Apport de la géophysique multi-méthodes aux risques naturels

Sara Bazin

To cite this version:

Sara Bazin. Apport de la géophysique multi-méthodes aux risques naturels. Géophysique [physics.geo-ph]. Université de Bretagne Occidentale, 2021. ⟨tel-03109448⟩

HAL Id: tel-03109448

https://hal.science/tel-03109448v1

Submitted on 13 Jan 2021

HABILITATION A DIRIGER DES RECHERCHES

UNIVERSITE
DE BRETAGNE OCCIDENTALE
COMUE UNIVERSITE BRETAGNE LOIRE

ECOLE DOCTORALE N° 598
Sciences de la Mer et du littoral

Par **Sara Bazin**

Apport de la géophysique multi-méthodes aux risques naturels

Présentée à Brest le 11 janvier 2021
Unité de recherche : UMR 6538 CNRS UBO UBS Géosciences Océan

Rapporteurs avant soutenance :

Anne Briais, CR, HDR, UMR 6538 Géosciences Océan, IUEM, UBO.

Roger Guérin Pr, UMR 7619 METIS, Sorbonne Université.

Colette Siriex Pr, UMR 5295 I2M, Université de Bordeaux.

Composition du Jury :

Anne Briais, CR, HDR, UMR 6538 Géosciences Océan, IUEM, UBO.

Roger Guérin Pr, UMR 7619 METIS, Sorbonne Université.

Frauke Klingelhoefer, HDR, Géosciences Marines, Ifremer, Plouzané.

Colette Siriex Pr, UMR 5295 I2M, Université de Bordeaux.

Pascal Tarits Pr, UMR 6538 Géosciences Océan, IUEM, UBO.

Table des matières

Glossaire 3

Préambule 4

Remerciements 6

1. Curriculum vitae 7
1.1. Statut civil et position actuelle …… 7
1.2. Thématiques de recherche …… 7
1.3. Formation et diplômes …… 8
1.4. Expérience professionnelle …… 8
1.5. Campagnes océanographiques…… 9
1.6. Encadrements de recherche …… 10
1.7. Jurys …… 11
1.8. Enseignement …… 12
1.9. Responsabilités collectives…… 12
1.10. Animation scientifique et diffusion…… 12
1.11. Bibliométrie…… 14
1.12. Liste de mes publications…… 16
    1.12.1. Journaux de rang A…… 16
    1.12.2. Journaux de rang B, abstracts étendus avec comité de lecture, chapitres……18
    1.12.3. Communications dans des congrès …… 20

2. L'aléa sismique aux Petites Antilles 25
2.1. Une nouvelle loi d'atténuation aux Petites Antilles…… 25
2.2. Mise en commun des données sismologiques de l'arc Antillais…… 39
2.3. Campagnes d'intervention rapide après les séismes des Saintes…… 53

3. Le risque tsunami aux Antilles 67
3.1. Modélisation de la propagation de tsunami …… 67
3.2. Base de données des tsunamis dans les Caraïbes…… 85

4. **Développements méthodologiques en géophysique de proche surface, appliqués aux risques naturels** 109
4.1. Amélioration de la méthodologie pour inverser la résistivité électrique : l'inversion contrainte…… 110
4.2. Etude multi-disciplinaire pour améliorer l'interprétation géologique dans le contexte de l'argile sensible…… 120
4.3. Développement d'un capteur géophysique pour caractériser les argiles sensibles en laboratoire …… 134
4.4. Inversion conjointe : application de l'ERT/PP aux schistes toxiques…… 145
4.5. La géophysique pour la surveillance des glissements de terrain…… 157

5. **L'hydroacoustique** 173
5.1. Mes travaux antérieurs sur la dorsale médio-Atlantique…… 173
5.2. Mes projets en hydroacoustique…… 190
5.2.1. Hydroacoustique pour étudier les dorsales indiennes…… 190
5.2.2. Hydroacoustique pour étudier la crise sismo-volcanique de Mayotte…… 192

6. **Perspectives et conclusions** 195

7. **Références** 199

Glossaire

AEM	Airborne Electro-Magnetic (levé électromagnétique aéroporté)
CDSA	Centre de Données Sismologiques des Antilles
ERT	Electrical Resistivity Tomography (tomographie de résistivité électrique)
GPR	Ground Penetrating Radar (géo-radar)
INSU	Institut National des Sciences de l'Univers
IP	Induced Polarisation (Polarisation Provoquée ou PP)
IPGP	Institut de Physique du Globe de Paris
IUEM	Institut Universitaire Européen de la Mer
LET	Local Earthquake Tomography
MARMOR	Marine Advanced geophysical Research equipment and Mayotte multidisciplinary Observatory for Research and response
NGI	Norges Geoteknisk Institutt (Institut Géotechnique de Norvège)
OBS	Ocean Bottom Seismometer (sismomètre de fond de mer)
OHASISBIO	Observatoire HydroAcoustique de la SISmicité et de la BIOdiversité
OSU	Observatoire des Sciences de l'Univers
OVSG	Observatoire Volcanologique et Sismologique de Guadeloupe
OVSM	Observatoire Volcanologique et Sismologique de Martinique
RAP	Réseau d'Accéléromètre Permanent
REVOSIMA	RÉseau de surveillance VOlcanologique et SIsmologique de Mayotte
SIG	Sytème d'Information Géographique
SIO	Scripps Institution of Oceanography (Institut d'Océanographie Scripps)
SNO	Services Nationaux d'Observation
SOFAR	SOund Fixing and Ranging
UBO	Université de Bretagne Occidentale
UCSD	University of California San Diego
UiO	Universitet i Olso (Université d'Oslo)
WOS	Web Of Science

Préambule

Le statut d'enseignant-chercheur-observateur implique un équilibre parfois difficile à trouver. J'ai, pendant les 20 dernières années, vécu des périodes où les observations occupaient la plus grande partie de mon temps (comme dans les observatoires) et des périodes où je me consacrais surtout à la recherche. Ce n'est que depuis mon arrivée à l'IUEM que je peux remplir ces trois fonctions de façon simultanée, et j'en suis finalement satisfaite !

A ce point de ma carrière, j'ai souhaité faire un bilan. La démarche pour obtenir l'habilitation à Diriger des Recherches m'a semblé être une bonne occasion. C'est dans cette optique qu'a été rédigé ce document. Les qualités humaines essentielles pour encadrer des étudiants sont difficiles à mettre en évidence dans un document écrit. Une position que j'essaie en général d'enseigner aux jeunes chercheurs est le recul "scientifique". Le recul est essentiel en géophysique pour éviter toutes sortes de surinterprétation. La qualité de l'interprétation de tout modèle géophysique dépend souvent de l'expérience du scientifique. En effet, il est important de bien comprendre derrière tout modèle, les enjeux et les difficultés (résolues ou non) et d'avoir une vue d'ensemble. Une culture générale des méthodes existantes est ainsi souvent un atout. Ma carrière est diverse et donc difficile à résumer dans un manuscrit mais la variété de mes expériences m'a apporté le recul et cette "culture pluridisciplinaire". C'est ce que je me suis efforcée de montrer dans ce recueil de travaux variés. Il a fallu faire un choix, je n'ai pas choisi d'y présenter les articles les plus récents, ni les plus prestigieux, mais ceux qui pouvaient illustrer au mieux ma démarche scientifique.

Ce manuscrit présente donc essentiellement mes travaux de recherche, et quelques-uns des étudiants que j'ai encadrés. J'ai essayé autant que possible de faire ressortir le fil conducteur de mes travaux. Le point commun que l'on retrouve dans mes recherches consiste à combiner différentes techniques en géophysique pour aller au-delà des résultats habituels. Ces travaux ont été réalisés à l'IPGP avec mon recrutement en tant que Physicienne Adjointe (2001) puis mon affectation dans les observatoires volcanologiques et sismologiques des Antilles (2003-2009), ma mise en disponibilité à Oslo, puis enfin à l'IUEM depuis 2019.

Le mémoire comprend trois parties présentant successivement un curriculum détaillé (**chapitre 1**), un mémoire des travaux de recherches et enfin mes projets de recherche. Les activités relatives à l'accompagnement de la recherche (responsabilités, encadrement d'étudiants, enseignement) sont présentées dans le chapitre 1. Mes différents chantiers et thèmes de recherche sont ainsi développés dans les **chapitres 2, 3, 4 et 5**, en présentant les éléments de réponses spécifiques aux différents contextes abordés.

Lors de mon doctorat à l'Institut Océanographique Scripps (SIO), je me suis intéressée à la structure fine de la croûte océanique et à sa genèse en utilisant la sismique grand-angle. Contrairement aux habitudes françaises, le projet de thèse aux Etats-Unis n'est pas défini à l'avance par l'encadrant, mais au cours de ses recherches par le doctorant. Ceci explique en partie pourquoi une thèse y dure en moyenne 6 ans. Après ma thèse, j'ai continué à approfondir cette analyse des processus d'accrétion océanique par la sismique réflexion, dans le cadre de mon post-doctorat à l'Université de Cambridge en 2000. Mes travaux sur les dorsales ne sont pas exposés dans ce mémoire car j'ai choisi de ne présenter que les recherches que j'ai pu mener de façon plus autonome. Mes thèmes de recherche ont ensuite évolué vers le risque sismique lors de mon affectation dans les observatoires volcanologiques et sismologiques des Antilles de 2003 à 2009 (**chapitre 2**). Puis je me suis intéressée à plusieurs petits tsunamis que j'ai pu observer aux Antilles et j'ai développé cette thématique grâce une année sabbatique à Oslo auprès de spécialistes (**chapitre 3**). J'ai choisi de prolonger mon séjour norvégien et mes recherches ont évolué vers la géophysique de proche surface appliquée aux risques naturels (**chapitres 4**). J'ai bénéficié d'un environnement innovant pour développer de nouvelles façons de réaliser des campagnes géophysiques en relation avec la géotechnique. Je montrerai par exemple l'intérêt de contraindre une inversion ou de développer des inversions conjointes.

La dernière partie du document porte sur les projets que je propose de développer à l'IUEM (**chapitre 5**). Le premier consiste à utiliser les réseaux d'hydrophones mouillés dans le canal SOFAR pour mieux comprendre les processus d'accrétion océanique et ces cycles magmato-tectoniques au niveau des dorsales ou sur les volcans sous-marins: je retourne ainsi à mes thèmes de recherche doctorale. Le second projet consiste à utiliser les OBS pour compléter les réseaux sismologiques terrestres. Un outil magique qui ne m'a jamais vraiment quitté pendant ma carrière.

Pour finir, mes conclusions sont présentes dans le **chapitre 6** et les références sont citées dans le **chapitre 7**.

Remerciements

Tout d’abord, je tiens à remercier vivement les membres du jury qui ont accepté de rapporter et d’examiner ce mémoire malgré leur emploi du temps chargé et le contexte difficile de la crise sanitaire.

Mes projets de recherche ont permis de nombreuses rencontres et de collaborations fructueuses. En commençant par mes encadrants et collègues de Scripps : John Orcutt, Alistair Harding, Harm Van Avendonk et Graham Kent, et des collaborations amicales qui se révèleront durer dans le temps avec Valérie Ballu et Wayne Crawford. A Paris, je remercie Satish Singh, Javier Escartin, Christine Deplus, Laurent Béguery, Catherine Mével, Mathilde Cannat. Dans les observatoires des Antilles, j'ai eu la chance de travailler avec François Beauducel, Alberto Tarchini (†), Nathalie Feuillet, Alex Nercessian, Patrick Tuchais, Jean-Marie Saurel, Arnaud Leridant, Mendy Bengoubou-Valérius, Georges Boudon, Jean-Claude Delmond (†), Anne Le Friant, Didier Bertil, Christian Anténor-Habazac et avec bien d'autres, en particulier mes collègues de la diffusion scientifique et de la prévention sismique. Au NGI à Oslo, j'ai appris une nouvelle façon de travailler avec une équipe de choc : Carl Harbitz, Finn Løvholt, Farrokh Nadim, Guillaume Sauvin, Andi Pfaffhuber, Helgard Anschütz, Maarten Vanneste, Asgeir Lysdahl, Regula Frauenfelder, Craig Christiansen, Guro Skurdal, Anders Solheim, Dominik Lang, et Heidi Hefre. A l'UiO, c'est avec Isabelle Lecomte, Bernd Etzelmüller, Valérie Maupin, Andreas Köhler, et Karianne Lillehøren, que j'ai appris de nouvelles compétences.

Depuis l'automne 2019, je me suis lancée dans une nouvelle aventure. Je remercie ma nouvelle équipe bretonne pour son accueil : Jean-Yves Royer, Julie Perrot, Marc-André Gutscher, Fred Jean, Mickaël Beauverger, Pascal Gente, Pascal Tarits, Jacques Deverchère, et enfin Claude Guénou (que je retrouve après 25 ans). Je remercie Margot Sauvadet et Charlotte Quiniou pour l’efficacité de leur travail administratif et Christophe Martin pour son assistance informatique. Chez nos voisins, à IFREMER, je remercie Louis Géli et Bruno Marsset (que je retrouve aussi après 25 ans) ainsi que Frauke Klingelhoefer, Chastity Aiken, Emmanuel Rinnert et Livio Raffine avec qui j'espère poursuivre une collaboration naissante.

Parmi ces vingt dernières années, j'ai particulièrement apprécié les missions de terrain (à terre et en mer), riches en moments intenses et souvenirs. Merci mille fois à toutes celles et tous ceux qui m’ont fait confiance, m’ont soutenue, et qui m’ont proposé de me lancer ou accepté de me suivre dans de nouveaux projets.

Enfin, toutes ces aventures lointaines ont été possibles grâce au soutien de ma famille. Je remercie mon mari Marc-Elie Pau pour ses encouragements indéfectibles et nos deux filles Anna et Agata pour supporter mes horaires et mes absences.

Et pour finir, je remercie Yane Bizouarn qui nous a laissé la jolie maison dans laquelle j’ai pu écrire ces lignes.

1. Curriculum vitae

1.1 Statut civil et position actuelle

Sara Bazin - Physicienne Adjointe

Institut Universitaire Européen de la Mer
Université de Bretagne Occidentale
UMR 6538 – Laboratoire Géosciences Océan
Place Nicolas Copernic, 29280 Plouzané
Tél. +33 2 98 49 87 18, sbazin@univ-brest.fr

Née le 21.12.1971
Nationalité française. Mariée, deux enfants

1.2 Thématiques de recherche

Mes thématiques de recherche sont très variées (Figure 1). Mes premiers sujets d'étude sont la géophysique marine et l'étude des dorsales océaniques. Mes travaux les plus récents abordent le développement des méthodes géophysiques pour résoudre des problèmes de société, tels que les risques de glissement de terrain, la dégradation du pergélisol et les schistes toxiques. Cette transition s'est faite après avoir dirigé l'observatoire de Martinique qui m'avait donné l'envie de travailler sur des thématiques plus proches de la société. J'ai, depuis ma mutation à l'IUEM, effectué un retour vers la sismologie marine tout en restant attachée aux risques naturels.

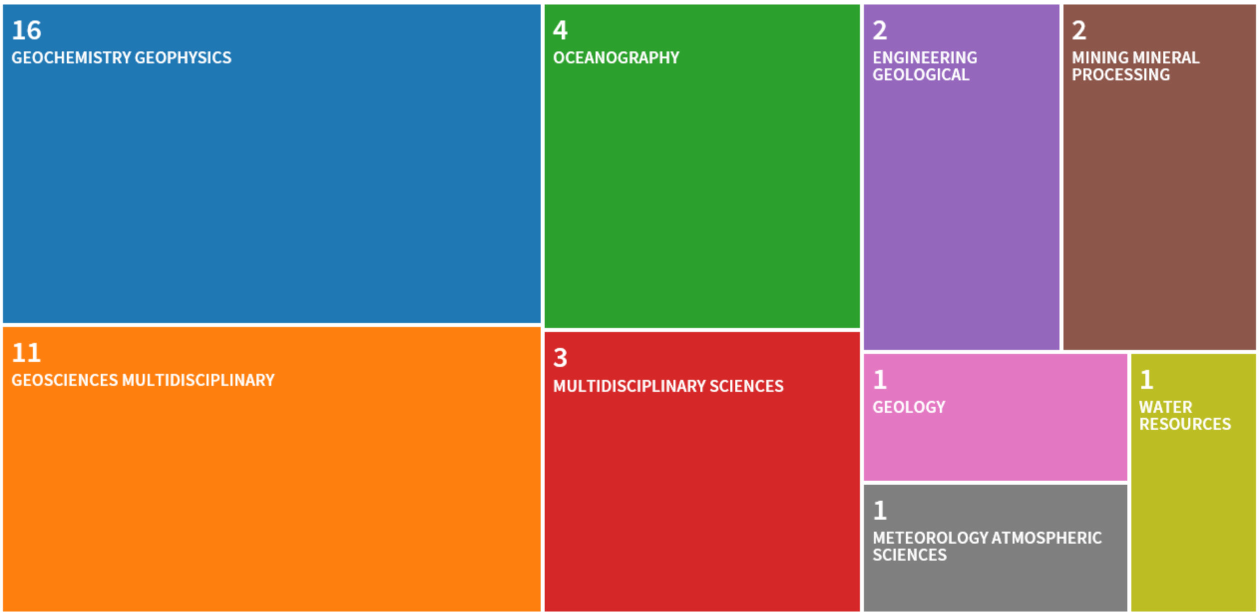

Figure 1: Thématiques de recherches illustrées par les publications dans Web Of Sciences.

1.3 Formation et diplômes

1994 - 2000 **Scripps Institution of Oceanography San Diego, USA**

Ph.D. en Géophysique Marine sous la direction de Prof. J. Orcutt et Dr. A. Harding.
Three-dimensional crustal structure of East Pacific Rise discontinuities from tomographic inversions.

1989 - 1994 **Institut des Sciences et Technologies, Paris**

Diplôme d'Ingénieur en Géophysique et Géotechnique (mention Bien).

1.4 Expérience professionnelle

Depuis septembre 2019 **Université de Bretagne Occidentale, Brest**

Physicienne Adjointe dans le Laboratoire de Géosciences Océan et ses observatoires hydroacoustiques (OSU de l'Institut Universitaire Européen de la Mer).

2016 - 2019 **Université d'Oslo, Norvège**

Professeure associée dans le département de Géosciences depuis 2018. Enseignante extérieure depuis 2016. Recherche en méthodes électriques et interférométrie sismique. Enseignement en géophysique de subsurface et risques naturels, et encadrement d'étudiants en Master.

2010 - 2019 **Norwegian Geotechnical Institute, Oslo, Norvège**

Chercheure dans un institut de recherche privé. Responsable scientifique de l'équipe de géophysique (ERT/IP, GPR, AEM, en forages, sismique terrestre et OBS). Montage de projets scientifiques avec collaborations internationales et partenariat avec l'industrie. Développements instrumentaux.

2009 - 2010 **International Center for Geohazards, Oslo, Norvège**

Chercheure invitée en année sabbatique. Modélisation de tsunamis, création d'une base de données tsunamis dans les Caraïbes et évaluation des risques associés dans l'arc Antillais.

2005 - 2009 **Observatoire Volcanologique et Sismologique de Martinique**

Physicienne Adjointe – directrice et responsable scientifique de l'observatoire. Coordonne les missions de surveillance, de recherche scientifique, d'information auprès des autorités et du public. Élabore les bulletins de sismicité des Antilles Françaises. Porteur du projet INTERREG Tsuareg (TSUnami Alerte RÉGionale). Coordonne le déploiement rapide d'OBS après un séisme fort (campagnes MARTOBS).

2003 - 2005 **Observatoire Volcanologique et Sismologique de Guadeloupe**

Physicienne Adjointe – sismologue. Installation de nouveaux réseaux sismologiques (large-bande sur le volcan et réseau RAP) et création du consortium CDSA (Centre de Données Sismologique des Antilles). Coordonne le déploiement rapide d'OBS après un séisme fort (campagnes GUADOBS).

2001 - 2003 **Institut de Physique du Globe de Paris**

Physicienne Adjointe au Laboratoire de Géosciences Marines. Étude de la structure des dorsales océaniques. Participation à la création du parc OBS de l'INSU. Développement d'un hydrophone SOFAR (financement BQR et Ministère de l'Outre Mer d'un projet d'instrumentation du canal SOFAR pour améliorer la surveillance sismologique aux Antilles).

2000 - 2001 **University of Cambridge, UK**

Recherche post-doctorale «Marie Curie Fellow». Imagerie sismique réflexion 3D. Application aux hydrates de gaz et au réflecteur de la chambre magmatique sous la dorsale Est Pacifique.

Un chronogramme simplifié de ma carrière depuis mon Doctorat à l'Institut Océanographique Scripps en 2000 est présenté sur la Figure 2.

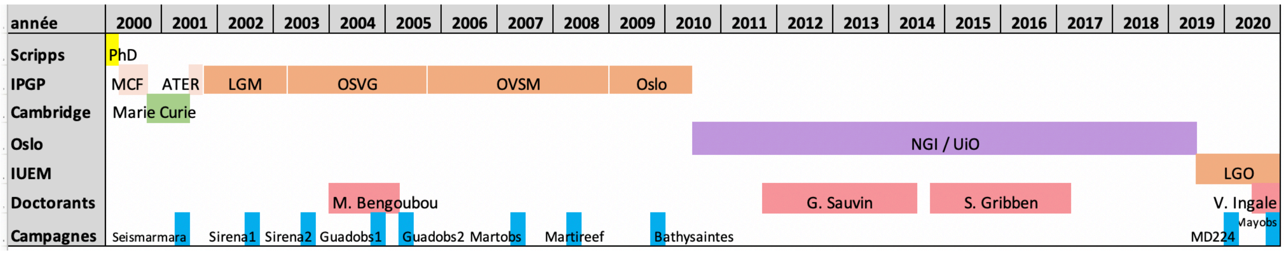

Figure 2: Chronogramme simplifié de ma carrière depuis la fin de mon PhD (bloc jaune). Les blocs colorés en orange représentent les périodes d'activité en tant que Physicienne Adjointe depuis 2001. Le bloc mauve représente une disponibilité pour raison familiale pendant laquelle j'ai travaillé en tant que chercheure dans une fondation de droit privé, le NGI, et à l'université d'Oslo. Les blocs roses représentent les doctorants que j'ai co-encadrés. Les blocs bleus représentent les campagnes en mer, les durées des missions ne sont pas respectées à cette échelle.

1.5 Campagnes océanographiques

- Campagne **MAYOBS15** à bord du N/O Marion Dufresnes, sous la direction d'I. Thinon et E. Rinnert (25 j) en 2020
- Campagne **OHASISBIO** à bord du N/O Marion Dufresnes, sous la direction de J.Y. Royer (9 j) en 2020.
- Campagne **BATHYSAINTES** à bord du N/O Pourquoi Pas, sous la direction de C. Deplus (11 j) en 2010.
- Campagne **MARTIREEF** à bord du N/O Antéa, sous la direction de N. Feuillet (4 jours de mer) en 2008.
- Campagne **MARTOBS** à bord du Maïto, chef de mission (2 jours de mer) en 2007.
- Campagnes **GUADOBS 1-2** à bord du Kahouanne, chef de mission (deux fois 2 jours de mer) en 2004-05.
- Campagne **SIRENA 2** à bord du RRV Discovery sous la direction de J. Goslin (19 jours de mer) en 2003.
- Campagne **SIRENA 1** à bord du N/O Suroît sous la direction de J. Goslin (17 j) en 2002.
- Campagne sismique pour étudiants à bord du N/O Thétys II sous la direction de J. Ségoufin (2 j) en 2002.
- Campagne **SEISMARMARA** à bord du N/O Nadir sous la direction de A. Hirn et S. Singh (32 j) en 2001.
- Campagne américaine **MOHOLE** à bord du N/O Maurice Ewing sous la direction de D. Wilson (35 j) en 1999.
- Campagne américaine **SWELL** à bord du N/O Monoa Wave sous la direction de J. Phipps-Morgan (7 j) en 1997.
- Campagne américaine **EW9602** à bord du N/O Maurice Ewing sous la direction de M. McNutt (53 j) en 1996.
- Campagne franco-américaine **MELT** à bord du N/O Melville sous la direction de J. Orcutt (40 j) en 1995.

- Campagne américaine d'essais à bord du N/O Robert Gordon Sproul sous la direction de S. Constable (1 j) en 1995.
- Transit bathymétrique à bord du N/O Melville sous la direction de P. Lonsdale (14 j) en 1995.

1.6 Encadrements de recherche

Avec J.-Y. Royer nous co-dirigeons Vaibhav Ingale pour une thèse intitulée «Dynamique de l'accrétion océanique vue par l'analyse d'essaims de séismes détectés depuis 10 ans sur trois dorsales à taux d'ouverture contrastés» depuis septembre 2020.

Les noms des étudiants avec qui j'ai publié des articles scientifiques sont soulignés (aussi dans l'annexe "publications scientifiques").

J'ai déjà co-encadré 3 thèses de Doctorat :

- 2014-17 - Co-encadrement du Doctorat de Shane Gribben «Developing an understanding of the factors that influence the geophysical properties of quick clays» à Queen's Univ. de Belfast. Nous avons avec Shane développé un capteur de résistivité et de célérité pour échantillons d'argile dans une presse triaxiale du laboratoire de mécanique des sols du NGI. Cet outil nous a permis de concilier les mesures en laboratoire, la mécanique de sols avec la géophysique de subsurface (sismique et ERT). S.G. a interrompu sa thèse à Belfast après un long arrêt-maladie et travaille actuellement dans une petite entreprise de géophysique en Irlande. Il reprendra son Doctorat quand sa santé le permettra. Depuis, le NGI utilise pour des projets industriels ce nouveau capteur que nous avons développé ensemble.
- 2011-14 - Co-encadrement du Doctorat de Guillaume Sauvin «Integrated geophysics for mapping and monitoring of landslide-prone valley and coastal grounds in Norway» à l'Univ. d'Oslo. J'ai encadré G.S. sur les méthodes électriques alors qu'Isabelle Lecomte l'encadrait sur les méthodes sismiques. Ce dernier a brillamment soutenu sa thèse et rapidement obtenu un poste de chercheur au NGI. Nous continuons nos collaborations en géophysiques de subsurface.
- 2004-2005 - Co-encadrement du Doctorat de Mendy Bengoubou-Valérius «Apport des données accélérométriques à l'étude de l'aléa sismique aux Antilles Françaises». Je n'ai co-encadré M.B.-V. que pendant la première moitié de sa thèse à l'OVSG, essentiellement pour définir les contours de ses recherches et mettre en place les données nécessaires. Elle a suspendu ses recherches pendant un congé maternité, puis je suis partie en poste à l'OVSM pendant la seconde moitié de sa thèse. M.B.-V. a obtenu un poste de sismologue au BRGM de Guadeloupe et elle est actuellement chargée de mission Risques sismique et volcanique au Ministère de la Transition Écologique et Solidaire.

J'ai encadré ou co-encadré 9 thèses de Master :

- 2020 Co-encadrement M2 en sismologie de Maël Thomas à l'IUEM-UBO. M.T. poursuit ses études.
- 2019-2020 Encadrement M2 en géophysique et glaciologie de Shakir Syed Gilani à l'Univ. d'Oslo, Norvège. S.S.G. soutiendra son Master en décembre 2020 en raison de la crise sanitaire.
- 2018 Encadrement M2 en géophysique de Guro Skurdal à l'Univ. d'Oslo, Norvège. G. S. travaille maintenant pour Emerald Geomodeling, une start-up du NGI.
- 2018 Co-encadrement M2 en géophysique d'Isiris Haugen à l'Univ. d'Oslo, Norvège. I. H. travaille dans une entreprise de géophysique de proche surface près d'Oslo.
- 2017 Co-encadrement de M2 en géophysique de Vilde Jørdre Øybekk à l'Univ. d'Ås, Norvège. V. J. Ø. est responsable des risques naturels dans une mairie de Norvège.
- 2015 Encadrement M2 en géophysique et géotechnique de Birara Ashagrie Yilma à l'Univ. d'Oslo. B. A. Y. travaille dans un bureau d'étude en Norvège.

- 2009 Co-encadrement M2 en modélisation de runup de tsunami de Rolf Bredesen à l'Univ. d'Oslo.
- 2006 Encadrement M2 de Célia Duclos à l'IPGP.
- 2001 Co-encadrement du stage de DEA de Angèle Ricolleau à l'IPGP.

J'ai encadré de nombreux stages :

- 2016 Encadrement du stage M1 de Craig Christensen en géophysique de subsurface au NGI.
- 2012 Encadrement du stage d'ingénieur de Patrice Aoun en géophysique de subsurface au NGI.
- 2011 Encadrement du stage d'ingénieur de Sylvain Tissot en géophysique de subsurface au NGI.
- 2010 Encadrement du stage M1 de Marianne Lanzky Kolstrup en géophysique de subsurface au NGI.
- 2006 Co-encadrement du stage ST2 de Matthieu Broncel, campagnes de nivellement et de GPS en Martinique et en Guadeloupe.
- 2006 Encadrement du stage M1 de Jean-Elie Athanase, mesures géophysiques sur le terrain à l'OVSM.
- 2006 Encadrement du stage L2 de Morgane Houssais, mesures géophysiques sur le terrain à l'OVSM.
- 2005 Encadrement du stage M1 de Romain Poujardieu sur la relocalisation des OBS de la campagne GUADOBS, à l'OVSG.
- 2004 Encadrement du stage d'ingénieur de Antoine Saglio sur les signaux sismologiques de la Soufrière de Guadeloupe, à l'OVSG.
- 2004 Encadrement de 2ème année STU, de Fabienne Zami sur une Synthèse des documents Soufrière 1976, à l'OVSG.

1.7 Jurys

Jury de soutenance de 3 thèses de Doctorat :

- 2009, Cécile Finco, «*Étude de l'impact simultané des propriétés électriques, diélectriques et magnétiques du sous-sol sur la mesure géophysique par méthode électromagnétique inductive dans le domaine temporel (TDEM)*». Sorbonne Université
- 2009, Silvia Salas Romero, «*Multidisciplinary near-surface investigation of a quick-clay landslide prone area in southwest Sweden*». Uppsala Universitet, Suède
- 2006, Joseph Mavoungo, «*La vulnérabilité des populations de Petites Antilles face au risque sismique, l'exemple de la Martinique*». Université des Antilles-Guyane.

Jury de soutenance de 2 thèses de Masters M2:

- 2009, Simon Olsen. Norwegian University of Science and Technology, Trondheim, Norvège
- 2008, Ragnhild Anderssen Myhre. Université d'Oslo, Norvège.

Jury de soutenance de Masters M1:

- 2020, la promotion Géosciences Océans, IUEM.

1.8 Enseignement

En raison de la charge exceptionnelle liée aux missions dans les observatoires, la direction de l'IPGP m'a déchargée d'enseignement formel entre 2003 et 2009 (statut du corps des astronomes et physiciens du décret n°86-434 du 12 mars 1986). Lors de mon séjour en Norvège, j'ai enseigné à temps partiel à l'Université d'Oslo au niveau Master.

En plus des enseignements généraux au niveau Licence de l'UBO, les Masters «Sciences de la Terre et des Planètes, Environnement, parcours Géosciences Océan» et «Sciences de la Mer et du Littoral» proposés à l'IUEM dispensent plusieurs enseignements sur lesquels je peux intervenir. Par ailleurs, je souhaite participer à l'élaboration d'une nouvelle maquette pour un Cursus de Master en Ingénierie (CMI) en «géosciences marines appliquées» en partenariat avec l'IFREMER. Mes contacts avec les entreprises seront alors utiles. Par ailleurs, je propose d'encadrer les étudiants en Master participant aux Universités Flottantes. La dernière devait avoir lieu à bord du Marion Dufresne lors de la mission GHASS2 en juillet 2020, mais a été annulée à cause de la crise sanitaire. Les campagnes GHASS étudient les hydrates de méthane présents en mer Noire, qui sont en train de fondre à cause de la diffusion du sel dans les sédiments.

Les enseignements que j'ai déjà dispensés sont :

- 2020 Enseignement Atelier Partagé en Master «Sciences de la Mer et du Littoral» , UBO
- 2020 Enseignement en Géolocalisation en L1, UBO
- 2019 Enseignement en Géophysique de terrain en L2, UBO
- 2019 Enseignement Atelier Partagé en Master «Sciences de la Mer et du Littoral» , UBO
- 2018 Master GEO4120 Near-Surface Geophysics, Université d'Oslo
- 2018 Master GEO4181 Natural Hazards, Université d'Oslo
- 2017 Master GEO4120 Near-Surface Geophysics, Université d'Oslo
- 2016 Master GEO4120 Environmental Geophysics, Université d'Oslo
- 2001 Acquisition sismique en DESS, campagne en mer, Villefranche sur Mer
- 2001 Traitement sismique en DESS, Institut de Physique du Globe de Paris
- 2001 Géophysique de Surface et de Subsurface niveau DESS, stage de terrain, Garchy.

1.9 Responsabilités collectives

Mes responsabilités collectives lors de mon affectation dans les observatoires comprenaient l'installation et la maintenance des réseaux de mesure, les astreintes, le pointé et la rédaction des bulletins sismologiques des Antilles Françaises (2003-2008), ainsi que la mise de place du CDSA. J'ai par ailleurs assuré pendant plus de 3 années la direction de l'observatoire de Martinique et de son équipe avec au total : 2 chercheurs PHAD (sismologie et tectonique), 1 doctorant, 2 IE/IR CNRS (informatique, électronique), 2 techniciens (électrotechnique), 2 adjoints administratifs et 2 techniciens d'entretien.

J'ai été honorée de plusieurs responsabilités dans le fonctionnement de la recherche :

- Relecteur pour Geophysical Research Letters, Journal of Applied Geophysics, Journal of Geophysical Research, Tectonophysics, Near Surface Geophysics, Sensor.
- Évaluatrice pour l'European Council (programme FET), le Research Council of Norway, l'ANR, la Commission flotte et engins nationaux, la National Science Fundation (USA), l'Académie Allemande (DAAD).
- Co-organisateur et chairman dans plusieurs congrès internationaux.
- Tsunami National Contact de la France pour le Caribbean Tsunami Warning System organisé par l'UNESCO (2004-2008).
- Représentatrice de la Norvège au Global Volcano Model (2013-2019).
- Board of OSEG, Oslo Society of Exploration Geophysicists, Norvège.

1.10 Animation scientifique et diffusion

Depuis mon installation à l'UEM, j'ai participé au rayonnement de la science en tenant un stand à la *Fête de la Science* au Quartz à Brest et en répondant aux interviews des journalistes (radio, TV et journaux) après des séismes ressentis dans la région.

Pendant la période 2002-2009 à l'OVSG puis à l'OVSM, je me suis investie dans de nombreux événements grand public dont les *Fêtes de la Science*, les *Journées du Patrimoine*, les *Journées Replik* (Figure 3 et Figure 4), les *Caravanes des Sciences*, etc. J'ai coordonné les missions d'information auprès des autorités de Martinique en tant que directrice de l'OVSM. J'ai organisé des visites grand public dans les deux observatoires et ai régulièrement participé au *Carbet des Sciences*. J'ai aussi formé les enseignants du rectorat de Martinique et du personnel de la Préfecture de Martinique au risque sismique et volcanique. J'ai par exemple participé à l'élaboration d'un fascicule sur le risque tsunami (Figure 4 centre). J'ai aussi participé à de nombreux évènements médiatiques (émissions radio RFO, deux émissions *C'est Pas Sorcier* sur les volcans et les séismes, émission *Le Club* sur ATV, journaux télévisés RFO, etc).

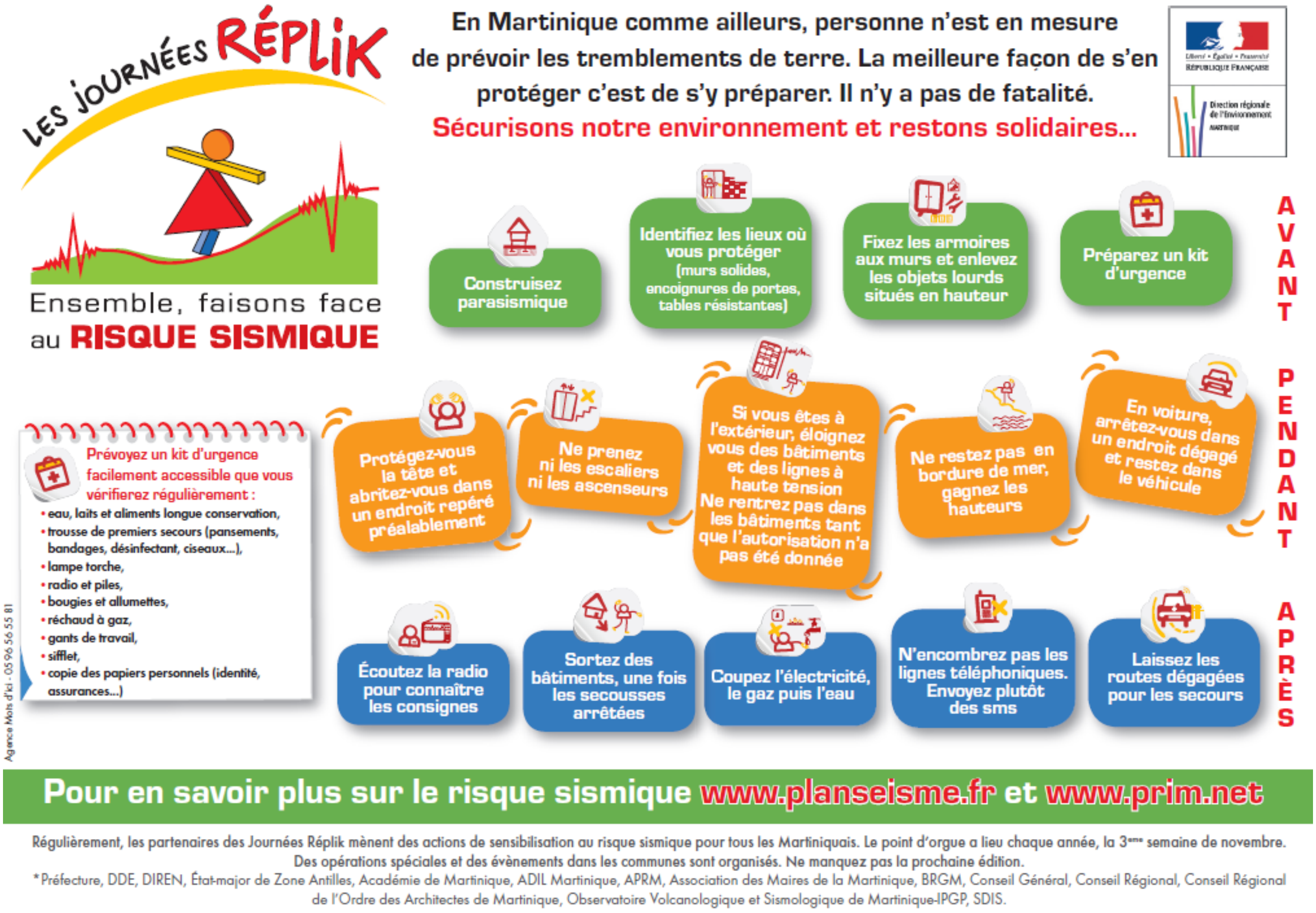

LES JOURNÉES RÉPLIK

Ensemble, faisons face au **RISQUE SISMIQUE**

En Martinique comme ailleurs, personne n'est en mesure de prévoir les tremblements de terre. La meilleure façon de s'en protéger c'est de s'y préparer. Il n'y a pas de fatalité.

Sécurisons notre environnement et restons solidaires...

Liberté • Égalité • Fraternité
RÉPUBLIQUE FRANÇAISE
Direction régionale de l'Environnement
MARTINIQUE

AVANT

- Construisez parasismique
- Identifiez les lieux où vous protéger (murs solides, encoignures de portes, tables résistantes)
- Fixez les armoires aux murs et enlevez les objets lourds situés en hauteur
- Préparez un kit d'urgence

PENDANT

- Protégez-vous la tête et abritez-vous dans un endroit repéré préalablement
- Ne prenez ni les escaliers ni les ascenseurs
- Si vous êtes à l'extérieur, éloignez vous des bâtiments et des lignes à haute tension
Ne rentrez pas dans les bâtiments tant que l'autorisation n'a pas été donnée
- Ne restez pas en bordure de mer, gagnez les hauteurs
- En voiture, arrêtez-vous dans un endroit dégagé et restez dans le véhicule

APRÈS

- Écoutez la radio pour connaître les consignes
- Sortez des bâtiments, une fois les secousses arrêtées
- Coupez l'électricité, le gaz puis l'eau
- N'encombrez pas les lignes téléphoniques. Envoyez plutôt des sms
- Laissez les routes dégagées pour les secours

Prévoyez un kit d'urgence facilement accessible que vous vérifierez régulièrement :
- eau, laits et aliments longue conservation,
- trousse de premiers secours (pansements, bandages, désinfectant, ciseaux...),
- lampe torche,
- radio et piles,
- bougies et allumettes,
- réchaud à gaz,
- gants de travail,
- sifflet,
- copie des papiers personnels (identité, assurances...)

Agence Mots d'ici - 0596 56 55 81

Pour en savoir plus sur le risque sismique www.planseisme.fr et www.prim.net

Régulièrement, les partenaires des Journées Réplik mènent des actions de sensibilisation au risque sismique pour tous les Martiniquais. Le point d'orgue a lieu chaque année, la 3ème semaine de novembre. Des opérations spéciales et des évènements dans les communes sont organisés. Ne manquez pas la prochaine édition.

*Préfecture, DDE, DIREN, État-major de Zone Antilles, Académie de Martinique, ADIL Martinique, APRM, Association des Maires de la Martinique, BRGM, Conseil Général, Conseil Régional, Conseil Régional de l'Ordre des Architectes de Martinique, Observatoire Volcanologique et Sismologique de Martinique-IPGP, SDIS.

Figure 3: Exemples de diffusion scientifique sur le risque sismique. En 2006, nous avons mise en place en Martinique le Réseau Actions RÉPLIK qui existe encore. Les partenaires RÉPLIK effectuent des actions de sensibilisation au risque sismique pour informer les martiniquais par des actions concrètes de sensibilisation.

Figure 4: À gauche: Exposition d'arts plastiques originale avec 14 artistes antillais qui avaient réalisé des œuvres sur le thème des séismes pendant que l'OVSM présentait une exposition sur les séismes historiques en Martinique. Au centre: Organisation du premier Exercice Richter avec l'État Majeur de Zone en 2008. À droite: simulateur de séismes financés par la Conseil Général de Martinique.

1.11 Bibliométrie

À ce jour en juillet 2020, 36 publications sont répertoriées dans le Web of Science (WOS ResearcherID: AAL-3694-2020) depuis 1998 (Figure 5). Ces publications ont donné lieu à 677 citations dans le WOS, soit en moyenne 29 citations par an et 19 citations par article. 15 de ces publications sont citées au moins 15 fois (Indice H -WOS = 15). L'indice H est de 19 dans Google Scholar (pour 1122 citations) et de 18 dans Research Gate (pour 1077 citations).

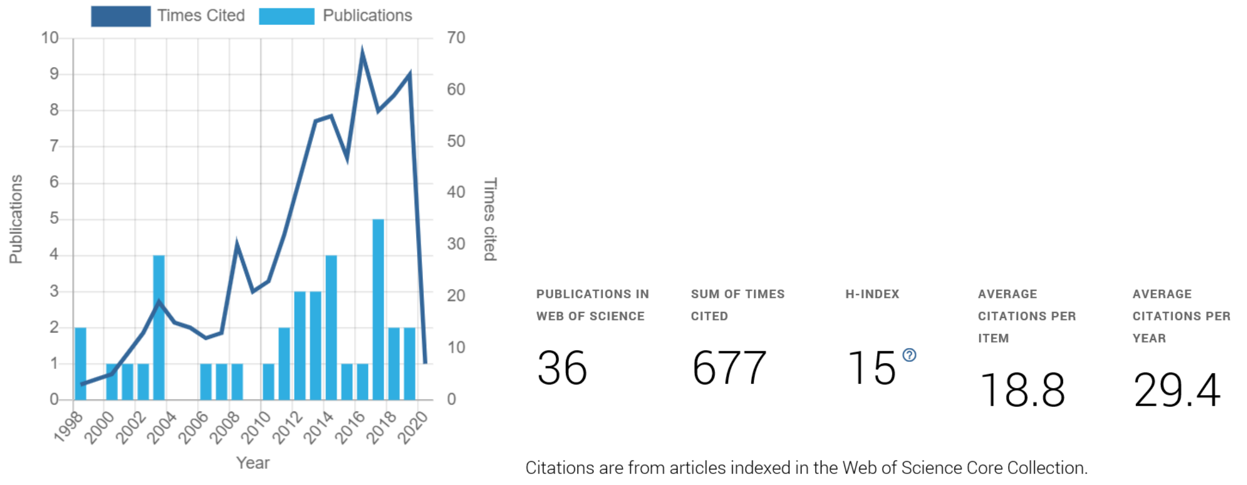

PUBLICATIONS IN WEB OF SCIENCE
36

SUM OF TIMES CITED
677

H-INDEX
15

AVERAGE CITATIONS PER ITEM
18.8

AVERAGE CITATIONS PER YEAR
29.4

Citations are from articles indexed in the Web of Science Core Collection.

RG Score
29.18

h-index
18

h-index
17
excluding self-citations

Top *h* cited research:

Evidence from three-dimensional seismic reflectivity images for enhanced melt supply beneath mid-ocean-ridge discontinuities

Article September 2000 · Nature

Sara Bazin
Institut Universitaire Européen de la Mer
Verified email at univ-brest.fr
geophysics seismology volcanology

	All	Since 2015
Citations	1122	514
h-index	19	13
i10-index	25	17

Figure 5: Bibliométrie avec the Web of Science (en haut), Research Gate (au centre) et Google Scholar (en bas).

La diversité des journaux scientifiques dans lesquels mes articles ont été publiés est illustrée dans la Figure 6. Les collaborations qui ont donné lieu à des publications communes sont illustrées dans la Figure 7.

Figure 6: Couvertures des journaux scientifiques dans lesquels mes articles ont été publiés.

Figure 7: Universités ou centres de recherche avec qui j'ai rédigé des publications scientifiques.

1.12 Liste de mes publications

1.12.1 Journaux de rang A (34 articles, impact >1)

El Houssein A., **Bazin,** S., Chazot, G., Youbi, N., Bensalah, M. K., Sabar, M. S., Boumehdi, M. A., Bertrand, H. The deep structure of the Richat magmatic intrusion (Northern Mauritania) from geophysical modeling. Insights about its kinematics of emplacement. Soumis à *Journal of African Earth Sciences*.

Skurdal, G., Pfaffhuber, A.A., Davis, A., **Bazin,** S. Improved near-surface resolution in geotechnical applications using very early AEM time gates. *Exploration Geophysics*. doi: 10.1080/08123985.2019.1691441, 2019.

Long, M., Pfaffhuber, A.A., **Bazin**, S., Kåsin, K., Gylland, A., Montafia, A. Glacio-marine clay resistivity as a proxy for remoulded shear strength - correlations and limitations. Quarterly Journal of Engineering Geology and Hydrogeology, https://doi.org/10.1144/qjegh2016-136, 2018.

Bazin, S., Lysdahl, A.K., Viezzoli, A., Günther, T. Anschütz, H., Scheibz, J., Pfaffhuber, A.A., Radic, T., Fjermestad, H. Resistivity and chargeability survey for tunnel investigation: a case study on toxic black shale in Norway. *Journal of Near Surface Geophysics*, doi:10.3997/1873-0604.2017036, 2017.

Anschütz, H., Vöge, M., Lysdahl, A., **Bazin**, S., Sauvin, G., Pfaffhuber, A.A. and Berggren, A.L. From manual to automatic AEM bedrock mapping. Special issue Airborne Geophysics of *J. of Environmental and Engineering Geophysics*, doi: 10.2113/JEEG22.1.35, 2017.

Anschütz, H., **Bazin**, S., Kåsin, K., Pfaffhuber, A.A, Smaavik, T.F. Airborne mapping of sensitive clay - stretching the limits of AEM resolution and accuracy. *Journal of Near Surface Geophysics*, 10.3997/1873-0604.2017018, 2017.

Lysdahl, A.K., Ahrens, S., **Bazin**, S., Christensen, C., Günther, T. 2D versus 3D ERT for site investigations– A case study from Oslo medieval Harbor. *Journal of Near Surface Geophysics*, doi: 10.3997/1873-0604.2016052, 2017.

Leclerc, F., Feuillet, N., Perret, M., Cabioch, G., **Bazin**, S., LeBrun, J.F., Saurel, J.M. The reef platform of Martinique: Interplay between eustasy, tectonic subsidence and volcanism since Late Pleistocene. *Marine Geology*, 10.1016/j.margeo.2015.08.001, 2015.

Leclerc, F., Feuillet, N., Cabioch, G., Deplus, C., LeBrun, J.F., **Bazin**, S., Beauducel, F., Boudon, G., Le Friant, A., De Min, L., Melezan, D. The Holocene drowned reef of Les Saintes plateau as a witness of a long-term tectonic subsidence along the Lesser Antilles volcanic arc in Guadeloupe. *Marine Geology*, 355, 115-135, 2014.

Sauvin G, Lecomte I, **Bazin** S, Hansen, L, and Vanneste M. On the integrated use of geophysics for quick-clay mapping: The Hvittingfoss case study, Norway. *Journal of Applied Geophysics*, doi: 10.1016/j.jappgeo.2014.04.001, 2014.

Bazin, S., Pfaffhuber, A.A. Mapping of quick clay by Electrical Resistivity Tomography under structural constraint. *Journal of Applied Geophysics*, doi: 10.1016/j.jappgeo.2013.09.002, 2013.

Michoud, C., **Bazin**, S., Blikra, L.H., Derron, M.-H., and Jaboyedoff, M.S. Experiences from Site-Specific Landslide Early Warning Systems. *Natural Hazards and Earth System Sciences*, doi: 10.5194/nhess-13-2659-2013, 2013.

Sauvin G, Lecomte I, **Bazin** S, L'Heureux JS, and Vanneste M. Towards geophysical and geotechnical integration for quick clay mapping in Norway. *Journal of Near Surface Geophysics*, doi: 10.3997/1873-0604.2012064, 2013.

Løvholt, F., G. Pedersen, S. **Bazin**, D. Kühn, R. Bredesen, C. Harbitz. Stochastic analysis of tsunami runup due to heterogeneous coseismic slip and dispersion. *J. Geophys. Res.*, doi:10.1029/2011JC007616, 2012.

Harbitz, C.B., S. Glimsdal , S. **Bazin,** N. Zamora, F. Løvholt, H. Bungum, H. Smebye, P. Gauer, O. Kjekstad. Tsunami hazard in the Caribbean: Regional exposure derived from credible worst case scenarios. *Continental Shelf Research*, doi: 10.1016/j.csr.2012.02.006, 2012.

Goslin, J., Perrot, J. Royer, J.-Y., Martin, C., Lourenço, N., Luis, J., Dziak, R.P., Matsumoto, H., Haxel, J., Fowler, M.J., Fox, C.G., Lau, A.T.-K., **Bazin**, S. Spatiotemporal distribution of the seismicity along the Mid-Atlantic Ridge north of the Azores from hydroacoustic data: Insights into seismogenic processes in a ridge–hot spot context. *Geochem. Geophys. Geosyst.,* doi: 10.1029/2011GC003828, 2012.

Feuillet, N., Beauducel, F., Jacques, E., Tapponnier, P. Delouis, B. **Bazin**, S. Vallée, M., King, G. C. P. The Mw = 6.3, November 21, 2004, Les Saintes earthquake (Guadeloupe): Tectonic setting, slip model and static stress changes. *J. Geophys. Res*, doi: 10.1029/2011JB008310, 2011

Beauducel, F., S. **Bazin**, M. Bengoubou-Valérius, M.-P. Bouin, A. Bosson, C. Anténor-Habazac, V. Clouard, J.-B.de Chabalier. Empirical model for rapid macroseismic intensities prediction in Guadeloupe and Martinique. *C. R. Geoscience*, doi: 10.1016/j.crte.2011.09.004, 2011.

Bazin, S., Feuillet, N., C. Duclos, W. Crawford, A. Nercessian, M. Bengoubou-Valerius, F. Beauducel, S. C. Singh. The 2004–2005 Les Saintes (French West Indies) seismic aftershock sequence observed with ocean bottom seismometers. *Tectonophysics,* doi: 10.1016/j.tecto.2010.04.005, 2010.

Bengoubou-Valerius, M. S **Bazin**, D Bertil, F Beauducel, A Bosson. CDSA: a new seismological data center for the French Lesser Antilles. *Seismological Research Letters*, doi: 10.1785/gssrl.79.1.90, 2008.

Carton, H., S.C. Singh, A. Hirn, S. **Bazin**, B. de Voogd, A. Vigner, A. Ricolleau, S. Certin, N. Oçakoglu, F. Karadoç, V. Sevilegen. Seismic imaging of the three-dimensional architecture of the Çınarcık Basin along the North Anatolian Fault. *J. Geophys. Res.*, doi: 10.1029/2006JB004548, 2007.

Singh, S.C., A.J. Harding, G.M. Kent, M.C. Sinha, V. Combier, S. **Bazin**, C.H Tong, J.W. Pye, P.J. Barton, R.W. Hobbs, R.S. White, J.A. Orcutt. Seismic reflection images of the Moho underlying melt sills at the East Pacific Rise. *Nature,* doi: 10.1038/nature04939, 2006.

Tong, C.H., C. Lana, R.S. White, M.R. Warner, P.J. Barton, S. **Bazin**, A.J. Harding, R.W. Hobbs, G.M. Kent, J.A. Orcutt, J.W. Pye, S.C. Singh, M.C. Sinha. Subsurface tectonic structure between overlapping mid-ocean ridge segments. *Geology*, doi: 10.1130/G21245.1, 2005.

Goslin, J., **Bazin**, S., Dziak, R., Fox, C., Fowler, M., Haxel, J., Lourenço, N., Luis, J., Martin, C., Matsumoto, H., Perrot, J. and Royer, J.-Y. Long-term seismicity of Northern (15°N-60°N) Mid-Atlantic Ridge recorded by two regional hydrophone arrays : widespread along-ridge influenced of the Azores and Iceland hotspots. *Geophysical Journal International,* doi: 10.1111/j.1365-246X.2005.02678.x, 2004.

Tong, C.H., R.S. White, M.R. Warner, P.J. Barton, S. **Bazin**, A.J. Harding, R.W. Hobbs, G.M. Kent, J.A. Orcutt, J.W. Pye, S.C. Singh, M.C. Sinha. The effects of tectonism and magmatism on cracks structure in oceanic crust : A seismic anisotropy study. *Geology,* doi: 10.1130/G19962.1, 2004.

Hulme, T., A. Ricolleau, S. **Bazin**, C. Crawford, S.C. Singh. Shear wave structure from joint analysis of seismic and seafloor compliance data. *Geophysical Journal International,* doi: 10.1046/j.1365-246X.2003.02061.x, 2003.

Tong, C.H., P.J. Barton, R.S. White, M.C. Sinha, S.C. Singh, J.W. Pye, R.W. Hobbs, S. **Bazin**, A.J. Harding, G.M. Kent, J.A. Orcutt. The influence of enhanced melt supply on upper crustal structure at a mid-ocean ridge discontinuity: A three-dimensional seismic tomographic study of 9°N East Pacific Rise *J. Geophys. Res.*, doi: 10.1029/2002JB002163, 2003.

Smith, D.K., J. Escartin, M. Cannat, M. Tolstoy, C.G. Fox, D.R. Bohnenstiehl, S. **Bazin**. Spatial and Temporal Distribution of Seismicity Along the Northern Mid-Atlantic Ridge (15-35°N). *J. Geophys. Res.*, doi: 10.1029/2002JB001964, 2003.

Bazin, S, A.J. Harding, G.M. Kent, J.A. Orcutt, S.C. Singh, C.H. Tong, J.W. Pye, P.J. Barton, M.C. Sinha, R.S. White, R.W. Hobbs, H.J.A. van Avendonk. A three-dimensional study of axial low velocity region beneath the 9°03'N overlapping spreading center. *Geophysical Research Letters*, doi:10.1029/2002GL015137, 2003.

Tong, C.H., J.W. Pye, P.J. Barton, R.S. White, M.C. Sinha, S.C. Singh, R.W. Hobbs, S. **Bazin**, A.J. Harding, G.M. Kent, J.A. Orcutt. Asymmetric melt sills and upper crustal construction beneath overlapping ridge segments. *Geology*, 30, 83-86, 2002.

Bazin, S., A. Harding, G. Kent, J. Orcutt, C.H. Tong, S. Singh, P. Barton, M. Sinha, R. White, H. Van Avendonk. 3-D crustal emplacement at the 9°03'N overlapping spreading center on the East Pacific Rise: correlations between magnetization and tomographic imaging. *J. Geophys. Res.,* doi: 10.1029/2001JB000371, 2001.

Kent, G.M., S.C. Singh, A.J. Harding, M.C. Sinha, J.A. Orcutt, P.J. Barton, R.S. White, S. **Bazin**, R.W. Hobbs, C.H. Tong, P.W. Pye. Evidence from three-dimensional seismic reflectivity images for enhanced melt supply beneath mid-ocean ridge discontinuities. *Nature*, 406, 614-619, 2000.

Bazin, S., H. Avendonk, A. Harding, J. Orcutt, J. P. Canales, R. Detrick. Crustal structure of the flanks of the East Pacific Rise: Implications for overlapping spreading centers. *Geophysical Research Letters*, 25, 2213-2217, 1998.

Canales, J. P., R. S. Detrick, S. **Bazin**, A. J. Harding, J. A. Orcutt,. Off-axis crustal thickness variations across and along the East Pacific Rise within the MELT area. *Science*, doi: 10.1126/science.280.5367.1218, 1998.

1.12.2 Journaux de rang B, abstracts étendus avec comité de lecture, chapitres (41 articles)

Helle, T. E., Aagaard, P., Nordal, S., Long, M., **Bazin, S**. A geochemical, mineralogical and geotechnical characterization of the low plastic, highly sensitive glaciomarine clay at Dragvoll, Norway. *AIMS Geosciences*, doi: 10.3934/geosci.2019.4.704, 2019.

Bazin, S., Lysdahl, A., Anschütz, H., Jørdre Øybekk, V., Frauenfelder, R., Glimsdal, S., Eidsvig, U. Waterborne Electrical Resistivity and Land-Based GPR Surveys for Characterization of Potential River Erosion in Larvik, Norway. *25th European Meeting of Environmental and Engineering Geophysics*, doi: 10.3997/2214-4609.201902485, 2019.

Bazin, S., Lysdahl, A., Olaus Harstad, A., Frauenfelder, R. Resistivity and Induced Polarization (ERT/IP) Survey for Bedrock Mapping in Permafrost, Svalbard. *25th European Meeting of Environmental and Engineering Geophysics*, doi: 10.3997/2214-4609.2019023622019, 2019.

Ólafsdóttir, E.Á., Bessason, B., Erlingsson S., L'Heureux, J.S., **Bazin, S.** Benchmarking of an open-source MASW software using data from three Norwegian GeoTest Sites. Proceedings of the XVII ECSMGE-2019, *Geotechnical Engineering foundation of the future*, doi: 10.32075/17ECSMGE-2019-0772, 2019.

Pfaffhuber, **Bazin, S.,** Frauenfelder, R. Near-surface methods in the geotechnical industry: Challenges, opportunities and limitations, *5th International Conference on Engineering Geophysics*, doi:10.3997/2214-4609.201901666, 2019.

Bazin, S., Köhler, A., Sauvin, G., Park, J., Johansson, J., Senna, S. Site characterization with ambient seismic noise at the Norwegian Geo Test Sites. *2nd Near Surface Geophysics in Asia*, 2019.

Bazin, S., Kvistedal, Y., Anschütz, H., Tunbridge, L., Jankowski, P., Fannian, K., Strømsvik, H., Grøv, E. Case study of crosshole GPR tomography for grouting distribution in rock fractures. *1st Near Surface Geophysics in Asia*, 10.3997/2214-4609.201800428, 2018.

Skurdal, G. H., Pfaffhuber, A. A., Davis, A., **Bazin, S.**, Anschütz, H., Nyboe, N. S. and Foged, N. Applying system response to improve the near-surface resolution of AEM models. *7th International Workshop on Airborne Electromagnetics*, Kolding, Denmark. Extended Abstracts, 2018.

Skurdal, G.H., Pfaffhuber, A.A., Davis, A., **Bazin**, S., Anschütz, H., Nyboe, N.S., Foged, N., Wiig T. Stretching AEM Near-surface Resolution Limits Related to Low- and Very High Resistivity Contrasts. S*econd European Airborne Electromagnetics Conference* DOI: 10.3997/2214-4609.201702158, 2017.

Skurdal, G. H., Pfaffhuber, A. A., Davis, A., **Bazin, S.**, Anschütz, H., Nyboe, N. S., Foged, N., Thomassen, T. and Wiig, T. Stretching AEM near-surface resolution limits related to low-and very high resistivity contrasts. *AEGC*, Sydney, Australia. Extended Abstracts, 2017.

Pfaffhuber, A.A., Lysdahl, A.K., Sørmo, E. **Bazin**, S. Skurdal, G.H., Thomassen, T. Anschütz, H., Scheibz, J.Delineating hazardous material without touching — AEM mapping of Norwegian alum shale. *First Break*, 35 (8), 35-39, 2017.

Pfaffhuber, A.A., Persson, L., Lysdahl, A.K., Kåsin, K., Anschütz, H., Bastani, M., **Bazin**, S., Löfroth, H. Integrated scanning for quick clay with AEM and ground-based investigations. *First Break*, 35 (8), 73-79, 2017.

Lysdahl, A.K.,Pfaffhuber, A.A., Anschütz, H.,Kåsin, K., **Bazin,** S. Probability of Sensitive Clay from AEM Data. *23rd European Meeting of Environmental and Engineering Geophysics*, DOI: 10.3997/2214-4609.201702007, 2017.

Sauvin, G., **Bazin**, S., Lysdahl, A.K. Shear-wave Reflection-seismic and ERT Investigation for Slope Stability. *23rd European Meeting of Environmental and Engineering Geophysics*, DOI: 10.3997/2214-4609.201701969, 2017.

Pfaffhuber, A.A., Kåsin, K., Anschütz, H., Lysdahl, A.K., **Bazin, S.** Vöge, M. Geotechnical ground investigations from the air - opportunities and limitations of airborne geoscanning. GeoOttawa conference, 2017.

Gribben, S., Donohue, S., **Bazin,** S. Investigating how the changes in geotechnical properties of sensitive clays influence their geophysical properties. Second International Workshop on Landslides in Sensitive Clays, Trondheim. In: Thakur et al. (Eds.), *Landslides in Sensitive Clays: From research to implementation, Advances in Natural and Technological Hazards Research*, 36, Springer, 2017.

Lysdahl, A. O. Pfaffhuber, A. A., Anschütz, H., Kåsin, K., **Bazin**, S., 2017. Helicopter electromagnetic scanning as a first step in regional quick clay mapping. Second International Workshop on Landslides in Sensitive Clays, Trondheim. In: Thakur et al. (Eds.), *Landslides in Sensitive Clays: From research to implementation, Advances in Natural and Technological Hazards Research*, 36, Springer, 2017.

Anschütz, H., **Bazin**, S., Kåsin, K., Pfaffhuber, A., and Smaavik, T.F., 2016, Airborne sensitive clay mapping – stretching the limits of AEM resolution and accuracy. *22nd European Meeting of Environmental and Engineering Geophysics*, 2016.

Malehmir, A., Socco, L. V., Bastani, M., Krawczyk, C. M., Pfaffhuber, A. A., Miller, R. D., Maurer, H., Frauenfelder, R., Suto, K., **Bazin**, S., Merz, K. & Dahlin, T. Near-Surface Geophysical Characterization of Areas Prone to Natural Hazards: A Review of the Current and Perspective on the Future. In Nielsen. L. (Ed.), *Advances in Geophysics,* doi: 10.1016/bs.agph.2016.08.001, 2016.

Lysdahl, A.K., Scheibz, J., Pfaffhuber, A.A., Rømoen, M. & **Bazin**, S., 2016. River-crossing Resistivity Survey for Bridge Foundation Design - A Case-study from Skarnes, Norway. *22nd European Meeting of Environmental and Engineering Geophysics*, DOI: 10.3997/2214-4609.201602049, 2016.

Anschutz, H., Voege, M., Lysdahl, A.K., **Bazin**, S., Sauvin, G., Pfaffhuber, A.A. & Berggren, A.L., 2016. Comparing Automatic and Manual Methods for Determination of the Bedrock Interface Using AEM Data. *22nd European Meeting of Environmental and Engineering Geophysics*, DOI: 10.3997/2214-4609.201602049, 2016.

Bazin, S., Sauvin, G., Dehghannejad, M., Lundberg, E., Lysdahl, A.K., Malehmir, A., Kveldsvik, V, Boge, K. & Pfaffhuber, A.A., 2016. Seismic and Electrical Resistivity Investigations for the Planning of a Tunnel in Oslo Outskirts. *22nd European Meeting of Environmental and Engineering Geophysics*, DOI: 10.3997/2214-4609.201602049, 2016.

Gribben, S., Donohue, S., Sivakumar, V., **Bazin**, S., Berre, T.& L'Heureux, J.S. Geophysical methods for assessing the geotechnical properties of sensitive clays. In Proceedings of the 69th Canadian Geotechnical Conference - GEOVancouver, 2016.

Pfaffhuber, A. A., Anschütz, H., Ørbech, T., **Bazin**, S., Lysdahl, A. O. K., Vöge., M., Sauvin, G., Waarum, I.-K., Smebye, H. C., Kåsin, K., Grøneng, G., Berggren, A.-L., Pedersen J. B., and Foged, N. Regional geotechnical railway corridor mapping using airborne electromagnetics. *5th International Conference on Geotechnical and Geophysical Site Characterisation*, Gold Coast, Australia, 2016.

Bazin, S., Anschütz, H., Sauvin, G., Helle, T.E., Gribbten, S., Donohue, S & Long, M. Geophysical characterisation of marine and quick clay sites: field and laboratory tests. *5th International Conference on Geotechnical and Geophysical Site Characterisation*, Gold Coast, Australia, 2016.

Pfaffhuber, A. A., **Bazin**, S., Kåsin, K., Anschütz, H., Sandven, R., Montafia, A., Gylland, A. S., and Long, M. In-situ detection of sensitive clays from a geophysical perspective. *5th International Conference on Geotechnical and Geophysical Site Characterisation*, Gold Coast, Australia, 2016.

Bhasin, R., Pabst, T., **Bazin, S**. Arnstein, A. Airborne Electromagnetic Surveys for Carrying Out Feasibility Studies for Constructing Road and Rail Tunnels in Himalaya. Journal of Rock Mechanics & Tunnelling Technology, 22 (2), 99-112, 2016.

Bazin, S., Anschütz, H., Pfaffhuber, A.A., Lysdahl, A.K. and Scheibz, J. On the Use of ERT and AEM Resistivities for a Tunnel Pre-investigation. *21st European Meeting of Environmental and Engineering Geophysics*, DOI: 10.3997/2214-4609.201413670, 2015.

Lysdahl, A.K., **Bazin**, S., Anschütz, H., and Pfaffhuber, A.A. Black Shale Mapping by AEM for Geotechnical Applications. *21st European Meeting of Environmental and Engineering Geophysics*, DOI: 10.3997/2214-4609.201413879, 2015.

Anschütz, H., **Bazin**, S. and Pfaffhuber. Towards Using AEM for Sensitive Clay Mapping - A Case Study from Norway. *21st European Meeting of Environmental and Engineering Geophysics*, DOI: 10.3997/2214-4609.201413863, 2015.

Bazin, S. Anschütz, H., Lysdahl, A.K., Pfaffhuber, Scheibz, J. ERT inversion industry standard versus cutting edge developments, time for a change? SAGEEP 2015 - *28th Annual Symposium on the Application of Geophysics to Engineering and Environmental Problems*, https://doi.org/10.4133/SAGEEP.28-076, 2015.

Scheibz, J., **Bazin**, S., Pfaffhuber, A.A., and Fiandaca, G. Total Chargeability versus Full Wave Form Time Domain IP Inversion - A Case Study from a DNAPL Contamination in Norway. *21st European Meeting of Environmental and Engineering Geophysics*, DOI: 10.3997/2214-4609.201413780, 2015.

Pfaffhuber, A.A., **Bazin**, S., Helle, T. E. An integrated approach to quick-clay mapping based on resistivity measurements and geotechnical investigations. In: L'Heureux et al. (Eds.), Landslides in Sensitive Clays: From Geosciences to Risk Management, *Advances in Natural and Technological Hazards Research*, 36, Springer, 2014.

Pfaffhuber A.A., **Bazin S.**, Helle T.E. An integrated approach to quick-clay mapping based on resistivity measurements and geotechnical investigations. Landslides in sensitive clays. *Advances in Natural and Technological Hazards Research*, 36, 193-204, 2014.

Sauvin G, Lecomte I, **Bazin** S, L'Heureux JS, and Vanneste M. Geophysical data integration for quick-clay mapping: the Hvittingfoss case study, Norway. In: L'Heureux et al. (Eds.), *Landslides in Sensitive Clays: From Geosciences to Risk Management, Advances in Natural and Technological Hazards Research*, 36, Springer, 2014.

Lysdahl, A.K., **Bazin**, S., Stokkeland, C., Ahrens, S., Helander, R., Høiseter, Å., Scheibz, J., Pfaffhuber, A.A. 2.5D ERT Survey in Oslo Harbor – Medieval Heritage in an Urban Development Area. *20th European Meeting of Environmental and Engineering Geophysics*, DOI: 10.3997/2214-4609.20142103, 2014.

Bazin, S., Pfaffhuber, A.A., Anschütz, H., Grøneng, G. and Christensen, C. Tunnel Pre-investigation - Towards a Resistivity to Rock-quality Transform. *20th European Meeting of Environmental and Engineering Geophysics*, DOI: 10.3997/2214-4609.20141960, 2014.

Bazin, S., Reiersen, K., Anschütz, H., Lato, M.J. and Pfaffhuber, A.A. The Use of Electrical Resistivity Tomography for an Archaeological Investigation in the Old Oslo Harbor, Norway. *18th European Meeting of Environmental and Engineering Geophysics*, DOI: 10.3997/2214-4609.20143309, 2012.

Sauvin, G., Lecomte, I., **Bazin**, S., L'Heureux, J.S., Vanneste, M. Geophysical Investigations of Quick-clay Slide Prone Areas. *18th European Meeting of Environmental and Engineering Geophysics*, DOI: 10.3997/2214-4609.20143319, 2012.

Sauvin, G., Lecomte, I., **Bazin**, S., L'Heureux, J.S., Malehmir, A. Quick-clay Landslide-prone Grounds in Norway and Sweden: A Complex Problem Requiring a Combined Geophysical and Geotechnical Approach. *74th EAGE Conference and Exhibition – Workshops*, DOI: 10.3997/2214-4609.20149783, 2012.

Pfaffhuber, A.A., **Bazin**, S., Integrating geophysics with geotechnical data for engineering projects, *First EAGE International Conference on Engineering Geophysics*, DOI: 10.3997/2214-4609.20143988, 2011.

Sauvin, G. **Bazin**, S. Vanneste, M. Lecomte I. Pfaffhuber A.A. Towards Joint Inversion/Interpretation for Landslide-prone Areas in Norway - Integrating Geophysics and Geotechnique. *17th EAGE European Meeting of Environmental and Engineering Geophysics*, DOI: 10.3997/2214-4609.20144416, 2011.

1.12.3. Communications dans des congrès sans comité de lecture

Smebye, H., Salazar, S., Gisnås, K., Paulsen, E.M., Lysdah, A.O.K., **Bazin, S.**, Frauenfelder, R. RPAS as a tool in geo-hazards mitigation: case studies from Norway and South Asia and best practices. Geophysical Research Abstracts Vol. 20, EGU2018-18477, *EGU General Assembly*, 2018.

Liu, Z., Lysdahl, A.K., Nadim, F., **Bazin**, S., Kalsnes, B., Lacasse, S. Bayesian kriging for the mapping of sensitive clay. *12th International Conference on Structural Safety & Reliability*, Vienna, Austria, 2017.

Pfaffhuber, A.A., **Bazin, S.,** Helle, T. E. An integrated approach to quick-clay mapping based on resistivity measurements and geotechnical investigations. *1st International Workshop on Landslides in Sensitive Clays*, Laval, Canada, 2013.

Sauvin G, Lecomte I, **Bazin S**, L'Heureux JS, and Vanneste M. Geophysical data integration for quick-clay mapping: the Hvittingfoss case study, Norway. *1st International Workshop on Landslides in Sensitive Clays*, Laval, Canada, 2013.

Pfaffhuber, A.A., **Bazin, S.,** Lato, M., Domaas, U. Correlating ERT with AEM in a rock slide mapping project, same shape but different quantities, *ASEG*, Melbourne, Australia, 2013.

Sauvin, G., Lecomte, I, **Bazin, S**., L'Heureux, J.-S. Quick-clay landslide-prone grounds in Norway and Sweden: a complex problem requiring a combined geophysical and geotechnical approach, *EAGE* conference, Copenhague, 2012.

Michoud, C., **Bazin, S.,** Blikra, L.-H., Derron, M.-H., Jaboyedoff, M., Overview of Existing Landslide Early-Warning Systems in Operation, Geophysical Research Abstracts, Vol. 14, EGU2012, *EGU General Assembly*, 2012.

Bazin, S., and the Dand Team, SafeLand guidelines for landslide monitoring and early warning systems in Europe - Design and required technology, Geophysical Research Abstracts, Vol. 14, EGU2012-1347-1, *EGU General Assembly*, 2012.

Bazin, S., Pfaffhuber, Cappelen, P., Holmström, P., Rudoplh-Lund, K, Non intrusive geophysics for pollution plume mapping inside an operating plant- 2D electrical resistivity tomography and time domain induced polarization surveying, *2nd workshop on geophysical measurements in waste management*, Malmö, Sweden, 2012.

Pfaffhuber, A., **Bazin, S**., Integrating Geophysics with Geotechnical Data for Engineering Projects, *First International Conference on Engineering Geophysics*, Al Ain, United Arab Emirates, 2011.

Pfaffhuber, A., **Bazin, S.,** Domaas, U., Grimstad, E., Electrical Resistivity Tomography to follow up an airborne EM rock slide mapping survey – Linking rock quality with resistivity, *12th International Congress of the Brazilian Geophysical Society*, Rio, Brazil, 2011.

Bazin, S., Pfaffhuber, A., Cappelen, P., Fiandaca, G., Dahlin, T., French, H., Bloem, E., Is IP instrumentation ready for commercial pollution plume mapping?, *2nd International Workshop on Induced Polarization in Near-Surface Geophysics*, Colorado School of Mines, CO, USA, 2011.

Bazin, S., Pfaffhuber, A., Filling the gaps between drill-hole data with high resolution geophysics - 2D electrical resistivity tomography (ERT) & induced polarization (IP) surveying, 8th International Symposium on Field Measurements in GeoMechanics, Berlin, Germany, 2011.

Bouin, M.P., de Chabalier, J.B., Clouard, V,. Beauducel, F., Feuillet, N., Nercessian, A., **Bazin, S.** Tait, S.. Seismicity and deformation processes in the Lesser Antilles subduction zone, New Horizons in Earth Sciences, Paris, 2011.

Løvholt, F., G. Pedersen, **S. Bazin**, D. Kühn, C. Harbitz, Tsunami run-up variability due to heterogeneous slip on the fault plane, *Geophysical Research Abstracts*, EGU, 2011.

Bazin, S., Case histories on the use of Electric Resistivity Tomography (ERT) and Induced Polarization (IPT) in sediments, Teknologidagene workshop, Trondheim, Norway, 2010.

Løvholt, F., **S. Bazin**, R. E. Bredesen, C. Harbitz, D. Kühn, H. Bungum, Stochastic variation of tsunami run-ups due to heterogeneous slip on reverse faults, *Geophysical Research Abstracts*, Vol. 12, EGU, 2010.

Feuillet, N., F. Beauducel,, E. Jacques, P. Tapponnier, **S. Bazin,** B. Delouis, M. Vallée, G. C. P. King, The Mw = 6.3, November 21, 2004, Les Saintes earthquake (Guadeloupe): Tectonic setting and static stress modeling, *Geophysical Research Abstracts*, Vol. 12, EGU, 2010.

Bouin, M.-P., M. Bouchon, O. Coutant, **S. Bazin**, J.L., Latchman, Source parameters of the Mw 7.4 Martinique intermediate-depth earthquake (Leeward islands) of November 29, 2007: A slab-pull event with horizontal fault plane, *Geophysical Research Abstracts*, Vol. 12, EGU, 2010.

Harbitz, C.B., Glimsdal, S., Zamora, N., Gour, N., Frauenfelder, R., Smebye, H., Dverdrup-Thygeson, K., Løvholt, F., Bungum, H., Gaure, P., Eldsvig, U.K., **Bazin, S**. Tsunamis in the Caribbean: regional exposure and local risk assessment, *EGU Conference*, Vienna, 2009.

Bazin, S., N. Feuillet, M.P. Bouin, J.B. de Chabalier, Le séisme de Martinique, contexte tectonique et historique, Gestion de crise*, Journées du RAP*, 2008.

Bouin, M-., O Coutant, **S. Bazin**, P Bernard, M Bouchon, B Delouis, N. Feuillet, T Mohammad, M Vallée, Mécanismes du séisme de Martinique : Analyse des données et études préliminaires, *Journées du RAP*, 2008.

Guéguen, Ph., **S. Bazin,** Analyse du comportement sous séisme des appuis du Centre de Découverte des Sciences de la Terre (Martinique), *Journées du RAP*, 2008.

Bengoubou-Valerius, M., J. Ruiz, P. Bernard, M.-P. Bouin,**S. Bazin**. Modélisation des mouvements forts du séisme des Saintes Mw 6.3 par fonctions de Green empiriques préliminaires*, Journées du RAP*, 2008.

Bazin, S., N. Feuillet, M.P. Bouin, C. Duclos, M. Bengoubou-Valérius, J.B. de Chabalier, The Mw=7.4 Martinique (Lesser Antilles) intermediate depth earthquake of November 29, 2007 : A first analyse, *18th Caribbean Geological Conference*, 2008.

Feuillet, N., F. Beauducel, E. Jacques, **S. Bazin**, P. Tapponnier, G.C.P. King, The Mw=6.3, 21 November 2004 les Saintes earthquake (Guadeloupe, FWI) : tectonic setting and associated stress changes, *18th Caribbean Geological Conference*, 2008.

Duclos, C., **S. Bazin**, W. Crawford, N. Feuillet, A. Nercessian, S. Singh, Analysis of Les Saintes (Guadeloupe) seismic crisis using ocean bottom seismometers (OBS), *EUG Journal of Conference*, Vol. 9, 07281, 2007.

Beauducel, F., C. Anténor-Habazac, **S. Bazin**, J.B. De Chabalier, A. Nercessian, N. Feuillet, E. Jacques, D. Bertil, J.C. Komorowski, G. Boudon, A. Lefriant, P. Tapponier, A. Hirn, J.C. Lépine, P. Bernard, G. King, OVSG team, The Mw 6.3 earthquake of Les Saintes (Guadeloupe) on November 21, 2004, *Journées du RAP*, Les Houches, 2006.

Beauducel, F., **S. Bazin**, M. Bengoubou-Valérius, Le Réseau Accélérométrique Permanent des Antilles Françaises (RAP-IPGP): spécificités, traitements automatiques et première loi d'atténuation, *Journées du RAP*, Les Houches, 2006.

Bengoubou-Valérius, M, D. Bertil, **S. Bazin**, A. Bosson, F. Beauducel, A. Randrianasolo, CDSA : A new seismological data center for French West Indies, *The Caribbean Academy of Sciences*, 15th Annual Meeting, Guadeloupe, 2006.

Bazin, S., F. Beauducel, J-C Komorowski, A. Nercessian, G. Boudon, A. Saglio, C. Anténor-Habazac, A. Tarchini, B. Figaro, J-C Delmond, A. Lemarchand, C. Lambert, D. Mallarino P. Bernard, B. Chouet, Volcano-seismic signals and monitoring network on La Soufrière of Guadeloupe, *European Seismological Commission Annual Workshop* - Quantifying Volcanic Activity, Guadeloupe, 2005.

Beauducel, F., C. Anténor-Habazac, **S. Bazin**, J.B. De Chabalier, A. Nercessian, N. Feuillet, E. Jacques, D. Bertil, J.C. Komorowski, G. Boudon, A. Lefriant, P. Tapponier, A. Hirn, J.C. Lépine, P. Bernard, G. King, The Mw 6.3 earthquake of Les Saintes (Guadeloupe) on November 21, 2004, *European Seismological Commission Annual Workshop* - Quantifying Volcanic Activity, Guadeloupe, 2005.

Vallée, M., B. Delouis, **S. Bazin**, Rupture process of the mainshocks of the Guadeloupe, West Indies, seismic crisis (November 2004-February 2005), *Workshop on fracture dynamics : Theory and application to earthquakes*, Madrid, 2005.

Bazin, S., F. Beauducel, J-C Komorowski, A. Nercessian, G. Boudon, A. Saglio, C. Anténor-Habazac, A. Tarchini, B. Figaro, J-C Delmond, A. Lemarchand, C. Lambert, D. Mallarino P. Bernard, B. Chouet, Volcano-seismic signals and monitoring network on La Soufrière of Guadeloupe, *Soufriere Hills Volcano, ten years on Workshop*, Montserrat, 2005.

Le Friant, A., G. Boudon, J-C Komorowskin, P. Heinrich, **S. Bazin**, F. Beauducel, Tsunami in the Lesser Antilles islands: Recent events and implications, *Soufriere Hills Volcano, ten years on,* workshop, Montserrat, 2005.

Goslin, J., J. Perrot, J.-Y. Royer, C. Martin, R. P. Dziak, C. G. Fox, M. Fowler, J. Haxel, H. Matsumoto, N. Lourenço, J. Luis, **S. Bazin,** Seismicity of the Mid-Atlantic Ridge at a regional scale : results from acoustic monitoring by two arrays of autonomous hydrophones, *MOMAR* workshop, Lisbonne, 2005.

Komorowski, J.C., Boudon, G., Semet, M., Beauducel, F., Anténor-Habazac, C., **Bazin, S.,** Hammouya, G. Guadeloupe. Volcanic hazard atlas of the Lesser Antilles. In: Lindsay J.M., Roberston, R.E.A., Sheperd, J.B., Ali, S. (eds)., 2004.

Goslin, J. and the SIRENA team : **S. Bazin,** R.P. Dziak, C. Fox, M. Fowler, J. Haxel, N. Lourenço, J. Luis, C. Martin, J. Perrot, J.-Y. Royer**,** Long-term seismicity of the northern (15°N-60°N) Mid-Atlantic Ridge recorded by two regional hydrophones arrays : a widespread along-ridge influence of the Azores and Iceland hotspots, *EOS*, 85, 2004.

Bazin, S., Attempt to improve the Caribbean seismic monitoring array with autonomous hydrophones, *Seismo-acoustic Applications in Marine Geology and Geophysics* workshop, Woods Hole, USA, 2004.

Goslin, J., J. Perrot, J.-Y. Royer, C. Martin, C. Fox, R.P Dziak, H. Matsumoto, M. Fowler, J. Haxel, J. Luis, N. Lourenço, **S. Bazin,** Interactions between the MAR and the Azores hotspot as imaged by seismicity distributions using autonomous hydrophone arrays, *Seismo-acoustic Applications in Marine Geology and Geophysics* workshop, Woods Hole, USA, 2004.

Singh, S.C., Harding, A.J., Sinha, M.C., Kent, G., Pye, J.W., **Bazin, S.,** Tong, C.H., Barton, P.J., Hobbs, R., White, R.S., Orcutt, J.A., Three-dimensional Reflectivity Images of Moho and Melt Sills beneath the 9 03'N Overlapping Spreading Centre at the East Pacific Rise, *EOS*, 84, 2003

Bazin, S., R. Bento, C. Fox, J. Goslin, N. Lourenco, J. Luis, L. Matias, H. Matsumoto, J. Perrot, P-F. Piserchia et J-Y. Royer, Deployment of new hydrophone array north of the Azores for seimic monitoring of the ridge and the Azores Plateau, *MOMAR workshop, Towards planning of seafloor observatory programs for the MAR region,* Açores, Portugal, 2002.

Ricolleau, A., **Bazin, S.,** Crawford, W., Singh, S., Joint analysis of seimsic and seafloor compliance data at 9°33', East Pacific Rise, *Annales Geophysicae*, 2002.

Singh, S., Hirn, A., De Voogd, B., Vigner, A., **Bazin, S**., Charvis, P., Géli, L., Saatcilar, R., Taymaz, T., Ozalaybey, S., Cetin, S., Oçakoglu, N., Ricolleau, A., Karakoç, F., Selvigen, V., 3D geometry of the North Anatolian Fault system in the Cinarcik Basin: preliminary results (SEISMARMARA 2001), *Annales Geophysicae*, 2002.

Hirn, A., Singh, S., Charvis, P., Géli, L., Laigle, M., Lépine, J-C, De Voogd, B., Saatcilar, R., Taymaz, T., Ozalaybey, S., Shimamura, H., Selvi, O. , Karabulut, H., Murai, Y., NIishimura, Y., Yamada, A., Vigner, A., **Bazin, S.**, Tan, O., Yolsal, S., Aktar, M., Galvé, A., Sapin, M., Marthelot, J.-M., Imren, C., Ergin, M., Tapirdamaz, C., Koçaoglu, A., Tarancioglu, A, Diaz, J., Verhille, J., Auffret, Y., Cetin, S., Ricolleau, A., Selvigen, V., Demirbag, E., Hakyemez, Y., Sarikawak, K., SEISMARMARA 2001: a marine seismic survey and offshore-onshore artificial source and natural earthquakes in the seismogenic region of the Sea of Marmara, *Annales Geophysicae*, 2002.

Hirn, A., Singh, S., Saatcilar, R., Laigle, M., De Voogd, B., Vigner, A., Taymaz, T., Ozalaybey, S., Imren, C., **Bazin, S.**, Charvis, P., Géli L., Klien, E., Reflection-seismic images and evolution at the scale of the crust and active faults of the Sea of Marmara trough (SEISMARMARA 2001), *Annales Geophysicae*, 2002.

Kent, G.M., Harding, A.J., Babcock, J.M., Orcutt, J.A., **Bazin, S.,** Singh, S., Detrick, R.S., Canales, J.P., Carbotte, S.M., Diebold, J., Magmatic Systems in 3-D, EOS, 2002.

Smith, D.K., M. Tolstoy, C.G. Fox, D.R. Bohnenstiehl, M. Cannat, J. Escartin, **S. Bazin**, Spatial and Temporal Distribution of Seismicity Along the Northern Mid-Atlantic Ridge, 15-35N, from an Autonomous Hydrophone Array, *EOS*, 82, 2001.

Bazin, S., S. Singh, G. Kent, A. Harding J. Orcutt et le groupe ARAD, Seismic structure of the EPR magma chamber : new constraints from the 9°03'N OSC, *EUG Journal of Conference*, 6, 1, 302, 2001.

Singh, S., A. Harding, M. Sinha, G. Kent and **ARAD group**, Three-dimensional reflectivity image of the melt sill and Moho- implications for crustal accretion process at fast spreading centers, *EUG Journal of Conference*, 6, 1, 302, 2001.

Pye, J., R.M. Shipp, C.H. Tong, P.J. Barton, R.S. White, R.W. Hobss, S.C. Singh, M.C. Sinha and **ARAD group**, Three-dimensional reflectivity image of teh melt sill and Moho- implications for crustal accretion process at fast spreading centers, *EUG Journal of Conference*, 6, 1, 806, 2001.

Bazin, S., G. Kent, S. Singh, A. Harding, J. Orcutt, C.H. Tong, J. Pye, M. Sinha, P. Barton, R. White, R. Hobbs, 3-D magma chamber structure beneath the 9°03' N OSC on the East Pacific Rise, *EOS,* 81, F1346, 2000, **communication orale invitée.**

Pye, J.W., R.M. Shipp, S. Singh, M. Sinha, P. Barton, R. Hobbs, C.H. Tong, S. **Bazin**, G. Kent, A. Harding, J. Orcutt, Physical Constraints on the Crustal Structure Beneath the East Pacific Rise at the 9°03' N Overlapping Spreading Centre, *EOS,* 81, F1329, 2000.

Bazin, S., A. Harding, G. Kent, J. Orcutt, C.H. Tong, J. Gee, S. Singh, P. Barton, M. Sinha, R. White, Crustal acretion at the 9°03'N overlapping spreading center, East Pacific Rise, *Annales Geophysicae*, CD-ROM, Vol. 2, 2000.

Bazin, S., G. Kent, A. Harding, J. Orcutt, C.H. Tong, S. Singh, P. Barton, M. Sinha, R. White, 3-D tomographic imaging of the oceanic crust, *Bull. Seism. Soc. Am.,* 71, 219, 2000, **communication orale invitée.**

Bazin, S., A. Harding, G. Kent, J. Orcutt, E. Hallenborg, C. Tong, M. Sinha, P. Barton, S. Singh, R. White, 3-D visualization of crustal accretion at the 9°03'N overlapping spreading center, East Pacific Rise, *EOS,* 80, F1049, 1999.

Bazin, S., A. Harding, G. Kent, J. Orcutt, E. Hallenborg, C. Tong, M. Sinha, P. Barton, S. Singh, R. White, 3D seismic tomography beneath the 9°03'N OSC on the East Pacific Rise, *EOS,* 79, F798, 1998.

Hallenborg, E., S. **Bazin**, G. Kent, A. Harding, J. Orcutt, S. Singh, M. Sinha, P. Barton, R. White, C. Tong, Improving bathymetric coverage of the 9°03'N OSC on the East Pacific Rise, *EOS*, 79, F803, 1998.

Harding, A. J., G. Kent, J. Orcutt, S. **Bazin**, E. Hallenborg, M. Sinha, S. Singh, P. Barton, C. Tong, R. Hobbs, and R. White, Overview of the ARAD 3-D seismic experiment at the 9°03'N overlapping spreading center, East Pacific Rise, *EOS*, 79, F798, 1998.

Kent, G. M., A. Harding, J. Orcutt, S. **Bazin**, E. Hallenborg, S. Singh, M. Sinha, P. Barton, V. Tong, R. Hobbs, R. White, The ARAD 3-D seismic experiment: a voxel approach, *EOS*, 79, F804, 1998.

Singh, S. C., G. Kent, M. Sinha, A. Harding, C. Tong, P. Barton, R. Hobbs, J. Orcutt, R. White, S. **Bazin**, 3D nature of the axial magma chamber beneath 9°03'N overlapping spreading center, East Pacific Rise, *EOS*, 79, F798, 1998.

Tong, C. H., P. Barton, M. Sinha, S. Singh, T. Owen, D. Boschi, R. White, R. Hobbs, S. **Bazin**, A. Harding, G. Kent, J. Orcutt, 3D crustal study of the 9°03'N Overlapping spreading center on the East Pacific Rise using densely sampled wide angle seismic data, *EOS*, 79, F904, 1998.

Canales, J.P., R.S. Detrick, S. **Bazin**, A.J. Harding, J.A. Orcutt, Off-axis crustal thickness variations across and along the East Pacific Rise within the MELT area, *EOS*, 79, S225, 1998.

Bazin, S., H. van Avendonk, A. Harding, J. Orcutt, Comparison of crustal structure beneath a robust and a non robust region of the Southern East Pacific Rise, *Annales Geophysicae*, 16, C291, 1998.

Bazin, S., H. van Avendonk, A. Harding, J. Orcutt, 2-D seismic tomography beneath the MELT region shows evidence of a variable magmatic regime at the East Pacific Rise, *EOS*, 78, F704, 1997, **communication orale invitée.**

Bazin, S., H. van Avendonk, A. Harding, J. Orcutt, Seismic refraction observations and tomographic study of 17 degrees south on the East Pacific Rise, *EOS*, 77, F664, 1996.

Harding, A.J., S. **Bazin**, J. Orcutt, Analysis of expanding spread profile data from the MELT area on the East Pacific Rise, *EOS*, 77, F664, 1996.

2. L'aléa sismique aux Petites Antilles

Le risque sismique aux Petites Antilles est un risque majeur du fait de la localisation de l'arc antillais au niveau d'une zone de subduction. En effet, la plaque Atlantique plonge sous la plaque Caraïbe avec une vitesse de rapprochement de 2 cm/an. Certains séismes sont directement liés à ce processus de subduction, ils sont en général profonds. D'autres plus superficiels et souvent moins forts résultent de la déformation de la plaque Caraïbe. Durant la période historique, plusieurs séismes ont causé des dégâts mais seulement deux séismes majeurs, ceux de 1974 à Antigua et de 1985 à Redonda, ont eu lieu depuis l'installation de réseaux de surveillance. La sismicité historique témoigne que l'arc des Petites Antilles a déjà été le siège de séismes destructeurs (1839, 1843) et d'autres sont à prévoir.

Dans cette section sont reproduits trois articles qui me semblent bien représenter les différents aspects du travail d'un sismologue aux Antilles:

- Le premier aspect est la nécessité de pouvoir estimer les mouvements du sol attendus après un séisme, en différents points du territoire. Ces estimations sont faites grâce à une « loi d'atténuation » et expriment l'accélération au niveau du sol en fonction de la magnitude et de la distance au séisme. Le premier article décrit la façon dont nous avons estimé une loi d'atténuation, la loi *Bcube*, représentative pour la région Guadeloupe-Martinique.
- Le second montre l'intérêt de compiler les données sismologiques issues des différents réseaux de la région pour améliorer la connaissance de l'aléa sismique dans les Petites Antilles. Il montre aussi la difficulté de grouper des données hétérogènes.
- Le dernier article montre la difficulté de surveiller l'ensemble de l'arc des Antilles en utilisant seulement des stations sismologiques localisées sur les terres émergées.

2.1 Une nouvelle loi d'atténuation aux Petites Antilles

L'objectif du Réseau d'Accélérométrie Permanent (RAP) est de permettre l'enregistrement de mouvements forts du sol sur tout le territoire français. Ce réseau n'a pas un rôle de surveillance mais les données servent à mieux comprendre les phénomènes relatifs au mouvement du sol lors de séismes en enregistrant les mouvements forts sans saturation. Plusieurs réseaux régionaux ont été installés sur le territoire depuis la création du GIS RAP en 2000. J'ai participé à l'installation de celui de l'OVSG puis celui de l'OVSM, dont chacun comprend 12 stations. J'ai étudié les effets de site en réalisant des mesures de H/V (mesures de bruit de fond sismique pour estimer l'épaisseur de sol meuble) puis participé à leur maintenance et leurs mises à jour, et j'ai validé quotidiennement des données enregistrées par déclenchements automatiques ou manuels (Bazin et al., 2005).

Une analyse des pics d'accélération (PGA) nous a permis de contraindre des modèles de prédiction de mouvement du sol (pour des sols durs et des sols meubles), en utilisant les magnitudes et les distances hypocentrales. La crise des Saintes a brutalement fourni assez de données accélérométriques pour pouvoir contraindre notre modèle de prédiction (Bertil et al., 2015). L'article présenté dans ce chapitre a été essentiellement rédigé par François Beauducel mais est issu d'un travail de recherche commun. J'ai associé et validé tous les signaux accélérométriques issus du réseau RAP pour le calcul des PGA. Nous avons développé une méthode indirecte consistant à ajuster une loi d'atténuation des ondes sismiques et d'y appliquer ensuite une relation amplitudes/intensités. Les paramètres de la loi ont été inversés par la méthode des moindres carrés à partir des données de plus de 400 événements de magnitudes comprises entre 1.1 et 6.3, et de distances hypocentrales variant entre 2 et 400 km. La loi régionale complète, dénommée *Bcube* (initiales des 3 auteurs), a été validée par comparaison avec les intensités réelles du séisme des Saintes (enquête officielle du BCSF) et de plusieurs séismes historiques.

Précédemment, lors d'un séisme ressenti par la population, les observatoires envoyaient un communiqué résumant les caractéristiques de l'événement (magnitude, localisation et heure). Or les autorités et la population souhaitaient davantage recevoir des informations sur les effets destructeurs du séisme. Seulement, ces derniers sont normalement recensés sur base de témoignages (volontaires ou par enquêtes sur le terrain) et arrivaient bien après l'envoi du communiqué de presse. L'excellente cohérence des résultats obtenus avec la loi d'atténuation *Bcube* nous a conduit à mettre en place un communiqué semi-automatique comprenant une carte des intensités prédites et la liste des communes concernées (*shakemaps* en anglais). Cette procédure est depuis quotidiennement utilisée dans les deux observatoires pour prédire les intensités macroscopiques dans les différentes communes et publier les bulletins « séisme ressenti » (Figure 8).

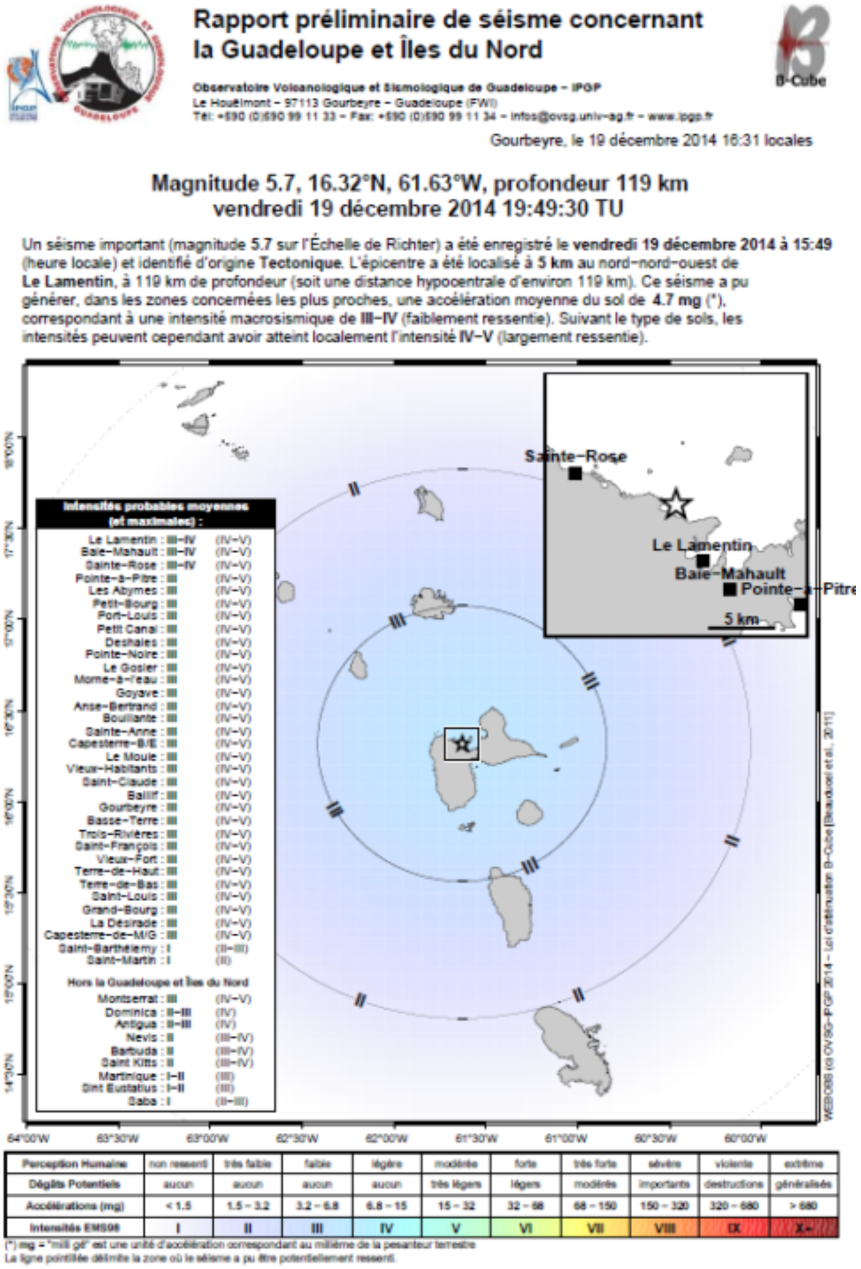

Rapport préliminaire de séisme concernant la Guadeloupe et Îles du Nord

Observatoire Volcanologique et Sismologique de Guadeloupe – IPGP
Le Houëlmont – 97113 Gourbeyre – Guadeloupe (FWI)
Tél: +590 (0)590 99 11 33 – Fax: +590 (0)590 99 11 34 – infos@ovsg.univ-ag.fr – www.ipgp.fr

Gourbeyre, le 19 décembre 2014 16:31 locales

Magnitude 5.7, 16.32°N, 61.63°W, profondeur 119 km
vendredi 19 décembre 2014 19:49:30 TU

Un séisme important (magnitude **5.7** sur l'Échelle de Richter) a été enregistré le **vendredi 19 décembre 2014 à 15:49** (heure locale) et identifié d'origine **Tectonique**. L'épicentre a été localisé à **5 km** au nord-nord-ouest de **Le Lamentin**, à 119 km de profondeur (soit une distance hypocentrale d'environ 119 km). Ce séisme a pu générer, dans les zones concernées les plus proches, une accélération moyenne du sol de **4.7 mg** (*), correspondant à une intensité macrosismique de **III–IV** (faiblement ressentie). Suivant le type de sols, les intensités peuvent cependant avoir atteint localement l'intensité **IV–V** (largement ressentie).

Intensités probables moyennes (et maximales) :

Le Lamentin : III–IV (IV–V)
Baie-Mahault : III–IV (IV–V)
Sainte-Rose : III–IV (IV–V)
Pointe-à-Pitre : III (IV–V)
Les Abymes : III (IV–V)
Petit-Bourg : III (IV–V)
Port-Louis : III (IV–V)
Petit Canal : III (IV–V)
Deshaies : III (IV–V)
Pointe-Noire : III (IV–V)
Le Gosier : III (IV–V)
Morne-à-l'eau : III (IV–V)
Goyave : III (IV–V)
Anse-Bertrand : III (IV–V)
Bouillante : III (IV–V)
Sainte-Anne : III (IV–V)
Capesterre-B/E : III (IV–V)
Le Moule : III (IV–V)
Vieux-Habitants : III (IV–V)
Saint-Claude : III (IV–V)
Baillif : III (IV–V)
Gourbeyre : III (IV–V)
Basse-Terre : III (IV–V)
Trois-Rivières : III (IV–V)
Saint-François : III (IV–V)
Vieux-Fort : III (IV–V)
Terre-de-Haut : III (IV–V)
Terre-de-Bas : III (IV–V)
Saint-Louis : III (IV–V)
Grand-Bourg : III (IV–V)
La Désirade : III (IV–V)
Capesterre-de-M/G : III (IV–V)
Saint-Barthélemy : I (II–III)
Saint-Martin : I (II)

Hors la Guadeloupe et Îles du Nord

Montserrat : III (IV–V)
Dominica : II–III (IV)
Antigua : II–III (IV)
Nevis : II (III–IV)
Barbuda : II (III–IV)
Saint Kitts : II (III–IV)
Martinique : I–II (III)
Sint Eustatius : I–II (III)
Saba : I (II–III)

Perception Humaine	non ressenti	très faible	faible	légère	modérée	forte	très forte	sévère	violente	extrême
Dégâts Potentiels	aucun	aucun	aucun	aucun	très légers	légers	modérés	importants	destructions	généralisés
Accélérations (mg)	< 1.5	1.5 – 3.2	3.2 – 6.8	6.8 – 15	15 – 32	32 – 68	68 – 150	150 – 320	320 – 680	> 680
Intensités EMS98	I	II	III	IV	V	VI	VII	VIII	IX	X+

(*) mg = "milli gé" est une unité d'accélération correspondant au millième de la pesanteur terrestre
La ligne pointillée délimite la zone où le séisme a pu être potentiellement ressenti.

Figure 8: Exemple de bulletin « séisme ressenti » donnant les prédictions de mouvement du sol (valeurs d'accélération du sol en mg) dans les communes de Guadeloupe et Martinique. Ce calcul est basé sur la loi d'atténuation qui permet de prédire les intensités macroscopiques (code couleur et chiffres romains).

C. R. Geoscience xxx (2011) xxx–xxx

Contents lists available at SciVerse ScienceDirect

Comptes Rendus Geoscience

www.sciencedirect.com

Internal geophysics

Empirical model for rapid macroseismic intensities prediction in Guadeloupe and Martinique

Modèle empirique pour la prédiction rapide des intensités macrosismiques en Guadeloupe et Martinique

François Beauducel [a,*], Sara Bazin [b], Mendy Bengoubou-Valérius [c], Marie-Paule Bouin [a], Alexis Bosson [a], Christian Anténor-Habazac [a], Valérie Clouard [a], Jean-Bernard de Chabalier [a]

[a] *Institut de physique du globe de Paris, Sorbonne Paris Cité, Univ. Paris Diderot, UMR 7154 CNRS, 1, rue Jussieu, 75238 Paris cedex 05, France*
[b] *Norwegian Geotechnical Institute, N-0806 Oslo, Norway*
[c] *BRGM, Guadeloupe, 97113 Gourbeyre, Guadeloupe*

ARTICLE INFO

Article history:
Received 16 May 2011
Accepted after revision 21 September 2011
Available online xxx

Presented by Jean-Paul Poirier

Keywords:
Earthquake
Ground motion
Macroseismic intensity
Lesser Antilles
Peak ground acceleration

Mots-clés :
Séisme
Mouvements du sol
Intensité macrosismique
Petites Antilles
Accélérations maximales du sol

ABSTRACT

We describe a simple model for prediction of macroseismic intensities adapted to Guadeloupe and Martinique (Lesser Antilles), based on a combination of peak ground acceleration (PGA) predictive equation and a forward relation between acceleration and intensity. The PGA predictive equation is built from a 3-parameter functional form constrained by measurements from permanent accelerometer stations, mostly associated with Les Saintes crustal earthquake (21/11/2004, $M_w = 6.3$) and its many aftershocks. The forward intensity model is checked on a database of recent instrumental events of various origins with magnitudes 1.6 to 7.4, distances from 4 to 300 km, and observed intensities from I to VIII. Global sigma residual equals 0.8 in the MSK scale, suggesting a larger applicability range than the intermediate PGA predictive equation. The model is presently used by the French Lesser Antilles observatories to produce automatic reports for earthquakes potentially felt.

RÉSUMÉ

Nous proposons un modèle simple de prédiction des intensités macrosismiques, adapté à la Guadeloupe et à la Martinique (Petites Antilles), basé sur la combinaison d'une loi d'atténuation des accélérations horizontales maximales (PGA) et d'une relation directe entre accélération et intensité. Le modèle prédictif des PGA est contruit à partir d'une équation fonctionnelle à 3 paramètres contrainte par des données provenant de stations accélérométriques permanentes, principalement associées au séisme des Saintes (21/11/2004, $M_w = 6,3$) et ses nombreuses répliques. Le modèle prédictif d'intensité est testé sur une base de données instrumentale de séismes récents, de magnitudes 1,6 à 7,4, de distances 4 à 300 km et d'intensités observées entre I et VIII. Le résidu RMS final est de 0,8 sur l'échelle MSK, ce qui suggère un plus large domaine d'applicabilité que le modèle intermédiaire des PGA. Le modèle est actuellement utilisé par les observatoires des Antilles françaises pour produire des communiqués semi-automatiques, lors de séismes susceptibles d'être ressentis.

---

* Corresponding author.
E-mail address: beauducel@ipgp.fr (F. Beauducel).

1631-0713/$ – see front matter © 2011 Académie des sciences. Published by Elsevier Masson SAS. All rights reserved.
doi:10.1016/j.crte.2011.09.004

1. Introduction

The Lesser Antilles arc is a zone of convergence between the American plate and the Caribbean plate at a rate of about 2 cm/yr (Lopez et al., 2006). This movement is absorbed by the subduction of the American plate below the Caribbean plate and deformation of the wedge of the upper plate on a 100-250 km-wide zone, producing an extended system of active crustal faults (Fig. 1 insert, (Feuillet et al., 2002)). It results in a high seismicity level (about 1000 detected events per year) located on the subduction interface and within the slab with hypocentral depths ranging from 10 km up to 220 km, and within the deformed Caribbean plate with shallow crustal seismicity from 2 km up to 15–20 km in depth. Very shallow earthquakes occurring below/or very close to Guadeloupe archipelago islands can be felt sometimes with magnitude less than 2.0.

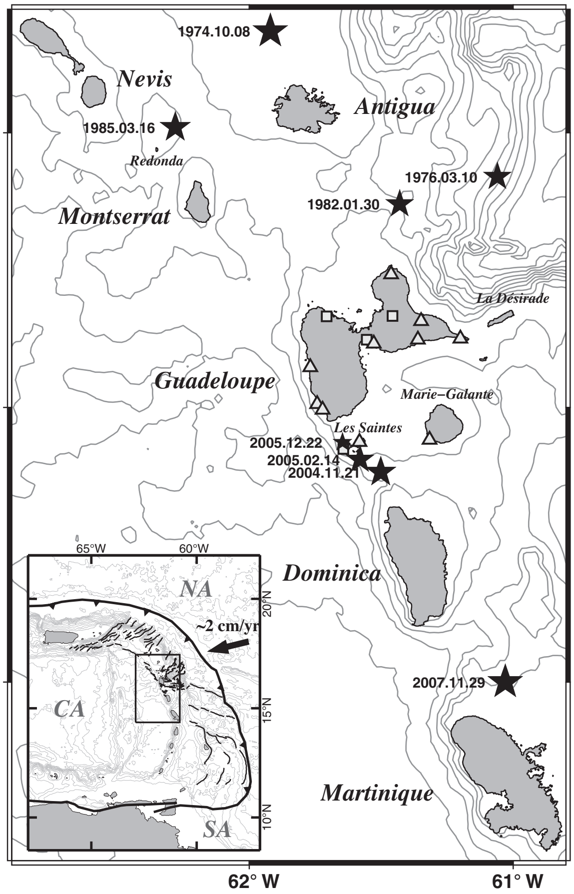

Fig. 1. Permanent network of digital accelerometers (TITAN AGECODAGIS, see http://www-rap.obs.ujf-grenoble.fr/) in Guadeloupe: soil (squares) and rock (triangles) site conditions (see Bengoubou-Valérius et al. (2008) for further details). Epicenters of some recent instrumental earthquakes are shown as black stars with dates (see text for details). Insert: Tectonic context of Lesser Antilles. CA = Caribbean plate, NA = North American plate, SA = South American plate. Black thick line with triangles: accretionary prism frontal thrust. Black lines: crustal faults from Feuillet et al. (2002). NA Euler vector of Lopez et al. (2006). Bathymetry data are 500 m contour lines (Smith and Sandwell, 1997).

Fig. 1. Réseau permanent d'accéléromètres du Rap (numériseurs Titan Agecodagis, voir http://www-rap.obs.ujf-grenoble.fr/) en Guadeloupe: conditions de site type sol (carrés) ou rocher (triangles) (voir (Bengoubou-Valérius et al., 2008) pour plus de détails). Les épicentres de quelques séismes instrumentaux sont indiqués par des étoiles avec dates (voir texte). Encart: contexte tectonique des Petites Antilles. CA = plaque Caraïbe, NA = plaque Nord-Américaine, SA = plaque Sud-Américaine. Courbe noire avec triangles: fosse frontale du prisme d'accrétion. Lignes noires: système de failles crustales d'après Feuillet et al. (2002). Vecteur d'Euler pour la plaque NA d'après Lopez et al. (2006). Données de bathymétrie: courbes de niveaux 500 m (Smith et Sandwell, 1997).

Since the French volcanological and seismological observatories (OVSG and OVSM) located in the Lesser Antilles are maintaining operational real-time seismic networks, they are responsible for detecting and informing local authorities and public of any felt earthquake occurrence and main event characteristics: location (epicenter and depth), type (tectonic or volcanic), magnitude, and maximum reported intensity in Guadeloupe and Martinique islands. Location and magnitude calculation are determined in a systematic way, using hand-picked phase arrivals and hypocenter inversion, and are available within few tens of minutes after an event, thanks to observatory permanent duty. Macroseismic intensities are determined later, as a result of detailed investigations in the field. However, in the case of a strongly felt earthquake, the first need of the local authorities is to get practical information on event location and maximum possible effects in the living areas. If this information can be delivered rapidly, it may be used to evaluate and focus assistance in the most affected zones.

On November 21, 2004, the occurrence of Les Saintes event, $M_w = 6.3$ and thousands of aftershocks in few days (Bazin et al., 2010; Beauducel et al., 2005; Bertil et al., 2004; Courboulex et al., 2010; IPGP, 2004) offered an exceptional new strong-motion database thanks to the French permanent accelerometric network (Pequegnat et al., 2008) installed in 2002–2004. Combined with collected testimonies and official intensity estimations for largest events, this provided a unique opportunity to establish a first local ground motion model adapted to the observatory needs.

In this article, we present the modeling strategy, dataset, results and applications of our empirical model. This work has been previously described in an internal report (Beauducel et al., 2005), named B^3 (from initials of the three original authors), and is presently used in Guadeloupe and Martinique seismological observatories to produce automatic reports.

2. Methodology

Our goal is to produce a predictive model of macroseismic intensities with a final uncertainty of about one intensity level, paying special attention to the maximum values that will be published after each earthquake. To be usable in an operative way, the model must be applicable to a wide range of magnitudes and hypocentral distances, and, ideally, independently from its tectonic context or depth.

Due to insular configuration of Lesser Antilles, most of epicenters occur offshore: it concerns 95 of $M \geq 2.5$ detected events (OVSG-IPGP database). Classical macroseismic intensity models cannot be used because they are

Please cite this article in press as: Beauducel F, et al. Empirical model for rapid macroseismic intensities prediction in Guadeloupe and Martinique. C. R. Geoscience (2011), doi:10.1016/j.crte.2011.09.004

based on maximum intensity at epicenter, I_0 (see for instance Pasolini et al. (2008), Sorensen et al. (2009)), a meaningless parameter for offshore events. Moreover, we do not have sufficient intensity data to well-constrain a predictive model for intensities. We have then proceeded by combining, first, a ground motion predictive equation (GMPE) constrained by peak ground accelerations (PGA) local data, and second, applying a forward empirical relation between intensities and accelerations.

Many empirical relations to predict earthquake ground motions have been developed for engineering purposes (see Abrahamson and Shedlock (1997), Bommer et al. (2010), Douglas (2003), Strasser et al. (2009) for a short review). Due to the necessary high precision for these specific applications (like building damage studies), models are developed using very selected datasets for specific applicability ranges of site conditions, magnitude and depth. Moreover, none of them is valid for magnitudes lower than 4.

Furthermore, a recent study Douglas et al. (2006), shows that ground motions observed on Guadeloupe and Martinique are poorly estimated by commonly-used GMPE, having smaller and more variable amplitudes than expected.

In this work, we do not intend to produce a new GMPE for the engineering community; we need a more general model with certainly higher uncertainty, but applicable over a wide range of earthquakes to be used in an operative way. In the following, we check results and residuals of our obtained PGA model as an intermediate stage, but in order to validate the choices made to produce automatic reports, we emphasize tests of the final intensity model performance in terms of medians across full range of intensity and distance applicability and beyond.

3. Intermediate PGA predictive equation

3.1. Formulation and dataset

Due to the limited database and model purpose, we use one of the simplest form of GMPEs with only 3 parameters (Berge-Thierry et al., 2003):

$$\log(PGA) = aM + bR - \log(R) + c \tag{1}$$

where PGA is the horizontal acceleration peak (in g), M is the magnitude, R is the hypocentral distance (in km), and a, b, c are constant parameters.

This functional form implies many hypothesis. In particular, a radial distribution of ground motion around a point source, neglecting geological heterogeneities, tectonic origin, source extension and radiation pattern. Fukushima (1996) also points out that a linear $\log(D)/M$ formulation is not verified for magnitudes ≥ 6.5 for which a M^2 term should be necessary. This concerns magnitudes

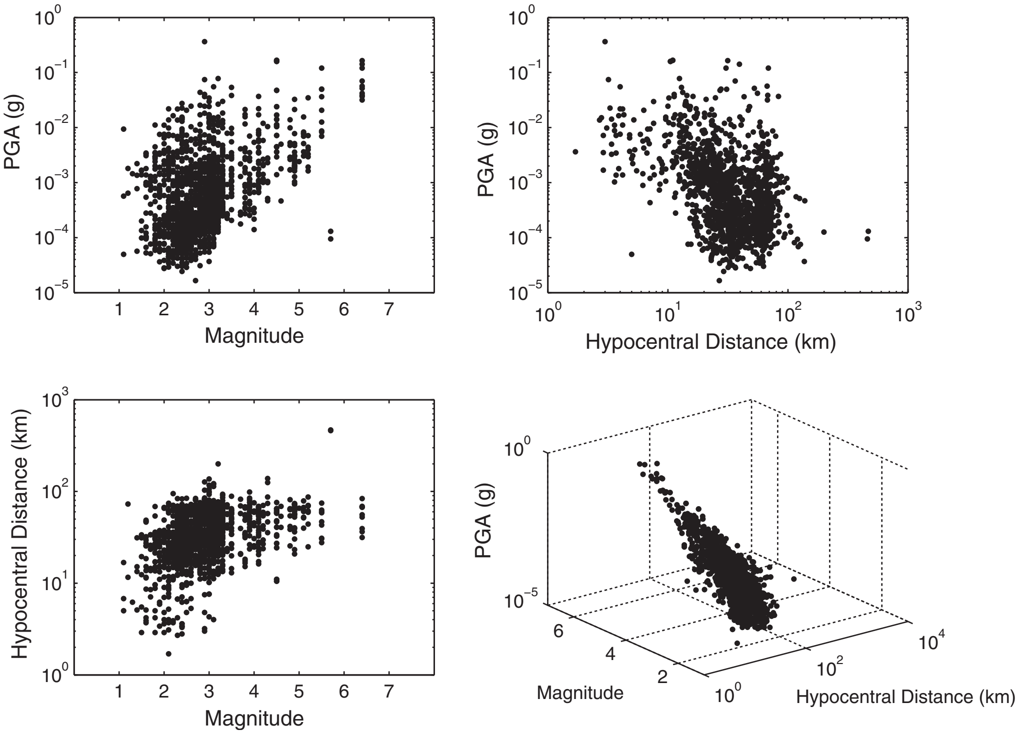

Fig. 2. Presentation of the seismic events dataset: 1430 triggers recorded by 14 permanent accelerometer stations from 2004.11.21 to 2004.12.28. Data are presented in 3-D view for different X-Y combinations of magnitudes, hypocentral distances (in km) and PGA values (in g). In the 3-D graph the view angle has been chosen to highlight the planar characteristic of the dataset.

Fig. 2. Données sismiques utilisées: 1430 déclenchements enregistrés par 14 stations accélérométriques permanentes entre le 21 novembre 2004 et le 28 décembre 2004. Les données sont présentées pour différentes combinaisons X-Y de magnitudes, distances hypocentrales (en km) et valeurs de PGA (en g). Sur le graphe 3D, l'angle de vue a été ajusté pour mettre en évidence l'aspect planaire du jeu de données.

Please cite this article in press as: Beauducel F, et al. Empirical model for rapid macroseismic intensities prediction in Guadeloupe and Martinique. C. R. Geoscience (2011), doi:10.1016/j.crte.2011.09.004

out of our study range, but we will keep in mind that accelerations should be underestimated at long distance for large magnitudes.

To inverse the three parameters, we use seismic data recorded at 14 strong-motion permanent stations in Guadeloupe (see Fig. 1), with mixed site conditions, rock and soil (details about the seismic stations can be found in (Bengoubou-Valérius et al., 2008)), in the period from November 21 to December 28, 2004. The dataset includes about 400 earthquakes associated to 1430 triggers of 3-component acceleration waveforms. These events correspond to Les Saintes main shock $M_w = 6.3$ and mostly the associated aftershocks, but also some regional events that we voluntarily kept in the database.

Locations and magnitudes come from the seismic catalog of the Guadeloupe observatory (OVSG-IPGP). Magnitudes were computed using the classical formula of duration magnitude from Lee et al. (1975) for events $M_d \leq 4.5$ (Clément et al., 2000; Feuillard, 1985), and we imposed the moment magnitude from worldwide networks for greater events. This allows us to overcome the problem of duration magnitude saturation for magnitude greater than 4.5. The consistency of magnitude scale (M_d versus M_w) has been checked by Bengoubou-Valérius et al. (2008).

For each event, a value of PGA is calculated as the maximum amplitude of horizontal acceleration signals, using the modulus of a complex vector defined by the two horizontal and orthogonal components $x(t)$ and $y(t)$. The PGA dataset is presented in Figs. 2 and 3. Magnitudes range from 1.1 to 6.3, hypocentral distances from 2 to 450 km, and PGA from 16 μg to 0.36 g.

3.2. *Best model determination and residuals*

To calculate the 3 parameters in Eq. (1), we minimized a misfit function using the L_2-norm. Due to the inhomogeneous dataset (magnitudes follow a power-law and there is more short-distance values), we applied a simple weighting function by multiplying the misfit by the magnitude and a power of the hypocentral distance. This gave more weight for large magnitudes and long distances.

The inversion scheme yields the following parameters: $a = 0.61755$, $b = -0.0030746$, and $c = -3.3968$. It produced an RMS residual on $\log(PGA)$ of 0.47 (a factor of 3 in PGA, see Fig. 4). This value is higher than classical published GMPE results (around 0.3, see Strasser et al. (2009)), and it confirms the observation of Douglas et al. (2006) about abnormal data variability in Lesser Antilles. However, interestingly, this factor corresponds to the average ratio between rock and soil conditions in the observed PGA (Bengoubou-Valérius et al., 2008). This might also reflect the wide range of magnitudes and distances in a too simple functional form. In order to follow some of the key considerations used to develop GMPEs (Bommer et al., 2010), we checked medians and sigmas of PGA residuals (Fig. 4): it shows a very consistent distribution in the full magnitude range (from 2 to 6), while we observe a significant PGA underestimation (median around +0.5 so a factor 3 in amplitude) for $D < 15$ km.

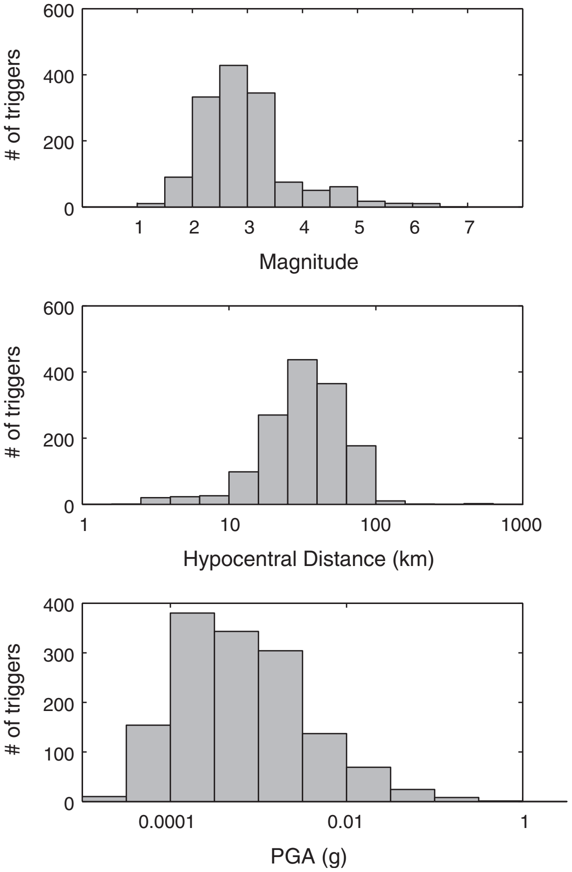

Fig. 3. Histograms of the seismic dataset: number of trigger versus magnitude, hypocentral distance (in km) and PGA value (in g).

Fig. 3. Histogrammes des données: nombre de déclenchements en fonction de la magnitude, de la distance hypocentrale (en km) et du PGA (en g).

Eq. (1) with the parameters found is represented as an abacus in Fig. 5 showing calculated PGA as a function of hypocentral distance (from 3 to 500 km) and magnitudes 1 to 8.

Note that we voluntarily limited the minimum hypocentral distance for each magnitude, as we do not take into account the near fault saturation term. It is reasonable to assume that this minimum hypocentral distance is greater than rupture size. Earthquake magnitude reflects the seismic moment which is proportional to the total displacement averaged over the fault surface (Aki, 1972; Kanamori, 1977). Many authors propose a simple formula to express the relationship between magnitude and fault length or rupture area (Liebermann and Pomeroy, 1970; Mark, 1977; Wells and Coppersmith, 1994; Wyss, 1979). Here we use Wyss's formula (Wyss, 1979):

$$M = \log(A) + 4.15 \tag{2}$$

where M is the magnitude and A the rupture surface. We decide to restrict the attenuation law of Eq. (1) to the domain $R > L$, where $L \approx A^{\frac{1}{2}}$ is an estimation of the fault characteristic size.

Please cite this article in press as: Beauducel F, et al. Empirical model for rapid macroseismic intensities prediction in Guadeloupe and Martinique. C. R. Geoscience (2011), doi:10.1016/j.crte.2011.09.004

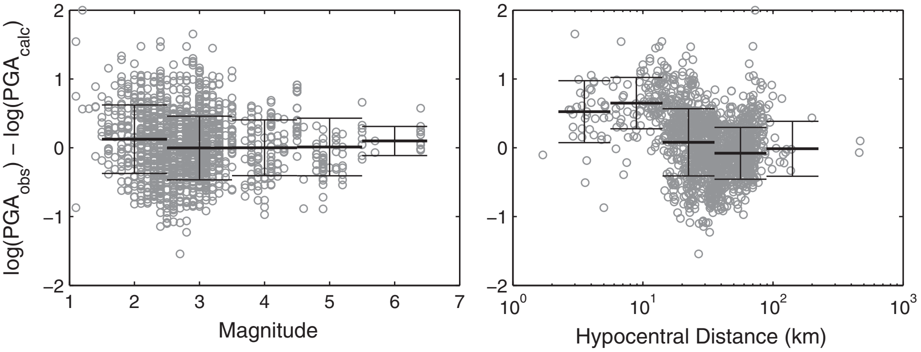

Fig. 4. PGA model residuals distribution: difference between observed and calculated log(PGA) versus magnitude and hypocentral distance (km). Horizontal segments with error bars stand for median values and associated standard deviations for each corresponding intervals. Global sigma of PGA residuals equals 0.47 (a factor of 3).

Fig. 4. Résidus du modèle PGA: différence entre log(PGA) observé et calculé en fonction de la magnitude et de la distance hypocentrale. Les segments horizontaux avec barres d'erreur représentent les valeurs médianes et l'écart-type associé pour chaque intervalle. L'écart-type global des résidus est égal à 0.47 (un facteur 3).

3.3. *Examples of predicted and observed PGA*

Fig. 6 shows representative events with observed PGA compared to our model predictions. We do not limit examples to the events from the dataset which reflects the previous residual analysis (Fig. 4), but present events in the period 2004 to 2007 with various depths, in crustal or subduction context, and for which sufficient triggers were available. As seen in Fig. 6, most of PGA values are predicted within the model uncertainty. Medians of $\log(PGA)$ residuals are equal to $+0.15$, $+0.28$, $+0.10$, $+0.19$, $+0.24$, and -0.01 for Fig. 6a to f events, respectively.

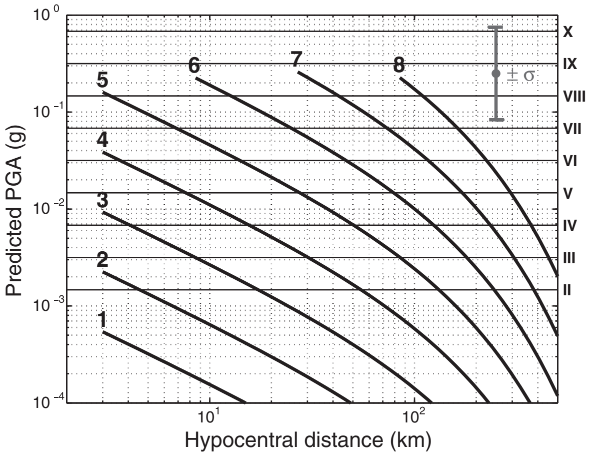

Fig. 5. The B^3 prediction model: simulation of PGA (left Y-axis and log dotted horizontal grid) and MSK intensities (right Y-axis with roman numerals and solid thin horizontal lines) versus hypocentral distance (X-axis) and magnitude (thick solid lines and numbers). Uncertainty interval (σ = factor 3 in PGA) is indicated as gray vertical error bar. MSK is defined in Medvedev et al. (1967).

Fig. 5. Modèle B^3: simulation des PGA (axe des ordonnées à gauche et grille logarithmique horizontale) et intensités MSK (axe des ordonnées de droite avec chiffres romains et lignes horizontales) en fonction de la distance hypocentrale (abscisses) et de la magnitude (lignes épaisses et chiffres en gras). L'intervalle d'incertitude (σ = facteur 3 sur le PGA) est indiqué par une barre d'erreur verticale grise. L'échelle MSK est définie dans Medvedev et al. (1967).

We denote, for these 6 particular examples, a light tendency for PGA underestimation, which seems independent from magnitude. This is consistent with Fig. 4 residual analysis. The only significant PGA misfit appears for one soil condition station in the near field ($\approx$ 15 km) for Les Saintes aftershocks (Figs. 6b and c), that is systematically underestimated by a factor of about 10.

We also compare these results with two published GMPE adapted to shallow crustal events: Sadigh et al. (1997) and Ambraseys (1995). The Sadigh et al. (1997) model is very similar to our PGA model for magnitudes ≥ 5.0 (Figs. 6a, c and f) but has poor fitting for lower magnitudes (Figs. 6b, d and e) with a systematic overestimation. The Ambraseys (1995) model has a globally poor fitting, with an overestimation of PGA, particularly for $M < 5.0$.

4. Macroseismic intensities

4.1. *Formulation*

Although we know that the spectral frequency content of ground acceleration and peak velocity have important implications on building damage, establishing a direct relation between a single PGA value and macroseismic intensity has proved its efficiency in many cases (Chiaruttini and Siro, 1981; Margottini et al., 1992; Murphy et al., 1977; Wald et al., 1999). For the Lesser Antilles, we follow the suggestion of Feuillard (1985) who studied the historical and instrumental seismicity using the simple empirical relation of Gutenberg and Richter (1942):

$$I = 3\log(PGA) + 3/2 \qquad (3)$$

where I is the mean intensity (MSK scale), PGA is maximum acceleration (in cm.s$^{-2} \approx$ mg). Combining Eqs. (1), (2) and (3) made the final empirical model formulation (hereafter called the B^3 prediction):

$$\begin{cases} I & = & 1.85265M - 0.0092238R - 3\log(R) + 0.3096 \\ R & > & 10^{\dfrac{M-4.15}{2}} \end{cases} \qquad (4)$$

Please cite this article in press as: Beauducel F, et al. Empirical model for rapid macroseismic intensities prediction in Guadeloupe and Martinique. C. R. Geoscience (2011), doi:10.1016/j.crte.2011.09.004

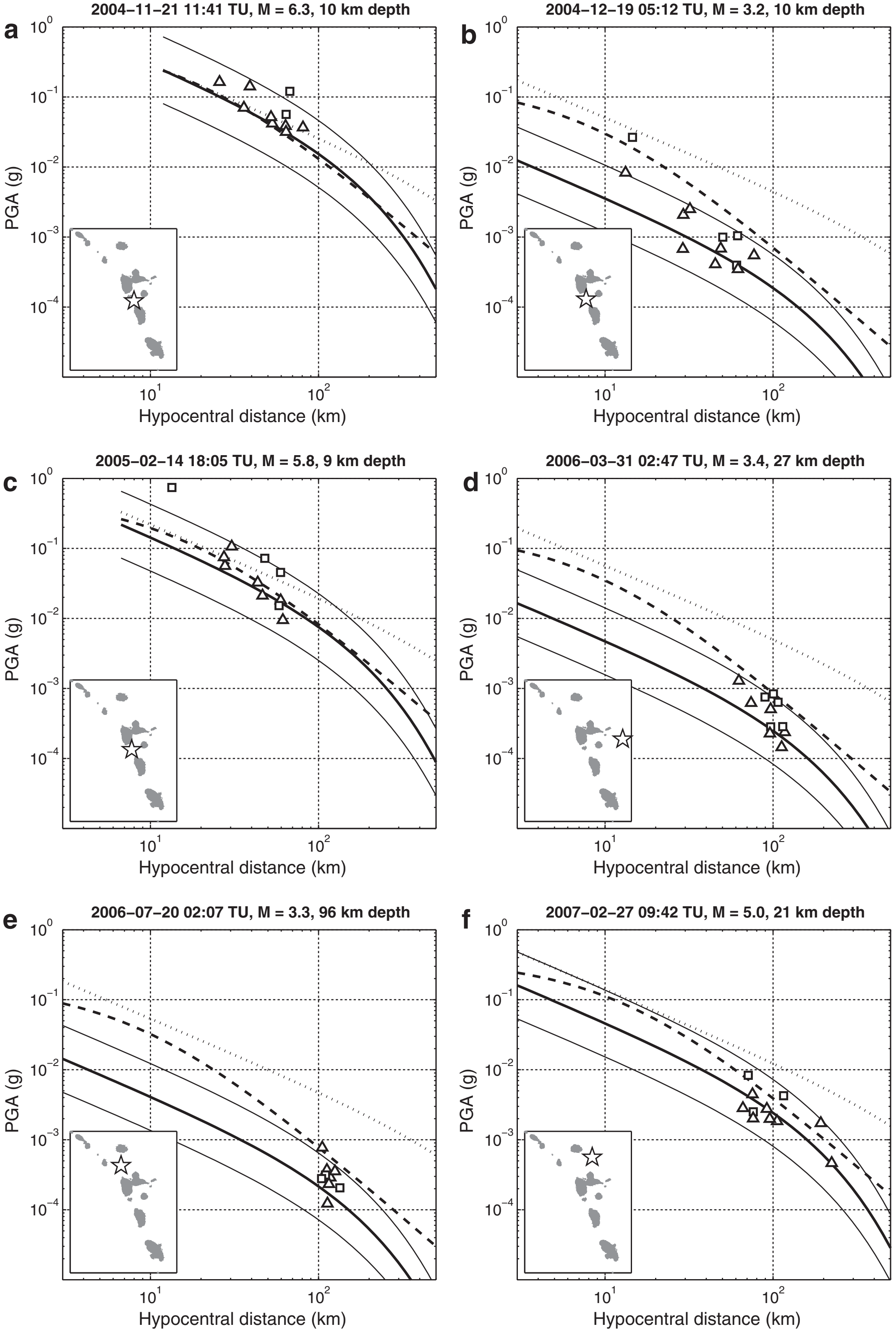

Fig. 6. PGA prediction (solid thick curve) and uncertainty (solid thin curves) for various magnitudes and depths. The recorded PGA values are presented in squares in the case of soil site condition and in triangles for rock site condition. Are also shown other attenuation laws: Sadigh et al. (1997) (dashed curve) and Ambraseys (1995) (dotted curve). Inset maps show epicenter location for each event (star). *a*) Les Saintes main shock, *b*) and *c*) are aftershocks. *d*) is a shallow subduction event located east of Guadeloupe. *e*) is a deep subduction event located north of Guadeloupe. *f*) is a shallow crustal event located south of Antigua.

Please cite this article in press as: Beauducel F, et al. Empirical model for rapid macroseismic intensities prediction in Guadeloupe and Martinique. C. R. Geoscience (2011), doi:10.1016/j.crte.2011.09.004

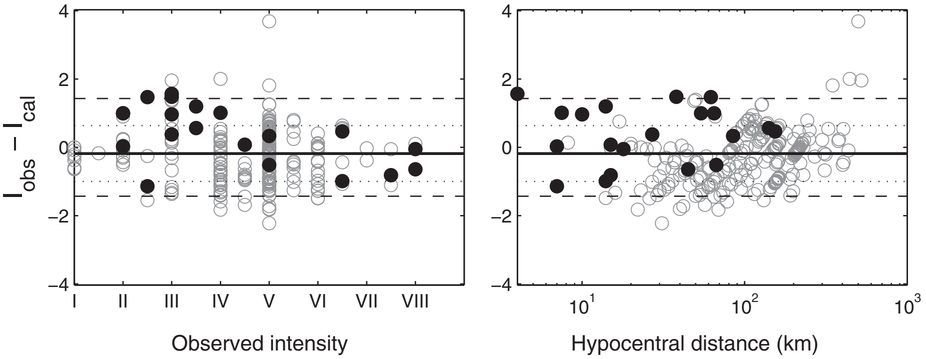

Fig. 7. Intensity model residuals distribution for 20 earthquakes (254 macroseismic observations): difference between observed and calculated intensities versus observed intensity and hypocentral distance (km). Solid black circles indicate the maximum observed intensity for each event. Thick black line = median value (−0.2). Dotted lines = standard deviation (±0.85). Dashed lines = PGA standard deviation equivalent (±1.4).

Fig. 7. Distribution des résidus du modèle prédictif des intensités pour 20 séismes (254 observations macrosismiques): différence entre intensité observée et calculée en fonction des intensités observées et de la distance hypocentrale (km). Les disques noirs indiquent l'intensité observée maximum pour chaque événement. Ligne épaisse = valeur médiane (−0, 2). Lignes pointillées = écart-type (±0, 85). Lignes tiretées = écart-type PGA équivalent (±1, 4).

Note that following the MSK scale, intensity must be an integer value. In this article, we decided arbitrarily to round I to the nearest and smallest integer (e.g., $I = 6.0$ to 6.9 correspond to intensity of VI).

The resulting model for intensities is presented as right Y-axis in Fig. 5. Following Eq. (3), the 0.47 uncertainty on our predicted log(PGA), would imply an uncertainty on I of ±1.4, on which we should add the uncertainty of Eq. (3) itself, which is unknown.

4.2. Intensity model residuals

We test our model on a database of 20 recent earthquakes for which we have intensity reports (a total of 254 observations) as well as instrumental magnitudes and hypocenter locations. Events are from various origins with magnitudes 1.6 to 7.4, distances from 4 to 500 km, and observed intensities from I to VIII. This wide panel of event characteristics allows us to check our model applicability.

We present in Fig. 7 the intensity residuals versus observed intensity and hypocentral distance. Global standard deviation equal 0.8, with a near zero median value. Residuals are also well distributed over the intensity and distance ranges. Since this database is not statistically sufficient, we will keep uncertainty on intensities deduced from the PGA residuals, i.e., $\sigma = 1.4$ corresponding to 68 confidence interval. We also checked that maximum observed intensity for each event is strictly below this probability level (see Fig. 7 solid circles).

4.3. Examples of simulated and observed intensities

In Fig. 8, we detail eight examples of the most significant events with observed and predicted intensities (see epicenters in Fig. 1).

Fig. 8a shows the October 10, 1974 "Antigua" earthquake (McCann et al., 1982; Tomblin and Aspinall, 1975), $M_s = 7.4$, a shallow 30 km-depth with normal-fault mechanism, M_s from NEIC USGS, location and MSK intensities from McCann et al. (1982). Maximum intensities and distance of observations vary from VIII at 45 km in Antigua to II at 400 km in Virgin Islands. All the observations (9 sites) are within the B^3 prediction uncertainty limits. The median of intensity residuals equals −0.6, sigma is 0.5. This is an unexpected positive result since the model is extrapolated for magnitudes larger than Les Saintes ($M_w = 6.3$); so this magnitude 7.4 is formally out of our interval of validity. Note also that near-field intensities (at 45 km) seem correctly fitted by the model while this hypocentral distance is very close to our limit defined by Eq. (2), which gives $L = 42$ km.

Fig. 8b shows the March 10, 1976 earthquake, a magnitude $M_b = 5.9$, 56 km-depth on subduction interface north of Guadeloupe (M_b from USGS-NEIC, location and MSK intensities from Feuillard (1985)). Maximum intensities and distances of observations vary from V in Le Moule (Guadeloupe) at 85-km, to II in Martinique at 150 km distance. Most of the 22 observed intensities are underestimated (median of residuals is +0.4) but still within one sigma uncertainty (RMS equals 0.5).

Fig. 8c shows the January 30, 1982 earthquake, a magnitude $M_w = 6.0$, 63 km-depth on subduction interface north of Guadeloupe (M_w and location from Global CMT Project, MSK intensities from Feuillard (1985)). Maximum intensities and distances of observations vary from V in various urban districts of Guadeloupe and Antigua at 90 km distance, to II in Barbuda (130 km). Most of the 34 observed intensities are within the B^3 uncertainty limits, with a zero median and RMS on intensity residuals equal to 0.7.

Fig. 6. Prédiction des PGA (courbe épaisse) et incertitudes (courbes fines) pour différentes magnitudes et profondeurs. Les PGA observés sont présentés par des carrés pour les conditions de site type sol, et par des triangles pour les conditions de site type roche. Sont aussi indiquées d'autres lois d'atténuation: Sadigh et al. (1997) (courbe tiretée) et Ambraseys (1995) (courbe pointillée). Les cartes en encart indiquent la position de l'épicentre pour chaque événement (étoile). *a*) Choc principal du séisme des Saintes, *b*) et *c*) sont des répliques. *d*) Séisme superficiel sur le plan de subduction à l'est de la Guadeloupe. *e*) Séisme profond de subduction au nord de la Guadeloupe. *f*) Séisme crustal superficiel au sud d'Antigua.

Please cite this article in press as: Beauducel F, et al. Empirical model for rapid macroseismic intensities prediction in Guadeloupe and Martinique. C. R. Geoscience (2011), doi:10.1016/j.crte.2011.09.004

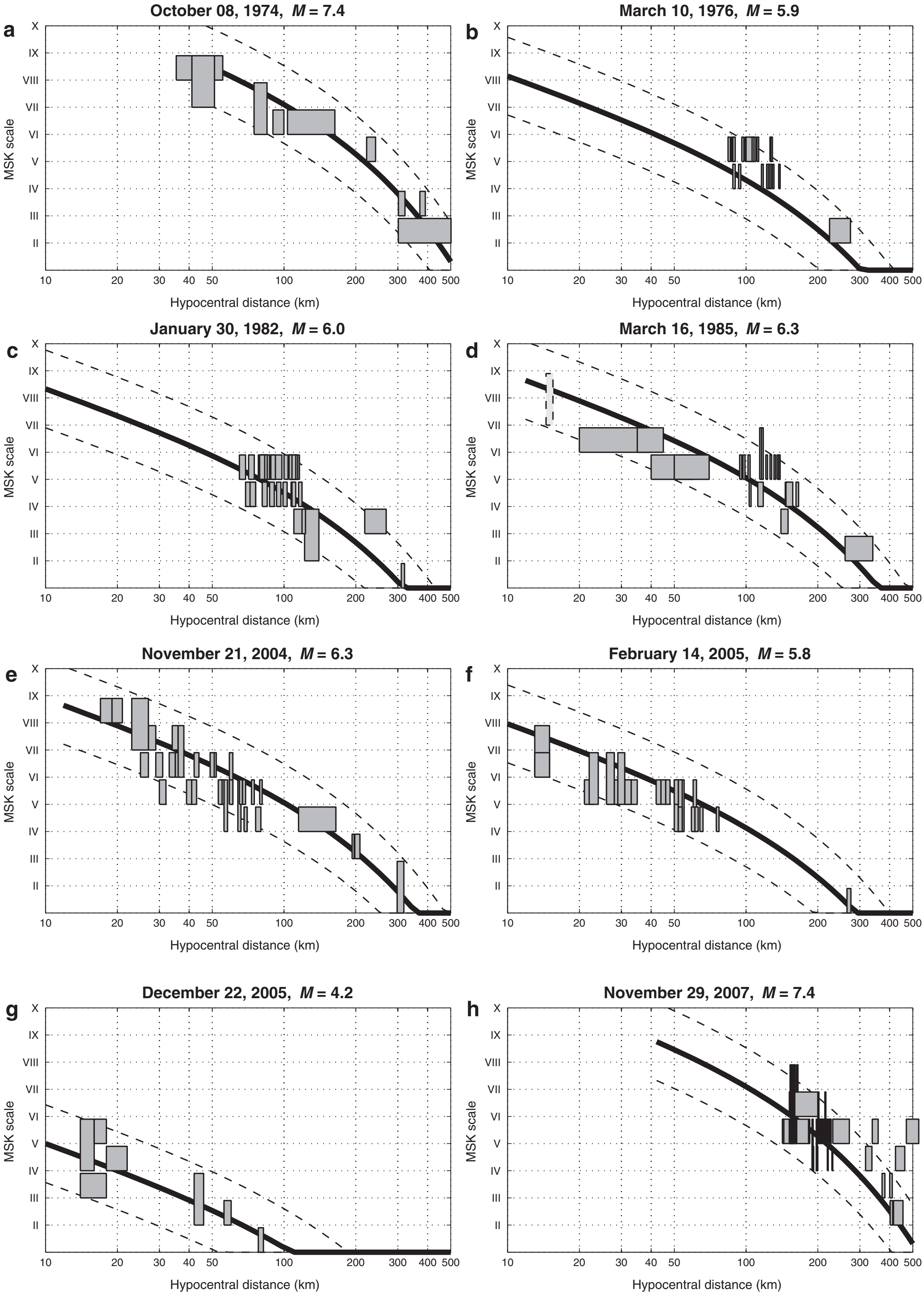

Fig. 8. Examples of B^3 predicted intensities for 8 instrumental earthquakes: observed macroseismic intensities (MSK) are presented versus hypocentral distance (km). Gray thick curve stands for the predicted intensity for given magnitude, dashed curves indicate uncertainties, solid rectangles represent

Fig. 8d shows the March 16, 1985 "Redonda" earthquake (Feuillet et al., 2010; Girardin et al., 1991), a magnitude $M_w = 6.3$, 10 km-depth normal-fault (M_w and location from Global CMT Project, MSK intensities from Feuillard (1985)). Maximum intensities and distances of observations vary from VI at 30 km in Montserrat to II at 300 km in Martinique. We added a supposed intensity of VII-VIII (light gray dashed rectangle) because important cliff collapses have been observed in the Redonda island, at 10 km-distance from epicenter. All the 23 observed intensities are within the B^3 uncertainty limits ($RMS = 0.7$) with zero median. Note a very local amplification effect that occurred in the region of Pointe-à-Pitre (Guadeloupe) with an intensity of V to VI at 120 km from the hypocenter.

Fig. 8e shows the November 21, 2004 Les Saintes main shock earthquake of magnitude $M_w = 6.3$, M_w from Global CMT Project, location from Bazin et al. (2010), EMS98 intensities (see definition in Grunthal et al. (1998)) from an official survey by the BCSF (Cara et al., 2005). Maximum intensities and distances of observations vary from VIII at 20 km in Les Saintes to IV at 140 km in Martinique, and correspond to detailed studies carried on by BCSF in 33 different urban districts. All the 29 observed intensities are within the B^3 uncertainty limits ($RMS = 0.6$, median = -0.9).

Fig. 8f shows the largest Les Saintes aftershock, on February 14, 2005 of magnitude $M_w = 5.8$, located south of Terre-de-Haut (M_w and location from Global CMT Project, MSK intensities from OVSG-IPGP). Maximum intensities and distances of observations vary from VII at 14 km in Les Saintes to IV at 74 km in Anse-Bertrand (Guadeloupe). All the 25 observed intensities are within the B^3 uncertainty limits ($RMS = 0.3$, median = -1.0) with a global light overestimation.

Fig. 8g shows one of the numerous Les Saintes aftershocks, on December 22, 2005 of magnitude $M_d = 4.2$, located north of Terre-de-Bas (M_d, location and MSK intensities from OVSG-IPGP, unpublished). Maximum intensities and distances of observations vary from V at 15 km in Basse-Terre to II at 58 km in Saint-François (Guadeloupe). All the 7 observed intensities are within the B^3 uncertainty limits ($RMS = 0.6$, median = -0.3).

Fig. 8h shows the November 29, 2007 Martinique intermediate-depth (152 km) intraslab earthquake of magnitude $M_w = 7.4$, M_w and location from Bouin et al. (2010) and Global CMT Project, with EMS98 intensities from an official survey by the BCSF (Schlupp et al., 2008). Maximum intensities and distances of observations vary from VII at 150 km in Martinique to II at 400 km in St-Barthelemy, and correspond to detailed studies carried on by BCSF in 70 different urban districts in Guadeloupe and Martinique, plus other islands reports. Most of the 74 observed intensities are within the B^3 uncertainty limits ($RMS = 0.83$, median = -0.1), but we note three underestimated intensities at long distances: V in Saint-Vincent (250 km) and Trinidad (500 km), and IV in Anguilla (443 km). This may be due to local site amplifications because of low frequency content of the seismic waves.

These eight examples confirm that B^3 model seems able to predict average intensities within a global residual of $\sigma = 1.4$ degree in the MSK scale, for events of magnitudes up to 7.4 in Lesser Antilles context with various hypocentral distances. This value corresponds to 68 of confidence interval and gives a convincing maximum possible intensity even when local site effects are observed.

5. Automatic intensity report

These good results and the apparent robustness of the B^3 model made us confident of the release of a semi-automatic theoretical intensity report at the Guadeloupe and Martinique observatories. For each located event, maximum intensity is computed for all towns of Lesser Antilles islands. If at least one location reaches an intensity of II, it means that the event has been potentially felt and an automatic report is produced, waiting for seismologist validation.

This simulation allows us: (1) to confirm that inhabitants may have (or not) felt the event when intensity interval varies from II to III in a town; and (2) to publish immediately and blindly (without any testimonies) the information of a possible felt earthquake when the predicted maximum intensity reaches IV, which means a 68 confidence level for an intensity between I-II and IV.

The report (see an example in Fig. 9) includes a synthetic text resuming the date, location and type of event, the maximum intensity prediction value and corresponding town name and distance. To better take into account potential site effects and increase the precision of the result, the average prediction is given together with the upper limit value ($I + \sigma = I + 1.4$) for potential site effects, and MSK intensities are indicated in half-unit values, i.e., $I = 6.0$ to 6.4 is "VI", and $I = 6.5$ to 6.9 is "VI-VII". The exhaustive list of urban districts for which theoretical intensity reaches at least II is given. Note that it includes all islands in the Lesser Antilles, while our model has been mainly checked with Guadeloupe and Martinique intensities. This may constitutes a future extension of our study.

The report also includes a location map that presents the islands and towns, earthquake epicenter and theoretical isoseist curves using a shaded color map. A detailed table legend explains the MSK scale and corresponding name, color, PGA interval, potential damage and human perception.

intensity observations. *a*), *d*), *e*), *f*) *g*) are shallow crustal earthquakes, *b*) and *c*) are ≈ 60 km-depth subduction slab interface, *h*) is an intermediate depth intraslab subduction.

Fig. 8. Exemples des intensités prédites B^3 pour 8 séismes instrumentaux: intensités macrosismiques observées (MSK) en fonction de la distance hypocentrale (km). La courbe épaisse grise réprésente l'intensité prédite pour une magnitude donnée, les courbes tiretées indiquent l'incertitude, les rectangles pleins représentent les intensités observées. *a*), *d*), *e*), *f*) *g*) sont des séismes crustaux, *b*) et *c*) sont des séismes à l'interface de subduction à ≈ 60 km de profondeur, *h*) est un séisme de subduction *intraslab* de profondeur intermédiaire.

Please cite this article in press as: Beauducel F, et al. Empirical model for rapid macroseismic intensities prediction in Guadeloupe and Martinique. C. R. Geoscience (2011), doi:10.1016/j.crte.2011.09.004

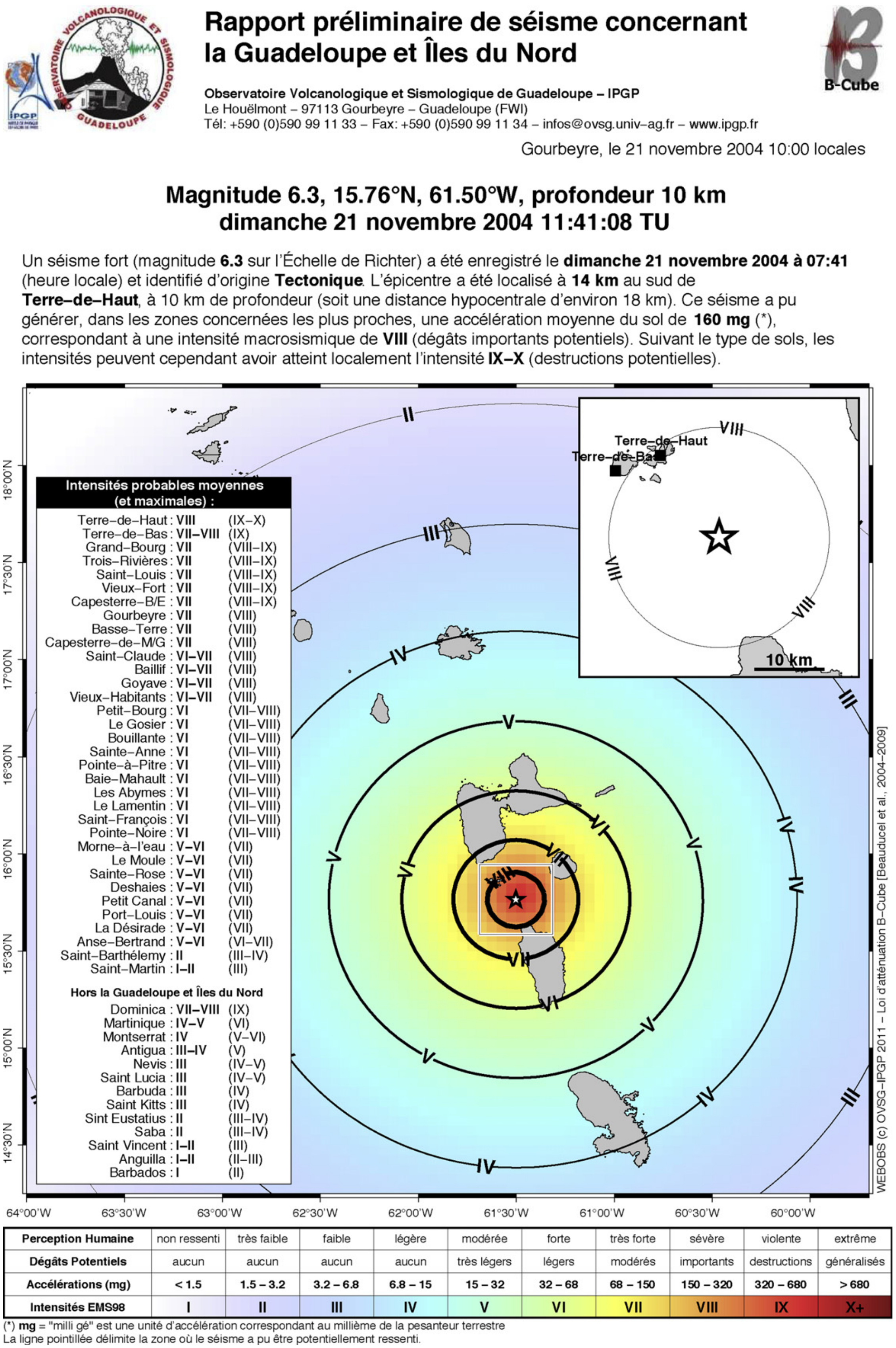

Rapport préliminaire de séisme concernant la Guadeloupe et Îles du Nord

Observatoire Volcanologique et Sismologique de Guadeloupe – IPGP
Le Houëlmont – 97113 Gourbeyre – Guadeloupe (FWI)
Tél: +590 (0)590 99 11 33 – Fax: +590 (0)590 99 11 34 – infos@ovsg.univ-ag.fr – www.ipgp.fr

Gourbeyre, le 21 novembre 2004 10:00 locales

Magnitude 6.3, 15.76°N, 61.50°W, profondeur 10 km
dimanche 21 novembre 2004 11:41:08 TU

Un séisme fort (magnitude **6.3** sur l'Échelle de Richter) a été enregistré le **dimanche 21 novembre 2004 à 07:41** (heure locale) et identifié d'origine **Tectonique**. L'épicentre a été localisé à **14 km** au sud de **Terre-de-Haut**, à 10 km de profondeur (soit une distance hypocentrale d'environ 18 km). Ce séisme a pu générer, dans les zones concernées les plus proches, une accélération moyenne du sol de **160 mg** (*), correspondant à une intensité macrosismique de **VIII** (dégâts importants potentiels). Suivant le type de sols, les intensités peuvent cependant avoir atteint localement l'intensité **IX–X** (destructions potentielles).

Intensités probables moyennes (et maximales) :

Terre–de–Haut : **VIII** (IX–X)
Terre–de–Bas : **VII–VIII** (IX)
Grand–Bourg : **VII** (VIII–IX)
Trois–Rivières : **VII** (VIII–IX)
Saint–Louis : **VII** (VIII–IX)
Vieux–Fort : **VII** (VIII–IX)
Capesterre–B/E : **VII** (VIII–IX)
Gourbeyre : **VII** (VIII)
Basse–Terre : **VII** (VIII)
Capesterre–de–M/G : **VII** (VIII)
Saint–Claude : **VI–VII** (VIII)
Baillif : **VI–VII** (VIII)
Goyave : **VI–VII** (VIII)
Vieux–Habitants : **VI–VII** (VIII)
Petit–Bourg : **VI** (VII–VIII)
Le Gosier : **VI** (VII–VIII)
Bouillante : **VI** (VII–VIII)
Sainte–Anne : **VI** (VII–VIII)
Pointe–à–Pitre : **VI** (VII–VIII)
Baie–Mahault : **VI** (VII–VIII)
Les Abymes : **VI** (VII–VIII)
Le Lamentin : **VI** (VII–VIII)
Saint–François : **VI** (VII–VIII)
Pointe–Noire : **VI** (VII–VIII)
Morne–à–l'eau : **V–VI** (VII)
Le Moule : **V–VI** (VII)
Sainte–Rose : **V–VI** (VII)
Deshaies : **V–VI** (VII)
Petit Canal : **V–VI** (VII)
Port–Louis : **V–VI** (VII)
La Désirade : **V–VI** (VII)
Anse–Bertrand : **V–VI** (VI–VII)
Saint–Barthélemy : **II** (III–IV)
Saint–Martin : **I–II** (III)

Hors la Guadeloupe et Îles du Nord

Dominica : **VII–VIII** (IX)
Martinique : **IV–V** (VI)
Montserrat : **IV** (V–VI)
Antigua : **III–IV** (V)
Nevis : **III** (IV–V)
Saint Lucia : **III** (IV–V)
Barbuda : **III** (IV)
Saint Kitts : **III** (IV)
Sint Eustatius : **II** (III–IV)
Saba : **II** (III–IV)
Saint Vincent : **I–II** (III)
Anguilla : **I–II** (II–III)
Barbados : **I** (II)

WEBOBS (c) OVSG–IPGP 2011 – Loi d'atténuation B-Cube [Beauducel et al., 2004–2009]

Perception Humaine	non ressenti	très faible	faible	légère	modérée	forte	très forte	sévère	violente	extrême
Dégâts Potentiels	aucun	aucun	aucun	aucun	très légers	légers	modérés	importants	destructions	généralisés
Accélérations (mg)	**< 1.5**	**1.5 – 3.2**	**3.2 – 6.8**	**6.8 – 15**	**15 – 32**	**32 – 68**	**68 – 150**	**150 – 320**	**320 – 680**	**> 680**
Intensités EMS98	**I**	**II**	**III**	**IV**	**V**	**VI**	**VII**	**VIII**	**IX**	**X+**

(*) **mg** = "milli gé" est une unité d'accélération correspondant au millième de la pesanteur terrestre
La ligne pointillée délimite la zone où le séisme a pu être potentiellement ressenti.

Please cite this article in press as: Beauducel F, et al. Empirical model for rapid macroseismic intensities prediction in Guadeloupe and Martinique. C. R. Geoscience (2011), doi:10.1016/j.crte.2011.09.004

6. Discussion and conclusions

We propose a simple empirical model for macroseismic intensities prediction for observatory operational purpose. The model is based on intermediate PGA model that has been adjusted using a shallow crustal normal-fault sequence of events. The functional form is only 3-parameters dependent which implies many assumptions and simplifications, but makes it also extremely robust with an uncertainty higher than usual GMPE (a factor of 3). This can be explained also by the fact that we do not select specific site conditions in the database, mixing rock and soil stations. The obtained PGA model has strong potential limits and may not be very useful for engineering purposes, but it exhibits a better fit than previous existing GMPE for Lesser Antilles. Its application domain should be limited to crustal events, magnitude range up to 6.3, and distance range up to 100–200 km.

The deduced intensity model is tested on a wider range of magnitudes, distances and source types of earthquakes. We suggest that the B^3 model is able to correctly predict intensities within ± 1.4 (1σ), for magnitudes up to 7.4 and hypocentral distance up to 300 km. At longer distances, we observe a clear underestimation of intensities. A major result of our work is that the final equation seems to exhibit a larger applicability range than intermediate PGA predictive equation. In particular, greater magnitudes and other types of earthquakes such as those located in the subduction slab are well modeled within the given uncertainties.

This model is currently used to produce automatic reports in Guadeloupe (since January 2005) and Martinique (since September 2008) observatories in order to anticipate potentially felt events immediately after the location and magnitude calculation. On a total amount of about 10,000 located events in Guadeloupe, a third has been potentially felt (minimal intensity of II) and has produced an automatic report. Following the observatory convention, only 200 reports were effectively sent as a public communiqué, when the minimum theoretical intensity reached IV or, in case of lower intensity (II or III), when immediate testimonies were received from inhabitants.

During more than 5 years of continuous seismic monitoring and thanks to inhabitants testimonies, the B^3 model is daily controlled by observatory team: comparisons between observations and predicted intensities exhibit an average uncertainty less than ±1 unit in the MSK scale.

The reports were also used for seismic hazard awareness and education of the public and local authorities. Particularly, explaining the fundamental difference between magnitude and intensity of an earthquake, the MSK scale, the uncertainty of prediction due to the law's empirical aspect and simplicity, and the potential site condition effects, thus earthquake-resistant construction advice.

Acknowledgments

FB thanks Pascal Bernard and Nathalie Feuillet for useful discussions, Victor Huerfano and Fabrice Cotton for very constructive comments that helped us to greatly improve the initial manuscript. Acceleration data come from the French national strong motion permanent network *Réseau Accélérométrique Permanent* (RAP), available at http://www-rap.obs.ujf-grenoble.fr/. Stations have been installed and maintained from 2002 to 2004 thanks to the effort of technicians from the observatory of Guadeloupe (OVSG-IPGP): Alberto Tarchini†, Christian Lambert, Laurent Mercier, Alejandro Gonzalez, and Thierry Kitou. Authors warmly thank Guadeloupe inhabitants for their collaboration in collecting testimonies. This is an IPGP contribution #3222.

References

Abrahamson, N., Shedlock, K., 1997. Overview (of modern attenuation relationships). Seismol. Res. Lett. 68 (1), 9–23.

Aki, K., 1972. Earthquake mechanism. Tectonophysics 13 (1-4), 423–446.

Ambraseys, N., 1995. The prediction of earthquake peak ground acceleration in Europe. Earthquake Engin. & Struct. Dyn. 24 (4), 467–490.

Bazin, S., Feuillet, N., Duclos, C., Crawford, W., Nercessian, A., Bengoubou-Valérius, M., Beauducel, F., Singh, S., 2010. The 2004-2005 Les Saintes (French West Indies) seismic aftershock sequence observed with ocean bottom seismometers. Tectonophysics 489 (1-4), 91–103.

Beauducel, F., Anténor-Habazac, C., Bazin, S., de Chabalier, J., Nercessian, A., Feuillet, N., Jacques, E., Bertil, D., Boudon, G., Le Friant, A., Tapponnier, P., Hirn, A., Lépine, J., Bernard, P., Komorowski, J., King, G., OVSG team, 2005a. The Mw 6.3 earthquake of Les Saintes (Guadeloupe) on November 21, 2004.In: European Seismological Commission Annual Workshop. IAVCEI.

Beauducel, F., Bazin, S., Bengoubou-Valérius, M., 2005b. Loi d'atténuation B-Cube pour l'évaluation rapide des intensités sismiques probables dans l'Archipel de Guadeloupe. Internal Report pp 16, Institut de Physique du Globe de Paris. http://www.ipgp.fr/~beaudu/download/2004_Beauducel_B3.pdf.

Fig. 9. Example of observatory communiqué published in case of potential felt event: here an a posteriori simulation of Les Saintes main shock (data from OVSG-IPGP). The B^3 model is used to estimate the probable macroseismic intensities. Are indicated the exhaustive list of towns or neighborough islands where the event could be felt, with maximum intensity in case of site amplification (after Beauducel et al. (2005))

Title: *"Preliminary report of earthquake in Guadeloupe and Northern Islands"*

Main text: *"A strong earthquake (magnitude 6.3 on the Richter Scale) was recorded on Sunday, November 21, 2004 at 07:41 (local time) and identified with tectonic origin. The epicenter was located 14 km south of Terre-de-Haut, 10 km-depth (hypocentral distance of about 18 km). This earthquake may have generated, in the closest areas from epicenter, an average ground acceleration of 160 mg (*), corresponding to macroseismic intensity of VIII (severe potential damages). However, depending on the type of soil, the intensities may have reached locally an intensity of IX-X (potential destructions)."*

Towns list: *"Average (and maximum) probable intensities:"*

Table: *"Human perception / Potential damages / Accelerations (mg) / MSK Intensity"*

Note: *"(*) 'mg' is a unit of acceleration equal to one thousandth of Earth's gravity"*

Fig. 9. Exemple de communiqué publié par l'observatoire en cas de séisme ressenti: ici une simulation a posteriori du séisme des Saintes (données OVSG-IPGP). Le modèle B^3 est utilisé pour estimer les intensités moyennes probables. Est mentionnée la liste exhaustive des communes ou îles voisines ayant pu ressentir le séisme, avec les intensités maximales (en cas d'effets de sites) (d'après Beauducel et al. (2005)).

Please cite this article in press as: Beauducel F, et al. Empirical model for rapid macroseismic intensities prediction in Guadeloupe and Martinique. C. R. Geoscience (2011), doi:10.1016/j.crte.2011.09.004

Bengoubou-Valérius, M., Bazin, S., Bertil, D., Beauducel, F., Bosson, A., 2008. CDSA: A New Seismological Data Center for the French Lesser Antilles. Seismol. Res. Lett. 79 (1), 90.

Berge-Thierry, C., Cotton, F., Scotti, O., Griot-Pommera, D., Fukushima, Y., 2003. New empirical response spectral attenuation laws for moderate European earthquakes. J. Earthquake Eng. 7 (2), 193–222.

Bertil, D., Bazin, S., Mallarino, D., Beauducel, F., 2004. Séisme des Saintes: rapport de synthèse. Tech. rep., Centre de Données Sismologiques des Antilles (CDSA), BRGM/IPGP/UAG.

Bommer, J., Douglas, J., Scherbaum, F., Cotton, F., Bungum, H., Fah, D., 2010. On the selection of ground-motion prediction equations for seismic hazard analysis. Seismol. Res. Lett. 81 (5), 783.

Bouin, M.-P., Bouchon, M., Coutant, O., Bazin, S., Latchman, J., 2010. Source parameters of the Mw 7.4 Martinique intermediate-depth earthquake (Leeward islands) of November 29, 2007: A slab-pull event with horizontal fault plane.In: EGU General Assembly 2010, held 2-7 May, 2010, Vienna, Austria, p. 5555.

Cara, M., Bertil, D., Feuillet, N., Jacques, E., Tapponnier, P., Guéguen, P., Bengoubou-Valérius, M., Sira, C., Lebrun, B., Beauducel, F., 2005. Séisme des Saintes (Guadeloupe) du 21 novembre 2004, note préliminaire. Tech. rep., Bureau Central de Sismologie Française.

Chiaruttini, C., Siro, L., 1981. The correlation of peak ground horizontal acceleration with magnitude, distance, and seismic intensity for Friuli and Ancona, Italy, and the Alpide belt. Bull. Seismol. Soc. Am. 71 (6), 1993.

Clément, C., Bernard, P., Viodé, J., Anténor-Habazac, C., Lépine, J., Beauducel, F., 2000. Compilation et validation du catalogue de sismicité des observatoires IPGP des Antilles. Tech. rep., Ministère de l'Aménagement du Territoire et de l'Environnement, Institut de Physique du Globe de Paris.

Courboulex, F., Converset, J., Balestra, J., Delouis, B., 2010. Ground-motion simulations of the 2004 mw 6.4 Les Saintes, Guadeloupe, earthquake using ten smaller events. Bull. Seismol. Soc. Am. 100 (1), 116.

Douglas, J., 2003. Earthquake ground motion estimation using strong-motion records: a review of equations for the estimation of peak ground acceleration and response spectral ordinates. Earth Sci. Rev. 61 (1-2), 43–104.

Douglas, J., Bertil, D., Roullé, A., Dominique, P., Jousset, P., 2006. A preliminary investigation of strong-motion data from the French Antilles. J. Seismol. 10 (3), 271–299.

Feuillard, M., 1985. Macrosismicité de la Guadeloupe et de la Martinique. Ph.D. thesis, Institut de Physique du Globe de Paris.

Feuillet, N., Leclerc, F., Tapponnier, P., Beauducel, F., Boudon, G., Le Friant, A., Deplus, C., Lebrun, J., Nercessian, A., Saurel, J., et al., 2010. Active faulting induced by slip partitioning in Montserrat and link with volcanic activity: New insights from the 2009 GWADASEIS marine cruise data. Geophys. Res. Lett. 37 .

Feuillet, N., Manighetti, I., Tapponnier, P., Jacques, E., 2002. Arc parallel extension and localization of volcanic complexes in Guadeloupe, Lesser Antilles. J. Geophys. Res. 107, 2331.

Fukushima, Y., 1996. Scaling relations for strong ground motion prediction models with m2 terms. Bull. Seismol. Soc. Am. 86 (2), 329.

Girardin, N., Feuillard, M., Viodé, J., 1991. Réseau régional sismique de l'arc des Petites Antilles; sismicité superficielle (1981-1988). Bull. Soc. geol. France 162 (6), 1003.

Grunthal, G., Musson, R., Schwarz, J., Stucchi, M., 1998. European Macroseismic Scale 1998 (EMS-98). Cahiers du Centre Européen de Géodynamique et de Séismologie 15 .

Gutenberg, B., Richter, C., 1942. Earthquake magnitude, intensity, energy, and acceleration. Bull. Seismol. Soc. Am. 32 (3), 163–191.

IPGP, 2004. Bilan mensuel de l'activité volcanique de la Soufrière de Guadeloupe et de la sismicité régionale. Public reports of OVSG-IPGP ISSN 1622-4523, Institut de Physique du Globe de Paris. http://www.ipgp.fr.

Kanamori, H., 1977. The energy release in great earthquakes. J. Geophys. Res. 82 (20), 2981–2987.

Lee, W., Lahr, J., N.C.E.R., 1975. HYPO71 (revised): a computer program for determining hypocenter, magnitude, and first motion pattern of local earthquakes. US Dept. of the Interior, Geological Survey, National Center for Earthquake Research.

Liebermann, R., Pomeroy, P., 1970. Source dimensions of small earthquakes as determined from the size of the aftershock zone. Bull. Seismol. Soc. Am. 60 (3), 879.

Lopez, A., Stein, S., Dixon, T., Sella, G., Calais, E., Jansma, P., Weber, J., LaFemina, P., 2006. Is there a northern Lesser Antilles forearc block? Geophys. Res. Lett. 33 (L07313).

Margottini, C., Molin, D., Serva, L., 1992. Intensity versus ground motion: a new approach using Italian data. Eng. Geol. 33 (1), 45–58.

Mark, R., 1977. Application of linear statistical models of earthquake magnitude versus fault length in estimating maximum expectable earthquakes. Geology 5 (8), 464.

McCann, W., Dewey, J., Murphy, A., Harding, S., 1982. A large normal-fault earthquake in the overriding wedge of the Lesser Antilles subduction zone: The earthquake of 8 October 1974. Bull. Seismol. Soc. Am. 72 (6A), 2267.

Medvedev, S., Sponheuer, W., Karnik, V., 1967. Seismic intensity scale version 1964. Inst. Geody. Publ. 48 .

Murphy, J., O'Brien, l., 1977. The correlation of peak ground acceleration amplitude with seismic intensity and other physical parameters. Bull. Seismol. Soc. Am. 67 (3), 877.

Pasolini, C., Gasperini, P., Albarello, D., Lolli, B., D'Amico, V., 2008. The attenuation of seismic intensity in Italy, part I: Theoretical and empirical backgrounds. Bull. Seismol. Soc. Am. 98 (2), 682.

Pequegnat, C., Gueguen, P., Hatzfeld, D., Langlais, M., 2008. The French accelerometric network (RAP) and national data centre (RAP-NDC). Seismol. Res. Lett. 79 (1), 79–89.

Sadigh, K., Chang, C., Egan, J., Makdisi, F., Youngs, R., 1997. Attenuation relationships for shallow crustal earthquakes based on California strong motion data. Seismol. Res. Lett. 68 (1), 180.

Schlupp, A., Sira, C., Cara, M., Bazin, S., Michel, C., Régnier, J., Beauval, C., Feuillet, N., De Chabalier, J., Barras, A., et al., 2008. Séisme de Martinique du 29 novembre 2007. Synthèse sismologique et étude macrosismique BCSF2008-R1, Bureau Central Sismologique Français 266 .

Smith, W., Sandwell, D., 1997. Global sea floor topography from satellite altimetry and ship depth soundings. Science 277 (5334), 1956.

Sorensen, M., Stromeyer, D., Grunthal, G., 2009. Attenuation of Macroseismic Intensity: A New Relation for the Marmara Sea Region, Northwest Turkey. Bull. Seismol. Soc. Am. 99 (2A), 538.

Strasser, F., Abrahamson, N., Bommer, J., 2009. Sigma: Issues, insights, and challenges. Seismol. Res. Lett. 80 (1), 40–56.

Tomblin, J., Aspinall, W., 1975. Reconnaissance report of the antigua, west indies, earthquake of october 8, 1974. Bull. Seismol. Soc. Am. 65 (6), 1553.

Wald, D., Quitoriano, V., Heaton, T., Kanamori, H., 1999. Relationships between peak ground acceleration, peak ground velocity, and modified Mercalli intensity in California. Earthquake Spectra 15, 557.

Wells, D., Coppersmith, K., 1994. New empirical relationships among magnitude, rupture length, rupture width, rupture area, and surface displacement. Bull. Seismol. Soc. Am. 84 (4), 974–1002.

Wyss, M., 1979. Estimating maximum expectable magnitude of earthquakes from fault dimensions. Geology 7 (7), 336.

Please cite this article in press as: Beauducel F, et al. Empirical model for rapid macroseismic intensities prediction in Guadeloupe and Martinique. C. R. Geoscience (2011), doi:10.1016/j.crte.2011.09.004

2.2 Mise en commun des données sismologiques de l'arc Antillais

L'arc des Petites Antilles couvre une région de 1 000 km du Nord au Sud et 700 km d'Ouest en Est. Cinq institutions émettent des bulletins sismologiques dans cette région : l'IPGP avec les bulletins compilés de l'OVSG et de l'OVSM depuis 1950, le Puerto Rico Seismic Network (PRSN), le Fundacion Venezolana de Investigationes Sismologicas (FUNVISIS) au Venezuela, le Seismic Research Unit (SRU) à Trinidad, et le U.S. Geological Survey (USGS) pour les événements de magnitude supérieure à 4. Ces centres utilisent des formats de données sismologiques hétérogènes, des modèles de vitesse de propagation sismique distincts et réalisent leurs calculs de magnitudes de façons différentes. Par exemple, les observatoires de l'IPGP utilisaient depuis très longtemps une magnitude locale basée sur la durée, mais cette dernière était imprécise et n'avait pas de signification physique.

Le CDSA est né d'une collaboration entre les trois organismes de recherche de Sciences de la Terre présents dans les Antilles Françaises (IPGP, BRGM, UAG). Sa mission principale a été de compiler toutes les données sismologiques disponibles sur l'ensemble de l'arc, de les rendre homogènes et de les mettre à disposition de la communauté scientifique et du public. Les réseaux utilisés présentent une très grande hétérogénéité dans les types des capteurs, les fréquences des mesures, les formats de stockage, le délai de récupération des données et la qualité de leur base temps. Plus de 120 stations provenant de 10 réseaux différents et de différents types de capteurs (courte-période, large-bande, accéléromètres) sont concernées. Le Centre a pu être créé grâce à un cofinancement de la Région Guadeloupe qui a également financée une bourse de thèse, celle de Mendy Bengoubou-Valerius. Nous avons, avec les informaticiens des observatoires et les collègues du BRGM conçu et installé le Centre dans les locaux de l'OVSG alors que j'étais en poste. Il a finalement été inauguré dans les locaux du BRGM en 2008.

L'article présenté dans ce chapitre a été rédigé par M.B.-V. dans le cadre de sa thèse, il porte sur l'exploitation de la base de données du CDSA, pour essayer de mieux contraindre les caractéristiques de la sismicité de l'arc grâce à la relocalisation des cinq premières années du CDSA. Je n'ai co-encadré M.B.-V. que pendant la première moitié de sa thèse à l'OVSG, essentiellement pour définir les contours de ses recherches et mettre en place les données nécessaires. Elle a suspendu ses recherches pendant un congé maternité, puis je suis partie en poste à l'OVSM pendant la seconde moitié de sa thèse.

Cet article a permis une vision plus homogène de la sismicité de l'arc des Petites Antilles mettant ainsi en évidence des zones de plus faible activité, au nord près des Iles Vierges et au sud entre Sainte-Lucie et Grenade. L'amélioration de la précision de localisation permet d'aligner les séismes « intraslab » jusqu'à une profondeur de l'ordre de 200 km, avec un angle relativement constant, proche de 50°, entre Sainte-Lucie et Nevis. Ses relocalisations permettent aussi de faire un parallèle entre les structures tectoniques et la sismicité superficielle détectée autour de la Guadeloupe et de la Martinique. Par ailleurs, son travail a permis de définir les paramètres de la distribution de Gutenberg-Richter. Cette loi de puissance découverte par Gutenberg et Richter en 1954, met en relation le nombre de séisme N dépassant une certaine magnitude M et les magnitudes observées. La relation $\log(N) = a - b.M$ met en évidence le niveau d'activité des régions étudiées. L'aplatissement de la courbe de distribution à faible magnitude met en évidence la magnitude de complétude des réseaux de surveillance. Cette magnitude est estimée entre 2 et 3 le long de l'arc.

CDSA: A New Seismological Data Center for the French Lesser Antilles

**Mendy Bengoubou-Valerius,[1, 2] Sara Bazin,[2] Didier Bertil,[3]
François Beauducel,[2] and Alexis Bosson[2]**

INTRODUCTION

The Lesser Antilles, in the eastern Caribbean, is prone to a large seismic hazard due to the subduction of the Atlantic lithosphere beneath the Caribbean plate, with a slow convergence rate of 2 cm/yr (Demets *et al.* 2000; Mann *et al.* 2002). The largest historical earthquake in the region, in 1843 between Guadeloupe and Antigua, had a magnitude estimate of 7.5 to 8 (Bernard and Lambert 1988), but historical seismicity covers too short a period of time (less than three and one-half centuries) to estimate the recurrence time of strong events or their plausible maximum magnitude. The latest destructive earthquake, Les Saintes in Guadeloupe in 2004, had a magnitude 6.3 (Institut de Physique du Globe de Paris 2004; Bertil *et al.* 2004).

To better understand the regional geodynamics and assess the related seismic hazard, we must improve our knowledge and our understanding of the area's present seismicity. Since the 1950s, several regional research institutes have monitored local seismicity. The Institut de Physique du Globe de Paris (IPGP) and Bureau de Recherches Géologiques et Minières (BRGM) have set up various seismological and accelerometric arrays to monitor the French islands of Guadeloupe and Martinique. As a consequence, several large datasets with very different formats and time spans exist, scattered among several sites. Providing a more integrated database for the seismicity of the Lesser Antilles arc was the primary motivation for creating the French Antilles Seismological Data Base (Centre de Données Sismologiques des Antilles, CDSA).

The aim of this paper is to introduce the newly created CDSA and to illustrate its capacity for improving our knowledge of the region's seismicity. In the first part of this study, we present the various arrays, waveform databases, and seismicity catalogs used by the CDSA. In the second part, we present and discuss new results provided by the CDSA database, particularly in terms of variations of seismic intensity along the arc, geometry of the subducting slab, and peak acceleration attenuation law.

WEAK- AND STRONG-MOTION REGIONAL ARRAYS

The study area is located at the eastern border of the Caribbean plate between 10° and 20° N and 58° and 65° W. It is bounded to the north by the Puerto Rico trench and to the South by El Pilar fault in Venezuela, and it extends as far west as the Aves Rise. Therefore, it completely covers the Lesser Antilles volcanic arc, the Barbados accretionary prism and the subduction trench. This area spans 1,000 km north to south and 700 km east to west and is much wider than the area covered by the French monitoring network. So far, the French observatories of Guadeloupe and Martinique (OVSG and OVSM) have been able to locate seismic events only within a 300-km radius.

Five institutions (listed in table 1) publish regular seismic catalogs for the Lesser Antilles. Figure 1 presents examples of seismicity during a five-year period from these five catalogs. Each provides complementary information. The Puerto Rico Seismic Network (PRSN) is centered on the island of Puerto Rico, while the Fundacion Venezolana de Investigationes Sismologicas (FUNVISIS) is centered on Venezuela. IPGP

TABLE 1
Sources of Seismic Catalogs for the Lesser Antilles.

Institution	Institution Code
Puerto Rico Seismic Network (PRSN)/ University of Puerto Rico http://redsismica.uprm.edu/	PRSN
Institut de Physique du Globe de Paris (IPGP) http://www.ipgp.jussieu.fr/	OVSG/OVSM
Seismic Research Unit (SRU)/ University of West Indies (UWI) http://www.uwiseismic.com/	SRU
Fundacion Venezolana de Investigationes Sismologicas (FUNVISIS) http://www.funvisis.gob.ve/	FUNVISIS
United State Geological Survey (USGS) http://earthquake.usgs.gov/	USGS

---

1. Université des Antilles et de la Guyane
2. Institut de Physique du Globe de Paris
3. Bureau de Recherches Géologiques et Minières

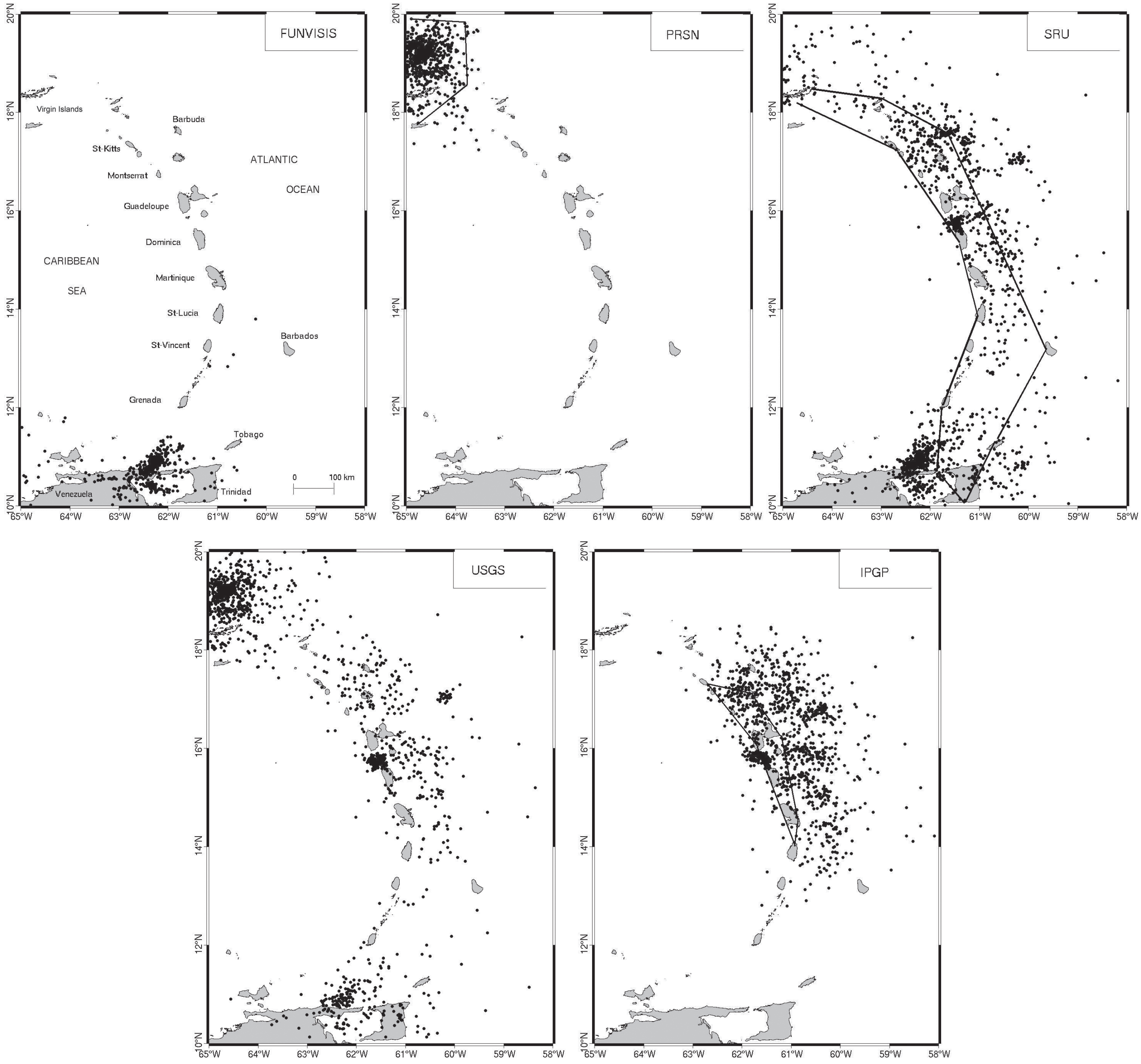

▲ **Figure 1.** Seismicity maps for magnitude > 2.7 from the five regional reports used by CDSA: PRSN, FUNVISIS, SRU, USGS, IPGP. The volcanic arc of the Lesser Antilles is located between the Caribbean Sea and the Atlantic Ocean, resulting from the subduction of the American plate under the Caribbean plate. The polygons show the area covered by each network by linking the outermost stations.

publishes a monthly synthesis from the OVSG and OVSM arrays, which cover the region between Antigua and St. Lucia. The Seismic Research Unit (SRU) array covers the whole arc, but its detection threshold is relatively high. The U.S. Geological Survey (USGS) provides a world seismicity catalog with a detection threshold of magnitude 4 in the Lesser Antilles.

The Eastern Caribbean region is known as a moderate-to-high seismic hazard area (Bernard and Lambert 1988; Tanner and Shedlock 2004). But until the mid-1990s, very little strong-motion data had been recorded. Until now, strong-motion data have not been included in attenuation models for the Lesser Antilles. Regional seismic hazard assessments are based on general attenuation models such as Youngs *et al.* (1997), Sadigh *et al.* (1997), or Ambraseys *et al.* (2005), which are not necessarily suitable for the local tectonic context. Local geology and topography in Martinique and Guadeloupe show large zones where strong amplification of surface ground motions are reported (Gagnepain-Beyneix *et al.* 1995; Castro *et al.* 2003; Lebrun *et al.* 2004).

BRGM installed its first strong-motion array in Guadeloupe in 1977, equipped with SMA-1 Kinemetrics analog instruments. Only one earthquake (16 March 1985, M_w =

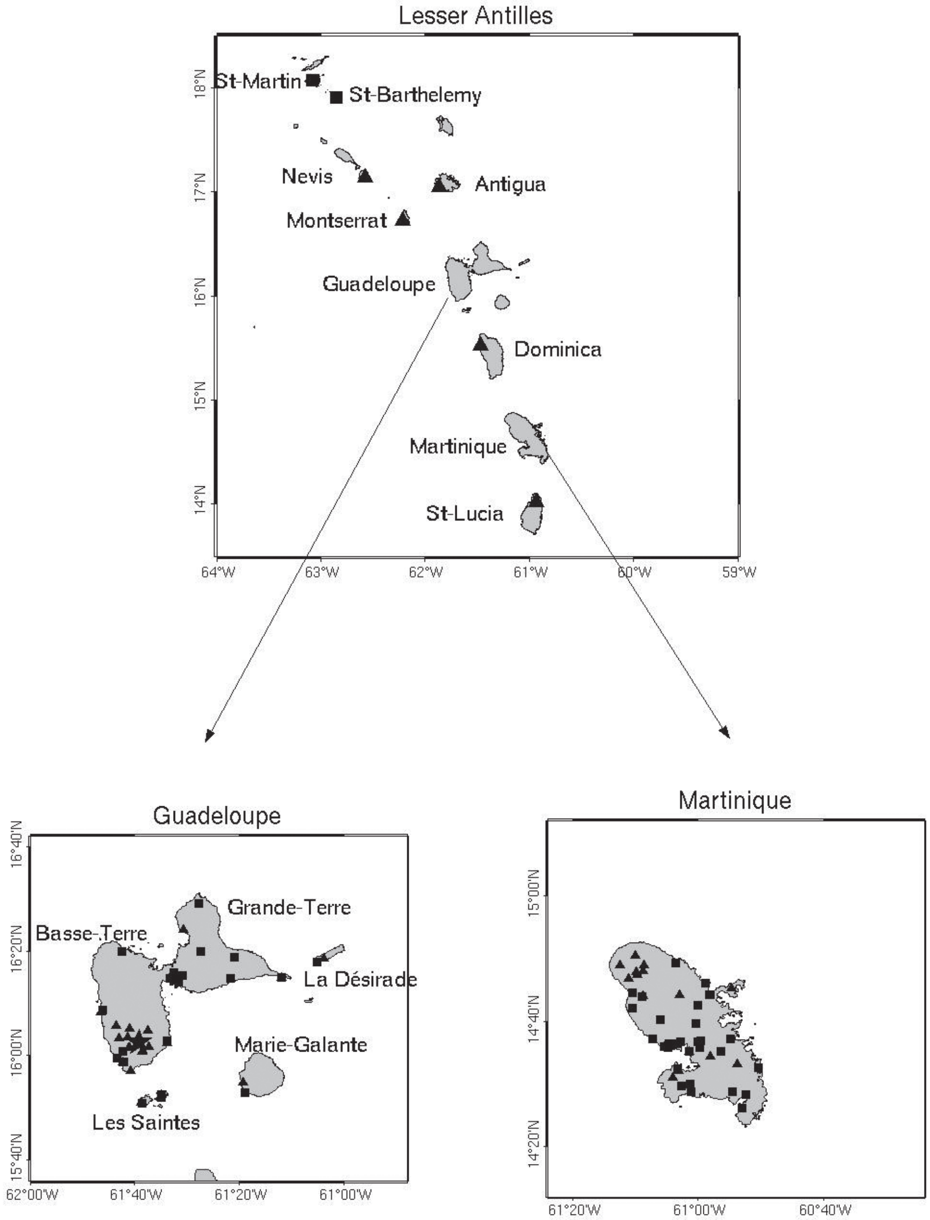

▲ **Figure 2.** Station maps used by CDSA in Lesser Antilles, Guadeloupe, and Martinique. Squares indicate accelerometric stations, triangles indicate short-period seismometers, and the star shows the location of the broadband network of Soufriére volcano in Guadeloupe.

6.4 at epicentral distances of more 100 km) was recorded by these stations (Bernard and Lambert 1986). During the past 10 years, several digital accelerometric arrays have been established in the French West Indies. In 1994, BRGM installed the first digital accelerometric network to study site effects in urban areas. The Conseil Général Martinique has instrumented public buildings in Martinique since 1999. IPGP installed 27 permanent stations in Martinique and Guadeloupe from 2001 to 2005 as part of the French Permanent Accelerometric Array (Réseau Accélérométrique Permanent, RAP) and of CDSA. Two of those accelerometers have been installed in St. Martin and St. Barthélemy islands, which are French overseas collectivities or territories in the northern Lesser Antilles arc. Figure 2 shows the spatial distribution of stations, and table 2 describes the arrays. The RAP records are transmitted to the RAP central office (http://www-rap.obs.ujf-grenoble.fr) at the Laboratoire de Géophysique interne et tectonophysique (LGIT) at the Université Joseph Fourier (UJF) in Grenoble (France). All these strong-motion records, which are scattered among three institutions and in various numerical formats, are collected by CDSA.

CDSA DATA PROCESSING

The Centre de Données Sismologiques des Antilles (CDSA) was created to make available on request technical and scientific information about seismic activity in the Lesser Antilles. The Center involves three institutions: the Institut de Physique

TABLE 2
Sources of Seismic Data Used by CDSA. In total, for 2005 the CDSA used 120 stations including 42 short-period stations, 10 broadband stations, and 69 accelerometric stations.

Network Name	Owner institution	Operator	Installation date	Sensors	Station numbers in 2005	Objective
Seismic monitoring network of OVSG	IPGP	OVSG	1950	Short-period	25	Regional and volcanic seismicity survey around Guadeloupe
Broadband volcanic network of OVSG	IPGP	OVSG	2003	Broadband	5	Broadband surveyance of Soufrière Guadeloupe
Permanent accelerometric network of Guadeloupe	RAP	OVSG	2002	Accelerometer	12	Ground motion observations and estimation of site effects
Accelerometric network of BRGM Guadeloupe	BRGM	BRGM	1994	Accelerometer	6	Site effects studies
CDSA accelerometric network	IPGP BRGM	OVSG	2005	Accelerometer	7	RAP network extension for ground motion observations
"Sismo des Ecoles" network of Guadeloupe	BRGM	BRGM	2003	Short-period	1	Project of seismometer installation in public school
Broadband network of Bouillante Guadeloupe	BRGM	BRGM	2004	Broadband	5	Study the geothermal field of Bouillante
Seismic monitoring network of Martinique	IPGP	OVSM	1950	Short-period	16	Regional and volcanic seismicity survey around Martinique
Permanent accelerometric network of Martinique	RAP	OVSM	2002	Accelerometer	8	Ground motion observations and site effects estimation
BRGM accelerometric network of Martinique	BRGM	BRGM	1994	Accelerometer	7	Site effects studies
Accelerometric network of Conseil Général Martinique	Conseil General Martinique	OVSM	1998	Accelerometer	29	Ground motion estimations in buildings of the Conseil Général

du Globe de Paris (IPGP), which is interested in fundamental research on seismic source and hazard; the Bureau de Recherches Géologiques et Minières (BRGM), which studies seismic hazard and risk; and the Université des Antilles et de la Guyane (UAG), which is involved in geological research in the Lesser Antilles.

CDSA collects all available data from French West Indies arrays, centralizing them into a single database. The data processing consists of several steps:

- creating a unified seismic catalog;
- collecting all available signal records and seismic bulletins;
- calculating a new location; and
- presenting information about the strong motion and the felt seismicity.

Unified Seismic Catalog

CDSA has built a single reference catalog by merging the regional catalogs listed in table 1. A classification for different types of events has been defined: regional, volcanic, indeterminate, quarry blasts, and others (T and sonic waves). When several arrays provide different locations for the same event, the location of the closest array is kept and becomes the reference.

Data Collecting

The next step consists of collecting all available data: waveform records and phase data bulletins. Thanks to various cooperative agreements, the CDSA receives records collected by IPGP and BRGM in the French West Indies, as well as from accelerometric stations of the Conseil Général de Martinique. In table 2, we list the characteristics of the arrays. Figure 2 shows accelerometric, short-period, and broadband stations located in the Lesser Antilles. CDSA also gathers waveforms from one SRU station on St. Lucia (SLW) and from one Montserrat Volcanologic Observatory (MVO) station (MGH) on Montserrat. These waveform records and wave-arrival times are included in the database.

CDSA reduces the heterogeneity of the original recording formats to only two formats: IASPEI-SUDS and SAC. SUDS is used to visualize the data and pick the phase arrival times, because it was already used by the two observatories (OVSG and OVSM) that provide most of the data. SAC was also chosen because it is widely used, mainly for accelerometric data. All the waveforms related to phase picks are included in the database.

The data is validated by suppressing noisy records and by controlling time synchronization. An association process is used to identify each data file with a seismic event listed in the regional reference catalog. For events that are not referenced (teleseismic events, and regional events detected by too few stations to be located), the catalog is completed by adding the first arrival time detected for such events.

New Location

For each event with enough data (more than three stations and four phases), a new location is computed with the HYPOINVERSE-2000 program (Klein 2002) using velocity and ground-motion data. Earthquake focal depths can be as deep as 200 km in the subduction zone. Therefore the location process begins by determining a preliminary epicenter for a set of fixed depths between 0 and 200 km. The solution with the best root mean square (rms) is chosen as the trial hypocenter for definitive location. When epicentral distance for the closest station is greater than 200 km, the best fixed-depth solution is kept. Next, a seismologist manually validates each new location by keeping or rejecting the new solution. We don't keep the new solution if:

- no *S* wave is used for the location of a regional event;
- horizontal error is too large compared to $D_{\min}$, the minimum distance at the closest station (for example, an error more than 15 km for $D_{\min} > 50$ km); and
- $D_{\min}$ is more than 500 km.

A 1D velocity model determined by Dorel (1978) is used for the new location. It consists of a three-layer model with *P* velocities of, respectively, 3.5 km/s, 6.0 km/s, and 7.0 km/s, and a mantle velocity of 8.0 km/s. The thicknesses of the three layers are 3, 12, and 15 km. The *P*- to *S*-wave velocity ratio is taken to be 1.76.

Presently, CDSA calculates earthquake magnitude by using the duration form of Lee and Lahr (1975) for velocity records:

$$Md = 2 \log(T) + 0.0035 \times \mathrm{ED} - 0.87,$$

where *T* is the time lag in seconds between *P*-wave arrival time and the end of the *S* coda wave and ED is epicentral distance (km). This magnitude scale has been used by IPGP observatories OVSG and OVSM since their very first seismological bulletins. The correlation between *Md* (IPGP) and M_w or m_b (USGS) is plotted in figure 3. The *Md* magnitudes are shifted by 0.1 to 0.2 below the m_b values for magnitudes above 4.

The reference catalog is regularly updated with CDSA relocation results, except for distant events (greater than 200 km at the closest station). In the latter case, initial source parameters from the closest regional bulletin are kept as the best reference.

Strong Motion and Felt Seismicity

CDSA gathers strong-motion data provided by the French regional three-component accelerometric arrays. Hypocentral distance and peak ground acceleration (PGA) are computed for defining future attenuation laws. PGA is defined here as the maximum value of the two horizontal components for a given record. CDSA includes information about site conditions (rock, soil, or building). Site-effects evaluation is performed by Nakamura's technique (1989) based on the calculation of horizontal-to-vertical component spectral ratios (*H/V*) from ambient noise measurements (Douglas *et al.* 2006). When *H/V* measurements have been made on a station site, they are added to the database.

Information about the felt events is also stored. Observatories OVSG and OVSM list felt earthquakes in Guadeloupe and Martinique, respectively. On average, five to six earthquakes are felt locally every year. Moreover, CDSA collaborates with the French Central Seismology Office (BCSF; `http://www.franceseisme.fr`) for macroseismic investigation in the French West Indies. In particular, the CDSA team contributed to a BCSF macroseismic investigation that determined EMS98 intensities (European macroseismic scale) for each community of Guadeloupe after the 21 November 2004 Les Saintes earthquake (BCSF 2004).

Database

The CDSA database is managed by postgresSQL. The first dataset introduced in the database covers the period from January 2001 to May 2005. The CDSA seismic catalog provides a list of 11,860 events. Of these, 8,844 (75%) have signal or phase data detected by Guadeloupe and Martinique arrays. Among these, 4,967 (56%) have been relocated by CDSA, 503 (6%) are teleseismic events, and 3,374 (38%) do not have enough records for reliable hypocentral calculations. Accelerometric records exist for 2,260 events (26%).

On average, 74% of CDSA locations have a horizontal error less than 5 km, and 78% have less than 10 km of vertical error. Due to errors in the velocity model, we expect that the actual errors are larger. Magnitude thresholds are evaluated from Gutenberg-Richter relations (Gutenberg and Richter 1954). We consider two categories of events: intraslabs (subduction earthquakes with depths > 50 km) and shallow events (depths < 30 km). For the second group, we have eliminated aftershocks of the 21 November 2004 event because the catalog is not complete for this seismic swarm. The magnitude threshold ($Md = 2.7$) is similar for the two types. The *b* values are quite close: $b = 1.13$ (intraslab) and $b = 1.38$ (shallow).

NEW EPICENTRAL LOCATION FROM CDSA

The seismicity of the new CDSA catalog is presented in figure 4. Note that the seismic activity is not distributed homogeneously along the plate border, and two particular regions show a lack of seismicity:

- between the Virgin Islands and St. Kitts (area called Anegada passage), to the north; and
- between St. Lucia and Grenada, to the south.

The USGS seismicity map (figure 1) shows the same two regions, which suggests that the lack of seismicity is not an artifact related to array geometries. To better quantify this heterogeneous seismic activity, we identify three zones defined by latitude: zone A (14.8°–18°), zone B (13.1°–14.8°), and zone C (12°–13.1°). We also consider zone D to the north with a latitude range of 17.8–20° and a longitude range 62–64°W. There aren't enough events in each of these zones to make accurate estimates of the parameter *b* of a Gutenberg-Richter law, so we

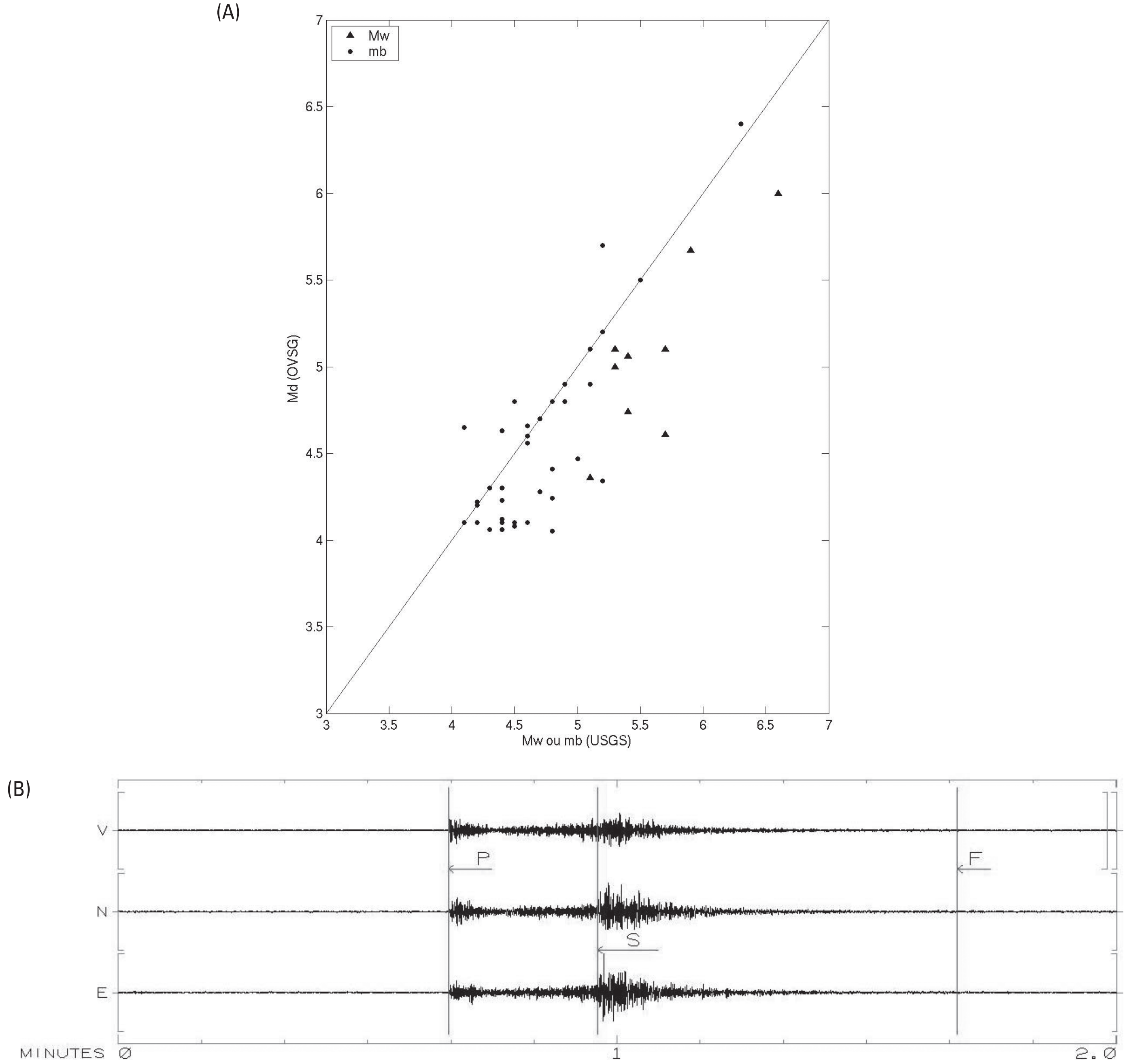

▲ **Figure 3.** (A) Comparison between *Md* (IPGP) used and M_w or m_b (USGS); (B) An example waveform where the *P* and *S* picks and the end of the *S* coda are shown.

followed a simpler approach. We calculate the number of events above magnitude 2.7 and magnitude 3 for the CDSA catalog and above magnitude 4 for the USGS catalog. The results are presented in table 3, together with the observed ratio between the number of small earthquakes (**M** > 2.7 or > 3) and large earthquakes (**M** > 4).

Ratios in zones C and D are twice smaller than in zone A for magnitude cutoff 2.7 and nearly equal for magnitude cutoff 3. Thus, to the first order, zones C and D have the same seismicity behavior as zone A (a factor of 2 might be due to random fluctuations for these small numbers). Zone B, however, shows small-to-large magnitude ratios much larger than does zone A (factor of 4 for magnitude cutoff 3). Therefore, the decrease of large magnitudes in zone B is most probably real, leading to higher *b* values. These results also show that the detection capabilities of the arrays in zones B, C, and D do not seem significantly different than in zone A for **M** > 2.7.

The lower seismic activity observed south of St. Lucia was first reported by Dorel (1981) and Wadge and Shepherd (1984). The authors explained this feature by a lower coupling between the two tectonic plates. Our results provide a finer image of the seismicity by identifying zone B as a low-seismicity area with

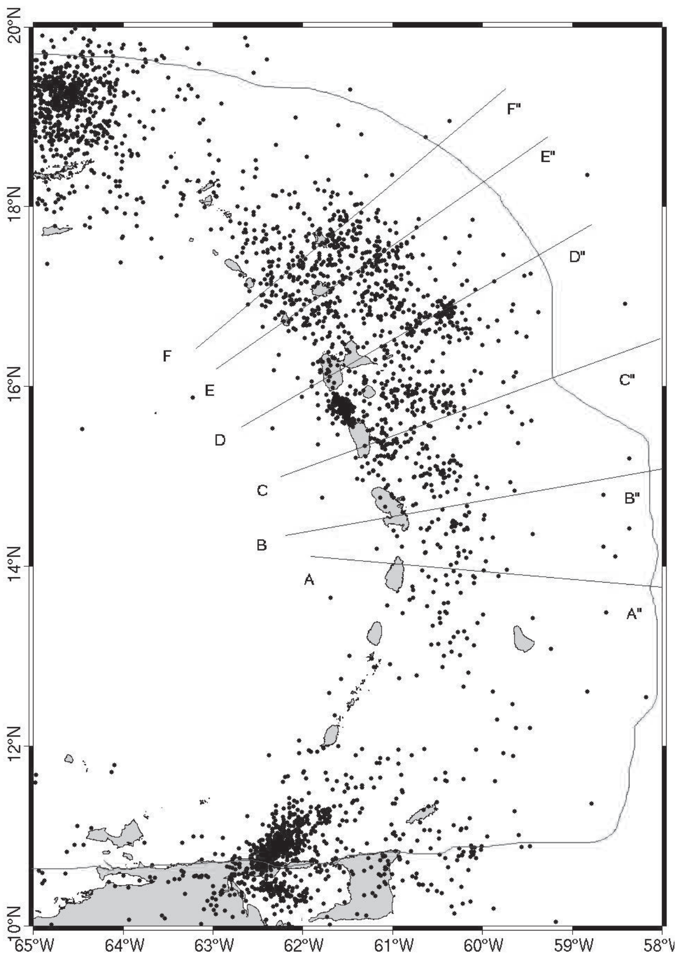

▲ **Figure 4.** Seismicity map for magnitude *Md* > 2.7 of CDSA complete catalog. Profiles AA″, BB″, CC″, DD″, EE″, and FF″ indicate the orientations of the cross-sections shown in figure 6. The continuous line represents the oceanic trench.

a lack of moderate earthquakes and zone C as an almost quiescent area. To the north, our study provides evidence for the relative seismic quiescence of area D, for which no explanation has yet been proposed.

From CDSA data, we can study the relationship between shallow seismicity (between 0 and 50 km) and active faults. The cutoff depth is based on the observed seismicity distribution and is in agreement with Tichelaar and Ruff (1993), who observed that worldwide intraslab earthquakes nearly all occur at depths deeper than 50 km. The shallow seismicity presents the same heterogeneity as for the complete catalog within the same zones. The change from high seismic activity (zone A) to lower activity (B and C) coincides with changes in the active tectonic structures mapped by Feuillet *et al.* (2002) and the deepening of the Barbados accretionary wedge. Interestingly, the quiescent area coincides with the deepest part of the wedge. This correlation might be related to high pore pressure within the sediments, which allows stable aseismic creep or volumetric anelastic strain. We have no explanation at present for the seismicity change from zone A to zone D to the north.

At a more detailed scale, we clearly see the high seismicity of Marie-Galante graben, which is a major active tectonic structure southeast of Guadeloupe (figure 4). Two other dense clusters are visible: one between Guadeloupe and Dominica, which corresponds to the aftershocks of Les Saintes 2004 earthquake; and the other, northeast of Guadeloupe, which corresponds to a seismic swarm in 2001. The latter contains earthquakes of magnitude 3.3–4.8 that occurred between April and July 2001. Christeson *et al.* (2003) proposed that this cluster is located at the intersection of the subducted Barracuda Ridge with a backstop, forming a block of buoyant crust, accreted during the Late Miocene (Bangs *et al.* 2003). We note that the USGS National Earthquake Information Center (NEIC) location from this cluster is shifted by 40 km to the northeast with respect to the CDSA location. The latter appears more in agreement with this geodynamic interpretation.

The improvement of CDSA locations within zone A (close to Guadeloupe and Martinique) allows more detailed study of the area's seismicity. We observe that seismic swarms are more clustered than in the original catalogs. This can be illustrated by the case of Les Saintes 2004 sequence. The 21 November 2004 ($M_w = 6.3$) earthquake is the most recent destructive event to strike the French West Indies. This shallow earthquake, which occurred south of Les Saintes archipelago between Guadeloupe and Dominica, was followed by numerous aftershocks. We use these data to test CDSA locations and compare them with USGS and IPGP catalogs. Figure 5 shows the location of the mainshock and 28 main aftershocks with magnitudes greater than 4.0, as computed by the three arrays. The swarm detected by the USGS is scattered over 30 km and the mainshock is located 15 km westward. IPGP stations clipped on the mainshock, and only one *S* phase could be picked up on the short-period network. The mainshock is shifted toward the east in comparison to the aftershock swarm. CDSA included accelerometric stations

TABLE 3
Number of events above magnitudes 2.7 and 3 in the CDSA catalog and above magnitude 4 in the USGS catalog, and respective ratios between the two catalogs.

	CDSA (M > 2.7)	CDSA (M > 3)	USGS (M > 4)	CDSA/USGS (M > 2.7)	CDSA/USGS (M > 3)
A(14.8°–18°)	1,021	539	109	13.4	4.9
B(13.1°–14.8°)	106	68	4	26.5	17
C(12°–13.1°)	25	21	4	6.2	5.2
D(17.8°–20°)	98	92	21	4.7	4.4

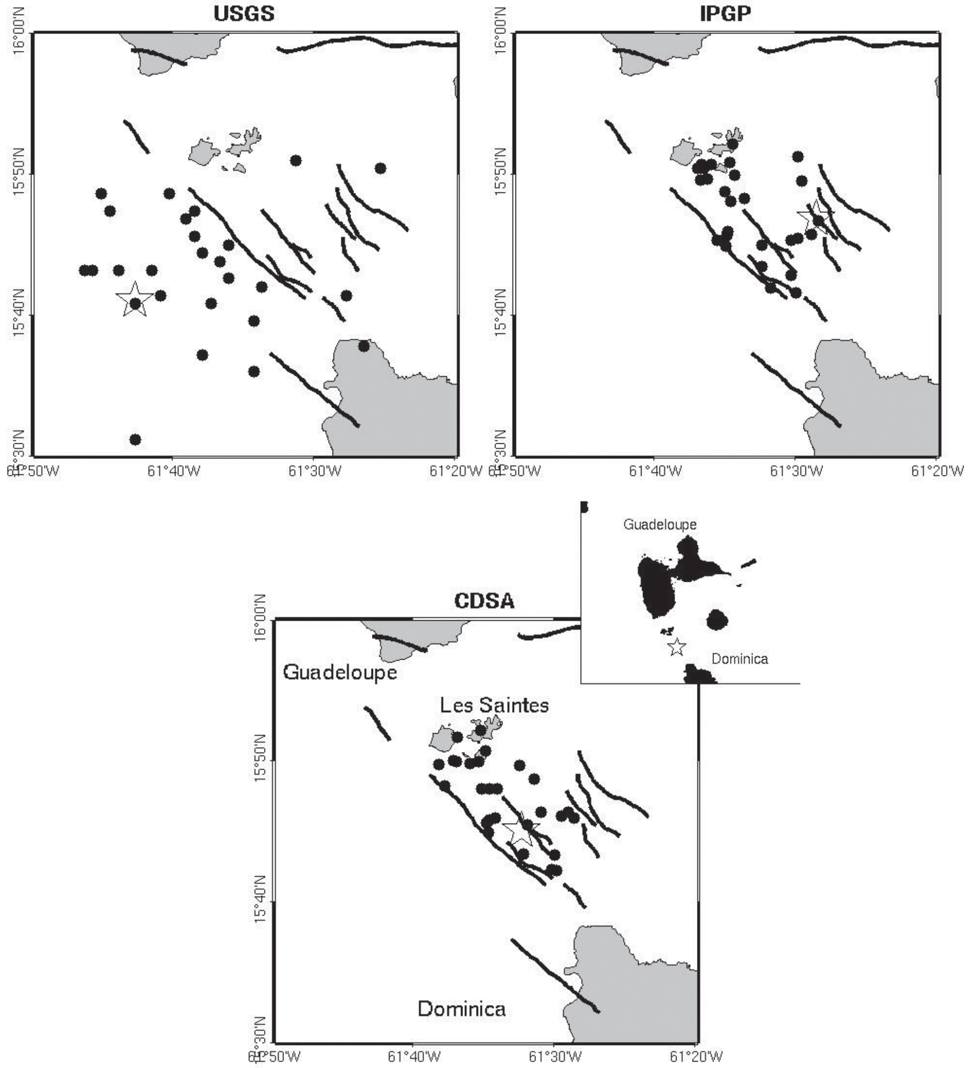

▲ **Figure 5.** Position of the main shock (21/11/04, Les Saintes event) and the 28 largest aftershocks (with magnitude *Md* > 4) located by different regional networks: USGS, IPGP, and the new catalog. Regional faults of Feuillet (2000) are outlined.

providing good *S* phases and obtained a location error of about 1 km for the mainshock. As a result, the CDSA swarm is less scattered than the others, and the mainshock epicenter is more accurately located within the swarm. The aftershocks are spread within a 25-km-long area, elongated in the NNW–SSE direction and fitting the fault systems mapped by Feuillet (2000).

SPATIAL VARIABILITY OF BENIOFF PLANE DIP ANGLE

The Lesser Antilles subducting plate has quite a complex structure, as described by a few authors who have shown a variable dip angle of the slab along the arc (Dorel 1981; Girardin and Gaulon 1983; Wadge and Shepherd 1984; Girardin *et al.* 1991; Feuillet *et al.* 2002). However, their results significantly differ from each other. For instance, to the north of Antigua, Wadge and Shepherd (1984) find a 50 to 60° dip whereas Dorel (1981) finds 30°, and to the south near St. Vincent, Wadge and Shepherd (1984) find a 45 to 50° dip whereas Dorel (1981) finds 30°. This apparent contradiction results from the small number and/or the large location uncertainties of the events in the catalogs. Others studies have provided evidence for a kink affecting the whole slab at depth, related to a triple junction between the Caribbean and the separated North and South American plates (Wadge and Shepherd 1984).

To investigate the variation of dip angle along the arc inferred from the new CDSA locations, we present vertical cross-sections for six profiles perpendicular to the arc through several active volcanic islands. These are shown in figure 6. The sections are 150 km wide, and the seismicity associated with the subduction slab is clearly observed from 50 to 200 km.

There is no clear dip variation from north to south as a 50° dipping line globally fits the seismic clusters. This contradicts the results of Wadge and Shepherd (1984) because the contour of the mean position of the Benioff zone decreases in slope toward the north. However, for areas corresponding to profiles AA' and FF', the 50° dip angle value differs from the results of Dorel (1981) but agrees with the results of Wadge and

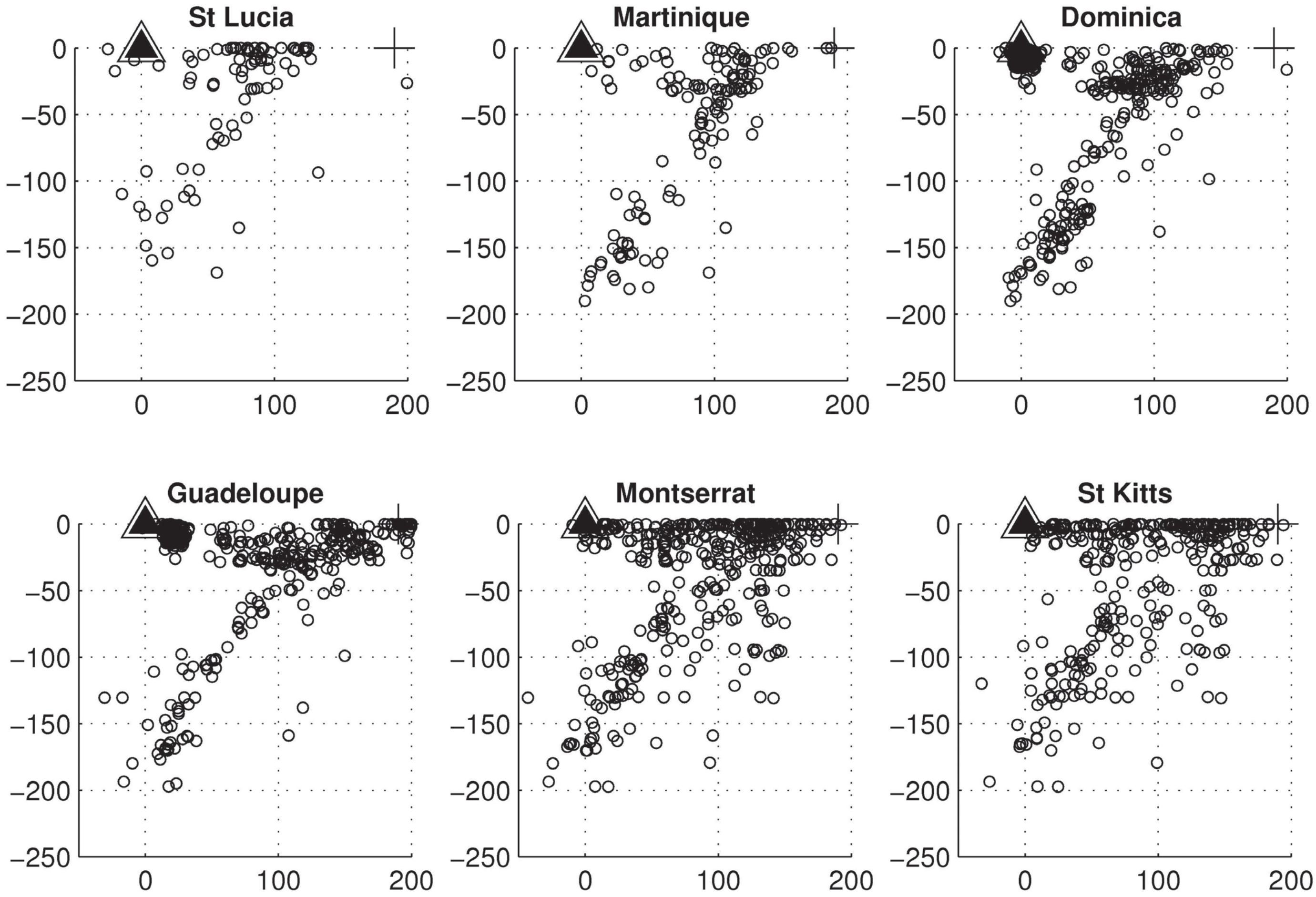

▲ **Figure 6.** Seismicity cross-sections (magnitude > 2.7) for six profiles perpendicular to the arc, through active volcanic islands (AA″ to FF″ shown in figure 4). The sections are 150 km wide. Triangles on the horizontal axis indicate the active volcanic front. Plus signs show the position of the negative gravity anomaly.

Shepherd (1984). All these results remain preliminary, because only five years of data could be relocated by CDSA.

ATTENUATION LAWS

Here we distinguish shallow crustal earthquakes (< 50 km) from intraslab subduction earthquakes (occurring within the subducting oceanic plate). The CDSA has gathered enough data from 2,260 events to allow us to compute PGA values. PGA estimates vary between 0.1 mg and 200 mg for hypocentral distances from 5 to 500 km. Figure 7 shows the magnitude-distance distribution of the strong-motion dataset collected for analysis. A large portion of the data comes from shallow crustal earthquakes, a majority of them from Les Saintes aftershock area. Magnitudes range from 1 to 6 and hypocentral distances from 2 to 500 km (figure 7A). For subduction earthquakes (figure 7B), magnitude and distance ranges are much smaller (about 2–5 km for magnitude, 20–200 km for hypocentral distances).

The Les Saintes islands earthquake (2004/11/21, M_w = 6.3) is the event for which we have the largest amount of accelerometric data. PGA distribution with distance is represented in figure 8 and table 4. The event was recorded by 46 stations at distances between 30 and 150 km. An illustration of site effects is presented in the seismograms of figure 9. For the mainshock, one compares the records at Ste. Rose (soil site) and Le Moule (rock site), both at 70 km from the epicenter, which provides a peak amplitude ratio of 2.

Unfortunately, there was no accelerometric station at Les Saintes Islands, near the activated fault. Therefore, the peak accelerations at these islands could only be estimated by interpolating the trend of its attenuation at a shorter distance. We estimate a PGA of 200–300 mg or larger, which is consistent with the EMS98 intensity VIII reported by BCSF on these islands (BCSF 2005).

In figure 8, we compare the acceleration data with the predicted acceleration using two attenuation laws computed for shallow crustal earthquakes (Sadigh *et al.* 1997; Chang *et al.* 2001). The Sadigh *et al.* (1997) model for rock sites is applicable to earthquakes with moment magnitudes of 4 to 8+ and distances up to 100 km. The Chang *et al.* (2001) model is valid for magnitudes of about 4 to 7 and for distances of about 5 to 250 km. The PGA prediction is rather good for Guadeloupe records at less than 100 km, but clearly overestimates the PGA observed in Martinique at about 150 km by a factor of 2 to 3.

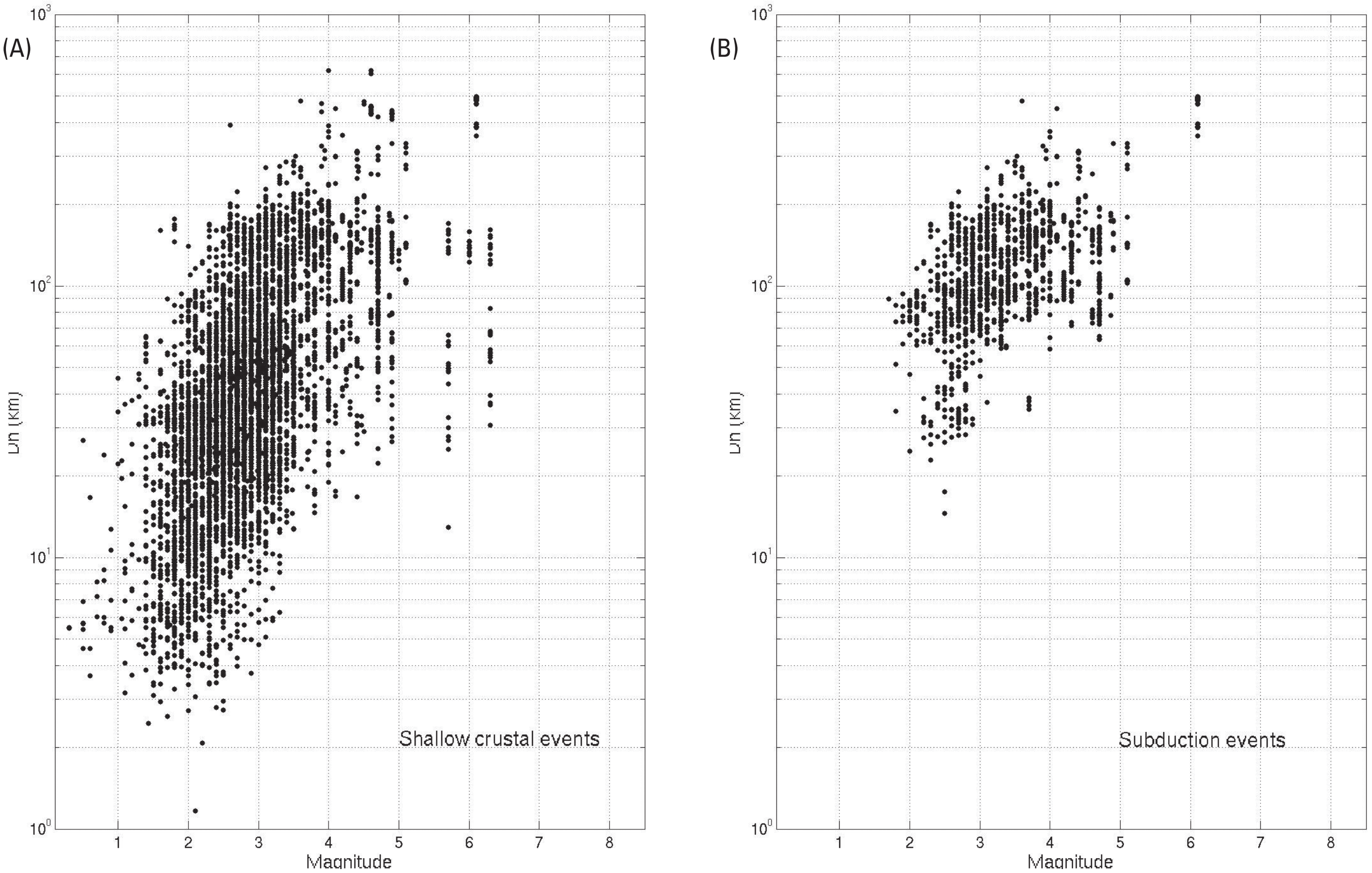

▲ **Figure 7.** Magnitude-distance distributions of peak ground-motion data used in this study. (A) shallow crustal earthquakes; (B) subduction zone earthquakes.

There presently are not enough magnitude 6 or larger earthquakes in the database to reliably constrain parameters for a new attenuation law.

CONCLUSIONS

The Lesser Antilles arc is prone to a large seismic hazard. The geodynamic context is relatively complex, the historical seismicity covers too-short a period of time (less than 3.5 centuries) to estimate the recurrence time of strong events, and seismicity associated with shallow active faults near the islands is not well-understood. Although several regional institutions produce catalogs of seismicity, the information remains partial. Under such conditions, the seismic hazard assessment is still relatively approximate and needs to be improved, which motivated the creation of the French Antilles Seismological Data Base, CDSA.

The purpose of CDSA is to collect and merge the data existing in the French Antilles. CDSA generates a new seismicity catalog that is as complete as possible. The five years of seismicity presently analyzed allow us to compare seismic activity on the whole arc and to see clearer evidence for variations in the seismicity level along the arc. The magnitude threshold is 2.7, and even lower near the islands of Guadeloupe and Martinique. We have been able to confirm a progressive increase of seismic activity from south to north between Martinique and Antigua and identify two presently quiescent zones, near St. Kitts to the north and Grenada to the south.

In the central part of the arc (17.5°N–13.5°N), the CDSA catalog improves our knowledge of the subduction zone and of the shallow seismicity because its hypocenter locations have smaller uncertainties than the original catalogs. It better defines the slab structure and dip angle: the latter seems constant between St. Lucia and St. Kitts, with a mean value of 50°. Moreover, the CDSA catalog better constrains the relationship between tectonic structures and seismicity, such as a backstop near Guadeloupe, and offshore active faults around Guadeloupe and Martinique, in particular for the 2004 Les Saintes seismic crisis. Including accelerometric data in CDSA has reduced location errors, but azimuth coverage is not improved: the problem of island–arc alignment remains. Only ocean-bottom instruments could improve this drawback. For this purpose, IPGP installed ocean bottom seismometerin 2006.

High-quality digital accelerometric data are recent in the Lesser Antilles, and there is not yet any attenuation relationship adapted for the Lesser Antilles. Preliminary results from the CDSA compilation show that standard attenuation laws overestimate peak accelerations at large distances by a factor of 2 to 3.

In conclusion, the newly created CDSA will improve regional hazard assessment and bring valuable input to applied and fundamental research, in particular through its accessibil-

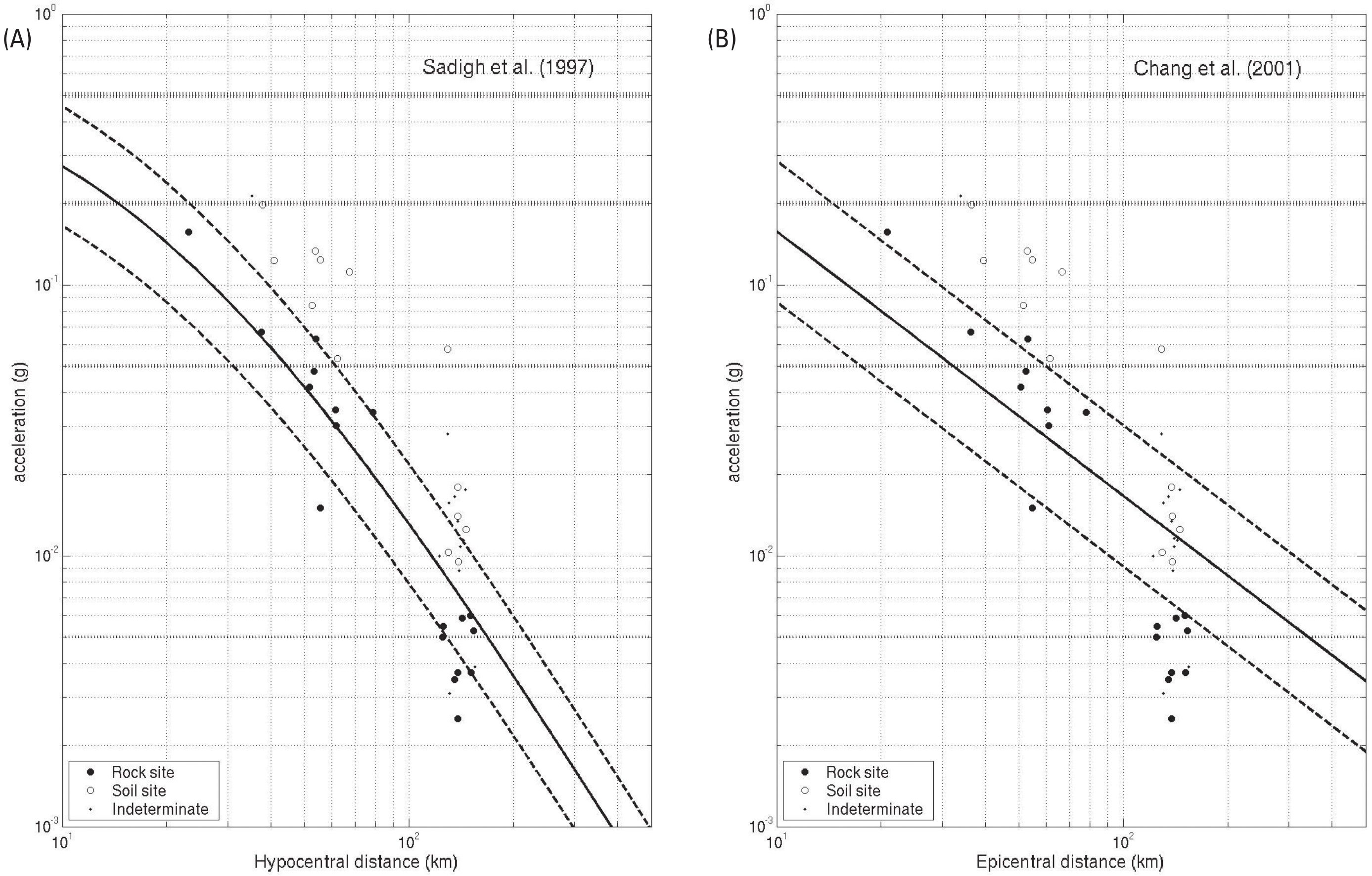

▲ **Figure 8.** Comparison between PGA for the mainshock (Les Saintes, 21/11/04, M_w 6.3) and the predicted values using two attenuation equations (Sadigh *et al.* 1997; Chang *et al.* 2001). The solid line indicates the predicted PGA, the broken lines indicate the standard error of the equation. Horizontal lines indicate empirical limits for degree of perception based on Feuillard (1984): from bottom to top, the earthquake is felt by few people, the earthquake is felt by a large majority of people, the earthquake can cause important damages, the earthquake can cause general panic.

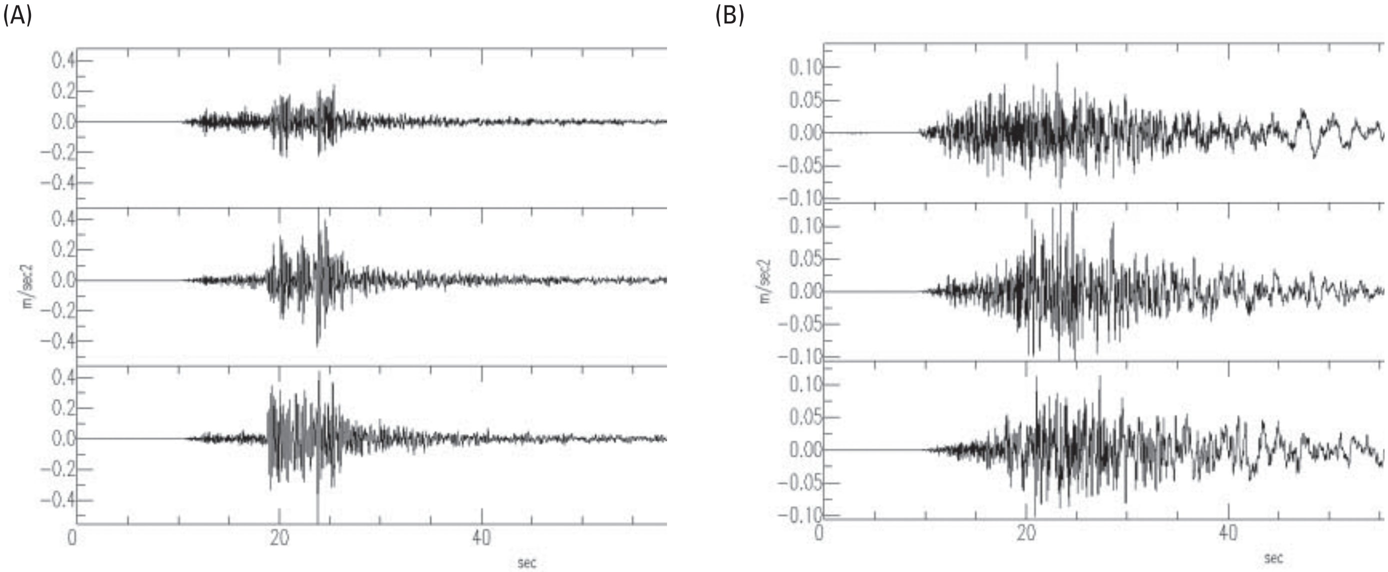

▲ **Figure 9.** Comparison between records from two stations at the same distance (70 km) from the epicenter (21/11/04) with different site conditions: (A) SROA (soil site) and (B) MOLA (rock site).

TABLE 4
Strong motions recorded by accelerometric stations in the French West Indies for the mainshock (Les Saintes, 21/11/04). Site conditions are indicated R for rock, S for soil, NA for indeterminate; the number indicates the type of classification: (1) for H/V measurements, (2) for geological determination (Douglas *et al.* 2005).

Stations	Code	Networks	Type	Hypocentral distance (km)	PGA (g)
Grand-Bourg-Marie-Galante	GBGA	RAP-IPGP	R (1)	32.4	0.157
Houelmont-Gourbeyre	GHMA	BRGM-GUA	R (1)	35.0	0.213
Préfecture-Basse-Terre	PRFA	RAP-IPGP	R (1)	37.1	0.067
Belfont-Saint-Claude	GJYA	BRGM-GUA	R (1)	37.9	0.198
Aérodrome de Baillif	ABFA	RAP-IPGP	S (1)	40.1	0.123
Ecole de Pigeon-Bouillante	PIGA	RAP-IPGP	R (1)	53.3	0.048
Institut-Pasteur-Abymes	IPTA	RAP-IPGP	R (1)	55.9	0.042
Fengarol Pointe-à-Pitre	GFEA	BRGM-GUA	S (1)	56.6	0.084
Lauricisque Pointe-à-Pitre	GLAA	BRGM-GUA	S (1)	57.6	0.133
Antéa-Abymes	GBRA	BRGM-GUA	R (1)	58.3	0.063
Aéroport Glide fond	GGFA	BRGM-GUA	R (2)	59.5	0.015
Aéroport Glide surface	GGSA	BRGM-GUA	S (1)	59.5	0.124
Morne à l'Eau	MESA	RAP-IPGP	S (1)	67.3	0.053
Le Moule	MOLA	RAP-IPGP	R (1)	68.0	0.030
St-François	SFGA	RAP-IPGP	R (1)	68.9	0.034
Sainte-Rose	SROA	RAP-IPGP	S (1)	69.1	0.112
Anse-Bertrand	BERA	RAP-IPGP	R (1)	83.5	0.034
Observatoire Morne des Cadets	CGOB	CG-MAR	R (1)	121.9	0.010
Piscine Carbet	CGCA	CG-MAR	R (1)	124.1	0.005
Sainte Marie	MASM	RAP-IPGP	R (1)	126.4	0.006
Collège Saint-Just Trinité	CGTR	CG-MAR	S (1)	130.0	0.028
Mairie-Trinité	MTRA	BRGM-MAR	S (1)	130.1	0.058
Hôpital Trinité	MATR	RAP-IPGP	S (1)	130.3	0.010
Centre Thermal Absalon	CGAS	CG-MAR	S (1)	130.4	0.003
Réservoir Deux Terres	CGDT	CG-MAR	S (1)	131.0	0.016
Météo Desaix	MAME	RAP-IPGP	R (1)	134.9	0.006
Collège Saint Joseph	CGSJ	CG-MAR	S (1)	135.7	0.017
Exotarium-Fort-de-France	MEXA	BRGM-MAR	S (1)	137.7	0.018
Immeuble Concorde DDST	CGCO	CG-MAR	R (1)	137.8	0.003
Archives Départementales Haut	CGAH	CG-MAR	R (1)	137.9	0.013
Archives Départementales Bas	CGAS	CG-MAR	S (1)	137.9	0.004
Théâtre-Fort-de-France	MTHA	BRGM-MAR	S (1)	138.1	0.014
Dillon-Fort-de-France	MDIA	BRGM-MAR	S (1)	138.6	0.010
Centre culturel Atrium	CGAT	CG-MAR	S (1)	138.8	0.009
Collège Petit Manoir Lamentin	CGPB	CG-MAR	S (1)	140.6	0.011
Collège Place d'Armes	CGPA	CG-MAR	S (1)	140.8	0.012
Zone Aéro-Militaire	MAZM	RAP-IPGP	R (2)	142.3	0.006
Collège du François	CGFR	CG-MAR	NA	144.2	0.011
Barrage de la Manzo Haut	CGMH	CG-MAR	NA	146.1	0.018
Barrage de la Manzo Bas	CGMB	CG-MAR	NA	146.2	0.013
Diamant	MADI	RAP-IPGP	R (2)	150.8	0.004
Marin	MAMA	RAP-IPGP	R (1)	150.8	0.006
Collège Diamant	CGDI	CG-MAR	R (1)	153.3	0.005
Collège Vauclin	CGVA	CG-MAR	S (1)	155.6	0.004

ity on the Internet (http://www.seismes-antilles.fr). Presently, CDSA focuses on data collected by the French arrays, but it would be a great opportunity to set up a cooperative data exchange among different Caribbean countries and institutes involved in assessing the seismic hazard of this region.

ACKNOWLEDGMENTS

The framework for creating CDSA was funded by the French government and Europe (CPER-DOCUP 2000-2006), the Guadeloupe region, and the main collaborators IPGP, BRGM, and UAG. We used data from IPGP observatories, BRGM, and RAP-IPGP to compute and plot figures in this paper. We would like to thank Auran Randrianosolo, Pascal Bernard, and Fabrice Cotton for their beneficial discussion and Didier Mallarino for his contribution to the creation of the CDSA database.

REFERENCES

Ambraseys, N. N., J. Douglas, S. K. Sarma, and P. M. Smit (2005). Equations for the estimation of strong ground motions from shallow crustal earthquakes using data from Europe and the Middle East: Horizontal peak acceleration and spectral acceleration. *Bulletin of Earthquake Engineering* **3** (1), 1–53.

Bangs, N. L., G. L. Christeson, and T. H. Shipley (2003). Structure of the Lesser Antilles subduction zone backstop and its role in a large accretionary system. *Journal of Geophysical Research* **108** (B7), 2,358.

BCSF (French Central Seismology Office) (2005). *Séisme des Saintes (Guadeloupe) du 21 Novembre 2004*. Note préliminaire, BCSF2005-NP3, 62 pps.

Bernard, P., and J. Lambert (1986). *Macrosismicité des Petites Antilles: Compte-rendu des effets du séisme du 16 mars 1985 et exploitation des accélérogrammes*. Technical Report 86 SGN 003 GEG, BRGM, France.

Bernard, P., and J. Lambert (1988). Subduction and seismic hazard in the Northern Lesser Antilles: Revision of the historical seismicity. *Bulletin of the Seismological Society of America* **78**, 1,965–1,983.

Bertil, D., S. Bazin, D. Mallarino, and F. Beauducel (2004). *Séisme des Saintes*. Rapport de synthèse, Centre de Données Sismologiques des Antilles, 8 décembre 2004.

Castro, R. R., H. Fabriol, M. Bour, and B. Le Brun (2003). Attenuation site effects in the region of Guadeloupe, Lesser Antilles. *Bulletin of the Seismological Society of America* **93** (2), 612–626.

Chang, T.-Y., F. Cotton, and J. Angelier (2001). Seismic attenuation and peak ground acceleration in Taiwan. *Bulletin of the Seismological Society of America* **91**, 1,229–1,246.

Christeson, G. L., N. L. Bangs, and T. H. Shipley (2003). Deep structure of an island arc backstop, Lesser Antilles subduction zone. *Journal of Geophysical Research* **108** (B7), 2,327–2,342.

Demets, C., P. E. Jansma, G. S. Mattioli, T. H. Dixon, F. Farina, R. Bilham, E. Calais, and P. Mann (2000). GPS geodetic constraints on Caribbean–North America plate motion. *Geophysical Research Letters* **27**, 437–440.

Dorel, J. (1978). Sismicité et structure de l'arc des Petites Antilles et du bassin atlantique. PhD diss., Université Pierre et Marie Curie, Paris, 326 pps.

Dorel, J. (1981). Seismicity and seismic gap in the Lesser Antilles arc and earthquake hazard in Guadeloupe. *Geophysical Journal of the Royal Astronomical Society* **67**, 679–695.

Douglas J., D. Bertil, A. Roullé, P. Dominique, and P. Jousset (2006). A preliminary investigation of strong-motion data from the French Antilles. *Journal of Seismology* **10**, 271–299.

Douglas, J., A. Roullé, P. Dominique, C. Maurin, and F. Dunand (2005). *Traitement des données accélérométriques du Conseil Général de la Martinique*. Rapport BRGM/MP-53906-FR.

Feuillard, M. (1984). *Macrosismicité de la Guadeloupe et de la Martinique*. Observatoire Volcanologique et Sismologique de la Guadeloupe, 349 pps.

Feuillet, N. (2000). Sismotectonique des Petites Antilles. Liaison entre activité sismique et volcanique. PhD diss., Université Paris 7- Denis Diderot, 284 pps.

Feuillet, N., I. Manighetti, and P. Tapponnier (2002). Arc parallel extension and localization of volcanic complexes in Guadeloupe, Lesser Antilles. *Journal of Geophysical Research* **107** (B12), 2,331.

Gagnepain-Beyneix, J., J. C. Lepine, A. Nercessian, and A. Hirn (1995). Experimental study of site effects in the Fort-de-France area (Martinique island). *Bulletin of the Seismological Society of America* **85**, 478–495.

Girardin, N., and R. Gaulon (1982). Microseismicity and stresses in the Lesser Antilles dipping seismic zone. *Earth and Planetary Science Letters* **62**, 340–348.

Girardin, N., M. Feuillard et J.-P. Viode (1991). *Bulletin de la Société Géologique de France* **162** (6), 1,003–1,015.

Gutenberg, B., and C. F. Richter (1954). *Seismicity of the Earth*. Princeton, NJ: Princeton University Press.

Institut de Physique du Globe de Paris (2004). *Bilan mensuel de l'activité volcanique de la Soufrière de Guadeloupe et de la sismicité régionale*. Public reports of OVSG-IPGP, Institut de Physique du Globe de Paris, http://www.ipgp.jussieu.fr, ISSN 1622-4523.

Klein, F. W. (2002) *User's Guide to Hypoinverse-2000, A Fortran Program to Solve for Earthquake Locations and Magnitudes.* USGS Open File Report 02-171.

Lebrun, B., A.-M. Duval, P.-Y. Bard, O. Monge, M. Bour, S. Vidal, and H. Fabriol (2004). Seismic microzonation: A comparison between geotechnical and seismological approaches in Pointe-à-Pitre (French West Indies). *Bulletin of Earthquake Engineering* **2** (1), 27–50.

Lee, W. H. K., and J. C. Lahr (1975). *HYP071 (Revised): A Computer Program for Determining Hypocenter, Magnitude, and First Motion Pattern of Local Earthquakes*. USGS Open File Report 75-311, 113 pps.

Mann, P., E. Calais, J. C. Ruegg, C. Demets, P. E. Jansma, and G. S. Mattioli (2002). Oblique collision in the northeastern Caribbean from GPS measurements and geological observations. *Tectonics* **21** (6), 1,057.

Nakamura, Y. (1989) A method for dynamic characteristics estimation of subsurface using microtremor on the ground surface. *Quaterly Report of the Railway Technical Research Institute*, **30** (1), 25–33.

Sadigh, K., C. Y. Chang, J. A. Egan, F. Makdisi, and R. R. Youngs (1997). Attenuation relationships for shallow crustal earthquakes based on California strong motion data. *Seismological Research Letters* **68**, 180–189.

Tanner, J. G., and K. M. Shedlock (2004). Seismic hazard maps of Mexico, the Caribbean and Central and South America. *Tectonophysics* **390**, 159–175.

Tichelaar, B. W., and L. J. Ruff (1993). Depth of seismic coupling along subduction zones. *Journal of Geophysical Research* **98,** 2,017–2,037.

Wadge, G., and J. B. Shepherd (1984). Segmentation of the Lesser Antilles subduction zone. *Earth and Planetary Science Letters* **71**, 297–304.

Youngs, R. R, S. J. Chiou, W. J. Silva, and J. R. Humphrey (1997). Strong ground motion attenuation relationships for subduction zone earthquakes. *Seismological Research Letters* **68**, 58–73.

Observatoire Volcanologique et Sismologique de la Guadeloupe
Le Houelmont, 97113 Gourbeyre Guadeloupe (FWI)
mendy@ovsg.univ-ag.fr
(M.B.-V.)

2.3 Campagnes d'intervention rapide après les séismes des Saintes

Un séisme intraplaque de magnitude 6,3 s’est produit en mer à 15 km au sud des îlets des Saintes en 2004 (Figure 9). Ce séisme était le plus important séisme enregistré aux Antilles Françaises depuis plusieurs décennies. Il s’est produit sur le réseau de failles normales situé entre les Saintes et la Dominique. Le réseau sismologique de l'OVSG ne permettait pas de localiser correctement les répliques en raison de la mauvaise couverture des stations par rapport à la zone active. Les localisations formaient artificiellement deux clusters de part et d'autre d'un graben sous-marin précédemment cartographié (Feuillet et al., 2001). J'ai rapidement déployé 6 sismomètres de fond de mer (OBS) du nouveau parc communautaire de l'INSU. Nous avons pu mettre temporairement à l'eau ces instruments autonomes autour de la zone activée à partir du bateau des Phares et Balises (chef de projet et chef de mission GUADOBS, Figure 9) de Guadeloupe. Plus de 4000 séismes ont été enregistrés par les OBS pendant les 6 semaines de l'expérience, ils ont permis de préciser la localisation des répliques par Local Earthquake Tomography (LET). La magnitude de complétude du réseau d'OBS est de l'ordre de 1, soit plus de 100 fois plus sensible de celle de l'OVSG. Un cluster de répliques profondes et alignées le long de la faille de Roseau souligne la zone de la faille qui n'avait pas rompu lors du choc principal. Par ailleurs, cette crise a réactivé les failles secondaires antithétiques de Rodrigues et du Souffleur, moins profondes. La tomographie locale image une anomalie négative du rapport Vp/Vs autour des failles de Rodrigues et du Souffleur mais positive autour de la faille de Roseau. Un fort rapport Vp/Vs pourrait caractériser une faille lubrifiée et expliquer l'inhabituelle longueur de la crise sismique, qui dure encore actuellement. Le rôle des fluides dans cette crise est d'autant plus remarquable que tous les OBS ont enregistré des signaux monochromatiques à 6.35Hz et que des bulles ont été observées par des témoins visuels à la surface de l'eau.

Figure 9: Église des Saintes détruite par le séisme de 2004. Campagne d'intervention rapide GUADOBS à bord du bateau des Phares et Balises pour déployer six sismomètres de fond de mer du parc INSU.

Tectonophysics 489 (2010) 91–103

Contents lists available at ScienceDirect

Tectonophysics

journal homepage: www.elsevier.com/locate/tecto

The 2004–2005 Les Saintes (French West Indies) seismic aftershock sequence observed with ocean bottom seismometers

S. Bazin [a,b,c,*], N. Feuillet [c,d], C. Duclos [b,c], W. Crawford [b,1], A. Nercessian [e], M. Bengoubou-Valérius [a,f], F. Beauducel [a,e], S.C. Singh [b]

[a] Observatoire Volcanologique et Sismologique de Guadeloupe, IPGP, 97113 Gourbeyre, Guadeloupe, French West Indies
[b] Géosciences Marines, IPGP, CNRS-INSU, 4 place Jussieu, 75005 Paris, France
[c] Observatoire Volcanologique et Sismologique de Martinique, IPGP, 97250, Fonds Saint-Denis, Martinique, French West Indies
[d] Tectonique et Mécanique de la Lithosphère, IPGP, CNRS-INSU, 4 place Jussieu, 75005 Paris, France
[e] Sismologie, IPGP, CNRS-INSU, 4 place Jussieu, 75005 Paris, France
[f] BRGM Guadeloupe, 97113 Gourbeyre, Guadeloupe, French West Indies

ARTICLE INFO

Article history:
Received 18 December 2009
Received in revised form 12 March 2010
Accepted 9 April 2010
Available online 20 April 2010

Keywords:
Ocean bottom seismometer
Local earthquake tomography
Normal-fault earthquake
Aftershock sequence
Fault–fluid interactions
Les Saintes
Lesser Antilles

ABSTRACT

On November 21, 2004 an M_w6.3 intraplate earthquake occurred at sea in the French Caribbean. The aftershock sequence continues to this day and is the most extensive sequence in a French territory in more than a century. We recorded aftershocks from day 25 to day 66 of this sequence, using a rapidly-deployed temporary array of ocean bottom seismometers (OBS). We invert P- and S-wave arrivals for a tomographic velocity model and improve aftershock locations. The velocity model shows anomalies related to tectonic and geologic structures beneath the Les Saintes graben. 3D relocated aftershocks outline faults whose scarps were identified as active in recent high-resolution marine data. The aftershocks distribution suggests that both the main November 21 event and its principal aftershock, on February 14, 2005, ruptured Roseau fault, which is the largest of the graben, extending from Dominica Island to the Les Saintes archipelago. Aftershocks cluster in the lower part of the Roseau fault plane (between 8 and 12.6 km depth) that did not rupture during the main event. Shallower aftershocks occur in the Roseau fault footwall, probably along smaller antithetic faults. We calculate a strong negative Vp anomaly, between 4 and 8 km depth, within the graben, along the Roseau fault plane. This low Vp anomaly is associated with a high Vp/Vs ratio and may reflect a strongly fracturated body filled with fluids. We infer from several types of observation that fault lubrication is the driving mechanism for this long-lasting aftershock sequence.

1. Introduction

On November 21, 2004, an M_w6.3 earthquake struck the Les Saintes archipelago (Guadeloupe, French West Indies). The earthquake epicenter was located 15 km south-east of the Les Saintes (Guadeloupe, French West Indies). This is the largest earthquake recorded in the Lesser Antilles arc since the 1985 M_w6.2 Redonda earthquake, offshore Montserrat Island (Girardin et al., 1991). It killed one child and was felt with a maximum intensity of VIII in the Les Saintes archipelago (Cara et al., 2005). It is the most damaging earthquake in a French territory since the 1967 M_w 5.1 Arette event (intensity VIII, (Cara et al., 2008)). A strong M_w5.8 aftershock occurred on February 14, 2005 and the aftershock sequence continues to this day. There is still debate about which fault or faults ruptured during this on-going sequence. In order to better study the aftershocks, six ocean bottom seismometers (OBS) were deployed around the active zone 25 days after the main event. The OBS array was deployed for 41 days, recording up to 250 events per day. In this paper, we present the results of a simultaneous inversion of the aftershock arrivals for event hypocenters and 3D subsurface velocities.

2. Seismotectonic setting

Along the Lesser Antilles arc, the North American and South American plates dip beneath the Caribbean plate at a rate of 2 cm/yr in a WSW direction (DeMets et al., 2000). As a consequence, the Eastern Caribbean is prone to a moderate to large seismic hazard (Bernard and Lambert, 1988). Three types of damaging seismicity can be distinguished in the arc (Stein et al., 1982). The first type is directly related to the subduction at the plate interface. The second type is within the subducting slab at greater depth. The third type of seismicity, which we study here, occurs within the Caribbean plate. Deformation within the Caribbean plate is accommodated by normal and oblique faults (Feuillet et al., 2001, 2004). A large en echelon fault system running

---

[*] Corresponding author. Temporarily at: International Centre for Geohazards/Norwegian Geotechnical Institute, P.O. Box. 3930 Ullevål Stadion, Oslo N-0806, Norway.
E-mail address: bazin@ipgp.fr (S. Bazin).

[1] Temporarily at: Institut de Recherche pour le Développement, c/o Dept Geology and Mines, Private Mail Bag 9001, Port Vila, Vanuatu.

0040-1951/$ – see front matter © 2010 Elsevier B.V. All rights reserved.
doi:10.1016/j.tecto.2010.04.005

from north of Montserrat Island to Dominica Island cuts active subaerial volcanoes (Soufrière Hills on Montserrat and Soufrière volcano on Guadeloupe) as well as submarine volcanoes (Fig. 1, (Feuillet, 2000; Feuillet et al., 2001)). These arc parallel normal faults have steep scarps that can reach up to several tens of meters high. The main fault segments dip toward the NE.

Between Guadeloupe and Dominica islands, a 15 km wide, N135°E striking graben belonging to the en echelon fault system was mapped during the AGUADOMAR marine survey (Feuillet, 2000; Feuillet et al., in revision). The graben is bounded by Roseau fault to the SW and the smaller Rodrigues fault to the NE (Fig. 2). The Les Saintes graben crosscuts several underwater volcanic edifices (Roseau and Colibri) which are probably no longer active. The 21 November earthquake occurred along the Les Saintes fault system. Field observations, the aftershock distribution, Coulomb stresses and tsunami modelling present Roseau fault as the best candidate for the mainshock rupture (Beauducel et al., 2005; Le Friant et al., 2008; Feuillet et al., in revision). It is the largest fault of the graben running 18 km in length with a cumulative scarp of up to 120 m (Feuillet, 2000). The centroid moment tensors (CMT) computed by the Harvard and Geoscope groups show a dominant normal-faulting mechanism with a slight strike–slip component. The two focal mechanisms do not differ by much (Table 1 and Fig. 2) and are compatible with the Roseau fault azimuth.

More than 30 000 events were recorded by the Earthquake and Volcano Observatory of Guadeloupe (OVSG-IPGP) during the 5 years following the main event (Beauducel et al., 2005; IPGP, 2009). At the time of the main shock and the first days of aftershocks, the precision

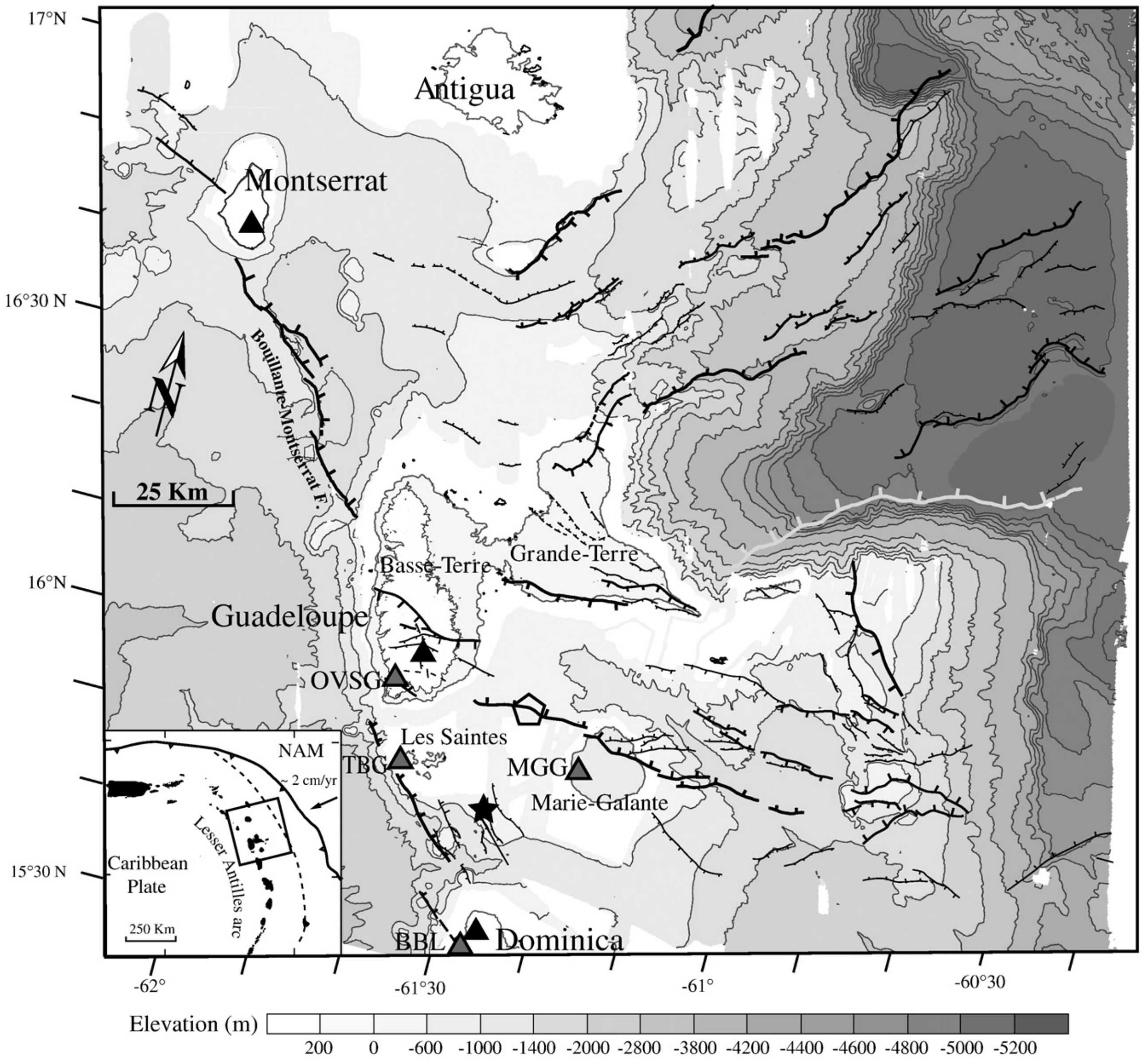

Fig. 1. Map of Guadeloupe Island along the East Caribbean volcanic arc (modified from Feuillet et al., 2004). The M_w6.3 earthquake discussed here occurred at sea between Guadeloupe and Dominica Islands, 15 km south-east of the Les Saintes archipelago (epicenter displayed as star). Black triangles indicate active volcanoes. The main seismic stations of the regional network are BBL in northern Dominica, MGG on Marie-Galante Island, and the Soufrière volcano seismic network south of Basse-Terre (regrouped under OVSG on this map). MGG was the closest station to the mainshock, 27 km away. A permanent vertical seismometer TBG was installed on Terre de Bas Island in the Les Saintes archipelago a few days after the mainshock, which improved the network's local detection threshold and location accuracy. The pentagone indicates the region where a geyser was observed by Blainville in 1843 (Bouysse, 1980) on Morne–Piton fault (cf Appendix A). The inset displays the Lesser Antilles arc at the eastern boundary of the Caribbean plate. The vector indicates the convergence rate between North American and Caribbean plates (DeMets et al., 2000).

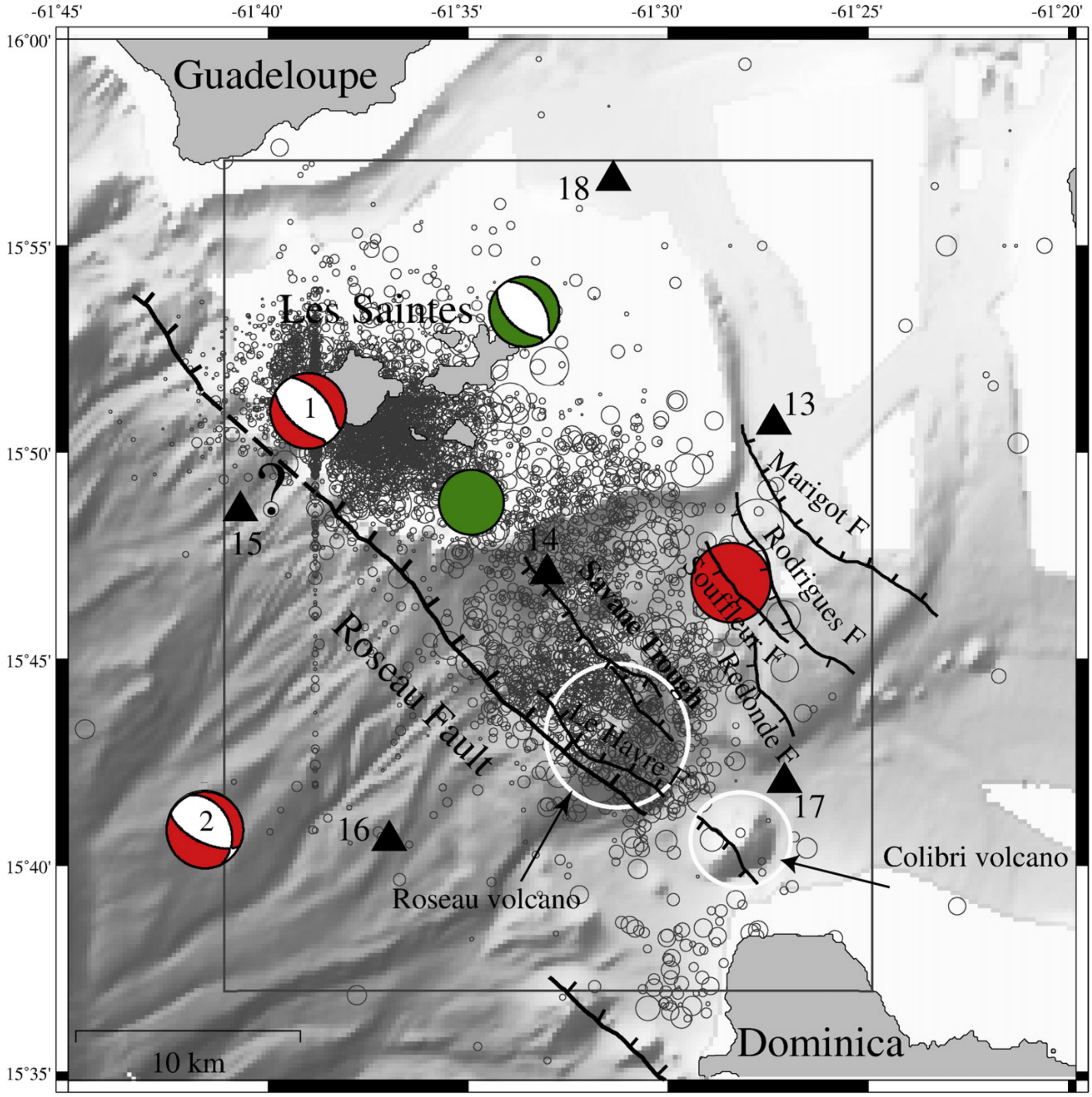

Fig. 2. Locations of the 5547 aftershocks manually picked by OVSG seismologists between 21 November 2004 and 17 September 2009 (IPGP, 2009). The data collected during this swarm is so voluminous, especially during the first year, that the whole period has not been processed. These preliminary locations present artefacts due to the limited monitoring array. The aftershocks distribution is cloudy but reveals a seismic gap near 15°47′N, which we will discuss below. Magnitudes detected are between 1 and 5.8, hypocentral depths range from the surface to 34 km with an average depth of 8.6 km. Position errors are 2.9 km horizontally. The filled red circle marks the mainshock as initially located by the OVSG network (15.77°N, 61.48°W, 14.5 km depth). Red beach balls show CMT and epicenters for the mainshock (1 is Harvard and 2 is Geoscope solution). The filled green circle marks the main aftershock as located by the OVSG network (15.81°N, 61.58°W, 11.7 km). The Harvard CMT solution for the main aftershock is displayed in green beach ball symbol. Underwater volcanoes are marked and the simplified fault scarps from Feuillet (2000) show the geometry of a graben in the channel between Guadeloupe and Dominica Islands. Les Saintes Islands are plotted above the seismicity symbols for clarification. Bathymetry relief in grey shading is from AGUADOMAR cruise (Deplus et al., 2001). Regions above 200 m below sea level, were not mapped, not permitting fault mapping on the Les Saintes insular shelf. Hence, the northern end of Roseau fault was not mapped, it may continue and connect to a branch mapped NW of the plateau. The triangles show the positions of the six OBS deployed after the mainshock for this study. The grey box delineates the area of map views of the velocity model shown in Fig. 8.

and detection threshold of the permanent network was limited by its geometry. In general, the alignment of monitoring stations along the island arc makes it difficult to accurately locate earthquakes in the EW direction. Several seismological networks located the November 21, 2004 event but positions differ by more than 15 km (Fig. 2 and Bertil et al. (2004)). More than 2000 events were detected during the first day. Seismic activity decreased very rapidly during the first week and more progressively after the first two months. The aftershocks form an elongated pattern, 22 km long and 10 km wide, following the graben azimuth and covering the whole fault system (Fig. 2). The aftershocks located by the permanent network do not indicate a clear fault plane and they cluster in two regions: one located beneath the Les Saintes islands and the other beneath the submarine Roseau volcano. The activity of this southern cluster faded through time and, 5 years later, only the cluster underneath Les Saintes remains active (IPGP, 2009; Feuillet et al., in revision).

Table 1
CMT solutions.

		Moment	NP1			NP2		
Event	Solution	(N m)	Strike	Dip	Rake	Strike	Dip	Rake
21 Nov 2004	Harvard[a]	3.44 10^{18}	325°	44°	−77°	127°	48°	102°
	Geoscope[b]	4.63 10^{18}	334°	34°	−54°	115°	63°	−112°
14 Feb 2005	Harvard[a]	0.698 10^{18}	326°	41°	−79°	132°	50°	−99°

[a] Global Centroid Moment Tensor database, formerly known as the Harvard CMT catalog: http://www.globalcmt.org/CMTsearch.html.

[b] Computed by E. Clévédé and G. Patau with IPGP-INSU data from http://www.geosp6.ipgp.jussieu.fr/CMT/Default_cmt_previous.htm.

3. Data and technique

To better locate aftershocks and determine the fault responsible for the main event, we deployed an array of six OBSs around the Les Saintes graben from 16 December 2004 to 25 January 2005, using the Ports and Lighthouses vessel *Kahouanne*. The OBSs are from an instrument pool owned by the Institut National des Sciences de l'Univers (INSU) and operated by the Institut de Physique du Globe de Paris (IPGP, http://www.ipgp.fr/pages/02120601.php). Each OBS is composed of a Hitech HYI-90-U hydrophone and a Mark Products L-22 vertical geophone mounted in a separate pressure case. The OBSs are designed by the Scripps Institution of Oceanography: detailed descriptions of the L-Cheapo package are given by Constable et al. (1998) and are available at http://www.obsip.org. The OBSs recorded at 125 samples per second per channel. Five OBSs encircled the active zone and one was placed in the center of the network to better constrain aftershock depths. The analysis of OBS data requires more pre-processing than for land stations because the instruments can neither be positioned or time synchronized by GPS while they are at the seafloor. A GPS time synchronization is made just before and just after deployment, and a linear drift correction applied. The OBS clock drift rates ranged from 11 to 37 ms during the 41 days of deployment (0.3–0.9 ms/day before correction). The drifts of the OBS Seascan clocks are typically rated to <0.5 ms/day. We estimate the OBS coordinates and depths by inverting travel times of direct water wave arrivals. The initial coordinates are taken from GPS coordinates of the instrument drop locations and the initial instrument depths are taken from sonar soundings or derived by interpolating the bathymetry grid at the drop locations. We sent acoustic pings from the vessel within a radius of 2.5 km around each instrument in order to triangulate for their position and depth. New instrument coordinates and depths as well as the average velocity in the water column are estimated using least-squares fit of travel times through the water column. The instruments experienced lateral drifts from 16 to 77 m during descent, the drift distance being proportional to the water depth at the drop site. Estimated water column velocities range from 1520 m/s to 1582 m/s. These velocities are inversely proportional to the water depth at the drop site and are compatible with regional conductivity-temperature–depth (CTD) profiles. The data recovery is 100% for the six OBS and the data quality is generally good, but we observe a puzzling monochromatic noise centered at 6.35 Hz on all geophones (Fig. 3). This noise is not recorded by any of the six hydrophones, nor by the land seismometers. It is almost continuous on OBS 15 and less intensive on OBS 13 and 18. It occurs only twice a day in average for OBS 14, 16 and 17. These monochromatic infrasound waves are not correlated in time with seismicity and do not occur simultaneously on all geophones. We believe that the noise source was localized at the seafloor. A similar 6–7 Hz noise was recorded offshore of Equator by geophones with a different design than our sensors. Pontoise and Hello (2002) interpreted them as methane seepage from underwater canyons due to erosion processes. They suggested a model for pressure waves resulting from oscillating clouds of bubbles.

The OBS recorded continuous data during 41 days of active seismicity. More than 4000 events are detected using an automated software running on the Earthworm platform (open source developed by USGS, see http://www.isti2.com/ew for details) based on an STA[3]/LTA[4] algorithm originally developed by Allen (1978). A visual selection removes interfering signals and seismic events from other regions. Events are then manually picked using the Seisan software package (see Havskov and Ottemöller, 2005). P- and associated S-time arrivals are carefully checked using the Wadati (1933) method. Generally, S-wave arrivals are difficult to read because their onset lies in the P-wave coda and their amplitude is usually not much greater than that of the P-wave arrival. Having the two channels with the vertical geophone and the hydrophone helps the picking. A total of 3905 earthquakes are manually picked, of which 3767 had enough arrival time picks to be located. The picking accuracy is on the order of 0.024 s for the P coda and 0.048 s for the S coda.

During the same period, the OVSG permanent monitoring network recorded 392 events. OVSG seismologists routinely calculate earthquake magnitude using the duration form of Lee and Lahr (1975): $M_d = 2\log T + 0.0035D - 0.87$, where T (s) is the time lag between the P-wave arrival time and the end of the S coda, log is logarithm to the base 10, and D (km) is the epicentral distance. This local scale has been in use since the first seismological bulletins in this network. According to Bengoubou-Valérius et al. (2008) the M_d scale is shifted by 0.1 to 0.2 below the m_b computed by the USGS for magnitude above 4. Five significant events occurred during the OBS experiment: on 19 December (M_d4.0), 21 December (M_d4.2), 26 December (M_d4.5), 27 December (M_d4.8) and 10 January (M_d4.3). M_d estimation is impossible on the OBS dataset so we used the maximum amplitude of the S coda, following a method developed by the Japan Meteorological Agency (JMA) for shallow earthquake monitoring. JMA has been publishing local magnitudes using the empirical form: $M_l = a\ \log A + b\ \log D + c$ where a, b, and c are constants, log is logarithm to the base 10, A is the maximum velocity amplitude, and D (km) is the epicentral distance (JMA, 2004). We use a minimum least-squares search algorithm to determine the values of a, b and c best fitting the M_d values of the OVSG database. The coefficients obtained for the JMA empirical formula are $a = 1.15$, $b = 1.42$ and $c = -6.12$ and the magnitude distribution for the 3542 events is shown on Fig. 4a. The M_l values range from −0.7 to 4. For $M_d \geq 3.5$, the OBS geophones generally saturate and no M_l value is assigned to the event. The local magnitude of completeness is on the order of 1 for the OBS array, while the regional value is 2.7 (Bengoubou-Valérius et al., 2008). A Gutenberg-Richter cumulative curve reveals a b-value of 0.94 during this period (Fig. 4b).

4. 1D velocity model

The velocity model used for the OVSG permanent network was derived from a seismic refraction survey (Dorel et al., 1974; Dorel, 1978). The land station network was not dense at the time and the shot interval was only 15 km, limiting the resolution of the refraction method. This velocity model was the only one available before our study. It was averaged for land and oceanic regions of the Lesser Antilles (Table 2). Although Dorel (1978) computed a regional Vp/Vs value of 1.85, the OVSG routinely uses 1.76 after a recent analysis of

Fig. 3. Monochromatic noise recorded on the OBS geophones. a) Raw signal recorded on the vertical geophone of OBS 15. Left: a representative 2 min time window without earthquake; Right: a representative 34 min time window with many aftershocks. The noise needs to be filtered out to allow accurate picking. b) Spectral analysis of the two time-windows. The fundamental peak, at 6.35 Hz, is visible for both time periods. c) Sonograms of the two time-windows. Two overtones are visible, at 12.7 and 19 Hz. The amplitude of the principal peak and overtones does not correlate with the occurrence of aftershocks. d) Occurrence of the monochromatic noise on each OBS over 1 week. The noise was almost continuous on OBS 15 and less intensive on OBS 13 and 18. It only occurred about twice a day for OBS 14, 16 and 17. e) Corrosion on the OBS metallic parts after recovery from the seafloor.

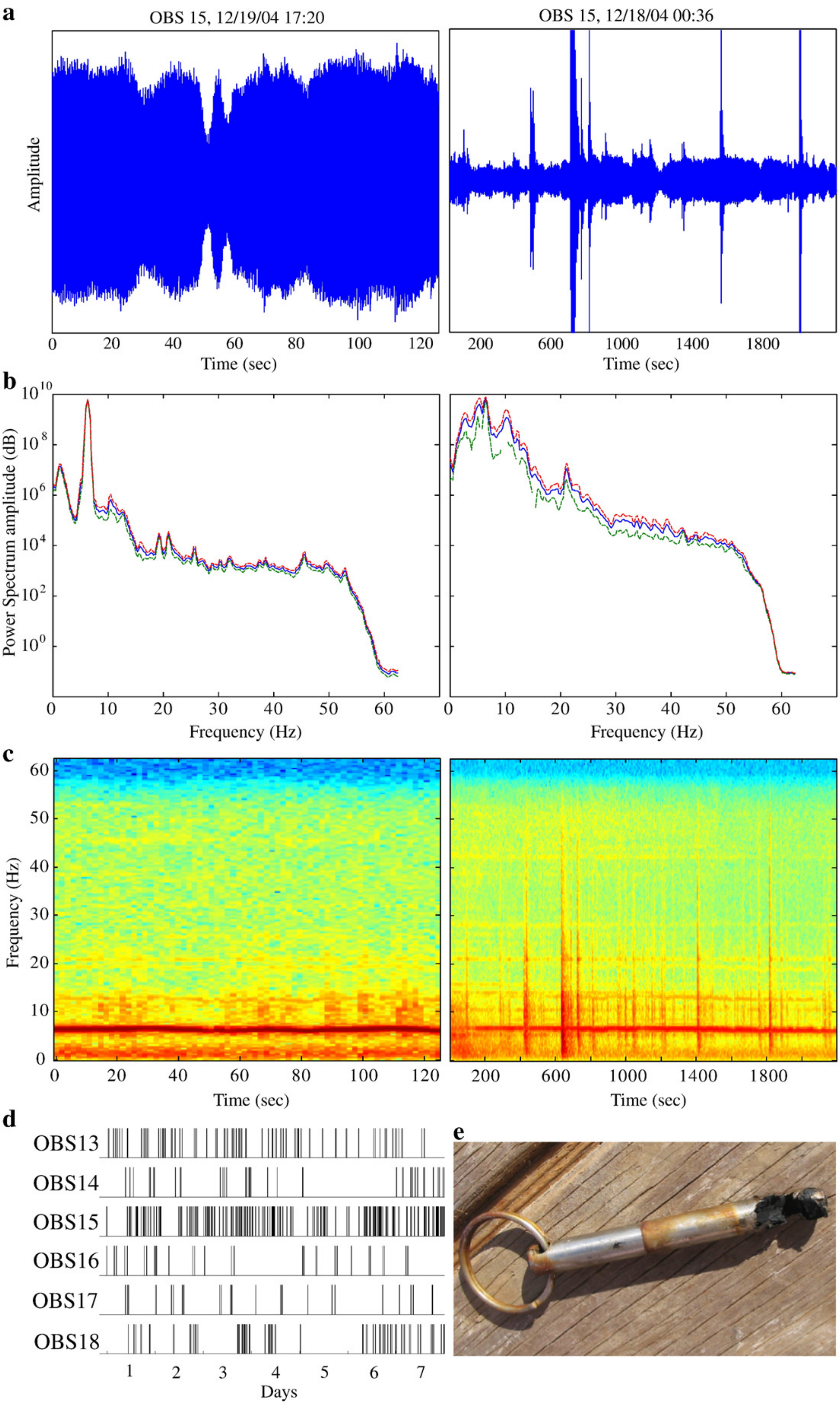
a
OBS 15, 12/19/04 17:20
OBS 15, 12/18/04 00:36
Amplitude
0 20 40 60 80 100 120
Time (sec)
200 600 1000 1400 1800
Time (sec)
b
10^{10}
10^{8}
10^{6}
10^{4}
10^{2}
10^{0}
Power Spectrum amplitude (dB)
0 10 20 30 40 50 60
Frequency (Hz)
0 10 20 30 40 50 60
Frequency (Hz)
c
Frequency (Hz)
0 10 20 30 40 50 60
0 20 40 60 80 100 120
Time (sec)
200 600 1000 1400 1800
Time (sec)
d
OBS13
OBS14
OBS15
OBS16
OBS17
OBS18
1 2 3 4 5 6 7
Days
e

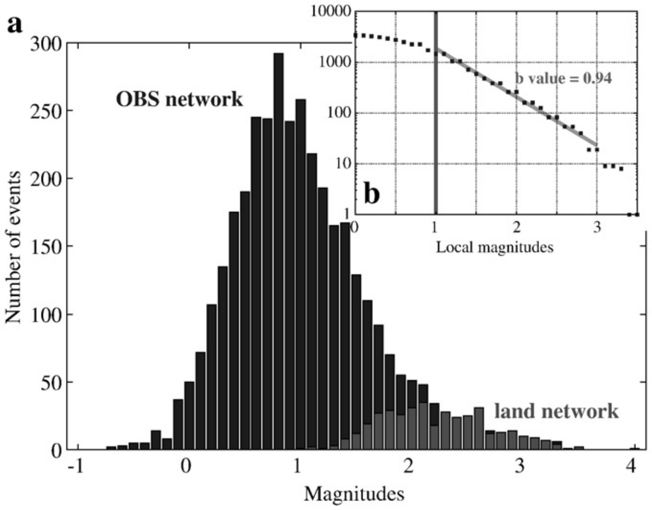

Fig. 4. a) Magnitude distribution of earthquakes recorded by the OBS and the permanent land network over the same 41-day period. The OBS array is sensitive to 9 times more events than the land network. b) Frequency-magnitude distribution for earthquakes recorded by the temporary OBS array. The *b*-value is calculated for events with $M_l \geq 1$, which is the magnitude of completeness of the OBS dataset. The *b*-value was 0.94 during this very active period.

the historical database (Clément et al., 2001). Preliminary earthquake locations using the same velocity model and Vp/Vs as the OVSG are computed for the 3767 OBS events that have sufficient P- and S-arrival times. Localized events are spread over the entire graben (Fig. 5a) and it is difficult to distinguish any clear feature from vertical profiles (therefore sections are not included here). In order to better constrain earthquake locations and to improve the layered velocity model, the data are inverted for a 1D model of velocity versus depth. Events with more than 3 P-S time lags, azimuth coverage ≥ 180° are initially selected. An additional data selection is achieved by slightly varying the velocity model and computing hypocentral shift (a proxy for real hypocentral error, (Lienert, 1994)). Only a subset of data with real epicentral error <2 km and real depth error <3 km are used for the 1D inversion. Travel times from these 1288 events (6225 rays) are inverted using the Velest code (see Kissling et al., 1995) and Dorel (1978) velocity profile as the starting model. The inversion simultaneously computes hypocenters and seismic velocities. The selected events are split into two subsets and each subset was run through the inversion (Kissling et al., 1994). The velocity models and RMS (root mean square) residuals obtained using the two subsets are quite similar which verifies the uniqueness of the solution: the two velocity models differ by 9% at the most and the starting travel-time RMS was reduced from 0.152 s to 0.101 s for the first selection and from 0.158 s to 0.108 s for the second selection. In Fig. 6, we show the two computed 1D velocity models compared to the a-priori one. The so-called minimum 1D model (Table 2) is chosen as that with the lowest RMS travel-time residual of the two subsets. We then test the dependence of the inverted model on the starting model, using high-velocity (+1 km/s) and low-velocity (−1 km/s) starting models (Fig. 6).

We compute hypocenters for the whole dataset using our minimum 1D model. A comparison of hypocenters obtained with the Dorel (1978) model and our inverted velocities (Fig. 5a, b) show a marked improvement in the clustering of events with the new 1D model. Using the Wadati (1933) method, the mean Vp/Vs value is 1.81 with a standard variation of ±0.1.

5. 3D modelling

To compute Vp and Vp/Vs anomalies and further improve earthquake locations, we calculate a 3D velocity model using the local earthquake tomography (LET) algorithm Simul2000 (Thurber, 1983; Eberhart-Phillips, 1990; Eberhart-Phillips and Reyners, 1997). Simul2000 iteratively solves for Vp, Vp/Vs, and updated earthquake locations and origin times. We space velocity nodes 5 km apart in the horizontal and 1 to 3 km apart in the vertical. The damping parameter has an important effect on tomography results: we select the optimum value by following the method described by Evans et al. (1994). We run one inversion iteration for 20 damping values from 1 to 1000. For each damping value, we compute the model complexity and data variance. The damping value of 12 gives the best trade-off between both properties (Fig. 7). Weaker damping would give a more complex velocity model without significantly better fitting the travel-time data. We begin by selecting a subset of 1183 earthquakes of the 1288 already selected for the 1D inversion (the original selection is S phases ≥3, epicentral error <2 km and depth error <3 km), by adding a threshold of 0.25 s for the localization RMS and 180° for the minimum azimuth coverage. As a starting model, we use the minimum 1D model, including its started Vp/Vs ratio of 1.81. The number of observations is 11063 (6630 P- and 4433 S-wave first arrival times) and we inverted for 255 velocity nodes.

Table 2
Compressional velocity depth models used in this study.

Dorel (1978)		Minimum 1D	
Depth (km)	Vp (km/s)	Depth (km)	Vp (km/s)
0–3	3.5	0–1	2.7
		1–2	3.6
		2–3	3.9
3–15	6.0	3–5	5.1
		5–9	5.5
		9–11	5.8
		11–13	5.9
15–30	7.0	13–30	7.0
30+	8.0	30+	8.0

The inversion reduces the RMS travel-time residual from 0.095 s to 0.053 s and the data variance from 0.009 s^2 to 0.003 s^2 after six iterations. Horizontal slices of the 3D velocity model solutions at upper and mid-crustal depths show the internal structure of the Les Saintes graben (Fig. 8). Vertical sections perpendicular to the faults direction reveal anomalies in the vicinity of the faults (Fig. 9). The final Vp velocity model (Figs. 8a, 9a) is highly variable (anomaly ranging between −19 and +13%), whereas Vp/Vs (Figs. 8b, 9b) is less variable (from −6 to +7 %). The Vp/Vs heterogeneity observed in the 3D model (−6 to +7% of 1.81) is on the same order of magnitude as the standard deviation of the minimum 1D model (±0.1). Moreover, the minimum and maximum values for the Vp anomaly (i.e. −19% and +13%) match the discrepancies between the 1D minimum model and the two end-members using high initial velocities and low initial velocities, which do not exceed 1 km/s in the middle crust (Fig. 6). The most striking features are the positive Vp/Vs anomaly in most of the graben region and the negative Vp/Vs anomaly SE of the Les Saintes Islands. A wide negative Vp anomaly of −19% lies between 4 and 8 km depth at the graben center, which at depth tracks the Roseau fault plane. At 6 km depth the Vp anomaly inversely mirrors the Vp/Vs anomaly and we will analyse this observation in the discussion about faulting processes. A very shallow positive Vp anomaly lies SE of the Les Saintes islands, which we interpret as an effect of the reef platform (Fig. 8a, plate $z = 2$ km). A positive Vp anomaly lies 10 km deep near the SE end of the aftershock swarm, *N* of Roseau volcano (Fig. 8a, plate $z = 10$ km). This +10 to +15% anomaly could be related to a frozen magmatic intrusive body.

Different tools exist to verify the LET solution quality and estimate the resolving power of the data set (Kissling et al., 2001). A simple evaluation of the resolution of the 3D seismic model can be obtained from the distribution of ray paths. The hit count distribution sums up the number of rays that contribute to the solution at each node. It

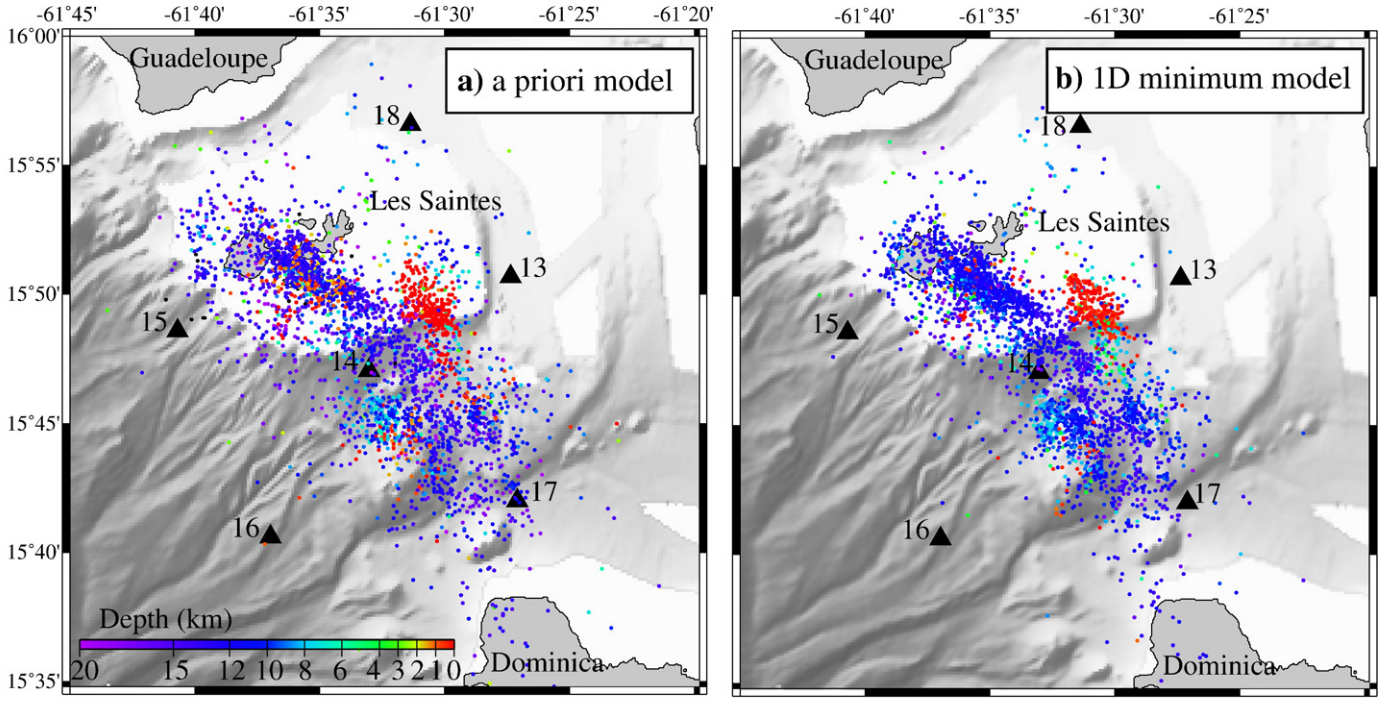

Fig. 5. Map of the seismicity recorded by the temporary OBS array preliminary located using 1D velocity models. The triangles show the positions of the six OBS. Les Saintes and Dominica coastlines are plotted, a) using the 1D velocity model of Dorel (1978). This regional model is the one routinely used for OVSG hypocenter localisations, b) using the minimum 1D model.

outlines the ray coverage but cannot assess the validity of the inversion parameterization. Hit count varies from 2000 to 8000 in most of our model volume. The derivative weight sum (DWS, see Toomey et al.(1994)) are interpreted as a measure of the density of seismic rays influencing each model parameter and therefore outlines the model resolving power. DWS distributions are shown in map views at six depths including those of our velocity model solutions (Fig. 10). The diagonal elements of the resolution matrix (RDE) can also be used as they describe how independent the solution is for one model parameter. It is common to define well-resolved models when RDE >0.2 (e.g. Haslinger et al., 1999). After analyzing the resolution matrix, we define the solution as reliable for areas with a DWS over 5000. This is a conservative choice as areas with DWS >5000 always verify RDE >0.2 in our model. The resolving power is adequate within the OBS array, and is best between 4 and 8 km depth.

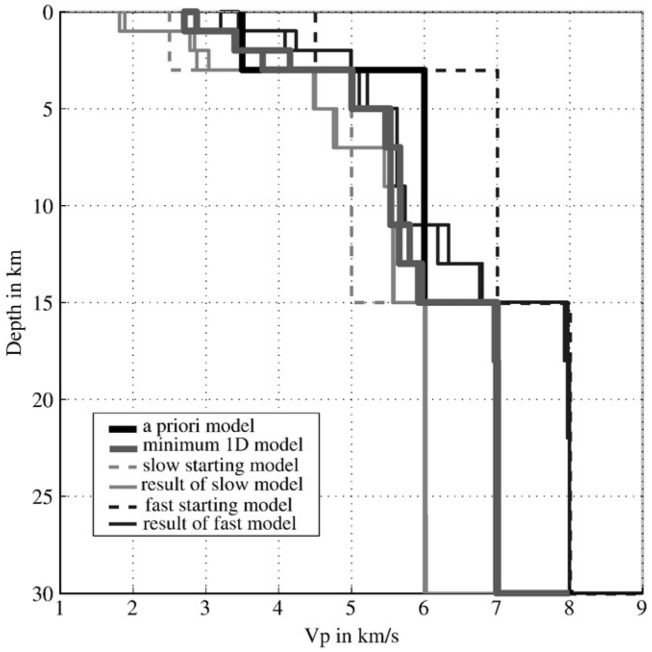

Fig. 6. Comparison of compressional velocity versus depth models from a regional study (thick black line from Dorel (1978)) and the models obtained using the Velest inversion. The solutions for the two subsets of data (two thick dark grey lines) are very similar; this verifies the uniqueness of the solution. The dependence on the starting model is tested using high-velocity and low-velocity starting models. Both solutions (thin black and thin pale grey lines) converge towards the minimum 1D model.

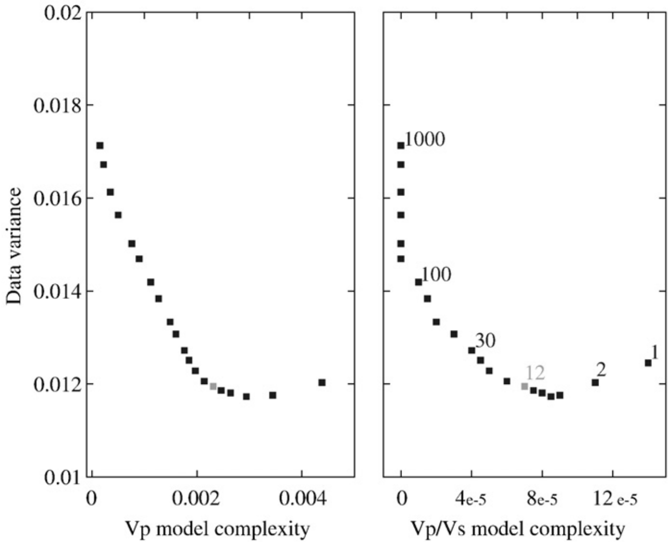

Fig. 7. The effect of damping on the relationship between data variance and model complexity. 20 damping values from 1 to 1000 are tested, the best trade-off between variance and complexity is obtained for a damping parameter value of 12.

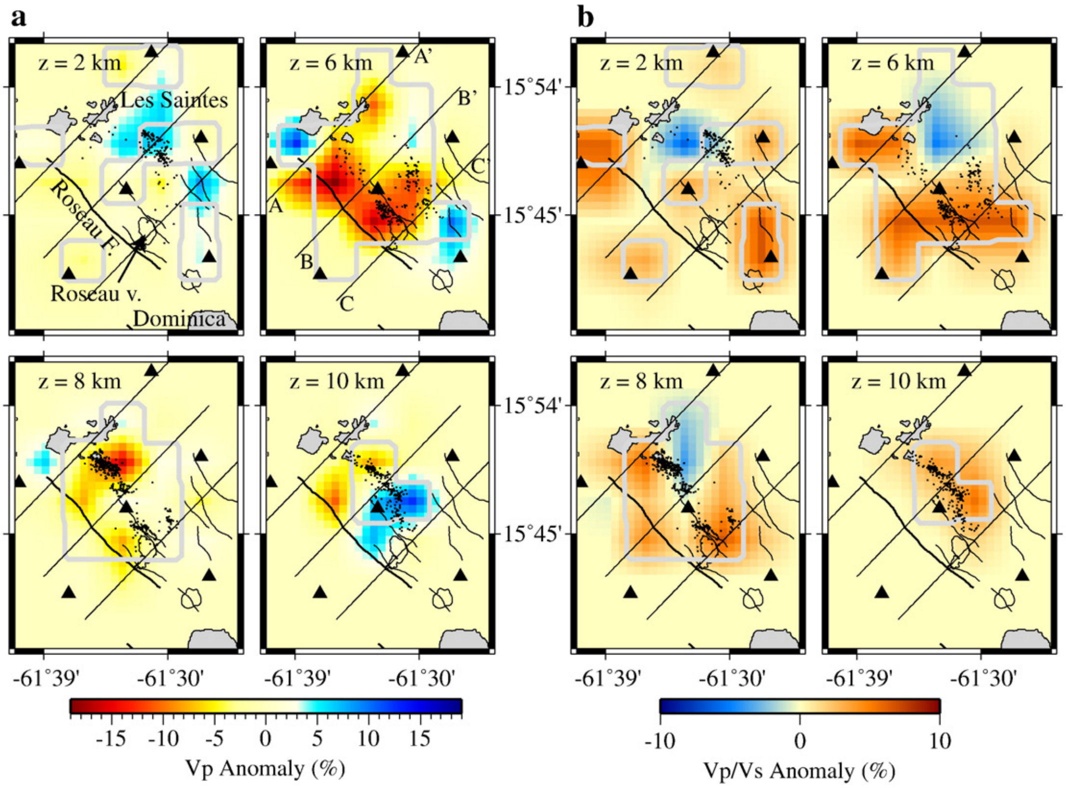

Fig. 8. Map views of the velocity anomalies on four constant-depth planes in the upper crust, mid crust and lower crust. Blue colors represent fast P-wave velocities or low Vp/Vs ratios, while red colors represent slow velocities or high Vp/Vs ratios. The grey lines are the isolines of the well-resolved regions (DWS > 000, see Fig. 10). LET hypocenters located near to each plane are plotted in black (in order, from 0–4, 4–7, 7–9 and 9+ km depth). Black lines mark the positions of the three vertical profiles presented in Fig. 9. Triangles show the OBS positions. The coastlines of the Les Saintes group and Dominica Island, and, the faults and the contour of the underwater volcanoes are plotted. a) Vp anomaly, b) Vp/Vs anomaly.

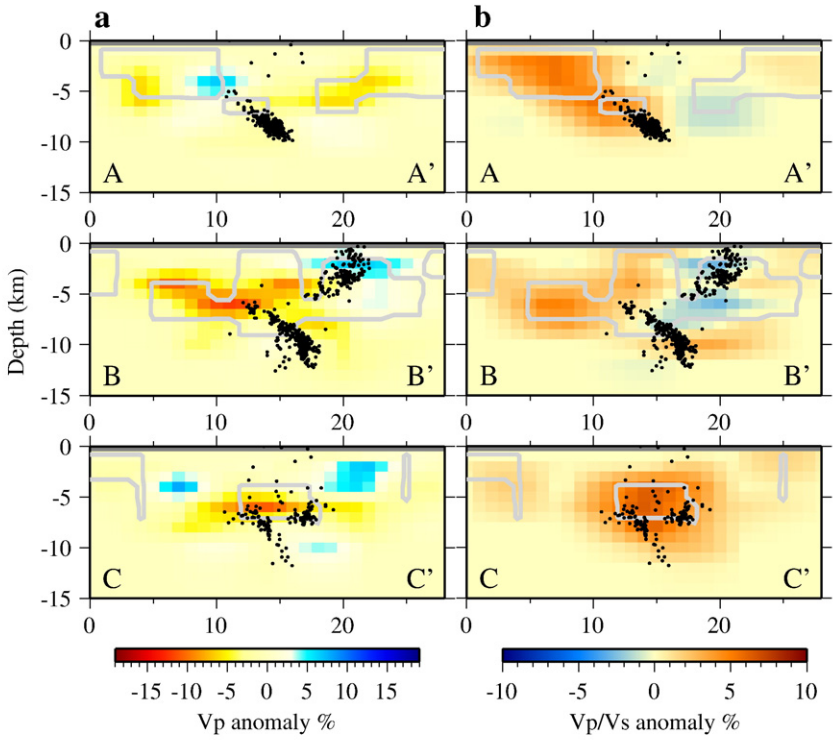

Fig. 9. Cross-sectional views of the velocity anomalies across the fault system. The three panels display profiles that step progressively southward from top to bottom. Transect AA′ shows a profile running across Les Saintes Islands. Transect BB′ presents the structure crossing through the middle of the seismic sequence while transect CC′ presents the structure across Roseau Volcano. Blue colors represent fast P-wave velocities or low Vp/Vs ratios, while red colors represent slow P-wave velocities or high Vp/Vs ratios. The grey lines are the isolines of the well-resolved regions (DWS >5000, see Fig. 10). LET hypocenter locations within 5 km of each plane are plotted in black. a) Vp anomaly and b) Vp/Vs anomaly.

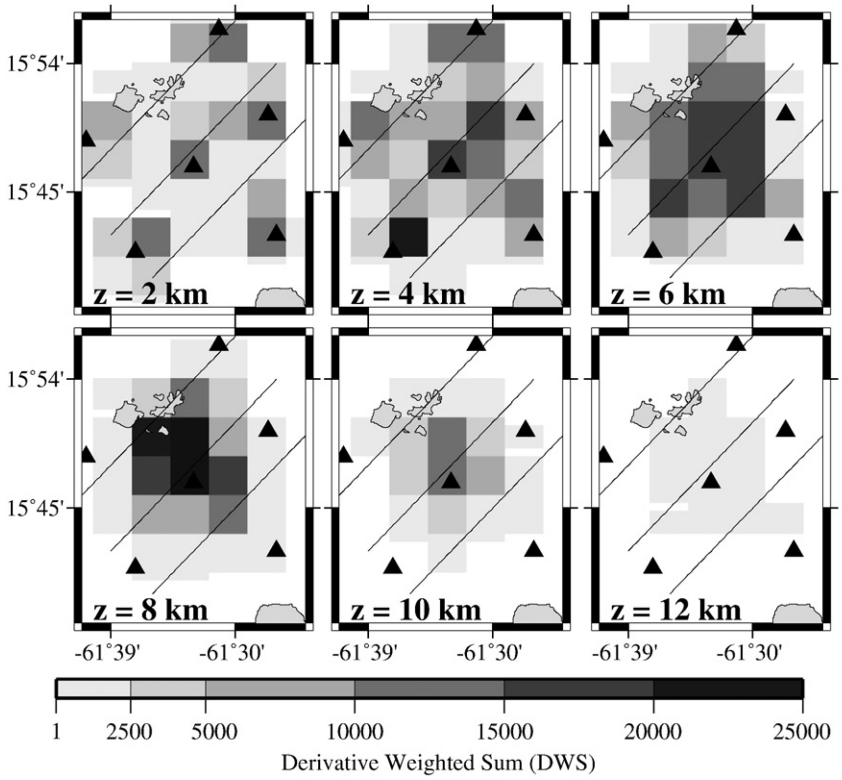

Fig. 10. Map view of derivative weight sum (DWS) values for 6 constant-depth planes. DWS is used as proxy for imaging model resolution. Here, values above 5000 are considered to have adequate resolution (Toomey and Foulger, 1989; Toomey et al., 1994; Haslinger et al., 1999). Black lines mark the locations of the three vertical profiles shown in Fig. 9. Triangles show the positions of the six OBS. Les Saintes and Dominica coastlines are plotted.

6. Aftershock sequence

The 1183 3D-located aftershocks are plotted with the faults and volcanoes in Fig. 11. The average change of epicenter location is 2 km. The locations are now precise enough to image the clustering of aftershocks along planes, allowing us to make a tectonic interpretation. There are two well-defined clusters, with opposite dip. The events of the main cluster align perfectly at depth, on a plane dipping at 50 ± 3° toward the NE. Seismicity on this fault plane is limited to between 5 and 12.6 km depth, with the highest density between 8 and 10 km. The best-fit plane to this cluster has an azimuth of N327°. This plane intersects the surface at the Roseau fault scarp.

The hypocenters computed by OVSG, Harvard, and Geoscope for the main November 21 event lie 15 km apart (Fig. 2) and do not lie on the fault plane identified by the aftershock cluster. The normal mechanisms computed by Harvard and Geoscope are composed of two nodal planes from which it has been so far impossible to decide on the actual fault geometry (Vallée et al., 2005; Delouis et al., 2007). Both CMT nodal planes agree with the N135° azimuth of the normal faults in the Les Saintes graben. From the dip of the relocated fault plane, we propose that the mainshock (21 November 2004, $M_w = 6.3$) and the second major event (14 February 2005, $M_w = 5.8$) both ruptured Roseau fault. The OBS array was not in place during these two main events, but we are able to relocate them with master events that are simultaneously located by the OVSG permanent network using a master-slave technique. Master events are chosen within our 3D-located aftershock dataset with at least 5 P- and 5 S-arrivals in the permanent network and short distances (<5 km) to the slave events. For each slave, three master events verify these conditions. As the slave (the event that we wish to relocate) and its master are close to each other, we can consider similar source-station ray paths. For each master event, we calculate the delay times at the permanent seismic stations by fixing the hypocenter at the position inverted by our LET. These time delays are then applied as station corrections for the relocation of the two slaves. The description of this procedure can be found in Bengoubou-Valérius (2008). The three possible solutions for each of the main events are listed in Table 3 and displayed in Fig. 11a. The deepest solutions do not lie on the fault plane outlined by the relocated aftershocks. Although they do not provide the smallest RMS, our preferred solutions are the shallowest ones (i.e. 8.0 and 8.1 km depth, respectively, for the 21 November and 14 February events) because their projections fall perfectly on the fault plane outlined by the 3D-located cluster. Between these two main shocks, which sit 8 km apart, there seems to be a seismic gap in the aftershock distribution (centered near 15°47′N 61°33′E in Fig. 11a). This lack of seismic activity was already visible between the north and south clusters in the dataset located by the permanent network (Fig. 2) and it persists with the OBS low detection threshold.

The Roseau seismicity distribution is perfectly planar to the north (section 1, Fig. 11b) but widens towards the south (section 3, Fig. 11b). The cloudy cluster may suggest that the postseismic deformation affected several parallel faults, including Le Havre fault, and probably connected at depth with the Roseau main fault. The NE cluster (Fig. 11) probably corresponds to slip on several parallel and smaller fault planes antithetic to Roseau fault (Rodrigues and Souffleur faults). This shallow cluster extends on the Les Saintes plateau suggesting that these antithetic faults continue northward. However, the lack of multibeam bathymetric data in this area cannot confirm this hypothesis. The dipping angle of the antithetic faults cannot be measured with accuracy but it is on the order of 50° as well. Roseau fault and the smaller antithetic ones may connect at depth where a positive Vp anomaly is detected (Fig. 8a, plate $z = 10$km), but the present data cannot confirm it.

The absence of shallow seismicity between the Roseau fault seafloor scarp and the depth of 5 km is not an artifact of the experiment geometry and truly illustrates the fault processes (Fig. 11). However the absence of relocated seismicity below Les Saintes islands, and, south of Roseau volcano is an artifact of the LET

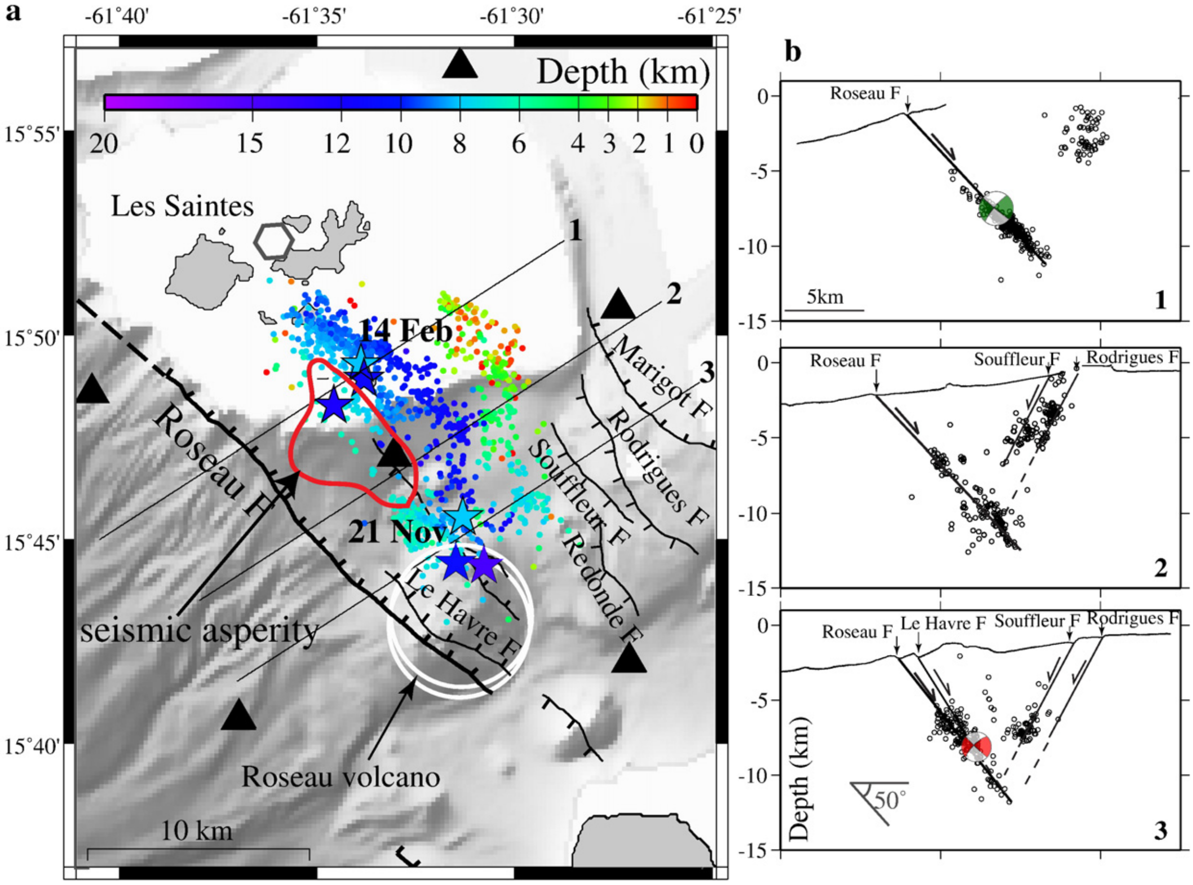

Fig. 11. 3D-located seismicity from the OBS dataset. a) Map view. Simplified fault scarps are from Feuillet (2000). Epicenters are coloured according to the hypocenter depth. Stars indicate the three possible solutions for the mainshock (21 Nov.) and its strongest aftershock (14 Feb.), calculated using slave–master technique (table 3). Our preferred solutions are the shallowest ones, i.e. the lightest blue stars. The patch of high coseismic slip (≥0.5 m) inferred from a teleseismic inversion for the main event (Salichon et al., 2009) is contoured in red. The 3D-located, aftershocks cluster in the lower part of the Roseau fault plane that had not ruptured during the main event. Les Saintes coastlines are plotted and the pentagone indicates the region where a geyser was observed by locals on February 14th (cf Appendix A). The triangles show the positions of the six OBS. b) The three panels display sections that step progressively southward from top to bottom and are perpendicular to the 327°N Roseau cluster azimuth. LET hypocenter locations within 2 km of each plane are plotted in black. The best fitting planes for the Roseau fault cluster and antithetic cluster are drawn; they connect to the surface fault scarps. The antithetic faults do not continue on the Les Saintes plateau but regions above 200 m below sea level were not mapped. Roseau fault dips at 47° for the two northern sections (1 and 2) and at 53° for the southern one (3). A 50° benchmark is shown for reference. The red and green beach balls mark Harvard CMT of the main shock and the main aftershock respectively, at their 3D-relocated positions. They perfectly lie on the LET relocated fault plane.

because events with 180° minimum azimuth coverage are selected for the 3D inversion. There is no seismicity below 12.6 km in the surveyed area, which probably represents the base of the graben formed by the antithetic faults. An antithetic fault was similarly reactivated after the M_S6.6 Kozani-Grevena normal-fault earthquake in 1995, and it connected to the main fault at 12 km depth (Meyer et al., 1996; Chiarabba and Sevaggi, 1997; Hatzfeld et al., 1997). This depth may correspond to the brittle–plastic transition. The typical seismogenic thickness is 15 km but can range from 0 to 40 km in the oceanic crust (Watts and Burov, 2003). Here, the thin seismogenic layer may be controlled by the local geothermal regime as the Les Saintes graben lies along the Lesser Antilles volcanic chain. The thickness of the seismogenic layer influences both the maximum width of grabens and the continuity of the faults (i.e. the maximum segment length) that bound them in extensional provinces (Hayward and Ebinger, 1996). It therefore has important implications for seismic hazard estimation in the region.

The main and antithetic clusters were active simultaneously during the 41 days of the OBS deployment; there is no clear temporal evolution within the aftershock sequence. The sequence has a *b*-value of 0.94 (Fig. 4a). Bengoubou-Valérius et al. (2008) computed a regional *b*-value of 1.13 for intraslab events and 1.38 for shallow events. *B*-values ≤1 are typical of magmatic regions but can also be interpreted as regions awaiting a major earthquake. The *b*-value of our dataset is 32% lower than the regional average. It might be due to the fact that the OBS survey took place before the main aftershock on February 14th 2005, or that this active fault system cuts several underwater volcanoes. The ages of these volcanoes are currently unknown, but nearby volcanoes in the Les Saintes archipelago and in the north of Dominica Island were dated to Pliocene Quaternary volcanism (Jacques et al., 1984; Bellon, 1988; Jacques and Maury, 1988).

Table 3

Latitude	Longitude	Depth (km)	RMS (s)
Three master–slave solutions for the first shock of November 21 2004			
15° 44.43	−61° 31.49	10.85	0.08
15° 45.55	**−61° 31.31**	**8.02**	**0.14**
15° 44.37	−61° 30.78	14.78	0.10
Three master–slave solutions for the strongest aftershock of February 14 2005			
15° 49.29	**−61° 33.88**	**8.11**	**0.12**
15° 48.28	−61° 34.57	12.19	0.11
15° 48.93	−61° 33.81	11.25	0.09

The preferred solutions are in bold. A description of the master–slave procedure can be found in Bengoubou-Valérius (2008).

7. Discussions

7.1. Aftershocks, low P-wave velocities and rupture geometry

After 25 days from the mainshock, most of aftershocks along Roseau fault are confined between 8 and 12.6 km and there were none shallower than 5 km. Our master–slave results indicate that the two main ruptures of the seismic sequence most probably started at 8 km depth. The negative Vp anomaly outlines the fault plane from 4 to 8 km depth (Fig. 9a, section BB′) and therefore is mostly located above the mainshock and aftershocks. P- and S-wave velocities in the crust depend on rock mineralogy, temperature, pressure, intrinsic porosity and fracturing as well as the presence of fluids (Christensen, 1996). Low P-wave velocities are typical in faulted regions and we propose that the wide negative Vp anomaly imaged by our LET at 4 to 8 km depth at the graben center (Fig. 8a) outlines sections of Roseau fault where most slip occurred. If we assume that the 21 November rupture reached the surface with a dip angle of 50° and a maximum depth of 8 km, the rupture zone width is on the order of 10.4 km. It is not as wide as previously assumed for the down-dip dimension of the 21 November failure plane (Le Friant et al., 2008; Feuillet et al., in revision) but still compatible with typical rupture dimensions for normal events of such magnitude (Wells and Coppersmith, 1994). Whether the rupture broke the surface or not is difficult to conclude using this dataset only and high-resolution underwater imagery will be necessary to solve this issue. However, as shear stress along a fault plane is required to vanish at the free surface, a shallow earthquake such as the 21 November one is likely to result in surface rupture. Indeed, Le Friant et al. (2008) assumed that the rupture reached the seafloor and successfully reproduced the observed 2–3 m tsunami. They modeled the tsunami wave generated by the November 21 event using a dip angle of 50°, a fault length of 15 km, an epicenter depth of 14 km, a strike angle of 320° and a 1 m uniform slip.

When earthquakes occur, they release the shear stress on the ruptured area and increase the stress beyond their rupture edges, by amount that declines with distance (Mendoza and Hartzell, 1988). Indeed, Chiarabba et al. (2009a) have located aftershocks that cluster around patches of large slip defined by SAR models for the Aquilla earthquake (central Italy). Here, we believe the deep aftershock cluster between 8 and 12.6 km depth was triggered by a stress increase at the rupture bottom–edge following the main shock rupture. The geometry of this deep cluster is in agreement with static Coulomb stress change models (Nostro et al., 1997; Feuillet et al., in revision). As the deep cluster geometry appears planar (Fig. 11b, section 1), we propose that these aftershocks ruptured sections of Roseau fault that had not slipped during the 21 November shock. Salichon et al. (2009) have recently achieved a teleseismic inversion of the 21 November rupture. Without knowing which one of the two nodal planes ruptured they proposed two models. Our preferred solution, model 2 (strike N327° and dip 55°), consists of a main asperity where the maximum slip reaches about 1 m, and a smaller one of 25 cm slip. The main asperity is located NW of the relocated 21 November event, between 8 and 16 km down–dip (which correspond to 6.5–13 km depth assuming the 55° dip, see its projection in Fig. 11a). The smaller asperity is located at the same depth and 10 km to the SE of the main asperity. Although the resolution of the teleseismic inversion is limited and the finite fault model geometry assumed for the rupture (30 km long and 21 km wide plane intersecting the preliminary hypocentral location at 14 km depth) does not coincide with our fault plane solution, the patch of high slip is in agreement with the aftershock pattern. According to Salichon et al. (2009), the 21 November nucleation started at depth (the authors assumed 14 km but we suggest 8 km depth) and propagated up–dip in two patches and probably reached the seafloor. As this event did not rupture the entire width of Roseau fault, aftershocks cluster in the lower part of the fault plane that had not slipped. The aftershock geometry, with the long-lasting cluster near the Les Saintes and a fading cluster near Roseau volcano, is in agreement with the teleseismically inverted rupture showing a main asperity NW of the hypocenter and a smaller one SE of it. Dense monitoring networks have previously imaged diffuse clouds of aftershock which indicate that aftershocks do not always cluster along the main fault planes or aftershock geometries do not always agree with rupture dimensions estimated by geodetic or teleseismic inversions (e.g. Hauksson et al., 1995; Massonnet et al., 1996; Donnellan and Webb, 1998). The present sequence shows a simple planar geometry that matches the surface fault scarp as well as the expected dip and strike determined teleseismically, and which dimensions are consistent with the event magnitude. The reason may be the moderate magnitude of the event and a simple source mechanism as previously suggested by Mellors et al. (1997).

7.2. Fluids

The monochromatic noise recorded by geophones 15 (with lower rate by geophones 13 and 18) may be produced by fluid seepage into the ocean. The proximity of these geophones to the two active faults (OBS 15 is ≤3 km away Roseau fault and OBS 13 is ≤3.5 km away from Rodrigues fault) favors this interpretation. The island shelf was not mapped during the AGUADOMAR high-resolution bathymetric survey and further mapping would be necessary to identify whether an active fault lies near OBS 18. Moreover, some metallic parts of the OBS mounting were extremely corroded when we recovered the instruments from the seafloor (Fig. 3e). This type of corrosion has not been observed before for such a short deployment time. We infer that the water chemistry near the seafloor was not of normal composition. This is another evidence that the 21 November event ruptured the seafloor. Further sea-bottom investigation would be necessary to solve this enigma. In addition, locals witnessed a bubbling white discharge associated with vapor in the ocean between Terre de Haut and Terre de Bas Islands in the Les Saintes group (location marked on map in Fig. 11a), forming a circular trace that lasted for several hours after the main aftershock (witnesses statements and pictures are presented in Appendix A). Scuba divers also reported zones of higher temperature around the Les Saintes coast, but we were not able to verify this information. Fluids may have been discharged from an underwater fault between these islands. A comparable manifestation was observed at sea on March 17, 1843, 37 days after an M_w8 earthquake NE of Guadeloupe (de Blainville, 1843). A geyser spouting with vapor occurred above Colombie Bank, located along the Morne Piton normal fault, NW of Marie-Galante Island (location marked on map in Fig. 1). Although, the 1843 geyser did not occur shortly after any earthquake, we infer that the Morne Piton fault released a high volume of fluids in a fashion similar to what happened near the Les Saintes Islands on February 14 2005.

Low P-wave velocities are typical in faulted regions while high Vp/Vs anomalies are characteristic of fluid-filled pores and cracks (Eberhart-Phillips and Michael, 1993) or molten bodies (Bazin et al., 2003). Here, the concomitant low Vp and high Vp/Vs anomalies (Fig. 8) could indicate transient fluid in the Roseau fault. In fluid-saturated rocks, high Vp/Vs anomalies may indicate high pore pressure, perhaps because large shallow earthquakes induce changes in the fluid pore pressure that are comparable to stress drop on faults (Nur and Booker, 1972). The pore pressure changes induced by the 21 November event may have caused postseismic fluid flow that slowly decreased the strength of rock (Chiarabba et al., 2009b,c) and resulted in the delayed fracture of the 14 February main aftershock. In addition, large-amplitude long-period motions are observed on broadband data collected during the same aftershock sequence (Jousset and Douglas, 2007). The authors suggest that 5 to 10 s peaks in displacement response spectra are specific oscillating source mechanisms possibly involving fluids within the source. The long-period peak is present during the $M_w5.3$ aftershock that occurred on November 21 at

13:37 TU, 2 h after the main rupture. We suppose that fluids were near the source region prior to the main rupture. Brodsky and Kanamori (2001) have shown that the mechanical effect of viscous fluid lubricating a fault zone has implication on the rupture dynamics. Elevated fluid pressure in a thin film between rock surfaces supports parts of the load reducing the effective normal stress across the fault and, therefore, can facilitate earthquake nucleation. Byerlee (1993) has proposed a compartment model to explain the cyclic behaviour of earthquake triggering: during an earthquake, the fault zone compacts and water flows into the damaged and porous country rock until the fault zone pore pressure reaches the country rock hydrostatic pressure. This new state can trigger another earthquake. Overall, fluid moving in and out of the fault zone could be the driving mechanism for such a long-lasting aftershock sequence. The negative Vp/Vs anomaly in the region of the antithetic Rodrigues and Souffleur faults suggests that fluids may not be involved in their rupture process. For that reason, the activity on the antithetic faults has ended after a few months. In comparison, the seismic sequence that followed the M_s6.2 strike–slip Redonda event that occurred north of Montserrat Island on March 16 1985, lasted only for a few months (Girardin et al., 1991). A late M_s5.2 aftershock occurred on February 12 1986 and was followed by a short aftershock sequence. We propose that the difference between the >5 year-long Les Saintes sequence and the 1 year-long Redonda sequence is caused by different fluid regimes. The reason why Roseau fault is lubricated while Redonda fault seems not, could be due to its occurrence in a volcanic region. It would be interesting in the future to identify the source of these high-pressure fluids by isotropic studies and define whether they come from the country rock at the base of the fault.

8. Conclusions

The 21 November 2004 M_w6.3 Les Saintes earthquake induced a very long-lasting aftershock sequence. We have successfully applied three-dimensional seismic tomographic inversions to an OBS dataset collected during 41 days of the aftershock sequence. Our results indicate that Roseau fault triggered the 21 November earthquake and that the seismicity is not concentrated along one single fault but also along several antithetic normal faults in the Les Saintes graben. The seismogenic thickness is lower than normal, probably due to the geothermal regime in this volcanic region. The relocated aftershock sequence and the velocity anomalies correspond to the continuation of Roseau fault at depth. The fault plane azimuth of the aftershock distribution is N327° and the dip is 50° toward the NE, which corresponds well with the surface alignment of Roseau Fault. The deep aftershock cluster is in agreement with the slip distribution of the 21 November rupture. The inverted Vp/Vs is 1.81, much higher than the regional value of 1.73. A positive Vp/Vs anomaly in the region of the Roseau fault plane might indicate pore-fluid flow. We suggest that mainshock-induced pore pressure changes controlled the timing of the strongest aftershock (75 days later), 8 km further north on the same fault. A negative Vp/Vs anomaly in the region of the antithetic Rodrigues and Souffleur faults might indicate a different state of pore pressure distribution than for Roseau fault. This study illustrates the scientific benefits of post-earthquake surveys. Although it was a challenge to mount this marine experiment, it provides a dataset that is crucial to understanding the region's seismotectonics. Further marine surveys are needed to address, among other questions, the possibility that the November 21, 2004 rupture reached the seafloor, and the presence of fluid seepage along the fault scarps.

Acknowledgments

We thank Captain N. Radenne and the crew of the *Kahouanne* for the success of the two legs of the GUADOBS marine experiment. We thank L. Beguery and O. Aouji for rapidly preparing and deploying the OBSs. We are grateful to the Guadeloupe authorities and Phares et Balises for providing the vessel and also to SIO team for providing OBS batteries that permitted this rapid response experiment. We thank OVSG technical team for the seismic analysis of the regional network. We thank the IPGP seismic crisis team that helped with the organization and INSU for financing airfare and equipment. We thank R. Poujardieu for relocating the OBS coordinates during a summer internship and C. Deplus for providing the AGUADOMAR bathymetric grid. We acknowledge the use of TOMO2GMT shareware of S. Husen and F. Haslinger. Figs. 1, 2, 5, 8, 9, 10, and 11 were created with GMT (Wessel and Smith, 1995). Useful suggestions to improve the paper were given by the editor and two anonymous reviewers. IPGP contribution 2614.

Appendix A. Supplementary data

Supplementary data associated with this article can be found, in the online version, at doi:10.1016/j.tecto.2010.04.005.

References

Allen, R.V., 1978. Automatic earthquake recognition and timing from single traces. Bull. Seismol. Soc. Am. 68, 1521–1532.

Bazin, S., Harding, A.J., Kent, G.M., Orcutt, J.A., Singh, S.C., Tong, C.H., Pye, J.W., Barton, P.J., Sinha, M.C., White, R.S., Hobbs, R.W., van Avendonk, H.J.A., 2003. A three-dimensional study of axial low velocity region beneath the 9°03′N overlapping spreading center. Geophys. Res. Lett. 30, 1039–1042.

Beauducel, F., Anténor-Habazac, C., Bazin, S., de Chabalier, J.-B., Nercessian, A., Feuillet, N., Jacques, E., Bertil, D., Boudon, G., Le Friant, A., Tapponnier, P., Hirn, A., Lépine, J.-C., Bernard, P., Komorowski, J.-C., King, G.C.P., 2005. The Mw 6.3 earthquake of Les Saintes (Guadeloupe) on November 21, 2004. IAVCEI European Seismological Commission Annual Workshop, Saint-Claude Guadeloupe, Sep. 2005.

Bellon, H., 1988. Reconnaissance Chronologique des deux premières phases d'activité volcanique en Dominique (Petites Antilles). C. R. Acad. Sci. 306, 1487–1492.

Bengoubou-Valérius, M., 2008. Contribution à la connaissance de l'Aléa sismique dans les Antilles Françaises. Univ. des Antilles et de la Guyane, Ph.D. thesis, 189 pp.

Bengoubou-Valérius, M., Bazin, S., Bertil, D., Beauducel, F., Bosson, A., 2008. CDSA: a new seismological data center for French Lesser Antilles. Seismol. Res. Lett. 79, 90–102.

Bernard, P., Lambert, J., 1988. Subduction and seismic hazard in the Northern Lesser Antilles—revision of the historical seismicity. Bull. Seismol. Soc. Am. 78, 1965–1983.

Bertil, D., Bazin, S., Mallarino, D., Beauducel, F., 2004. Séisme des Saintes — Rapport de Synthèse. Centre de Données Sismologiques des Antilles, 8 décembre 2004. 36 pp.

Bouysse, Ph., 1980. Sur l'existence d'un volcan sous-marin dans l'archipel de la Guadeloupe. BRGM, Rapport 80 SGN 084 MAR. 36 pp.

Vallée, M., Delouis, B., Bazin, S., 2005. Rupture process of the mainshocks of the Guadeloupe, West Indies, seismic crisis (November 2004–February 2005). Workshop on fracture dynamics: Theory and application to earthquakes, Madrid.

Brodsky, E., Kanamori, H., 2001. Elastohydrodynamic lubrication of faults. J. Geophys. Res. 106, 16 357–16 374.

Byerlee, J., 1993. Model for episodic flow of high-pressure water in fault zones before earthquake. Geology 21, 303–306.

Cara, M., Bertil, D., Feuillet, N., Jacques, E., Tapponnier, P., Guéguen, P., Bengoubou-Valérius, M., Sira, C., Lebrun, B., Beauducel, F., 2005. Séisme des Saintes (Guadeloupe) du 21 novembre 2004, note préliminaire. BCSF2005-NP3. 62 pp.

Cara, M., Alasset, P.-J., Sira, C., 2008. Magnitude of historical earthquakes, from macroseismic data to seismic waveform modelling: application to the Pyrenees and a 1905 earthquake in the Alps. Hist. Seismol. 2, 369–384. doi:10.1007/978-1-4020-8222-1.

Chiarabba, C., Sevaggi, G., 1997. Structural control on fault geometry: example of the Grevena Ms 6.6, normal faulting earthquake. J. Geophys. Res. 102, 22 445–22 457.

Thurber, C.H., 1983. Earthquake locations and three-dimensional crustal structure in the Coyote lake area, Central, California. J. Geophys. Res. 88, 8226–8236.

Chiarabba, C., Amato, A., Anselmi, M., Baccheschi, P., Bianchi, I., Cattaneo, M., Cecere, G., Chiaraluce, L., Ciaccio, L., De Gori, M.G., De Luca, P., Di Bona, G., Di Stefano, M., Faenza, R., Govoni, A., Improta, L., Lucente, F.P., Marchetti, A., Margheriti, L., Mele, F., Michelini, A., Monachesi, G., Moretti, M., Pastori, M., Piana Agostinetti, N., Piccinini, D., Roselli, P., Seccia, D., Valoroso, L., 2009a. The 2009 L'Aquila (central Italy) Mw 6.3 earthquake: Main shock and aftershocks. Geophys. Res. Lett. 36. doi:10.1029/2009GL039627.

Chiarabba, C., De Gori, P., Boschi, E., 2009b. Pore-pressure migration along a normal-fault system resolved by time-repeated seismic tomography. Geology 37 (1), 67–70. doi:10.1130/G25220A.1.

Chiarabba, C., Piccinini, D., De Gori, P., 2009c. Velocity and attenuation tomography of the Umbria Marche 1997 fault system: evidence of a fluid-governed seismic sequence. Tectonophysics. doi:10.1016/j.tecto.2009.04.004.

Christensen, N.I., 1996. Poisson's ratio and crustal seismology. J. Geophys. Res. 101, 3139–3156.

Clément, C., Bernard, P., Viodé, J.-P., Antenor-Habazac, C., Lépine, J.-C., Beauducel, F., 2001. Compilation et validation du catalogue de sismicité des observatoires IPGP des Antilles Françaises. Rapport MATE-IPGP. 95 pp.

Constable, S.C., Orange, A.S., Hoversten, G.M., Morrison, H.F., 1998. Marine magnetotellurics for petroleum exploration, part 1, a seafloor equipment system. Geophysics 63, 816–825.

de Blainville, C., 1843. Sur un volcan qui a fait éruption entre la Guadeloupe et Marie-Galante. C. R. Acad. Sci. 16 (19), 1083–1084.

Delouis, B., Vallée, M., Cruz-Atienza, V., 2007. The Mw = 6.3 Saintes earthquake (West Indies): source kinematics determination and uncertainties in a poorly known crustal structure. Geophys. Res. Abstr. 9, 10050.

DeMets, C., Jansma, P.E., Mattioli, G.S., Dixon, T.H., Farina, F., Bilham, R., Calais, E., Mann, P., 2000. GPS geodetic constraints on Caribbean–North America plate motion. Geophys. Res. Lett. 27, 437–440.

Deplus, C., Le Friant, A., Boudon, G., Komorowski, J.-C., Villemant, B., Harford, C., Ségoufin, J., Cheminée, J.-L., 2001. Submarine evidence for large-scale debris avalanches in the Lesser Antilles Arc. Earth Planet. Sci. Lett. 192, 145–157.

Donnellan, A., Webb, F.H., 1998. Geodetic observations of the M 5.1 January 29, 1994 Northridge aftershock. Geophys. Res. Lett. 25, 667. doi:10.1029/98GL50323.

Dorel, J., 1978. Sismicité et structure de l'arc des Petites Antilles et du bassin Atlantique. Ph.D. thesis, Université Pierre et Marie Curie, 326 pp.

Dorel, J., Eschenbrenner, S., Feuillard, M., 1974. Profils sismiques dans les Petites Antilles. Ann. Geophys. 30, 117–126.

Eberhart-Phillips, D., 1990. Three-dimensional P and S velocity structure in the Coalinga region, California. J. Geophys. Res. 95, 15 343–15 363.

Eberhart-Phillips, D., Michael, A.J., 1993. Three-dimensional velocity structure and seismicity in the Parkfield region, central California. J. Geophys. Res. 98, 15 737–15 758.

Eberhart-Phillips, D., Reyners, M., 1997. Continental subduction and three-dimensional crustal structure: the northern South Island, New Zealand. J. Geophys. Res. 102, 11 843–11 861.

Evans, J.R., Eberhart-Phillips, D., Thurber, C.H., 1994. User's manual for SIMULPS12 for imaging Vp and Vp/Vs: a derivate of the Thurber tomographic inversion SIMUL3 for local earthquakes and explosions. U.S. Geol. Surv. Open File Rep., 94-431, 101pp.

Feuillet N., 2000. Sismotectonique des Petites Antilles, Liaison entre activité sismique et volcanique, Ph.D. thesis, Université Paris 7, 283 pp.

Feuillet, N., Manighetti, I., Tapponnier, P., 2001. Extension active perpendiculaire à la subduction dans l'arc des Petites Antilles (Guadeloupe). C. R. Acad. Sci. 333, 583–590.

Feuillet, N., Tapponnier, P., Manighetti, I., Villemant, B., King, G., 2004. Differential uplift and tilt of Pleistocene reef platforms and Quaternary slip rate on the Morne–Piton normal fault (Guadeloupe, French West Indies). J. Geophys. Res. 109. doi:10.1029/2003JB002496.

Feuillet, N., Beauducel, F., Jacques, E., Bazin, S., Tapponnier, P., King, G.C.P., The Mw = 6.3, November 21, 2004, Les Saintes earthquake (Guadeloupe): tectonic setting and static stress modeling. In revision.

Girardin, N., Feuillard, M., Viodé, J.-P., 1991. Réseau régional sismique de l'arc des Petites Antilles: sismicité superficielle (1981–1988). Bull. Soc. Géol. Fr. 162 (6), 1003–1015.

Haslinger, F., Kissling, E., Ansorge, J., Hatzfeld, D., Papadimitriou, E., Karakostas, V., Makropoulos, K., Kahle, H.-G., Peter, Y., 1999. 3D crustal structure from local earthquake tomography around the Gulf of Arta (Ionian region, NW Greece). Tectonophysics 304, 201–218.

Hatzfeld, D., Karakostas, V., Ziazia, M., Selvaggi, G., Leborgne, S., Berge, C., Guiguet, R., Paul, A., Voidomatis, P., Diagnourtas, D., Kassaras, I., Koutsikos, I., Makropoulos, K., Azzara, R., Di Bona, M., Baccheschi, S., Bernard, P., Papaioannou, C., 1997. The Kozani–Grevena (Greece) earthquake of 13 May 1995 revisited from a detailed seismological study. Bull. Seismol. Soc. Am. 87, 463–473.

Hauksson, E., Jones, L.M., Huttor, K., 1995. The 1994 Northridge earthquake sequence in California: seismological and tectonic aspects. J. Geophys. Res. 100, 12 3335–12 355.

Havskov, J., Ottemöller, L., 2005. SEISAN: the earthquake analysis software. Version 8.1, User's manual, University of Bergen, Norway, 259 pp.

Hayward, N.J., Ebinger, C.J., 1996. Variations in the along-axis segmentation of the Afar Rift system. Tectonics 15, 244–257.

IPGP, 2009. Bilan mensuel de l'activité volcanique de la Soufrière de Guadeloupe et de la sismicité régionale. Monthly Public Reports of OVSG-IPGP, Institut de Physique du Globe de Paris, Gourbeyre, 2004–2009.

Jacques, D., Maury, R.C., 1988. Carte géologique du département de la Guadeloupe: Les Saintes 1/20 000. BRGM, Orléans. 28 pp.

Jacques, D., Maury, R.C., Bellon, H., 1984. Géologie et géochronologie 40K–40Ar des îles des Saintes (Guadeloupe). C. R. Acad. Sci. 299, 721–726.

Japan Meteorological Agency, 2004. The seismological and volcanological bulletin of Japan for January 2004. http://www.fnet.bosai.go.jp/event2004.

Jousset, P., Douglas, J., 2007. Long-period earthquake ground displacements recorded on Guadeloupe (French Antilles). Earthquake Eng. Struct. Dyn. 36, 949–963.

Kissling, E., Ellsworth, W.L., Eberhart-Phillips, D., Kradolfer, U., 1994. Initial reference models in earthquake tomography. J. Geophys. Res. 99, 19635–19646.

Kissling, E., Kradolfer, U., Maurer, H., 1995. VELEST user's guide-short introduction. Institute of Geophysics and Swiss Seismological Service, ETH, Zurich. 25 pp.

Kissling, E., Husen, S., Haslinger, F., 2001. Model parameterization in seismic tomography: a choice of consequences for the solution quality. Phys. Earth Planet. Inter. 123, 89–101.

Le Friant, A., Heinrich, P., Boudon, G., 2008. Field survey and numerical simulation of the 21 November 2004 tsunami at Les Saintes (Lesser Antilles). Geophys. Res. Lett. 35, L12308. doi:10.1029/2008GL034051.

Lee, W.H., Lahr, J.H., 1975. HYPO71 (revisited): a computer program for determining hypocenter, magnitude and first motion pattern of local earthquakes. U.S. Geol. Surv., Open File Rep., Menlo Park, California, pp. 75–311.

Lienert, B.R., 1994. HYPOCENTER 3.2: a computer program for locating earthquakes locally, regionally and globally. Tech. rep., Hawaii Institute of Geophysics and Planetology, Honolulu, 74 pp.

Massonnet, D., Feigl, K.L., Vadon, H., Rossi, M., 1996. Coseismic deformation field of the M = 6.7 Northridge California earthquake of January 17, 1994 recorded by two radar satellites using interferometry. Geophys. Res. Lett. 23, 969–972.

Mellors, R.J., Vernon, F.L., Pavlis, G.L., Abers, G.A., Hamburger, M.W., Ghose, S., Iliasov, B., 1997. The Ms = 7.3 1992 Suusamyr, Kyrgyzstan, earthquake: 1. Constraints on fault geometry and source parameters based on aftershocks and body-wave modeling. Bull. Seismol. Soc. Am. 87, 11–22.

Mendoza, C., Hartzell, S.H., 1988. Aftershock patterns and main shock faulting. Bull. Seismol. Soc. Am. 78, 1438–1449.

Meyer, B., Armijo, R., Massonet, D., de Chabalier, J.-B., Delacourt, C., Ruegg, J.-C., Achache, J., Briole, P., Papanastassiou, D., 1996. The 1995 Grevena (Northern Greece) earthquake: fault model constrained with tectonic observations and SAR interferometry. Geophys. Res. Lett. 23, 2677–2680.

Nostro, C., Cocco, M., Belardinelli, M.E., 1997. Static stress changes in extensional regimes: an application to Southern Apennines (Italy). Bull. Seismol. Soc. Am. 87, 234–248.

Nur, A., Booker, J.R., 1972. Aftershocks caused by pore fluid flow? Science 175 (4024), 885–887.

Pontoise, B., Hello, Y., 2002. Monochromatic infra-sound waves recorded offshore Ecuador: possible evidence of methane release. Terra Nova 14, 1–11.

Salichon, J., Lemoine, A., Aochi, H., 2009. Validation of teleseismic inversion of the 2004 Mw 6.3 Les Saintes, Lesser Antilles, earthquake by 3D finite-difference forward modelling. Bull. Seismol. Soc. Am. 99, 3390–3401.

Stein, S., Engeln, J.F., Wiens, D.A., Fujita, K., Speed, R.C., 1982. Subduction seismicity and tectonics in the Lesser Antilles arc. J. Geophys. Res. 87 (B10), 8642–8664.

Toomey, D.R., Foulger, G.R., 1989. Tomographic inversion of local earthquake data from the Hengill-Grensdalur Central volcano complex, Iceland. J. Geophys. Res. 94, 17 497–17 510.

Toomey, D.R., Purdy, S.C., Purdy, G.M., 1994. Tomographic imaging of the shallow crustal structure of the East Pacific rise at 9°30′N. J. Geophys. Res. 99, 24 135–24 157.

Wadati, K., 1933. On the travel time of seismic wave. Geophys. Mag. 7, 87–153.

Watts, A.B., Burov, E.B., 2003. Lithospheric strength and its relationship to the elastic and seismogenic layer thickness. Earth Planet. Sci. Lett. 213, 113–131.

Wells, D.L., Coppersmith, K.J., 1994. New empirical relationships among magnitude, rupture length, rupture width, rupture area, and surface displacement. Bull. Seismol. Soc. Am. 84, 974–1002.

Wessel, P., Smith, W.H.F., 1995. New version of the generic mapping tools released. Eos Trans. AGU. 76, 329.

3. Le risque tsunami aux Antilles

Dans les Antilles Françaises, autant des automatismes ont été acquis, face au risque cyclonique transmis de génération en génération, autant le risque tsunami était pratiquement inconnu des habitants avant celui du 2 décembre 2004 dans l'Océan Indien. Le risque tsunami n'apparaissait d'ailleurs pas dans le Plan de Prévention des Risques, et pourtant ce risque existe. Le 13 juillet 2003, une vague de 1 à 2 m de hauteur s'est abattue sur la Côte-sous-le-vent de la Guadeloupe et a fait quelques dégâts matériels. Ce petit tsunami a été provoqué par un écroulement du dôme de lave du volcan Soufriere Hills de Montserrat situé à 50 km au Nord de la Guadeloupe. A la suite de cet évènement, j'ai mené une étude ponctuelle pour recueillir des témoignages et des observations. Le séisme des Saintes avait lui aussi engendré un tsunami de 2 à 3 mètres (Le Fiant et al., 2008). A la suite de ces deux tsunamis mineurs, nous avons obtenu en 2004 un financement auprès du Ministère d'Outre-Mer pour l'installation de quatre marégraphes sur les côtes Guadeloupéennes. Ce petit projet nous a surtout permis de débuter un projet d'envergure internationale et de participer activement au système de surveillance CARTWS (Caribbean Regional Tsunami Warning System). J'ai alors été tsunami National Contact pour la France et cela m'a rendue sensible au besoin de me former sur la thématique. Cela m'a conduit en 2009 à une année sabbatique au Norwegian Geotechnical Institute (NGI) où j'ai appris à modéliser la propagation des tsunamis auprès d'un expert dans le domaine, Carl Harbitz. Ma présence dans son équipe lui a permis de mieux comprendre la complexité des sources de tsunami aux Antilles. J'ai aussi pu co-encadrer ses étudiants, Finn Løhvolt et Rolv Bredesen, experts en modélisation et informatique mais peu formés en sciences de la terre. Je me suis aussi familiarisée pour la première fois avec des outils SIG, en particulier avec le logiciel ArcGIS, si utile pour prendre en compte les différents facteurs de vulnérabilités dans l'évaluation des risques naturels. Cette collaboration, courte mais fructueuse, a permis de publier plusieurs rapports et articles, dont deux sont retranscrit dans cet ouvrage :

- Le premier article consiste à tenir compte d'un modèle de rupture plus compliqué qu'un simple rectangle uniforme, pour la géométrie faille.
- Le second article, a permis d'évaluer le risque tsunami dans toute la Caraïbe grâce à une nouvelle base de données des tsunamis historiques. Ce travail de synthèse et de modélisation a servi de référence pour la mise en place du système d'alerte CARTWS déjà mentionné.

3.1 Modélisation de la propagation de tsunami

La plupart des modèles de propagation de vagues de tsunami font l'hypothèse que le déplacement cosismique est uniforme sur le plan de la faille. Ici, j'ai modélisé la source du tsunami comme étant une rupture hétérogène le long de la faille. En utilisant la formule d'Okada (1985) pour calculer le déplacement vertical du fond de la mer, j'ai réalisé une analyse stochastique de 500 simulations de Monte Carlo pour chaque géométrie de failles. Celle-ci a ensuite été utilisée par avec un étudiant en Master en informatique, Rolv Bredesen pour étudier la variabilité observée sur le runup au niveau d'une côte. Nous avons ainsi évalué l'effet de différentes géométries de source (magnitudes, profondeurs de la faille et pendages variables) sur les statistiques de runup. Cette analyse a ensuite été intégrée par un étudiant en thèse, Finn Løvholt, qui a ajouté une variabilité au niveau de la bathymétrie côtière, dans un article plus général, présenté ici. Cet article a mis en évidence que la rupture non uniforme a une grande influence sur la valeur maximale de runup. Ce qui avait été observé pour certains tsunamis (Geist, 2002) mais qui, jusqu'à présent, avait été négligé dans les modélisations.

JOURNAL OF GEOPHYSICAL RESEARCH, VOL. 117, C03047, doi:10.1029/2011JC007616, 2012

Stochastic analysis of tsunami runup due to heterogeneous coseismic slip and dispersion

F. Løvholt,[1,2,3] G. Pedersen,[2,3] S. Bazin,[1,3] D. Kühn,[3,4] R. E. Bredesen,[5] and C. Harbitz[1,2,3]

Received 21 September 2011; revised 3 February 2012; accepted 7 February 2012; published 31 March 2012.

[1] Most tsunami models apply dislocation models that assume uniform slip over the entire fault plane, followed by standard analytical models based on Volterra's theory of elastic dislocations for the seabed deformation. In contrast, we quantify tsunami runup variability for an earthquake with fixed magnitude but with heterogeneous rupture distribution assuming plane wave propagation (i.e., an infinitely long rupture). A simple stochastic analysis of 500 slip realizations illustrates the expected variability in coseismic slip along a fault plane and the subsequent runup that occurs along a coastline in the near field. Because of the need for systematically analyzing different fault geometries, grid resolutions, and hydrodynamic models, several hundred thousand model runs are required. Thus, simple but efficient linear models for the tsunami generation, propagation, and runup estimation are used. The mean value and variability of the maximum runup is identified for a given coastal slope configuration and is analyzed for different dip angles. On the basis of the ensemble runs, nonhydrostatic effects are discussed with respect to their impact on generation, nearshore propagation, and runup. We conclude that for the geometry and magnitude investigated, nonhydrostatic effects reduce the variability of the runup; that is, hydrostatic models will produce an artificially high variability.

Citation: Løvholt, F., G. Pedersen, S. Bazin, D. Kühn, R. E. Bredesen, and C. Harbitz (2012), Stochastic analysis of tsunami runup due to heterogeneous coseismic slip and dispersion, *J. Geophys. Res.*, *117*, C03047, doi:10.1029/2011JC007616.

1. Introduction

[2] This study is motivated by the need for a quantification of expected variability in runup for a subduction earthquake of given magnitude and mean slip. Tsunami runup prediction has for a long time been based on homogeneous slip distributions of rupture on the fault. Using empirical relationships relating earthquake slip to its magnitude [*Wells and Coppersmith*, 1994; *Henry and Das*, 2001; *Blaser et al.*, 2010; *Leonard*, 2010], one can therefore simply compute the profile of the initial waveform. Modern teleseismic and geodetic inversion techniques however, have shown that the assumption of a uniform slip over the entire rupture plane is invalid. Although several studies have addressed tsunami generation by heterogeneous slip with a relatively complex rupture pattern, it is often in the context of hindcasting past events [e.g., *Wang and Liu*, 2006; *Løvholt et al.*, 2006]. In the present paper, we analyze how heterogeneous coseismic slip affects the initial water surface elevation and consequently the tsunami runup on the coast for a high number of stochastic slip realizations, thereby addressing also the runup uncertainty. The number of studies including this effect is limited [e.g., *Geist*, 2002; *McCloskey et al.*, 2007, 2008], but conclusive on the fact that the common deterministic practice understates the complexity of the problem. Papers addressing the variations of mean quantities such as the slip and fault dimensions based on magnitude scaling relations [e.g., *Bolshakova and Nosov*, 2011; *Blaser et al.*, 2011] also emphasize the importance of stochastic runup. Herein we choose to only concentrate on slip variations in the dip direction. The available studies in literature addressing tsunamis due to random slip earthquakes are so far limited to the nearshore wave height, thus not attempting the explicit calculation of the runup. This paper quantifies the runup for an ensemble of plane waves generated by earthquakes with different realizations of heterogeneous slip. Because of the need for systematically analyzing different geometries, grid resolutions, and hydrodynamic models, several hundred thousand model runs are required. Thus, simple but efficient linear models for the tsunami generation, propagation, and runup estimation are employed, and an idealized bathymetry is applied. For the same reason, we limit the analysis to plane wave runup; it is stressed that this study is focusing on the theoretical and fundamental aspects of the tsunami generation and runup rather than attempting a description of any historical event. Opposed to previous studies, the present paper includes an elaborate analysis of dispersive effects originating from short-wave components introduced by the slip heterogeneity. *Geist and Dmowska* [1999] indicate that tsunami water levels associated with slip variations in strike direction are greater than those due to corresponding variations in dip direction. This exemplifies

---

[1] NGI, Oslo, Norway.
[2] Department of Mathematics, University of Oslo, Oslo, Norway.
[3] International Center for Geohazards, Oslo, Norway.
[4] NORSAR, Kjeller, Norway.
[5] Simula Research Laboratory, Lysaker, Norway.

0148-0227/12/2011JC007616

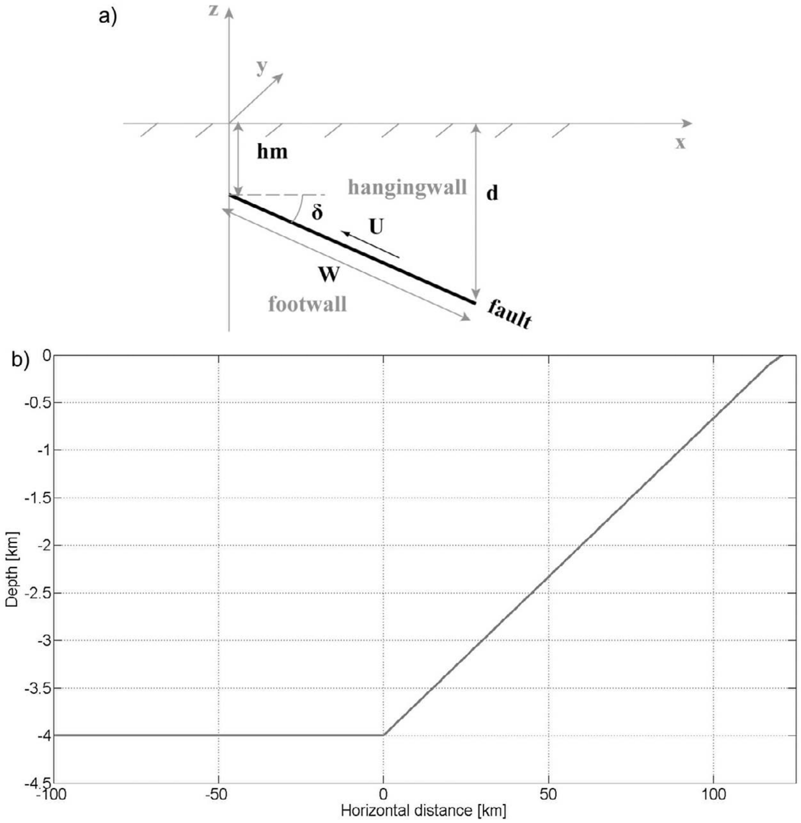

Figure 1. (a) Geometry of the source in the analytical model. The surface displacement due to a rectangular reverse fault in a half-space is computed using the work of *Okada* [1985]. The y axis is taken to be parallel to the strike direction of the fault. The x axis is taken to be perpendicular to the strike direction of the fault, pointing horizontally in the downdip direction. The z axis corresponds to the vertical direction pointing upward from the seabed; δ is the dip angle of the fault plane, and h_m is its shallowest depth below the seabed. W is the width of the fault (downdip dimension). (b) Geometry of the bathymetry used in the tsunami simulations. The small bottom section with the gentlest slope closest to the shoreline is not shown in this figure because of the scale.

that additional factors adding to the variability is neglected in this study. Such factors may include the slip variation and rupture speed in the strike direction, bathymetry and topography effects, tidal variations, and finally two-dimensional wave phenomena such as refraction, reflection, focusing, and edge wave evolution.

2. Elastic Seabed Response to a Subduction Earthquake

2.1. Seabed Response to Coseismic Slip

[3] *Okada* [1985] derived analytical expressions for the surface displacement due to an inclined fault in a half-space for finite rectangular sources. These expressions have been broadly used to model ground surface deformations associated with earthquakes. In this study, we concentrate on interplate subduction events which are the most common source for large tsunamis observed around the world. We therefore limit our analysis to vertical displacement of the seabed due to pure dip slip on a reverse fault. U is taken as the movement of the hanging wall side block relative to the footwall side block (Figure 1). Considering pure dip slip only, we set strike and tensile components to zero. At the seabed, the vertical permanent deformation u_z due to a dislocation along a surface in an isotropic elastic medium is given by *Okada* [1985, equation 26].

[4] In order to compute the vertical displacement due to a fault rupture with nonuniform slip distribution, we implement the *Okada* [1985] analytical solution for n equal elements with width W/n along the two-dimensional (2D) fault. We calculate and sum the local vertical displacements due to constant slip on each element, allowing for heterogeneous slip by varying U piecewise from segment to segment.

[5] The earthquake rupture process has for long been considered to follow a self-similar scaling relationship, since the stress drop has been observed to be independent of magnitude [*Aki*, 1967]. Earthquake self-similarity means that small earthquakes are not physically different from large earthquakes. Indeed, recent inversions of rupture mechanism have provided increasingly detailed slip distributions. *Mai and Beroza* [2000, 2002] analyzed published slip maps for different earthquakes to model mechanics of the rupture process. They derived a series of laws accounting for spatial complexity of earthquake slip along a fault plane. The authors proposed that the slip distribution follows an autocorrelation function only depending on the distance between

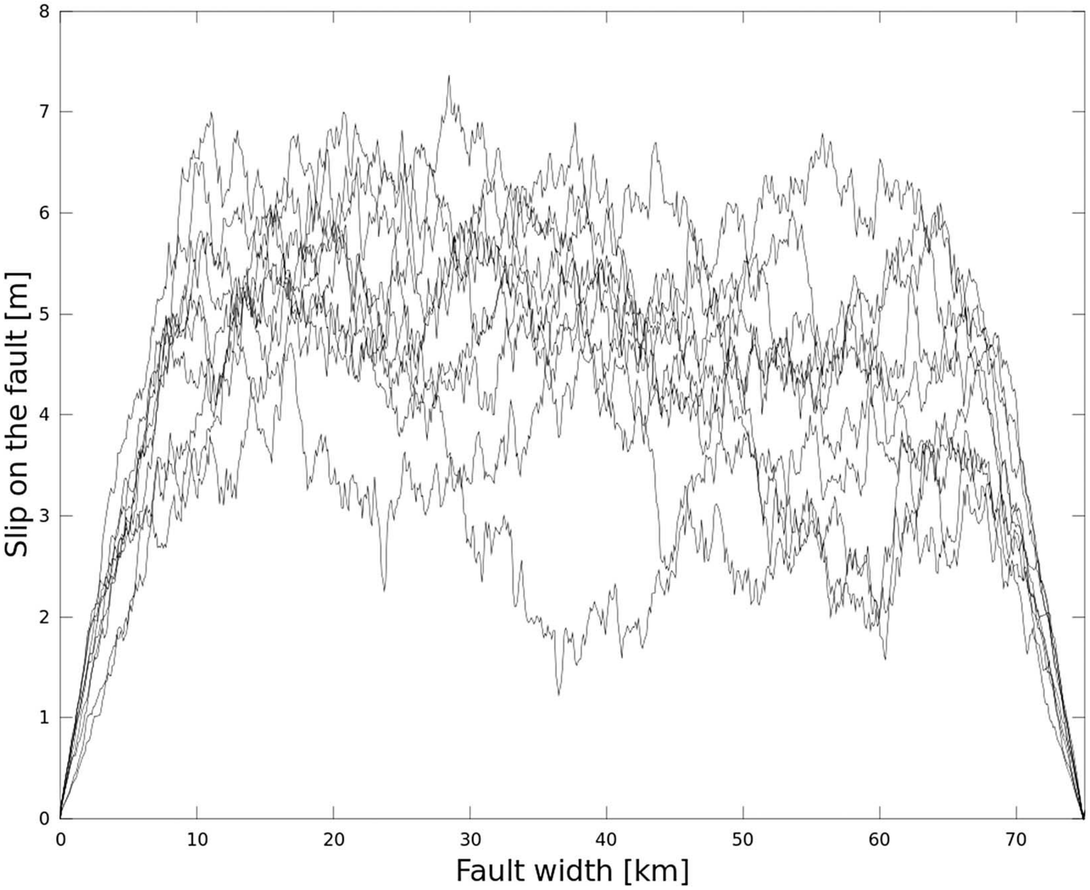

Figure 2. Example of a subset of the variable slip distributions used in the simulations.

two points on the fault plane and a downdip correlation length a. The correlation length can be derived from fault dimensions using $a \sim 1 + W/3$ where W is width (downdip dimension) of the fault in km. Among the possible autocorrelation functions, we chose to implement the exponential one that is characterized in space by $C(x) = e^{-x/a}$ and in the Fourier domain by the power spectrum $F(k) = 2a/(1 + a^2k^2)$, where x is distance and k is wave number. The actual fluctuation of the slip is added to the mean slip by a multiplication of the spectral amplitude with a random phase term $e^{i\varphi(k)}$, subsequently transformed back to space using an inverse Fourier transformation. The fluctuation of slip is then scaled to 30% of the mean slip value of 5 m. The procedures for computing the distributed slip stochastically is adopted from *Roth and Korn* [1993].

[6] For this study, the fault width is set to 75 km, which leads to a correlation length a of 26 km. To be able to analyze the results stochastically, we generate 500 random slip distributions following the exponential autocorrelation function. For each rupture simulation, the slip value varies in the downdip direction and is tapered at the upper and lower edges of the fault. Examples of several randomly generated slip distributions are given in Figure 2.

2.2. Geometry and Seabed Displacements

[7] To design realistic trench topography, we use the continental slope along the Sumatra trench as a suitable example. An average slope is computed along a section perpendicular to the subduction trench: 1:30 for Sumatra, with a nearshore slope of 1:39.5 at water depths less than 100 m. Outside of the trench, a constant ocean depth of 4000 m is assumed. The topography is shown in Figure 1. Naturally, the bathymetric profile affects the runup; a mild slope generally provides a larger amount of amplification than a steeper slope. Varying the slope of the bathymetric profile is beyond the scope of this paper.

[8] The fault segments are divided into $n = 746$ parts over the fault plane. Each of the 500 slip distributions is applied to the rectangular fault plane located along the plate interface. As we limit the study to plane wave propagation, we extract the solution in x-z space at the center of the fault plane. The dip angle δ is changed from 10° to 70°, and the depth of the upper edge h_m varies from 100 m to 30 km below the seabed. The shallowest depth of $h_m = 100$ m represents a rupture extending to the surface. However, it is necessary to place the fault at a certain depth to avoid mathematical singularities. In this particular case, the slip profile was not tapered at the upper edge of the fault. The results of the simulations for a limited number of realizations are plotted in Figure 3.

[9] The displacement due to a shallow dipping dip-slip event is very different from a steep fault event, which corresponds to the standard theory. For dip angles <30°, the initial seabed waveform is composed of a surface elevation

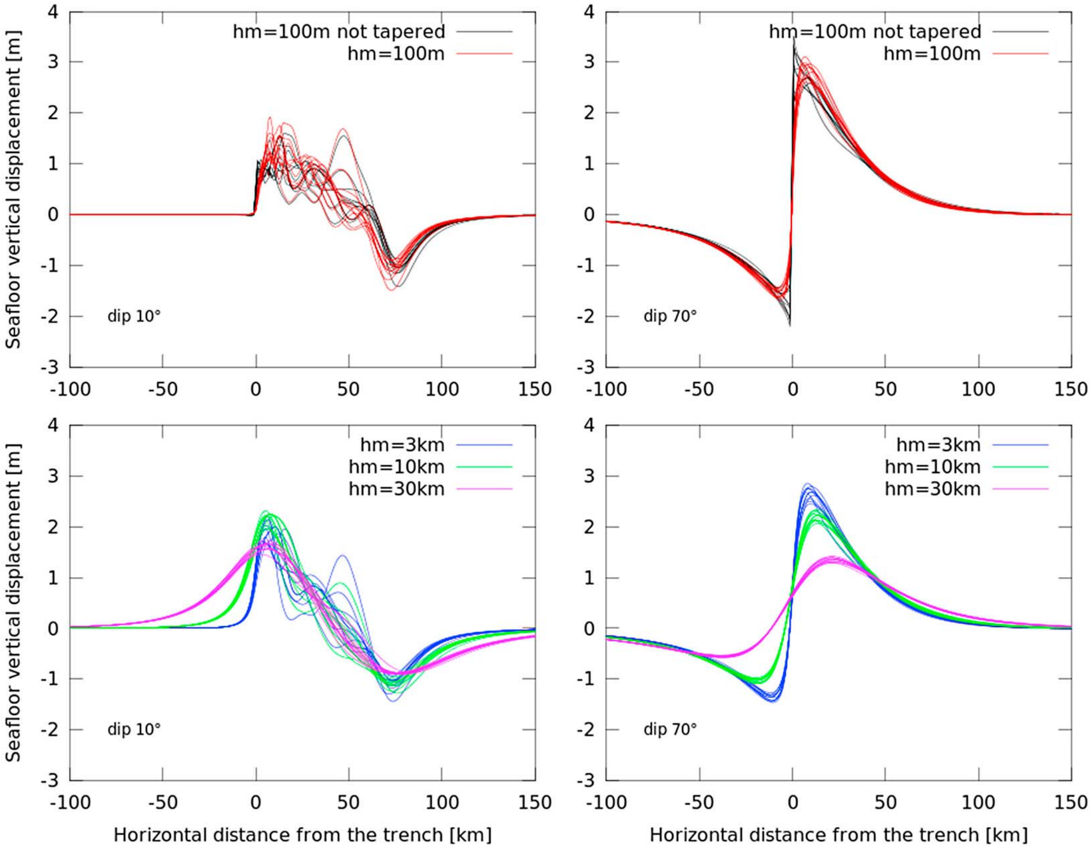

Figure 3. Permanent vertical displacement at the seabed due to thrust events with different fault geometries as a function of the distance from the trench for a subset of the realizations. Different colors are used for different fault depths h_m. We investigate two types of slip distributions for the subsurface fault (h_m = 100 m): the slip values are tapered (red lines) or not (black lines) at the upper edge. We observe a change in the wave polarity between dip angles shallower or steeper than 30°. For clarity, we only present the two end-members of dip angles δ. (left) Shallow dipping fault with δ = 10°, (right) steep fault δ = 70°, (top) h_m = 100 m, and (bottom) h_m = 3, 10, 30 km.

flanked by a depression on its right. As a consequence, coasts located along the volcanic arc in the dip direction of the subduction zone (i.e., to the right of the *x* axis) will first observe a sea withdrawal. For steep faults (with dip angles >30°), the initial seabed waveform is composed of a depression followed by an elevation. As a consequence, coasts located along the volcanic arc in the dip direction of the subduction zone (i.e., to the right on the *x* axis) will only observe a small sea withdrawal, followed by a much larger increase in water level. We observe that for a thrust earthquake, the maximum predicted elevation is always larger than the maximum depression.

[10] In terms of runup estimation, we are interested in the maximum value of the vertical displacement and the total volume of water displaced. These two variables are analyzed with respect to their coefficient of variation (standard deviation σ divided by the mean μ). This coefficient displayed larger values in the cases of shallow rupturing and shallow dipping faults, whereas the imbedded faults and the faults with larger dip resulted in less variation (for brevity, the results are not displayed). A reduction of the coefficient of variation with increasing fault depth h_m was found, and is interpreted as the depth acting as a low-pass filter on the seabed response.

3. Tsunami Propagation and Runup Estimation

3.1. Methodology

3.1.1. Initial Conditions for Tsunami Simulations

[11] Most tsunami models encountered in literature copy the seabed displacement directly from the seabed without taking the hydrodynamic response that filter out short-wave components at the seabed during tsunami generation into account. This approach may introduce nonphysical short wavelengths. To explore this issue, we therefore use both the seabed copied to the surface as well as modified seabed elevations as initial conditions in the subsequent tsunami simulations. Thus, we label the simulations using the seabed response directly as “copied,” whereas the initial conditions modified due the hydrodynamic response are labeled “filtered.” The methodology for quantifying the filtered initial water level is based on full potential wave theory. The method for filtering is derived from *Pedersen* [2001], and is similar to the model of *Kaijiura* [1963] applying a

hyperbolic cosine filter. The seabed uplift is instantaneous, and represented with piecewise constant values. The resulting initial water elevation represents the average elevation in the interval centered at each node.

3.1.2. Wave Propagation and Quantification of Runup in Large Ensembles

[12] Naturally, the crucial feature of a tsunami is its runup. A variety of approaches for nonlinear shoreline tracking has been attempted over the years; see for instance the review by *Pedersen* [2008a]. Today runup models are included in state of the art tsunami models based on the shallow water equations [*Titov and Synolakis*, 1995, 1998; *Imamura*, 1996; *LeVeque and George*, 2008; *Gayer et al.*, 2010], as well as in widespread coastal engineering codes based on Boussinesq type equations [e.g., *Kennedy et al.*, 2000; *Lynett et al.*, 2002; *Lynett*, 2006; *Son et al.*, 2011; *Zhou et al.*, 2011]. Still, in the present context where we need to perform several hundred thousands of simulations in a controlled and comparable manner, a simpler computational strategy is crucial.

[13] A few analytical solutions for runup on an inclined plane have been obtained by applying the hodograph transformation to the nonlinear shallow water equations, as first published by *Carrier and Greenspan* [1958] and later employed in a series of articles. However, the hodograph transformation essentially links the nonlinear problem to its linear counterpart, a wave equation with variable coefficients that still must be solved. This is generally obtained through the application of a Hankel transform, which put restrictions on the shape of the incident wave to obtain an explicit transformed waveshape. With a few notable exceptions, such as the asymptotic formula for solitary wave runup published by *Synolakis* [1987], the inverse transformation requires numerical integration. For our randomly generated initial conditions this kind of procedure is unsuitable. Fortunately, the analysis of runup based on the hodograph technique has also provided general and useful insight in the relation between linear and nonlinear shallow water solutions for runup. Provided that the incident wave is well described by linear theory, maximum runup and withdrawal are the same for the linear and the nonlinear description. On the other hand, the shoreline motion between these extreme values does depend on the nonlinearity. This is discussed by, for instance, *Synolakis* [1987] and, more elaborately, by *Didenkulova* [2009]. In the latter reference it is also demonstrated that other properties, e.g., the breaking limit, may be obtained from linear solutions. Breaking is here defined as a singularity in the hodograph transformation corresponding to a vanishing Jacobian determinant at the shoreline, implying that the surface elevation is becoming multivalued as a function of the horizontal coordinate. When the breaking criterion is expressed in terms of the vertical acceleration of the shoreline it reads [*Didenkulova*, 2009]

$$\gamma = \frac{1}{(\alpha^2 g)}\frac{\partial^2 \eta}{\partial^2 t} = -\frac{1}{(\alpha g)}\frac{\partial u}{\partial t} > 1,$$

where α is the slope of the beach and the shoreline is to the left of the fluid. Implicit in the use of this criterion is the assumption that a bore will persist whenever breaking does occur. Hence, an incident wave that will produce breaking anywhere will also yield breaking at the shoreline. This is definitely the case within nonlinear shallow water theory. In view of the geometry, which is two-dimensional and comprises a monotonous slope, this assumption is reasonable also from a physical point of view.

[14] As will be shown subsequently, dispersion may have a noticeable effect on the runup height. However, dispersion will be most important in the deep water part of the propagation [see *Pedersen*, 2008a] and we assume that the wave motion close to the shoreline is hydrostatic. Then, provided the dispersive deep water region and the nonlinear shallow water region do not overlap nonlinear, extreme shoreline excursions may again be obtained by linear theory. This is demonstrated by *Pedersen* [2008b] (benchmark 1). For waves that come close to breaking in finite depth dispersive effects may become important again, because of the steep wavefront, and lead to the evolution of undular bores that are sometimes observed for tsunamis [e.g., *Glimsdal et al.*, 2006; *Grue et al.*, 2008; *Madsen et al.*, 2008]. Undular bores are nonlinear and dispersive wave forms that are outside the framework of our modeling strategy that may be regarded as a combination of linear dispersive equations with nonlinear shallow water equations. Further, in the present investigation we are primarily concerned with non-breaking runup heights or the occurrence of breaking of such. The first is presumably not affected by undular bores, while the breaking limits may be slightly modified, only, by dispersive effects at the shoreline.

[15] In the present article the topography is not represented by a single inclined plane, but by a broken plane joined to a deep sea region of constant depth. Still, as long as nonlinear effects are important only on the innermost slope leading to the shoreline, while dispersive effects then have become very small because of shoaling, both the breaking criterion and the linear values for the maximum runup will be valid. Again, it is emphasized that the general shoreline motion between the extreme values is not reproduced by linear theory, even though it can be derived from the linear time story of the shoreline [*Didenkulova*, 2009]. In the present filtered simulations, γ is in most cases less than unity during first runup (see Figure 4), implying validity of the employed linear theory. On the other hand, it should be noted that nonphysical breaking is frequent in the copied model runs for small dip angles and shallow rupture.

[16] In view of the discussion above we employ linear numerical models for the runup. We then solve the linear shallow water (LSW) equations, the linearized Boussinesq equations on standard form [*Peregrine*, 1967] and the linearized Nwogu formulation [*Nwogu*, 1993] that has better dispersion properties than the standard Boussinesq equations. To this end we employ a simple finite difference method with a staggered grid in space and time and centered differences. Further details on the method is found in work by *Løvholt and Pedersen* [2008], with the differential equations given in their equations 1–2 and Table 1, while the discretizations are defined in their equations 5–7 and Table 2. The extension to nonuniform grids is obtained simply by invoking the local grid increments in the discrete equations. Since the methods are linear, no tracing of the shoreline is needed. However, it is important that a velocity node is located at the shoreline, in which case no onshore extrapolation or fictitious nodes are needed. The runup performance of this method, for the LSW and standard Boussinesq equations, has been tested by *Pedersen* [2008b]

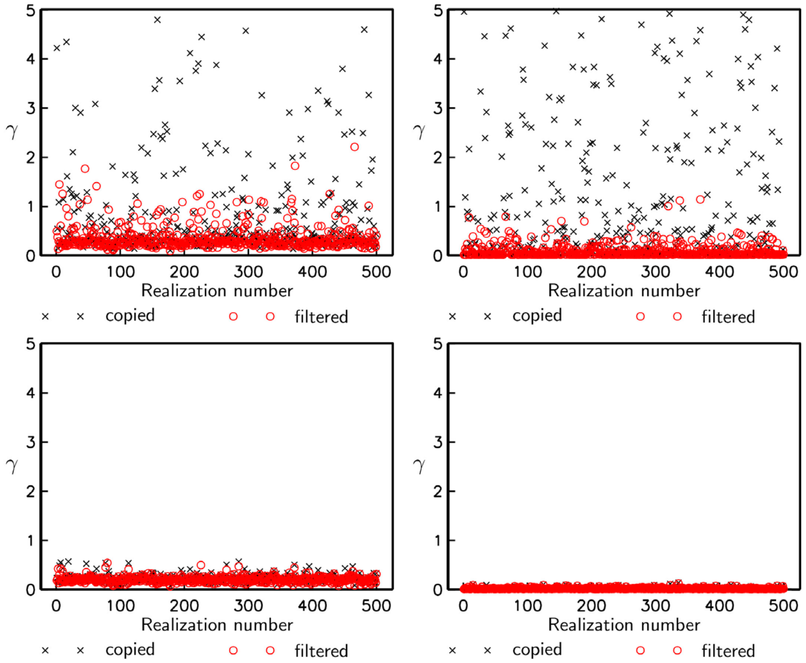

Figure 4. Breaking factor γ for all simulations on the shallow rupture geometry (h_m = 100 m) computed using the fluid acceleration at the shoreline. Crosses show the breaking factor for simulations using the seabed displacements as initial conditions, and circles show the breaking factor for simulations using the smoothed initial conditions. (top) Results for 10° dip and (bottom) results for 40° dip. (left) Results for the LSW simulations and (right) results for the dispersive (Nwogu) simulations.

and compared to fully nonlinear, Lagrangian models (NLSW, Boussinesq, full potential theory) with an accurate shoreline representation. For a benchmark test (numbered 1) it was found that the linear model reproduced the nonlinear maximum runup value very closely also for the Boussinesq equations, in accordance with the above discussion.

3.1.3. Grid Effects

[17] A variable grid is employed where the maximum grid increment at depths of 4000 m is Δx_{max}. Subsequently, the local Courant number is kept nearly constant at 0.9 until a given minimum water depth, H_{min} where a minimum spatial grid increment is employed, Δx_{min}. For water depths smaller than the threshold depth H_{min}, the grid increment remains equal to Δx_{min}.

[18] For each hydrodynamic model (LSW, standard linear dispersive, and linearized Nwogu; both copied and filtered initial elevation) and for each realization, minimum depth, and dip angle, simulations are conducted for three different grid resolutions, employing 500, 1000, and 2000 grid points. The finest resolution then corresponds to Δx_{max} = 160 m and Δx_{min} = 5 m. The convergence is evaluated on the ensemble level by computing the percentage error for mean values and standard deviations between the two finest resolutions. It is computed for each hydrodynamic model and parameter combination of δ and h_m. The largest relative error for the computed runup comparing the different grid resolutions is found for the LSW model with the copied initial conditions and a minimum fault depth of 100 m, ranging from 2.3% (for a 10°dip angle) to 3.1% (for a 70°dip angle) for the mean and 4.7% to 8.5% for the standard deviation. For the imbedded faults, and for all other combinations of initial conditions and models, errors were below 0.3% both for the mean and the standard deviation, decreasing with increasing h_m.

3.2. Examples of Results From Single Realizations

[19] Figure 5 shows the initial water surface computed for 10° and 40° dip angles using the same slip realization at three different minimum depths h_m. For the case of shallow rupture, the difference between the filtered and copied initial conditions is distinct. For the 10° dip angle, short wavelength seabed undulations are clearly filtered on seabed response. In case of the 40° dip angle, the filtering results in a reduction in the peak of the initial water level and a gentler slope for the steep gradient located above the upper fault edge. However, the effect of filtering is small for the imbedded faults, and in the case of h_m = 30 km, the difference is barely visible.

[20] Figure 6 shows the simulated runup for the LSW model, using the water levels displayed in Figure 5 as initial conditions. As shown, the effect of filtering is most distinct for the shallow rupture. For h_m = 100 m, the difference between the two solutions (copied and filtered) is relatively limited during the first wave cycle. During the second wave cycle however, the corresponding solutions are distinctly different, and it is shown that the simulation using the copied initial condition overestimates the runup by about a factor 2 for the 10° case. The drawdown obtained for shallow rupture using the copied initial conditions largely exceeds the solution using the filtered initial condition. In fact, for most simulations breaking occurs during the drawdown after the first positive peak. This also holds for the dispersive simulations, see below for a discussion. Hence, the solution at later times may no longer be valid. For this reason, we

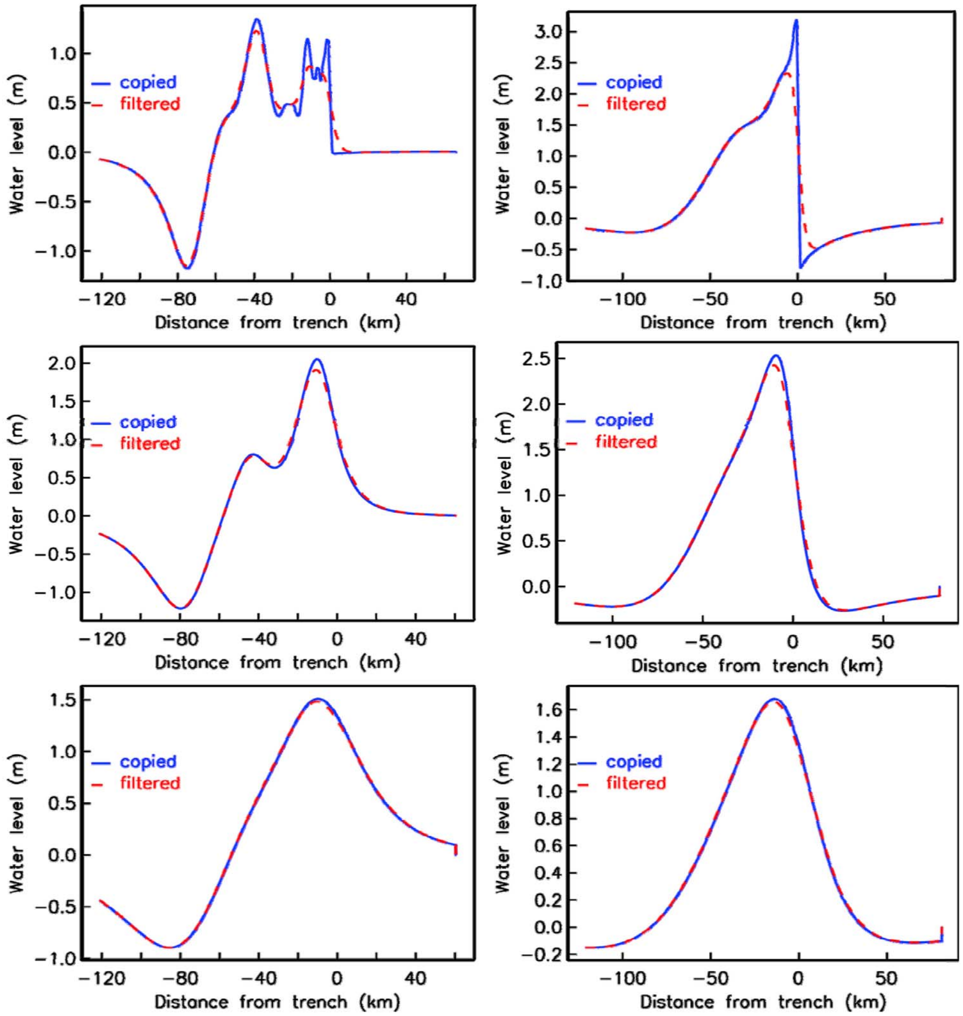

Figure 5. Comparison of the initial water surface obtained by copying the seabed displacement without filtering (solid curves) and with filtering (dashed curves) for six different realizations. Results for (top) h_m = 100 m, (middle) h_m = 10 km, and (bottom) h_m = 30 km. (left) Fault plane dip angle of 10°; (right) fault plane dip angle of 40°.

restricted subsequent analyses and statistics on the maximum runup to the first positive peak. We will claim that it still represents the maximum runup reasonably well, as the maximum runup arises within the first positive wave in most dispersive simulations. Given the small difference in initial conditions this relatively large overestimation in runup caused by the nonphysical short wavelengths may seem surprising. Nevertheless, this example demonstrates that even relatively small deviations due to artificial short wavelengths may contribute considerably to the runup or drawdown using a hydrostatic model.

3.3. Effects of Fault Parameters on the Maximum Runup

[21] We investigate the maximum runup for both the LSW and dispersive tsunami simulations for all shallow rupturing geometries and all realizations with respect to the fault parameters. Both copied and filtered initial conditions are used. We notice that comparing the higher-order dispersive model of *Nwogu* [1993] with a standard dispersive model resulted only in negligible deviations. The effect of higher-order dispersion will hence not be addressed further.

[22] Figure 7 shows examples of the distributions of the simulated maximum runup with Poissonian and lognormal fits, established using built-in fitting functions in Matlab. The distributions are associated with a distinct skewness, enabling maximum runups markedly larger than the mean of the ensemble. The widest distributions are found for the LSW model with copied initial condition and a shallow rupture. The randomness of the runup is however clearly reduced by introducing dispersion, as the dispersive simulations show no extreme values such as the ones from the LSW model shown in Figures 7a and 7d. This is due to filtering of high-frequency components in the dispersive simulations during the arrival of the leading at the coastline. Submerging the fault to larger depths also reduces variability; moreover, the skewness of the maximum runup distribution is much less pronounced for imbedded faults.

[23] The mean value, standard deviations, and coefficient of variation of the maximum runup were computed for the different parameter and model combinations for the

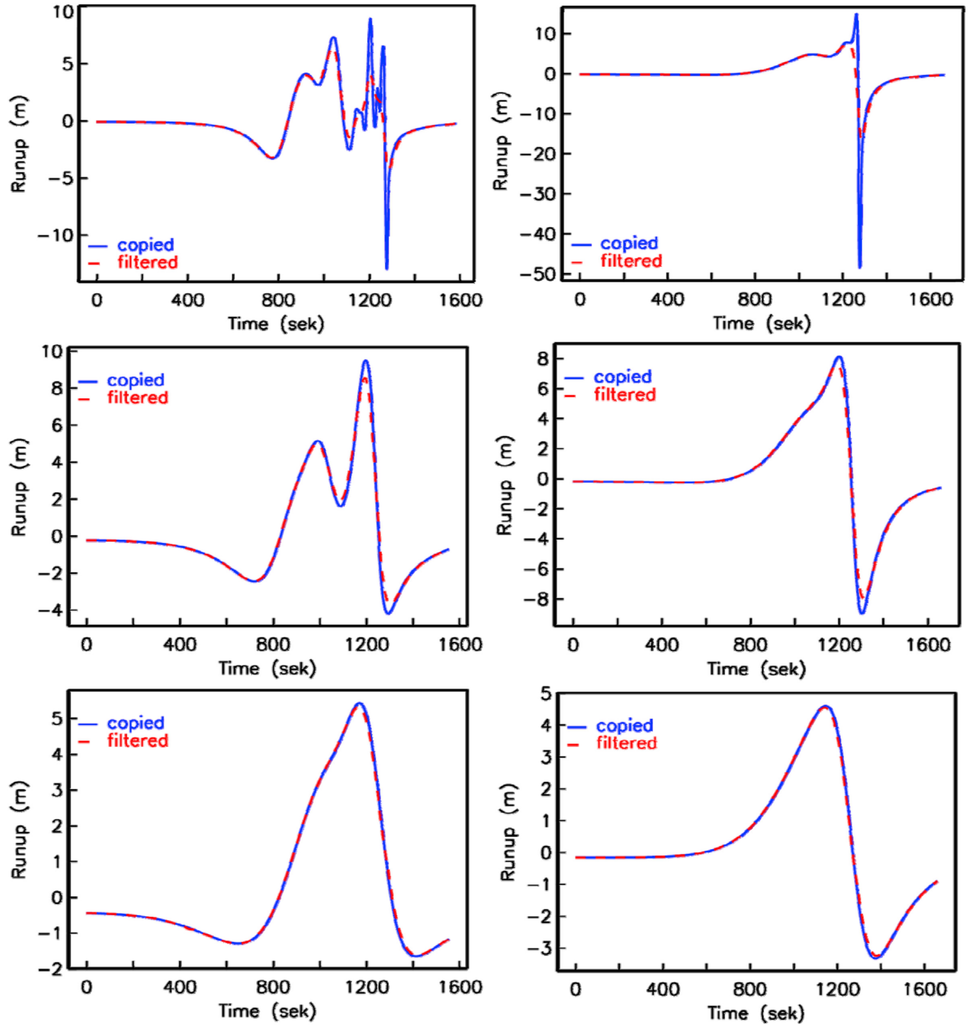

Figure 6. Simulated shoreline evolution as a function of time using the initial conditions shown in Figure 5. Simulations with initial water surface obtained by copying the seabed displacement without filtering (solid curves) and with filtering (dashed curves). Results for (top) $h_m = 100$ m, (middle) $h_m = 10$ km, and (bottom) $h_m = 30$ km. (left) Fault plane dip angle of 10°; (right) fault plane dip angle of 40°.

500 realizations. This statistic is presented below. To obtain a measure of the accuracy of the Monte Carlo simulation, we also computed the corresponding statistics for half subsets of the realizations. Deviations in the mean, the standard deviation and the coefficient of variation were typically found in the range of 1 to 5% comparing the sets with 250 and 500 realizations. Trends in these statistical outputs as functions of the different model parameters discussed below were not changed because of the finite number of realizations. It was therefore concluded that the 500 realizations were sufficient for this study, although a larger number of realizations would increase the accuracy. However, it is noted that a similar number of realizations would be needed for generalization into two horizontal dimensions, which would enable the need for quite large computational resources.

[24] Figures 8a and 8b show mean value and standard deviation of the maximum runup as a function of the dip angle for the LSW and the dispersive model, respectively. For the LSW model, the effect of filtering the initial water level on the mean increases as a function of the dip. For the dispersive model, the effect of filtering is still clear, but more moderate and only pronounced for dip angles exceeding 40°. Comparing Figures 8a and 8b we note that the standard

Figure 7. Distributions of maximum runup and fitted probability density functions. (a) LSW model with copied initial conditions for dip angle of 10° and a minimum depth of 100 m. (b) Nwogu model with filtered initial conditions for a dip angle of 10° and a minimum depth of 100 m. (c) LSW model with copied initial conditions for dip angle of 10° and a minimum depth of 30 km. (d) LSW model with copied initial conditions for dip angle of 40° and a minimum depth of 100 m. (e) Nwogu model with filtered initial conditions for a dip angle of 40° and a minimum depth of 100 m. (f) Nwogu model with copied initial conditions for dip angle of 40° and a minimum depth of 30 km.

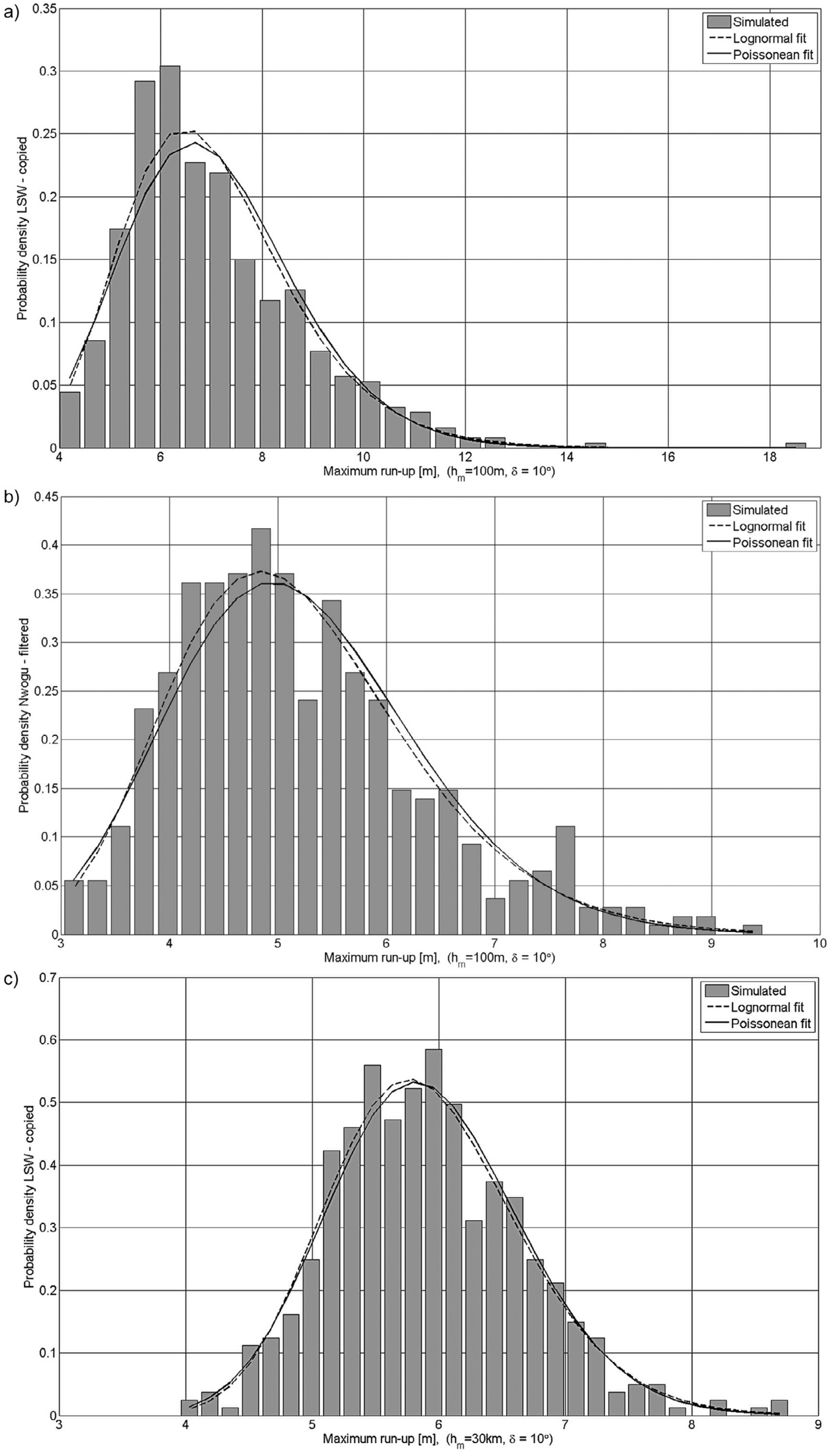
a)
Simulated
Lognormal fit
Poissonean fit
Probability density LSW - copied
0
0.05
0.1
0.15
0.2
0.25
0.3
0.35
4
6
8
10
12
14
16
18
Maximum run-up [m], (h_m=100m, δ = 10°)
b)
Simulated
Lognormal fit
Poissonean fit
Probability density Nwogu - filtered
0
0.05
0.1
0.15
0.2
0.25
0.3
0.35
0.4
0.45
3
4
5
6
7
8
9
10
Maximum run-up [m], (h_m=100m, δ = 10°)
c)
Simulated
Lognormal fit
Poissonean fit
Probability density LSW - copied
0
0.1
0.2
0.3
0.4
0.5
0.6
0.7
3
4
5
6
7
8
9
Maximum run-up [m], (h_m=30km, δ = 10°)

Figure 7

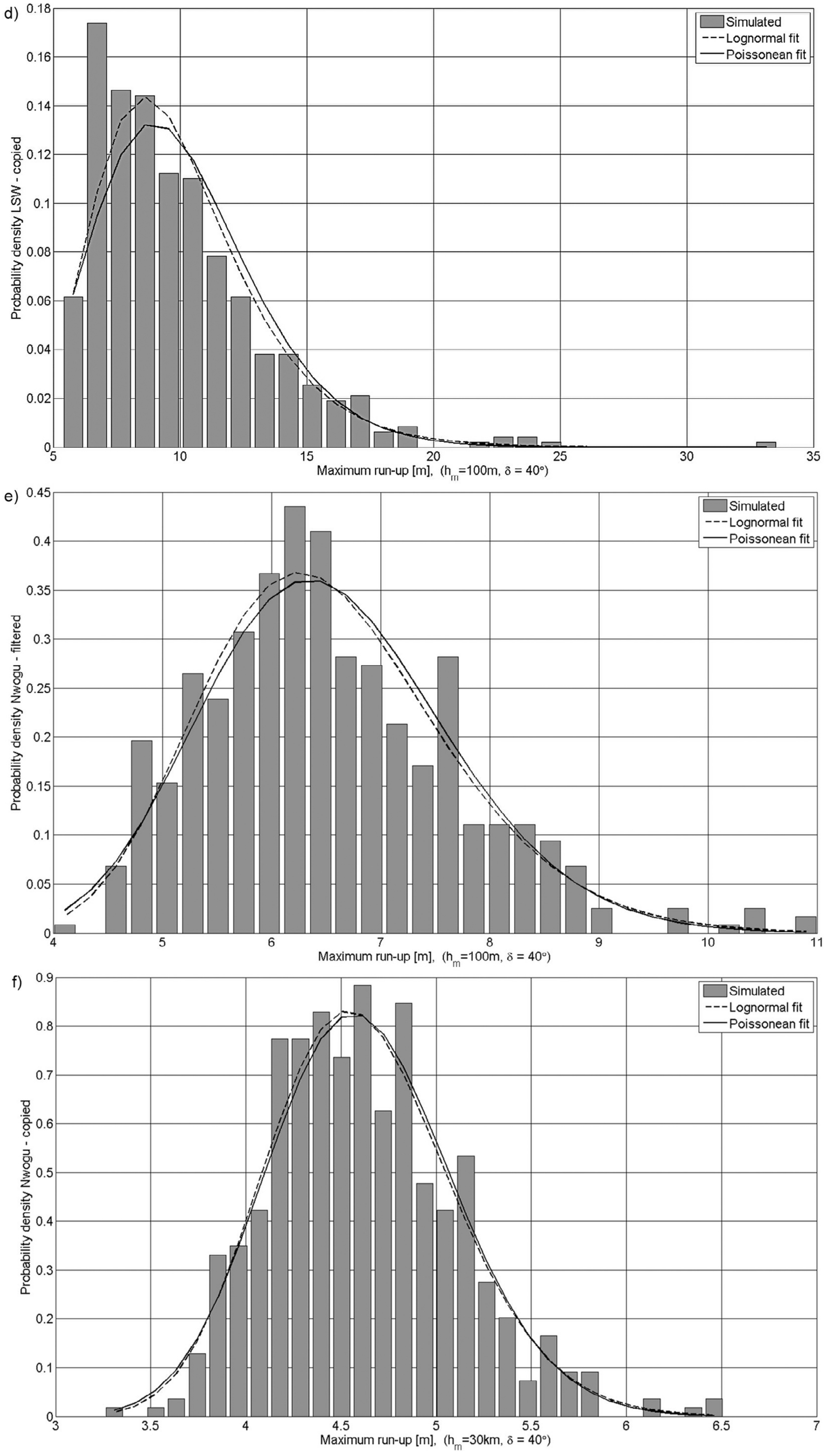

Figure 7. (continued)

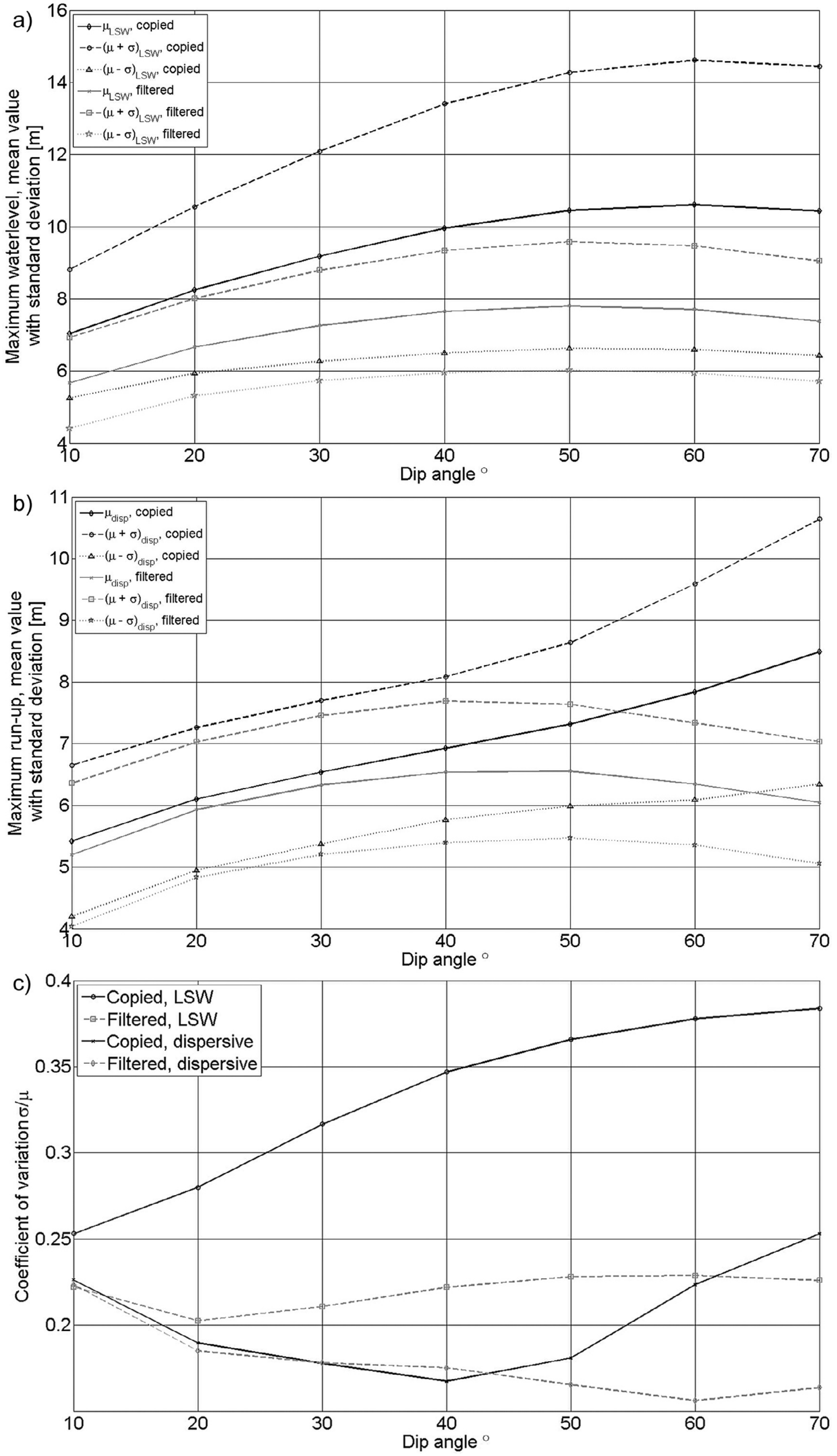

Figure 8. Mean value of maximum runup including standard deviation as a function of dip angle for (a) the LSW model and for (b) the dispersive model; (c) coefficient of variation as a function of dip angle.

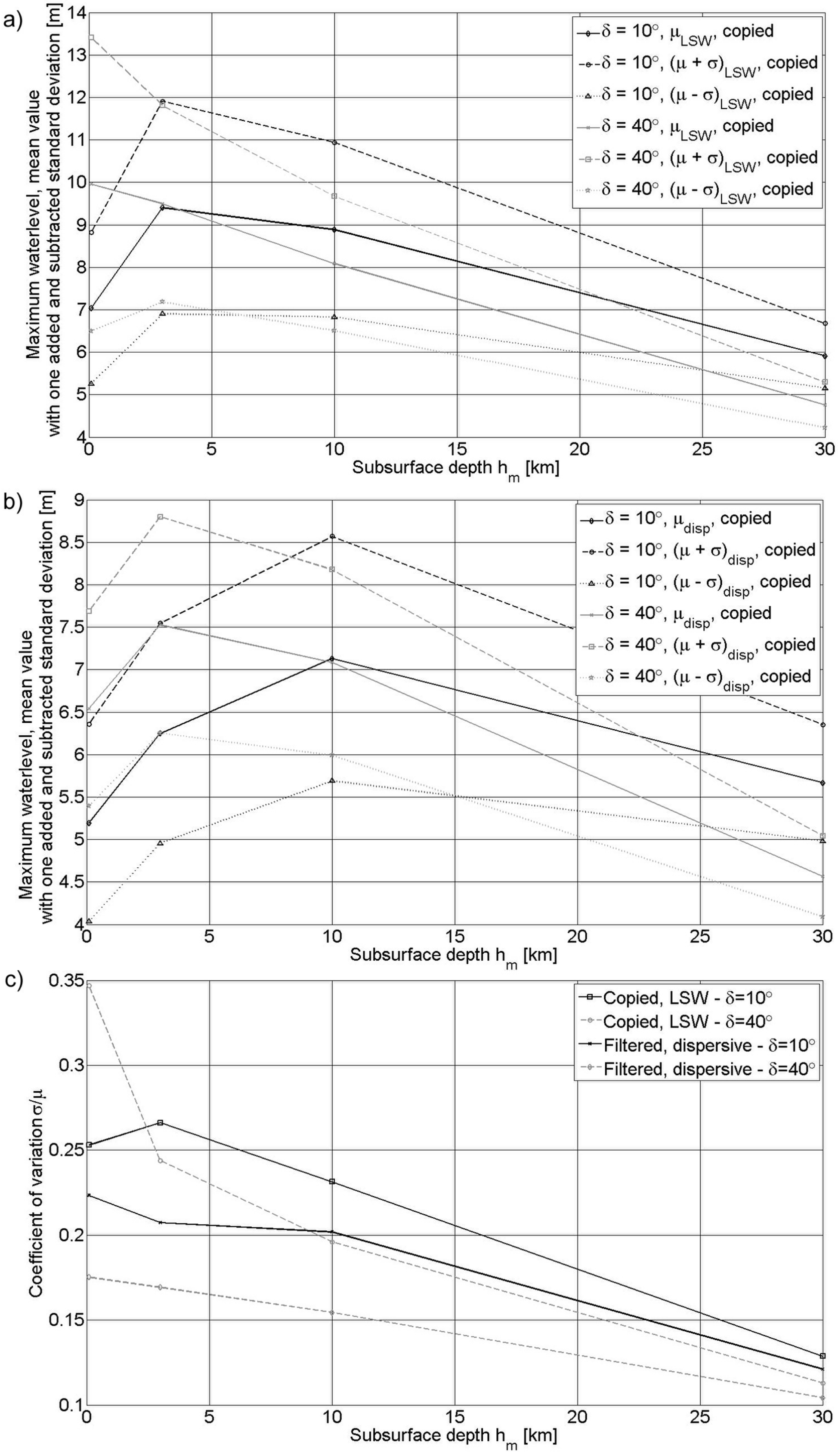

Figure 9. Mean value of maximum runup including standard deviation as function of the minimum fault depth for (a) the LSW model and for (b) the dispersive model; (c) coefficient of variation as function of the minimum fault depth.

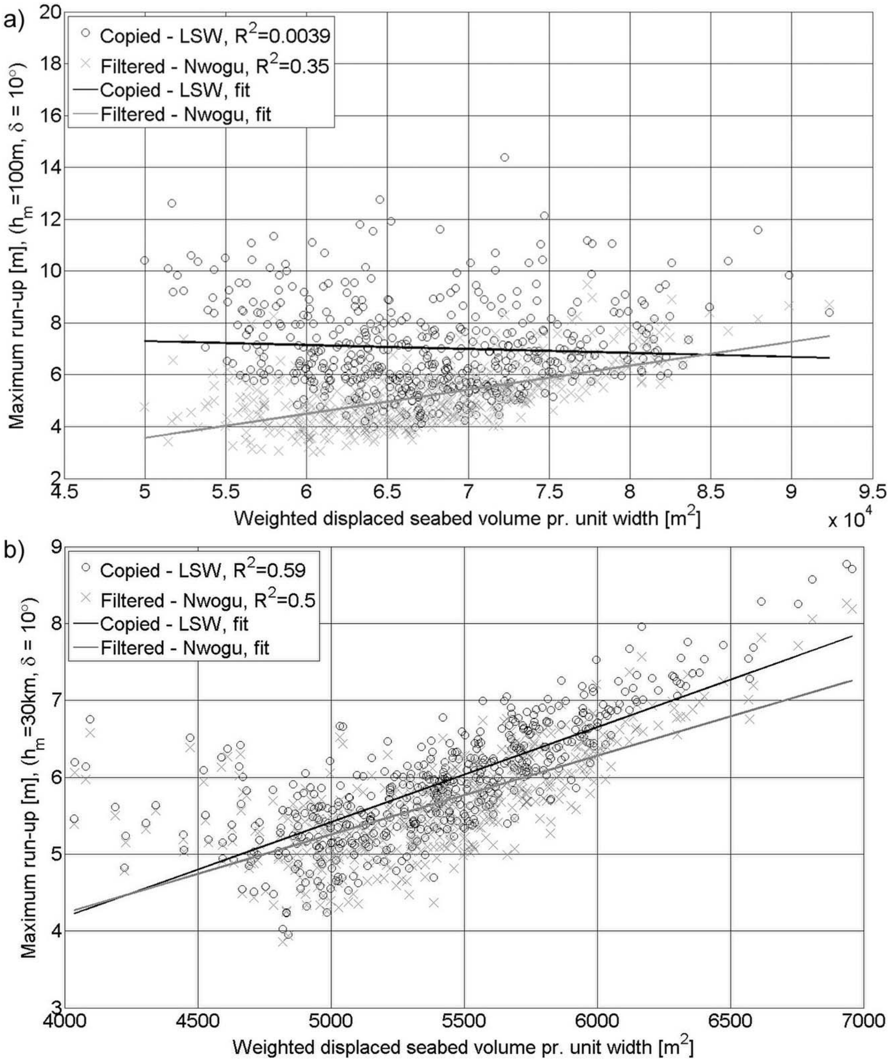

Figure 10. Maximum runup as a function of weighted displaced water volume for different minimum fault depths and dip angles. (a) Minimum fault depth of 100 m and 10° dip angle, (b) minimum fault depth of 30 km and 10° dip angle, (c) minimum fault depth of 100 m and 40° dip angle, and (d) minimum fault depth of 30 km and 40° dip angle.

deviation of the maximum runup is smaller for the dispersive model. The coefficient of variation is visualized in Figure 8c for the different combinations of initial conditions and models, showing clearly that filtering the initial water level reduces the variation of runup due to heterogeneous slip. It also shows that dispersion during propagation reduces the coefficient of variation. For the most general solution (filtered initial water level and usage of dispersive model), the coefficient of variation is decreasing as a function of the dip angle, i.e., the standard deviation is 22% of the mean for the 10° dip angle, compared to 16% for 70°.

[25] Figures 9a and 9b show mean value and standard deviation of the maximum runup as a function of the minimum fault depth for LSW and dispersive model, respectively. For shallow dip angles, the mean value first increases from h_m = 100 m to h_m = 3 km. A likely reason for this is the accumulation of localized strain close to the uppermost part of the imbedded faults leading to increased seabed elevation close to the fault tip. This effect is most pronounced for dispersive simulations. For larger values of the minimum fault depth, the maximum runup decreases as expected. Figure 9c depicts the coefficient of variation, showing that the variability of the maximum runup decreases as a function of increasing minimum fault depth. This is interpreted as an effect of the imbedded faults acting as a low-pass filter on the surface displacement.

3.4. Maximum Runup Correlation With Seabed Response

[26] The different slip realizations result in a range of initial seabed responses. We investigate to which extent the simulated maximum runup was governed by the characteristics of the seabed displacements, by investigating different parameters.

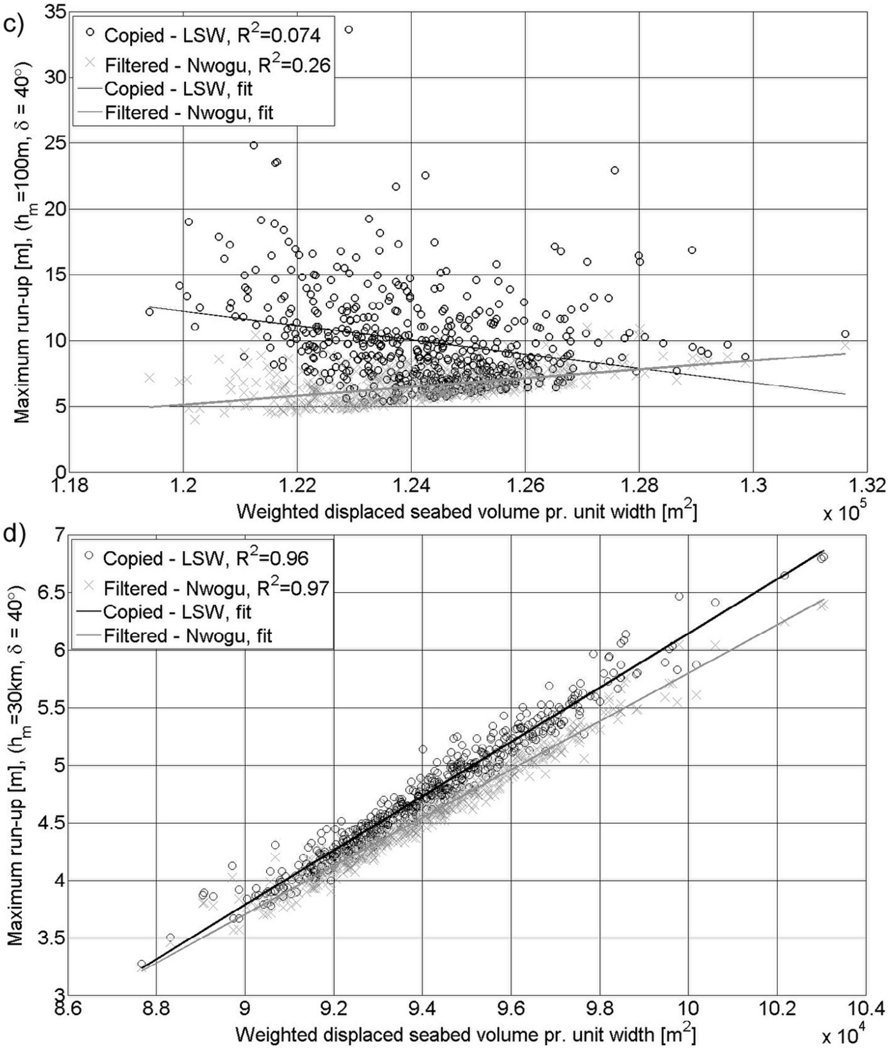

Figure 10. (continued)

[27] The first parameter is the integrated absolute seabed displacement times the 1/4 power of the absolute water depth H normalized by the maximum water depth H_0 = 4500 m, denoted weighted displaced water volume V_w below, i.e.,

$$V_w = \int |u_z(H)| \cdot (H/H_0)^{1/4} dx.$$

[28] The idea behind scaling with the water depth is to take into account the potential for amplification due to shoaling following Green's law, i.e., that wave components generated at larger depth amplify more. The maximum runup as a function of weighted displaced water volume is shown in Figure 10. For the shallow rupture (h_m = 100 m), the correlation is almost zero for the LSW model with copied initial water level, whereas somewhat more distinct for the dispersive simulations. For the imbedded faults, the correlation is improved, and a very good correspondence with little variability is found when combined with the steepest dipping faults, as exemplified for h_m = 30 km in Figure 10.

[29] A second set of parameters comprises the maximum vertical seabed elevation, the maximum seabed depression, and the peak-to-peak vertical distance between these two quantities (mimicking roughly the maximum initial wave height). Of all these, the latter provides the best correlation. Figure 11 shows the maximum runup for all realizations as a function of the maximum peak-to-peak vertical seabed distance. Compared to the weighted volume, improved correlation is observed, also regarding the surface rupturing faults (h_m = 100 m). A possible explanation for the increased correlation for the peak-to-peak displacement compared to the weighted volume is that fluctuations in the surface elevation that contribute to the volume contribute less to the maximum runup. The peak-to-peak seabed displacement is therefore a better measure of the tsunamigenic potential than

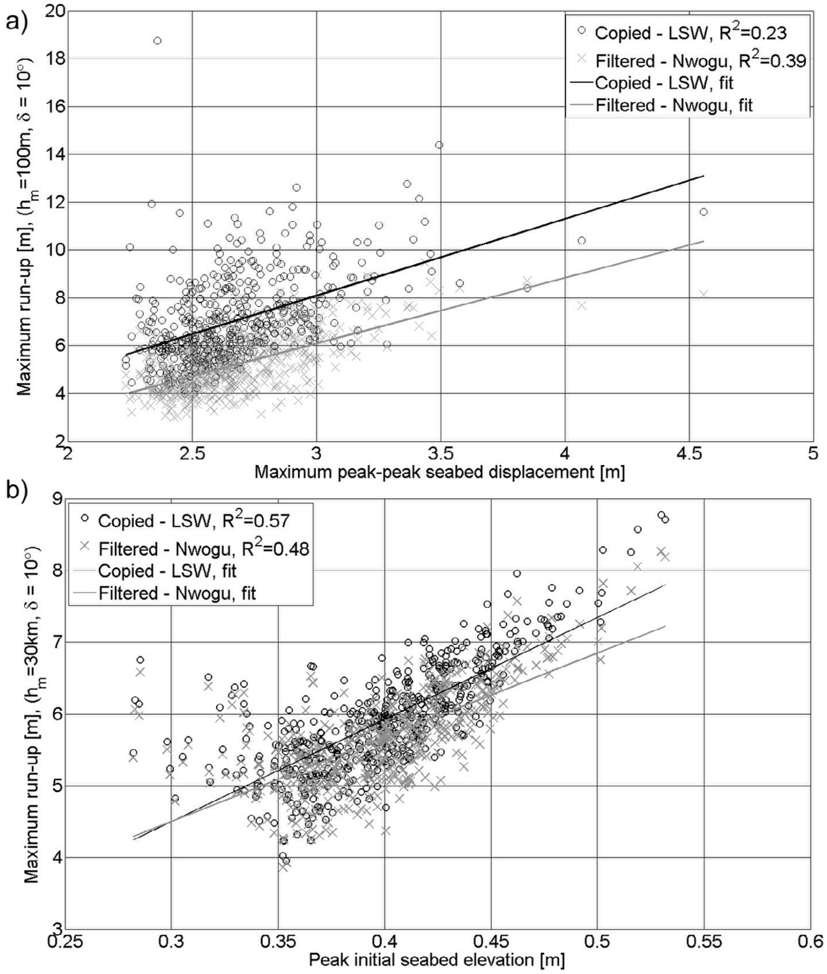

Figure 11. Maximum runup as function of peak-to-peak initial seabed displacement for different minimum fault depths and dip angles. (a) Minimum fault depth of 100 m and 10° dip angle, (b) minimum fault depth of 30 km and 10° dip angle, (c) minimum fault depth of 100 m and 40° dip angle, and (d) minimum fault depth of 30 km and 40° dip angle.

the weighted volume, particularly for shallow dip when displaced seabed fluctuations are prominent.

4. Concluding Remarks

[30] The purpose of this study is to quantify the effects of nonuniform coseismic slip in the dip direction on stochastic tsunami runup variability. We investigate tsunami generation and maximum runup due to subduction earthquakes with idealized geometries for a large number of numerical simulations by exploring the dependence of predicted tsunami heights on the heterogeneous coseismic slip distribution and dispersion. The seabed configurations are represented by a piecewise linear profile, and wave propagation is plane. The simplified geometry enables transparent results when varying fault and hydrodynamic properties compared to a more realistic topography. The dip angle varies from 10° to 70° and the fault depth from 100 m to 30 km. A total of 500 rupture realizations are modeled in each case.

[31] Seabed displacements are computed using a generalization of the *Okada* [1985] model. The sea surface response is either a direct copy of the seabed displacement, or computed using the Green's function approach by *Pedersen* [2001]. A simple computational strategy using linear models was employed because of the need of performing several hundred thousand model runs. Correct values for maximum runup of nonbreaking waves, and breaking limits, may then be obtained as long as shoaling effects make dispersion very weak before nonlinearity starts to matter. By analyzing the breaking number given by *Didenkulova* [2009], we find that for most cases and for the first wave cycle, breaking does not occur for the current combination of fault, seabed, and slip configuration for dispersive simulations. The results obtained by dispersive wave models therefore resemble closely a "realistic" runup distribution.

[32] The current paper supports the conclusion of earlier studies on stochastic shoreline response due to earthquake tsunamis, suggesting large possible runup variations even for a given magnitude. Still, we find that there are various factors related to the wave generation and propagation that reduces the variability, and that not all of these factors are commonly applied. The coefficient of variation of the runup displays its largest values for shallow faults. Increasing fault depth is found to reduce the observed variability (in terms

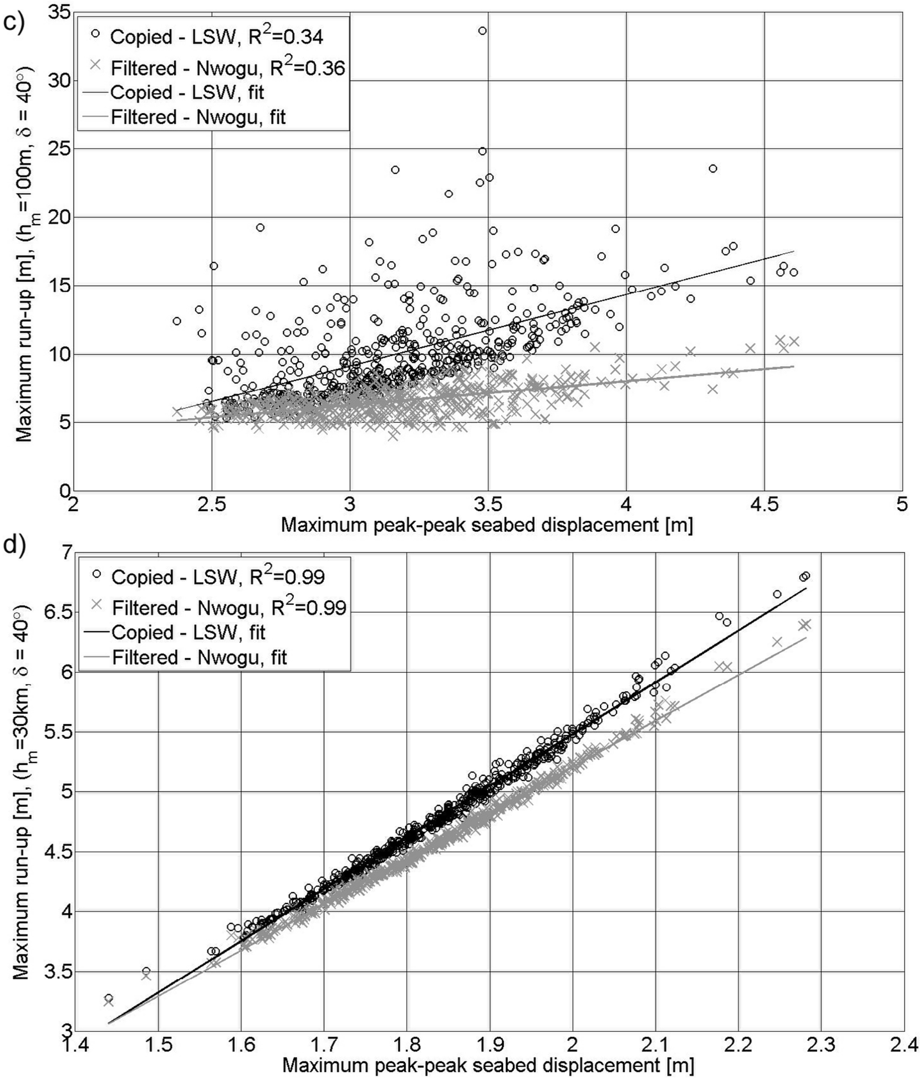

Figure 11. (continued)

of the coefficient of variation) of the seabed response. Frequency dispersion reduces the variability of the runup further, first by filtering high-frequency seabed undulations during tsunami generation, and second during the propagation phase. Shallow water models may therefore overestimate the maximum runup and its variation because of heterogeneity where such heterogeneities persist over a longer distance in the strike direction. Wave breaking may however reduce this variation to a certain extent. It is noted that by tuning the grid resolution in a shallow water model, numerical dispersion that mimics the dispersion curve may be obtained at a given water depth [see, e.g., *Shuto*, 1991]. However, for the current geometry with a considerable depth gradient; this strategy is not recommended.

[33] Furthermore, correlations between the maximum runup with various sets of seabed displacement parameters are sought. The best candidates found in this study are the scaled seabed volume per unit length and the maximum peak-to-peak vertical seabed displacement. For the deepest faults (h_m = 30 km), both parameters provide a strong correlation with the runup. Generally, the steepest dipping faults show better correlation than the shallow ones. For the shallow dipping faults, the peak-to-peak seabed displacement offers better correlation than the scaled seabed volume.

[34] The coefficient of variation varies between 16% and 22% for a surface rupturing earthquake in the configuration studied here. These are substantial variations, and points to the fact that stochastic effects should be taken into account in tsunami hazard mapping. However, the present case considers plane wave propagation and a uniform shoreline. Factors such as wave breaking and three-dimensional effects on the initial conditions and the shoreline configuration are believed to reduce the variability further as demonstrated by *Geist* [2002]. Hence, the current results should not be interpreted in absolute terms. On the other hand, the results highlight some fundamental effects that influence the variability of the maximum runup that previously have been neglected.

[35] **Acknowledgments.** The work described in this paper was financed by the Norwegian Ministry of Foreign Affairs, the International Centre for Geohazards, and NGI. Their support is highly appreciated. Furthermore, we thank Hilmar Bungum for his advice during the early stages of this work. We also thank Thea Knudsen for her work in developing the first version of the heterogeneous Okada model. Finally, the authors are indebted to two anonymous reviewers who greatly improved the quality of the paper. The present article is contribution 373 from the International Centre for Geohazards, Oslo, Norway.

References

Aki, K. (1967), Scaling law of seismic spectrum, *J. Geophys. Res.*, *72*(4), 1217–1231, doi:10.1029/JZ072i004p01217.

Blaser, L., F. Krüger, M. Ohrnberger, and F. Scherbaum (2010), Scaling relations of earthquake source parameter estimates with special focus on subduction environment, *Bull. Seismol. Soc. Am.*, *100*, 2914–2926, doi:10.1785/0120100111.

Blaser, L., M. Ohrnberger, C. Riggelsen, A. Babeyko, and F. Scherbaum (2011), Bayesian networks for tsunami early warning, *Geophys. J. Int.*, *185*(3), 1431–1443, doi:10.1111/j.1365-246X.2011.05020.x.

Bolshakova, A., and M. Nosov (2011), Parameters of tsunami source versus earthquake magnitude, *Pure Appl. Geophys.*, *168*, 2023–2031, doi:10.1007/s00024-011-0285-3.

Carrier, G. F., and H. P. Greenspan (1958), Water waves of finite amplitude on a sloping beach, *J. Fluid Mech.*, *4*, 97–109, doi:10.1017/S0022112058000331.

Didenkulova, I. (2009), New trends in the analytical theory of long sea wave runup, in *Applied Wave Mathematics: Selected Topics in Solids, Fluids, and Mathematical Methods*, edited by E. Quak and T. Soomere, pp. 265–296, Springer, Berlin, doi:10.1007/978-3-642-00585-5_14.

Gayer, G., S. Leschka, I. Nöhren, O. Larsen, and H. Günther (2010), Tsunami inundation modelling based on detailed roughness maps of densely populated areas, *Nat. Hazards Earth Syst. Sci.*, *10*, 1679–1687, doi:10.5194/nhess-10-1679-2010.

Geist, E. L. (2002), Complex earthquake rupture and local tsunamis, *J. Geophys. Res.*, *107*(B5), 2086, doi:10.1029/2000JB000139.

Geist, E. L., and R. Dmowska (1999), Local tsunamis and distributed slip at the source, *Pure Appl. Geophys.*, *154*, 485–512, doi:10.1007/s000240050241.

Glimsdal, S., G. Pedersen, K. Atakan, C. Harbitz, H. P. Langtangen, and F. Løvholt (2006), Propagation of the Dec. 26, 2004 Indian Ocean tsunami: Effects of dispersion and source characteristics, *Int. J. Fluid Mech. Res.*, *33*(1), 15–43, doi:10.1615/InterJFluidMechRes.v33.i1.30.

Grue, J., E. N. Pelinovsky, D. Fructus, T. Talipova, and C. Kharif (2008), Formation of undular bores and solitary waves in the Strait of Malacca caused by the 26 December 2004 Indian Ocean tsunami, *J. Geophys. Res.*, *113*, C05008, doi:10.1029/2007JC004343.

Henry, C., and S. Das (2001), Aftershock zones of large shallow earthquakes: Fault dimensions, aftershock area expansion and scaling relations, *Geophys. J. Int.*, *147*, 272–293, doi:10.1046/j.1365-246X.2001.00522.x.

Imamura, F. (1996), Simulation of wave-packet propagation along sloping beach by TUNAMI-code, in *Long-Wave Runup Models*, edited by H. Yeh, P. L.-F. Liu, and C. Synolakis, pp. 231–241, World Sci., Singapore.

Kaijiura, K. (1963), The leading wave of a tsunami, *Bull. Earthquake Res. Inst. Univ. Tokyo*, *41*, 535–571.

Kennedy, A. B., Q. Chen, J. T. Kirby, and R. A. Dalrymple (2000), Boussinesq modeling of wave transformation, breaking, and runup. I: 1D, *J. Waterw. Port Coastal Ocean Eng.*, *126*(1), 39–47, doi:10.1061/(ASCE)0733-950X(2000)126:1(39).

Leonard, M. (2010), Earthquake fault scaling: Self-consistent relating of rupture length, width, average displacement, and moment release, *Bull. Seismol. Soc. Am.*, *100*, 1971–1988, doi:10.1785/0120090189.

LeVeque, R., and D. L. George (2008), High-resolution finite volume methods for the shallow water equations with bathymetry and dry states, in *Advanced Numerical Models for Simulating Tsunami Waves and Runup*, edited by P. L.-F. Liu, H. Yeh, and C. Synolakis, pp. 43–73, World Sci., Hackensack, N. J., doi:10.1142/9789812790910_0002.

Løvholt, F., and G. Pedersen (2008), Instabilities of Boussinesq models in non-uniform depth, *Int. J. Numer. Methods Fluids*, *61*, 606–637, doi:10.1002/fld.1968.

Løvholt, F., H. Bungum, C. B. Harbitz, S. Glimsdal, C. D. Lindholm, and G. Pedersen (2006), Earthquake related tsunami hazard along the western coast of Thailand, *Nat. Hazards Earth Syst. Sci.*, *6*, 979–997, doi:10.5194/nhess-6-979-2006.

Lynett, P. (2006), Nearshore wave modeling with high-order Boussinesq-type equations, *J. Waterw. Port. Coastal Ocean Eng.*, *132*, 348–357, doi:10.1061/(ASCE)0733-950X(2006)132:5(348).

Lynett, P. J., T.-R. Wu, and P. L.-F. Liu (2002), Modeling wave runup with depth-integrated equations, *Coastal Eng.*, *46*, 89–107, doi:10.1016/S0378-3839(02)00043-1.

Madsen, P. A., D. R. Fuhrman, and H. A. Schäffer (2008), On the solitary wave paradigm for tsunamis, *J. Geophys. Res.*, *113*, C12012, doi:10.1029/2008JC004932.

Mai, P. M., and G. C. Beroza (2000), Source scaling properties from finite-fault rupture models, *Bull. Seismol. Soc. Am.*, *90*, 604–615, doi:10.1785/0119990126.

Mai, P. M., and G. C. Beroza (2002), A spatial random field model to characterize complexity in earthquake slip, *J. Geophys. Res.*, *107*(B11), 2308, doi:10.1029/2001JB000588.

McCloskey, J., A. Antonioli, A. Piatanesi, K. Sieh, S. Steacy, S. Nalbant, M. Cocco, C. Giunchi, J. D. Huang, and P. Dunlop (2007), Near-field propagation of tsunamis from megathrust earthquakes, *Geophys. Res. Lett.*, *34*, L14316, doi:10.1029/2007GL030494.

McCloskey, J., A. Antonioli, A. Piatanesi, K. Sieh, S. Steacy, S. Nalbant, M. Cocco, C. Giunchi, J. D. Huang, and P. Dunlop (2008), Tsunami threat in the Indian Ocean from a megathrust earthquake west of Sumatra, *Earth Planet. Sci. Lett.*, *265*, 61–81, doi:10.1016/j.epsl.2007.09.034.

Nwogu, O. (1993), Alternative form of Boussinesq equations for nearshore wave propagation, *J. Waterw. Port Coastal Ocean Eng.*, *119*(6), 618–638, doi:10.1061/(ASCE)0733-950X(1993)119:6(618).

Okada, Y. (1985), Surface deformation due to shear and tensile faults in a half-space, *Bull. Seismol. Soc. Am.*, *75*, 1135–1154.

Pedersen, G. (2001), A note on tsunami generation by earthquakes [online], *Preprint Ser. Mech. Appl. Math.*, *4*, 1–8. [available at http://www.duo.uio.no/sok/work.html?WORKID=126788]

Pedersen, G. (2008a), Modeling runup with depth integrated equation models, in *Advanced Numerical Models for Simulating Tsunami Waves and Runup*, edited by P. L.-F. Liu, H. Yeh, and C. Synolakis, pp. 3–41, World Sci., Hackensack, N. J., doi:10.1142/9789812790910_0001.

Pedersen, G. (2008b), A Lagrangian model applied to runup problems, in *Advanced Numerical Models for Simulating Tsunami Waves and Runup*, edited by P. L.-F. Liu, H. Yeh, and C. Synolakis, pp. 311–315, World Sci., Hackensack, N. J., doi:10.1142/9789812790910_0017.

Peregrine, D. H. (1967), Long waves on a beach, *J. Fluid Mech.*, *27*, 815–827, doi:10.1017/S0022112067002605.

Roth, M., and M. Korn (1993), Single scattering theory versus numerical modelling in 2-D random media, *Geophys. J. Int.*, *112*, 124–140, doi:10.1111/j.1365-246X.1993.tb01442.x.

Shuto, N. (1991), Numerical simulation of tsunamis—Its present and near future, *Nat. Hazards*, *4*, 171–191, doi:10.1007/BF00162786.

Son, S., P. J. Lynett, and D.-H. Kim (2011), Nested and multi-physics modeling of tsunami evolution from generation to inundation, *Ocean Modell.*, *38*(1–2), 96–113, doi:10.1016/j.ocemod.2011.02.007.

Synolakis, C. E. (1987), The runup of solitary waves, *J. Fluid Mech.*, *185*, 523–545, doi:10.1017/S002211208700329X.

Titov, V. V., and C. E. Synolakis (1995), Modeling of breaking and non-breaking long-wave evolution and runup using VTCS-2, *J. Waterw. Port Coastal Ocean Eng.*, *121*(6), 308–316, doi:10.1061/(ASCE)0733-950X(1995)121:6(308).

Titov, V. V., and C. E. Synolakis (1998), Numerical modeling of tidal wave runup, *J. Waterw. Port Coastal Ocean Eng.*, *124*(4), 157–171, doi:10.1061/(ASCE)0733-950X(1998)124:4(157).

Wang, X., and P. L.-F. Liu (2006), An analysis of 2004 Sumatra earthquake fault plate mechanisms and Indian Ocean tsunami, *J. Hydraul. Res.*, *44*(2), 147–154, doi:10.1080/00221686.2006.9521671.

Wells, D. L., and K. J. Coppersmith (1994), New empirical relationships among magnitude, rupture length, rupture width, rupture area, and surface displacement, *Bull. Seismol. Soc. Am.*, *84*(4), 974–1002.

Zhou, H., C. W. Moore, Y. Wei, and V. V. Titov (2011), A nested-grid Boussinesq-type approach to modelling dispersive propagation and runup of landslide-generated tsunamis, *Nat. Hazards Earth Syst. Sci.*, *11*, 2677–2697, doi:10.5194/nhess-11-2677-2011.

S. Bazin, C. Harbitz, and F. Løvholt, NGI, PO Box 3930, Ullevål Stadion, N-0806 Oslo, Norway. (finn.lovholt@ngi.no; sara.bazin@ngi.no; carl.bonnevie.harbitz@ngi.no)

R. E. Bredesen, Simula Research Laboratory, PO Box 134, N-1325 Lysaker, Norway. (rolv@simula.no)

D. Kühn, International Center for Geohazards, c/o NGI, PO Box 3930, Ullevål Stadion, N-0806 Oslo, Norway. (daniela@norsar.no)

G. Pedersen, Department of Mathematics, University of Oslo, PO Box 1072, Blindern, N-0316 Oslo, Norway. (geirkp@math.uio.no)

3.2 Base de données des tsunamis dans les Caraïbes

J'ai aussi revisité les cinq différents catalogues des tsunamis historiques qui existaient dans les Caraïbes. Je les ai comparés et compilés puis j'ai croisé ma compilation avec différentes sources comme le catalogue de sismicité, celui des éruptions volcaniques et les archives des cyclones de façon à filtrer les vagues de tempêtes et à associer les tsunamis aux bonnes causes. La base de données ainsi mise à jour, m'a permis de remarquer que seulement 17 des 85 tsunamis historiques avaient fait des victimes. Mais plus de 15 000 personnes auraient péri dans des tsunamis dans les Caraïbes depuis 1498. Ce chiffre dépasse le nombre total de morts sur la côte ouest des Etats Unis, à Hawaii et en Alaska. 74% des tsunamis y sont d'origine sismiques, 14% d'origine volcanique et 7% ont été générés par des glissements de terrain. La vague la plus haute (8.8-10 m) a été mesurée après le séisme des Iles Vierges le 18 novembre 1867. Ce tsunami avait touché toutes les iles des Petites Antilles.

Le risque lié au tsunami est en général plus difficile à quantifier que celui du risque sismique. La première raison est qu'il a différentes origines (sismique, volcanique et glissement de terrain). La seconde raison est que, comme nous l'avons vu dans le chapitre précédent, la taille d'un tsunami est complexe et non linéaire. Les séismes de subduction comme celui d’Indonésie en 2004, sont en général considérés comme les plus tsunamigéniques, mais le séisme des Iles Vierge en est un contre-exemple. La nouvelle base de données a pu fournir différents types de scénarios qui ont servi à mes collègues du NGI pour estimer les risques associés, à l'aide de modélisation de runup et d'estimation des vulnérabilités. La durée de la base de données a permis d'évaluer quelques périodes de retour. Par ailleurs, les populations exposées ont été estimées en utilisant des outils SIG. Nous avons ainsi calculé que l'ile de la Guadeloupe présente l'exposition relative (par rapport à sa population totale) la plus élevée (6,5%) dans le pourtour de la plaque Caraïbe.

ARTICLE IN PRESS

Continental Shelf Research ▮ (▮▮▮▮) ▮▮▮–▮▮▮

Contents lists available at SciVerse ScienceDirect

Continental Shelf Research

journal homepage: www.elsevier.com/locate/csr

Research papers

Tsunami hazard in the Caribbean: Regional exposure derived from credible worst case scenarios

C.B. Harbitz [a,b,*], S. Glimsdal [a,b], S. Bazin [a,b,c], N. Zamora [b,d], F. Løvholt [a,b], H. Bungum [e,b], H. Smebye [a,b], P. Gauer [a,b], O. Kjekstad [a,b]

[a] *Norwegian Geotechnical Institute (NGI), Norway*
[b] *International Centre for Geohazards (ICG), Norway*
[c] *Institut de Physique du Globe de Paris (IPGP), France*
[d] *Research collaboration with University of Costa Rica, Costa Rica*
[e] *NORSAR, Norway*

ARTICLE INFO

Article history:
Received 11 July 2011
Received in revised form
12 November 2011
Accepted 15 February 2012

Keywords:
Caribbean
Tsunami
Earthquake
Volcano
Landslide
Run-up

ABSTRACT

The present study documents a high tsunami hazard in the Caribbean region, with several thousands of lives lost in tsunamis and associated earthquakes since the XIXth century. Since then, the coastal population of the Caribbean and the Central West Atlantic region has grown significantly and is still growing. Understanding this hazard is therefore essential for the development of efficient mitigation measures. To this end, we report a regional tsunami exposure assessment based on potential and credible seismic and non-seismic tsunamigenic sources. Regional tsunami databases have been compiled and reviewed, and on this basis five main scenarios have been selected to estimate the exposure. The scenarios comprise two M_w8 earthquake tsunamis (north of Hispaniola and east of Lesser Antilles), two subaerial/submarine volcano flank collapse tsunamis (Montserrat and Saint Lucia), and one tsunami resulting from a landslide on the flanks of the Kick'em Jenny submarine volcano (north of Grenada). Offshore tsunami water surface elevations as well as maximum water level distributions along the shore lines are computed and discussed for each of the scenarios. The number of exposed people has been estimated in each case, together with a summary of the tsunami exposure for the earthquake and the landslide tsunami scenarios. For the earthquake scenarios, the highest tsunami exposure relative to the population is found for Guadeloupe (6.5%) and Antigua (7.5%), while Saint Lucia (4.5%) and Antigua (5%) have been found to have the highest tsunami exposure relative to the population for the landslide scenarios. Such high exposure levels clearly warrant more attention on dedicated mitigation measures in the Caribbean region.

1. Introduction

Tsunami hazard is more difficult to assess than earthquake hazard for two main reasons, firstly that the tsunamigenic processes are diverse (earthquakes, volcanoes, landslides, or some combination of these) and secondly that the relation between the energy released in the process (such as the earthquake magnitude) and the size of the tsunami generally is quite complex, and non-linear. Moreover, a problem that tsunami hazard shares with earthquake hazard is the extreme scaling laws, demonstrated by the way the consequences (the risk) increase with decreasing occurrence probabilities. What this means in real life is that the most severe earthquake and tsunami disasters are very rare and have scaling characteristics such that they saturate only at a very high level (as compared for instance to winds and ocean waves) and that they therefore are difficult to predict when based on empirical data that cover only a few hundred years, even though paleoseismic and paleotsunamic studies have now significantly increased the time frames here. For these (and other) reasons, probabilistic assessment of tsunami hazard is still at an early stage of development (Løvholt et al., 2011), and we find therefore that scenario based assessments represent a more viable approach, as used in this study.

The Caribbean is one of the most highly exposed regions of the world with respect to natural hazards, as seen recently by the January 2010 Haiti earthquake and tsunami (Calais et al., 2010; Hornbach et al., 2010; see also ISDR, 2009). Climatic hazards such as strong winds and heavy rains, storms and hurricanes frequently give rise to landslides, sediment flows, and water

---

* Corresponding author at: Norwegian Geotechnical Institute (NGI), P.O. Box 3930, Ullevål stadion, N-0806 Oslo, Norway. Tel.: +47 22023000; fax: +47 22230448.
E-mail address: ch@ngi.no (C.B. Harbitz).

0278-4343/$ - see front matter © 2012 Elsevier Ltd. All rights reserved.
doi:10.1016/j.csr.2012.02.006

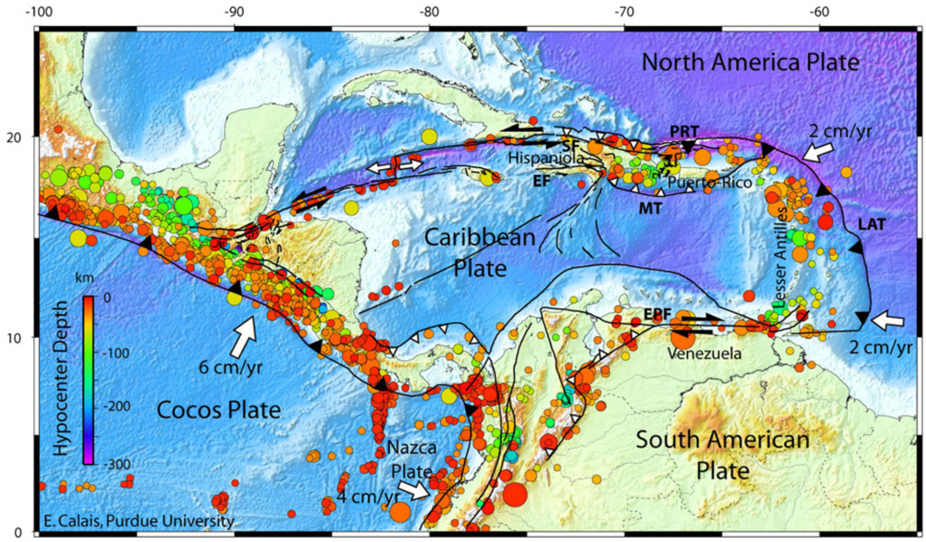

Fig. 1. Seismotectonic context of the Caribbean Plate. Seismicity is from USGS/NEIC database (1974—present). This map is modified from E. Calais, http://web.ics.purdue.edu/~ecalais/haiti/. BAP: Barbados Accretionary Prism; CAT: Central American Trench; EF: Enriquillo Fault; EPF: El Pilar Fault; LAT: Lesser Antilles Trench; MT: Muerto Trench; PRT: Puerto Rico Trench; and SF: Septentrional Fault. Country names are shown in Fig. 2.

floods. Earthquakes and volcanic activity in the eastern Caribbean are also significant in addition to the relatively high risk levels for coastal flooding, including tsunami risk. In fact, one out of seven tsunamis worldwide is found in the Caribbean Sea (O'Loughlin and Lander, 2003). With few exceptions, the capabilities in the region to deal with these hazards in terms of efficient preventive measures have so far been limited (Intergovernmental Oceanographic Commission (IOC), 2006). This is largely a result of limited technological and human resources, combined with the fact that the region comprises a number of small autonomous states with limited collaboration and integration of capabilities. Experience from most countries exposed to natural disasters is that efforts to build awareness and improve preparedness are crucial in mitigating the large consequences of natural hazards.

This paper presents a study of regional tsunami hazard and related exposure in the Caribbean region, including potential seismic and non-seismic tsunamigenic sources. The paper contains calculations demonstrating a methodology that could easily be expanded into a more comprehensive tsunami hazard and exposure assessment. The regional tsunami risk is assessed as the sum of the effects from a number of scenarios that may affect the various elements at risk. As already mentioned, the tsunami risk is often dominated by large scale 'credible worst case scenarios' (Nadim and Glade, 2006), and the scenarios developed in this paper clearly fall into this category. However, since the scenarios cover only the presumed most important of the potential scenarios, they do not represent the complete tsunami risk. Further applications of the tsunami simulations in a more local and detailed way, with tsunami vulnerability and risk analysis for Bridgetown, Barbados, are presented by NGI (2009a).

2. Geodynamics and potential tsunami sources in the Caribbean region

In the Caribbean region, both earthquakes and non-seismic sources (volcanic eruptions, flank collapses, and submarine landslides) are known to have caused a large number of tsunamis, many of them destructive. Hence, both seismic, volcanic, and landslide activity must be understood for a balanced combination of credible worst case tsunami scenarios and for disaster risk reduction.

2.1. Seismic activity

The Caribbean Plate is bounded to the east by the Lesser Antilles subduction zone and to the west by the Central America subduction zone (Fig. 1). The North American and South American plates dip beneath the Caribbean plate at a rate of about 2 cm/yr in a WSW direction along the Lesser Antilles Trench (DeMets et al., 2000; Mann et al., 2002). As a consequence, the Eastern Caribbean is prone to a moderate to large seismic hazard. Three kinds of damaging seismicity can be distinguished in the arc (Stein et al., 1982), firstly, the seismicity directly related to the subduction at the plate interface, secondly, the seismicity within the subducting slab at greater depth, and thirdly, the seismicity occurring within the Caribbean plate.

The largest historical earthquake in the region occurred in 1843 between Guadeloupe and Antigua (geographical names are presented in Fig. 2), with a magnitude of 7.5–8 (Bernard and Lambert, 1988). Since the historical seismicity in this region covers only three and a half centuries, and with variable quality, it is difficult on this basis to estimate the recurrence time of strong events and also their magnitudes. The geometries of the subduction processes in the Caribbean are also quite complex, so it is difficult also on this basis to estimate the potentials. Using the instrumental seismicity available since 1950 in the Lesser Antilles, several authors have described a variable dip angle (from 30° to 60° dip) of the slab along the main arc (Dorel, 1981; Girardin and Gaulon, 1982; Wadge and Shepherd, 1984; Girardin et al., 1991; Feuillet et al., 2002). However, according to Bengoubou-Valérius et al. (2008), with more accurate earthquake locations there is no significant dip variation from north to south and a constant 50° dip angle fits the Wadati–Benioff plane quite well. In general, the subduction rate (the downgoing slab velocity) often tends to increase with the age of the subducted plate due to the density of old oceanic lithosphere (Carlson and Raskin, 1983). In the Lesser Antilles, however, the subduction is slow (the rate of convergence is 2 cm/yr according to DeMets et al., 2000), while the subducting lithosphere is old (80–85 Ma according to Müller et al., 1997), which is what Ruff and Kanamori (1982) showed in their classical paper to be important criteria for limiting the maximum magnitude. However, the 2004 Sumatra event violated significantly the rule that only young plates with a fast subduction can create megathrust earthquakes, so apparently the

Please cite this article as: Harbitz, C.B., et al., Tsunami hazard in the Caribbean: Regional exposure derived from credible worst case scenarios. Continental Shelf Research (2012), doi:10.1016/j.csr.2012.02.006

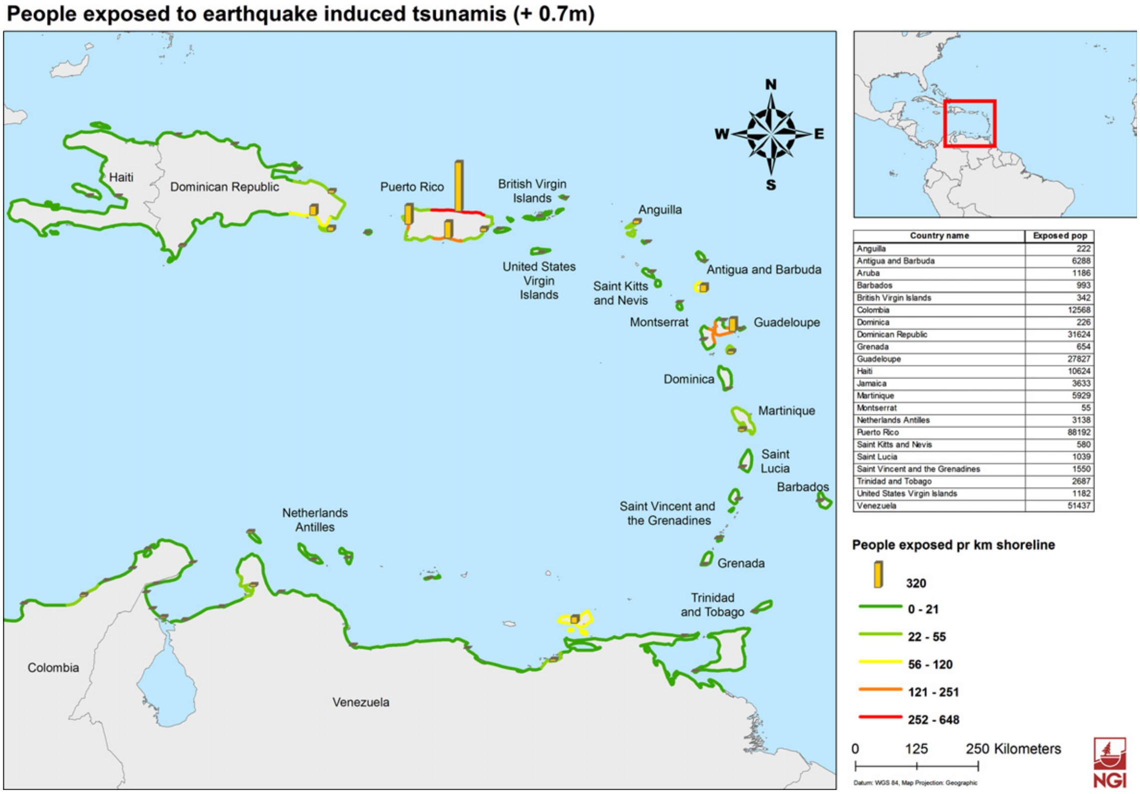

Country name	Exposed pop
Anguilla	222
Antigua and Barbuda	6288
Aruba	1186
Barbados	993
British Virgin Islands	342
Colombia	12568
Dominica	226
Dominican Republic	31624
Grenada	654
Guadeloupe	27827
Haiti	10624
Jamaica	3633
Martinique	5929
Montserrat	55
Netherlands Antilles	3138
Puerto Rico	88192
Saint Kitts and Nevis	580
Saint Lucia	1039
Saint Vincent and the Grenadines	1550
Trinidad and Tobago	2687
United States Virgin Islands	1182
Venezuela	51437

Fig. 2. Number of people exposed to earthquake induced tsunami per km shoreline. The bars indicate the exposed population per km shoreline calculated by defining line segments along the coast with approximately similar population density per unit area. The statistics from these areas are projected into the shoreline for the same area using different colours. The effect of high tide and sea level rise is taken into account. Estimated individual return period is about 500 years.

Ruff–Kanamori paradigm is too simple. It has also been suggested (Ruff, 1989) that the existence of trench sediments could explain part of the remaining variance in maximum earthquake size, which is interesting here since the southern part of the Lesser Antilles Trench is buried by a large wedge of sediments forming the Barbados accretionary prism (Bengoubou-Valérius et al., 2008). However, a close examination of these and other criteria made Stein and Okal (2007) conclude that the strongest one was possibly age in itself, since no mega-earthquakes (e.g. larger than M_w9.0) are known to have occurred in a subducting lithosphere older than 90 Ma. Even so, it is worth keeping in mind that tsunamis driven by sub-mega-earthquakes can also be highly hazardous (Løvholt et al., 2006).

The strike-slip motions relative to the North and South American plates occurs along two major fault zones (Calais et al., 1998; see also Fig. 1): the northern plate boundary (Hispaniola and Puerto Rico) dominated by the Enriquillo and Septentrional faults, and the southern plate boundary (Venezuela) dominated bythe El Pilar fault. The type of seismicity associated with strike-slip faulting is shallow and can be damaging, as demonstrated by the 2010 Haiti earthquake. The tsunamigenic potentials of earthquakes are tied to the focal mechanism as the tsunami generation implies a significant vertical displacement (Tanioka and Satake, 1996; Hebert et al., 2005); thrust events in subduction zones are therefore generally the most tsunamigenic ones. Grilli et al. (2010) present numerical simulations of both near- and far-field impact of tsunamis generated in the Puerto Rico trench, revealing run-up heights of about 20 m along the northern shore of Puerto Rico for a M_w9.1 source. However, faulting mechanisms are complex in the Caribbean region and do not always reflect only the first order plate motions; for instance, oblique motions at the tip of a strike-slip fault could also produce vertical dislocations. In addition, pure strike-slip earthquakes could trigger submarine landslides that generate tsunamis. A more comprehensive review of the large scale tectonics of the region and of potential seismic sources for tsunamis is presented by NORSAR (NGI, 2009b).

The Lesser Antilles volcanic arc has been built up by the subduction of the northern and southern American plates under the Caribbean plate (Molnar and Sykes, 1969). It has a curved shape and extends from 12°N to 18°N latitude. North of the island of Martinique, the Lesser Antilles arc is composed of an outer arc, made of Plio-Quaternary coral reef platforms, and of a recent upper Miocene inner volcanic arc. Active volcanoes are located in the western branch of the island chain, with twelve Holocene active volcanoes in the ten major islands of the younger arc. Catastrophic flank collapses are quite frequent for these volcanoes (Boudon et al., 2007).

2.2. *Volcanic activity, flank collapses, and landslides*

In Guadeloupe, the Grande Découverte-Soufrière composite volcano has experienced at least 12 flank collapse events over the last 50 ka (Komorowski et al., 2002, 2005). During the last 8500 years, 8 small flank-collapse events with volumes of 0.1–0.3 km^3 are known, and some of them reached the Caribbean Sea (Le Friant et al., 2006). The Caracasbaai in Curaçao, Netherlands Antilles, is also the result of a huge slide. With the use of echosounding, a limestone block of about 150 million m^3 has been identified. The block separated from the south-western part of the island and fell into the sea, displacing around 700 million m^3 of globigerina ooze about 5–10 ka BP (de Buisonje and Zonneveld, 1976).

Kick'em Jenny is an active growing submarine volcano located 8 km off the northern side of the island of Grenada. According to Pararas-Carayannis (2004) submarine explosive eruptions would be expected to generate tsunamis as a series of smaller events

Please cite this article as: Harbitz, C.B., et al., Tsunami hazard in the Caribbean: Regional exposure derived from credible worst case scenarios. Continental Shelf Research (2012), doi:10.1016/j.csr.2012.02.006

over more than 24 h. The wave periods and wave lengths will probably be short, however, and wave height will therefore decay rapidly with distance. Based on the pattern of Kick'em Jenny's eruptive activity, a present 'worst case tsunami scenario' would be a repeat of the 1939 event, but with the shallower depth of the present summit. Such a large and violent eruption can be expected to generate waves with a run-up height of 3 m in Northern Grenada and the Grenadines, and as much as 1–2 m along the west coast of the Barbados, Trinidad, and Saint Vincent. The wave heights along the nearest coastline of northern Bonaire, Netherlands Antilles, and Venezuela may be up to 1 m (Pararas-Carayannis, 2004).

Gisler et al. (2006b) demonstrated by 2D numerical simulations of explosive eruptions that a medium scenario for this volcano could generate a wave with a height of 130 m at a distance of 3 km from the source and a height of 21 m at 10 km distance, comparable to an explosion of about 20,000 kT. However, in the simulations the submerged top was only 100 m below the water surface, thus significantly shallower than the true cone summit. They also state that the water depth above the volcano summit is now 190 m, and is not significantly diminishing. Hence, the water pressure confines the explosive effects, and the coupling of the explosive energy to wave energy is inefficient compared to slower mechanisms such as landslides (only a few percent of the explosive source energy is transferred). Gisler et al. (2006b), therefore, concluded that there is presently a modest danger related to explosive eruptions except for gases and missiles threatening shipping, and that the tsunami danger from Kick'em Jenny is larger for a slope failure similar to that which caused the horse-shoe shaped cleft in which the volcano currently nestles. The debris flows of Kick'em Jenny were described by Sigurdsson et al. (2006). These flows extend from the western side of the submarine volcano for about 15 km to maybe 30 km to the west into the Grenada Basin (west of Grenada) with a thickness of tens to hundreds of metres. A conservative estimate of the volume of the smaller debris flow deposits is about 10 km^3. It is possible that hydromagmatic explosions associated with future eruptions could result in greater flank instability and maybe also slow the rate of growth of the volcano (Pararas-Carayannis, 2004).

Using high-resolution bathymetric data, Deplus et al. (2001) mapped large-scale debris flow deposits on the seafloor surrounding several active volcanoes. These flow deposits most likely represent catastrophic events also generating huge tsunamis. Three smaller debris flow deposits of about 20–120 km^2 were identified on the lower submarine flanks of the Soufriere Hills volcano in Montserrat. They are characterised by mega-blocks 100–400 m across and 20–40 m high in addition to smaller debris flow blocks, and they extend to about 15 km from the shoreline. The age of the debris flows is probably less than 100–200 ka (Deplus et al., 2001). The major English's Crater event about 4000 years BP involved a volume of 0.5 km^3 (Le Friant et al., 2004). Off the southern parts of Montserrat some of the observed deposits could have originated either as a submarine flank failure or as an older subaerial flank collapse that subsequently have been buried by the South Soufriere Hills volcano. Large-scale debris flow deposits are also identified west of the active volcanoes of Martinique, Dominique, and Saint Lucia. Off Martinique and Saint Lucia, the deposits are found at the opening of flat-floored channels in the continuity of the horseshoe-shaped structures of Mt Pelée (Martinique) and Qualibou (Saint Lucia). The deposits cover areas of about 3500 km^2 off Dominica, 800 km^2 off Martinique, and 2000 km^2 off Saint Lucia, with terrain covered by mega-blocks over 1100, 60 and 300 km^2, respectively. The run-out distances for the debris flow blocks are about 90 km for Dominica, 60 km for Martinique, and 75 km for Saint Lucia. The deposits probably resulted from several flank collapse events for each volcano, but the long run-out distances demonstrate that they were produced by major events. The age of the debris flows is probably also here less than 100–200 ka (Deplus et al., 2001).

Many forested volcanic islands of the Lesser Antilles have highly eroded oversteepened coastal cliffs that can cause large landslides, and therefore present significant tsunami hazards. Due to surveying difficulties these areas have not been properly studied to date, but new remote sensing techniques could provide appropriate methods of investigation (Teeuw et al., 2009).

Recent geomorphological landslide data obtained by marine geophysical surveys have also given interesting results for studying possible tsunami sources; for instance, the ones located in the Puerto Rico region are described by ten Brink et al. (2004). The Loiza amphitheatre (and a 15 km long fissure) and the Arecibo amphitheatre (50 km wide escarpment), both on the southern side of the Puerto Rico Trench, the northern side of the Puerto Rico trench, and the Mona rift (between Puerto Rico and Hispaniola) were all interpreted as failures capable of generating tsunamis. The Loiza debris extends for 40 km with a thickness of 200 m. From 160 landslides described in the area only 9 are supposed to have volumes of more than 5 km^3 (ten Brink et al., 2006a), and only these could have caused tsunami run-ups higher than 2.5 m. The numerical tsunami modelling by ten Brink et al. (2006a) predicted a maximum tsunami run-up of approximately 16 m on the northern coast of Puerto Rico. This region may generate significant tsunamis mainly towards the coast of Puerto Rico, Virgin Islands, and Dominican Republic. The conditions of the Mona Canyon and its secondary canyons with their steep slopes may possibly generate submarine landslides. Quantifying this hazard is difficult, however, due to scarce historical information (Moya and Mercado, 2006).

3. Past tsunami events

3.1. Historical tsunamis database

Historical Caribbean tsunamis have been studied by several researchers (e.g. McCann, 2006), but with only some of them going back to original data and analysing data from the many scattered archives in this region (Zahibo and Pelinovsky, 2001; BRGM, 2009; Nikolkina et al., 2010). We have compiled a new historical tsunami database for the Caribbean Sea largely based on the reports from the NOAA National Geophysical Data Center (NOAA/NGDC, 2008) and the Novosibirsk Tsunami Laboratory (NTL, 2002), which in turn are based on tsunami catalogues compiled by O'Loughlin and Lander (2003), Mercado-Irizarry and Liu (2006), and Shepherd et al. (1995). For many of the events we have updated the source information based on recent updates of earthquake locations, focal depths, magnitudes, and tsunami observations (Engdahl and Villaseñor, 2002; Engdahl et al., 2007; Villaseñor and Engdahl, 2007; BRGM, 2009). This reassessment has led to some significant adjustments. In our updated database (available in the Appendix), a total of 85 tsunamis are documented, comprising only definite, probable, or questionable events. Events labelled unlikely or erroneous have been removed. Some data have also been removed (by us) after a careful inspection of the literature sources.

The first reported tsunami in the new database occurred in Venezuela in 1498, while the first tsunami with definite tectonic origin occurred in 1530 in Cumanà, Venezuela. The database ends with the tsunami caused by the eruption of Soufriere Hills of Montserrat in 2006. Although unlikely, we cannot exclude the possibility that a significant historical tsunami may have escaped the above-mentioned catalogues during the past five centuries.

Please cite this article as: Harbitz, C.B., et al., Tsunami hazard in the Caribbean: Regional exposure derived from credible worst case scenarios. Continental Shelf Research (2012), doi:10.1016/j.csr.2012.02.006

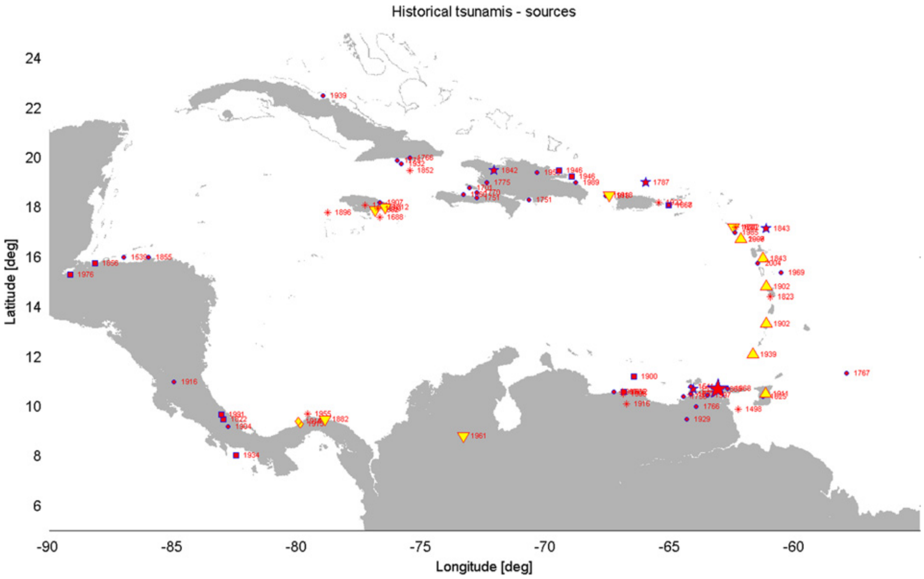

Fig. 3. Sources of tsunamis in the Caribbean. We refer to earthquake tsunamis if the tsunamigenic source is categorised in the original data as earthquake or probable earthquake. Red markers represent seismic sources (star means 8.5 > magnitude ≥ 8.0, square means 8.0 > magnitude ≥ 7.5, and circle means magnitude < 7.5), while the yellow upward triangle means volcanic sources, the yellow downward triangle means landslide sources, and yellow rhomboid means combined/unknown/other sources. (For interpretation of the reference to colour in this figure legend the reader is referred to the web version of this article.)

We find that 17 of the 85 tsunamis report fatalities and that more than 15,000 people have perished due to tsunamis since 1498, which means that the number of tsunami casualties in the Caribbean exceeds that of the U.S. West Coast, Hawaii, and Alaska combined (ten Brink et al., 2005). A total of 74% of the listed tsunamis were caused by earthquakes, 14% by volcanoes, 7% by landslides, and only 5% are of unknown origin (Fig. 3).

Both the NOAA/NGDC (2008) and the NTL (2002) databases include a mix of run-up heights and highest reported wave heights (H). It is assumed that most of these refer to the run-up heights and we have kept both these values together under maximum wave level in our database. In addition, tsunamis with intensity $I = \log_2(\sqrt{2}H)$ (Soloviev and Go, 1984) or tsunami magnitude $M_I = \log_2(H)$ (Iida et al., 1967) were referred to in the original databases, and we applied the H value derived from these expressions as maximum water level in our database. The reported tsunami heights and fatalities with respect to source types are presented in Fig. 4. The earthquake magnitude included in the original data was either unspecified or reported as the surface wave magnitude M_S or the moment magnitude M_W. We kept all original information in our database, presented the M_S or M_W values for the various events together, and favoured M_w when both values were available for the same event.

3.2. Historical seismic tsunami sources

According to O'Loughlin and Lander (2003), only two trans-oceanic tsunamis have been reported in the Caribbean Sea, the first of which resulted from the November 1, 1755 Lisbon earthquake (Baptista et al., 1998, 2003). The tsunami wave had an amplitude of up to 20 m at Lisbon and along the African and south European coasts, and of 6.4 m at the island of Saba in the Lesser Antilles (Baptista et al., 2003). A second trans-oceanic tsunami was recorded after the earthquake on the Iberian coast on March 31, 1761, causing considerable flux and reflux in Barbados, with a run up height of about 1.2 m (Lander and Whiteside, 1997; O'Loughlin and Lander, 2003).

Altogether 62 of the 85 reported Caribbean tsunamis (Fig. 4) are of regional seismic origin, and they occur in different tectonic contexts, as subduction and strike-slip events at the plate boundaries, and as intraplate events. The highest tsunami wave occurred on November 18, 1867, after a strong M_S 7.5 earthquake in the Virgin Islands. This severe tsunami travelled across all the Lesser Antilles islands. There is still disagreement about the maximum run-up heights (8.8 or 10 m in Table 1). The 1867 Virgin Island tsunami is simulated numerically by Zahibo et al. (2008) and their results are in close agreement with the observations in many islands of the Caribbean Sea except for the island of Guadeloupe where a run-up height of 18.3 m was originally reported; however, recently reduced to 10 m (NOAA/NGDC, 2008). The reduction is based on inspection of the site and investigation of historical documents by Zahibo and Pelinovsky (2001), who stated that a run-up height up to 10 m seems more realistic in Deshaies, perhaps as small as 5 m (Zahibo et al. 2003). Barkan and ten Brink (2010) also performed simulations of the 1867 Virgin Island tsunami and found that the epicentre location was along the upper part of the northern wall of the Virgin Islands basin, and not in the Virgin Islands basin, as commonly assumed.

3.3. Historical non-seismic tsunami sources

A thorough literature survey on non-seismic tsunamigenic sources in the region is presented by NGI (2009c).

3.3.1. Volcanic eruptions and flank collapses

Eruptions accompanied by collapsed lava domes, flank failures, pyroclastic flows, lahars, and debris flows can all generate tsunamis (e.g., Brown et al., 1977). The eruption on Montserrat on December 26, 1997, was followed by a pyroclastic flow that reached the ocean and caused 3 m waves and 80 m of inundation (Heinrich et al., 1998; Pararas-Carayannis, 2004). The previous 1995 eruption did not generate a tsunami, but probably weakened the Soufriere Hills' flanks and thus caused the flank failures associated with the eruptions in 1997, 1999, 2003, and 2006, which did generate tsunamis. The July 12, 2003 tsunami following a major collapse of the lava dome and a pyroclastic flow that reached the sea was reported to about 4 m on Montserrat and about 0.5–1 m on Guadeloupe (Pelinovsky et al., 2004; Poisson

Please cite this article as: Harbitz, C.B., et al., Tsunami hazard in the Caribbean: Regional exposure derived from credible worst case scenarios. Continental Shelf Research (2012), doi:10.1016/j.csr.2012.02.006

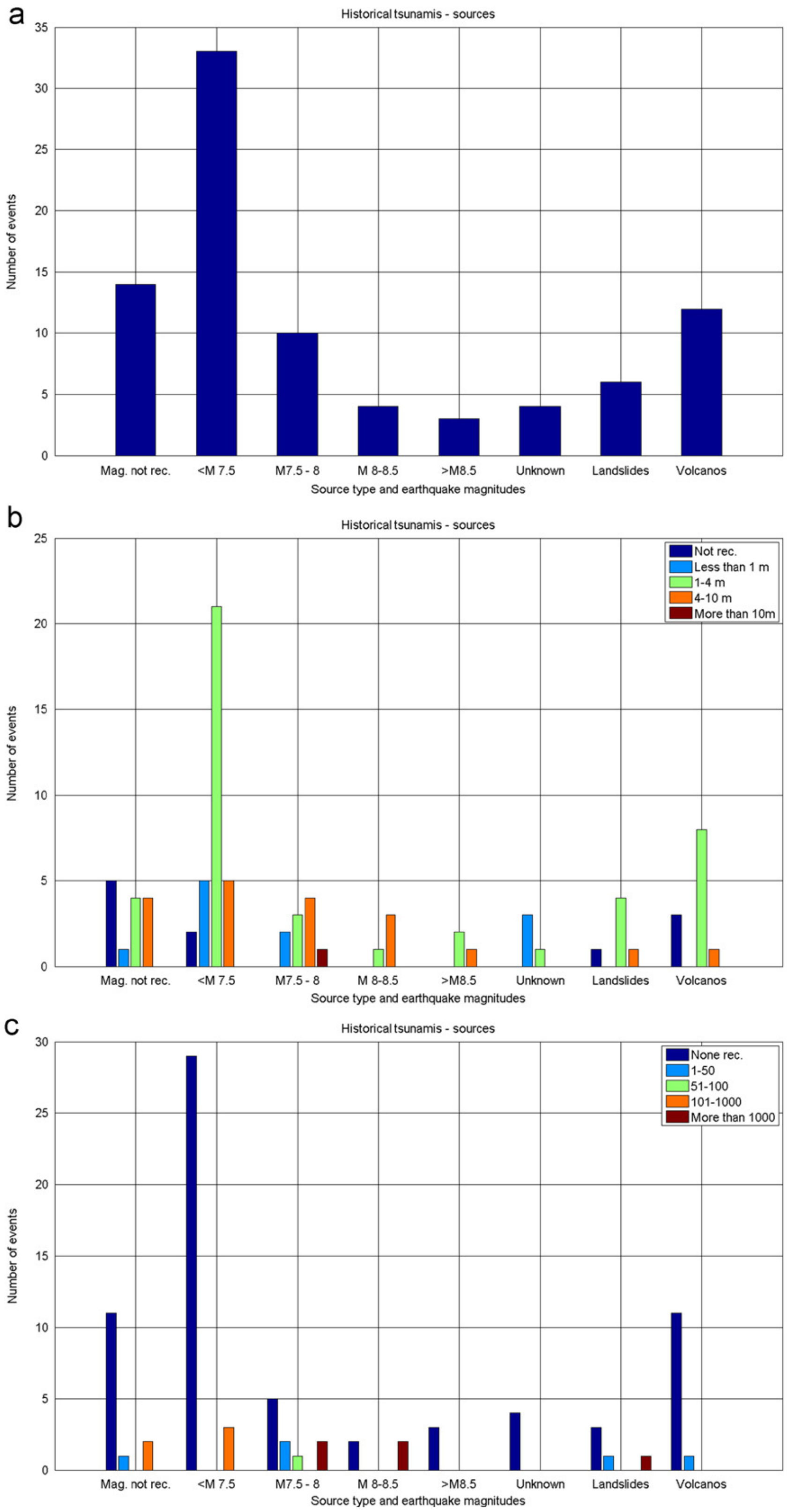

Fig. 4. Types of tsunamis in the Caribbean. (a) Number of events with regard to tsunami source type and earthquake source magnitude. M_w is most reliable magnitude estimate and therefore applied when available; (b) number of events split into ranges of maximum water levels versus tsunami source and earthquake magnitude; and (c) number of events split into ranges of number of fatalities versus tsunami source and earthquake magnitude.

and Pedreros, 2010). On May 20, 2006, another tsunami of volcanic origin reached Montserrat with a height of 1 m.

There are reports of a tsunami on Martinique in 1767, but the height of the waves and their origin are uncertain. Two important events related to the Mt Pelée, Martinique eruptions took place in 1902. On May 5 that year Mt Pelée began erupting and produced destructive lahars with speeds of about 100 km/hour. The lahars continued into the sea and generated a 4–5 m tsunami, affecting

Please cite this article as: Harbitz, C.B., et al., Tsunami hazard in the Caribbean: Regional exposure derived from credible worst case scenarios. Continental Shelf Research (2012), doi:10.1016/j.csr.2012.02.006

Table 1
Run-up data from the 1867 Virgin Islands tsunami.

Location	Latitude (°N)	Longitude (°E)	Distance to source (km)	Max water height[a] (m)	Observations[b]
St. George's, Grenada	12.01	−61.78	765	1.5	1.44 m recede
Gouyave, Grenada	12.17	−61.73	752	3	6.4 m run-up
Basse Terre, Guadeloupe	16.00	−61.72	429	1	2 m run-up
Deshaies, Guadeloupe	16.32	−61.78	404	**10**[*]	4 m recede
Sainte-Rose, Guadeloupe	16.33	61.70	411	**10**	4 m recede over 150 m distance
St. John's, Antigua	17.19	−62.42	302	2.4	2.88 minundations
Frederiksted, St. Croix	17.71	−64.88	48	7.6	**8.8** m wave height
Charlotte Amalie, St. Thomas	18.33	−64.92	32	6	7.36 m wave height

According to Zahibo et al. (2008), houses were destroyed and the sea receded 100 m at Deshaies, while the sea withdrew 100 m and damaged houses upon return as a 10 m wave at Sainte-Rose.

[*] In 2008, the NOAA/NGDC (2008) database listed 18.3 m maximum water height for Deshaies, it has been corrected since and is now (November 2011) reduced to 10 m.

[a] Maximum water heights listed by NOAA/NGDC (2008) database.

[b] Observations according to BRGM (2009) after revisiting existing archives.

the areas of St Pierre. Based on numerical simulations of the event, Poisson and Pedreros (2010) argue that the tsunami was generated by three successive lahars rather than a single instantaneous source. A second event occurred on May 8, 1902. The day before, sea disturbances of up to 1 m were reported in the harbours of Grenada, Barbados, and Saint Lucia (NOAA/NGDC, 2008). These disturbances were possibly caused by the flank failure of Mt Pelée or by pyroclastic flows reaching the sea from the eruption of the Soufrière volcano on Saint Vincent.

Kick'em Jenny's first recorded eruption occurred in 1939, causing a series of tsunami-like waves with amplitudes of about 2 m in the Grenadines and the Grenada Island. More eruptions occurred in 1943, 1953, 1965, 1966, 1972, 1977, 1988, and 1990, but with no tsunami triggering. Two more tsunami events, although with scarce information, occurred on February 17, 1843, in Antigua and on November 3, 1911, in Trinidad. Both are supposed to have a volcanic origin.

3.3.2. *Submarine landslides*

Tsunamis that are generated by submarine landslides are often associated with earthquakes (O'Loughlin and Lander, 2003), and they can cause considerable impacts even on distant shores (Masson et al., 2006; Harbitz et al., 2007). Pararas-Carayannis (2004) mentions that a fairly unknown event on May 7, 1902 cut the submarine communication cables from the island of Martinique to the outside world, and that the cable failures could have been caused by an underwater debris avalanche.

4. Tsunami modelling approach

4.1. *Seismic sources*

The earthquake rupture is generally a rapid process, and the main tsunami generation is therefore most often completed within a few minutes. Hence, the initial wave mimics the seabed elevation with a few modifications. For the purpose of tsunami modelling the co-seismic dislocations are normally converted to seabed displacements through a standard analytical formula (Okada, 1985). The input to this formula is the position, width, and length of fault, as well as dip-slip, strike-slip, focal depth, and dip angle. The seabed displacement is then transferred to the sea surface. Finally, a two-dimensional (2D) solution of the Laplace equation established by matched asymptotics is employed to smooth out sea surface discontinuities above the fault line (Pedersen, 2001). The sea surface elevation is finally applied as an initial condition for the tsunami propagation model with the water initially at rest. For further details on design of the seismic scenarios, see Løvholt et al. (in review).

4.2. *Landslide sources*

Tsunamis generated by landslides (submarine and subaerial) are caused mainly by the volume displacements of the flowing masses. In this process, the water is elevated above the front of the landslide, whereas a water depression is found above the tail of the landslide. Submarine landslides are often clearly sub-critical, i.e. the Froude number (defined as the ratio of the landslide speed to the linear hydrostatic wave speed) is much less than one. This implies that the wave will normally run away from the wave-generating landslide, limiting the build-up of the wave. However, critical effects (i.e. Froude number close to one) are often important for tsunamis generated by volcanic flank collapses or rock slides, where the sliding masses impact shallow water with high velocities.

In our modelling of the landslide scenarios (subaerial and submarine), the landslide is simplified as a flexible box with a prescribed velocity progression. The landslide box is rounded to avoid numerical noise due to sharp edges. The dimensions and configuration of the landslides are determined from the literature on previous events, from studies of the mapped deposits, and by visual reconstruction of the landslide scar topography. The impact velocity is determined by analytical energy considerations and from literature on simulations of pyroclastic flows (e.g., Heinrich et al., 1998; Le Friant et al., 2006). The submarine run-out distance is determined by the mapped deposits from previous events and by statistics of fall height to run-out distance ratios versus volumes (De Blasio et al., 2006). This returns run-out distances clearly shorter than those reported for debris flow blocks in Section 2.2, which is reasonable as such blocks most often reach longer than the full debris flow (that the block might originate from). Further, these blocks do not contribute much to the tsunami generation. In the model, the landslide follows a straight line (note that the initial phase of the landslide progression principally determines the characteristics of the generated waves, see e.g. Løvholt et al., 2005). The seabed displacement caused by the landslide is calculated and applied as input to the tsunami propagation model. From previous experience, the prescribed model for the landslide configuration and progression gives reasonable results for the tsunami propagation, in light of the overall uncertainty (landslide parameters, etc.). For further details on representation of and tsunami generation by landslides, see Harbitz (1992) and Løvholt et al. (2005).

4.3. *Tsunami propagation*

For the tsunami propagation, we apply the depth-averaged three-dimensional tsunami model (a model with two horizontal dimensions, 2HD) GloBouss (Pedersen and Løvholt, 2008; Løvholt et al., 2008, 2010). This model is based on the Boussinesq equations including higher order dispersion terms, Coriolis terms,

Please cite this article as: Harbitz, C.B., et al., Tsunami hazard in the Caribbean: Regional exposure derived from credible worst case scenarios. Continental Shelf Research (2012), doi:10.1016/j.csr.2012.02.006

and numerical hydrostatic correction terms. Boussinesq models capture both the effect of non-linearity (steepening of the wave front in shallower water) and dispersion (wavelength dependent wave speed). GloBouss further includes possibilities to utilise both Cartesian and geographical coordinates. Landslides are included through sink-source (velocity) distributions of the seabed deformations as function of time, whereas earthquake generated tsunamis are included as initial conditions for the sea surface (see above). The bathymetric data applied for this study is based on the General Bathymetric Chart of the Oceans (GEBCO, 2008) 1' grid.

4.4. Alongshore distribution of the maximum water levels

To find an estimate of the tsunami impact on land, the corresponding run-up or alternatively the shoreline water levels along all the affected coastlines must be calculated. For a regional study including hundreds of locations and hundreds to thousands of kilometres of shoreline, it is too time consuming to perform refined numerical inundation investigations for all scenarios for each of the locations. Instead a faster, but still reliable procedure to transfer the offshore tsunami surface elevation to the shoreline water levels was used, determining the amplification factors from the parameters describing the incoming wave, bathymetric slope, etc.

To find these factors, a series of simulations with different tsunami characteristics (leading depression/peak, wave period) were performed on a set of different idealised bathymetric profiles (Løvholt et al., 2011). These simulations serve as a database for the amplification factors between the offshore surface elevation and the onshore water level. Two different numerical models have been used to determine the amplification factors. Both models are of the Boussinesq type, but in this context the models are applied in a linear hydrostatic mode. Primarily, a tsunami propagation model in one horizontal dimension (1HD) for simulating waves along vertical transects is used (Vanneste et al., 2010), whereas the 2HD model GloBouss described above is used for determination of the amplification factors at smaller islands. The inclusion of a 2HD model for determining the amplification of the tsunami at smaller islands are needed due to three dimensional effects not captured along transects.

Outside each location to be investigated a ‘control point’ was put at a water depth of 50 m to measure the surface elevation (time series). The maximum surface elevation measured at the point was extracted and the shape of the leading wave (depression or peak) and the wave period were determined. By visual inspection of the bathymetry (from deep water to the shoreline), it is determined what idealised profile that matches the best way. The amplification factor for the given set of parameters is then extracted from the database. Finally, the maximum surface elevation measured at the control point is multiplied by the amplification factor to find the maximum shoreline water level. For a detailed description of this methodology, see NGI (2009c) and Løvholt et al. (2011). Effects such as refraction and focusing are of course not taken into account in a 1HD model. However, one advantage of this model is that it can apply grids of variable resolutions, allowing for finer grids in the shallowest waters. In the simulations we have designed the spatial grid to keep the Courant number (i.e. the ratio of the spatial grid increment to the temporal grid increment; Courant et al., 1967) constant. For a defined temporal resolution the spatial resolution is coarser in deeper water, enabling fewer grid cells and less CPU time spent. This is an advantage for tsunami modelling since higher resolution is needed in shallower areas to resolve the waves (waves become shorter) and since the presence of numerical dispersion is minimised due to a constant Courant number. Grid refinement tests were performed to ensure convergence for each run. For the 1HD simulations the Courant number was set to 0.5 with a temporal increment of 2.5 s, giving a spatial resolution from 34 m close to the shoreline up to 500 m in the deepest part. In the 2HD simulations around smaller islands the uniform spatial resolution was 500 m.

Although the models do not include the inundation on dry land, the surface elevation on the boundary close to the shoreline (at 0.5 m water depth) with a no-flux condition yields a good approximation. The results from the depth averaged models are validated by a subset of corresponding simulations performed with 1HD and 2HD non-linear inundation models including shock waves and wave breaking (Løvholt et al., 2011; NGI, 2009c).

The results show that the 1HD tsunami model applied in the present study estimates the shoreline water level mainly with a deviation of less than 20–30% from the non-linear model. However, larger deviation may occur for very long and gentle slopes due to omission of wave breaking. For a M_W 8 earthquake scenario (Lesser Antilles scenario as explained in Section 5.1) east of Guadeloupe, the regional approach based on the amplification factors gave a maximum shoreline water level of 2.6 m at Bridgetown, while a corresponding study with a 2HD model gave a run-up height of 2.9 m (NGI, 2009a; Løvholt et al., 2011). Naturally, we expect that the regional methodology do not capture local variations. However, for the purpose of a regional study, the approach gives reasonable results on the overall scale.

5. Tsunamigenic source scenarios

The scenario selection is principally based on a comprehensive analysis of the updated database on both seismic and non-seismic Caribbean tsunami events (above), a literature survey on non-seismic tsunamigenic sources in the region (NGI, 2009c), the study of the large scale tectonics of the region by NORSAR (NGI, 2009b), geological and topographical evaluations, information from R. Robertson, SRC (pers. comm., 2007–2008), and the volcanic hazard atlas of the Lesser Antilles (Lindsay et al., 2005). It should be noted that all areas have not been similarly well surveyed, nor have the survey data been available in order to evaluate the potential for tsunamigenic sources to the same extent all over the region. This is especially relevant for potential submarine landslides along the margins of the Caribbean Sea (Teeuw et al., 2009).

In addition to sensible choices based on all the sources of information listed above, the tsunami scenarios for this study should also represent various types of sources, provide a regional distribution to exemplify a regional exposure assessment, provide relevant examples for all partners in the project, avoid reproduction of previous studies, and be relevant as input for the Bridgetown tsunami disaster mitigation demonstration project (NGI, 2009a). The tsunami surface elevations shortly after the initiation of the five selected Caribbean scenarios are shown in Fig. 5, and an example of a trans-oceanic tsunami scenario is presented in Section 5.3.

5.1. Seismic scenarios

The Northern coastlines of Hispaniola and Puerto Rico were hit by 5–6 m tsunamis in 1918 and 1946 and we chose the subduction earthquake located on the strait between the two islands as a source scenario (hereafter called the Hispaniola scenario).[1] The northeast Lesser Antilles were hit in 1843 by the largest reported

---

[1] It should be noted that López-Venegas et al. (2008) identified a submarine landslide off the northwestern coast of Puerto Rico, and postulate that this landslide, which was likely triggered by the 1918 earthquake, was the primary cause of the October 11, 1918, tsunami.

Please cite this article as: Harbitz, C.B., et al., Tsunami hazard in the Caribbean: Regional exposure derived from credible worst case scenarios. Continental Shelf Research (2012), doi:10.1016/j.csr.2012.02.006

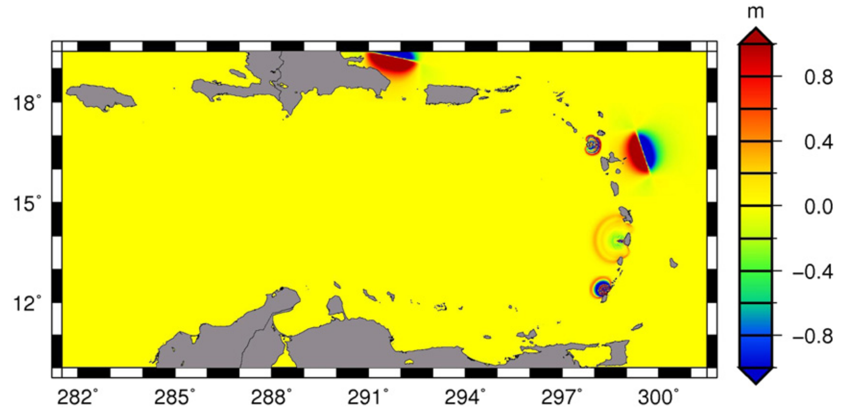

Fig. 5. The tsunami surface elevations shortly after the initiation of the five Caribbean scenarios evaluated: two earthquake sources (Hispaniola and Lesser Antilles scenarios) and three landslide sources (Montserrat, Saint Lucia, and Kick'em Jenny).

historical earthquake of the Lesser Antilles subduction arc (hereafter called the Lesser Antilles scenario). It produced seismic intensity IX on a segment about 100 km long between Antigua and Guadeloupe and generated a small tsunami.

An M_W 8 scenario represents a credible worst case earthquake scenario based on the 500 year history of earthquakes and tsunamis in the Caribbean region (NGI, 2009b, 2009c). Parsons and Geist (2009) state that the completeness threshold varies with time, and is likely about M_W 7 before the 20th century. Parsons and Geist (2009) further estimate a total tectonic moment for a 505-year period corresponding to M_W 9.18 and report an expressed seismic moment sum from the earthquake catalogue corresponding to M_W 8.85. This implies that the coupling coefficient (i.e. the ratio of expressed seismic to expected tectonic moment release) around the Caribbean plate is low, or that there is a large temporal seismic gap waiting to be expressed. Both the Lesser Antilles and the Hispaniola scenarios are built up by three fault segments, with a tapering of the co-seismic slip at the end-segments. The scenarios are close to identical except for location and orientation. The fault models are about 180 km long with slips of 6 m for the central segment and 3 m (mid value) for the end segments (seismic source geometries are listed in Table 2). The rigidity is set to 30 MPa (Bilek and Lay, 1999). Length, width, and slip are parameterised based on the empirical expressions by Wells and Coppersmith (1994).

Table 2
Parameter values for the earthquake scenarios.

Location	Segment	Dip-slip [m]		[km]		M_w
		Start	End	Length	Width	
Hispaniola	1	0	6	61	55	
	2	6	6	65	55	
	3	6	0	65	55	
	SUM			191		8.0
Lesser Antilles	1	0	6	59	55	
	2	6	6	58	55	
	3	6	0	58	55	
	SUM			173		8.0

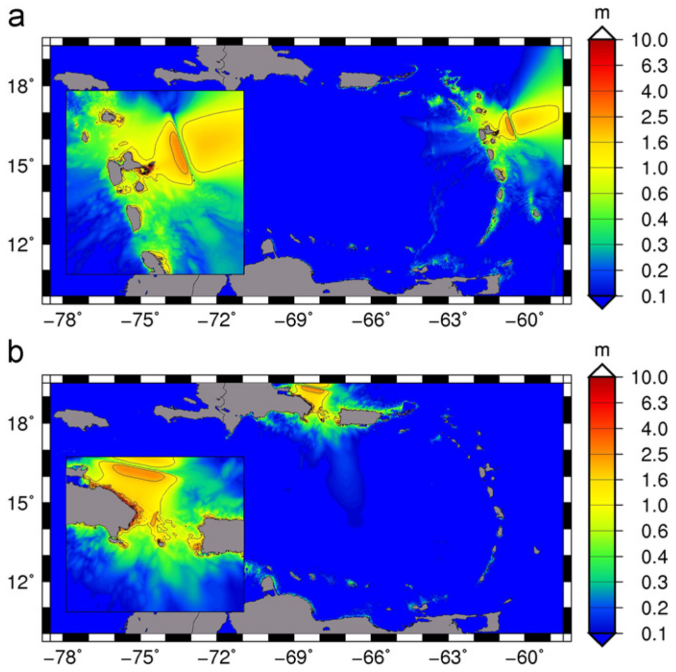

Fig. 6. (*a*) Maximum surface elevations for the Lesser Antilles earthquake scenario and (b) maximum surface elevations for the Hispaniola earthquake scenario. A zoom of the source area is shown in the frame to the left in each panel.

5.1.1. *Lesser Antilles scenario*

The source model in this case is based on the January 30, 1982, M_W 6 thrust event and its Harvard CMT solution. The fault plane chosen for the tsunami modelling has a strike of 340° and a dip of 80°. Its conjugate fault plane (strike of 166° and dip of 11°) might be more compatible with the regional tectonics, but it would have generated a smaller seabed elevation (Løvholt et al., in press). However, the purpose of this simulation is to estimate the credible worst scenario. This fault model scenario is also steeper than the average dip angle of the Wadati–Benioff plane and may therefore generate shorter waves favouring stronger amplification due to shoaling. The maximum tsunami surface elevation calculated in each computational cell during the total computational time is shown in Fig. 6. The values in shallow/near shore areas may be underestimated; the corresponding maximum shore line water levels landward from the control points are shown in Fig. 7.

The estimated maximum surface elevations and maximum shoreline water levels show that the Lesser Antilles scenario affects mostly the eastern part of the Lesser Antilles arc. The highest waves are found in an area directed east-west. The sea surface elevation around the generation area is 1–4 m, while the islands south and north of the most affected ones have sea surface elevations off the shore above 0.5 m. There is some effect of the tsunami (~0.5 m) found also in the southern part of Puerto Rico

Please cite this article as: Harbitz, C.B., et al., Tsunami hazard in the Caribbean: Regional exposure derived from credible worst case scenarios. Continental Shelf Research (2012), doi:10.1016/j.csr.2012.02.006

and along the north-western coast of Venezuela. The rest of the Caribbean Sea is only slightly affected. The area west of the Lesser Antilles arc is protected by the islands closest to the source area. This scenario is applied further in a local and more detailed tsunami vulnerability and risk analysis for Bridgetown, Barbados (NGI, 2009a).

5.1.2. Hispaniola Antilles scenario

The source model here is based on the June 24, 1984, M_W 6.7 thrust event and its Harvard CMT solution. The fault plane chosen for the tsunami modelling has a strike of 100° and a dip of 80°. Again, the conjugate fault plane which is much shallower dipping is more compatible with the regional tectonics, but the worst scenario was preferred for the tsunami modelling. The maximum tsunami surface elevation calculated in each computational cell during the total computational time is shown in Fig. 6. The tsunami from the Hispaniola scenario is directed more north-south, and especially impacts the north-eastern part of Hispaniola and parts of Puerto Rico. The values in shallow/near shore areas may be underestimated, but the corresponding maximum shore line water levels landward from the control points are shown in Fig. 7. The offshore surface elevations are up to 10 m locally. The Hispaniola and Puerto Rico islands serve as a shield protecting the rest of the Caribbean Sea. An exception occurs where the waves entering between Hispaniola and Puerto Rico hit the coast of the northern part of Venezuela and Colombia. However, due to diffraction and radial spread the offshore surface elevation there is below 0.5 m.

5.2. Non-seismic scenarios

Two subaerial/submarine volcano debris flow scenarios and one submarine landslide scenario are selected to demonstrate non-seismic sources. The model parameters for all three scenarios are found in Table 3 with the dimensions of the simplified rounded box landslide, the submarine run-out distance, as well as the impact velocity, V_{max}.

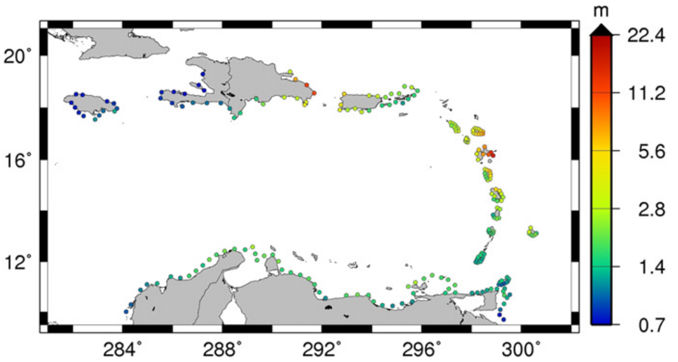

Fig. 7. Location of the points where the maximum shoreline water level is calculated with the described procedure. The colours in each point reflects the compilation of the highest estimated maximum water level given in metres for the two potential earthquake tsunami scenarios north of Hispaniola and east of Guadeloupe (Lesser Antilles scenario). (For interpretation of the reference to colour in this figure legend the reader is referred to the web version of this article.)

5.2.1. Montserrat scenario

The eruptive Soufrière Hills volcano on Montserrat has generated several small tsunamis in the recent past (1997, 1999, 2003, and 2006). We simulate a 1.7×10^8 m^3 landslide scenario mimicking a flank collapse in the English's Crater on the eastern side of the cone, and this volume corresponds approximately to the 4000 BP event. Le Friant et al. (2004) argue that the corresponding deposits were formed by one event. The simulated scenario can therefore be considered a subaerial/submarine worst case for the Soufrière Hills volcano. For comparison, the 1997 event had a volume of 2.5×10^7 m^3, while the 2003 event had a larger volume (2×10^8 m^3), but reached the sea as a series of smaller landslides with limited velocities.

The Montserrat scenario is clearly the most local of the five scenarios evaluated in this study (Figs. 8 and 9). The maximum

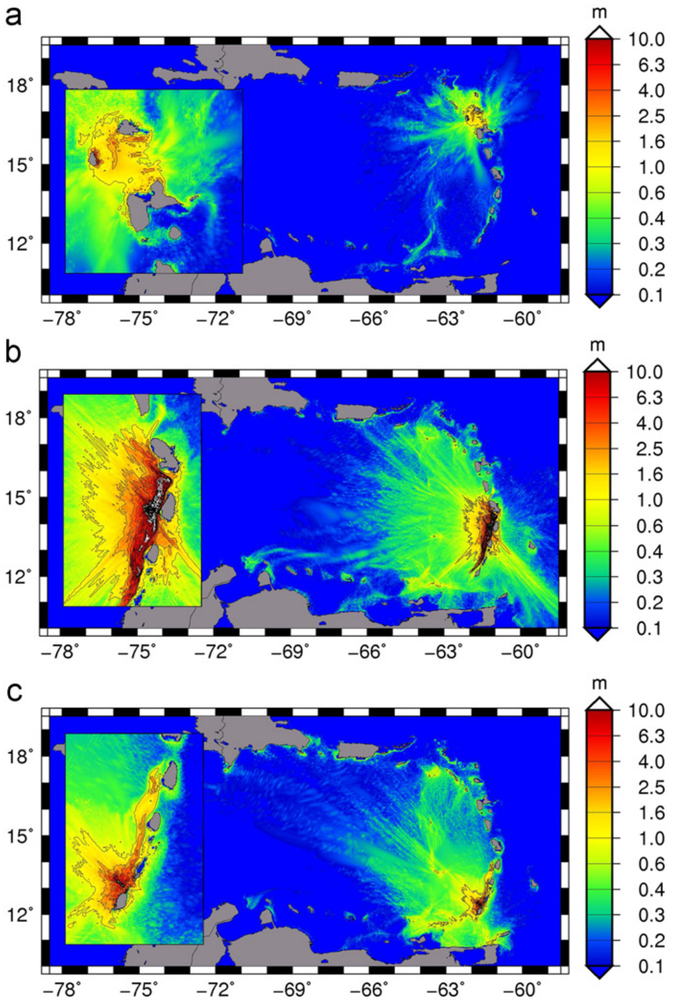

Fig. 8. Maximum surface elevations for the three landslide scenarios. (a) Flank collapse on Montserrat volcano; (b) dome collapse on Saint Lucia volcano; and (c) submarine landslide on Kick'em Jenny volcano. A zoom of the source area is shown in the frame to the left in each panel.

Table 3
Parameter values for the landslide scenarios.

Landslide	*Subaerial landslide*	*Submarine landslide*	*Width [km]*	*Height [km]*	*Length [km]*	*Submarine run-out [km]*	*Volume [km^3]**	*V_{max} [m/s]*
Montserrat	X	–	0.8	0.1	1.6	5.4	0.17	30
Kick'em Jenny	–	X	0.8	0.1	5.6	10	0.6	45
Saint Lucia	X	–	0.8	0.2	1.2	18	0.25	40

* The volume of the landslide is larger than the product of width, height, and length owing to the rounding of the slide box.

Please cite this article as: Harbitz, C.B., et al., Tsunami hazard in the Caribbean: Regional exposure derived from credible worst case scenarios. Continental Shelf Research (2012), doi:10.1016/j.csr.2012.02.006

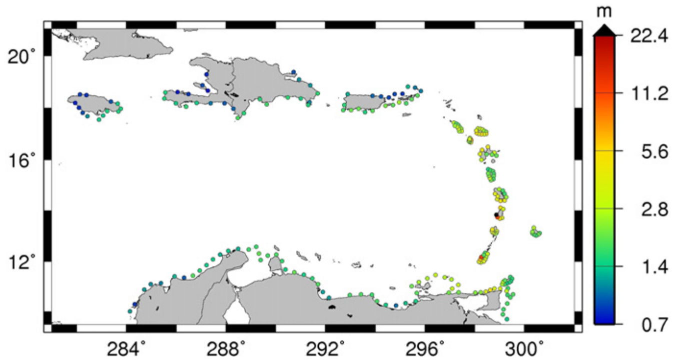

Fig. 9. A compilation of the highest estimated maximum water level given in metres for the three landslide scenarios (Montserrat, Saint Lucia, and Kick'em Jenny).

offshore surface elevation is 2.5 m, but it has minor effects on the islands south of Guadeloupe and west of the Lesser Antilles arc. In contrast to the earthquake scenarios where the maximum waves have a clear directional propagation, the landslide scenarios act more or less as point sources with no pronounced directivity. The results agree reasonably well with simulations by Heinrich et al. (1998, 1999), when taking their smaller volume of 40×10^6 m^3 (as for the 26 December 1997 event) and larger impact velocity of 40 m/s into account.

5.2.2. *Saint Lucia scenario*

According to Lindsay et al. (2005), a possible scenario for a magmatic eruption is a dome-forming eruption from within the Qualibou Caldera on Saint Lucia (this is not the least-likely worst case large explosive magmatic eruption scenario). Such an eruption would be similar to the ongoing eruption of the Soufrière Hills volcano in Montserrat and may generate, among others, dome-collapse pyroclastic flows. Lack of age data makes it impossible to develop an eruption frequency. However, the major activity seems to have been concentrated 35,000–20,000 years BP. It should be kept in mind that pyroclastic deposits are easily eroded, and it is possible that more eruptions have occurred over the last 20,000 years and that their products have not been preserved.

We consider a subaerial/submarine landslide from the Soufrière volcanic centre cone in Saint Lucia. Due to the combination of large volume, higher velocity, and longer run-out, the Saint Lucia scenario has a significantly greater impact in large areas than the Montserrat scenario (Figs. 8 and 9). Locally, the offshore surface elevations are above 10 m, and the surface elevation on the west side of the islands from the Virgin Islands down to Dominica is between 0.5 and 1 m. From Dominica down to Grenada, the elevation is between 3 and 10 m. Waves leak between Saint Lucia and Saint Vincent and the Grenadines, forming a south-easterly directed pattern south of Barbados. The surface elevation outside Bridgetown, Barbados is about 0.6 m.

5.2.3. *Kick'em Jenny scenario*

Kick'em Jenny 8 km north of Grenada is the most active volcanic centre in the Lesser Antilles arc. Based on the bathymetry and the information cited above, the tsunami generated by a 0.6 km^3 submarine landslide running westward on the flanks of the submerged volcano cone is simulated. The simulated waves are slightly lower than the Saint Lucia scenario (Figs. 8 and 9). The main part of the waves is kept on the western side of the Lesser Antilles arc. Some parts of the waves have a direction towards Puerto Rico and Hispaniola, leading to offshore surface elevations there between 0.5 and 1 m.

5.3. *Extreme trans-oceanic scenario*

Possible trans-oceanic tsunamis threatening the Caribbean Islands may be generated by strong earthquakes from distant seismic zones, or alternatively, by large submarine or subaerial landslides. One example of a strong earthquake is the 1755 Lisbon earthquake (Baptista et al., 1998, 2003; Gutscher et al., 2006; Horsburgh et al., 2008, Roger et al., 2010; Barkan et al., 2009), which generated a tsunami that killed more than 30,000 people in Portugal. The tsunami probably also maintained large amplitudes across the Atlantic Ocean. Potential non-seismic trans-oceanic sources may for instance include submarine landslides off the continental margin of western Africa, or subaerial and submarine landslides originating from the Canary and Cape Verde Islands (less likely from the Azores Islands). One of the most extreme scenarios would be a collapse of the La Cumbre Vieja volcano on the island of La Palma, releasing a volume of 375 km^3 simultaneously. The threat of such a scenario has been addressed by Ward and Day (2001), Mader (2001), Pararas-Carayannis (2002), Gisler et al. (2006a), and Løvholt et al. (2008). In Løvholt et al. (2008), near shore surface elevations of 5–15 m are found from Northern Brazil north to New York City, in addition to the enormous local waves generated along the coastlines of the Canary Islands and more nearby locations. Even larger waves are found by Ward and Day (2001), whereas Mader (2001) predicts clearly smaller waves.

5.4. *Scenario return periods*

A scenario is by definition not associated with an occurrence probability, since the only requirement is that it should only be within the realm of the possible. Even so, to be useful in a hazard and risk context, the applied scenarios should still be presented with some indication of likelihood. To this end, an attempt to roughly estimate possible return periods is presented below.

5.4.1. *Seismic sources*

Løvholt et al. (2006) found that for South America, Japan, and Sunda Arc combined, 34% of the shallow earthquakes with $M \geq 7$ were reported to have generated a tsunami, with 71% for $M \geq 7.5$ and 84% for $M \geq 8.0$. For reference, the probability that a shallow $M \geq 7$ earthquake occurs in the Puerto Rico region is 0.61 per decade (Panagiotopoulos, 1995).

The historical seismic database in the Caribbean is too short to estimate the earthquake potentials with confidence and the geologic framework is also quite complicated, but the largest credible earthquake for the entire region is estimated to be around $M8$ and with a return period of around 500 years, which corresponds to the duration of the historical records. A more detailed discussion on the return period of the tsunamigenic earthquakes is given by Parsons and Geist (2009), who complemented the earthquake and tsunami records with computations of the seismic moment balance, finding slip rates typically ranging from 5 to 15 m over 500 years in the Lesser Antilles, whereas slip rates of 1–3 m over 500 years were found from the historical records. By assuming a locked fault and a slip of 6 m, the seismic moment balance corresponds to lower bound return periods of about 200–500 years for the earthquake scenarios. Grilli et al. (2010) state that a $M_w9.1$ source corresponds to a 600 years or so return period, while a $M_w8.7$ source corresponds to a 200 years or so return period. Zahibo et al. (2008) suggest $M8$ earthquake return periods of about 200 years. It should be noted

Please cite this article as: Harbitz, C.B., et al., Tsunami hazard in the Caribbean: Regional exposure derived from credible worst case scenarios. Continental Shelf Research (2012), doi:10.1016/j.csr.2012.02.006

that the individual tsunami scenario return periods are generally longer than the lower bound earthquake return periods, partly because an individual earthquake scenario has a longer return period than the return period for the corresponding earthquake magnitudes in question within the study region, and partly because only some of the earthquakes will be tsunamigenic.

5.4.2. *Non-seismic sources*

Ten Brink et al. (2006a) calculated the return periods of submarine landslide in the Puerto Rico trench by considering the number of large failures. For the Loiza amphitheatre the average recurrence rate is about 250–825 ka and it is about 130–470 ka for the Arecibo amphitheatre. The combined landslide tsunami recurrence rate for the north coast of Puerto Rico from the entire carbonate platform is about 70–250 ka. In comparison, Kick'em Jenny has erupted at about 5 year intervals since 1939. ten Brink et al. (2006b) established a power-law volume frequency distribution for submarine slope failures north of Puerto Rico.

Deplus et al. (2001) state that the age of the large-scale debris flows mapped offshore of the Lesser Antilles Arc is younger than 100–200 ka. Boudon et al. (2007) identified 15 flank collapses within the last 12 ka in the Lesser Antilles Arc (there may have been several collapses from the same volcano, and not all flows enter the sea even though the Caribbean Islands are small). The Lesser Antilles include 21 live volcanoes that could erupt in the future (Lindsay et al., 2005). From this information, a rough estimate gives a collapse return period of 20,000 years for each volcano (~20 sources causing ~10 collapses during ~10,000 years). Boudon et al. (2007) further state that in the northern part of the arc, flank collapses are smaller (~1 km^3), repetitive, and occur in all directions. In contrast, larger (up to tens of km^3) and infrequent sector collapses all directed to the west are typical in the southern part.

A rough estimate based on the age determination data from deposits of Holocene tsunami events in the wider Caribbean by Scheffers and Kelletat (2006) gives a return period of 1000–3000 years. However, their data may originate from the same tsunami event being detected in several places, i.e. high energy tsunami sources have return periods longer than 3000 years. On the other hand, small deposits suffer erosion and may disappear. Scheffers and Kelletat (2006) say further that "risk analyses [...] based solely upon historical sources underestimate the real tsunami risk by a factor of five to ten and the so far neglected coasts facing the open Atlantic Ocean are particularly endangered."

In summary, the individual return period of the smaller non-seismic events in the northern part of the arc can be estimated to be more than 1000 years, while the individual return period of larger events in the southern part of the arc is more on the order of 10,000 years. It should also be mentioned that Zahibo and Pelinovsky (2001) estimate the return period for all kinds of tsunamis (seismic and non-seismic tsunamis) in the Lesser Antilles exceeding 2–3 m to be 100 years.

5.4.3. *Extreme trans-oceanic sources*

In the latest 1 Ma or so, the Canary Islands have produced one large landslide approximately every 100 ka, with typical volumes of 50–200 km^3 (Masson et al., 2006). However, these landslides are believed to develop retrogressively (Wynn and Masson, 2003), and thus being less effective in generating a tsunami than a single volume. As pointed out by Wynn and Masson (2003), the separation time between each landslide volume is expected to be so large that a visible contrast in the turbidite deposit may be identified for each retrogressive element comprising the total volume. The effective tsunamigenic volume is therefore likely to be significantly smaller than the total volume.

A simultaneous release of a landslide may, however, not be completely ruled out, both because the retrogressive effects are not quantified, and also because a future landslide does not necessarily follow the nature of previous landslides. For a simultaneously and extreme released volume of 375 km^3 we expect that the annual probability is clearly smaller than the 10^{-5} obtained from the recurrence rate of all the past landslide events within the Canaries, taking into account that a gradual release of the slide is more likely. An expert judgment may crudely suggest an annual probability of at least one order of magnitude less, i.e. roughly $< 10^{-6}$. Still, it may obviously be disputed whether it is at all possible to quantify this return period. It is also noted that the risk of the extreme event may exceed the more likely ones as the consequence may increase faster than the probability decays. This extreme event should therefore be studied. However, in the future it is important to include a study of a smaller and more realistic volume and investigate its far-field impact. The low probability combined with longer arrival times and thereby longer warning times and reduced risk for trans-oceanic tsunamis, substantiates why this scenario is not pursued further in this study.

5.5. *Tsunami simulations and results*

5.5.1. *Seismic and non-seismic Caribbean scenarios*

The maximum tsunami surface elevation calculated in each computational cell is shown in Figs. 6 and 8 for all five scenarios. The maximum surface elevation should not, however, be used to determine the impact on land (i.e. how high the waves are near the shore or during inundation) since the near shore amplification is not captured in the simulations. The waves typically amplify several times on their way towards the shoreline, and these effects are taken into account in the estimations of the maximum shoreline water levels in Figs. 7 and 9. In the simulations, the uniform spatial resolution was 1' (about 1.85 km).

The highest waves for the earthquake scenarios are of course found closest to the sources, with values up to about 20 m (Hispaniola/Puerto Rico and east part of Guadeloupe and the surrounding islands). The waves for the landslide scenarios along the islands in the eastern part of the Caribbean Sea are mainly in the range of 1–5 m. Close to the landslide areas, the maximum shoreline water levels can be several times higher. The predicted arrival times for the two furthest north and south scenarios (i.e. Hispaniola and Kick'em Jenny) are depicted in Fig. 10. The tsunami arrival time is generally short for the Caribbean Islands; typically one should prepare for less than one hour.

5.5.2. *Extreme trans-oceanic scenario*

For this study, we combined results of the numerical simulations by Gisler et al. (2006a) for the wave propagation in the central Atlantic Ocean and Løvholt et al. (2008) for a local simulation of the tsunami propagation near the Lesser Antilles. The overall trends rather than detailed results are investigated.

Gisler et al. (2006a) used the numerical model SAGE (Gittings et al. 2008) to simulate the simultaneous landslide and water wave motion. The landslide motion was close to critical with a maximum landslide speed up to approximately 150 m/s, effectively generating a large tsunami. The far-field propagation was simulated using the Globouss model. For the trans-atlantic propagation in Løvholt et al. (2008), a grid resolution of 2′ was used. In our local simulations near the Lesser Antilles, the results from the Atlantic propagation are extracted and used as initial conditions in a smaller domain covering the Lesser Antilles. In our computations, different grid resolutions of 2′, 1′, and 0.5′ are used

Please cite this article as: Harbitz, C.B., et al., Tsunami hazard in the Caribbean: Regional exposure derived from credible worst case scenarios. Continental Shelf Research (2012), doi:10.1016/j.csr.2012.02.006

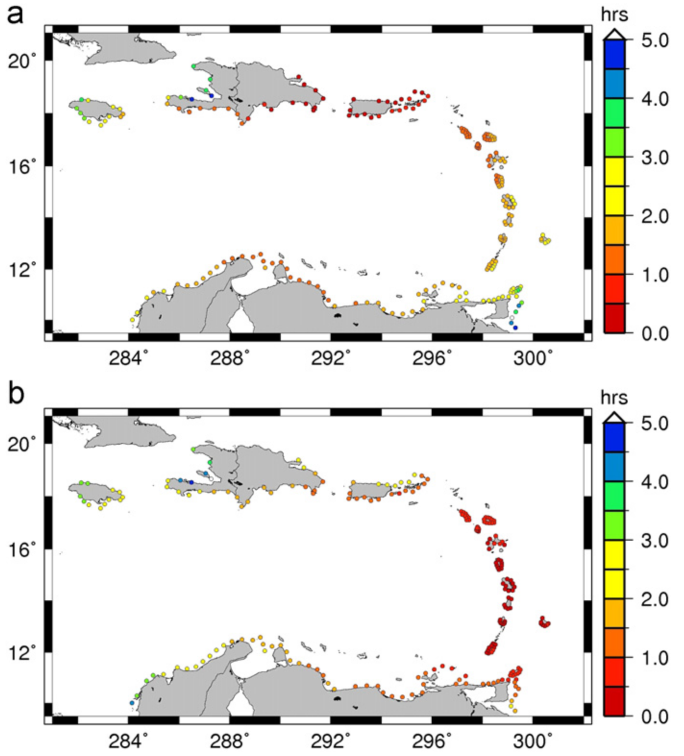

Fig. 10. Arrival times (hours) for two selected scenarios: the Hispaniola earthquake (a) and the Kick'em Jenny submarine landslide (b).

(the two latter are interpolated from the 2′ grid using bi-linear interpolation). Along the Northern, Western, and Southern boundaries, an absorbing layer of width 0.4° is used, whereas the Eastern boundary is reflective.

Snapshots of the simulated extreme wave as it approaches and impacts the Caribbean Islands are shown in Fig. 11. A sequence of large incident waves is observed. The increased wave heights, especially towards Trinidad and Tobago, result as a combination of refraction and source directivity. The maximum run-up heights are expected to clearly exceed the maximum offshore surface elevations of 5–10 m typically found in the locations displayed in Fig. 11 (at depths of 500 m or more) as a result of amplification due to shoaling. Effects of edge waves, interference of reflecting waves, etc., may also enhance the maximum water levels. Fig. 11 further reveals that the wavelengths in question are generally longer than the typical extensions of the islands, which together with the steep shelves prevents significant amplification due to shoaling. In addition, it is expected that possible wave breaking and friction will to some extent counteract the amplification. Fig. 11 also shows how the Lesser Antilles provide a screening for the westerly located islands and coastlines.

The solution converged for the first few wave cycles for most of the locations in Fig. 11 (NGI, 2009c). An exception was the Barbados west location (site C). In time series from other locations not displayed here, there is generally a tendency that the time series affected by island reflection, etc., tend to give results that deviate more. However, the eastward time series are less influenced by such effects, and better accuracy is therefore found in these locations (site A, B, D, E, and F).

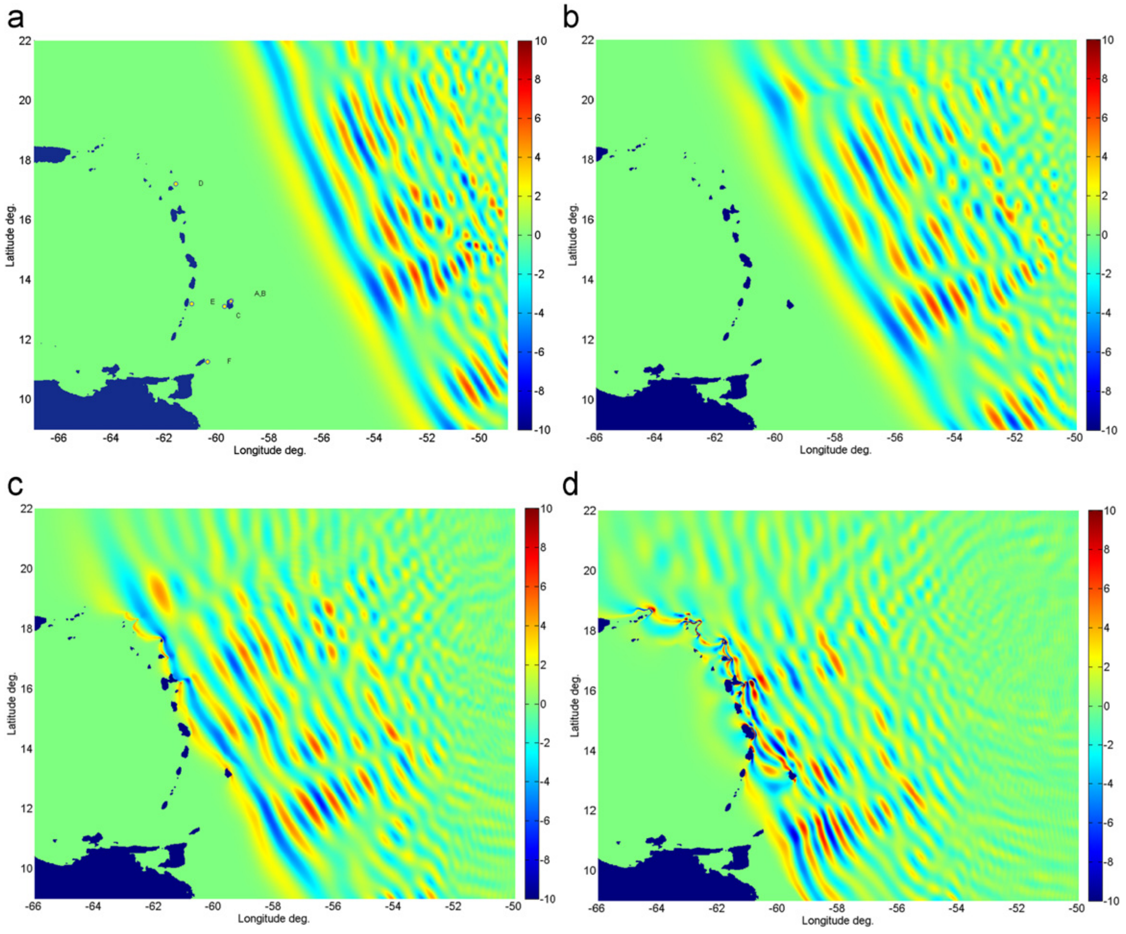

Fig. 11. Extreme trans-oceanic tsunami scenario. Snapshots of the simulated surface elevation at 5 h 15 min (a); 5 h 45 min (b); 6 h 15 min (c); and 6 h 45 min (d).

Please cite this article as: Harbitz, C.B., et al., Tsunami hazard in the Caribbean: Regional exposure derived from credible worst case scenarios. Continental Shelf Research (2012), doi:10.1016/j.csr.2012.02.006

6. Regional exposure assessment

One of the main goals for a study of this kind is clearly to estimate the number of people exposed to the tsunamis triggered by landslides and earthquakes in the region, and to this end we have employed a GIS analysis. The maximum water level raster along the shoreline has been interpolated from the shoreline water level points using the Inverse Distance Weighted (IDW) method, and the inundated area is obtained by subtracting a digital elevation model with 3 arc s resolution from the shoreline maximum water level raster (NGI, 2009c). Hence, the inundated area first covered all the topography below the maximum shoreline water level. However, it turned out that for some gentle and low-lying near shore locations, the inundation distance could be unreasonably long. A simple formula was therefore used to limit the maximum inundation distance

$$I_{\max} = \sqrt{g\eta}\,T/4$$

where η is the maximum shoreline waver level, g the acceleration of gravity, and T the wave period set to 600 s (the wave period for the combination of slide- and earthquake-generated waves varies from 400 to 1000 s with a mean value of about 600 s). The formula assumes that the wave travels inland with a propagation speed of $(g\eta)^{1/2}$ for a quarter of a predefined wave period (i.e. during the time the tsunami is still rising at the shore line), and therefore gives a rough upper bound of the inundation length. The expression is obviously inaccurate (the wave can travel faster inland than $(g\eta)^{1/2}$ from the beginning of the inundation, the flow depth decreases and causes lower velocities further inland, the wave can travel inwards for a longer time than $T/4$, obstructions influence the travel distance, etc.), but we still believe that it is a good first order approximation of inundation distance for a regional study.

The Shuttle Radar Topography Mission (SRTM) elevation data used here is the most complete high-resolution digital topographic database available to us (Rabus et al. 2003). The population dataset is taken from the Global Rural–Urban Mapping Project (GRUMP) which consists of estimates of human population for the years 2007 (Center for International Earth Science Information Network (CIESIN), 2007) and has a spatial resolution of 30 arc seconds. The exposed population is defined as the number of people in the inundated areas. The exposed population per km shoreline is created by manually defining line segments along the coast with approximately similar population density per unit area. The statistics from these areas are then projected into the shoreline for the same area.

During the last century, a relative sea level rise of about 20 cm has been observed in the Caribbean and the rate is increasing. Relative sea level was estimated to rise on average 2.8–5.0 mm/year during the 1990s. Regional projections state a rise in sea level of 10–50 cm by 2025 as realistic (Maul, 1993; Parry et al., 2007). Moreover, the global sea level rise within year 2100 is estimated to be in the range from 20 to 50 cm (Bindoff et al., 2007). Inside the Caribbean region the high tide is about 50–90 cm above mean lower low water (NOAA, 2008). The topography is measured relative to Mean Sea Level (MSL). A high tide may roughly be set to 25–45 cm above MSL. A combined effect of sea level rise and high tide is taken into account in our investigations by adding 0.7 m to the estimated maximum shoreline water levels. The probability of two independent extreme events, namely a design tsunami and an extreme high tide, happening at the same time is so low that it contributes very little to the total hazard.

Figs. 2 and 12 show the number of people exposed to landslide or earthquake induced tsunamis in the Caribbean region. The results for the two groups of tsunamigenic sources are kept separate owing to different estimated probabilities. The different colour scales in the figures should be noted. The total number of exposed people for each country is presented in Fig. 13 for the seismic sources and in Fig. 14 for the landslides sources. The exposure is presented both as the total number of exposed people and as a percentage of the total number of inhabitants in each country. The tsunami exposure with and without the effect of possible sea level rise and high tide is also compared. The strongest effect of higher sea level is found for Puerto Rico (total exposure), Antigua and Barbuda and Anguilla (relative exposure) both for the earthquake and landslide scenarios, and for Venezuela (total exposure) and Saint Lucia (relative exposure)

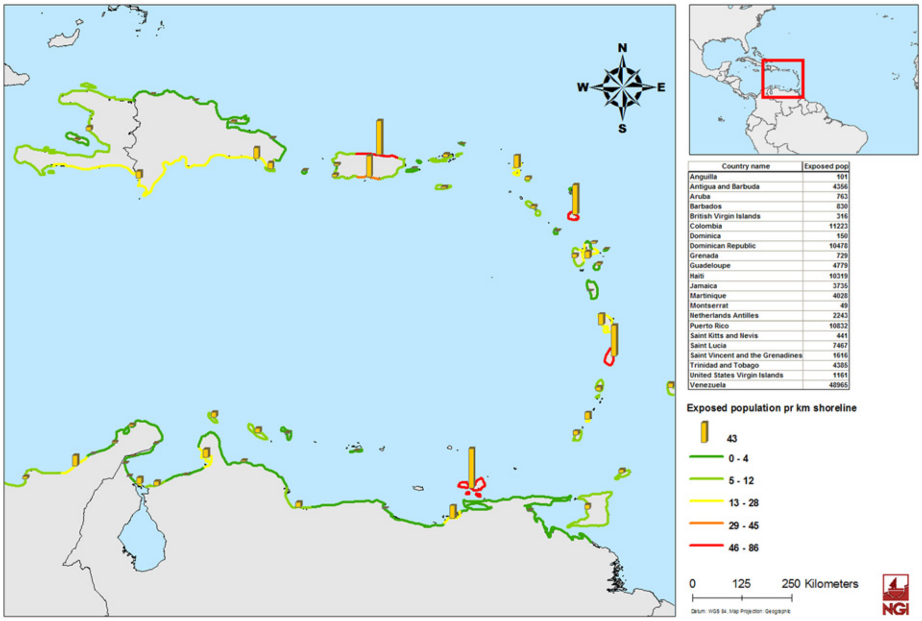

Country name	Exposed pop
Anguilla	101
Antigua and Barbuda	4356
Aruba	763
Barbados	830
British Virgin Islands	316
Colombia	11223
Dominica	150
Dominican Republic	10478
Grenada	729
Guadeloupe	4779
Haiti	10319
Jamaica	3735
Martinique	4028
Montserrat	49
Netherlands Antilles	2243
Puerto Rico	10832
Saint Kitts and Nevis	441
Saint Lucia	7467
Saint Vincent and the Grenadines	1616
Trinidad and Tobago	4385
United States Virgin Islands	1161
Venezuela	48965

Fig. 12. Number of people exposed to landslide induced tsunami per km shoreline. The effect of high tide and sea level rise is taken into account. Estimated individual return period is more than 1000 years for smaller events in the north and about 10,000 years for larger events in the southern part of the arc. *Note*: different scales of bars and colours compared to Fig. 2.

Please cite this article as: Harbitz, C.B., et al., Tsunami hazard in the Caribbean: Regional exposure derived from credible worst case scenarios. Continental Shelf Research (2012), doi:10.1016/j.csr.2012.02.006

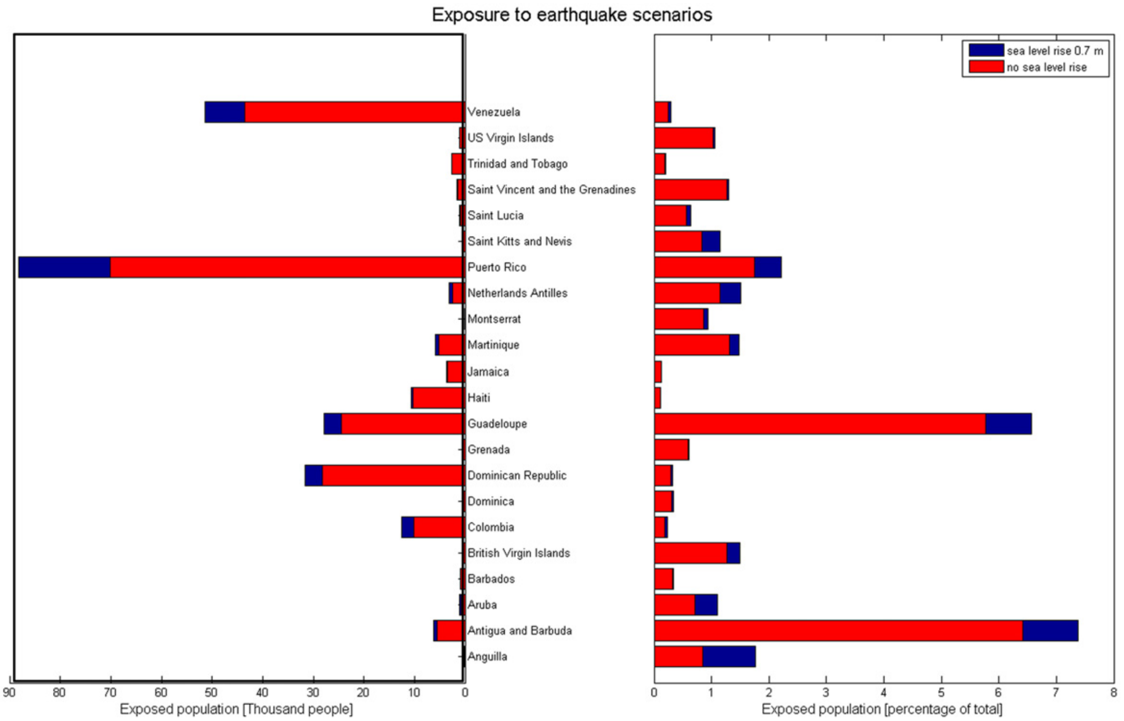

Fig. 13. Overview of population exposed to earthquake induced tsunamis (estimated individual return period of about 500 years). Left part of the figure shows the total number of people exposed, while the number of exposed people relative to number of inhabitants in each country is shown to the right. The effect of sea level rise is taken into account.

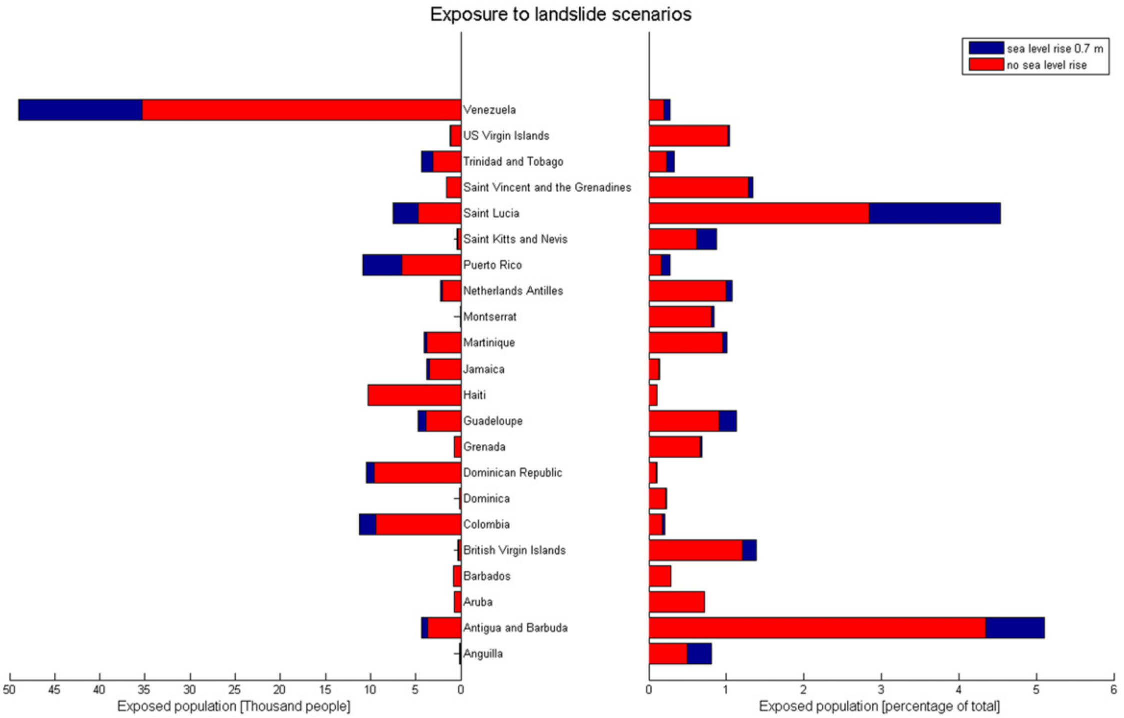

Fig. 14. Overview of population exposed to landslide induced tsunamis (estimated individual return period is more than 1000 years for smaller events in the north and about 10,000 years for larger events in the southern part of the arc). Left part of the figure shows the total number of people exposed, while the number of exposed people relative to number of inhabitants in each country is shown to the right. The effect of sea level rise is taken into account.

for the landslide scenarios. The high exposure along the coasts of Puerto Rico and the southern coast of the Dominican Republic is due to the very gentle, low-lying terrain and dense population. For the earthquake scenarios, Puerto Rico (90,000 exposed people), Venezuela (50,000), the Dominican Republic (35,000), and Guadeloupe (30,000) have the highest exposure in terms of total number of people. The highest exposure relative to the population is found in Antigua (7.5%) and in Guadeloupe (6.5%).

Please cite this article as: Harbitz, C.B., et al., Tsunami hazard in the Caribbean: Regional exposure derived from credible worst case scenarios. Continental Shelf Research (2012), doi:10.1016/j.csr.2012.02.006

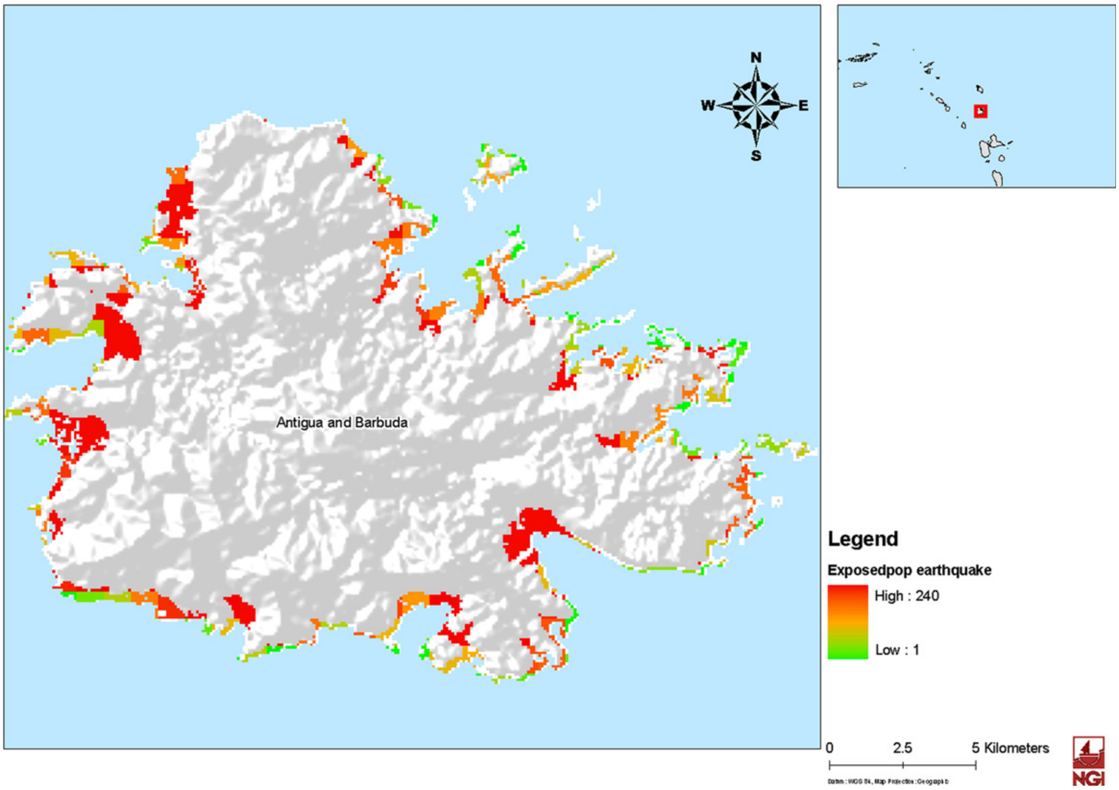

Fig. 15. Number of people exposed to earthquake induced tsunamis per 30 arc s square (0.75 km^2) in Antigua. The effect of high tide and sea level rise is taken into account. Estimated individual return period is about 500 years.

The highest number of exposed people for the landslide scenarios is found for Venezuela (50,000 exposed people), while there are several countries with approximately 10,000 people exposed (Saint Lucia, Puerto Rico, Haiti, Dominican Republic, and Colombia). Antigua (5%) and Saint Lucia (4.5%) have the highest exposure relative to the population. The fact that a landslide acts as a point source with possible higher damping rates than for earthquake sources can also be seen by comparing Figs. 2 and 12.

The exposure for Venezuela is high (in terms of total number of exposed people) for both types of scenarios. This is due to both the effect of low topography and of course high coastal population density. In Figs. 15 and 16 the distribution of the exposure is shown as an example for Antigua which is the most exposed island relative to its population according to our study. The two maps are very similar and therefore the same mitigation measures should be put in place for the two sources of tsunamis. Predicted tsunami arrival times vary between about 30 min (for the Lesser Antilles scenario) to 2 h 20 min (for the Hispaniola and Kick'em Jenny scenarios, Fig. 10).

It should be noted that the results may be biased owing to the limited number of scenarios assessed, implying higher surface elevations and number of exposed people in the vicinity of the presented tsunami source areas. This is especially relevant for the near shore and non-seismic tsunami scenarios. Further, the resolution of the bathymetry, elevation, and population data is too coarse for the hazard and exposure maps to be applied at a local scale.

7. Concluding remarks

A tsunami exposure assessment for the Caribbean region is performed. Compared to previous studies, a first step forward is that both seismic and non-seismic tsunamigenic sources are studied together, enabling a more complete hazard and exposure comparison. The probability, location, and size of the largest credible earthquake and gravity mass flow tsunami sources are based on historical earthquake and tsunami occurrence, large scale tectonics, and geology. Both submarine and initially subaerial tsunamigenic debris flows and landslides are included. The seabed displacements related to earthquakes are determined by analytical calculations, while the seabed displacements and mass flow dynamics related to mass flows are determined by a combination of analytical calculations and numerical simulations. The seabed displacements are used as input to the numerical tsunami simulations. Both linear hydrostatic and non-linear dispersive (Boussinesq) models are applied to describe the tsunami propagation. Dispersive effects turn out to be particularly important for the trans-oceanic tsunamis.

A second step forward compared to earlier tsunami studies for the Caribbean is the use of a recently developed procedure to transfer the offshore tsunami surface elevation to the shoreline water levels, determining the amplification factors from the parameters describing the incoming wave and bathymetric slope. Possible overestimation is due to lack of friction and breaking in the method of amplification factors. Finally, the total number of people exposed to the tsunamis triggered by landslides and earthquakes in the region is estimated, applying the maximum shoreline water level, a high-resolution digital topographic database, and a population dataset in a GIS analysis.

Large scale tectonics and compilation of the historical data for hazardous tsunami events in the region indicate that the return period for the selected M_W 8 earthquake tsunami scenarios is to the order of 500 years. The return period for landslide triggered tsunami scenarios is even more difficult to estimate, but the individual return period of the smaller non-seismic events in the northern part of the arc can be estimated to more than 1000 years, while the individual return period of larger events in the

Please cite this article as: Harbitz, C.B., et al., Tsunami hazard in the Caribbean: Regional exposure derived from credible worst case scenarios. Continental Shelf Research (2012), doi:10.1016/j.csr.2012.02.006

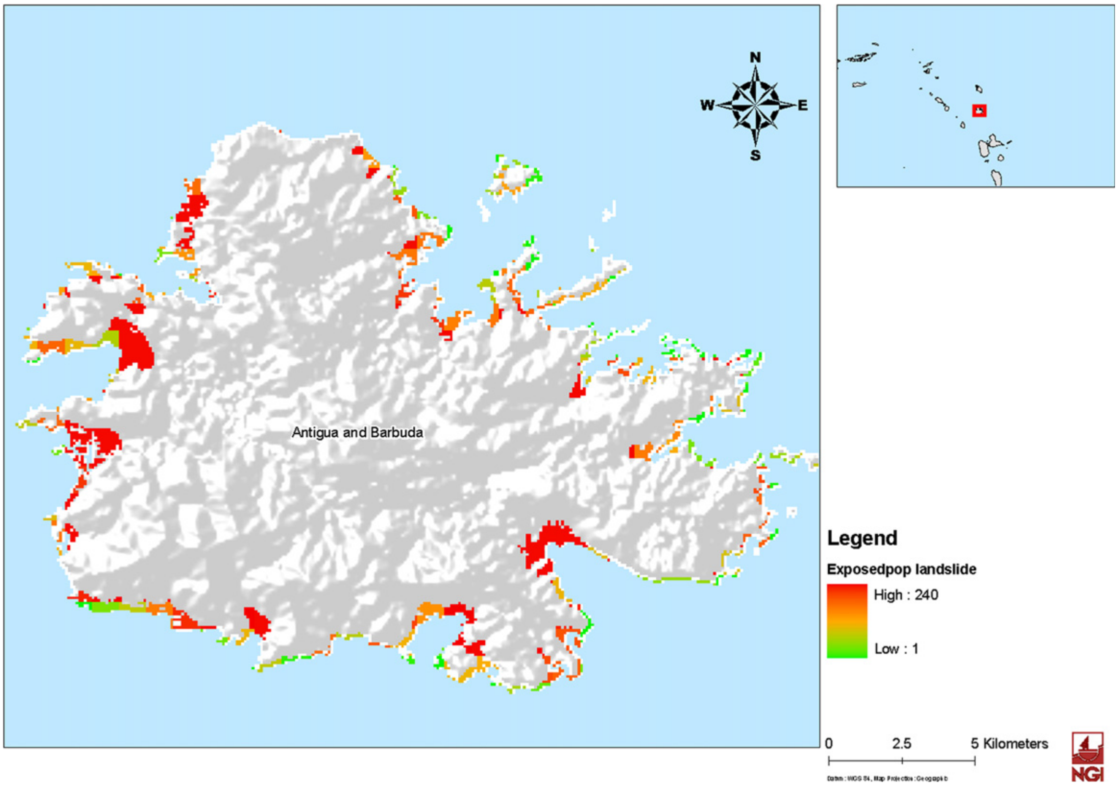

Fig. 16. Number of people exposed to landslide induced tsunamis per 30 arc s square (0.75 km^2) in Antigua. The effect of high tide and sea level rise is taken into account. Estimated individual return period is more than 1000 years for smaller events in the north and about 10,000 years for larger events in the southern part of the arc.

southern part of the arc is more along the order of 10,000 years. It should be noted that the return periods for the future tsunamis are not to be interpreted as precise estimates. For the seismic scenarios, the “memory free” (i.e. the probability of a future event is independent of the occurrence of recent events) assumption should be alluded. For the non-seismic scenarios, a more precise quantification of the probabilities could probably be achieved by in-depth individual studies of the potential landslide and debris flow source areas.

A maximum shoreline water level up to about 20 m is found closest to the sources (Hispaniola/Puerto Rico and the eastern section of Guadeloupe and the surrounding islands) for the seismically induced tsunami scenarios. The maximum shoreline water level for the landslide tsunami scenarios along the islands in the eastern part of the Caribbean Sea is mainly in the range of 1–5 m. Locally, the shoreline water level can be several times higher close to the landslide areas. A volcano flank collapse from the Soufrière Volcano at Saint Lucia is found to give maximum shoreline water levels of 3–10 m in the coastal areas from Dominica down to Grenada.

Using predicted tsunami maximum shoreline water levels together with available population data, it is found that Puerto Rico is the most exposed island, with as many as 90,000 people located in the likely tsunami inundation zones for the 500 years earthquake events that have been selected. Other highly exposed countries are Venezuela with 50,000, the Dominican Republic with 35,000, and Guadeloupe with 30,000 people. Measuring exposure relative to the population, Antigua is highest with 7.5%, followed by Guadeloupe with 6.5%. Exposure for tsunamis triggered by the selected landslide sources shows the highest figure for Venezuela (50,000 people), while there are several countries with approximately 10,000 people exposed (Saint Lucia, Puerto Rico, Haiti, Dominican Republic, and Colombia). The total risk is probably higher for the earthquake induced tsunamis than for the landslide induced tsunamis, owing to a higher number of exposed people and a shorter return period. The tsunami arrival time is generally short for the Caribbean Islands, typically one should prepare for less than one hour. This will certainly influence on the design and effectiveness of a tsunami early warning system and the possibility of evacuating the residents.

The presented regional hazard maps and population exposure are based on approximate and simplified methods as well as coarse resolution bathymetry, elevation, and population data to cover large geographical areas. Such hazard maps should therefore not be interpreted nor applied locally, but rather as a tool to produce reasonable regional estimates for risk comparison and management. The scenarios cover only the presumably most important ones. Hence, the results may be biased owing to the limited number of scenarios assessed. A higher number of sources would reveal a more complete picture of the regional tsunami risk. This would also illuminate the risk related to more frequent, but lower energy scenario sources. Finally, the maximum water levels, the inundated areas, and the resulting exposure of people should be further investigated, preferably with higher data resolution, in certain areas of complex terrain.

Acknowledgements

L. Brewster, L. Inniss, F.Hinds, and R. Roach (CZMU Barbados), R. Mahon, L. Nurse, N. Gour, J. Blackwood, and R. Goodridge (UWI/CERMES Cave Hill Barbados), R. Robertson and L. Lynch (SRC Trinidad), R. Ahmad (UWI Mona, Jamaica), J. Collymore, E. Riley, and A. Brome (CDERA Barbados), J. Thomas (DEM Barbados), as well as disaster coordinators throughout the Caribbean region are all thanked for helpful support to render possible and facilitate the project, including information and data sharing, arranging

Please cite this article as: Harbitz, C.B., et al., Tsunami hazard in the Caribbean: Regional exposure derived from credible worst case scenarios. Continental Shelf Research (2012), doi:10.1016/j.csr.2012.02.006

workshops and seminars, and capacity building. R. Goodridge is thanked for her assistance with the linguistics of the manuscript. The Norwegian Ministry of Foreign Affairs is greatly acknowledged for the financial support to execute the 2006–2008 UWI/NGI capacity building programme on natural disasters mitigation in the Caribbean. The Norwegian Geotechnical Institute (NGI), the International Centre for Geohazards (ICG), NORSAR, the Institut de Physique du Globe de Paris (IPGP), and the Research Council of Norway are thanked for supporting the conversion of the project reports into this journal paper. Finally, the two anonymous referees are thanked for valuable comments to the manuscript. This is contribution no. 372 of the International Centre for Geohazards and no. 3242 of IPGP.

Appendix A. The NGI/NORSAR Caribbean tsunami database

See Table A1.

Table A1

Year	Month	Day	Hour	Tsunami cause code	Magnitude type not specified		Magnitude (*Ms*)		Magnitude (*Mw*)		Magnitude (Mt —Abe)	Focal depth (km)	Tsunami eventvalidity
1498	8	2		1									3
1530	9	1	14	1			7		8			10	4
1539	11	24	23	1			7						3
1541	12	25		1			7						2
1688	3	1		1									2
1690	4	5		3	7.6		7						3
1692	6	7	16	3	7.5		7					10	4
1701	11	9		1			7						2
1750				1			7						3
1751	10	18	19	1	7.3		7					33	3
1751	11	21		1			7						3
1755	11	1	9	1			8.5						4
1755	11	18	9	1			7						3
1761	3	31	0	1			8.5				8.5		4
1766	6	11	24	1			7						2
1766	10	21		1			7						3
1767	4	24	6	1			7						3
1770	6	3	9	1			7					10	4
1775	2	11		1			7						3
1775	12	18		1			7						3
1781	8	1		2									2
1787	3	28		1			8						4
1802	3	19		1									3
1802	8	15		1								0	3
1812	3	26	20	1	7.7							33	2
1812	11	11	10	3									2
1822	5	7	23	1			7.6						3
1823	11	30	3	1									4
1825	9	20	4	1			7						2
1842	5	7	21	1	8.05		8.1						4
1843	2	8	14	1	8		8.3					33	4
1843	2	17		6									2
1852	7	17		1									2
1853	7	15	14	1	6.7		6.7					14	4
1855	9	25	10	1			6.5						2
1856	8	9		1	7.5							0	4
1860	4	8	10	1	7.5		7						4
1867	11	18	18	1	7.5		7.5					33	4
1868	3	17	6	1			7						4
1868	8	13		1	8.5								3
1882	9	7	7	3	7.9		7.9						4
1893	2	19	1	1									2
1896	2	6	13	1									2
1900	10	29	4	1	7.7	MsAN2	7.6	P&S	7.7	P&S		60	3
1902	5	5	13	7									4
1902	5	7		6									4
1902	5	8	8	6									3
1902	5	20		6									2
1902	8	30	21	6									3
1904	12	20	5	1	7.8	G&R	7.2	AN2	7.2	P&S			2
1906	1	31		1									2
1906	2	16		1									2
1907	1	14	21	1	6.5	GAN							3
1911	11	3		6									4
1913	10	2		0									2
1914	5	28		0									2
1915	11	26		0									2
1916	4	26	2	1	7.3	G&R	7.4	AN1	7.2	P&S		0	4
1916	7	30		1								0	2
1918	10	11	14	1	7.5	MsABE1	7.3	P&S	7.3	P&S		60	4
1918	10	24	3	3									4
1922	5	2	20	1									2

Please cite this article as: Harbitz, C.B., et al., Tsunami hazard in the Caribbean: Regional exposure derived from credible worst case scenarios. Continental Shelf Research (2012), doi:10.1016/j.csr.2012.02.006

Table A1 (*continued*)

Year	Month	Day	Hour	Tsunami cause code	Magnitude type not specified		Magnitude (*Ms*)		Magnitude (*Mw*)		Magnitude (Mt —Abe)	Focal depth (km)	Tsunami eventvalidity
1929	1	17	11	1	6.9	G&R						35	4
1932	2	3	6	1	6.8	G&R						25	4
1934	7	18	1	1	7.6	MsABE1	7.4	P&S	7.6	P&S		25	4
1939	7	24		4									2
1939	8	15	3	1	5.6	G&R							2
1946	8	4	17	1	8.1	G&R	8	ABE1	7.9	P&S		60	4
1946	8	8	13	1	7.6	G&R	7.6	ABE1	7.5	P&S		25	4
.1953	5	31	19	1	6.9	ROTHE	6.8	PAS				33	2
1955	1	18		1								33	2
1961	6	16	10	8	6	PAS						114.9	2
1967	7	29	23	1			6.5					10	2
1968	9	20	6	1	6.2	mbGS	6.2	ISC				102.6	2
1969	12	25	21	1	7	MsABE1	7	P&S	7.2	P&S		9.7	4
1976	2	4	9	1	7.7	MwP&S	7.5	P&S	7.5	HRV		12.1	4
1985	3	16	14	1	6.5	*Mw*GS	6.4	ISC	6.4			15.8	4
1989	11	1	10	1	5.2	mbISC	4.4	ISC				18	3
1991	4	22	21	1	7.3	*Mw*GS	7.5	ISC	7.6	HRV		12.3	4
1997	4	10		0									2
1997	7	9	19	1	6.9	*Mw*GS	6.8	ISC	7	HRV		10	3
1997	12	26	8	7								0	4
1999	1	20		6									4
2003	7	13	3	6									4
2004	11	21	11	1	6.3	*Mw*GS	6.1	GS	6.3	HRV		14	4
2006	5	20	7	6									4

Year	Country	Region	Lat	Long	Magnitude (Lida)	Intensity (Soloviev)	Max. wave height [m]	Number of deaths	Casualty idx.
1498	VENEZUELA	BOCADE LA SIERPE	9.9	– 62.3		1			3
1530	VENEZUELA	CUMANA	10.7	– 64.1	2.6	2	7.3		
1539	HONDURAS	CABO DE HIGUERAS	16	– 87		1			
1541	VENEZUELA	CUBAGUA ISLAND	10.8	– 64.2		1			
1688	Port Royal.	Jamaica	17.6	– 76.7		2			
1690	Antigua; Nevis, St. Thomas, etc		17.2	– 62.5		1	2	2	
1692	JAMAICA	PORT ROYAL	17.9	– 76.9		3	1.8	2500	4
1701	Gon(n)ave.	Haiti	18.8	– 73.1		1			
1750	Cumana.	Venezuela	10.4	– 64.5		1			
1751	DOMINICAN REPUBLIC	AZUA DE COMPOSTELA	18.3	– 70.7		2			
1751	All	All	18.4	– 72.8		2	7		
1755	All	All	36	– 11	3.6	3.5	6.4		
1755	All	All	42.7	– 70.3		4	6.3		
1761	Barbados	Barbados	34.5	– 13	1.3	2	1.2		
1766	Jamaica	Jamaica	20	– .5		2			
1766	Cumana.	Venezuela	10	– 64		1			
1767	Martinique and Barbados	Martinique and Barbados	11.35	– 57.95		1	2.8		
1770	HAITI	PORT–AU-PRINCE	18.6	– 72.8		1		200	
1775	CUBA	SANTIAGO DE CUBA	19.9	– 76		1			
1775	HAITI	HAITI & DOMINICAN REPUBLIC	19	– 72.4		1			
1781	JAMAICA	JAMAICA: UNKNOWN LOCATION	18.1	– 77.3					
1787	S. MEXICO	MEXICO	19	– 66		2.5	4		
1802	Antigua and St. KittsAntigua and St. Kitts	Antigua and St. KittsAntigua and St. Kitts	17.2	– 62.4		1			
1802	VENEZUELA	CUMANA	10.48	– 64.2					
1812	VENEZUELA	LA GUAIRA	10.6	– 66.9		2			
1812	JAMAICA	KINGSTON	18	– 76.5		2			
1822	COSTA RICA	MATINA	9.5	– 83		1			
1823	MARTINIQUE	SAINT PIERRE	14.4	– 61		2			
1825	TRINIDAD AND TOBAGO	PORT–OF-SPAIN	10.4	–61.3		1			
1842	HAITI	Port de Paix	19.5	–72.1	4.2	3	4.6	4500.00	3
1843	Antigua	St John	17.15	–61.17	0.3	1	1.2	5000	
1843	Guadeloupe	Marie-Galante	15.93	–61.3		0			
1852	CUBA	SANTIAGO DE CUBA	19.5	–75.5		2			
1853	VENEZUELA	CUMANA	10.5	–64.2		1			3
1855	Honduras. Trujillo Bay		16	–86		1			
1856	HONDURAS	OMOA	15.75	–88.17		2	5		
1860	HAITI	ANSE-A-VEAU	18.52	–73.35		1			
1867	all	all	18.1	–65.1	2.3	3	9	30	1
1868	USA TERRITORY	VIRGIN ISLANDS	18.1	–65.1	–0.7	1	1.5		
1868	VENEZUELA	RIO CARIBE	10.7	–63.1		1			
1882	PANAMA	SAN BLAS ARCHIPELAGO	9.5	–78.9		1.5	3	100	2
1893	JAMAICA	KINGSTON	17.97	–76.8		1			
1896	Kingston. Jamaica		17.8	–78.8		1			
1900	VENEZUELA	MANCUTO	11.2	–66.5		3	10		4

Please cite this article as: Harbitz, C.B., et al., Tsunami hazard in the Caribbean: Regional exposure derived from credible worst case scenarios. Continental Shelf Research (2012), doi:10.1016/j.csr.2012.02.006

Table A1 (*continued*)

Year	Country	Region	Lat	Long	Magnitude (Lida)	Intensity (Soloviev)	Max. wave height [m]	Number of deaths	Casualty idx.
1902	MARTINIQUE	Saint-Pierre	14.82	–61.17		2	2		
1902	Barbados, Grenada, Saint Lucia	Barbados, Grenada, Saint Lucia	13.33	–61.18			1		
1902	MARTINIQUE	Saint-Pierre	14.82	–61.17					
1902	MARTINIQUE	Basse-Pointe,Le Prêcheur, Fort de France, Le Carbet	14.82	–61.17				2	
1902	MARTINIQUE	Fort-de-France	14.82	–61.17		0	1		
1904	Panama. Costa Rica		9.2	–82.8					
1906	VENEZUELA	CARACAS	10.5	–66.916				500	
1906	VENEZUELA	Cabo Blanca	10.6	–66.95					
1907	JAMAICA	JAMAICA	18.2	–76.7	1.3	2	2.5	1000	
1911	TRINIDAD AND TOBAGO	TRINIDAD	10.5	–61.2		1			
1913	Gatun. Panama		9.3	–79.9		−2	0.03		
1914	Gatun. Panama		9.4	–80		−1	0.15		
1915	Gatun. Panama		9.4	–80		−2	0.01		
1916	PANAMA	BOCAS DEL TORO	11	–85		1	1.2		
1916	VENEZUELA	OCUMARE DE LA COSTA DE ORO	10.1	−66.8					
1918	USA TERRITORY	PUERTO RICO: MONA PASSAGE	18.473	–67.631	2.6	2.5	6.1	142	3
1918	USA TERRITORY	PUERTO RICO	18.5	–67.5					
1922	USA TERRITORY	PUERTO RICO: VIEQUES	18.2	–65.5		0	0.64		
1929	VENEZUELA	CUMANA	9.499	–64.381		1			
1932	CUBA	SANTIAGO DE CUBA	19.77	–75.85		1			
1934	Panama. Puerto Armueles		8.045	–82.48			1.3		
1939	Grenada		12.1	–61.7					
1939	CUBA	SANTA CLARA	22.5	–79		1			
1946	DOMINICAN REPUBLIC	NORTHEASTERN COAST	19.25	–69	2.2	2	5	1790	4
1946	DOMINICAN REPUBLIC	NORTHEASTERN COAST	19.5	–69.5		0	0.6	75	2
.1953	DOMINICAN REPUBLIC	PUERTO PLATA	19.4	–70.4	–3.3	0.5	0.6		
1955	PANAMA	PANAMA: OFF NORTHERN COAST	9.7	–79.6		2		0	
1961	COLOMBIA	NORTHEASTERN COLOMBIA	8.824	–73.337		1			
1967	VENEZUELA	CARACAS	10.6	–67.3		−1	0.07		
1968	VENEZUELA	CARUPANO	10.731	–62.719					
1969	Barbados	Barbados	15.37	–60.58	–3.3	0	0.46		
1976	Guatemala. Gulf of Honduras		15.297	–89.145		0	0.45		
1985	GUADELOUPE	Basse–Terre	16.982	–62.446	–3.3	−2	0.03		
1989	USA TERRITORY	PUERTO RICO	19	-68.83		−1	0.1		
1991	COSTA RICA	LIMON, PANDORA	9.675	–83.072	1	1.5	3	2	1
1997	Honduras								
1997	VENEZUELA	CARIACO-CUMANA	10.448	–63.533		1			
1997	MONTSERRAT	WHITE RIVER VALLEY	16.72	–62.18		1	3		
1999	MONTSERRAT	SOUFRIERE HILLS VOLCANO	16.72	–62.18			2		
2003	MONTSERRAT	SOUFRIERE HILLS VOLCANO	16.72	–62.18		0	4		
2004	GUADELOUPE	Les Saintes	15.75	–61.53			2		
2006	Guadeloupe	Deshaies	16,72	–62.18			1		

From NOAA:
Tsunami event validity:
Valid values: **0–4**
Validity of the actual tsunami occurrence is indicated by a numerical rating of the reports of that event:
0 = Erroneous entry
1 = Very doubtful tsunami
2 = Questionable tsunami
3 = Probable tsunami
4 = Definite tsunami

Description of number of deaths from the tsunami:
Valid values: **0–4**

When a description was found in the historical literature instead of an actual number of deaths, this value was coded and listed in the deaths D column.
If the actual number of deaths was listed, a descriptor was also added for search purposes.
0 = None
1 = Few (∼1–50 deaths)
2 = Some (∼51–100 deaths)
3 = Many (∼101–000 deaths)
4 = Very many (over 1000 deaths)

Please cite this article as: Harbitz, C.B., et al., Tsunami hazard in the Caribbean: Regional exposure derived from credible worst case scenarios. Continental Shelf Research (2012), doi:10.1016/j.csr.2012.02.006

Table A1 (*continued*)

Tsunami cause code:
Valid values: 0–11
The source of the tsunami:
0=Unknown cause
1=Earthquake
2=Questionable earthquake
3=Earthquake and landslide
4=Volcano and earthquake
5=Volcano, earthquake, and landslide
6=Volcano
7=Volcano and landslide
8=Landslide
9=Meteorological
10=Explosion
11=Astronomical tide

Magnitude (Lida)=Log 2(H)
Intensity (Soloview)=log 2(H/sqrt(2))

Abbreviations:

NOAA—National Geophysical Data Centre, NOAA/WDC Historical Tsunami Database at NGDC, http://www.ngdc.noaa.gov/hazard/tsu_db.shtml.

TLN—Historical Tsunami Database for the World Ocean (HTDBWLD), Tsunami Laboratory, Novosibirsk, http://tsun.sscc.ru/On_line_Cat.htm.

EHB—Engdahl, E.R., R van der Hilst and R. Buland (1998): Global teleseismic earthquake relocation with improved travel times and procedures for depth determination. Bull. Seism. Soc. Am., 88, 722–743.

—Engdahl, E.R. and A. Villasenor (2002): Global Seismicity: 1900–1999. International Handbook of Earthquake and Engineering Seismology, Volume 81A, pp. 665–690. Published by IASPEI, Committee of Education.

—Engdahl, E.R., A. Villasenor, H.R. DeShon, and C.H. Thurber (2007): Teleseismic Relocation and Assessment of Seismicity (1918–2005) in the Region of the 2004 M_w 9.0 Sumatra–Andaman and 2005 M_w 8.6 Nias Island Great Earthquakes. Bull. Seism. Soc. Am., V.

—Bilek, S.L., and E.R. Engdahl (2007), Rupture characterisation and aftershock relocations for the 1994 and 2006 tsunami earthquakes in the Java subduction zone, Geophys. Res. Lett., 34, L20311, doi:10.1029/ 2007GL031357.

—Villaseñor, A. and E.R. Engdahl (2007): Systematic Relocation of Early Instrumental Seismicity: Earthquakes in the International Seismological Summary for 1960–1963. Bull. Seism. Soc. Am., Vol. 97, No. 6, pp. 1820–1832, December 2007.

—Personal communication (data files).

GS–USGS (earthquake locations reported under different acronyms over the years, including NEIC, NElS and C&GS, NOAA, NGDC and PDE—Prelimary Determination of Epicentres).

ABE—Catalogue of large earthquakes, mostly magnitude 6.8 and larger, 1897–1980, from Abe (1981, 1984) and Abe and Noguchi (1983a,b). The magnitude sources ANI, AN2, ABEl, and ABE2 are from this catalogue.

B&D—Catalogue of large earthquakes, 1897–1977, compiled by Bath and Duda (1979).

G&R—Catalogue of hypocenters and magnitudes, 1904–1952 (Gutenberg and Richter, 1954).

ISC—Hypocenters and magnitudes from bulletins prepared by the International Seismological Centre, Newbury, UK, 1964.

ISS—Hypocenters listed in the International Seismological Summary (predecessor of ISC), 1918–1963.

P&S—Complete and uniform catalogue of worldwide earthquakes with *Ms* magnitudes of 7.0 and larger at depths less than or equal to 70 km, 1900–1989 (Pacheco and Sykes, 1992).

PAS—Magnitudes reported by the Califomia Institute of Technology, Pasadena, USA.

References

Baptista, M.A., Heitor, S., Miranda, J.M., Miranda, P., Mendes, L., 1998. The 1755 Lisbon Tsunami; Evaluation of the tsunami parameters. Journal of Geodynamics 25 (2), 143–157.

Baptista, M.A., Miranda, J.M., Chierici, F., Zitellini, N., 2003. New study of the 1755 earthquake source based on multi-channel seismic survey data and tsunami modeling. Natural Hazards and Earth System Sciences 3, 333–340.

Barkan, R., ten Brink, U.S., 2010. Tsunami Simulations of the 1867 Virgin Island Earthquake: Constraints on epicenter location and fault parameters. Bulletin of the Seismological Society of America 100 (3), 995–1009.

Barkan, R., ten Brink, U.S., Lin, J., 2009. Far field tsunami simulations of the 1755 Lisbon earthquake. Implications for tsunami hazard to the U.S. East Coast and the Caribbean. Marine Geology 264, 109–122.

Bengoubou-Valérius, M., Bazin, S., Bertil, D., Beauducel, F., Bosson, A., 2008. CDSA: A new seismological data center for French Lesser Antilles. Seismological Research Letters 79, 90–102.

Bernard, P., Lambert, J., 1988. Subduction and seismic hazard in the Northern Lesser Antilles: Revision of the historical seismicity. Bulletin of the Seismological Society of America 78, 1965–1983.

Bilek, S.L., Lay, T., 1999. Rigidity variations with depth along interplate megathrust faults in subduction zones. Nature 400, 443–446.

Bindoff, N.L., Willebrand, J., Artale, V., Cazenave, A., Gregory, J., Gulev, S., Hanawa, K., Le Quere, C., Levitus, S., Nojiri, Y., Shum, C.K., Talley, L.D., Unnikrishnan, A., 2007. Observations: Oceanic climate change and sea level. In: Solomon, S., Qin, D., Manning, M., Chen, Z., Marquis, M., Averyt, K.B., Tignor, M., Miller, H.L. (Eds.), Climate Change 2007: The Physical Science Basis. Contribution of Working Group I to the FourthAassessment Report of the Intergovernmental Panel on Climate Change. Cambridge University Press, Cambridge.

Boudon, G., Le Friant, A., Komorowski, J.C., Deplus, C., Semet, M.P., 2007. Volcano flank instability in the Lesser Antilles Arc: Diversity of scale processes and temporal recurrence. Journal of Geophysical Research, 112. doi:10.1029/2006JB004674.

BRGM, 2009. Data Extracted from Tsunamis. BRGM 〈www.tsunamis.fr〉.

Brown, G.M., Holland, J.G., Sigurdsson, H., Tomblin, J.F., Arculus, R.J., 1977. Geochemistry of the lesser Antilles volcanic island arc. Geochimica et Cosmochimica Acta 41, 785–801.

Calais, E., Freed, A., Mattioli, G., Amelung, F., Jónsson, S., Jansma, P., Hong, S.-H., Dixon, T., Prépetit, C., Momplaisir, R., 2010. Transpressional rupture of an unmapped fault during the 2010 Haiti earthquake. Nature Geoscience 3, 794–799. doi:10.1038/ngeo992 〈http://www.nature.com/ngeo/focus/haiti/index.html〉.

Calais E., Perrot J., Mercier de Lepinay B., 1998. Strike-slip tectonics and seismicity along the northern Caribbean plate boundary from Cuba to Hispaniola. In: Dolan, J.F., Mann, P. (Eds.), Active Tectonics of the Northern Caribbean Plate Boundary Zone, GSA Special Paper 326, pp. 125–141.

Carlson, R.L., Raskin, G.S., 1983. Density of the ocean crust. Nature 311, 555–558.

Center for International Earth Science Information Network (CIESIN), 2007. Columbia University; International Food Policy Research Institute (IPFRI) the World Bank; and Centro Internacional de Agricultura Tropical (CIAT) Global Rural–Urban Mapping Project (GRUMP): Gridded Population of the World available at: 〈http://beta.sedac.ciesin.columbia.edu/gpw〉.

Courant, R., Friedrichs, K., Lewy, H., 1967. On the partial difference equations of mathematical physics. IBM J 11, 215–234.

De Blasio, F.V., Elverhøi, A., Engvik, L., Issler, D., Gauer, P., Harbitz, C.B., 2006. Understanding the high mobility of subaqueous debris flows. Norwegian Journal of Geology 86, 275–284.

de Buisonje, P.H., Zonneveld, J.I.S., 1976. Caracasbaai: A submarine slide of a high coastal fragment in Curaçao. Nieuwe West-Indische gids 5, 55–88.

Please cite this article as: Harbitz, C.B., et al., Tsunami hazard in the Caribbean: Regional exposure derived from credible worst case scenarios. Continental Shelf Research (2012), doi:10.1016/j.csr.2012.02.006

DeMets, C., Jansma, P.E., Mattioli, G.S., Dixon, T.H., Farina, F., Bilham, R., Calais, E., Mann, P., 2000. GPS geodetic constraints on Caribbean–North America plate motion. Geophysical Research Letters 27, 437–440.

Deplus, C., Le Friant, A., Boudon, G., Komorowski, J.C., Villemant, B., Harford, C., Segoufin, J., Cheminee, J.L., 2001. Submarine evidence for large-scale debris avalanches in the Lesser Antilles Arc. Earth and Planetary Science Letters 192 (2), 145–157.

Dorel, J., 1981. Seismicity and seismic gap in the Lesser Antilles arc and earthquake hazard in Guadeloupe. Geophysical Journal of the Royal Astronomical Society 67, 679–695.

Engdahl, E.R., Villaseñor, A., 2002. Global seismicity: 1900–1999. IASPEI International Handbook of Earthquake and Engineering Seismology 81, 665–690.

Engdahl, E.R., Villaseñor, A., DeShon, H.R., Thurber, C.H., 2007. Teleseismic relocation and assessment of seismicity (1918–2005) in the region of the 2004 *Mw* 9.0 Sumatra–Andaman and 2005 *Mw* 8.6 Nias Island Great Earthquakes. Bulletin of the Seismological Society of America 97 (1A), 43–61.

Feuillet, N., Manighetti, I., Tapponnier, P., 2002. Arc parallel extension and localization of volcanic complexes in Guadeloupe Lesser Antilles. Journal of Geophysical Research 107 (B12), 2331.

GEBCO, 2008. Information and downloadable data at 〈http://www.bodc.ac.uk/products/bodc_products/gebco/〉 (Accessed December 2008).

Girardin, N., Feuillard, M., Viodé, J.P., 1991. Réseau régional sismique de l'arc des Petites Antilles: Sismicité superficielle (1981–1988). Bulletin de la Société Géologique de France 162 (6), 1003–1015.

Girardin, N., Gaulon, R., 1982. Microseismicity and stresses in the Lesser Antilles dipping seismic zone. Earth and Planetary Science Letters 62, 340–348.

Gisler, G., Weaver, R., Gittings, M., 2006a. SAGE calculations of the tsunami threat from La Palma. Science of Tsunami Hazards 24, 288–301.

Gisler, G., Weaver, R., Mader, C., Gittings, M., 2006b. Two-dimensional simulations of explosive eruptions of Kick'em Jenny and other submarine volcanoes. Science of Tsunami Hazards 25 (1), 34–41.

Gittings, M., Weaver, R., Clover, M., Betlach, T., Byrne, N., Coker, R., Dendy, E., Hueckstaedt, R., New, K., Oakes, W.R., Ranta, D., Stefan, R., 2008. The RAGE radiation-hydrodynamic code. Computational Science & Discovery 1, 015005. doi:10.1088/1749-4699/1/1/015005. 63 pp〈http://iopscience.iop.org/1749-4699/1/1/015005/pdf/1749-4699_1_1_015005.pdf〉.

Grilli, S.T., Dubosq, S., Pophet, N., Pérignon, Y., Kirby, J.T., Shi, F., 2010. Numerical simulation and first-order analysis of large co-sesimic tsunamis generated in the Puerto Rico trench: near-field impact on the North shore of Puerto Rico and far-field impact on the US East Coast. Natural Hazards and Earth System Sciences 10, 2109–2125.

Gutscher, M.-A., Baptista, M.A., Miranda, J.M., 2006. The Gibraltar Arc seismogenic zone 20 (part 2): Constraints on a shallow east dipping fault plane source for the 1755 Lisbon 21 earthquake provided by tsunami modeling and seismic intensity. Tectonophysics 22 426 (1–2), 153–166.

Harbitz, C.B., 1992. Model simulations of tsunamis generated by the Storegga Slide. Marine Geology 105, 1–21.

Harbitz C.B., Løvholt F., Glimsdal S., 2007. Tsunamis Generated by Landslides and Earthquakes—Wave Characteristics and Numerical Modeling for Hazard Assessment in Offshore Geohazards. Proceedings of the 2007 Offshore Technology Conference, Houston, Texas, 30 April-3 May 2007. OTC 18602.

Hebert, H., Schindele, F., Altinok, Y., Alpar, B., Gazioglu, C., 2005. Tsunami hazard in the Marmara Sea (Turkey): A numerical approach to discuss active faulting and impact on the Istanbul coastal areas. Marine Geology 215 (1–2), 23–43.

Heinrich, P., Mangeney, A., Guibourg, S., Roche, R., 1998. Simulation of water waves generated by a potential debris avalanche in Montserrat Lesser Antilles. Geophysical Research Letters 25 (9), 3697–3700.

Heinrich, P., Roche, R., Mangeney, A., Boudon, G., 1999. Modéliser un raz de marée créé par un volcan. La Recherche 318, 67–71.

Hornbach, M.J., Braudy, N., Briggs, R.W., Cormier, M.-H., Davis, M.B., Diebold, J.B., Dieudonne, N., Douilly, R., Frohlich, C., Gulick, S.P.S., Johnson III, H.E., Mann, P., McHugh, C., Ryan-Mishkin, K., Prentice, C.S., Seeber, L., Sorlien, C.C., Steckler, M.S., Symithe, S.J., Taylor, F.W., Templeton, J., 2010. High tsunami frequency as a result of combined strike-slip faulting and coastal landslides. Nature Geoscience 3, 783–788. doi:10.1038/ngeo975 〈http://www.nature.com/ngeo/focus/haiti/index.html〉.

Horsburgh, K.J., Wilson, C., Baptie, B.J., Cooper, A., Cresswell, D., Musson, R.M.W., Ottemöller, L., Richardson, S., Sargeant, S.L., 2008. Impact of a Lisbon-type tsunami on the U.K. coastline and the implications for tsunami propagation over broad continental shelves. Journal of Geophysical Research. 113, C04007. doi:10.1029/2007JC004425.

Iida K., Cox D.C., Pararas-Carayannis G., 1967. Preliminary catalog of tsunamis occurring in the Pacific ocean. Hawaii Institute of Geophysics, Data Report 5:67-10.

Intergovernmental Oceanographic Commission, 2006. Establishment of an intergovernmental coordination group for tsunami and other coastal hazards warning system for the Caribbean and adjacent regions UNESCO Resolution XXIII-13 〈http://ioc3unescoorg/ioc-24/documents/CARIBE-EWS-II-3pdf〉.

ISDR, 2009. Global assessment report (GAR) on disaster risk reduction 〈http://www.preventionweb.net/gar09/〉.

Komorowski, J.C., Boudon, G., Semet, M., Beauducel, F., Anténor-Habazac, C., Bazin, S., Hammouya, G., 2005. Guadeloupe. In: Lindsay, J., Robertson, R., Shepherd, J., Ali, S. (Eds.), Volcanic Hazard Atlas of the Lesser Antilles. Seismic Research Unit, the University of the West Indies, Trinidad and Tobago, pp. 65–102.

Komorowski J.C., Boudon G., Semet M.P., Villemant B., Hammouya G., 2002. Recurrent flank-collapses at Soufrière of Guadeloupe volcano: Implications of acid hydrothermal fluids on edifice stability. In: Proceedings of the International Congress Montagne Pelée 1902–2002 Martinique May 12–16, 2002.

Lander J.F., Whiteside L.S., 1997. Caribbean Tsunamis: An Initial History. Tsunami Workshop June 11–13, Mayaguez, Puerto Rico.

Le Friant, A., Boudon, G., Komorowski, J.C., Heinrich, P., Semet, M.P., 2006. Potential flank-collapse of Soufrière volcano Guadeloupe Lesser Antilles? Natural hazards 39 3, 381–393.

Le Friant, A., Hardford, C.L., Deplus, C., Boudon, G., Sparks, R.S.J., Herd, R.A., Komorowski, J.C., 2004. Geomorphological evolution of Montserrat (West Indies): importance of flank collapse and erosional processes. Journal of the Geological Society London 161, 147–160.

Lindsay, J., Robertson, R., Shepherd, J.B., Ali, S. (Eds.), 2005. Volcanic Hazard Atlas of the Lesser Antilles. Seismic Research Unit, the University of the West Indies, Trinidad and Tobago.

López-Venegas, A.M., ten Brink, U.S., Geist, E.L., 2008. Submarine landslide as the source for the October 11, 1918 Mona Passage tsunami: Observations and modelling. Marine Geology 254, 35–46.

Løvholt, F., Bungum, H., Harbitz, C.B., Glimsdal, S., Lindholm, C.D., Pedersen, G., 2006. Earthquake related tsunami hazard along the western coast of Thailand. Natural Hazards and Earth System Sciences 6, 1–19.

Løvholt, F., Glimsdal, S., Harbitz, C.B., Zamora, N., Nadim, F., Peduzzi, P., Dao, H.I., Smebye, H., 2011. Tsunami hazard and exposure on the global scale. Earth-Science Reviews0012-8252. doi:10.1016/j.earscirev.2011.10.002 〈http://www.sciencedirect.com/science/article/pii/S0012825211001619〉.

Løvholt, F., Harbitz, C.B., Haugen, K.B., 2005. A parametric study of tsunamis generated by submarine slides in the Ormen Lange/Storegga area off western Norway. Marine and Petroleum Geology 22, 219–231. doi:10.1016/jmarpetgeo200410017.

Løvholt F., Kühn D., Bungum H., Harbitz C.B., Glimsdal S., in review. Historical tsunamis and present tsunami hazard in Eastern Indonesia and the Philippines. Submitted for publication in Journal of Geophysical Research - Solid Earth.

Løvholt F., Pedersen G., Bazin S., Kühn D., Bredesen R.E., Harbitz C.B. in press. Stochastic analysis of tsunami run-up due to heterogeneous co-seismic slip and dispersion. Accepted for publication in Journal of Geophysical Research – Oceans. 〈http://www.agu.org/journals/jc/papersinpress.shtml#id2011JC007616〉.

Løvholt, F., Pedersen, G., Gisler, G., 2008. Oceanic propagation of a potential tsunami from the La Palma Island. Journal of Geophysical Research 113. doi:10.1029/2007JC004603.

Løvholt F., Pedersen G., Glimsdal S., 2010. Coupling of dispersive tsunami propagation and shallow water coastal response. In: Zahibo, N., Pelinovsky, E., Yalciner, A., Titov, V. (Eds.), Proceedings of the Caribbean Waves 2008 Workshop in Guadeloupe December 2008. The Open Oceanography Journal, vol. 4, pp. 71–82.

Mader, C.L., 2001. Modeling the La Palma Landslide Tsunami. Science of Tsunami Hazards 19, 150–170.

Mann, P., Calais, E., Ruegg, J.C., DeMets, C., Jansma, P.E., Mattioli, G., 2002. Oblique collision in the northeastern Caribbean from GPS measurements and geological observations. Tectonics 21 (6). doi:10.1029/2001TC001304.

Masson, D.G., Harbitz, C.B., Wynn, R.B., Pedersen, G., Løvholt, F., 2006. Submarine landslides: Processes triggers and hazard prediction. Philosophical Transactions of the Royal Society, 364. doi:10.1098/rsta20061810.

Maul, G.A., 1993. Climate Change in the Intra-Americas Sea. Edward Arnold, London.

McCann, W.R., 2006. Estimating the threat of tsunamigenic earthquakes and earthquake induced landslide in the Caribbean. In: Mercado-Irizarry, A., Liu, P. (Eds.), Caribbean Tsunami Hazard. World Scientific Publishing, pp. 43–65.

Mercado-Irizarry A., Liu P., 2006. Caribbean tsunami hazard (eds). World Scientific Publishing, 341 pp.

Molnar, P., Sykes, L., 1969. Tectonics of the Caribbean and Middle America regions form focal mechanisms and seismicity. Geological Society of America Bulletin 80, 1639–1684.

Moya, J.C., Mercado, A., 2006. Geomorphologic and stratigraphic investigations on historic and prehistoric tsunami in northwestern Puerto Rico: Implications for Long Term Coastal Evolution. In: Mercado-Irizarry, A., Liu, P. (Eds.), Caribbean Tsunami Hazard. World Scientific Publishing, pp. 149–177.

Müller, R.D., Roest, W.R., Royer, J.-Y., Gahagan, L.M., Sclater, J.G., 1997. Digital isochrons of the world's ocean floor. Journal of Geophysical Research 102 (B2), 3211–3214. doi:10.1029/96JB01781.

Nadim F., Glade T., 2006. On tsunami risk assessment for the west coast of Thailand. Nadim F, Pöttler R, Einstein H, Klapperich H, Kramer S (eds), ECI Symposium Series 7 〈http://services.bepress.com/eci/geohazards/28〉.

NGI, 2009a. Natural disaster mitigation in the Caribbean; local tsunami risk assessment—The Bridgetown demonstration project, Norwegian Geotechnical Institute, report 20061575-3.

NGI, 2009b. Natural disaster mitigation in the Caribbean; Scenarios for earthquake induced tsunamis. NORSAR July 2007, Norwegian Geotechnical Institute, report 20061575-4.

NGI, 2009c. Natural disaster mitigation in the Caribbean; Regional tsunami exposure assessment. Norwegian Geotechnical Institute, report 20061575-1.

Nikolkina, I., Zahibo, N., Pelinovsky, E., 2010. Tsunami in Guadeloupe (Caribbean Sea). In: Zahibo, N., Pelinovsky, E., Yalciner, A., Titov, V. (Eds.), Proceedings of

Please cite this article as: Harbitz, C.B., et al., Tsunami hazard in the Caribbean: Regional exposure derived from credible worst case scenarios. Continental Shelf Research (2012), doi:10.1016/j.csr.2012.02.006

the Caribbean Waves 2008 Workshop in Guadeloupe December 2008. The Open Oceanography Journal, vol. 4, pp. 44–49.

NOAA, 2008. Tide and currents. 〈http://tidesandcurrents.noaa.gov/〉 (Accessed December 2008 and November 2011).

NOAA/NGDC, 2008. The National Geophysical Data Center tsunami run-up database, 〈www.ngdc.noaa.gov/hazard/tsu.html〉 (Accessed March 1 2008 and November 11 2011).

NTL, 2002. Expert Tsunami Database for the Atlantics. Version 36 of March 15 2002, Tsunami Laboratory, Novosibirsk, Russia 〈http://tsun.sscc.ru/htdbwld/〉.

Okada, Y., 1985. Surface deformation due to shear and tensile faults ina half-space. Bulletin of the Seismological Society of America 74 (4), 1135–1154.

O'Loughlin, K.F., Lander, J.F., 2003. Caribbean Tsunamis, A 500-Year History from 1498–1998, Second edition Springer, The Netherlands 261 pp.

Panagiotopoulos, D.G., 1995. Long-term earthquake prediction in Central America and Caribbean Sea based on the time- and magnitude-predictable model. Bulletin of the Seismological Society of America 85, 1190–1201.

Pararas-Carayannis, G., 2002. Evaluation of the threat of mega-tsunami generation from postulated massive slope failures of island stratovolcanoes on La Palma, Canary Islands, and on the island of Hawaii. Science of Tsunami Hazards 20 (5), 251–277.

Pararas-Carayannis, G., 2004. Volcanic tsunami generating source mechanisms in the Eastern Caribbean region. Science of Tsunami Hazards 22 (2), 74–114.

Parry, M.L., Canziani, O.F., Palutikof, J.P., 2007. Climate Change 2007: Impacts Adaptation and Vulnerability. Contribution of Working Group II to the Fourth Assessment Report of the Intergovernmental Panel on Climate Change. Cambridge University Press, Cambridge.

Parsons, T., Geist, E., 2009. Tsunami probability in the Caribbean Region. Pure and Applied Geophysics 165, 2089–2116.

Pedersen, G., 2001. A Note on Tsunami Generation by Earthquakes. Preprint Series in Applied Mathematics, vol. 4. Department of Mathematics, University of Oslo, Norway.

Pedersen, G., Løvholt, F., 2008. Documentation of a Global Boussinesq Solver. Preprint Series in Applied Mathematics, vol. 1. Dept of Mathematics, University of Oslo, Norway 〈http://www.math.uio.no/eprint/appl_math/2008/appl_2008.html〉.

Pelinovsky, E., Zahibo, N., Dunkley, P., Edmonds, M., Herd, R., Talipova, T., Kozelkov, A., Nikolkina, A., 2004. Tsunami generated by the volcano eruption on July 12–13 2003 at Montserrat Lesser Antilles. Science of Tsunami Hazards 22 (1), 44–57.

Poisson, B., Pedreros, R., 2010. Numerical modelling of historical landslide-generated tsunamis in the French Lesser Antilles. Natural Hazards and Earth System Sciences 10, 1281–1292.

Rabus, B., Eineder, M., Roth, A., Bamler, R., 2003. The shuttle radar topography mission—a new class of digital elevation models acquired by spaceborne radar. Photogrammetric Engineering and Remote Sensing 57, 241–262.

Roger, J., Allgeyer, S., Hébert, H., Baptista, M.A., Loevenbruck, A., Schindelé, F., 2010. The 1755 Lisbon tsunami in Guadeloupe archipelago: Source sensitivity and investigation of resonance effects. In: Zahibo, N., Pelinovsky, E., Yalciner, A., Titov, V. (Eds.), Proceedings of the Caribbean Waves 2008 workshop in Guadeloupe December 2008. The Open Oceanography Journal, vol. 4, pp. 58–70.

Ruff, L., Kanamori, H., 1982. Seismicity and the subduction process. Physics of the Earth and Planetary Interiors 23, 240–252.

Ruff, L.J., 1989. Do trench sediments affect great earthquake occurrence in subduction zones? Pure Appl. Geophys. 129, 263–282. doi:10.1007/BF00874629.

Scheffers, A., Kelletat, D., 2006. New evidence and datings of Holocene paleo-tsunami events in the Caribbean (Barbados St Martin and Anguilla). In: Mercado-Irizarry, A., Liu, P. (Eds.), Caribbean Tsunami Hazard. World Scientific Publishing, pp. 178–202.

Shepherd J.B., Lynch L.L., Tanner J.G., 1995. An earthquake catalogue for the Caribbean. Pan-American Institute of Geography and History, 120 pp.

Sigurdsson, H., Carey, S., Wilson, D., 2006. Debris avalanches formation at Kick'em Jenny submarine volcano. In: Mercado-Irizarry, A., Liu, P. (Eds.), Caribbean Tsunami Hazard. World Scientific Publishing.

Soloviev S.L., Go C.N., 1984. A Catalogue of tsunamis on the western shore of the Pacific Ocean. Russian Academy of Sciences Moscow, 310 pp.

Stein, S., Engeln, J.F., Wiens, D.A., Fujita, K., Speed, R.C., 1982. Subduction seismicity and tectonics in the Lesser Antilles arc. Journal of Geophysical Research 87 (B10), 8642–8664.

Stein, R.S., Okal, E.A., 2007. Ultralong period seismic study of the December 2004 Indian Ocean Earthquake and implications for regional tectonics and the subduction process. Bulletin of the Seismological Society of America 97 (1A), 279–295. doi:10.1785/0120050617 〈http://edokappsrv1:8080/sites/1044/GetFile.aspx?fileId=613676〉.

Tanioka, Y., Satake, K., 1996. Tsunami generation by horizontal displacement of ocean bottom. Geophysical Research Letters 23, 861–864.

Teeuw, R., Rust, D., Solana, C., Dewdney, C., Robertson, R., 2009. Large coastal landslides and tsunami hazard in the Caribbean. EOS Transactions 90 (10), 81–82.

ten Brink, U.S., Danforth, W.W., Polloni, C., Andrews, B., Llanes, P., Smith, S.V., Parker, E., Uozumi, T., 2004. New seafloor map of the Puerto Rico Trench helps assess earthquake and tsunami hazards. EOS 85 (37), 349–354.

ten Brink, U., Geist, E.L., Andrews, B.D., 2006b. Size distribution of submarine landslides and its implication to tsunami hazard in Puerto Rico. Geophysical Research Letters 33 (L11307). doi:10.1029/2006GL026125. 4 pp.

ten Brink, U., Geist, E.L., Lynett, P., Andrews, B., 2006a. Submarine slides north of Puerto Rico and their tsunami potential. In: Mercado-Irizarry, A., Liu, P. (Eds.), Caribbean Tsunami Hazard. World Scientific Publishing, pp. 67–90.

ten Brink, U., Jaffe, B.E., Geist, E.L., 2005. Tsunami hazard potential in the Caribbean USGS-Woods Hole Science Center 〈http://woodshole.er.usgs.gov/projects/2921C4X.pdf〉 (Accessed April 30, 2008).

Vanneste, M., Harbitz, C.B., De Blasio, F.V., Glimsdal, S., Mienert, J., Elverhøi A., 2010. The Hinlopen–Yermak landslide Arctic Ocean—Geomorphology slide dynamics and tsunami simulations. In: Shipp, R.C., Weimer, P., Posamentier, H.W. (Eds.), The Importance of Mass-Transport Deposits in Deepwater Settings. SEPM Special Publication 95.

Villaseñor, A., Engdahl, R., 2007. Systematic relocation of early instrumental seismicity: Earthquakes in the International Seismological Summary for 1960–1963. Bulletin of the Seismological Society of America 97 (6), 1820–1832. doi:10.1785/0120060118.

Wadge, G., Shepherd, J.B., 1984. Segmentation of the Lesser Antilles subduction zone. Earth and Planetary Science Letters 71, 297–304.

Ward, S.N., Day, S., 2001. Cumbre Vieja volcano—potential collapse and tsunami at La Palma, Canary Islands. Geophysical Research Letters 28 (17), 3397–3400.

Wells, D.L., Coppersmith, K.J., 1994. New empirical relationships among magnitude rupture length rupture width rupture area and surface displacement. Bulletin of the Seismological Society of America 84, 974–1002.

Wynn, R., Masson, D., 2003. Canary Islands landslides and tsunami generation: Can we use turbidite deposits to interpret landslide processes. In: Locat, J., Mienert, J. (Eds.), Submarine Mass Movements and Their Consequences. Kluwer Acad., Dordrecht, Netherlands, pp. 325–332.

Zahibo, N., Pelinovsky, E., 2001. Evaluation of tsunami risk in Lesser Antilles. Natural Hazards and Earth System Sciences 3, 221–231.

Zahibo, N., Pelinovsky, E., Kurkin, A., Nikolkina, I., 2008. Tsunami hazard for the French West Indies Lesser Antilles. In: Krishnamurthy, R.R., Glavovic, B.C., Kannen, A., Green, D.R., Ramanathan, A., Han, Z., Tinti, S., Agardy, T. (Eds.), Integrated Coastal Zone Management (ICZM) 800 pp ISBN:978-981-05-8948-6.

Zahibo, N., Pelinovsky, E., Yalciner, A.C., Kurkin, A., Koselkov, A., Zaitsev, A., 2003. The 1867 Virgin Island tsunami. Natural Hazards and Earth System Sciences 3, 367–376.

4. Développements méthodologiques en géophysique de proche surface, appliqués aux risques naturels

Les méthodes géophysiques de proche surface fournissent des distributions de paramètres physiques en profondeur à un point donné (sondage en 1D), le long d'une ligne (section verticale en 2D) ou dans un cube (grille 3D). Les méthodes de prospection géophysique les plus connues, comme la réflexion sismique ou le géoradar (GPR), fournissent des images des interfaces géologiques en profondeur, qui sont relativement faciles à lire par les non-spécialistes. En revanche, l'inversion géophysique, comme par exemple celle des vitesses de propagation sismique ou des résistivités électriques, fournit un modèle continu du sous-sol, souvent représenté par des images colorées moins faciles à comprendre par les non-spécialistes. Les méthodes d'inversion sont mathématiquement complexes et l'interprétation de ces images colorées doit être faite avec un esprit critique, compte tenu des limites propres aux techniques d'investigation et des contraintes liées au calcul d'inversion. Par ailleurs, il est toujours nécessaire de croiser ou comparer les modèles obtenus avec des observations directes du terrain.

De façon générale, chaque géophysicien sait que le choix des méthodes géophysiques utilisées en proche-surface doit être fait en fonction de plusieurs critères tels que le site (profondeur d'investigation souhaitée, résolution souhaitée, étendue de la zone, type de surface, contraintes d'accès au site, contraintes de budget et de temps, etc), le type de matériaux présents (sédiments, socle, etc) et les cibles (géométrie structurelle, fractures ou failles, objets souterrains, etc). Une seule méthode, souvent liée à un paramètre physique, n'est généralement pas suffisante pour converger vers un modèle satisfaisant. Ainsi, la tendance actuelle en géophysique de proche surface est de combiner plusieurs méthodes pour mieux contraindre l'interprétation géologique des modèles calculés. Ceci peut se faire soit directement grâce à une inversion conjointe (deux paramètres sont estimés simultanément au cours de l'inversion, par exemple la résistivité électrique et la polarisation), soit en interprétant conjointement plusieurs paramètres physiques (par exemple la vitesse de propagation sismique et la résistivité électrique).

Mes préoccupations de recherche se situent dans l’amélioration de l'utilisation des méthodes géophysiques pour répondre à des problèmes de société, tels que les risques naturels. C'est un travail que j'ai essentiellement entrepris au NGI et à l'UiO entre 2010 et 2019. Nous parlons beaucoup de l'avantage de l'interdisciplinarité dans le monde de la recherche, mais en pratique cela est souvent chaotique. En tant que géophysicienne dans un institut de géotechnique (le NGI) et surtout lorsque j'y ai dirigé l'équipe de géophysique et télédétection, j'ai essayé de faciliter les échanges entre les géotechniciens, les géophysiciens et les SIGistes. Pareillement, en tant que géophysicienne dans une équipe en cryogénie à l'UiO, j'ai adapté différentes méthodes pour répondre au problème de la quantification de la détérioration du pergélisol, thème de recherche si important à l'heure actuelle chez les glaciologues.

Dans ce chapitre sont reproduits cinq articles où l'on propose de nouvelles méthodologies en utilisant des techniques conventionnelles. Le premier sujet étudié est commun aux trois premiers articles, il s'agit de l'argile sensible qui provoque des glissements de terrain destructeurs en Norvège. Le quatrième article, traite des schistes toxiques, un autre aléa géologique en Norvège, moins spectaculaire mais tout aussi dangereux. Le dernier article dresse un état des lieux des système de surveillance et de préalerte des glissements de terrain, de façon à proposer des procédures adaptées aux différents cas possibles.

- Le premier article est un travail personnel sur l'inversion contrainte lorsque l'on a accès à des informations structurales qui peuvent aider à modéliser les distributions de la résistivité électrique dans le sous-sol.

- Le second est le travail d'un de mes étudiants en thèse, Guillaume Sauvin, qui montre l'avantage de combiner plusieurs méthodes de prospection géophysique pour mieux cartographier les argiles sensibles en profondeur.

- Le troisième est un travail d'un autre étudiant en thèse, Shane Gribben, qui s'efforce de faire le lien entre les paramètres géophysiques mesurés sur le terrain et les propriétés mécaniques de l'argile, essentiel pour comprendre l'aléa de glissement de terrain dans les argiles sensibles.

- Le quatrième article montre l'intérêt d'inversion simultanément la résistivité électrique et la polarisation pour cartographier des couches qui ont des résistivités similaires mais différents niveaux de polarisation. Je l'ai appliqué dans les schistes noirs qui présentent différents niveaux de toxicité.

- Le cinquième article est une collaboration avec un doctorant de l'Université de Lausanne en Suisse. Il montre l'intérêt de combiner différentes méthodes pour la surveillance des glissements de terrain.

4.1 Amélioration de la méthodologie pour inverser la résistivité électrique : l'inversion contrainte

Les argiles déposées en milieu marin dans les régions côtières de la Norvège, de la Suède, de la Russie et du Canada peuvent être soumises à des glissements de terrain. En effet, l'argile dite « rapide » (*quick clay*) ou « argile sensible » est le résultat d'une argile saturée en eau de mer qui s'est retrouvée au-dessus du niveau de la mer depuis la dernière période glaciaire. La percolation de l'eau sous-terraine a pu lessiver le sel présent dans ses pores. Avec moins de liaisons chimiques entre ses minéraux, la structure floculée de l'argile lessivée devient alors instable. Ainsi, l'argile rapide peut se liquéfier lorsqu'elle est affectée par une augmentation de contraintes. Les causes peuvent être un séisme, de l'érosion en pied de pente, des travaux de construction ou l'augmentation de la saturation par l'excès d'eau de pluie. Aussi, la hausse de la fréquence et de l'intensité des phénomènes météorologiques extrêmes, découlant des changements climatiques actuels, amplifie cet aléa. Le phénomène se produit généralement de façon subite, sans signe précurseur, et peut être catastrophique en fonction de la densité de population. Environ 150 personnes sont mortes dans des glissements d'argiles sensibles en Norvège depuis la fin des années 1800. Les dépôts d'argile sensible doivent donc être cartographiés pour limiter leur vulnérabilité. La méthode la plus fiable pour confirmer la présence l'argile sensible dans le sous-sol est la prise d'échantillon avec mesure en laboratoire de la résistance au cisaillement et de l'index de sensibilité. Le forage ne fournit que des points d'information ponctuels et l'interprétation géologique doit ainsi être interpolée entre ces points. Les méthodes géophysiques de proche surface peuvent fournir des informations pour combler ces lacunes. Pendant dans les années 1950, Söderblom (1969) a utilisé une sonde spéciale pour mesurer la résistivité électrique du sol depuis la surface du sol, car cette dernière est inversement proportionnelle à la teneur en sel. Avec mes collègues géotechniciens du NGI, nous avons proposé d'utiliser la tomographie par résistivité électrique (ERT) pour interpoler entre les sondages ponctuels. En effet, les instruments de mesure et les outils d'interprétation se sont considérablement modernisés depuis 1950. Les argiles sensibles sont généralement caractérisées par une résistivité légèrement plus élevée que l'argile non sensible et l'ERT est par conséquent une approche appropriée pour identifier leur occurrence. Cependant, l'expérience montre que l'ERT ne peut pas résoudre le faible contraste en résistivité lorsqu'il se trouve à proximité de fortes anomalies en résistivité telles que l'interface du substratum rocheux. Pour cette raison, j'ai proposé de contraindre l'inversion des données ERT performances de deux logiciels d'inversion, le logiciel commercial Res2Dinv (Loke, 2002) et le logiciel académique BERT2 (Boundless Electrical Resistivity Tomography - Version 2, Günther et al. 2006) pour ce travail. Par rapport aux modèles obtenus sans contraintes, les modèles contraints présentent des contrastes de résistivité plus nets et leurs valeurs de résistivité correspondent mieux aux mesures faites in situ. Dans l'article présenté ici, je propose une façon de contraindre les modèles en utilisant les résultats de quelques forages pour délimiter la profondeur du substratum rocheux. Ce truchement permet de détecter le faible contraste en résistivité entre les argiles sensibles et non sensibles. Nous avons confirmé les modèles par des forages et analyses en laboratoire.

L'application de nouvelles méthodes en résistivité électrique pour cartographier les argiles sensibles a été poursuivie par la suite. Depuis environ 5 ans, l'AEM connait un essor rapide pour les projets de géotechnique en Norvège. En effet, nous avons adapté cette méthode d’investigation initialement utilisée pour des projets miniers profonds, en optimisant la résolution des modèles obtenus de façon à pouvoir les utiliser pour des projets géotechniques (e.g. Anschütz et al., 2017; Skurdal et al., 2019). Ce travail de recherche réalisé au NGI a permis la naissance d'une startup en 2019, Emerald Geomodeling (https://emeraldgeo.com/en/). Et c'est avec fierté mais aussi un peu de nostalgie, que je suis les projets concrétisés par mes anciens étudiants et stagiaires. L'application de l'Intelligence Artificielle (AI) a par ailleurs permis une interprétation plus rapide et plus efficace de la grande quantité de lignes de vol (Lysdahl et al., 2017; Pfaffhuber et al., 2019).

Journal of Applied Geophysics 98 (2013) 280–287

Contents lists available at ScienceDirect

Journal of Applied Geophysics

journal homepage: www.elsevier.com/locate/jappgeo

Mapping of quick clay by electrical resistivity tomography under structural constraint

S. Bazin *, A.A. Pfaffhuber

Norwegian Geotechnical Institute (NGI), Sognsveien 72, NO-0855 Oslo, Norway

ARTICLE INFO

Article history:
Received 11 June 2013
Accepted 7 September 2013
Available online 19 September 2013

Keywords:
ERT
RCPT
Constrained inversion
Quick clay
Case histories

ABSTRACT

Geotechnical projects usually rely on traditional sounding and drilling investigations. Drilling only provides point information and the geology needs to be interpolated between these points. Near surface geophysical methods can provide information to fill those gaps. Norwegian case studies are presented to illustrate how two-dimensional electrical resistivity tomography (ERT) can be used to accurately map the extent of quick clay deposits. Quick clay may be described as highly sensitive marine clay that changes from a relatively stiff condition to a liquid mass when disturbed. Quick clay slides present a geo-hazard and therefore layers of sensitive clay need to be mapped in detail. They are usually characterized by higher resistivity than non-sensitive clay and ERT is therefore a suitable approach to identify their occurrence. However, our experience shows that ERT cannot resolve this small resistivity contrast near large anomalies such as a bedrock interface. For this reason, a constrained inversion of ERT data was applied to delineate quick clay extent both vertically and laterally. As compared to the conventional unconstrained inversions, the constrained inversion models exhibit sharper resistivity contrasts and their resistivity values agree better with *in situ* measurements.

1. Introduction

Clays deposited in marine environments in the coastal regions of Norway, Sweden, and Canada can be subjected to quick clay landslides. Quick clay is the result of the highly water saturated clay being uplifted above sea-level after the last ice age and leached to low salinity by underground fresh water. With less chemical bindings between its minerals, the flocculated structure of the leached clay becomes unstable (*e.g.*, Løken, 1968; Rosenqvist, 1953). Consequently, quick clay can liquefy when affected by a stress increase. Slopes are particularly prone to quick clay landslides, which can be triggered by increased loading on top of the slope, erosion at the foothill, or increased saturation by excess rainwater. Since the late 1800s, about 150 people died in quick clay slides in Norway.

The most reliable method to confirm quick clay is sampling and index testing in the lab to measure the remolded shear strength and sensitivity. However these tests are costly for systematic quick clay hazard zonation. The methodology generally employed in Norway is based on several less costly Rotary Pressure Soundings (RPS) along the slope under investigation. The force needed to push the rod into the ground at a rate of 3 m/min gives a relative indication of the resistance in the soil and therefore an evidence of layers of quick clay in the subsurface. During the 1950s, Söderblom (1969) used a special probe pushed down into the soil to measure clay electrical resistivity. He reported a correlation between clay sensitivity and salt content measured in the lab with *in-situ* resistivity. For that reason, Solberg et al. (2008) suggested that quick clay investigations using RPS can be significantly enhanced with electrical resistivity tomography (ERT) to interpolate between soundings.

Recent studies have illustrated the advantages of geophysical investigations for quick clay with an increasing focus on combined methods (Donohue et al., 2012; Kalscheuer et al., 2013; Malehmir et al., 2013a, 2013b; Sauvin et al., 2013; Shan et al., 2012). Among the geophysical methods, ERT surveying can be efficient for quick clay mapping as it can greatly reduce the numbers of geotechnical soundings. However, an understanding of the limitations of the technique is important in order to fully exploit ERT. Additional information such as seismic reflectors and geotechnical logs are often used to suppress some of the pitfalls in resistivity data during the interpretation process for quick clay zoning. Still, it is less often that the data integration is performed using joint inversions (Kalscheuer et al., 2013; Shan et al., 2012). In this study, ERT and borehole data are integrated to constrain the inversion of the resistivity data. The potential of constrained inversions is examined by forward and inverse modeling on synthetic and real datasets. We run theoretical forward models to show that smoothness-constrained inversion which is standard in this field could induce misleading information for quick clay hazard zonation. Two representative case histories show the efficiency of 2D ERT with limited drilling data. In addition, the two real datasets point out that the standard resistivity threshold usually employed to outline quick clay bodies should be reassessed in the context of each site.

2. Method

ERT is a well established geophysical method and has been used for quick clay investigations because the resistivity of quick-clay (with low

---

* Corresponding author. Tel.: +47 458 06 824.
E-mail address: Sara.Bazin@ngi.no (S. Bazin).

0926-9851/$ – see front matter © 2013 Elsevier B.V. All rights reserved.
http://dx.doi.org/10.1016/j.jappgeo.2013.09.002

salt content in the pore water) is higher compared to unleached clay (with high salt content in the pore water). The resistivity of clay varies between 1 and 100 Ω·m depending on clay content, porosity, dissolved mineral content, and water saturation. Based on 2D ERT imaging, Solberg et al. (2008, 2012) proposed the following ranges of resistivity for Norwegian clays:

- Unleached marine clay: 1–10 Ω·m;
- Leached, possibly quick clay: 10–80/100 Ω·m;
- Dry crust clay, slide deposits, and bedrock: >100 Ω·m.

However, there is no general consensus for these resistivity ranges. Quick clay may occasionally have higher or lower values and this appears to be influenced by local conditions (*e.g.*, Pfaffhuber et al., in press; Rømoen et al., 2010; Solberg et al., 2012).

In most cases, the software employed to invert resistivity data acquired for quick clay studies (Donohue et al., 2012; Lundström et al., 2009; Sauvin et al., 2013; Solberg et al., 2008, 2012) is RES2DINV which is commercialized by Geotomo (Loke, 2013). This inversion program is based on a smoothness-constrained least-squares method (*e.g.*, de Groot-Hedlin and Constable, 1990). The 2D-model used in the forward modeling program consists of a number of rectangular blocks with increasing size towards depth. A standard smoothness-constrained inversion may provide unrealistic resistivity values in the clay layer because it cannot correctly resolve the sharp contrast with the underlying bedrock. We have tested different options in RES2DINV software to overcome this drawback (Loke, 2013). We have then tested an alternative inversion package called BERT2 (Boundless Electrical Resistivity Tomography, Version 2). BERT2 is a part of the open source software library called GIMLi (Generalized Inversion and Modelling Library, www.resisvity.net). The theory and technology of BERT2 are described in Günther et al. (2006). The main difference with RES2DINV is that BERT2 is based on unstructured tetrahedral meshes that can follow any geometry of the subsurface or any structural information. The depth of the modeling domain is automatically determined based on 1D sensitivity estimate and a shading effect permits to conveniently visualize the sensitivity within the model section. This software has the option to easily incorporate *a priori* data to constrain model parameters: a known discontinuity can be set to allow an arbitrary jump in resistivity.

3. Synthetic model of an ERT survey for quick clay mapping

This section introduces a synthetic example that resembles typical Norwegian quick clay sites. The intention is to illustrate the potential of an ERT investigation for quick clay mapping. The synthetic model is displayed in Fig. 1a and contains several geological units with three different resistivities: near the surface lie three conductive bodies of marine clay ($\rho = 3\ \Omega\cdot m$) within a resistive background typical of leached clay ($\rho = 50\ \Omega\cdot m$). The bedrock is made of gneiss ($\rho = 1000\ \Omega\cdot m$) and lies at 35–45 m depths. A deep body of marine clay ($\rho = 3\ \Omega\cdot m$) also lies on top of the bedrock in the center of the model section. A synthetic dataset is obtained by perturbing the theoretical solution of the forward problem with 5% Gaussian noise using RES2DMOD package (Loke, 2002). The noise added to the synthetic values is based on the potentials in order to take into account the sensitivity of the survey geometry (Zhou and Dahlin, 2003). It is computed assuming a multiple gradient array with 81 electrodes at 4 m spacing, which is the survey geometry of a real example that will be presented in the following section. The multiple gradient array has been designed for use in multichannel systems (Dahlin and Zhou, 2006) and is optimal for the instrument we use, a 12-channel Terrameter LS recording unit (ABEM, 2010).

This synthetic dataset is inverted with RES2DINV using standard parameters (L1-norm, model refinement that allows to get model cell size of half the unit electrode spacing, reduction of side blocks effect). The data fit is already good (RMS = 1.6%) after 4 iterations. The theoretical model (Fig. 1b) shows that the lateral limits between the leached clay (resistive) and unleached clay (conductive) are properly identified near the ground surface. The deeper unleached clay is less identified due to poorer resolution at depth. In addition to low resolution at depth, come the well-known principles of equivalence and suppression. The principle of equivalence relates to a layer which has a resistivity lower (here the embedded unleached clay body) than that of the layers above (leached clay) and below (bedrock) it: the thickness and resistivity of the clay unit cannot be derived independently. The principle of suppression relates to a layer which has a resistivity intermediate (here the leached clay unit) between the layer above (clay) and below it (bedrock). Unless such layer is fairly thick, its effect cannot be seen with ERT soundings. Besides, smoothness constrained inversion typically produces smoothly varying resistivity distributions, and so the bases of the geological units are difficult to determine in the synthetic model. As a result, the sharp interface between clay and gneiss is modeled as a 20 m thick gradient in the right part of the model section in Fig. 1b. The bedrock is not even recovered in the left part of the model section because of the equivalence problem introduced by the deep unleached clay body. Such smooth models are not convenient for slope stability calculations, which require a blocky model with the different geological units. To overcome this common problem that occurs in ERT data inversion, several authors have imposed *a priori* constraints to the RES2DINV inversion process. Indeed, this commercial package has the unrivaled advantage that the user can play with many inversion parameters. Solberg et al. (2012) performed inversions with a vertical to horizontal flatness filter ratio of 0.5 to emphasize horizontal structures in the subsurface. Although such technique improves results in the context of quick clay zoning, our synthetic test using the same option is not successful in recovering the interface between the clay and the bedrock (Fig. 1c). The data fit is also good (RMS = 1.5%) after 4 iterations. In the same way, Orlando (2013) overcomes RES2DINV smoothing problem by imposing *a priori* constraints on the boundary and resistivity of known bodies. We tested his technique by fixing the resistivity to 1000 Ω·m in the region below 35 m depth. The damping factor weight for the resistivity of that region is set to 2 such as in Orlando (2013) for this example but several values were tested and led to similar results. The resulting data fit is good (RMS = 1.4%) after 5 iterations. The synthetic model can now recover the base of the deep unleached clay body however the boundary between the clay and the bedrock is still modeled as a gradient instead of a sharp interface (Fig. 1d). This smooth gradient leads to unrealistically high resistivity at the base of the clay unit. For this reason, it is always advised that resistivity models are calibrated with borehole data. Yet, even when borehole investigation exists and is deep enough to provide point wise bedrock depths, it is often difficult to choose which resistivity contour should be used to delineate the bedrock topography. In Fig. 1d, the resistivity contour of 159 Ω·m (between the yellow and brown colors) would probably be the best candidate as a proxy for the clay/bedrock boundary. A way to obtain a more realistic resistivity model is to add controls on the depth to the bedrock in the inversion. As shown by Scott et al. (2000), the RES2DINV model can be divided into two zones, one above and one below a set boundary. This option removes any constrain between the resistivities below and above the boundary. The resistivity values are hence constrained to vary in a smooth manner within each zone. The synthetic solution in Fig. 1e reveals an abrupt transition across the set boundary with a good data fit (RMS = 1.6%) after 4 iterations. However it fails to recover the bedrock resistivity under the deep unleached clay body. The ideal model solution would be a combination between Fig. 1e and d.

This same synthetic dataset is then inverted with BERT2 software using a robust method (L1 norm). The solutions for the synthetic test without and with *a priori* information on the bedrock depth are shown in Fig. 1f and g, respectively. The unconstrained and the constrained models exhibit satisfactory data fits and smoothness levels (RMS = 1.6% and $\chi^2 = 0.80$ after 7 iterations for the unconstrained model, while RMS = 1.1% and $\chi^2 = 0.50$ after 6 iterations for the constrained model). Again, the two tests fail to recover the bedrock resistivity

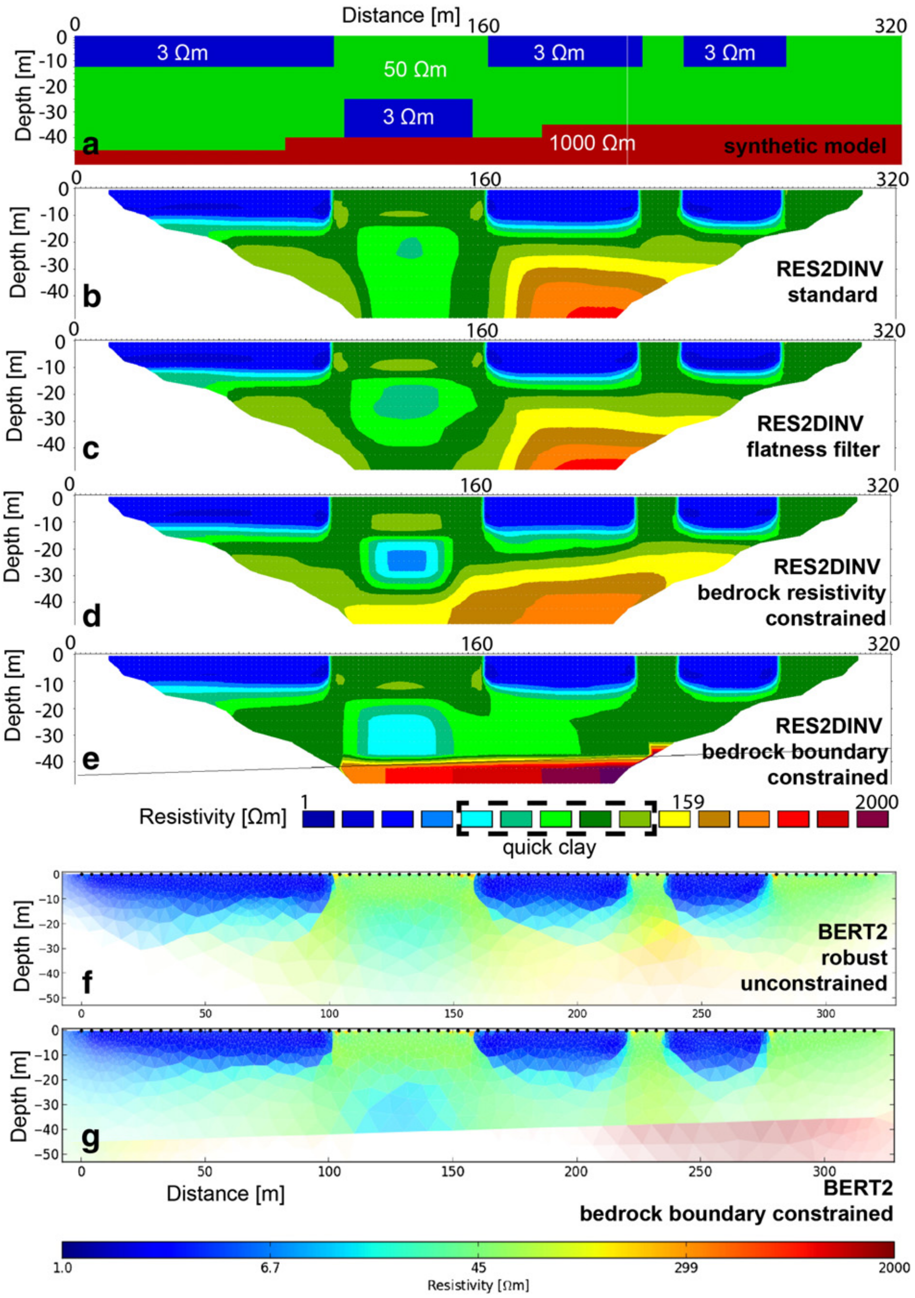

Fig. 1. Synthetic test. a) Synthetic resistivity model. b) Resistivity model inverted with RES2DINV standard options. c) RES2DINV solution with a vertical to horizontal flatness filter ratio of 0.5. d) RES2DINV solution with resistivity constrained at 1000 Ω·m below 35 m depth. e) RES2DINV solution with two independent zones. The boundary is marked as a black line. f) BERT2 solution without *a priori* constraint. g) BERT2 solution with bedrock topography constraint. Color scales are chosen so that unleached clay is blue, leached clay (potentially quick clay) is green and bedrock is red.

under the deep unleached clay body because of lack of data coverage (light shading indicates poor sensitivity). The poor sensitivity between x = 50 and 200 m below 40 m depth illustrates that the depth resolution is not uniform along the 2D profile. As for RES2DINV constrained solution (Fig. 1e) the additional information leads to a better resolution of the resistivities in the different blocks and there is no more vertical gradient within the leached clay unit. The resistivity at the base of the clay unit is now close to the theoretical value of 50 Ω·m and the bedrock resistivity is close to the theoretical value of 1000 Ω·m.

Our synthetic test illustrates the main limitation of the ERT inversion routine and data which is the strong reduction in resolution with depth. This limitation can usually be reduced by the use of model constraint. Indeed, our synthetic test demonstrates that imposing *a priori* constraints on the bedrock has a practical application in quick clay zoning. Still in reality, borehole investigations may supply information on the bedrock depth but not on the bedrock resistivity. In such cases, we therefore favor setting *a priori* constraint on the bedrock topography without imposing a fixed resistivity.

4. Case studies

We present the BERT2 solutions for ERT datasets collected in two Norwegian sites that are prone to quick clay landslides, but with very different settings.

4.1. Smørgrav

We have acquired a new ERT dataset in the already well investigated quick clay site, Smørgrav, located in Southern Norway, 60 km SW of Oslo (Fig. 2). A suite of near surface geophysical methods had already been applied there: seismic refraction and Multichannel Analysis of Surface Waves (MASW), ERT, Electromagnetic (EM-31), Radio-MagnetoTelluric (RMT) and Controlled-Source Radio-MagnetoTelluric CSAMT profiles (*e.g.*, Donohue et al., 2012; Kalscheuer et al., 2013). Bore samples, Rotary Pressure Soundings (RPS), Cone Penetration Testing (CPT), as well as resistivity logging (RCPT) and geochemical lab work had also been performed (Donohue et al., 2012; Pfaffhuber et al., in press). The published results shall briefly be reviewed but details can be found in the listed references. Donohue et al. (2012) describe how the ERT results are compatible with quick clay bodies detected by the RPS where the penetration resistance curves flatten with depth. They report that the quick clay layer could be interpreted as a single layer using only the geotechnical results. However, the geophysical data shows two separated bodies and their thickness varies considerably over the area. Pfaffhuber et al. (in press) discuss the excellent match between the *in situ* resistivities (RCPT logging), resistivity measured on clay samples, and those modeled with ERT. They further compare the different datasets of resistivity measurements with the salt content of the samples confirming the expected correlation. Kalscheuer et al. (2013) describe how the joint inversion of ERT, RMT and CSAMT data yields better constrained resistive structures than individual inversions. The ERT data covers the shallow part of the resistivity model down to a depth of 20 m while the CSAMT and RMT data allow a greater depth of investigation. CSAMT and RMT methods are indeed valuable near rivers where ERT fails to provide sufficient depth coverage (Malehmir et al., 2013a, 2013b). This benchmark site has therefore shown that ERT is a suitable indicator for quick clay if calibrated by conventional site investigation soundings. We shall now use this well understood site to illustrate the benefits of structural constraints in resistivity inversions.

The new ERT profile discussed in the present study is 370 m long with 5 m spacing (Fig. 2). It is twice as long as the ERT profiles discussed in Donohue et al. (2012) therefore allows a better data coverage and depth of investigation. Our interpretation of the resistivity profile inverted with BERT2 (Fig. 3a) agrees with that of Donohue et al. (2012): a thick surface layer of dry crust with resistivity on the order of 100 Ω·m (yellow color in Fig. 3a) in the first 1–5 m. Below 5 m depth, resistivity varies between 1 and 100 Ω·m, which falls in the typical range for Norwegian clay (Solberg et al., 2012). We observe a quick clay body (10–80 Ω·m, light blue to green color in Fig. 3a) in the shallow part of the profile between x = 100 m and 350 m as well as in the deeper part of the profile between x = 0 m and 100 m. Initial interpretation of RPS results suggested that a quick clay layer was continuous between boreholes 505 and 506. As noted before by Donohue et al. (2012), our resistivity model clearly images a layer of unleached clay (1–10 Ω·m, dark blue color in Fig. 3a) between two quick clay bodies. In this area, the bedrock is formed of alum shale and limestone (Fig. 2). Shale resistivities vary from a few Ω·m to tens of Ω·m while limestone has resistivities of a few thousands of Ω·m. Higher resistivity values in the SE part of the ERT profile reveal the presence of limestone. In the NW part the basement is probably made of shale with resistivities quite similar to unleached clay resistivities and therefore the ERT model alone would not be able to detect the basement in the center of the resistivity model.

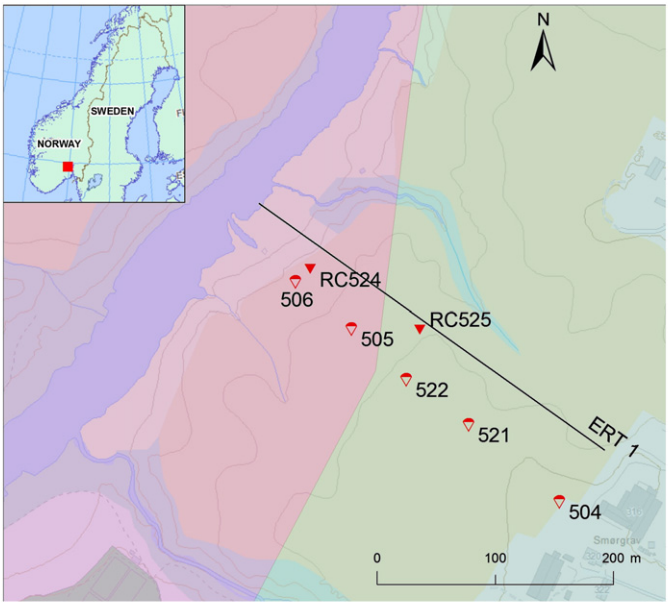

Fig. 2. Location of ERT investigation along with boreholes. The site is located in Smørgrav (inset, southern Norway) and the quick clay risk level is 5 on a scale from 1 to 5. The bedrock is made of shale (indicated as pink color) in the west part and of limestone (indicated as green color) in the east part of the area.

Four RPS investigations provide reliable bedrock depth estimates: these are 7.6 m, 37.0 m, 8.5 m, and 22.2 m in boreholes 504, 505, 521, and 522 respectively. Boreholes 506, 524 and 525 did not reach the bedrock. We can integrate a bedrock interface based on these four depth estimates into the model parameters. BERT2 inversion allows a sharp resistivity contrast along this subsurface interface without imposing a set resistivity value, it is only a structural constraint. The solution of the constrained inversion is shown in Fig. 3b. The unconstrained and the constrained models exhibit comparable data fits and smoothness levels (RMS = 1.5% and $\chi^2 = 1.03$ after 7 iterations for the unconstrained model, while RMS = 1.8% and $\chi^2 = 0.95$ after 7 iterations for the constrained model), and the two models are visually quite similar (Fig. 3a and b). However the additional information leads to a clearer image of the subsurface in relevant areas. The quick clay unit is thicker than expected near borehole 525. The shallow quick clay body that is present in the central part of the section is better delineated: it clearly extends all the way to the bedrock between x = 0 m and 350 m. Besides, a region of high resistivity (above 200 Ω·m, orange color in Fig. 3b) at 10 m depth and near x = 225 m, indicates that the bedrock bulges between boreholes 521 and 522. Although this finding does not have a large impact on safety computation, it clearly illustrates the high resolution of ERT and the benefit of a 2D section *versus* isolated geotechnical boreholes.

Three RCPT logs (Fig. 4) were acquired in the area and can be scrutinized in the context of the established resistivity range for quick clay (10–80 Ω·m as in Solberg et al., 2012). It is worth mentioning that clay can present resistivity higher than 10 Ω·m even though it is not sensitive. It has been shown that quick clay usually occurs at depth greater than 4–6 m as long as dry crust has developed in the top layer (Rosenqvist, 1953). This is observed in all RPS acquired in Smørgrav. For example, RPS505 reveals a thin dry crust layer on top of marine clay, and a quick clay layer from 5 m to 12–13 m depths indicated by the flat penetration resistance curve (lighter colors are used in Fig. 4 to depict quick clay as detected by the RPS). Marine clay is found again from 12–13 m to 37 m, which is when the bedrock is found. This interpretation of the penetration resistance curve is confirmed by lab analyses of samples from the same borehole. If one follows the resistivity threshold of 10 Ω·m (Solberg et al., 2012), RCPT505 would indicate that the quick clay body extends only down to 8 m depth. As other methods have confirmed the presence of quick clay down to 12–13 m depths, the resistivity threshold for quick clay might locally be as low as 5 Ω·m. The RCPT524 was performed in an area interpreted to contain non-quick clay. Yet, the increasing resistivity at the bottom of the RCPT log indicates that the clay is becoming more and more leached at depth. This infers a deep quick clay body as observed between x = 0 and 100 m in our ERT section. In addition, the neighboring RPS506

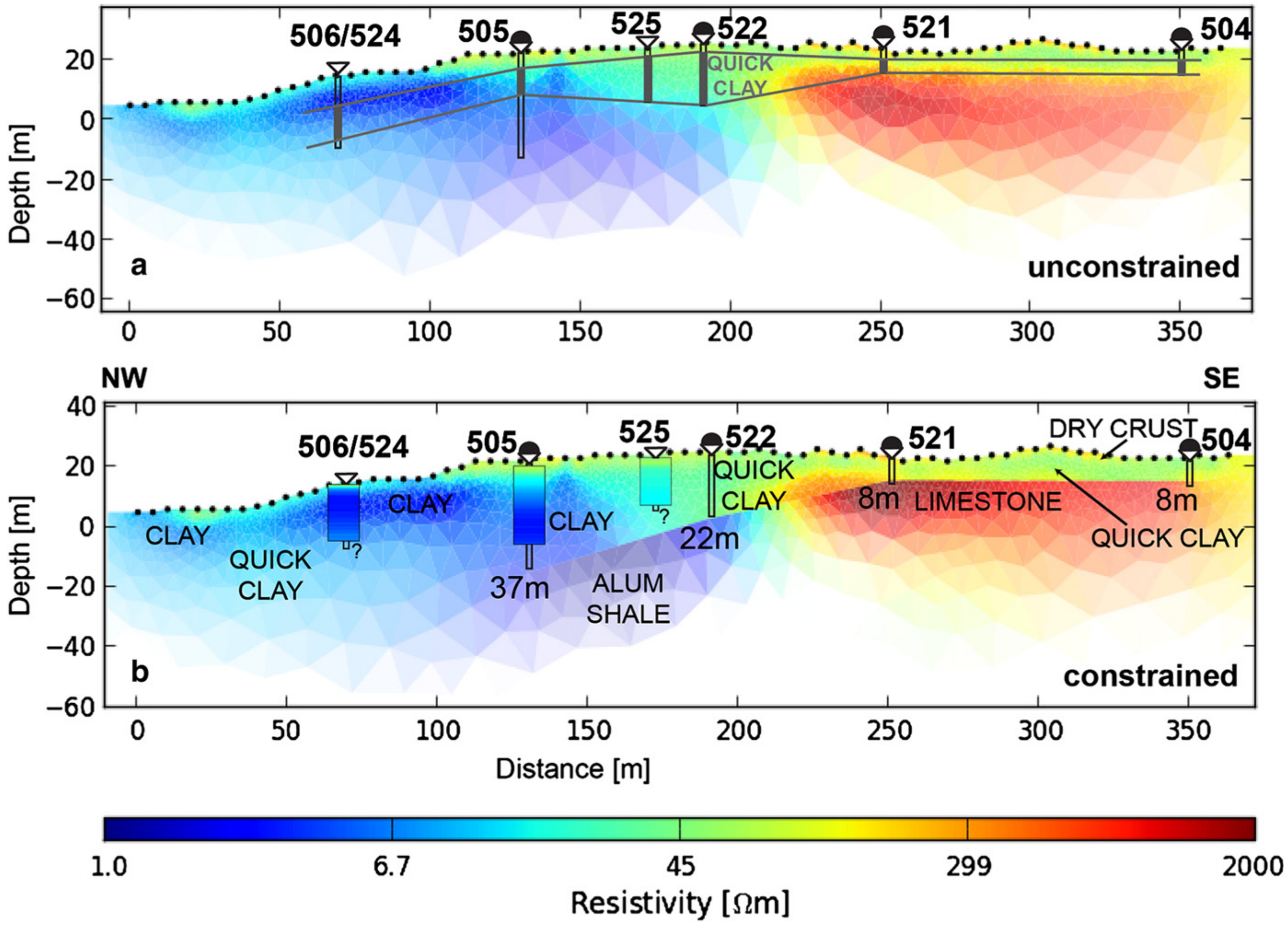

Fig. 3. Real dataset acquired in Smørgrav quick clay site and inverted with BERT2. Color scales are chosen so that unleached clay is blue while leached clay (potentially quick clay) is green, and there is no vertical exaggeration (as for Figs. 6 and 7). a) Resistivity model inverted without *a priori* constraint. The RPS results indicating a single quick clay layer are illustrated as gray filled boxes (modified from Donohue et al., 2012). b) Resistivity model inverted with *a priori* information on the bedrock topography. *In situ* resistivities acquired in RCPT505, RCPT524, and RCPT525 are also displayed with the same logarithmic color scale. A geological interpretation is indicated.

indicates quick clay between 10 and 21 m depth where the sounding stops. This again supports a local resistivity threshold below 10 Ω·m. The RCPT525 shows that the quick clay body extends to the bottom of the sounding. Moreover, we can compare the three sets of *in situ* resistivities with those inverted from the ERT data: three vertical logs are extracted from the constrained BERT2 model and plotted in Fig. 4. Although the two sets of measurements do not agree perfectly, the trends are similar. As often, resistivities measured *in situ* are lower than those inverted with ERT data. Indeed, the RCPT setup has a much smaller influence volume than the ERT array and this can cause discrepancies (*e.g.*, Solberg et al., 2012). In addition, drilling disturbs the clay particles and hence lowers the measured resistivity. The three resistivity logs (RCPT505, RCPT524, RCPT525) are also displayed in logarithmic color scale in Fig. 3b. The agreement between the ERT model and RCPT525 is even better for the constrained inversion than for the unconstrained inversion, as it does not suffer any smoothing artifact from the underlying bedrock.

4.2. Grong

We have reprocessed an ERT dataset acquired in 2009 at a quick clay site close to Grong, located in central Norway (Fig. 5). Four resistivity profiles were acquired on this site but only two of them are discussed here, lines 5 and 7. The electrode spacing is 4 m for both lines. The two unconstrained models obtained with BERT2 are presented in Figs. 6a and 7a. The two resistivity models indicate a rather homogeneous conductive (10 to 100 Ω·m) layer. Line 7 features significant heterogeneities close to the surface. The resistive material outcropping at the top of the slope could be a result of the landscape reshaping into farm fields: boulders had been pushed away by flattening or bulldozing of natural slopes in order to make the farming easier in the area. These resistive zones (red anomalies near the surface in Fig. 7a) will simply be referred as “filling” hereafter. The gradient to high resistivity at the base of the two profiles indicates that the bedrock is just barely reached.

Once more, the resistivity models are improved by constraining the depth to the bedrock using isolated geotechnical boreholes. For both lines, three bedrock depth estimates are taken from nearby boreholes. The bedrock is found at 48 m, 43 m, 28.5 m, 43 m, and 20 m depths in boreholes 104, 115, 125, 126, and 128 respectively (Figs. 6b and 7b). The model solution along line 5 (RMS = 1.7% and $\chi^2 = 1.05$ after 7 iterations for the unconstrained model, while RMS = 1.7% and $\chi^2 = 0.91$ after 8 iterations for the constrained model) is significantly better than along line 7 (RMS = 11.8% and $\chi^2 = 5.8$ after 7 iterations for the unconstrained model, while RMS = 12.0% and $\chi^2 = 2.2$ after 7 iterations for the constrained model). The poor data fit along line 7 is probably due to 3D effects and to the heterogeneity of the resistive filling.

For further interpretation of the resistivity models, resistivity ranges need to be empirically assigned to the different geological units using RPS results and samples collected in the area (Fig. 8). In borehole 104:

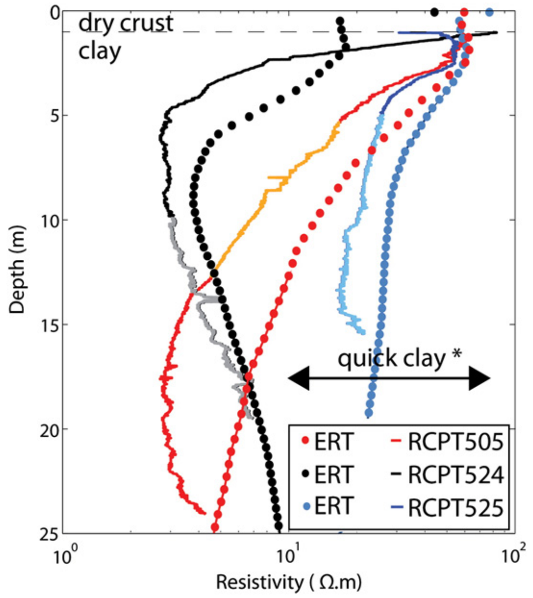

Fig. 4. *In situ* resistivity logs acquired during three RCPT sounding in Smørgrav quick clay site. Lighter colors depict measurements where the clay was characterized as "quick" by RPS investigations. The local quick clay resistivities are slightly lower than the established range of 10–80 Ω·m (*, Solberg et al., 2012). Three vertical logs (dots) extracted from the constrained BERT2 model are plotted for comparison.

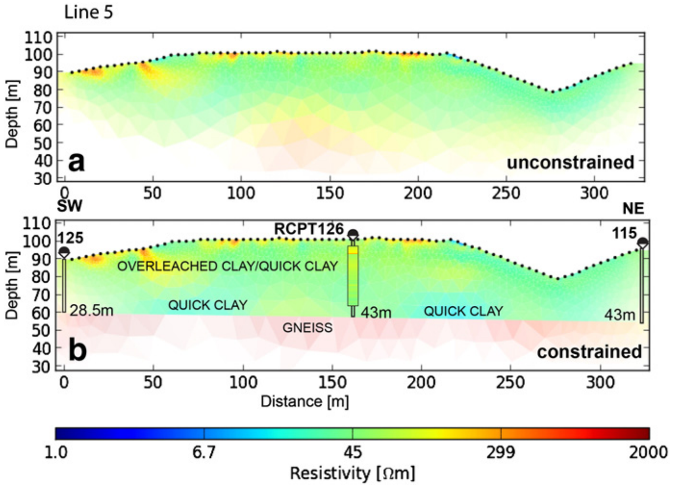

Fig. 6. Real dataset (line 5) acquired in Grong quick clay site and inverted with BERT2 program. Colors are chosen so that quick clay is green. a) Resistivity model inverted without *a priori* constraint. b) Resistivity model inverted with *a priori* information on the bedrock depth. *In situ* resistivities acquired in RCPT126 are also displayed with the same logarithmic color scale. A geological interpretation is indicated.

two samples collected between 9 and 12 m depths are identified as non-quick clay and three samples collected between 18 and 28 m depths are identified as quick clay. In borehole 126: four samples collected between 5 and 18 m depths are identified as non-quick clay and samples collected between 23 and 31 m depths are identified as quick clay. The penetration resistance curves flatten with depth indicating a transition from clay to quick clay near 14 m depth in RPS104 and near 20 m depth in RPS126. Surprisingly, the transition from clay to quick clay is not supported by an increase in the modeled resistivity but rather a small decrease (Figs. 6b and 7b). Resistivity data acquired in the two boreholes using a RCPT probe confirm the modeled resistivity: the two logs (RCPT104 and RCPT126) are displayed in logarithmic color scale and are in perfect match with BERT2 solutions. There is no increase in the modeled resistivity that would imply a usual transition from non-quick clay to quick clay at depth.

Based on the RCPT104 depth-log (Fig. 9), material with resistivity below 90 Ω·m could be assigned as quick clay while materials with resistivity above 90 Ω·m as non-quick clay. However this threshold does not hold in RCPT126, where the transition from non-quick clay to quick clay (near 20 m depth) is found around 65 Ω·m. The boundary between the two layers is difficult to pin down in the model sections. It is not possible to see a distinct transition between non-quick clay and quick clay but rather a gradual change in resistivity. Instead of a two-layer model suggested by the samples and the RPS results, the resistivity profiles indicate pockets of quick clay (green) embedded in clay

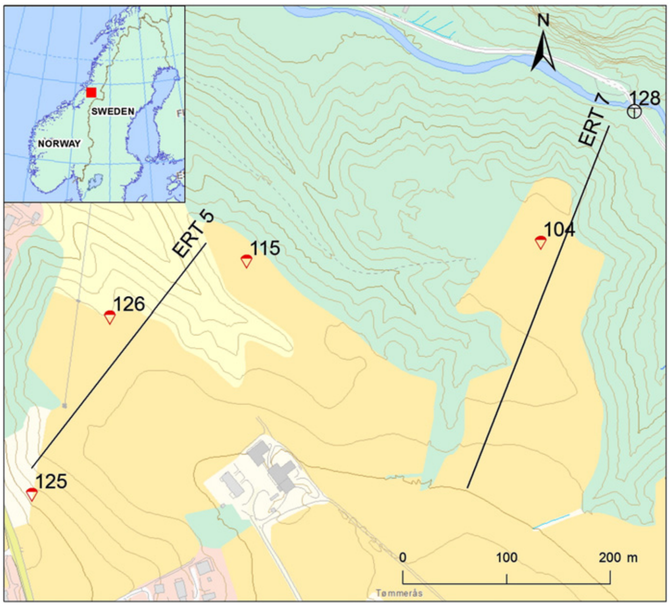

Fig. 5. Location of ERT investigation along with boreholes. The site is located in Gong (inset, central Norway) and the quick clay risk level is 5 on a scale from 1 to 5.

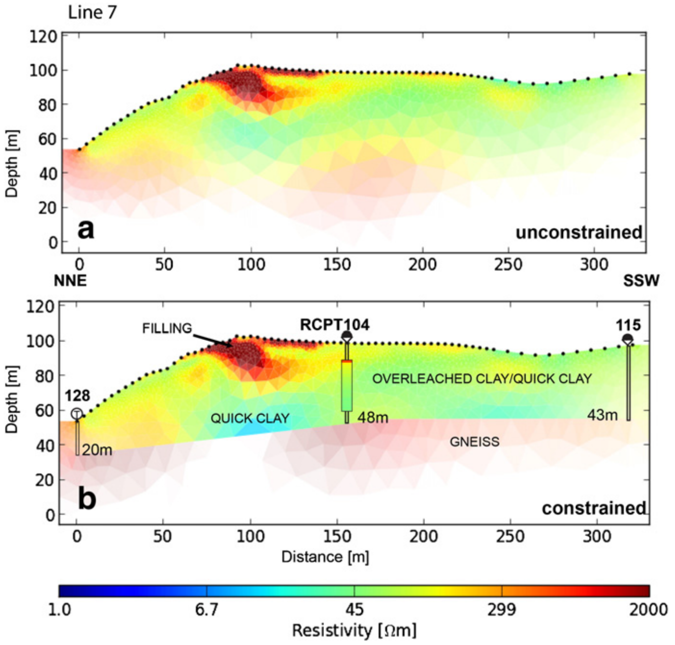

Fig. 7. Real dataset (line 7) acquired in Grong quick clay site and inverted with BERT2 program. Colors are chosen so that quick clay is green. a) Resistivity model inverted without *a priori* constraint. b) Resistivity model inverted with *a priori* information on the bedrock depth. *In situ* resistivities acquired in RCPT104 are also displayed with the same logarithmic color scale. A geological interpretation is indicated.

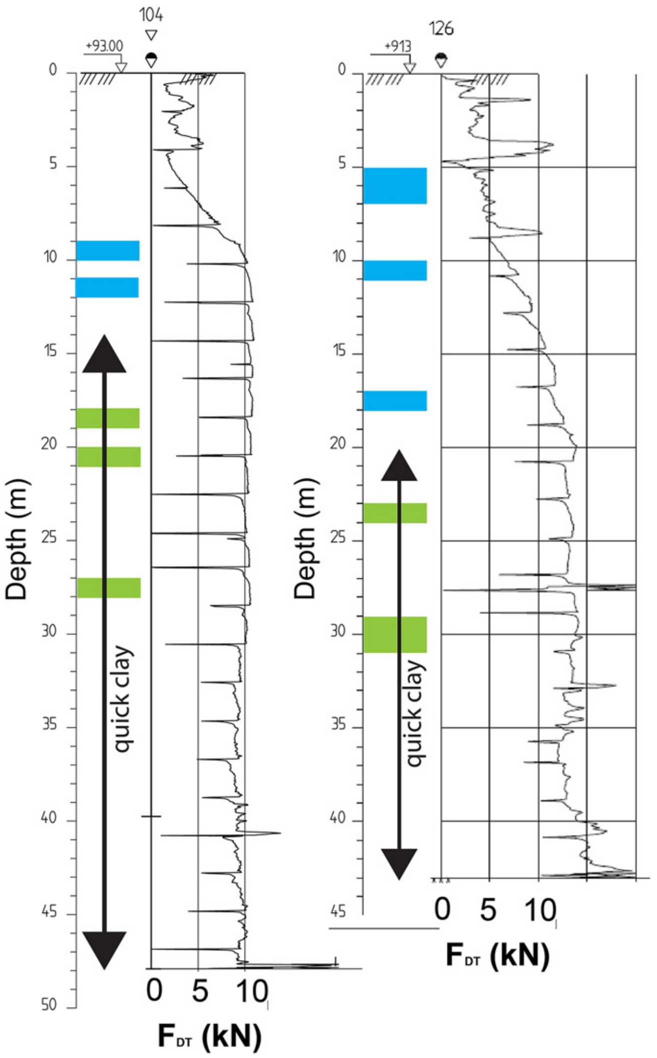

Fig. 8. RPS and collected samples in Grong boreholes 104 and 126. The penetration resistance curves flatten with depth indicating a transition from clay to quick clay near 14 m depth in RPS104 and near 20 m depth in RPS126. Lab analysis on collected samples shows that the shallow samples are non-quick clay (green) while the deeper samples are quick clay (blue).

(yellow). In contrast to the Smørgrav site and to the standard resistivity classification (Solberg et al., 2008, 2012), non-quick clay has a higher resistivity than quick clay in Grong. Moum et al. (1971) had introduced the term "desensitized clay" to describe clay that has been quick at some time in the past but now has reduced sensitivity. The authors suggested that "desensitized clay" can regain a salt content similar to or less than that observed in quick clay. They investigated normal consolidated Norwegian clay in two borings 25 m apart. Both boring exhibited similar low salt content but one boring contained less quick clay than the other one. They showed that leaching of the clay had progressed both from percolating of precipitation from the surface and upwards by ground water gradients from the bedrock. Weathering agents in the leaching water had restabilized the clay structure in part of the quick clay. Weathering and ion exchange can consequently transform the quick clay to non-quick stage, even though the salt content remains low. "Desensitized clay" would result in a higher resistivity than quick clay. A similar phenomenon is also observed after quick clay slides, where the clay that has slided quickly regains its strength thanks to the reorientation of the particles. Here, we propose that the clay with resistivity values above 90 Ω·m has been "desensitized" and does not have a quick behavior anymore. A simple explanation for this

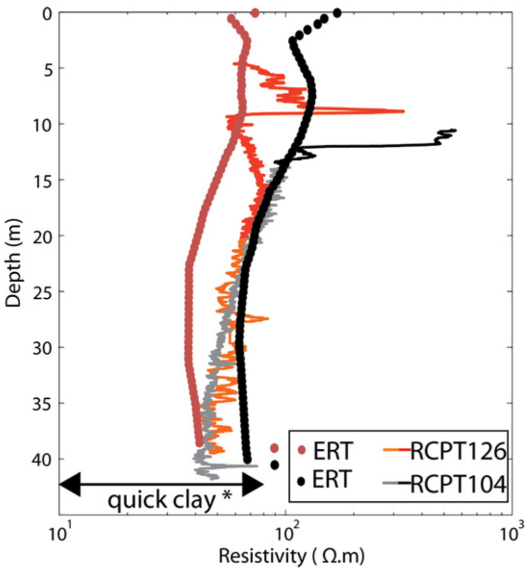

Fig. 9. *In situ* resistivity logs acquired during two RCPT sounding in Grong quick clay site. Lighter colors depict measurements where the clay was characterized as "quick" by RPS investigations and lab analysis of soil samples. The established range of 10–80 Ω·m (*, Solberg et al., 2012) is shown for reference. Two vertical logs (dots) extracted from the constrained BERT2 models are plotted for comparison.

observation may come from the landscape reshaping: the natural ground surface had been scrapped by bulldozers in order to flatten the fields and make the farming easier in the area. This could have favored chemical weathering as well as the reorientation of the clay particles.

At Grong, the bedrock is formed of gneiss which usually has resistivities above 1000 Ω·m (red in the color scale of Figs. 6 and 7). As explained in the synthetic test, the unconstrained models (Figs. 6a and 7a) cannot distinguish between the two alternatives for the lower part of the sediments unit: either the quick clay body extends all the way to the bedrock, or there is a more resistive material that might be clay but could be a different type of sediment. The deepest samples lie more than 10 m above the bedrock and it is therefore unconfirmed whether the quick clay pocket extends down to the bedrock. The constrained inversion canceled the smoothing effect that caused the ambiguity just above the bedrock: the quick clay body occurs to extend all the way to the bedrock. In addition, the constrained models exhibit an even better match with RCPT data than the unconstrained models (Figs. 6b and 7b).

5. Conclusions

This study demonstrates that setting *a priori* constraints is a key to the reduction of the uncertainty inherent in the inversion process of ERT data for quick clay mapping. Based on synthetic tests and representative case studies, a step approach is recommended starting by a systematic use of ERT profiling. Standard processing can provide a first idea of the subsurface and allow to better target geotechnical boreholes and reduce their number. Following the borehole investigation, the bedrock depth can then be used to reprocess the ERT data with a constrained inversion. A bedrock topography derived from seismic methods would provide even better constraints. The arbitrary jump in resistivity at the interface allows the model to invert for the bedrock resistivity. Bedrock can hence be of different nature/resistivity in the final model. Finally, the combined investigation provides a continuous and relatively detailed picture of the subsurface in cost effective manner. Indeed, the two case histories show the efficiency of ERT measurements with limited drilling data. Methods that would allow the depth to the sharp boundary to vary during the inversion may be considered if bedrock topography is not available (Auken and Christiansen, 2004; Loke, 2013; Smith et al., 1999).

The first case history suggests that quick clay investigations using discrete rotary pressure soundings can be significantly enhanced by using ERT profiles to interpolate between soundings. There, a layer of unleached clay wedged between two quick clay bodies was missed by the boreholes. Such a zone is important because it can limit a potential quick clay landslide. This case history portrays the potential risk of missing information between isolated geotechnical boreholes and emphasizes the need for near surface geophysics. In addition, the perfect agreement between *in situ* resistivities with those inverted from the ERT data gives confidence in the method resolution.

The second case history points out that the standard resistivity threshold employed for quick clay zoning should be reassessed with RCPT soundings in the context of each site. The resistivity range for quick clay is influenced by local conditions and there is often an overlap between classes. At Grong, the clay has been so leached that it seems to be "desensitized". The gradual character of the resistivity in the clay sequences makes it difficult to classify a material as quick clay using one threshold value. In addition, ERT often images pockets of non-quick and quick clay, instead of layers of homogeneous material such are required for the calculation of slope stability.

Acknowledgments

Funding was provided by the Research Council of Norway through NGI research programs ICG, SIP12, and SP1. Grong RCPT data is published with the authorization of the Norwegian Water Resources and Energy Directorate (NVE). We acknowledge M. Lanzky Kolstrup for her help on the field in Grong and K. Hetland Ekseth for the maps in Figs. 2 and 5. We thank Guillaume Sauvin for constructive discussions and NGI colleagues for their geotechnical insights. We thank T. Dahlin for providing the gradient array geometry and M.H. Loke for the continuous improvements of Geotomo softwares. We express gratitude to T. Günther for providing BERT2 software and supportive guidance. Constructive comments by Prof. Alireza Malehmir and an anonymous reviewer improved the clarity of our paper.

References

ABEM, 2010. Terrameter LS, Instruction Manual, ABEM100709. 63 (http://abem.se/files/upload/UserGuideTerrameterLS2020100709.pdf).

Auken, E., Christiansen, A.V., 2004. Layered and laterally constrained 2D inversion of resistivity data. Geophysics 69, 752–761.

Dahlin, T., Zhou, B., 2006. Gradient array measurements for multi-channel 2D resistivity imaging. Near Surf. Geophys. 4, 113–123.

De Groot-Hedlin, C., Constable, S.C., 1990. Occam's inversion to generate smooth, two-dimensional models from magnetotelluric data. Geophysics 55, 1613–1624.

Donohue, S., Long, M., O'Connor, P., Helle, T.E., Pfaffhuber, A.A., Rømoen, M., 2012. Multi-method geophysical mapping of quick clay. Near Surf. Geophys. 10, 207–219.

Günther, T., Rücker, C., Spitzer, K., 2006. Three-dimensional modelling and inversion of dc resistivity data incorporating topography — II. Inversion. Geophys. J. Int. 166, 506–517.

Kalscheuer, T., Bastani, M., Donohue, S., Perrsson, L., Pfaffhuber, A.A., Reiser, F., Ren, Z., 2013. Delineation of a quick clay zone at Smørgrav, Norway, with electromagnetic methods under geotechnical constraints. J. Appl. Geophys. 92, 121–136.

Loke, M.H., 2002. RES2DMOD Version 3.01.80. Rapid 2D Resistivity Forward Modeling Using the Finite-difference and Finite Element Methods. Instruction Manual. Geotomo Software. (http://www.geotomosoft.com/).

Loke, M.H., 2013. Tutorial: 2-D and 3-D Electrical Imaging Surveys. Revision Date: 8th March 2013. Geotomo Software. (http://www.geotomosoft.com/).

Løken, T., 1968. Kvikkleiredannelse og kjemisk forvitring i norske leirer. Publication, 75. Norwegian Geotechnical Institute, Oslo, pp. 19–26 (In Norwegian).

Lundström, K., Larsson, R., Dahlin, T., 2009. Mapping of quick clay formations using geotechnical and geophysical methods. Landslides 6, 1–15.

Malehmir, A., Bastani, M., Krawczyk, C., Gurk, M., Ismail, N., Polom, U., Persson, L., 2013a. Geophysical assessment and geotechnical investigation of quick-clay landslides — a Swedish case study. Near Surf. Geophys. 11. http://dx.doi.org/10.3997/1873-0604.2013010.

Malehmir, A., Saleem, M.U., Bastani, M., 2013b. High-resolution reflection seismic investigations of quick-clay and associated formations at a landslide scar in southwest Sweden. J. Appl. Geophys. 92, 84–102.

Moum, J., Løken, T., Torrance, J.K., 1971. A geochemical investigation of the sensitivity of a normally-consolidated clay from Drammen, Norway. Geotechnique 21, 329–340.

Orlando, L., 2013. GPR to constrain ERT data inversion in cavity searching: theoretical and practical applications in archaeology. J. Appl. Geophys. 89, 35–47.

Pfaffhuber, A.A., Bazin, S., Helle, T.E., 2013. An integrated approach to quick-clay mapping based on resistivity measurements and geotechnical investigations. In: L'Heureux, et al. (Ed.), Landslides in Sensitive Clays: From Geosciences to Risk Management. Advances in Natural and Technological Hazards Research, 36. Springer (in press).

Rømoen, M., Pfaffhuber, A.A., Karlsrud, K., Helle, T.E., 2010. Resistivity on marine sediments retrieved from RCPTU-soundings: a Norwegian case study. International Symposium on Cone Penetration Testing. CPT'10, Huntington Beach, CA. Proceedings, 2, pp. 289–296.

Rosenqvist, I.T., 1953. Considerations on the sensitivity of Norwegian clays. Geotechnique 3, 195–200.

Sauvin, G., Lecomte, I., Bazin, S., L'Heureux, J.S., Vanneste, M., Solberg, I.L., Dalsegg, E., 2013. Towards geophysical and geotechnical integration for quick-clay mapping in Norway. Near Surf. Geophys. 11. http://dx.doi.org/10.3997/1873-0604.2012064.

Shan, C., Bastani, M., Malehmir, A., Persson, L., 2012. Correlation between 2D RMT and ERT resistivity models and high-resolution reflection data at a quick clay site in Sweden. European Meeting of Environmental and Engineering Geophysics, Paris, France. Near Surface Geoscience Proceedings.

Smith, T., Hoversten, M., Gasperikova, E., Morrison, F., 1999. Sharp boundary inversion of 2D magnetotelluric data. Geophys. Prospect. 47, 469–486.

Söderblom, R., 1969. Salt in Swedish clays and its importance for quick clay formation. Results from Some Field and Laboratory Studies. Proceedings, 22. Swedish Geotechnical Institute, Stockholm.

Solberg, I.L., Rønning, J.S., Dalsegg, E., Hansen, L., Rokoengen, K., Sandven, R., 2008. Resistivity measurements as a tool for outlining quick-clay extents and valley-fill stratigraphy: a feasibility study from Buvika, Central Norway. Can. Geotech. J. 45, 210–225.

Solberg, I.L., Hansen, L., Rønning, J.S., Haugen, E., Dalsegg, E., Tønnesen, J.F., 2012. Combined geophysical and geotechnical approach to ground investigations and hazard zonation of a quick clay area, Mid Norway. Bull. Eng. Geol. Environ. 71, 119–133.

Zhou, B., Dahlin, T., 2003. Properties and effects of measurement errors on 2D resistivity imaging surveying. Near Surf. Geophys. 1, 105–117.

4.2 Etude multi-disciplinaire pour améliorer l'interprétation géologique dans le contexte de l'argile sensible

Le chapitre précédent a montré que l'ERT est la méthode géophysique à privilégier pour cartographier les argiles sensibles. Cependant, comme pour toute méthode inverse, les résultats de l'inversion sont loin d'être uniques, et même après calibration grâce à des forages, les modèles sont irrémédiablement lisses. Les modèles géophysiques par inversion sont en effet souvent sujets à ambiguïté et nécessitent autant que possible des informations supplémentaires. En Norvège, les campagnes de cartographie d'argiles sensibles sont toujours accompagnées d'un ou plusieurs forages, mais ces derniers sont généralement interprétés par des géotechniciens, alors que les profils géophysiques sont traités par des géophysiciens. Il semblerait naturel de traiter ces deux types de données de façon intégrée car elles se complètent bien. Cependant, les logiciels d’inversion disponibles permettent difficilement l'intégration de différents formats de données. Dans l'article présenté ci-dessous, nous nous sommes attaqués à ces insuffisances. Nous avons aussi testé différents paramètres physiques, tels que les vitesses de propagation sismique. En effets, des auteurs ont montré l'intérêt d'utiliser la vitesse des ondes de cisaillement pour la caractérisation des argiles en Norvège (Long et Donohue, 2007, 2010; L'heureux et Long, 2017).

Dans cet article, nous avons aussi essayé de montrer l'intérêt de réaliser les campagnes de caractérisation en plusieurs étapes, en succédant les forages et les profils géophysiques (Figure 10). La géophysique peut d'être utilisée initialement comme étude pilote pour tester la faisabilité des différentes méthodes dans les conditions du site (ERT, GPR, et ou sismique). Cette pré-étude sert aussi à optimiser les emplacements des forages géotechniques, réduisant ainsi leur coût total. Dans un second temps, la ou les méthodes géophysiques les plus appropriées sont déployées en profils 2D (ou en grille 3D) pour cartographier les propriétés, à la fois latéralement et verticalement. Par la suite, les données géophysiques sont analysées de façon intégrée et de préférence de manière quantitative, pour être directement utilisables par les géotechniciens pour leur calcul de stabilité.

Figure 10: Campagne de géophysique de proche surface (ERT, GPR et sismique) et sondages géotechniques pour caractériser une pente présentant un fort aléa de glissement de terrain à cause de la présence d'une épaisse couche d'argile sensible en bordure de rivière, à Hvittingfoss en Norvège.

Journal of Applied Geophysics 106 (2014) 1–13

Contents lists available at ScienceDirect

Journal of Applied Geophysics

journal homepage: www.elsevier.com/locate/jappgeo

On the integrated use of geophysics for quick-clay mapping: The Hvittingfoss case study, Norway

Guillaume Sauvin [a,b,c,*], Isabelle Lecomte [a,b,c], Sara Bazin [d], Louise Hansen [e], Maarten Vanneste [d], Jean-Sébastien L'Heureux [d]

[a] Oslo University, Box 1072 Blindern, 0316 Oslo, Norway
[b] International Centre for Geohazards (ICG), P.O. Box 3930, N-0806 Oslo, Norway
[c] NORSAR, P.O. Box 53, N-2027 Kjeller, Norway
[d] Norwegian Geotechnical Institute (NGI), P.O. Box 3930, N-0806 Oslo, Norway
[e] Geological Survey of Norway (NGU), Leiv Eirikssons vei 39, N-7491 Trondheim, Norway

ARTICLE INFO

Article history:
Received 6 November 2013
Accepted 3 April 2014
Available online 12 April 2014

Keywords:
Quick clay
Georadar
Resistivity
S-wave seismic reflection
Seismic refraction
Landslide

ABSTRACT

Quick-clay landslides are a known hazard in formerly glaciated coastal areas; hence, large efforts are devoted to map the distribution of quick clays. In this paper, we focus on one particular Norwegian site (Hvittingfoss, 80 km south-west of Oslo), which was remediated against potential landsliding in 2008. A set of geophysical methods including Electrical Resistivity Tomography, P-wave seismic refraction tomography, S-wave seismic reflection profiling, and Ground Penetrating Radar were jointly analysed and complemented with laboratory data and in situ geotechnical measurements (i.e., seismic and resistivity Cone Penetration Testing with pore pressure measurement) in order to improve our geological understanding of the site and to establish a suitable, integrated and multi-disciplinary approach to better map the special extent of the quick-clay zone. The integration of the different geophysical methods and geotechnical measurements allow a more precise imaging and characterisation, both spatially and vertically, of the sedimentary sequences and of the underlying bedrock. The resulting geological model is then populated with the quantitative parameters derived from the geophysical measurements. Considering the inherent complexity of quick-clay mapping, the collected data illustrate the benefit of an integrated approach, and emphasise the need for high resolution, proper imaging, calibration and ultimately joint inversion of the different data.

Contents

1. Introduction . . . 2
2. Geological setting . . . 3
3. Methods . . . 3
    3.1. ERT measurements . . . 3
    3.2. Seismic measurements . . . 3
    3.3. GPR measurements . . . 4
    3.4. Geotechnical investigations . . . 4
4. Results and interpretation . . . 5
    4.1. Geophysical results . . . 5
        4.1.1. Detailed presentation of results . . . 5
        4.1.2. Joint Interpretation and construction of the geological model . . . 6
    4.2. Correlation with geotechnical parameters . . . 8
5. Discussion . . . 9
6. Conclusions . . . 12
Acknowledgements . . . 12
References . . . 12

---

* Corresponding author at: Oslo University, Box 1072 Blindern, 0316 Oslo, Norway. Tel.: +47 96871869.
E-mail addresses: Guillaume.Sauvin@norsar.no (G. Sauvin), Isabelle.Lecomte@norsar.no (I. Lecomte), Sara.Bazin@ngi.no (S. Bazin), Louise.Hansen@ngu.no (L. Hansen), Maarten.Vanneste@ngi.no (M. Vanneste), Jean-Sebastien.LHeureux@ngi.no (J.-S. L'Heureux).

http://dx.doi.org/10.1016/j.jappgeo.2014.04.001

1. Introduction

A good understanding of soil conditions is a prerequisite for the safe development of urban zones. Some of the most densely populated regions of Norway lie within landslide-prone areas related to quick clays. According to Norwegian standards, quick clays have an undrained remoulded shear strength below 0.5 kPa (NGF, 1975). These sediments, originally deposited in a marine environment, emerged following glacio-isostatic rebound and fall of the relative sea level during the Holocene. Long-term leaching of salt due to groundwater flow and percolating surface water affects clay-particle bonding and makes the soil highly susceptible to liquefaction when disturbed (Brand and Brenner, 1981; Mitchell, 1976). Landslides involving quick clays often occur on low-angle slopes and they can be triggered by small perturbations in stress conditions caused by, e.g., human activity or erosion, e.g., Saint-Jean-Vianney in 1971 (Potvin et al., 2001; Tavenas et al., 1971), Rissa in 1978 (Gregersen, 1981; L'Heureux et al., 2012), Finneidfjord in 1996 (Longva et al., 2003), Kattmarka in 2009 (Nordal et al., 2009), and St-Jude in 2010 (Locat et al., 2012). Several factors determine the final extent of a landslide in clay. These include, topography, stratigraphy and the clay sensitivity (i.e., ratio of undrained shear strength in its undisturbed condition s_u and undrained remoulded shear strength s_{ur}, see Table 1 for a list of acronyms) as well as the spatial distribution of the highly sensitive clay deposit or “quick clay” (e.g., L'Heureux, 2012; Mitchell and Markell, 1974; Tavenas et al., 1983). As such, one requires a variety of physical and geotechnical data for a proper landslide hazard mapping in the framework of planning and protection in such areas (Gregersen, 2008).

As of yet, the standard way of investigating quick-clay sites is largely based on the interpolation of results from 1D geotechnical soundings, such as Rotary Pressure Sounding (RPS) or Cone Penetration Testing with pore pressure measurement (CPTU). Often, laboratory measurements, necessary for site-specific slope stability assessment, complement these in situ measurements. The soil properties necessary for determining the safety factor (i.e., density, internal angle of friction, effective cohesion, groundwater table height, undrained shear strength) are then assigned to each layer.

Whereas this traditional approach has been applied in several case studies and engineering projects, it suffers from spatial undersampling of the soil properties, which may have important implications for the project. Indeed, important stratigraphic features are not necessarily properly mapped using solely 1D boreholes. Geophysical techniques, such as P-wave seismic refraction and electric methods, are sometimes used to interpolate/extrapolate between/from geotechnical boreholes, in which the latter serve as the necessary points for ground-truth, validation and calibration (Adamczyk et al., 2013; Calvert and Hyde, 2002; Dahlin et al., 2005; Donohue et al., 2012; Löfroth et al., 2012; Lundström et al., 2009; Rankka et al., 2004; Solberg et al., 2008, 2012). The geophysical methods yield different and complementary properties of the sub-surface. P-wave seismic refraction, for example, allows determining the P-wave velocities as well as depth to bedrock, whereas resistivity (as a pore–water ion-concentration indicator) is a proxy to differentiate leached from unleached clays (Dahlin et al., 2005; Donohue et al., 2012; Lundström et al., 2009; Rankka et al., 2004; Sauvin et al., 2013; Solberg et al., 2012). However, geophysical methods do not directly provide static or geotechnical soil parameters, notwithstanding the fact that the geophysical methods add complementary information, like 2D stratigraphy which is essential in safety assessment, and for which seismic reflection profiling is ideally suited. With respect to elastic properties, shear wave velocity relates to the stiffness of the soil, and is therefore an important geophysical parameters, particularly when vibration is of concern. Shear wave velocities can be determined from either multi-channel analysis of surface wave (Donohue et al., 2012; Sauvin et al., 2013) or shear wave seismic reflection profiling and detailed velocity analysis and modelling (Crow et al., 2011; Hunter et al., 2010; Malehmir et al., 2013a; Polom et al., 2011, 2013; Pugin et al., 2009, 2013).

From our experience, there is no single geophysical method that yields the optimal information to accurately map the distribution of the quick-clay deposits. As a consequence, one should combine a variety of geophysical techniques (e.g., Electrical Resistivity Tomography — ERT; Multi — channel Analysis of Surface Wave; seismic refraction tomography; P- and S-wave seismic reflections; Ground Penetrating Radar — GPR); as well as geotechnical data (in-situ measurements using CPTU, seismic-CPTU and resistivity-CPTU, laboratory tests) to build a consistent geo-model that can be populated with multiple geophysical and geotechnical parameters. As such, quick-clay mapping gradually moves towards 2D or pseudo-3D site characterisation, thus improving the stability assessment of the area. The present study illustrates the benefits of such multi-disciplinary investigation, 1) to derive a consistent high-resolution geological model, as also supported by previous studies (Dahlin et al., 2013; Donohue et al., 2012; Malehmir et al., 2013b; Sauvin et al., 2013), and 2) for a more accurate correlation with relevant geotechnical parameters.

Hvittingfoss, 80 km South-West of Oslo, Southern Norway (Fig. 1), is located within a quick-clay area which has been mapped during the nationwide quick-clay mapping programme, i.e., based on topography and geotechnical soundings. Because of river erosion at the foot of the site, the steep slope and the inhabited area nearby, there was a concern about the soil conditions and stability. Hence, in 2008, following geotechnical investigations, the site was mitigated to prevent potential quick-clay landslide failure (Norwegian Geotechnical Institute, 2008). Geotechnical investigations included geotechnical drillings, mainly RPS, few CPTUs, and laboratory testing on samples extracted from one borehole. The factor of safety was then determined using soil parameters simply linearly interpolated between the boreholes for the interpreted soil units (Fig. 1).

Because of the large amount of geotechnical data, this site was selected as a field laboratory to evaluate the potential of geophysical quick-clay investigations. Geophysical techniques used include ERT, GPR, P-wave seismic refraction tomography, and S-wave seismic reflection data. In order to link the geophysical results to the geotechnical parameters of interest, we also acquired additional resistivity-CPTU and seismic-CPTU data.

The goals of the geophysical investigations are to obtain high-resolution information of the stratigraphy of the sedimentary deposits, to map the depth to bedrock, and to populate the resulting geological model with geotechnical parameters (e.g., determine elastic properties such as S-wave velocity of the sediment as a key proxy for their stiffness). Our objective is to test the benefits of such a multi-disciplinary and multi-method investigation to enhance the geological model that could then be used for stability assessment in quick-clay prone areas.

Table 1
List of acronyms.

Acronym	Meaning
AGC	Automatic Gain Control
CPTU	Cone Penetration Testing with pore pressure measurement
CMP	Common MidPoint
ERT	Electrical Resistivity Tomography
G_{max}	Small-strain shear modulus
GPR	Ground Penetrating Radar
RPS	Rotary Pressure Sounding
Vp	P-wave velocity
Vs	S-wave velocity
q_t	Corrected CPTU tip resistance
q_n	Net CPTU tip resistance
s_u	Undrained shear strength
s_{ur}	Undrained remoulded shear strength
ρ	Density

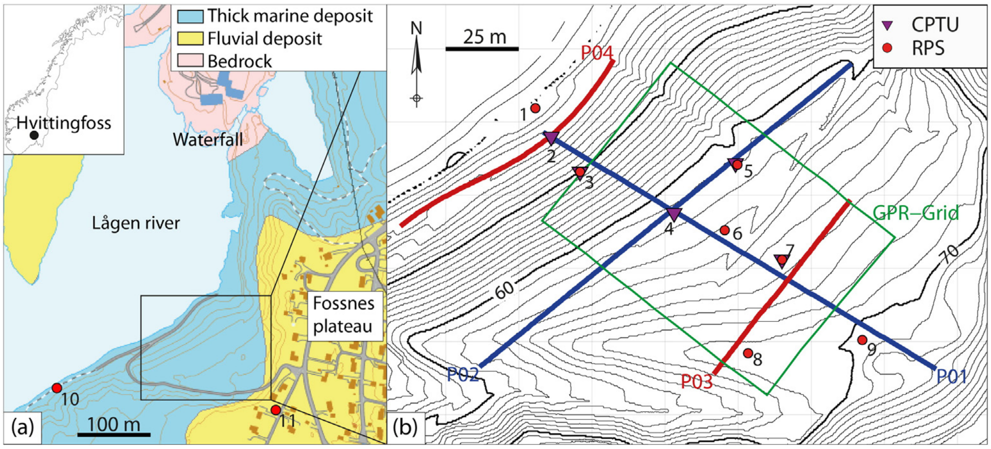

Fig. 1. Map showing the a) quaternary geology of the Hvittingfoss area and b) the topography of the investigation site, with location of geophysical measurements, blue lines for ERT and P-wave seismic, red and blue for S-wave seismic and green rectangle for GPR, as well as location of geotechnical data, red dots for Rotary Pressure Soundings and purple triangles for CPTU tests. (For interpretation of the references to colour in this figure legend, the reader is referred to the web version of this article.)

2. Geological setting

Bedrock around Hvittingfoss is dominated by syenite, quartz–syenite, romb porphyry, monzonite, and quartz–monzonite (Dahl et al., 1997). It crops out locally, to the waterfall just north of the investigated site and on Fossness plateau north-east of the site (Fig. 1). Geotechnical soundings in Hvittingfoss area show an up to 30-m thick valley-filled by sand and gravel “alluvium” lying on top of glacio-marine clays which in turns cover the bedrock (boreholes 9 and 11; Fig. 1; Norwegian Geotechnical Institute, 2008).

The top alluvial deposit is a sand and gravel unit, which is thickest on the Fossness plateau (Norwegian Geotechnical Institute, 2008) and thins both northwards and southwards across the investigated area. It overlays thick glacio-marine sediments, composed of silty clay with some thin layers of sand and gravel. These were deposited as the glacier ice was retreating in the Lågen valley (Dahl et al., 1997). Following deglaciation, the area was subject to glacio-isostatic rebound, causing a drop of relative sea level, thus locally exposing glacio-marine sediments above the present sea level and thereby to fresh groundwater leaching.

Laboratory measurements on samples from borehole 3 (Fig. 1) indicate that the clay fraction in the glacio-marine deposits ranges from 18 to 30%, and the plasticity index is lower than 10–15% down to 12 m depth. Layers of silt, sand, and gravel lie underneath (Norwegian Geotechnical Institute, 2008). Part of the glacio-marine deposit was interpreted as quick clay as the penetration resistance of the RPS is nearly constant with depth, indicating that the soil is extremely soft (Rygg, 1988). The sensitivity of the clay measured from the fall cone test on samples exceeds 200 in borehole 3 and 500 in borehole 10 located further south. These values are well above the lower-bound value of 30 used in Norway, and thus the soils are classified as quick clays (Fig. 1).

Due to the active erosion effect of the river to the west, stability has been gradually decreasing, endangering the housing area to the east. For that reason, the site was mitigated in 2008 by moving parts of the soil from the upper part of the slope downwards to the lower part, and erosion from the river was prevented by adding boulders at the bottom of the slope.

3. Methods

In this section, we describe the applied geophysical methods (ERT, GPR, P- and S-seismics, as well as resistivity-CPTU and seismic-CPTU), including data acquisition details and processing steps. We also present the existing geotechnical data used in our study.

3.1. ERT measurements

We used results from previous geotechnical investigations (Norwegian Geotechnical Institute, 2008), to define a preliminary simple earth resistivity model, which we used in forward modelling in order to design a proper data acquisition. We subsequently collected 2D resistivity measurements using a Terrameter LS (ABEM) with both gradient and dipole–dipole array configurations. Acquisition was performed in roll-along mode with 64 electrodes with 2 m spacing, resulting in two 160-m long profiles (Fig. 1). Full waveform data indicate that signal-to-noise ratio is high, and virtually no data had to be filtered out prior to inversion. 2D models of the earth subsurface resistivity were inverted from apparent resistivity using RES2DINV software (Loke, 2010) which uses the smoothness-constrained Gauss–Newton least-square inversion technique (Sasaki, 1992). Inversions converged to RMS errors of less than 5% after 7 iterations. Since both gradient and dipole–dipole array configurations give similar resistivity model, and because of its lower sensitivity to noise (Dahlin and Zhou, 2006), we only present the results from inversion of gradient array configuration here. The 2D ERT profiles were then combined to generate pseudo-3D displays.

There is a rapid and sharp resistivity change across the boundary between the fluvial (sand, above) and the fjord (clay, below) deposits. In order to better constrain the resistivity inversion within the clay deposits, the stratigraphic information from GPR and S-wave seismic reflection was used as inversion constraints for ERT, i.e., the subsurface in the inversion model can be divided into zones, one above and one below the interpreted interface between the coarse grained material cover and the underlying clay deposit. Within each unit, the resistivity values are constrained to vary smoothly, but an abrupt transition across the zone boundary is allowed by removing all constraints between the resistivity values below and above the zone boundary (Smith et al., 1999). Similar constrained inversion presented by Bazin and Pfaffhuber (2013) for quick-clay mapping gave promising results.

3.2. Seismic measurements

Both P- and S-wave seismic measurements were conducted. The P-wave seismic acquisition was initially designed for seismic refraction tomography alone. Acquisition was performed using 24 4.5 Hz geophones, a Geode (Geometrics) seismograph and a 5 kg sledgehammer as seismic source. Receivers and source spacing is 4 m, with shots in between receiver stations. The recording length is 2 s with a time sampling of 0.25 ms. The high quality of the seismic data (Fig. 2) allowed for an accurate picking of the P-wave. The S-wave seismic acquisition was designed for seismic reflection imaging, using three Geode seismographs with a seismic horizontal vibrator unit developed by Polom et al. (2011) as shear-wave source and 71 horizontal geophones (12 Hz natural frequency). Due to the field conditions along profiles 1 to 3 (high thick grass), geophones were planted, whereas a landstreamer (Krawczyk et al., 2013; Malehmir et al., 2013a) was used as a test on the gravel path for profile 4 (Fig. 3). Source and receiver spacing is 1 m with shots located at receiver stations, and "SH-mode" oriented, i.e., with vibration and recording oriented horizontally and perpendicularly to the profile. The recording length is 11 s and time sampling 1 ms, with a 10 s long 20–160 Hz up-sweep as source signal.

Picking of first-arrival travel times for seismic refraction tomography was performed semi-automatically on raw data and the inversion of the travel times was performed. The inversion algorithm adopts an iterative adaptation (Simultaneous Iterative Reconstruction Technique, Nolet, 1987), and the final result is cross-checked by modelling with an eikonal solver (Vidale, 1988).

The S-wave seismic data processing is summarised in Table 2. A similar processing was applied to an S-wave data set acquired in Trondheim Harbour and discussed in details in Polom et al. (2010) and Sauvin (2009). We refer to these documents for further information on the different processing steps. The overall seismic data quality is good, but strong surface wave energy hinders some of the useful reflection energy (Fig. 4).

Fig. 3. Pictures depicting S-wave seismic reflection acquisition using wheelbarrow mounted horizontal seismic vibrator with landstreamer along the gravel path for profile 4.

3.3. GPR measurements

A Ramac (Malå) non-shielded 50-MHz rough-terrain antenna was used for profiling and standard Ramac 50-MHz non-shielded antennas for Common MidPoint (CMP) measurements. The GPR grid covers 100 m by 70 m with 1 m spacing between in-lines and cross-lines, which gives a total of 172 2D profiles. In order to obtain a representative velocity field, CMP acquisition was performed at every 10th grid point (10-m spacing) in both in-line and cross-line directions (Fig. 1).

The fact that the pseudo-3D GPR cube is built up from several 2D near-zero-offset in-lines and cross-lines implies that some editing of each individual profile was necessary. First, we applied a static shift to each profile, in order to correctly position the zero time. To validate static shift value, we iteratively generated a cube from these profiles, inspect linear anomalies on time slices and adjust the static shifts. Then, standard dewow filtering (removal of low frequency noise related to the antenna characteristics), DC-shift subtraction and gain corrections as well as careful background noise removal were applied to all 2D profiles. Because of the topographic conditions, and since hip-chain was used for distance measurements between the grid point poles, the profile positions were iteratively verified by generating cubes from the 2D lines and shifting the anomalous ones from inspecting time slices. Finally, the resulting cube is depth converted using the velocity model extracted from diffraction hyperbolae and velocity analyses on CMP gathers.

3.4. Geotechnical investigations

Ground conditions in the study areas were previously investigated by different consulting companies (Norwegian Geotechnical Institute, 2008). The methods included 54 mm piston samplers (with laboratory testing), Rotary Pressure Sounding, CPTU, Total Sounding, Rotary Sounding and Vane Shear Tests. For the present study, we collected additional in situ data from resistivity-CPTU (3 locations) and seismic-CPTU (1 location) in order to link laboratory measurements with in situ measurements. One has to keep in mind that soft layers that are 75 to 100 mm thick can be fully detected by the cone resistance of the CPTU, whereas stiff layers may need to be as thick as 750 mm or more for the cone resistance to reach its full value (Lunne et al., 1997).

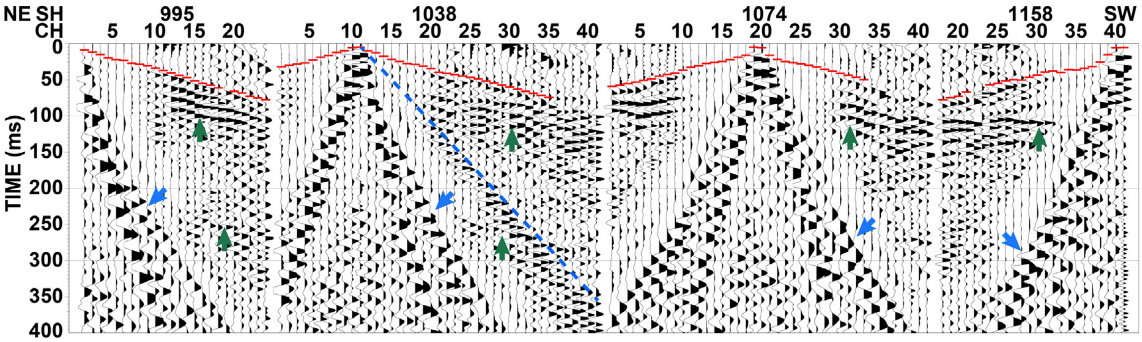

Fig. 2. Selected P-wave seismic pre-processed record examples of profile 2. X axis corresponds to shot and channel number (4-m spacing). The dashed blue lines correspond to the theoretical gradient of 333 m/s air wave velocity, which is not much recorded. The first arrival corresponding to the refracted waves is also displayed on these records (red picks). The blue arrows point at surface-wave energy and the green ones point at reflected energy. For the sake of the display, a 350 ms AGC is applied. (For interpretation of the references to colour in this figure legend, the reader is referred to the web version of this article.)

Table 2
Processing flowchart and corresponding parameters for S-wave seismic reflection data.

Processing step	Parameters
SEG-2	SEG-2 file import
Cross-correlation	Signal contraction: cross-correlation with pilot sweep
Subtractive stack	Sum of correlated records with opposite sweep–signal polarities
Geometry settings	CMP geometry binning
Elevation statics	Source/receiver elevation–statics corrections for P01 only
Amplitude recovery	Amplitude preserving analytical spherical–divergence correction of t^2
Deconvolution	Surface-consistent predictive deconvolution with 70–90 ms operator length, prediction lag of 5 ms and prewhitening of 0.1%
Time variant BP filter	Time-variant bandpass filter (zero-phase Ormsby filter), from 35–40–155–160 to 20–25–115–120 Hz
FK filtering	Dip filter varying along the profile to further suppress Love-wave energy
Mutes	Top and bottom mutes
Residual statics/velocity analysis	Velocity analysis (every 10 m) performed recursively with residual–statics corrections
NMO	Normal–move out corrections using best fitting velocity field with 25% stretch mute
Stacking	CMP gather stacking
Time-to-depth conversion	Time-to-depth conversion using smoothed velocity field

4. Results and interpretation

In this section, we present the results and interpretation from the integration of geophysical, geotechnical and geological data at the Hvittingfoss test site. We furthermore, assess how geophysical data can contribute to provide a more complete geological model, from a stratigraphic and quantitative point of view.

4.1. Geophysical results

4.1.1. Detailed presentation of results

Figs. 5 and 6 show the results of (a) ERT inversion together with (b) GPR profiles, (c) S-wave interval velocities from reflection seismic velocity analysis, (d) the S-wave seismic reflection section, and (e) P-wave velocities from seismic refraction tomography, for profiles 1 and 2, respectively.

The results of resistivity imaging are spatially consistent (Figs. 5a and 6a) and mismatch at intersection point could be explained by 3D effects or equivalence phenomena. Similarly, P- and S-wave velocity fields derived from P-wave seismic refraction tomography and S-wave seismic reflection velocity analyses are in good agreements and present generally increasing profiles with depth (Figs. 5c, e and 6c, e). Since the GPR depth penetration is limited due to the strong attenuation of the GPR signal in clay (Figs. 5b and 6b), the GPR data are mainly used for a detailed stratigraphic analysis of the upper, coarser material. The high-resolution of the S-wave seismic data (theoretical minimal vertical resolution of 0.4 m) allows for establishing a detailed geological interpretation at depth (Figs. 5d and 6d) and detailed features can be extracted within some of the identified units.

The anthropogenic fill (above the blue line in Fig. 5, and referred as unit D in Figs. 7, 8 and 9) has very high resistivity values (typically above 500 Ω·m), as well as low P- and S-wave velocities (less than 250 m/s and 150 m/s, respectively). The GPR data lack a coherent reflection pattern within the fill but its base (or top of the original topography) coincides with a strong reflection (Fig. 5b). Upslope from this manmade fill, there is a reasonably consistent upper layer (referred as unit C) with high resistivity (values above 300 Ω·m), ranging in depth from 2 m in the middle of the profiles to about 15 m towards the eastern end of profile 1. P- and S-wave velocities within this layer are continuous and range from 250 to 750 m/s, and 150 to 180 m/s, respectively. GPR reflections are continuous over short distances and the S-wave seismic reflection pattern is horizontally stratified with medium continuity. Underneath this upper soil units, resistivity decreases rapidly to low values (between 20 and 100 Ω·m) whereas P- and S-wave velocities increase from 1250 to 1750 m/s and 200 to 300 m/s, respectively. Both resistivity and seismic velocity results reveal some lateral variations within this layer (referred as subunits B3 and B4). The GPR signal is highly attenuated, showing only few very-low-amplitude reflectors. The S-wave seismic reflection pattern is horizontally stratified with fairly good continuity. Underneath (subunits B1 and B2), only S-wave velocities from seismic reflection data could be retrieved since the penetration depth of the seismic refraction and ERT data is not sufficient. S-wave velocity ranges from 250 to 380 m/s down to around 20 m elevation (around 40 m below the surface), and the reflection pattern is generally horizontally stratified

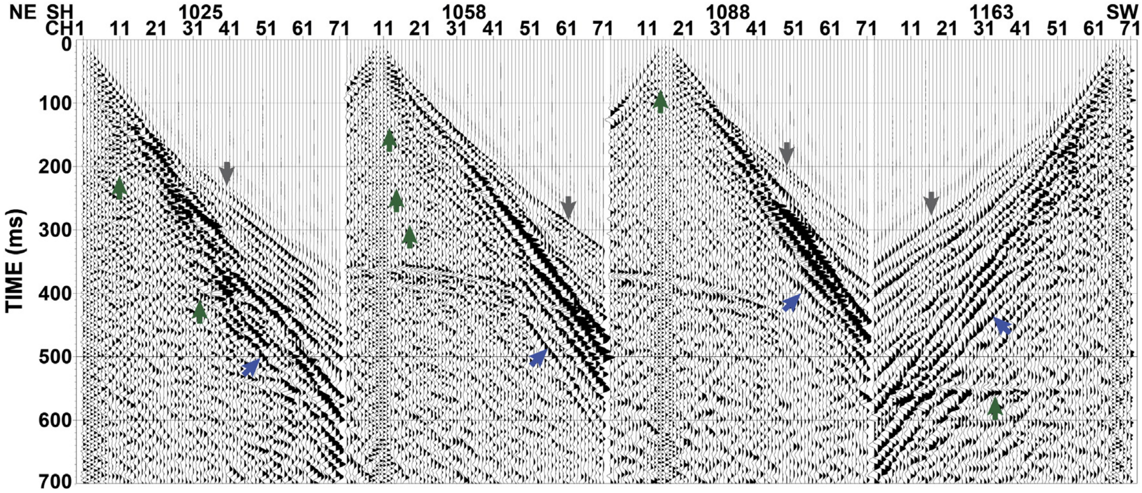

Fig. 4. Selected S-wave seismic pre-processed record examples of profile 2. X axis corresponds to shot and channel number (2-m spacing). Strong surface-wave energy was recorded (blue arrows) and hides some of the important reflections (green arrows). The grey arrows point at refracted wave energy. (For interpretation of the references to colour in this figure legend, the reader is referred to the web version of this article.)

Table 3
Table summarising the empirical factor for net tip resistance — Vs correlation, $q_n = a^*Vs + b$, for each CPTU along seismic lines and every layers. The last column indicates the correlation parameters for all the CPTU and all the layers together.

	CPTU-02		CPTU-109		RCPTU-02		RCPTU-03		All	
	a	b	a	b	a	b	a	b	a	b
B4-MB3	▨	▨	2	424.6	3.36	336.6	4.94	85.9	3.37	225.06
MB3-B3	0.9	800	-7.7	3162	-9.5	3501	-2.2	1813		
B3-B2	21.3	-4022	35.2	-8837	22.4	-4749	20	-4185		

with alternating low and high amplitudes. Below (unit A), the S-wave velocities exceed 400 m/s and the top is clearly delineated by a continuous high-amplitude reflection. S-wave velocity values derived from seismic reflection and seismic-CPTU correlate well (Figs. 5c and 6c), and, even if generally higher, resistivity values from ERT measurements and resistivity-CPTU are in good agreement as well (Figs. 5a and 6a), confirming the models derived from surface measurements.

4.1.2. Joint Interpretation and construction of the geological model

The benefit of a multidisciplinary approach lies in the quantified joint interpretation of different vintages of geophysical and geotechnical data. For Hvittingfoss, we present the interpretation along the S-wave seismic reflection profile 2 in Fig. 7, in a pseudo-3D fence of the S-wave seismic reflection in Fig. 8, and the properties of each interpreted unit are summarised in Fig. 9.

All profiles were interpreted correlating the picked events from one profile to another at the crossing points in the depth domain and matching each profile to the geotechnical data. Four main stratigraphic units (A to D, from bottom to top) are identified by the internal reflection patterns and reflection amplitudes in the seismic and GPR reflection sections as well as variations in resistivity, P- and S-wave velocities. Unit A is interpreted as bedrock, units B and C as fjord and fluviodeltaic deposits, and unit D as anthropogenic fill. Unit B can be further divided into four subunits (B1–B4), having slightly different reflection patterns. The units make up a typical fjord-fill succession above bedrock which corresponds to the model, proposed by, e.g., Corner (2006).

The anthropogenic fill, unit D, is known from the pre-existing topography and is characterised by very high resistivity as well as low P- and S-wave velocities. Unit C, interpreted as fluviodeltaic deposit, is characterised by high resistivity values, low P- and S-wave velocities, horizontally-stratified S-wave seismic reflection pattern and continuous to semi-continuous GPR reflections. RPS drilling resistance is typically high (up to 15 kN), but varies with depth. This unit is mainly composed of coarse-grained material (sand and gravel), with some thin clay layers. Distinct GPR reflections with noticeable amplitude variations within the sand deposit suggest spatial heterogeneity. Highly-attenuated zones along the profiles correspond to sediments with higher clay/silt content (Figs. 5b and 6b). The fjord deposit (unit B) is further divided in subunits according to changes in S-wave seismic reflection patterns, RPS drilling resistance variations and

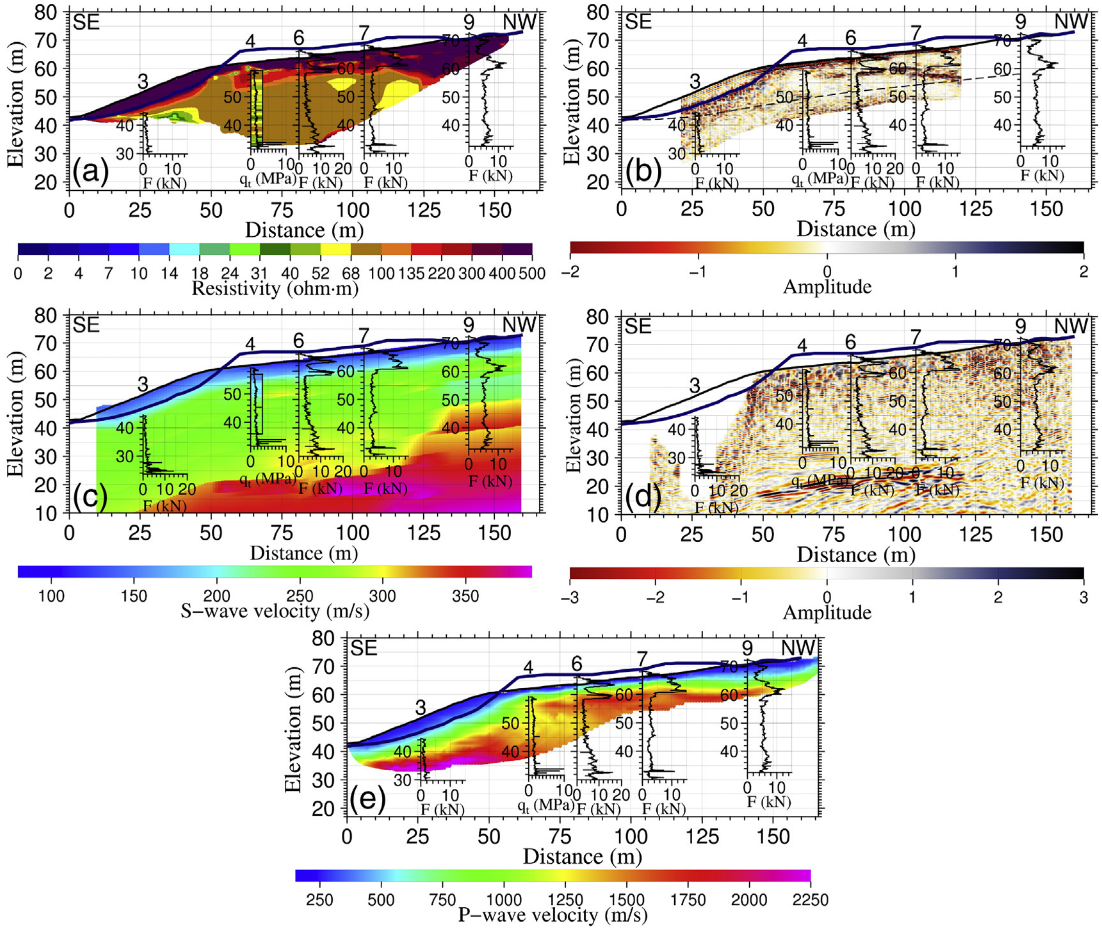

Fig. 5. Profile 1, a) inverted resistivity from gradient array, b) GPR profile extract from the depth converted GPR cube superimposed, c) S-wave interval velocity, d) depth converted S-wave seismic reflection, and e) P-wave velocity from seismic refraction tomography. One can notice the strong GPR reflection between the old (blue line) and new (black line) topography. Resistivity values as well as S-wave velocity from borehole 4 are also depicted with the same colour scale as for ERT and S-wave seismic respectively. The water table interpreted from GPR, seismic refraction and piezometer is also displayed in dashed line. (For interpretation of the references to colour in this figure legend, the reader is referred to the web version of this article.)

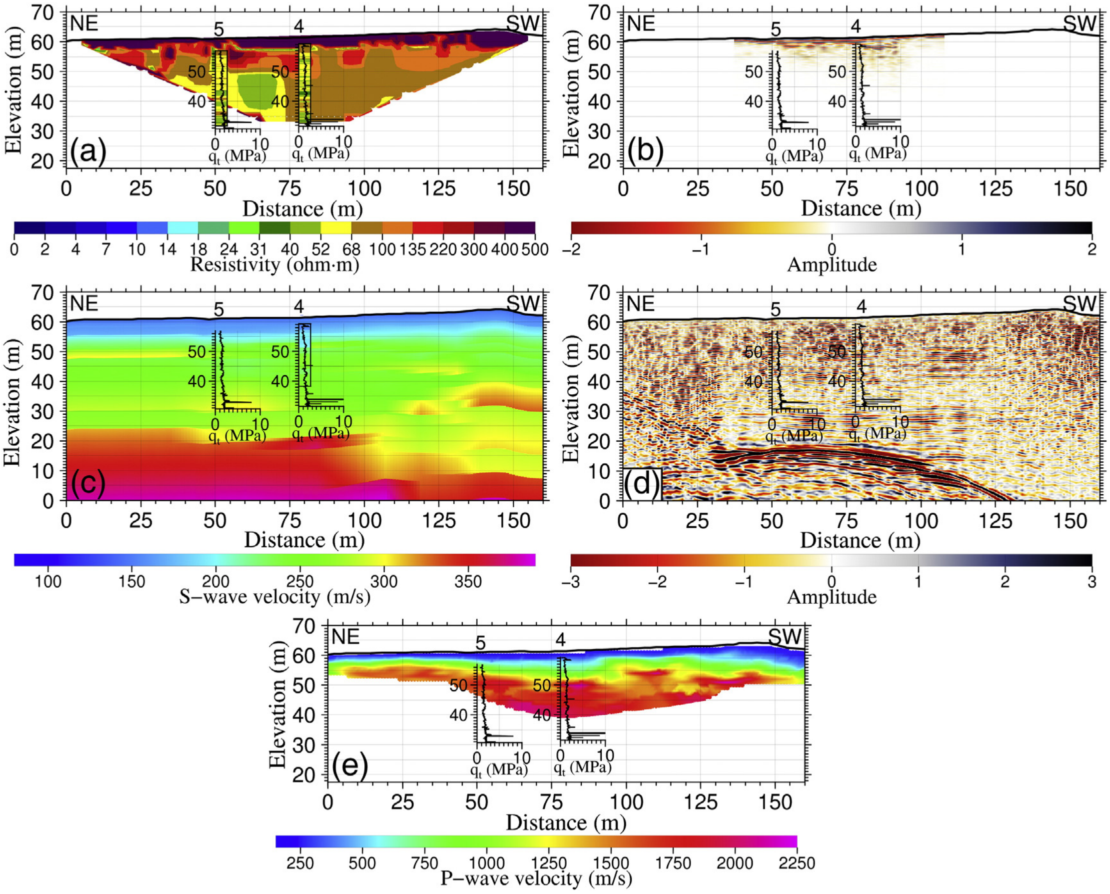

Fig. 6. Profile 2, a) inverted resistivity from gradient array, b) GPR profile extract from the depth converted GPR cube superimposed, c) S-wave interval velocity, d) depth converted S-wave seismic reflection, and e) P-wave velocity from seismic refraction tomography. Resistivity values from boreholes 4 to 5 as well as S-wave velocity from borehole 4 are also depicted with the same colour scale as for ERT and S-wave seismic respectively. (For interpretation of the references to colour in this figure legend, the reader is referred to the web version of this article.)

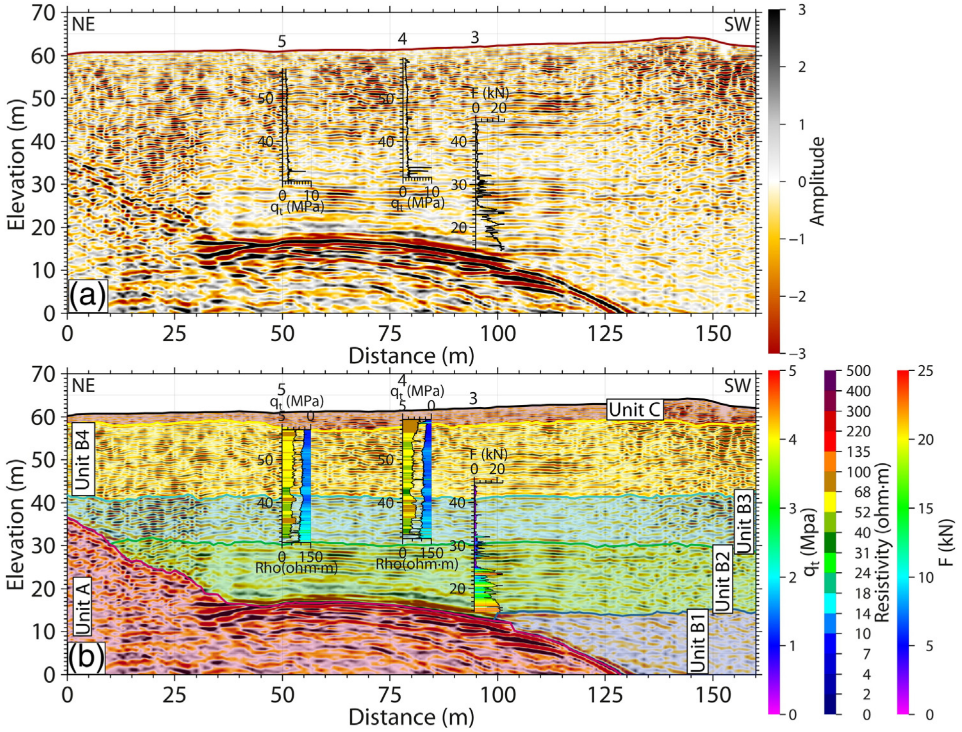

Fig. 7. Profile 2, S-wave seismic reflection profile with boreholes 3 (10 m offset), 4 and 5. The interpreted stratigraphy is superimposed on the S-wave seismic reflection profile and the corresponding layers are coloured in b). The resistivity values and the corrected tip resistance from boreholes 4 and 5, as well as the drilling resistance from borehole 3 are also depicted. (For interpretation of the references to colour in this figure legend, the reader is referred to the web version of this article.)

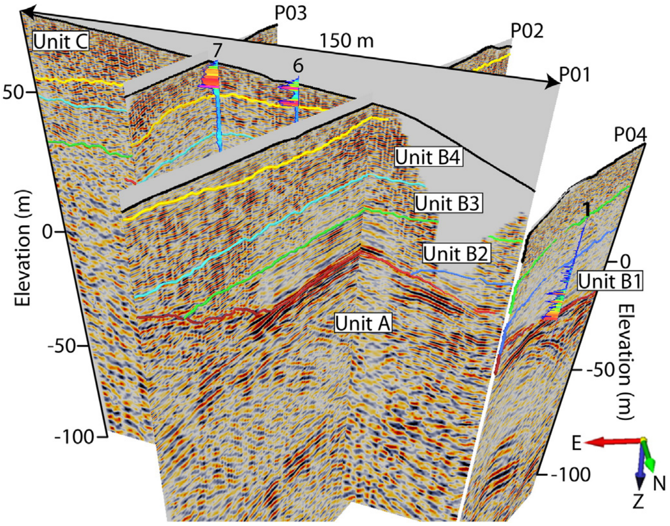

Fig. 8. Pseudo-3D view of time-to-depth converted S-wave seismic reflection profiles and boreholes 1, 6, and 7. The interpreted top of units is also displayed; black, top unit C (actual topography); yellow, turquoise, green, and blue, top subunits B4, B3, B2, and B1, respectively; red, top unit A. (For interpretation of the references to colour in this figure legend, the reader is referred to the web version of this article.)

geotechnical laboratory test results. Subunit B4 is a fjord-marine sediments deposited in a quiet fjord environment. B4 corresponds to continuous to semi-continuous, sub-horizontal, stratified sequences on the S-wave seismic profile. RPS drilling resistance is constant with depth indicating quick clays. Laboratory measurements confirm the presence of quick clay in the lowest part of this subunit, and low sensitive clay above. Resistivity values in this subunit range between 15 and 100 Ω·m, thus close to the resistivity range (10–80 Ω·m) characteristic of leached clay and potentially quick clay (Solberg et al., 2012). The low P-wave velocities within this layer correlate with higher resistivity and GPR amplitude variations, suggesting grain-size variation. Subunit B3 is interpreted as fjord-marine sediments deposited in a glacier-distal fjord environment. The S-wave seismic reflection pattern is generally horizontally stratified with low amplitudes. Laboratory measurements indicate fine-grained sediments (silty-clay) with some thin hard parts (clasts or lenses of thin sand layers) towards the base. The entire subunit has likely an elevated sensitivity, inferred from the nearly constant RPS drilling resistance with depth. Resistivity values in this subunit are similar to subunit B4, i.e. between 20 and 80 Ω·m. No resistivity values below 15 Ω·m are observed, suggesting that most of the imaged fjord deposits have been leached in the vicinity of the two ERT profiles. Subunit B2 is interpreted as glaciomarine sediments deposited in a fjord environment close to a glacier. This subunit is characterised by high amplitude, horizontally stratified S-wave seismic reflection pattern. Results from laboratory measurements indicate fine and coarse layers succession (silty-clay/sand/gravel). The RPS drilling resistance is generally high but varies with depth (borehole 3 in Fig. 7). Subunit B1 is interpreted as glaciomarine sediments deposited in an environment relatively close to the glacier. This subunit is interpreted from S-wave seismic reflection alone, since none of the other methods reach such depth. It is characterised by internal irregular reflection pattern with lower amplitudes and frequency content compared to the rest of unit B. Finally, unit A is the bedrock or stiff sub-stratum with internal irregular to poorly stratified reflection patterns, a continuous and very-high amplitude reflection at the top and high S-wave seismic velocity (>450 m/s).

Since the interfaces are known from GPR and S-wave seismic reflection data, they can be used as sharp geological boundaries to invert for resistivity, in order to retrieve the resistivity variations within subunits B3 and B4 decoupled from the high resistivity values of unit C (Fig. 10). Little changes are observed, but the north-eastern part of the profile has more uniform resistivity values within subunits B4 and B3 when using sharp boundaries as inversion constraints.

4.2. Correlation with geotechnical parameters

In addition to the stratigraphic information extracted from geophysical and geotechnical data, results from geophysical measurements can be used, 1) as direct quantitative information, 2) for correlation with geotechnical parameters, and 3) for inter/extrapolation from geotechnical soundings, in order to, ultimately, populate the geological model with relevant quantitative parameters, which will contribute to improved hazard assessment.

Correlation of the geophysical data with the existing RPS and CPTU is good, and allows for an accurate interpretation of the upper units (Figs. 5, 6 and 7). The geological model is therefore confirmed, and, wherever possible, filled with geophysical parameters. Parameters of interest for safety factor computation, e.g., density, internal angle of friction, effective cohesion, groundwater table height, undrained shear strength, and sensitivity, cannot be directly extracted from geophysical measurements (except maybe for the density, using micro-gravimetry,

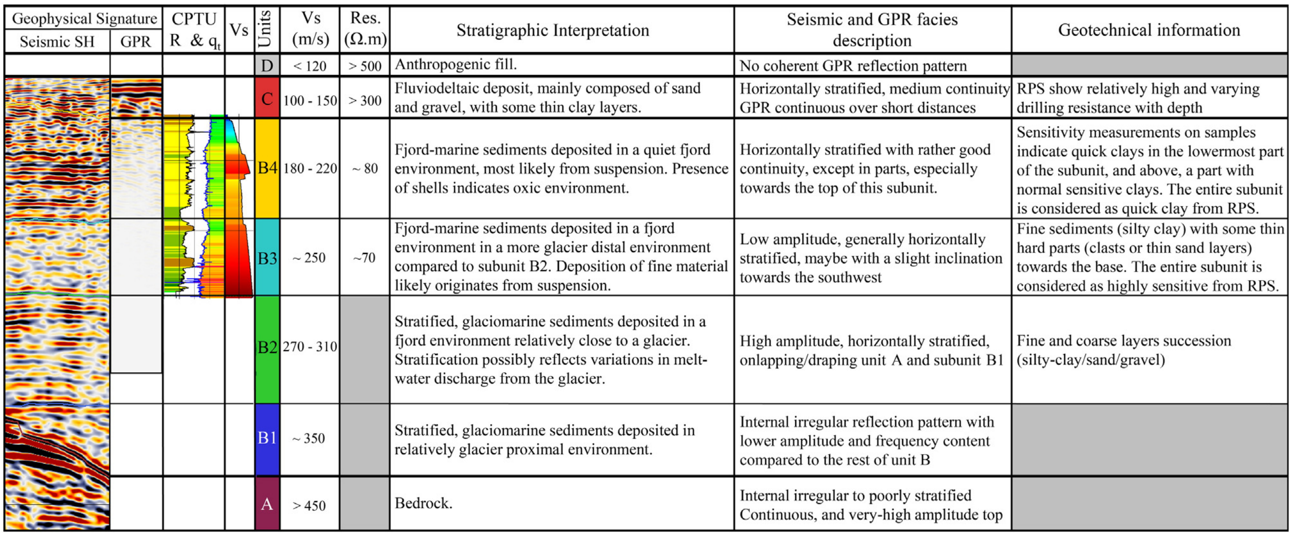

Geophysical Signature		CPTU	Vs	Units	Vs	Res.	Stratigraphic Interpretation	Seismic and GPR facies description	Geotechnical information
Seismic SH	GPR	R & q_t			(m/s)	(Ω.m)			
				D	< 120	> 500	Anthropogenic fill.	No coherent GPR reflection pattern	
				C	100 - 150	> 300	Fluviodeltaic deposit, mainly composed of sand and gravel, with some thin clay layers.	Horizontally stratified, medium continuity GPR continuous over short distances	RPS show relatively high and varying drilling resistance with depth
				B4	180 - 220	~ 80	Fjord-marine sediments deposited in a quiet fjord environment, most likely from suspension. Presence of shells indicates oxic environment.	Horizontally stratified with rather good continuity, except in parts, especially towards the top of this subunit.	Sensitivity measurements on samples indicate quick clays in the lowermost part of the subunit, and above, a part with normal sensitive clays. The entire subunit is considered as quick clay from RPS.
				B3	~ 250	~70	Fjord-marine sediments deposited in a fjord environment in a more glacier distal environment compared to subunit B2. Deposition of fine material likely originates from suspension.	Low amplitude, generally horizontally stratified, maybe with a slight inclination towards the southwest	Fine sediments (silty clay) with some thin hard parts (clasts or thin sand layers) towards the base. The entire subunit is considered as highly sensitive from RPS.
				B2	270 - 310		Stratified, glaciomarine sediments deposited in a fjord environment relatively close to a glacier. Stratification possibly reflects variations in melt-water discharge from the glacier.	High amplitude, horizontally stratified, onlapping/draping unit A and subunit B1	Fine and coarse layers succession (silty-clay/sand/gravel)
				B1	~ 350		Stratified, glaciomarine sediments deposited in relatively glacier proximal environment.	Internal irregular reflection pattern with lower amplitude and frequency content compared to the rest of unit B	
				A	> 450		Bedrock.	Internal irregular to poorly stratified Continuous, and very-high amplitude top	

Fig. 9. Main stratigraphic interpretation of the S-wave seismic reflection and GPR data. Correlation with resistivity and corrected tip resistance values from resistivity-CPTU as well as S-wave interval velocity derived from seismic reflection velocity analysis is also presented. The geotechnical information is also given wherever available.

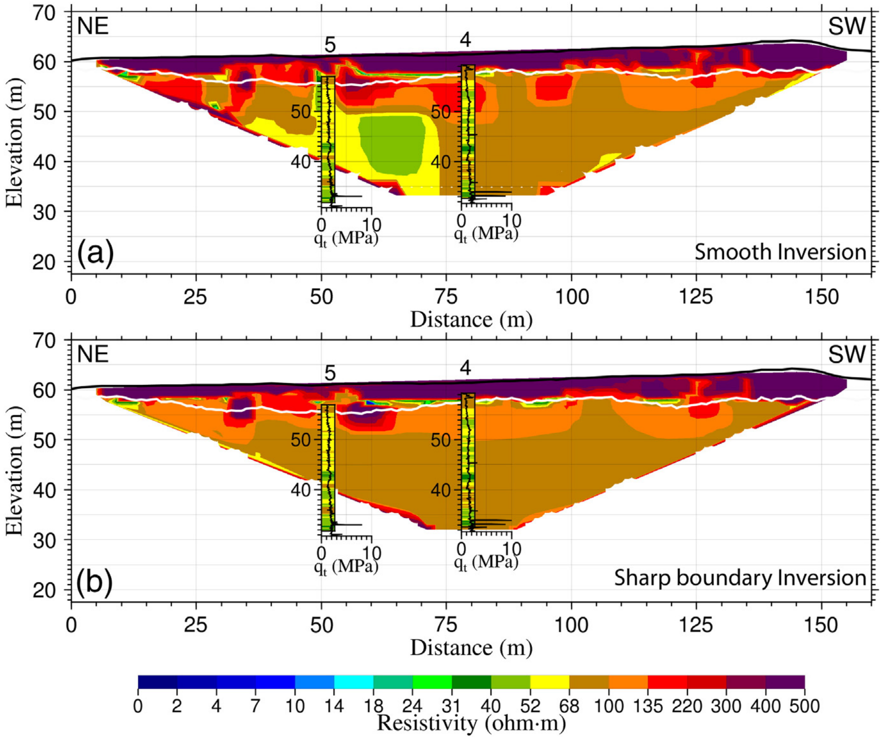

Fig. 10. Profile 2, resistivity inverted from gradient array, using a) smooth inversion, and b) sharp boundary inversion. The interface in-between unit C and unit B (white line) was used as the decoupled sharp boundary.

and the water table level), and therefore, one has to use the multidisciplinary data to establish empirical correlations between geophysical and geotechnical parameters.

Previous studies (Long et al., 2012) report good relationships between resistivity and pore–water salt content, as well as resistivity and clay content or plasticity. However, no simple connections between s_{ur} or sensitivity and resistivity exist as such relationship depends on particle size distribution, mineralogy, ionic content, role of dispersing agents, etc. According to Torrance (1983), salt concentration has to be below 2 g/l for a clay to be considered "quick", therefore, resistivity profiles inverted from ERT measurement can possibly be used as a necessary criterion for highly sensitive clay, based on salt content. From various Norwegian quick-clay sites, Long et al. (2012) derived the following regression correlation between the resistivity R and the salt concentration S_c with a regression coefficient of determination $R^2 = 0.8$:

$$R = 49.4 \times S_c^{-0.83}. \qquad (1)$$

As another salt-content indicator, the GPR attenuation could potentially be used. The higher the salt content, the lower the resistivity, and hence, the higher the GPR attenuation.

As directly related to pore–water pressure, the ground-water table level is important when it comes to stability assessment. The water table can generally be retrieved from GPR measurements, but, in our case, because of the clay layer attenuating the electromagnetic signal, the detection of the groundwater table was not viable everywhere. However, combined with P-wave seismic refraction, the water table could be traced along the profiles (Fig. 5). The ground-water table depth was also measured using piezometers in boreholes 1, 3 and 5, validating the results from the seismic refraction.

The internal angle of friction and effective cohesion are known from laboratory measurements on samples and are generally fixed for a given type of soil. Similarly, the density is measured and associated to a layer throughout the entire area. No correlations associated to these parameters were derived from geophysical measurements.

Since S-wave velocity (Vs) is directly connected to the small-strain shear modulus G_{max} ($G_{max} = \rho Vs^2$), it seems reasonable to use this parameter for correlation. As a first attempt, we correlate Vs to the net tip resistance q_n ($q_n = q_t - \sigma_{v0}$, corrected tip resistance minus the total vertical stress).

Even if the vertical resolution in the S-wave data and velocity results is too low for detection of very thin, decimetre-size layers evidenced on CPTU data, one can notice similar trends in q_n and Vs when directly compared (Fig. 11). Almost every sign change in q_n slope coincides with abrupt variations in S-wave velocity (Fig. 11). It is therefore possible to divide the Vs logs in sections (layers) corresponding to main sign changes in q_n derivative with depth (Fig. 11). Since the layering derived from q_n slope variations exhibits similarity with the actual stratigraphic interpretation, we can use the stratigraphy as main boundaries to infer empirical relationships between q_n and Vs (Fig. 12). Therefore, using the S-wave seismic reflection patterns, one can estimate the net tip resistance from the S-wave interval velocity field in between continuous reflections, in agreement with the stratigraphic interpretation. Additionally, if more than one CPTU log is available along the same seismic profile, one can define an empirical correlation between q_n en Vs for every layer and at each CPTU location. The coefficients of the empirical correlations can then be interpolated and used to derive a more consistent q_n field from Vs. The coefficients used for the linear empirical correlations are given in Table 2 and the inferred net tip resistance field using the interpolated coefficients is presented in Fig. 13.

5. Discussion

The stratigraphic model inferred from geophysical interpretation is used to fill the gap between the 1D geotechnical boreholes and it provides the missing stratigraphic information as a priori information in inversion and joint analysis of the data. The geo-model can then be populated with quantitative parameters.

Interpretation of the geophysical data provides detailed stratigraphic information and a consistent geological model (e.g. Figs. 8 and 9). The stratigraphy is of high importance in safety factor computations, and

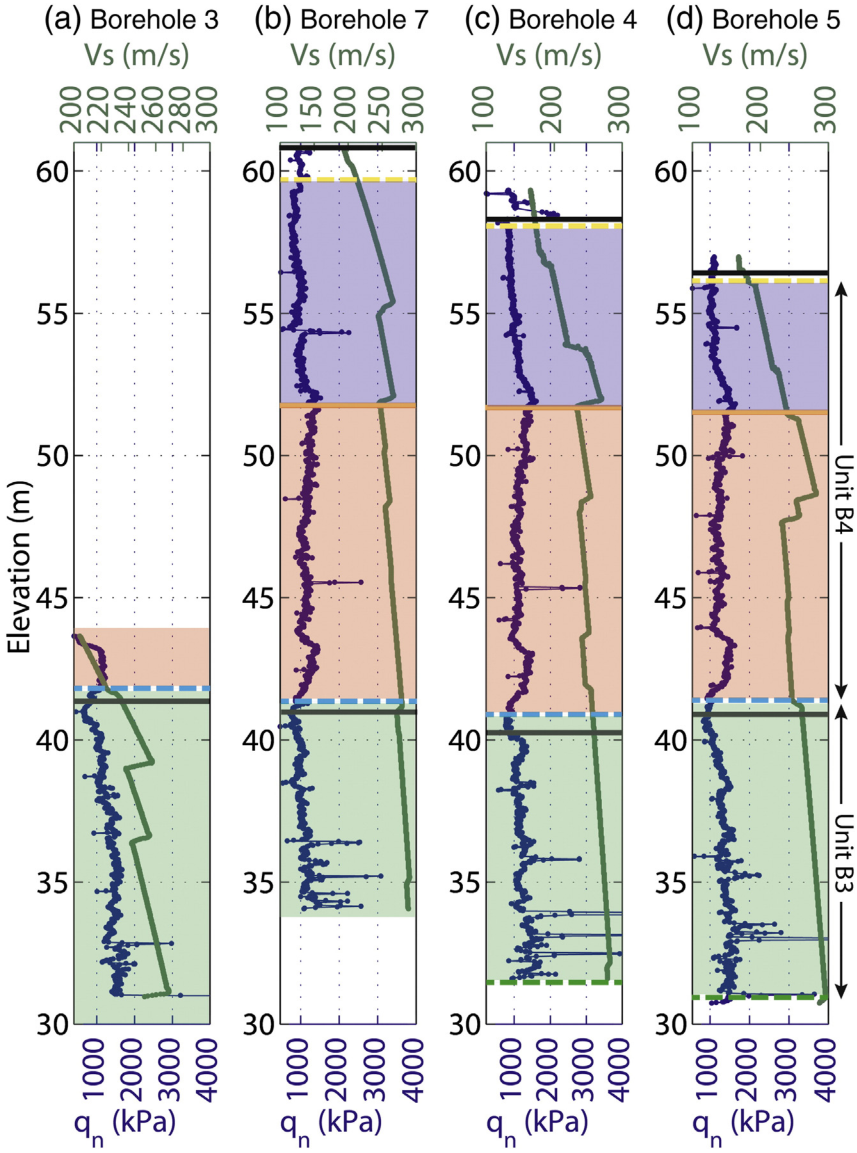

Fig. 11. q_n compared with the interval S-wave velocities at a) boreholes 3, b) 7, c) 4, and d) 5. The stratigraphic interpretation (horizontal dashed lines, top unit B4, yellow; top unit B3, blue; top unit B2 green) as well as the sections corresponding to general slope changes in q_n (horizontal black and orange lines) are also displayed. (For interpretation of the references to colour in this figure legend, the reader is referred to the web version of this article.)

therefore the more detailed it is, the better the hazard assessment can be conducted. In this particular case, the geometry of the main layers interpreted from geophysical measurements is not too different from the one established from geotechnical soundings alone. However, the interpretation from complementary geophysical data could make a distinct difference at other sites, e.g., in the case where the spatial undersampling of the geotechnical measurements leads to an inaccurate geological model. Additionally, when it comes to stability assessment relative to quick clay, one has to evaluate the remoulded shear strength of the clay. As the sensitivity of marine clays relates to the degree of leaching it has undergone, it is also important to know the preferential groundwater paths, i.e., locate the permeable layers and the highs in bedrock topography (Sauvin et al., 2013, and references therein). The topography of the bedrock and the geometry of the coarse grain layers were retrieved. This provides insights on the sub-surface groundwater migration and the preferential leaching paths for the clay which influence the local drainage (Løken, 1968) and therefore had a significant effect on the formation of quick clay at that site (Malehmir et al., 2013a,b). The stratigraphic model derived from geophysical interpretation is used to fill the gap between the 1D geotechnical soundings and provides the missing stratigraphic information. The model can then be populated with quantitative parameters.

As previously mentioned, the sensitivity of marine clays is related to the degree of leaching it has undergone. Leached clay has a lower pore–water ion concentration compared with unleached clay. Resistivity, being a function of pore–fluid conductivity, could potentially give an estimate of the salinity of the clay and therefore be correlated to the degree of leaching. Solberg et al. (2012) estimated that highly-sensitive or quick-clay resistivity values generally exceed 10 Ω·m, and this is in agreement with the resistivity–salt concentration correlation proposed by Long et al. (2012). Nevertheless, resistivity is also a function of many other physical properties such as porosity, water saturation, and grain size distribution, which means that resistivity alone could help mapping high sensitive clay, but also that it is insufficient.

Looking at the geophysical parameters variation within each unit/subunit, it appears that the sub-surface is more complex than initially thought using solely the geotechnical boreholes. The geophysical data reveal lateral variations in the physical properties. Looking at resistivity, P- and S-wave velocity variations in subunits B4–B3 along profile 2, and the corresponding GPR profile (Fig. 6), it appears that the interpreted

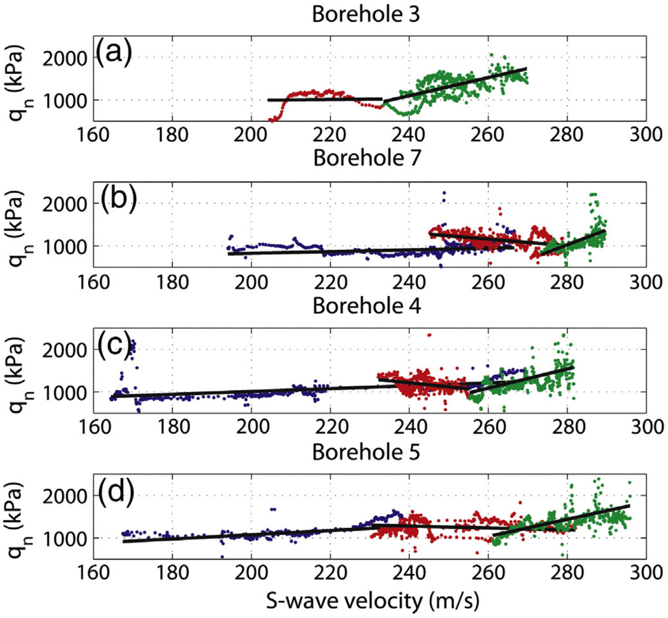

Fig. 12. Cross plot of q_n and Vs for a) boreholes 3, b) 7, c) 4, and d) 5. Blue, red and green colours correspond to the layers defined in Fig. 11. The black lines represent the linear fit for each section and their respective correlation coefficients are given in Table 3. (For interpretation of the references to colour in this figure legend, the reader is referred to the web version of this article.)

quick-clay layer (subunit B4) is not homogeneous and it includes non-quick clay zones with higher resistivity (even on the resistivity profile inverted using sharp boundaries, Fig. 10), higher S-wave velocity and better GPR depth penetration. Similarly, geophysical parameters vary along profile 1 (Fig. 5), suggesting an inhomogeneous distribution of the quick clays. These results suggest that quick-clay investigations using discrete and spatially isolated geotechnical boreholes can benefit significantly from complementary geophysical parameters profiles to interpolate in between, and extrapolate from these point-wise calibration points. This is further emphasised by the good consistency between S-wave velocity and resistivity values from seismic-CPTU and resistivity-CPTU measurements with those from S-wave seismic reflection and ERT.

Correlation of S-wave velocity with net tip resistance within layers defined upon net tip resistance slope variation is good and is used to populate the geological model (Fig. 13). For stability assessment, estimation of the undrained shear strength s_u is usually achieved through empirical correlations with CPTU results and laboratory measurements. One of the empirical approaches available for interpretation of s_u from CPT/CPTU results uses the net tip resistance as follows (Karlsrud et al., 1996):

$$s_u = \frac{q_n}{N_{kt}}, \tag{2}$$

where N_{kt}, is a cone factor based on effective cone resistance, and typically obtained from matching CPTU data with results from advanced geotechnical laboratory tests (e.g., triaxial shear strength tests under compression). Using this correlation, one can also correlate the S-wave velocity field to the undrained shear strength.

One critical aspect in our work is to establish empirical relationships between G_{max} and soil index properties, and hence, relating dynamic and static soil properties. Norwegian practice normalises G_{max} with respect to the sum of consolidation stress and attraction to obtain a dimensionless parameter that depends on friction only (e.g. Janbu, 1985). For the case of the small-strain shear modulus, Langø (1991) suggested that the normalised small-strain shear modulus g_{max} can be written as

$$g_{max} = \frac{G_{max}}{\sigma'_m + a} \tag{3}$$

where $\sigma_m{}'$ and a are the mean effective consolidation stress and the attraction measured in triaxial tests, respectively. According to Langø (1991), L'Heureux et al. (2013), and Long and Donohue (2007, 2010) a systematic variation in normalised shear modulus may be obtained by plotting g_{max} as a function of water content (Fig. 14). There is a reasonable correlation between g_{max} and the water content. Here, the attraction (a) was assumed to be equal to 3 kPa, which is a typical value for the clays studied by Janbu (1985). The results are consistent with data found in literature (Fig. 14) suggesting that the correlation defined previously between Vs and the net tip resistance could be extended to other clay sites.

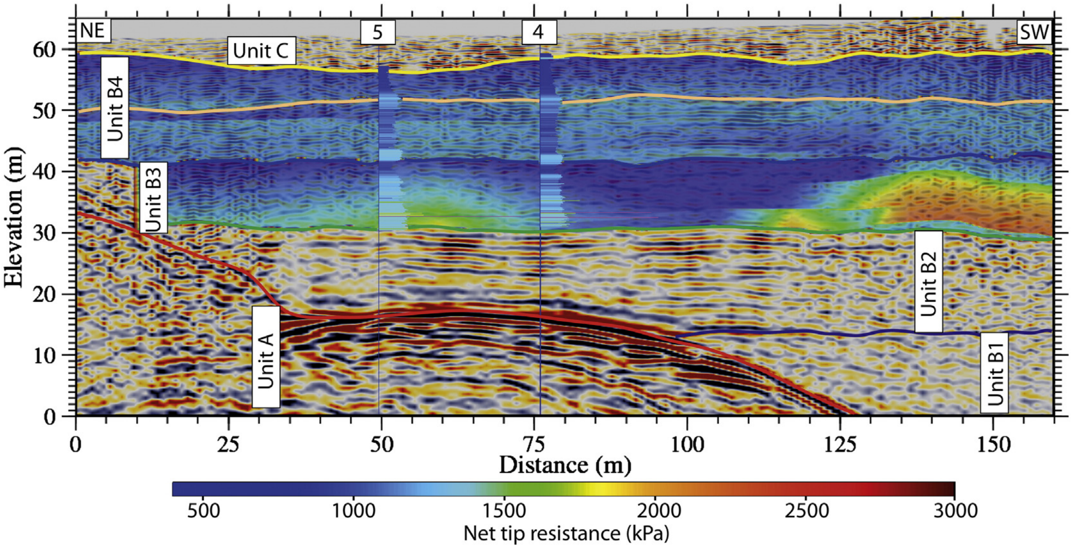

Fig. 13. S-wave seismic reflection profile 2 with net tip resistance estimated from S-wave seismic velocity within subunits B4 and B3 superimposed. The green, blue and yellow lines correspond to interpreted tops of units B2, B3, and B4. The orange line is the interpreted interface within unit B3 corresponding to slope change in q_n (orange line in Fig. 11). Net tip resistance from boreholes 4 and 5 are also displayed with the same colour scale. (For interpretation of the references to colour in this figure legend, the reader is referred to the web version of this article.)

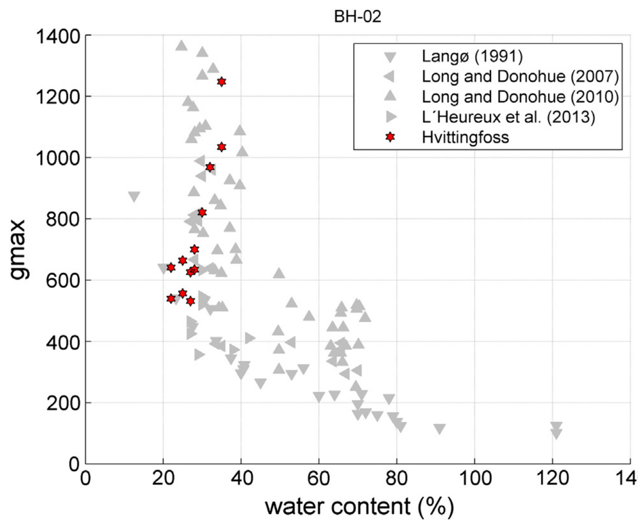

Fig. 14. Relationship between water content and normalised small strain shear modulus for Hvittingfoss and previous studies.

6. Conclusions

In addition to the dense geotechnical dataset available at the Hvittingfoss test site, a number of geophysical methods were combined in order to improve our geological understanding of the site, which can lead to an improved hazard assessment. Following careful planning, acquisition and processing of different types of geophysical data using geotechnical boreholes as ground proofing, we established a more detailed stratigraphy model based on the integration of all geophysical methods and geotechnical measurements available. As such, geophysics is used to fill the gap between the isolated 1D geotechnical boreholes. The resulting geological model also serves to better understand the local drainage system responsible for the salt leaching from the clay, information which cannot be derived unambiguously from geotechnical measurements alone. The geological model is then populated with the quantitative parameters derived from the geophysical measurements, which directly helps to map and identify the area where highly sensitive clay may be found (i.e. resistivity and GPR attenuation as proxy for salt concentration and degree of leaching, Vs for stiffness and Vp/Vs for saturation). S-wave velocity correlation with net tip resistance allows populating the geological model with geotechnical parameters, particularly suited for hazard assessment when vibrations are generated (e.g., blasting). The high-resolution geological model resulting from the integration of several geophysical methods and geotechnical data helps locating the potential quick clay and can subsequently be used as input for more realistic and advanced 2D to 3D stability simulations. Correlation between geophysical parameters and remoulded shear strength is still lacking, and therefore, more lab measurements would be required.

Acknowledgements

The authors are grateful to Magnus Rømoen for providing the geotechnical data previously acquired. The authors also thank Gedco and Sandmeier for providing academic licences to ICG (Vista and ReflexW, respectively). The authors acknowledge Nadège Langlet, Sylvain Tissot, Christian Maskrey, Håkon Akerholt, Tor Overskeid, Karine Petrus, Mesay Geletu Gebre, Gunther Druivenga (GEOSYM) and Berit Paulsen for their help in the field. We are most grateful to the two journal reviewers whose insightful comments helped us to improve the manuscript. Guillaume Sauvin thanks the sponsors of his PhD thesis: the Norwegian Public Roads Administration, the Norwegian National Railway Administration, the Norwegian Water Resources and Energy Directorate, and the International Centre for Geohazards.

References

Adamczyk, A., Malinowski, M., Malehmir, A., 2013. Application of first-arrival tomography to characterize a quick-clay landslide site in southwest Sweden. Acta Geophys. 61, 1057–1073.

Bazin, S., Pfaffhuber, A.A., 2013. Mapping of quick clay by electrical resistivity tomography under structural constraint. J. Appl. Geophys. 98, 280–287.

Brand, E.W., Brenner, R.P., 1981. Soft Clay Engineering. Elsevier.

Calvert, H.T., Hyde, C.S.B., 10–14 February 2002. Assessing landslide hazard in the Ottawa Valley using electrical and electromagnetic methods. Proceedings of the Symposium on the Application of Geophysics to Engineering and Environmental Problems (SAGEEP), Las Vegas. Environmental and Engineering Geophysical Society.

Corner, G., 2006. A trangressive-regressive model of fjord-valley fill: stratigraphy, facies and depositional controls. In: Leckie, Dalrymple RW., Tillman, R.W. (Eds.), Inceised valleys in time and space. Society of Sedimentary Geology, Tulsa, pp. 161–178.

Crow, H.L., Hunter, J.A., Motazedian, D., 2011. Monofrequency in situ damping measurements in Ottawa area soft soils. Int. J. Soil Dyn. Earthq. Eng. 31, 1669–1677.

Dahl Å., K. S. Olsen, and R. Sørensen, 1997, Holmestrand 1813 IV, Quaternary geological map — M 1:50000 with description. NGU.

Dahlin, T., Larsson, R., Leroux, V., Larsson, R., Rankka, K., 4–7 September 2005. Resistivity imaging for mapping of quick clays for landslide risk assessment. Proceedings of the 11th Annual Meeting EAGE — Environmental and Engineering Geophysics, Palermo, p. A046.

Dahlin, T., Zhou, B., 2006. Multiple-gradient array measurements for multichannel 2D resistivity imaging. Near Surf. Geophy. 4, 113–123.

Dahlin, T., Löfroth, H., Schälin, D., Suer, P., 2013. Mapping of quick clay using geoelectrical imaging and CPTU-resistivity. Near Surf. Geophys. 11, 659–670.

Donohue, S., Long, M., O'Connor, P., Eide-Helle, T., Pfaffhuber, A.A., Rømoen, M., 2012. Multi-method geophysical mapping of quick clay. J. Near Surf. Geophys. EAGE 10 (3), 207–219.

Gregersen, O., 1981. The quick clay landslide in Rissa, Norway. Norw. Geotech. Inst. Publ. 135, 1–6.

Gregersen, O., 2008. Program for økt sikkerhet mot leirskred - Metode for kartlegging og klassifisering avfaresoner, kvikkleire. Norwegian Geotechnical Institute Report 20001008-2 ((3rd revision). 24 pp. (In Norwegian)).

L'Heureux, J.S., 2012. A study of the retrogressive behaviour and mobility of Norwegian quick clay landslides. Proceedings of the 11th International and 2nd North American Symposium on Landslides, Banff, Canada.

L'Heureux, J.S., Eilertsen, R.S., Glimstad, S., Issler, D., Solberg, I., Harbitz, C.B., 2012. The 1978 quick clay landslide at Rissa, mid-Norway: subaqueous morphology and tsunami simulations. Sub-marine mass movements and their consequences. Advances in Natural and Technological Hazards Research, vol 31. Springer, Dordrecht pp. 507–516.

L'Heureux, J.S., Long, M., Vanneste, M., Sauvin, G., Hansen, L., Polom, U., Lecomte, I., Dehls, J., Janbu, N., 2013. On the prediction of settlement from high-resolution shear-wave reflection seismic data: the Trondheim Harbour case study, mid Norway. Eng. Geol. http://dx.doi.org/10.1016/j.enggeo.2013.10.006.

Hunter, J.A., Crow, H.L., Brooks, G., Motazedian, D., et al., 2010. Seismic site classification and site period mapping in the Ottawa area using geophysical methods. Geological Survey of Canada, Open File Report 6273.

Janbu, N., 1985. Soil models in offshore engineering. Geotechnique 35, 241–281.

Karlsrud, K., Lunne, T., Brattlien, K., 1996. Improved CPTU correlations based on block samples. Proc. Nordic Geotechnical Conference, Reykjavik. 1996, vol. 1, pp. 195–201.

Krawczyk, C.M., Polom, U., Beilecke, T., 2013. Shear-wave reflection seismic as a valuable tool for near-surface urban applications. Lead. Edge Spec. Sect. Urban geophys. 32, 256–263.

Langø, H., 1991. Cyclic Shear Modulus of Natural Intact Clays. (Ph.D. thesis) Norwegian Institute of Technology (NTH), Trondheim, Norway.

Locat, P., Demers, D., Robitaille, D., Fournier, T., Noël, F., Leroueil, S., Locat, A., Lefebvre, G., 2012. The Saint-Jude landslide of May 10, 2012, Québec, Canada. In: Eberhardt, E., Froese, C., Turner, A.K., Leroueil, S. (Eds.), Landslides and Engineered Slopes — Protecting Society through Improved Understanding, vol 1. CRC Press, London, UK, pp. 635–640.

Löfroth, H., Suer, P., Schalin, D., Dahlin, T., Leroux, V., 2012. Mapping of quick clay using sounding methods and resistivity in the Göta River valley. Geotechnical and geophysical site characterisation 4. In: Couthino, R.C., Mayne, P.W. (Eds.), Proceedings of the 4th International Conference on Site Characterisation (ISC-4) 2. CRC Press, Taylor & Francis Group, Balkema, pp. 1001–1008.

Loke, M.H., 2010. Res2DInv ver 3.59.102. Geoelectrical Imaging 2D and 3D. Instruction Manual. Geotomo Sotware, http://www.geotomosoft.com/.Long M., and S. Donohue, 2007, In situ shear wave velocity from multichannel analysis of surface waves (MASW) tests at eight Norwegian research sites. Can. Geotech. J. 44, 533–544.

Long, M., Donohue, S., 2007. In situ shear wave velocity from multichannel analysis of surface waves (MASW) tests at eight Norwegian research sites. Can. Geotech. J. 44, 533–544.

Long, M., Donohue, S., 2010. Characterization of Norwegian marine clay with combined shear wave velocity and piezocone cone penetration test (CPTU) data. Can. Geotech. J. 47, 709–718.

Long, M., Donohue, S., L'Heureux, J.S., Solberg, I.L., Rønning, J.S., Limacher, R., O'Connor, P., Sauvin, G., Rømoen, M., Lecomte, I., 2012. Relationship between electrical resistivity and basic geotechnical parameters for marine clays. Can. Geotech. J. 49, 1158–1168.

Longva, O., Janbu, N., Blikra, L.H., Boe, R., 2003. The 1996 Finneidfjord slide: seafloor failure and slide dynamics. In: Locat, J., Mienert, J. (Eds.), Submarine Mass Movements and Their Consequences. Kluwer, Dordrecht, pp. 531–538.

Lundström, K., Larsson, R., Dahlin, T., 2009. Mapping of quick clay formations using geotechnical and geophysical methods. Landslides 6, 1–15.

Lunne, T., Robertson, P.K., Powell, J.J.M., 1997. Cone Penetration Testing in Geotechnical Practice. Chapman & Hall, London.

Løken, T., 1968. Kvikkleiredannelse og kjemisk forvitring i norske leirer. Publication, 75. Norwegian Geotechnical Institute, Oslo pp. 19–26 (In Norwegian).

Malehmir, A., Bastani, M., Krawczyk, C., Gurk, M., Nazli, I., Polom, U., Persson, L., 2013a. Geophysical assessment and geotechnical investigation of quick-clay landslides — a Swedish case study. Near Surf. Geophys. 11, 341–350.

Malehmir, A., Saleem, U.M., Bastani, M., 2013b. High-resolution reflection seismic investigations of quick-clay and associated formations at a landslide scar in southwest Sweden. J. Appl. Geophys. 92, 84–102.

Mitchell, J.K., 1976. Fundamentals of Soil Behavior. John Wiley and Sons, Inc.

Mitchell, R.J., Markell, A.R., 1974. Flowslides in sensitive soils. Can. Geotech. J. 11, 11–31.

Norwegian Geotechnical Institute, 2008. Fossnes på Hvittingfoss, Vurdering av skredfare og sikringstiltak. Norwegian Geotechnical Institute Report (20071564-2 30).

NGF (Norsk Geoteknisk Forening), 1975. Retningslinjer for presentasjon av geotekniske undersøkelser (In Norwegian).

Nolet, G., 1987. Seismic Tomography. D. Reidel Publ. Co., Dordrecht.

Nordal, S., Alén, C., Emdal, A., Jendeby, L., Lyche, E., Madshus, C., 2009. Skredet i Kattmarkvegen i Namsos 13. mars 2009 - Rapport fra undersøkelsesgruppe satt ned av Samferdselsdepartementet. Tapir Uttrykk, Trondheim (In Norwegian).

Polom, U., Hansen, L., Sauvin, G., L'Heureux, J.S., Lecomte, I., Krawczyk, C.M., Vanneste, M., Longva, O., 2010. High-resolution SH-wave seismic reflection for characterization of on-shore ground conditions in the Trondheim Harbor, Central Norway. In: Miller, R. D., Bradford, J.D., Holliger, K. (Eds.), Advances in Near-surface Seismology and Ground-penetrating Radar. SEG, Tulsa, pp. 297–312.

Polom U., G. Druivenga, E. Grossmann, S. Grüneberg, and W. Rode, 2011, Transportabler Scherwel-lenvibrator. Patent application DE 103 27 757 A1, Deutsches Patent- und Markenamt (in German).

Polom, U., Bagge, M., Wadas, S., Winsemann, J., Brandes, C., Binot, F., Krawczyk, C.M., 2013. Surveying near-surface depocentres by means of shear wave seismics. First Break 31, 67–79.

Potvin, J., Pellerin, F., Demers, D., Robitaille, D., La Rochelle, P., Chagnon, J.Y., 2001. Revue et investigation supplémentaire du site du glissement de Saint-Jean-Vianney. 54th Canadian geotechnical conference. Calgary, vol. 2, pp. 792–800.

Pugin, A.J.M., Pullan, S.E., Hunter, J.A., 2009. Multicomponent high-resolution seismic reflection profiling. Lead. Edge 28 (10), 1248–1261.

Pugin, A.J.M., Brewer, K., Cartwright, T., Pullan, S.E., Perret, D., Crow, H., Hunter, J.A., 2013. Near surface S-wave seismic reflection profiling — new approaches and insights. First Break 31 (2), 49–60.

Rankka, K., Anderssen-Skold, Y., Hulten, C., Larsson, R., Leroux, V., Dahlin, T., 2004. Quick Clay in Sweden. Report 65Swedish Geotechnical Institute, Linkoping.

Rygg, N., 1988. Rotary pressure sounding: 20 years of experience. In: Ruiter, De (Ed.), Proc. Pen Testing, 1988, ISOPT-1. Balkema, pp. 453–457.

Sasaki, Y., 1992. Resolution of resistivity tomography inferred from numerical simulation. Geophys. Prospect. 40, 453–464.

Sauvin, G.I., Lecomte, S., Bazin, J.S., L'Heureux, Vanneste, M., 2013. Towards geophysical and geotechnical integration for quick clay mapping in Norway. J. Near Surf. Geophys. EAGE 11. http://dx.doi.org/10.3997/1873-0604.2012064.

Sauvin, G., 2009. S-wave Seismic for Geohazards: A Case Study from Trondheim Harbor: Diploma Engineering Thesis. University of Strasbourg (2009-6-1).

Solberg, I.L., Hansen, L., Rønning, J.S., Dalsegg, E., Hansen, L., Rokoengen, K., Sandven, R., 2008. Resistivity measurements as a tool for outlining quick-clay extent and valley-fill stratigraphy: a feasibility study from Buvika, central Norway. Can. Geotech. J. 45, 210–225.

Solberg, I.L., Hansen, L., Rønning, J.S., Haugen, E., Dalsegg, E., Tønnesen, J.F., 2012. Combined geophysical and geotechnical approach to ground investigations and hazard zonation of a quick clay area, Mid Norway. Bull. Eng. Geol. Environ. 71, 119–133.

Smith, T., Hoversten, M., Gasperikova, E., Morrison, F., 1999. Sharp boundary inversion of 2D magnetotelluric data. Geophys. Prospect. 47, 469–486.

Tavenas, F., Chagnon, J.Y., La Rochelle, P., 1971. The Saint-Jean-Vianney landslide: observations and eyewitnesses accounts. Can. Geotech. J. 8, 463–478.

Tavenas, F., Flon, P., Leroueil, S., Lebuis, J., 1983. Remolding energy and risk of retrogression in sensitive clays. Symposium on slopes on soft clays. Linkoping, Swedish Geotechnical Institute Report, No. 17 pp. 205–262.

Torrance, J.K., 1983. Towards a general model of quick clay development. Sedimentology 30, 547–555.

Vidale, J., 1988. Finite-difference calculation of travel times. Bull. Seismol. Soc. Am. 78, 2062–2076.

4.3 Développement d'un capteur géophysique pour caractériser les argiles sensibles en laboratoire

L'argile sensible est caractérisée par des valeurs de résistivité plus élevées en raison de la lixiviation du sel au fil du temps. Nous avons vu dans les deux articles précédents que l'ERT est utilisée depuis une dizaine d'année en Norvège pour cartographier les zones lessivées de leur salinité originelle. Par ailleurs, des études récentes ont montré que la vitesse des ondes de cisaillement pouvait aussi être utilisées. Cependant, il manquait un lien entre ces paramètres physiques (résistivité électrique et vitesse de propagation) à grande échelle et les propriétés mécaniques intrinsèques du sol, comme mentionné dans la dernière phrase de conclusion du papier présenté dans le chapitre précédent (Sauvin et al., 2014). Nous avons avec Shane Gribben, un étudiant en thèse de Queens University à Belfast, développé un capteur de résistivité et de célérité pour échantillons d'argile dans une presse triaxiale du laboratoire de mécanique des sols du NGI. L'idée est de lessiver un échantillon d'argile marine de façon continue à l'intérieur d'une presse triaxiale, de mesurer les variations de résistivité électrique et de célérité des ondes de cisaillement V_s au cours du temps, et enfin, de mesurer la teneur en sel, la résistance au cisaillement et la sensibilité du matériau. La sensibilité S_t d'un sol a un sens essentiellement pour les sols fins, elle se calcule comme le rapport de la résistance (définie conventionnellement) du sol intact sur la résistance du sol (mesurée dans les mêmes conditions) complètement remanié à teneur en eau constante. La notion de sensibilité a été introduite par Bjerrum (1954) dans le cas des argiles glaciaires. On retiendra qu'un sol ayant une résistance notable à l'état intact pourra littéralement se transformer en un liquide après remaniement si sa sensibilité est élevée. La limite utilisée en Norvège pour définir une argile sensible est $S_t < 30$. Ce nouvel outil nous a permis de concilier les mesures en laboratoire, la mécanique des sols avec la géophysique de subsurface (sismique et ERT). Le court article présenté dans ce chapitre décrit la procédure de test en laboratoire que nous avons imaginée ensemble. Des articles présentant les résultats des différentes séries de tests sont en préparation. Le NGI a depuis utilisé ce capteur que nous avons développé dans son laboratoire, pour des projets industriels.

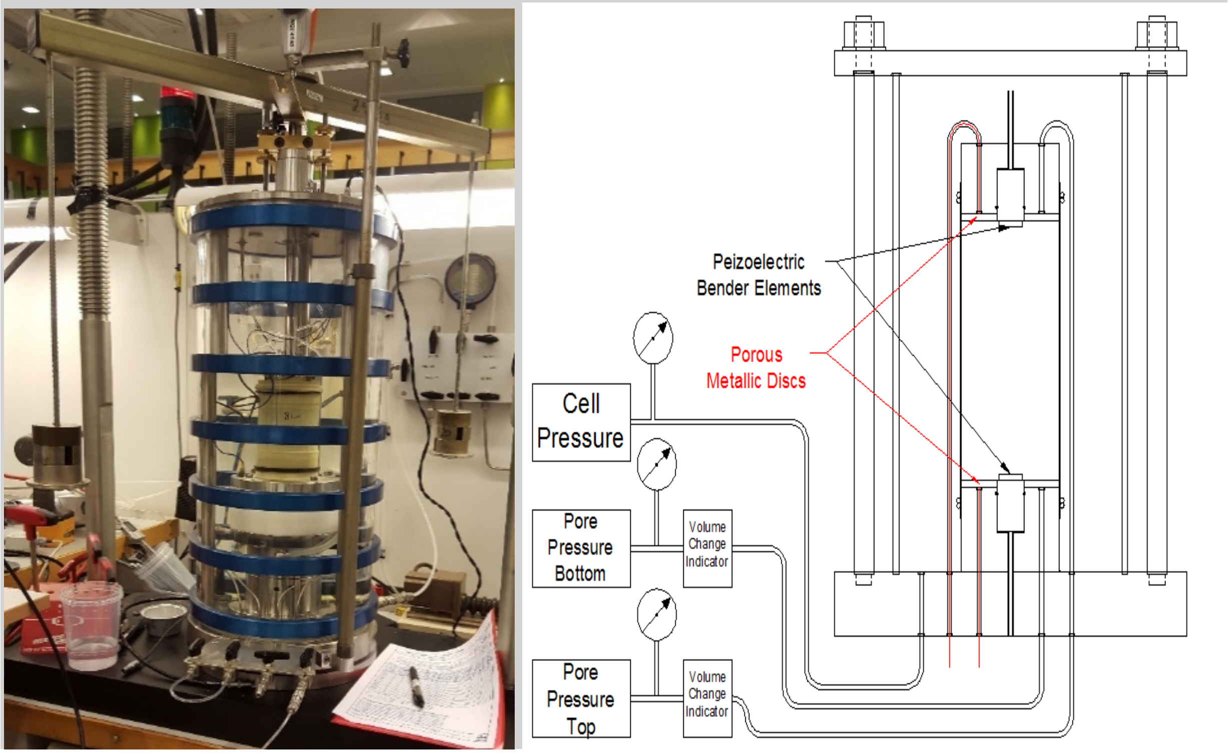

Figure 11 : Développement d'un capteur de résistivité et de célérité pour échantillons d'argile dans une presse triaxiale du laboratoire de mécanique des sols du NGI.

Chapter 8
Investigating How the Changes in Geotechnical Properties of Sensitive Clays Influence Their Geophysical Properties

Shane Gribben, Sara Bazin, Shane Donohue, V. Sivakumar,
and Jean-Sébastien L'Heureux

Abstract This laboratory study involves leaching clay from Onsøy, Norway. Deaired deionised water reduced the pore water salinity, potentially forming a quick clay, in a triaxial cell, modified to allow shear wave velocity and resistivity measurements to be made. This project aims to assess how changes in the geotechnical properties of the clay influence its geophysical properties. The testing procedure has been able to create a quick clay with a remoulded shear strength of 0.2 kPa, and a final salt content of 2.0 g/l. This corresponded to an increase in the resistivity of the clay from initially 0.9 Ωm to a final resistivity of 14.0 Ωm.

8.1 Introduction

Sensitive clays present a serious geological hazard, and are involved in some of the largest landslides that threaten infrastructure and people in countries such as Canada and Norway as demonstrated by the landslides at St-Jude in 2009 and Rissa in 1978. Deposits of quick clays are typically found in post glacial regions of Alaska, Canada and Scandinavia (Holmsen 1953; Engdahl 2006; Sauvin et al. 2014).

Quick clays are highly sensitive soils whose structure completely collapses upon remoulding, resulting in a significant reduction in its shear strength. Remoulded shear strengths less than 0.5 kPa are typical, due to the natural water content of the clay being greater than its liquid limit (Bjerrum 1954; Lundström et al. 2009). In

---

S. Gribben (✉) • S. Donohue • V. Sivakumar
Queen's University Belfast, Belfast, Northern Ireland, UK
e-mail: sgribben02@qub.ac.uk; s.donohue@qub.ac.uk; V.Sivakumar@qub.ac.uk

S. Bazin
Norwegian Geotechnical Institute (NGI), Oslo, Norway
e-mail: sara.bazin@ngi.no

J.-S. L'Heureux
Trondheim Division, Norwegian Geotechnical Institute (NGI), Trondheim, Norway
e-mail: jsl@ngi.no

V. Thakur et al. (eds.), *Landslides in Sensitive Clays*, Advances in Natural
and Technological Hazards Research 46, DOI 10.1007/978-3-319-56487-6_8

Norway a clay is considered to be quick if its remoulded shear strength is less than 0.5 kPa (Torrance 1983; Lundström et al. 2009; NIFS 2015).

These clays are formed as a result of fine glacial outwash material being deposited in a high salt content marine environment. This has resulted in a clay with a highly flocculated structure, a high pore water salt content and a natural water content that is greater than its liquid limit. Post depositional processes such as isostatic uplift has resulted in these deposits being above sea level, as well as percolation and groundwater flow have reduced the pore water salt content of the clay (Bjerrum 1954).

The reduction in the pore water salt content has been linked to the increase in sensitivity of the clay deposit, in particular the reduction in the remoulded shear strength, and reductions in consistency limits. Threshold values for pore water salt content of 2 g/l and 5 g/l have been suggested to identify quick clay (Bjerrum 1954; Torrance 1974), however quick clays with pore water salt content as high as 5.6 g/l have been found in south west Sweden (Lundström et al. 2009).

Current methods for identifying deposits of highly sensitive clays are based on a combination of *in situ* characterisation and geotechnical assessment in the lab. The Norwegian method of identification is based upon a combination of *in situ* testing using total soundings, cone penetration tests, and lab testing to confirm field observations (Lundström et al. 2009; Rankka et al. 2004; NIFS 2015).

Recent developments in the identification of sensitive clays have involved the use of geophysical methods to locate and map the extent of these deposits (Solberg et al. 2008; Lundström et al. 2009; Long et al. 2012; Donohue et al. 2012; Donohue et al. 2014). In particular, there has been a considerable amount of work published on the use of geoelectrical measurements (e.g. Electrical Resistivity Tomography (ERT)) for mapping quick clay. The resistivity of clays typically fall in the range of 1–100 Ωm. Solberg et al. (2008, 2012) suggested for Norwegian clays, that unleached marine clays had resistivities between 1–10 Ωm, fully leached potentially quick clay deposits typically have resistivities in the range of 10–80 Ωm and resistivities of 80+ Ωm are typical of dry crusts, slide deposits and bedrock. The change in resistivity is linked to the reduction in salt content (Long et al. 2012; Solberg et al. 2008). However recent investigations have shown that local conditions can have a major impact upon the threshold resistivity values for quick clays, Lundström et al. (2009) reported Swedish quick clays have resistivity values as low as 5 Ωm.

The purpose of this project is to identify and understand the factors that influence the geophysical properties of sensitive clays.

8.2 Methodology

The experimental procedure involved testing a sample of clay from Onsøy, Norway. The test samples were cut from a block sample, obtained using a Sherbrooke sampler used by the Norwegian Geotechnical Institute (NGI). The site is located 100 km South East of Oslo near the city of Fredrikstad. This site has been used by NGI as a research site for decades. As a result, the site is well characterised.

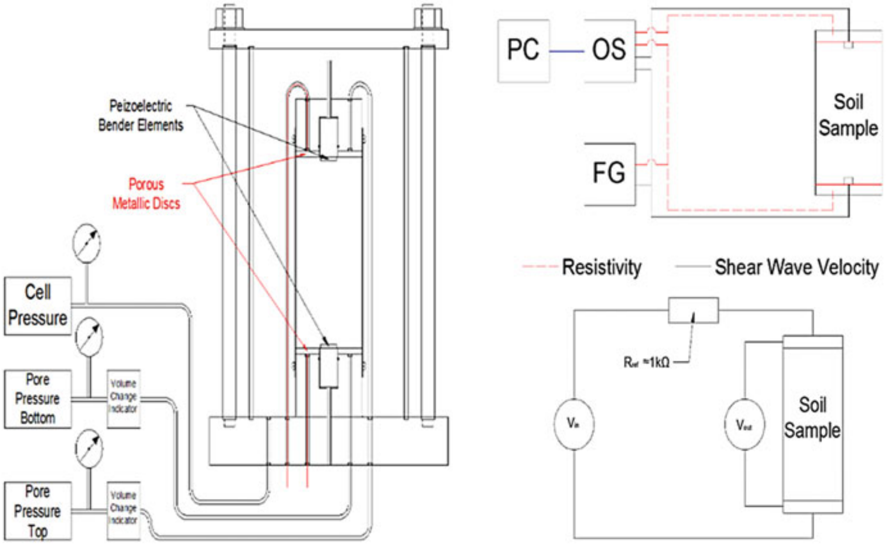

Fig. 8.1 (**a**) Triaxial cell with piezoelectric elements and axial resistance. (**b**) Schematic of sensors, Picoscope (*OS*), Function Generator (*FG*), and Computer (*PC*). (**c**) Electrode arrangement used to measure the complex impedance of the sample (After Wang et al. 2009)

The test procedure has been designed to reduce the pore water salt content of the sample by applying a hydraulic gradient to the sample, which was used to drive a flow of deaired, deionised water through the sample, reducing the pore water salt content of the marine clay, potentially forming a quick clay.

A triaxial cell, Fig. 8.1a, has been modified to measure the changes in resistivity and shear wave velocity of the sample as the pore water salt content is reduced. The shear wave velocity (V_S) is measured using piezoelectric bender element pairs and calculated from the travel time between the tips of the bender elements. Resistivity is measured by applying a current to the sample and measuring the potential difference, which allows the resistance to be determined, and the corresponding resistivity from the sample geometry and the resistance.

Figure 8.1a shows the layout of the triaxial cell including the configuration of the piezoelectric bender elements, used to measure V_S, and the metal porous discs used to measure the electrical resistance of the sample.

The hydraulic gradient across the sample was maintained using two pressure control systems. The pore water pressure at the bottom of the sample was 20 kPa higher than the top of the sample. Volume change due to consolidation/swelling of the sample was monitored using two volume change indicators connected to the pressure control systems that regulated the pore water pressure distribution.

Shear wave velocity and resistivity were measured at regular intervals during the test, using the set up shown in Fig. 8.1b, c. The resistance was measured using a setup modelled after Wang et al. (2009). An input voltage, V_{in}, generated by a sinusoidal function at the function generator (FG), was passed through a reference resistor, R_{ref}, and the potential difference across the sample, V_{out}, was measured by a Picoscope (OS), Fig. 8.1b, c.

The fluid that was flushed out of the sample was collected in the volume change unit connected to the top of the sample, and the salt content of the pore water fluid was measured using a WTW Cond 3110 conductivity probe. The sample was subsequently sheared to obtain the final undisturbed shear strength and a fall cone test, with a 60 g 60° cone, was used to obtain the final remoulded shear strength.

8.3 Results

Table 8.1 summarises information about the tests that have been carried out. Figures 8.2 and 8.3 illustrate the change in resistivity of the various tests as a function of (a) time and (b) the pore water salt content of the sample, respectively.

Table 8.1 Summary of the tests carried out to date

	Test number			
	1	2	3	4
Depth of Sample (m)	12.5	8.0	8.0	8.0
Initial Salt Content (g/l)	9.0	32.6	32.6	32.6
Final Salt Content (g/l)	0.3	0.6	2.0	0.9
Duration of test (days)	130	140	70	125
Initial Undisturbed Shear Strength (kPa)		20	20	20
Initial Remoulded Shear Strength (kPa)		2	2	2
Final Undisturbed Shear Strength (kPa)	–	–	9.0	14.0
Final Remoulded Shear Strength (kPa)	–	–	0.2	0.4

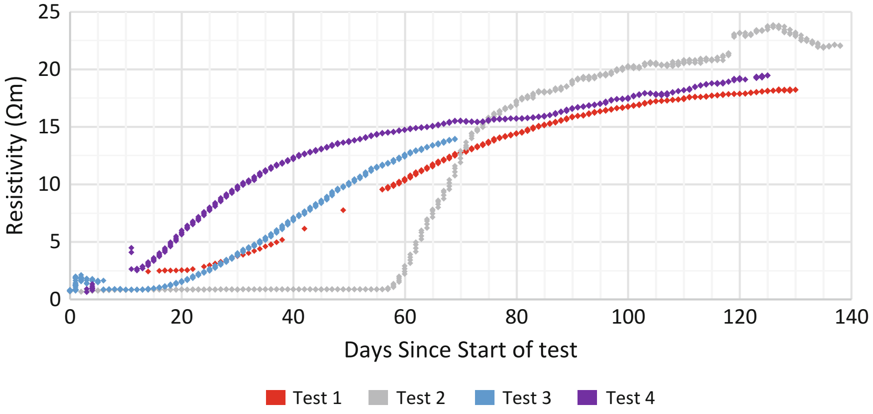

Fig. 8.2 Change in resistivity of the clay sample while undergoing leaching

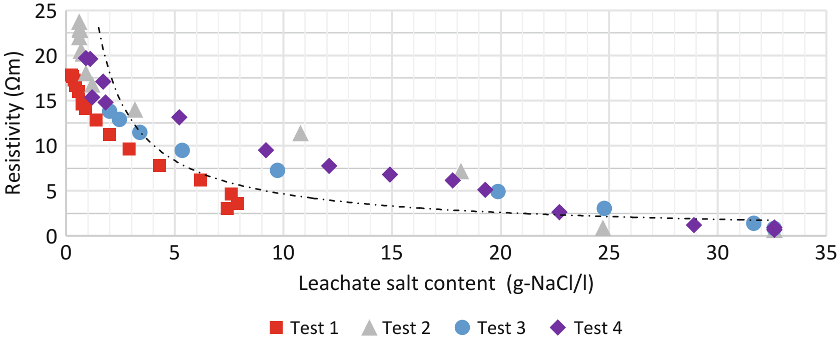

Fig. 8.3 Change in the resistivity of the clay sample as a function of pore water salinity. Dashed line is trend suggested by Long et al. (2012) of the form $y = Ax^n$

Test 1 was used to verify that the system was able to measure the change in resistivity and shear wave velocity as the pore water salt content was reduced by leaching. The sample used in Test 1 was a reconstituted sample of Onsøy clay, it was reconstituted using a pug mill in NGI's Schmertmann Research Laboratory.

The pore water salinity at the start of the test was 9 g-NaCl/l, the pore water salt content was reduced by the leaching method, described previously, to a salinity of 0.3 g-NaCl/l. This reduction in pore water salt content increased the resistivity of the sample from an initial resistivity of 2.4 Ωm to a final resistivity of 17.7 Ωm, see Fig. 8.2. The final shear strengths of this sample were not determined as the sample was reconstituted, this process destroyed the natural structure of the clay and, as a result, significant changes to the undisturbed shear strength, remoulded shear strength and resultant sensitivity were not expected.

Tests 2, 3 and 4 were conducted using a sample cut from a Sherbrooke block sample obtained from a depth of 8.0 m. Each sample had a starting pore water salt content of 32.6 g–NaCl/l. At this depth Onsøy clay typically has an undisturbed shear strength between 20 and 30 kPa, depending upon sampling and testing methods, and a remoulded shear strength of 2–3 kPa, and a resulting sensitivity between 8 and 16, according to Lunne et al. (2003).

During Test 2, one of the drainage lines was blocked, this is clearly visible in Fig. 8.2, as between days 20 and 60 there was no noticeable change in the resistivity of the sample. The method of clearing the drainage lines may have damaged the microstructure of the clay, and in this case neither the undisturbed or remoulded shear strength was calculated.

Figure 8.3 shows the change in resistivity of the marine clay as it was leached of its pore water salt content. Test 2 (shown in grey) had an initial pore water salt content of 32.6 g–NaCl/l and was leached to final pore water salt content of 0.6 g–NaCl/l. The reduction in pore water salinity resulted in an increase in the sample resistivity, from an initial value of 0.7 Ωm to a final resistivity value of 18.1 Ωm.

In Test 3, (shown in light blue), the pore water salt content was reduced to 1.8 g–NaCl/l. The resistivity of the sample increased from an initial value of 0.7 Ωm to a final value of 13.8 Ωm. The remoulded shear strength, measured using the fall cone method, decreased from an initial value of 2.0 kPa to a final value 0.2 kPa, which according to the Norwegian definition, making this leached marine clay, quick.

In Test 4, (purple), the pore water salt content was reduced to 0.9 g–NaCl/l. The resistivity of the sample increased from an initial value of 0.9 Ωm to a final value of 19.7 Ωm. The remoulded shear strength of this sample, measured via fall cone test, was found to have decreased from initially 2 kPa to 0.4 kPa, making the clay quick.

Figure 8.4 shows the change in the shear wave velocity of the sample in Tests 1, 2 and 4, as the sample was leached. No measurements were possible for Test 3 due to equipment malfunction. In Test 1 the initial V_s was 118 m/s which increased to a final velocity of 126 m/s this occurred over the same time period as a reduction in the pore water salt content, as previously stated, from 9.0 g–NaCl/l to 0.3 g–NaCl/l, Fig. 8.5.

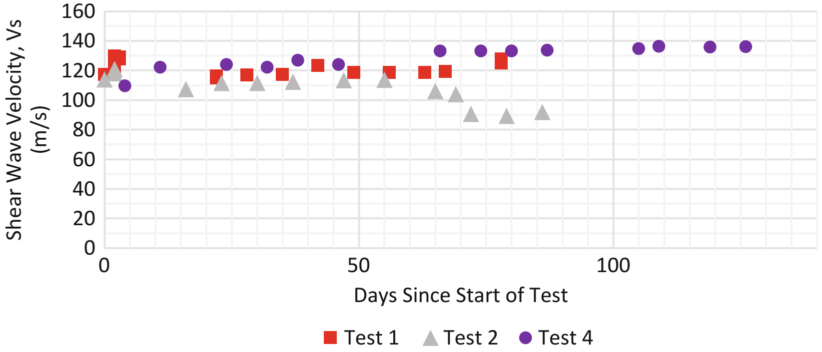

Fig. 8.4 Change in shear wave velocity of the clay samples while undergoing leaching

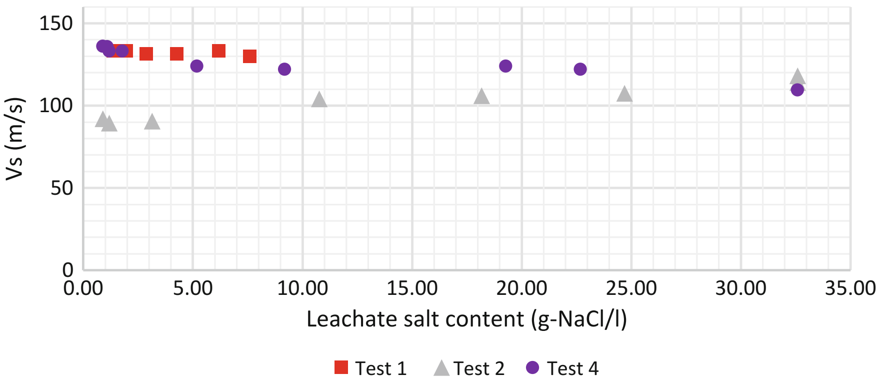

Fig. 8.5 Change in the shear wave velocity of the sample as a function of the pore water salinity

In Test 2 V_s decreased from 114 m/s to a final value of 92 m/s. This reduction in the shear wave velocity occurred over the same time period that the pore water salt content was reduced from an initial value of 32.6 g–NaCl/l to 0.6 g–NaCl/l, see Fig. 8.5. Due to the blockage in the drainage line in Test 2, nothing conclusive can be drawn from this reduction in V_s as any change in stiffness may be due to clearing the blockage.

In Test 4V_s increased from 109 m/s to a final value of 136 m/s. This increase in value occurred over the same time period that the pore water salt content reduced from an initial value of 32.6 g–NaCl/l to a final value of 0.9 g–NaCl/l, see Fig. 8.5.

8.4 Discussion

The reduction in the pore water salt content and consequent increase in the resistivity of the clay sample was expected as pore water salt is typically comprised of fully dissociated salts containing Na^+, K^+, Mg^{2+}, and Ca^{2+} ions which have lower electrolytic resistivity's than the clay dominated matrix. This was consistent in all four tests. The increase in the resistivity of the sample as a function of the salt content as shown in Fig. 8.3 appears to be of the form $y = Ax^n$ which is the same form as suggested by Long et al. (2012).

The results of Tests 3 & 4 suggest that the reduction in the remoulded shear strength, from 2 kPa in both cases to 0.2 kPa and 0.4 kPa in Tests 3 & 4 respectively, hence increase in the sensitivity, of the clay is linked to the reduction in the pore water salt content of the clay. This is consistent with Bjerrum (1954) conclusions regards the influence of salt content and the remoulded shear strength.

The initial laboratory resistivity and shear wave velocity measurements have been compared to values obtained from seismic and ERT surveys of the Onsøy research site, the values for resistivity measured in the lab for a sample at 8 m depth are in the range of 0.7–0.9 Ωm, while the value obtained from the ERT profile the resistivity at this depth is 0.8 Ωm (Bazin et al. 2016).

The small variation between the resistivity measured in the laboratory and those determined from ERT surveys indicates the laboratory setup is capable of accurately replicating the conditions encountered in the field. This also indicates that the storage method used for these samples had limited impact upon the salt content of the block sample, although more information on the ion composition and concentrations would be required to verify this.

It should, however, be noted that the pore water salinity according to Lunne et al. (2003), was expected to be 35 g/l whereas in both samples of Onsøy clay, the initial salinity was 32.6 g/l. A higher initial resistivity would therefore have been expected in the lab resistivity measurement, if the stress conditions in the lab accurately the *in situ* conditions at the site, than that obtained from the ERT survey (Bazin et al. 2016).

The lower than expected resistivity, given the salt content and stress conditions, is possibly as a result of changes in the consistency limits of the soil due to aging of the soil during storage including a possible increase in moisture content due to the sampling technique, and changes in the salinity of the sample due to oxidation (NGI 2013) which has been shown to cause variations in resistivity, in particular the moisture content and salinity, (Samouëlian et al. 2005; Hazreek et al. 2015).

The V_s measurements from laboratory tests suggest that the initial shear wave velocity is between 109 m/s and 127 m/s, whereas the seismic data in the field gives a value of 105 m/s to109m/s (Bazin et al. 2016). The difference between the value in the field and the laboratory is likely due to a number of factors including, sample disturbance during preparation of the sample for testing, ageing of the samples while they were kept in storage and methodological uncertainty associated with selecting travel time between bender elements.

The increase in V_s observed during Test 1 is likely due to a combination of volume change and the effects of secondary consolidation. Research by Anderson and Stokoe (1978) propose that the increase in V_s with time is expected to be about 5–20% for every log cycle of time, for normally consolidated clays.

Test 2 showed a reduction in V_s from 114 m/s to 92 m/s, this was likely caused by clearing a blockage in the drainage lines, which would have disturbed the sample, however the reduction in V_s of the sample does occur when the pore water salt content of the sample falls below a threshold value of 5 g/l, and this corresponds to the expected changes in strength and stiffness of highly sensitive and quick clays (Bjerrum 1954). However the results of Test 4 show a 5% increase in V_s, per log cycle time, of the sample which is likely due to a combination of volume change and the effects of secondary consolidation which is in line with what was proposed by Anderson and Stokoe (1978), indicating that the reduction in V_s shown in Test 2 was due to sample disturbance during testing.

The pore water salt content is determined by measuring the conductivity of the fluid collected in the volume control unit. There are a few issues with this method, firstly, the salinity of the fluid that was flushed out of the sample may not be the same as the salinity of the pore water in the sample at the time of collecting the fluid (i.e. there will be a time lag). Secondly the exact geochemical composition of the pore water is unknown, and it is unknown whether the change in conductivity is a result of changes in Na^+, K^+, Ca^{2+}, and Mg^{2+} and not as a result of other oxidised stabilising ions.

8.5 Conclusion

The results of the preliminary tests show that using a modified triaxial cell to quantify the changes in geotechnical and geophysical properties of a marine clay as its pore water salt content is reduced is possible. The results of Tests 3 and 4 show that it is possible to create a highly sensitive (or quick) clay using the leaching method outlined.

In addition to determining the changes in the undisturbed and remoulded shear strengths due to reduction in the pore water salt content, it is proposed that future work will assess the affect of moisture content, density, grain size distribution, consistency limits, pore water chemistry, grain size distribution and clay content on the geophysical properties during leaching of ‘salt’ clay samples.

Acknowledgements The authors wish to extend their sincere gratitude to Toralv Berre, Morten Andreas Sjursen, and Rune Dyvik at NGI geotechnical laboratory for all the help and expertise offered in laboratory work. We would also like to thank both NGI and Prof. JH Schmertmann for the use of both time and equipment in NGI’s Schmertmann Research Laboratory. Funding for this research has been provided by both the Department for Employment and Learning (NI) and the NGI Schmertmann Research Laboratory.

References

Anderson DG, Stokoe KH (1978) Shear modulus: a time-dependent soil property. ASTM Special Technical Publication, Philadelphia, pp 66–90

Bazin S, Anschütz H, Sauvin G, Gribben S, Donohue S, Long M (2016) Geophysical characterisation of marine and quick clay sites: field and laboratory tests. In: 5th International conference on geotechnical and geophysical site characterisation. pp 0–5

Bjerrum L (1954) Geotechnical properties of Norwegian marine clays. Géotechnique 4(2):49–69

Donohue S, Long M, L’Heureux JS, Solberg IL, Sauvin G, Rømoen M, Kalscheuer T, Bastani M, Persson L, Lecomte I, O’Connor P (2014) Landslides in sensitive clays: from geosciences to risk management. In J.-S. L’Heureux et al., (eds) Dordrecht, Springer Netherlands, pp 159–178

Donohue S, Long M, O’Connor P, Eide Helle T, Pfaffhuber AA, Rømoen M (2012) Multi-method geophysical mapping of quick clay. Near Surf Geophy 10(1828):207–219

Engdahl M (2006) Natural hazards in Nordic countries. Episodes J Int Geosci 31(1):176–184

Hazreek ZAM, Aziman M, Azhar ATS, Chitral WD, Fauziah A, Rosli S (2015) The behaviour of laboratory soil electrical resistivity value under basic soil properties influences. Aero Earth 23:12002

Holmsen PER (1953) Landslips in Norwegian quick-clays. Géotechnique 3(5):187–194

Long M, Donohue S, L’Heureux JS, Solberg IL, Rønning JS, Limacher R, O’Connor P, Sauvin G, Rømoen M, Lecomte I (2012) Relationship between electrical resistivity and basic geotechnical parameters for marine clays. Can Geotech J 49(10):1158–1168

Lundström K, Larsson R, Dahlin T (2009) Mapping of quick clay formations using geotechnical and geophysical methods. Landslides 6(1):1–15

Lunne T, Long M, Forsberg CF (2003) Characterisation and engineering properties of Onsøy clay. In: Characterisation and engineering properties of natural soils. Swets & Zeitlinger, Lisse, pp 395–428

NGI (2013) Effect of storage time on sample quality, Report number 68-2014

NIFS (2015) Detektering av kvikkleire - Sluttrapport (Detection of Sensitive Material), Report number 126-2015. ISSN 1501–2832

Rankka K, Andersson-Sköld Y, Hultén C, Larsson R, Leroux V, Dahlin T, (2004) Quick clay in Sweden, Linkoping, Goteborg. Lund

Samouëlian A, Cousin I, Tabbagh A, Bruand A, Richard G (2005) Electrical resistivity survey in soil science: a review. Soil Tillage Res 83(2):173–193

Sauvin G, Lecomte I, Bazin S, Hansen L, Vanneste M, L’Heureux JS (2014) On the integrated use of geophysics for quick-clay mapping: the Hvittingfoss case study, Norway. J Appl Geophys 106:1–13

Solberg IL, Hansen L, Rønning JS, Haugen ED, Dalsegg E, Tønnesen JF (2012) Combined geophysical and geotechnical approach to ground investigations and hazard zonation of a quick clay area, mid Norway. Bull Eng Geol Environ 71(1):119–133

Solberg IL, Rønning JS, Dalsegg E, Hansen L, Rokoengen K, Sandven R (2008) Resistivity measurements as a tool for outlining quick-clay extent and valley-fill stratigraphy: a feasibility study from Buvika, central Norway. Can Geotech J 45(2):210–225

Torrance JK (1974) A laboratory investigation of the effect of leaching on the compressibility and shear strength of Norwegian marine clays. Géotechnique 24(2):155–173

Torrance JK (1983) Towards a general model of quick clay development. Sedimentology 30(4):547–555

Wang Z, Gelius LJ, Kong FN (2009) Simultaneous core sample measurements of elastic properties and resistivity at reservoir conditions employing a modified triaxial cell – a feasibility study. Geophys Prospect 57(6):1009–1026

4.4 Inversion conjointe : application de l'ERT/PP aux schistes toxiques

Comme expliqué précédemment, il y a souvent nécessité de combiner plusieurs mesures physiques lorsque qu'il existe une ambiguïté dans l'interprétation d'un modèle géophysique. Par exemple, pour différencier des roches qui présentent la même résistivité électrique, il faut parfois faire appel à d'autres propriétés physiques. La polarisation provoqué (PP) présente alors un intérêt notable car elle ne nécessite pas de faire une acquisition supplémentaire. En effet, cette dernière peut être enregistrée sur le terrain par le même matériel que l'ERT et de façon simultanée. La méthode PP est une extension de la méthode électrique en courant continu. La méthode ERT classique cible la conductivité électrique du milieu (transport de charges) tandis que la PP mesure la polarisation du milieu (réorientation des charges). Celle-ci se manifeste par une tension secondaire transitoire dans les matériaux polarisables après l’interruption du courant continu. Longtemps utilisée pour l'exploration minière (recherche de métal précieux concentré dans des filons), la PP est en extension depuis les années 2000 dans les études environnementales, pour par exemple délimiter les zones contaminées ou pour étudier certains paramètres physico-chimiques. Je l'ai utilisée en contexte de pergélisol pour délimiter les sols gelés du substrat rocheux car ces deux matériaux ne présentaient pas de contraste en résistivité électrique. En revanche, le substrat rocheux avait une forte anomalie en PP par rapport aux sols gelés (Bazin et al., 2019).

L'application de la l’ERT couplée avec la PP présentée ici concerne les schistes toxiques alunifères dans la région d'Oslo. Les schistes argileux sont des roches sédimentaires argileuses fissiles, ce qui correspond à la définition du " shale" en anglais. Ce sont des roches cohérentes, non "schisteuses", finement cristallisées, dans lesquelles on peut rencontrer du quartz, de l'illite, de la chlorite, de la calcite, de la pyrite et de la magnétite. Parmi eux, les schistes alunifères contiennent de l'alun provenant en partie de la décomposition de la pyrite. Leur couleur les fait classer dans les schistes noirs. Ces derniers ont une forte concentration en Uranium qui les rend toxiques. Il y a nécessité de cartographier les zones où il existe une probabilité que du radon se dégage du sol, appelée « potentiel radon ». Celui-ci est mesuré par l’indice de concentration d’activités (I) en Bq/kg. Il existe dans certaines régions de Norvège de grandes quantités de schistes noirs, surtout dans le graben d'Oslo qui est de surcroît la région la plus densément peuplée. Or les schistes noirs se présentent en général dans une série géologique comprenant plusieurs types de schistes dont certains sont très riches en Uranium et d'autres moins. Ces différents schistes ont des résistivités électriques très faibles à faibles (ρ entre 0,02 et 0,5 Ωm), mais proches les uns des autres et il est difficile de les différencier sans faire d'analyse physico-chimiques. Or des mesures en laboratoire nous ont permis de montrer que les schistes d'alun qui ont le plus fort potentiel radon, présentent aussi des valeurs de PP les plus élevées. Nous nous sommes servis de cette observation, pour cartographier pour la première fois, les zones de schistes d'alun, en utilisant la résistivité électrique et la PP mesurées le long de profils géophysiques de surface mais aussi par mesures aéroportées avec l'AEM. L'article retranscrit ici montre l'intérêt d'inverser simultanément la résistivité électrique et la polarisation pour cartographier les différents types de schistes. Ce travail a bénéficié d'une collaboration avec Thomas Gunther, le concepteur du freeware BERT, avec qui nous avons développé une nouvelle méthode pour inverser les courbes de relaxation des profils de surface plutôt que l'amplitude moyenne de la polarisation, comme avec la plupart des logiciels dont Res2Dinv. Par ailleurs, un essai de survol héliporté nous a aussi permis de montrer que la résolution des modèles de résistivité électrique et de polarisation obtenus par AEM est suffisante pour ce type de cartographie. Nos modèles géophysiques sont ensuite confrontés aux observations directes faites par forages et lors de l'excavation d'un tunnel.

Near Surface Geophysics, 2018, **16**, 1-11 doi: 10.3997/1873-0604.2017036

Resistivity and chargeability survey for tunnel investigation: a case study on toxic black shale in Norway

Sara Bazin[1*], Asgeir K. Lysdahl[1], Andrea Viezzoli[2], Thomas Günther[3], Helgard Anschütz[1], Jürgen Scheibz[1], Andreas A. Pfaffhuber[1], Tino Radic[4] and Halldis Fjermestad[5]

[1] *Norwegian Geotechnical Institute, Sognsveien 72, 0855 Oslo, Norway*
[2] *Aarhus Geophysics, ApS. C.F. Møllers Allè 4, DK-8000 Aarhus C, Denmark*
[3] *Leibniz Institute for Applied Geophysics, D-30655 Hannover, Germany*
[4] *Radic Research, 13469 Berlin, Germany*
[5] *Statens vegvesen Region øst, Postboks 1010, 2605 Lillehammer, Norway*

Received March 2016, revision accepted July 2017

ABSTRACT

In the past few years, the focus on Alum shale hazards and the need for efficient mapping tools have increased in Norway. Alum shale is highly toxic and poses a substantial obstacle to infrastructure development such as tunnel projects. We present an evaluation of the ground-based electrical resistivity tomography, induced polarisation, and airborne electromagnetic methods for mapping purposes using a recent case study. This evaluation is done in combination with resistivity and chargeability laboratory measurements applied to drill cores. The aim of the geophysical survey was to improve the knowledge of Alum shale occurrence to assist a tunnel project in Gran, southeast Norway. Resistivity and chargeability models derived from an electrical resistivity tomography/induced polarisation survey enabled us to map the presence of Alum shale during the tunnel investigation. The resistivity models point to geological layers that are in agreement with the rock types observed from early drillings together with subsequent geological logging during tunnelling. The time-domain chargeability models are imperfect but nonetheless reveal the presence of polarisable minerals. These are likely due to the high levels of sulphides contained in black shale. An airborne electromagnetic survey was done close to the area of interest, which enabled us to fly some sparse lines across the tunnel alignment as a piggyback survey. Although the airborne electromagnetic resolution is lower than electrical resistivity tomography, the successful test flight lines illustrate the potential of airborne electromagnetic surveys for Alum shale mapping in Norway and affirm the promise of airborne electromagnetic in the early stages of project exploration.

INTRODUCTION

The Norwegian Road Authority is modernizing the highway Rv.4, located 80 km northwest of Oslo (Figure 1). Two parallel road tunnels, each 1700 m long, have been excavated to bypass the town of Gran. The rock overburden is between 15 m and 25 m. The blasting took place between November 2013 and May 2015, and roughly 335 000 m^3 of masses from 700 blasting units were driven out. The tunnel opened to traffic in summer 2017. We carried out a geophysical survey along the planned tunnel axis as blasting had just started. Exploratory drilling had already been conducted, and a preliminary geological model was available. However, the complexity of the project required a supplementary study to gather continuous information between the boreholes and, thus, decrease the overall project risk in terms of finances and scheduling. The first objective of this study was to characterize the rock mass and its overburden using resistivity derived either from ground-surface electrical resistivity tomography (ERT) or airborne electromagnetic (AEM) surveys.

Experience shows that ERT usually gives good results for tunnel investigations (Danielsen and Dahlin 2009), and it is a time and cost-effective method compared with other ground-based geophysical methods. Conversely, the use of AEM for tunnel pre-investigations is only starting for economic reasons,

---

[*] sara.bazin@ngi.no

and an increasing number of case studies shows that high-resolution AEM data are valuable and cost-saving tools in construction projects (Pfaffhuber *et al.* 2010, Okazaki *et al.* 2011, Anschütz *et al*. 2017). The typical size of an AEM survey for such projects is on the order of 200-km flight lines, which takes approximately 2–3 days to fly. Both methods, ERT and AEM, can model the lateral and vertical resistivity distribution of the subsurface; ERT has often a better lateral resolution but more limited depth of investigation than AEM (e.g., Anschütz *et al.* in press). The two methods are therefore complementary.

The second objective of this study was to determine the applicability of geophysics to identity the different shale types present in the tunnel. Some areas of the Norwegian capital Oslo and its surroundings feature a toxic black shale type, Alum shale. Excavated Alum shale is classified as toxic waste and must be disposed accordingly (NGI 2015). For this purpose, a special waste landfill needs to be established near the excavated site. Consequently, Alum shale occurrence is a massive cost for a tunnel project, and prior knowledge about its expected volume is crucial. The resistivity models were initially used to delineate the occurrence of the black shale along the tunnel axis. We observed that the black shale was chargeable enough to create induced polarisation (IP) signals in both the ground and airborne data. Laboratory measurements were then carried out at a later stage to help understand the different mechanisms involved in the IP signals observed in the field. The results of the different methods are first described, then compared and discussed. An evaluation of the different mapping methods is proposed.

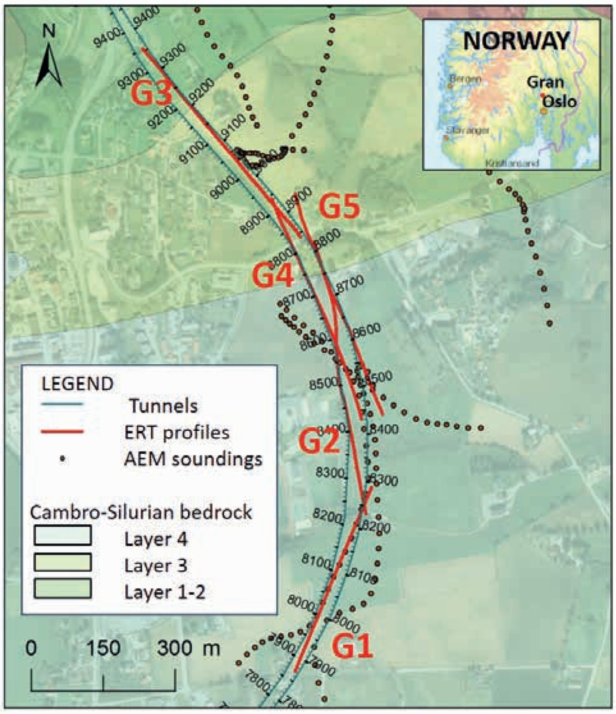

Figure 1 Detailed map of the study area in Gran town, 100 km north of Oslo, Norway. Superposition of the planned road tunnel, the ERT profiles, the AEM test survey, and the bedrock stratigraphy. The regional map is displayed with transparency effect to show the presence of urban infrastructure near the survey.

Geological context

The Alum Shale Formation is a formation of black shale of Middle Cambrian to Lower Ordovician in age, found only in southern Scandinavia (Nielsen and Schovsbo 2007). They were deposited in an alternation of reducing or oxidizing environmental conditions as dark, fine-grained sediments rich in organic material (NGU 2009). These shale formations have a high content of carbon, with total carbon values (TOC) up to 16–17% (wt). In certain extreme TOC values, up to 50% (wt) have been found. Alum shale is known to be environmentally harmful because of its high content of sulphides (> 15 g/kg) and heavy metals (60–200 mg/kg) (NGI 2013). Alum shale is also a source of radon gas and ionizing radiation. Adding to its toxicity, Alum shale swells significantly when it encounters oxygen, leading to deformation and damage risk to infrastructure in the vicinity: the oxidation changes the shale minerals such that a significant swelling perpendicular to the shale plane occurs (two to three times the original volume), which can cause differential uplift to nearby structures (NGI 2015). Moreover, when exposed to air and water, the sulphides are oxidised and produce sulfuric acid, which may corrode metallic structures. Black shale formations in Norway are mainly found in the Oslo rift, which extends as far north as Hamar, about 130 km north of Oslo. They are found on a small but densely inhabited area (roughly one third of the Norwegian population lives in southeast Norway). These clay-rich shales are part of the Cambro–Silurian stratigraphy, which includes a wide variety of shales and limestones of different compositions. The different lithological black shales in the Oslo graben have been formed under different anaerobic conditions. Less oxygen present under sedimentation generally produced higher sulphide and heavy metal contents and larger grain sizes. The shale layers are named chronologically: Layer 1 designates the oldest, deepest layer and consists mainly of sandstones. Layers 2–3a comprise the most harmful black shale, named Alum shale, usually in thick layers (up to 80 m). Alum shale is an argillaceous, often carbonaceous rock, containing iron sulphides (pyrite, pyrrhotite, and marcasite), which, when decomposed,

	Elnes	Huk	Galgeberg	Hagaberg	Alum
Max. resistivity (Ωm)	84	540	0.54	240	0.13
Min. resistivity (Ωm)	44	43	0.25	110	0.025

Table 1 Laboratory resistivity measurements in core samples from the five rock types of the Cambro–Silurian stratigraphy.

forms sulphuric acid that reacts with the aluminous and potassic materials of the rock to produce aluminium sulphates (AGI 1972). Layer 3bα is called Hagaberg and is a green–gray shale, usually with a thickness of over 10 m. Layer 3bβ is another black shale, called Galgeberg, with a thickness of over 15 m. Thereafter comes layer *3c*, typically a thin layer subdivided into limestones, called Huk, and limestone-rich shales. The last layer found in the Gran tunnel is 4aα, called Elnes, a gray shale that may have black shale properties and can occur in layers dozens of meter thick. The strata are tilted in the area, and the Alum shale layer is exposed in the northern tunnel end. Nyland and Teigland (1984) measured uranium (U) concentration in many samples from Cambro–Silurian rocks of the Oslo rift, and they reported that the Alum shale samples contained the highest U concentration (126 mg/kg), compared with an average of 29 mg/kg in the remaining samples.

Laboratory data

Resistivity measurements were carried out on cores drilled in the Gran tunnel. They correspond to the five rock types of the Cambro–Silurian stratigraphy. The samples were carefully sawn off, and their final average dimensions were 38 mm in diameter and 31 mm in length (Figure 2 right). Wang, Gelius and Kong (2009) have adapted a triaxial cell to measure resistivity in rock samples at *in situ* conditions while minimizing the polarisation effects with a two-electrode system (Figure 2 left). The modified triaxial cell was used at a confining pressure of 0.5 MPa and a varying effective vertical stress of 3–10 MPa. Both axial and radial resistivities were recorded. The maximum (perpendicular to the shale plane) and minimum (parallel to the shale plane) resistivities were estimated by rotating the conductivity tensor (Table 1).

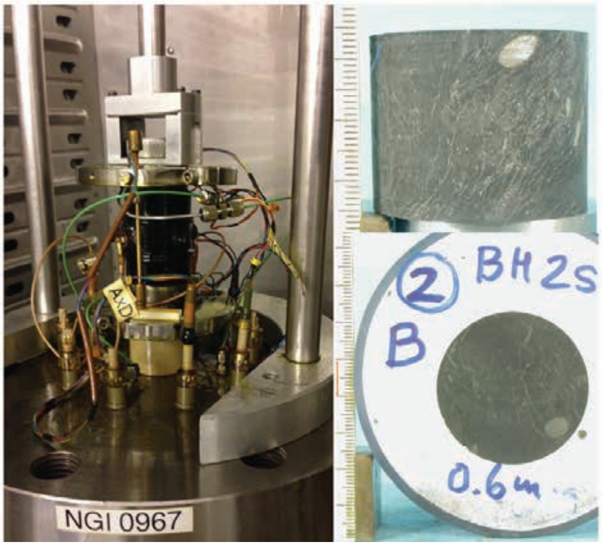

Figure 2 Left: the modified triaxial cell can measure resistivity at *in situ* conditions (Wang *et al*. 2009). The electrodes are encapsulated in the top cap and the pedestal and on the sides of the sample. Right: Alum shale sample used for the laboratory resistivity measurement. Notice the anisotropy and the large mineral sizes.

The laboratory set-up and the Alum shale sample are shown in Figure 2.

The two black shale types (Alum and Galgeberg) are highly conductive, $\rho < 1$ Ωm, the Alum shale being the most conductive. These extremely low values confirm the potential to use resistivity as a mapping tool for black shale. The gray shale Elnes, which may have some black shale properties, has a higher resistivity, whereas the Hagaberg and the limestone Huk have much higher values. The strong anisotropy, up to a factor of 10 for Huk limestone and Alum shale, is of particular interest. The former is explained by significant cracks visible in the sample; the latter is a result of the inherent sedimentation structure.

As explained in the introduction, the second objective of this study was to determine the applicability of geophysics to identity the different shale types of the Cambro–Silurian stratigraphy. The need to better understand the chargeability properties of Alum shale was raised while processing the ground-investigation data. Therefore, spectral IP (SIP) measurements were carried out on three core samples at a later stage using the "Chameleon" apparatus (Radic 2014) to measure the complex resistivity ρ^* ($\rho^* = |\rho| e^{i\phi}$ where ϕ is the phase shift between the injected current and the measured potential). These samples were not taken in the Gran tunnel but from the same Alum shale layer of the Cambro–Silurian stratigraphy in the Oslo graben. Again, the samples were carefully sawn off, and their final average dimensions were 45 mm in diameter and 96 mm in length. The SIP measurements were carried out with three different current densities (0.07 A/m^2, 0.7 A/m^2, and 7 A/m^2), but only the most representative one, at 0.07 A/m^2, is shown here. Figure 3 shows the resistivity spectra (amplitude $|\rho|$ and phase ϕ) in three Alum shale samples (E1, E2 and E3). The measured impedance is a combination of several mechanisms. The most important of these for the investigated samples is the current flowing through metallic particles, which creates a frequency dependent conduction. This mechanism is usually referred to as interfacial polarisation. We observe a decrease of the amplitude resistivity with increasing frequency (Figure 3a), which is connected with a negative phase shift between the injected current and the measured voltage (Figure 3b). The chargeability level can be estimated from the relative drop of resistivity from lowest to highest frequency by the formulation $m_o = (\rho_0 - \rho_{inf}) / \rho_0$. It ranges between 650 mV/V and 800 mV/V for the three samples over the entire spectrum (Figure 3a). The three phase spectra in Figure 3b seem to indicate that these Alum shale cores have different polarisation performance over the studied frequency (1 mHz to 100 kHz), but they all show three negative phase peaks at the same frequencies (at 3 mHz, between 2 Hz and 3 Hz, and near 100 kHz). The phase decrease near 100 kHz should not be considered a characteristic peak. The measured absolute peak amplitudes are between 1° and 19°. Normally, IP effects over 1° phase are due to electronic conducting minerals, that is, the iron sulphides present in these Alum shale cores. The

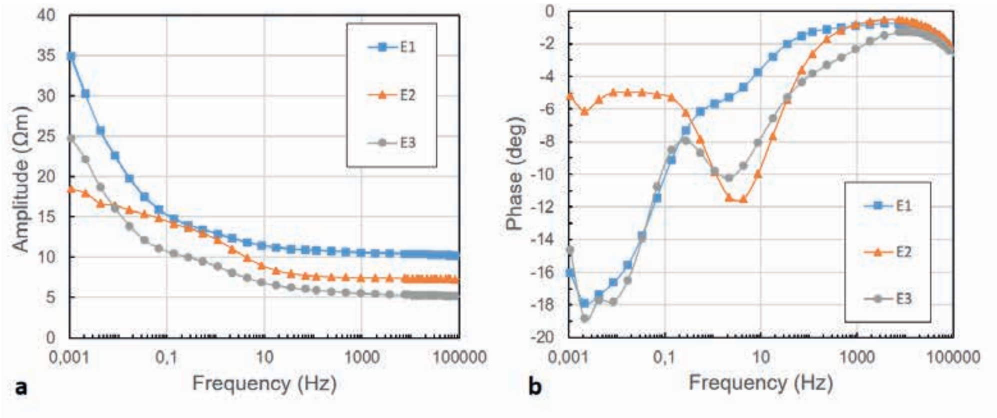

Figure 3 Complex resistivity spectra ($\rho^* = |\rho|\ ei\phi$) for three core samples E1, E2, and E3 of Alum shale. The resistivity amplitude $|\rho|$ is shown in *a*, whereas the phase ϕ shift (in degrees) between the injected current and the measured potential is shown in *b*.

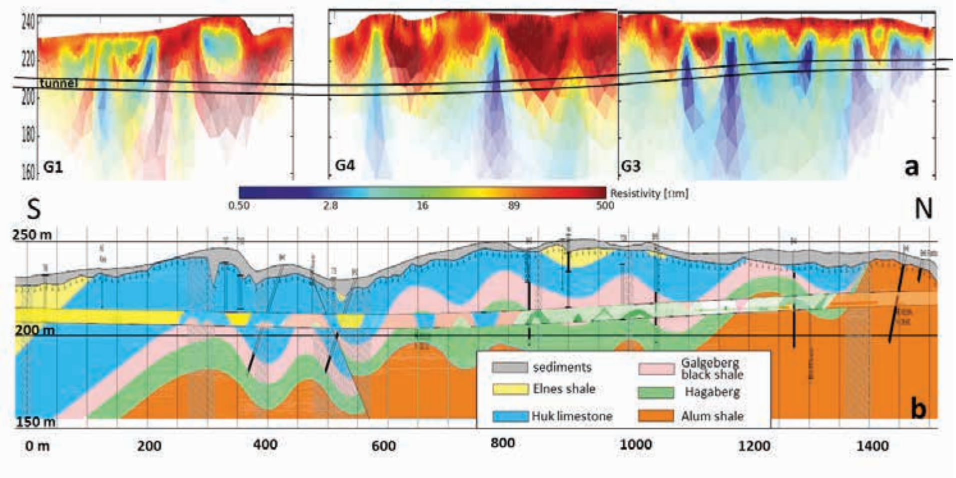

Figure 4 (a) Resistivity models along G1, G4, and G3. (b) Preliminary geological model based on drilling (background colours) and geological mapping during excavation (inside tunnel sketch). The preliminary geological model treats the Hagaberg layer (green color) as one unit, whereas the on-site geological mapping is able to differentiate between the limestone (light green) and the shale (dark green) sublayers. The vertical scale is exaggerated.

peaks in the spectrum are interpreted as related to the diameters of electronic conducting minerals (e.g., Pelton *et al.* 1978). The phase peak at 2–3 Hz corresponds with minerals' diameters of some millimetre, whereas the phase peak at 3 mHz corresponds with minerals' diameters of some centimetre. A visual inspection does not show minerals as large as cm and thus the phase peak at 2–3 Hz can be a result of connected conducting minerals, forming large polarisable aggregates. Such aggregates are visible in the samples and have the shape of foliations. In general, the amplitude of the phase peak correlates with the mineral content of the sample (Pelton *et al.* 1978; Revil *et al.* 2016). A chemical analysis of the three samples reveals that the two samples (E2 and E3) that present a strong peak near 3 mHz contain the most iron sulphides and the highest U levels and, are therefore, the most harmful. This result highlights the heterogeneity that can be found in one single Alum shale layer. These rocks have probably been formed under more anaerobic conditions, yielding higher sulphide content and larger grain sizes (Lysdahl, Endre and Radic 2016). This result also suggests that the amplitude of the phase peak may be a good proxy for the toxicity level of the Alum shale.

Resistivity ground investigation

ERT measurements were carried out along the tunnel axis to map the occurrence of black shale, motivated by prior laboratory tests indicating extremely low resistivity (< 1 Ωm, see above). The survey was performed with a 12-channel Terrameter Lund System (LS) recording unit (ABEM 2010). The multiple gradient array was chosen for the acquisition protocol (Dahlin and Zhou 2006), being the most efficient array for this multichannel instrument. Three ERT profiles with 3-m electrode spacing (profile lengths: G1 420 m, G2 582 m and G3 519 m) were acquired along most of the tunnel alignment. The maximum depth of investigation was ~46 m with this acquisition geometry. Two additional ERT profiles (G4 and G5) were acquired in the central part of the tunnel alignment with 5-m electrode spacing to increase the depth of investigation to 70 m where the tunnel is the deepest (the depth of the tunnel roof at its deepest point is 44 m). All ERT data were inverted with the academic boundless electrical resistivity tomography (BERT/GIMLi) code (Günther, Rücker and Spitzer 2006). Bazin *et al.* (2015) discuss the consistency between this inversion algorithm and the industry standard Res2Dinv program (Loke 2010) together with the Århus University's AarhusInv algorithm (Auken *et al.* 2005, 2014). Figure 4 illustrates the three different stratigraphy models that exist for the tunnel project: pre-investigation geological mapping and borehole lithology were used to build a preliminary stratigraphic model; resistivity models were used to foresee possible deviation from the preliminary stratigraphic model; finally, direct geological observation during the excavation were used as ground truth to evaluate the resolution of the resistivity models. Only the three most representative of the five ERT profiles are presented here for the interpretation considering the geology. The parallel profiles are consistent and corroborate our interpretation. Two-dimensional resistivity sections acquired during excavation (Figure 4a) enabled us to map geological layers in agreement with the rock types expected in the geological model based on early drill logs (Figure 4b). The folding of the resistive Huk limestone layer (its laboratory resistivity ranges from 43 to 540 Ωm, c.f. Table 1) is recovered by the resistivity models. The Hagaberg layer (ρ = 110–240 Ωm) is too thin to be resolved between the two conductive shale layers (Galgeberg with ρ = 0.25–54 Ωm and Alum with ρ = 0.025–0.13 Ωm). The presence of black shale is suggested by the very low resistivity (< 1 Ωm, dark blue in Figure 4a) within the northern two fifth of the tunnel. This was later confirmed by direct geological observation during the excavation; the final geological mapping is depicted in the tunnel outline (Figure 4b). The preliminary stratigraphic model provided a general understanding of the expected geology, but the direct geological observation revealed that the Huk layer thickness is variable and that all the layers are more folded than predicted.

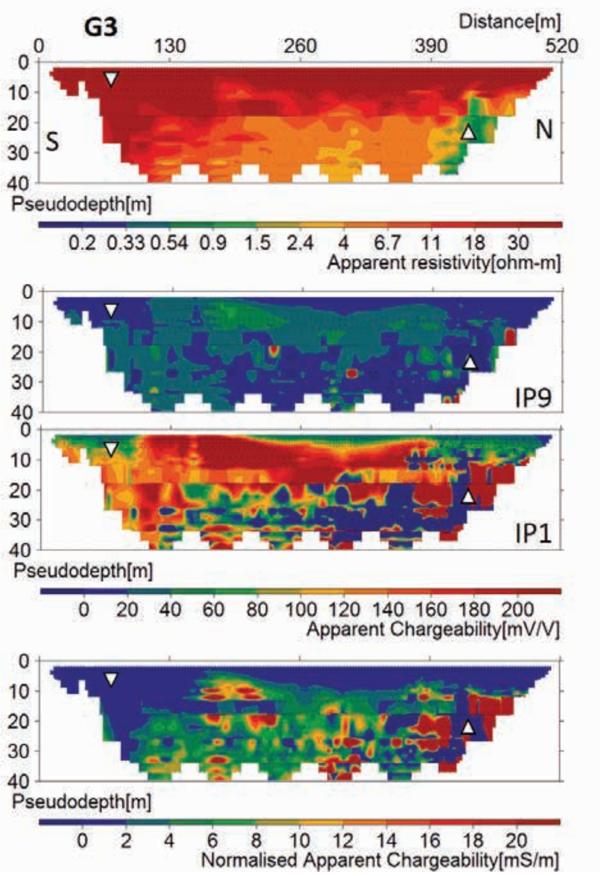

Figure 5 Pseudo-sections along G3 showing good quality apparent resistivity data (upper panel) and noisy IP data (three lower panels). The first gate, IP1, extends from 0.01 to 0.03 s. The last gate, IP9, extends from 0.75 to 0.99 s. The normalised apparent chargeability data are the integration over the nine time gates. The triangle pointing downward indicates the position of the measurement shown in Figure 6 for which the chargeability data are of good quality. The triangle pointing upward indicates the position of the measurement shown in Figure 7 for which the chargeability data are of bad quality.

Chargeability ground investigation

Time domain IP (TDIP) was also measured during the ERT survey. Acquisition settings were kept equal for the different profiles: a square-wave voltage input with 1 second on-and-off time was applied and full-waveform data were recorded. This short time period was chosen due to the survey's primary focus on resistivity. For the same reason, non-polarisable electrodes were not used as they are fragile and not practical in hard ground conditions. Stainless steel electrodes were used for current transmission as well as potential measurements. The Terrameter measurement protocol is specially designed to minimise electrode charge-up by making sure that electrodes are not used for measuring potentials immediately, or soon after, being used for transmitting current (Dahlin 2000). Logarithmically spaced gates windows were used for the IP acquisition during current time off (50% of the duty cycle).

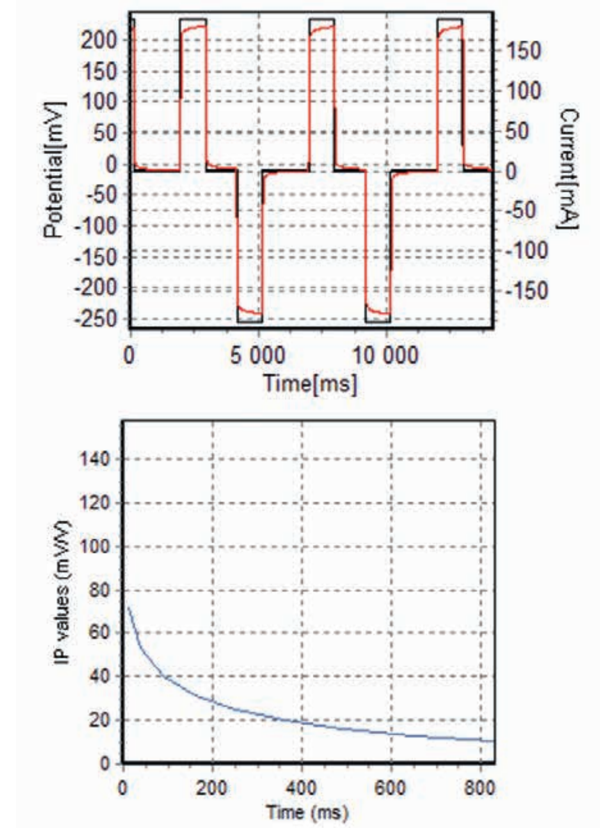

Figure 6 Voltage measurements (upper) and resulting decay curve (lower) collected along G3 at the location marked by triangle pointing downward in Figure 5. The voltage data are of good quality and so is the resulting decay curve.

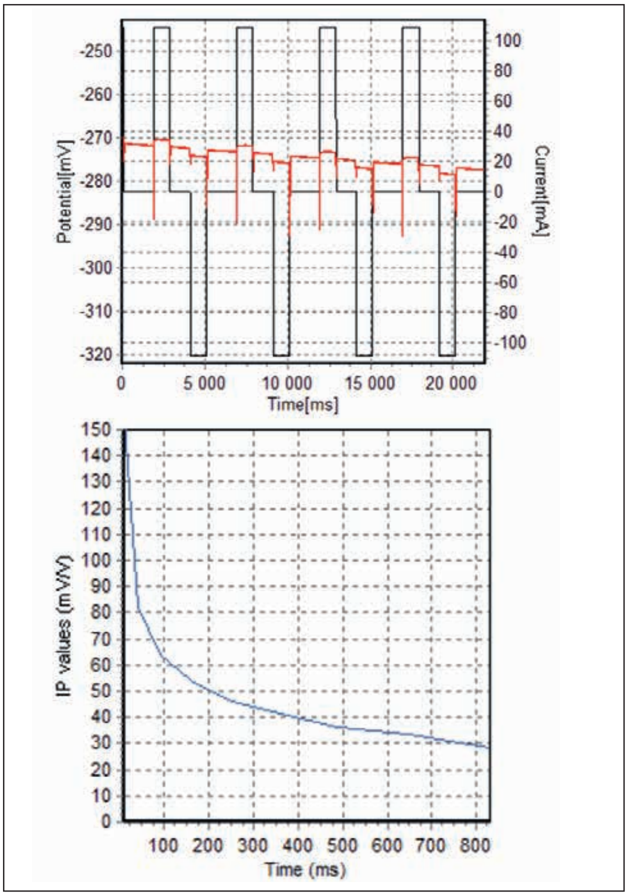

Figure 7 Voltage measurement (upper) and resulting decay curve (lower) collected at the location along G3 marked by a triangle pointing upward in Figure 5. The voltage data are influenced by noise.

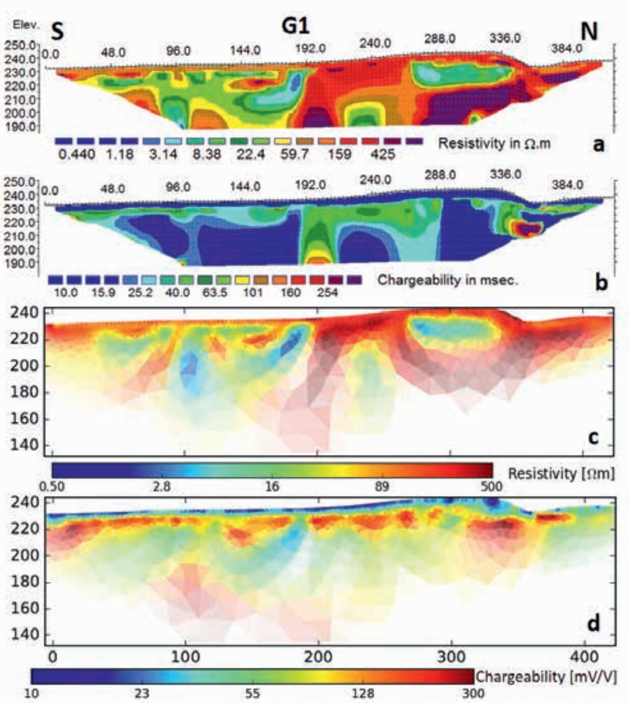

Figure 8 Resistivity (*a* and *c*) and chargeability (*b* and *d*) models along G1. Res2Dinv models are seen in *a* and *b* while BERT models are seen in *c* and *d*. The resistivity data is of good quality while the IP data is influenced by noise.

Figure 5 shows the raw field data as apparent resistivity and apparent chargeability sections along one representative profile, G3, with 3270 data points. The resistivity data are of generally good quality but the IP data appear erratic as we observe very negative and very positive apparent chargeability values next to each other. It is generally observed that field resistivity data acquisition is robust from a data quality point of view, whereas IP data acquisition is much more sensitive to noise contamination due to smaller signal levels in combination with shorter delays and integration times (Dahlin and Leroux 2012). Apparent chargeability values above 200 mV/V, as measured here, are usually considered unrealistic and affected by noise in near-surface investigations but are common in mineral exploration (e.g., Viezzoli and Kaminski 2016). In this case, the occurrence of high absolute apparent chargeability values is stronger for the early gate (IP1 gate goes from 0.01 to 0.03 s) than for the later gate (IP9 goes from 0.75 to 0.99 s). The injected current varied between 83 mA to 503 mA, with the low current values being concentrated in the conductive areas (mostly toward the north). This would indicate that the IP data quality is expected to be lower due to smaller signal levels in the vicinity of Alum shale, which was the aim of the survey. Negative apparent chargeability values can occur as a consequence of the distribution of chargeable zones in the ground (Dahlin and Loke 2015); they were therefore kept during the data processing. An inspection of the full-waveform voltage data measured along G3 indicates that some areas reveal good quality voltage data (Figure 6), which is the case for most of the shallow part of the profile. However, a large part of the full-waveform voltage data reveals ambient noise most likely due to the nearby infrastructures (Figure 7). Such noise is frequent, and Olsson *et al.* (2015) have improved the acquisition software and hardware to minimise this, but these developments were not available at the time of this survey. Some of the areas affected by ambient noise can still present the usual shape for the decay curves (Figure 7) even though the voltage measurements are erratic. This indicates that manual data editing is not possible based only on the shape of the decay curves. In addition to the anthropogenic noise, the voltage data might also be contaminated by electromagnetic (EM) coupling within the measuring cables, and this noise most often affects the first gate. EM coupling noise can be important, whereas using the multiple gradient array as the potential electrode pair is located inside the current electrode pair. Dahlin and Leroux (2012) have reduced this type of noise by using two separate multi-electrode cables for the potential and current dipoles. This was unfortunately not doable here with the limited time available for the survey and, again, because the resistivity measurements were the priority.

Some decay curves are so erratic that it was not possible to manually edit the raw data and keep enough decays to successfully invert for the Cole–Cole relaxation parameters with AarhusInv inversion algorithm (Fiandaca *et al.* 2013). At the time of this research, AarhusInv was not able to invert such sparse data. In the meantime, a constant phase angle inversion was implemented. Instead of fitting the full shape of the decay curves, one can limit the IP inversion to the integral chargeability, which is the integration of the area beneath each decay curve. The magnitude of the integral chargeability can be computed by discrete integration at the nine time gates with Res2DInv (Loke 2010). The Res2Dinv resistivity and integral chargeability results are presented in Figure 8(a,b), Figure 9(a,b), and Figure 10(a,b) for profiles G1, G4, and G3, respectively, going from S to N. As already discussed in Bazin *et al.* (2015), the resistivity models obtained with the two inversion algorithms, Res2inv (Figures 8–10a) and BERT/GIMLi (Figures 8–10c), are quite similar. The earlier comparison of Bazin *et al.* (2016) plotted the inverted models obtained from the different algorithms with the same visualisation tool. Here, for simplification, the two built-in visualisation tools are used but with the same range of values for the colour scales. The IP data fit is already very good (root mean square (RMS) = 2.3%) at iteration 4 for G1 but only fair (RMS = 10.5%) at iteration 5 for G3 and poor at iteration 5 for G4 (RMS = 13,6%) with Res2Dinv (Figures 8–10b). As is typical for noisy IP data, the inverted chargeability appears spotty. The background chargeability level is low for most of the G1 except in the northern end, which presents a strong but small-scale anomaly. Indeed, the later geological mapping revealed the presence of Galgeberg black shale near G1 northern end. The chargeability models along G4 and G3 are more variable than along G1. A quite contiguous feature is observed along G1 and G3 profiles in the first 15-m depth, which traces the sediment–bedrock interface. In addition, some strong blocky anomalies are seen along G3 and G4 within the bedrock, but it is difficult to interpret them in terms of geology.

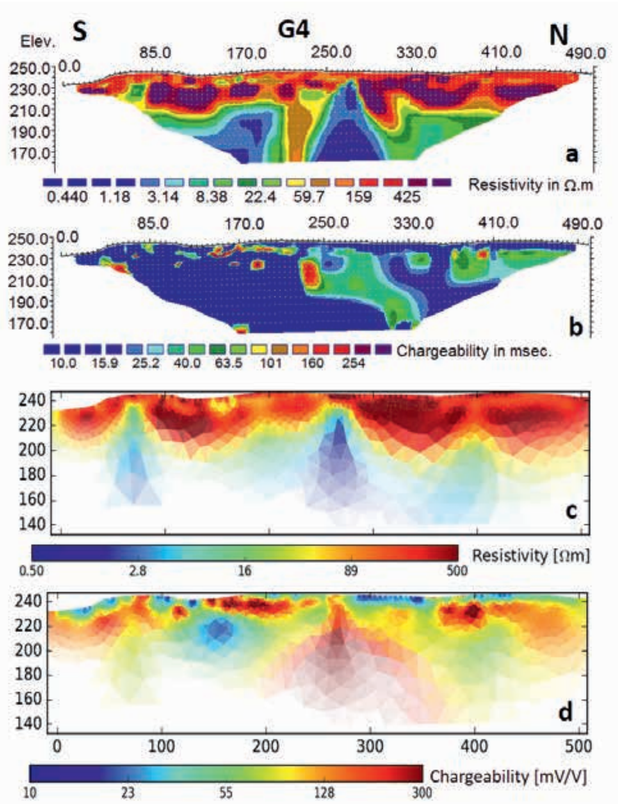

Figure 9 Resistivity (*a* and *c*) and chargeability (*b* and *d*) models along G4. Res2Dinv models are seen in *a* and *b*, whereas BERT models are seen in *c* and *d*. The resistivity data are of good quality, whereas the IP data are strongly influenced by noise.

Alternatively, the SIP effect can be modelled by the BERT/GIMLi algorithm (Günther and Martin 2016). Like other algorithms, it begins with a direct current (DC) resistivity inversion prior to inversion of the IP data. Usually it works in the frequency domain, either for single frequencies or simultaneously for the whole frequency spectrum (Günther and Martin 2016). However, this algorithm also includes an inversion for chargeability using an inversion approach based on the ideas of Oldenburg and Li (1994) and combining two different DC forward calculations. Data are the measured apparent chargeabilities for any time gate and inversion parameters are the subsurface chargeabilities (in mV/V), which are directly regularised by smoothness constraints and a logarithmic transformation. As a result, contiguous and, thus, more realistic IP models are obtained compared with linearised inversion approaches. The

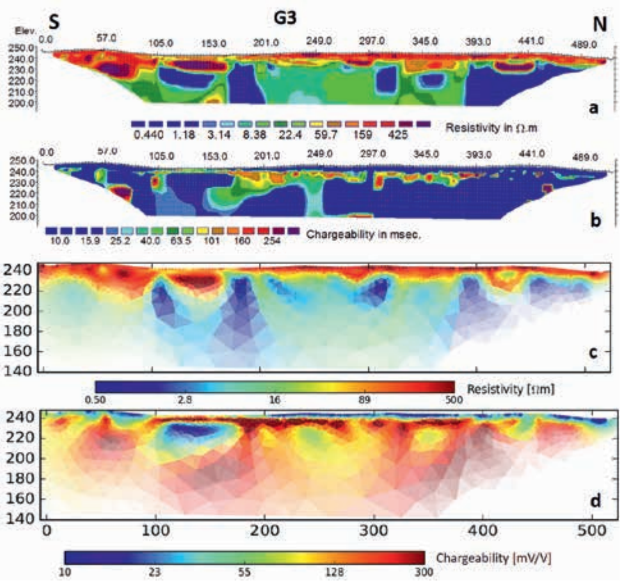

Figure 10 Resistivity (a and c) and chargeability (b and d) models along G3. Res2Dinv models are seen in *a* and *b*, whereas BERT models are seen in *c* and *d*. The raw data are shown in Figure 5: the resistivity data are of good quality, whereas the IP data are strongly influenced by noise.

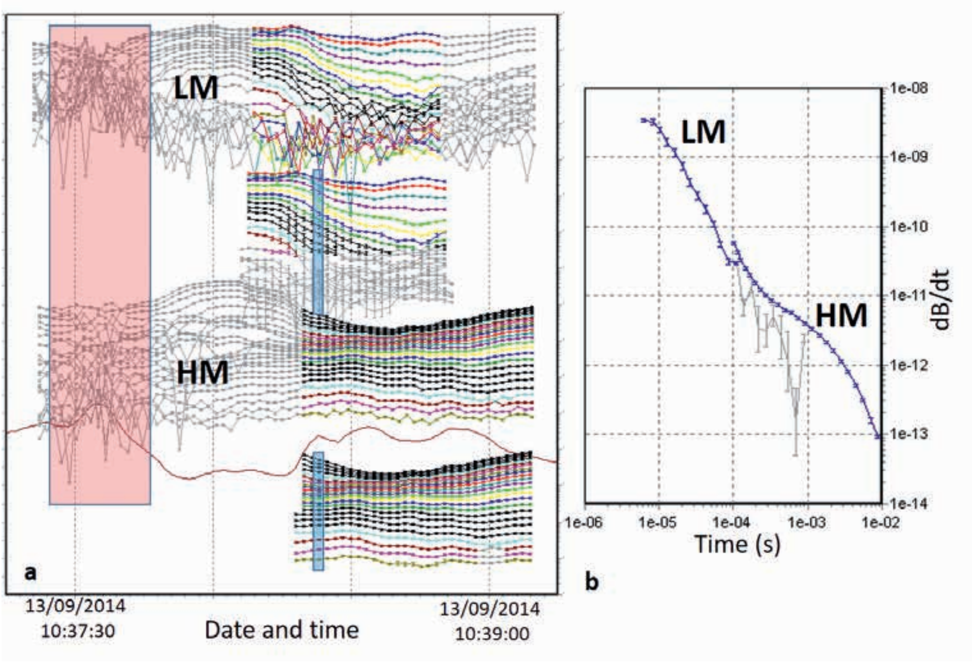

Figure 11 (a) AEM raw and stacked voltage soundings at low moment (LM) and high moment (HM), measured over 2 minutes of flight. The manually edited soundings are shown in gray. The area marked in red shows noisy data affected by capacitive coupling due to man-made infrastructures. (b) Transient of LM and HM as a result of the averaged data marked in blue in (a).

BERT resistivity (Figures 8–10c) and chargeability (Figures 8–10d) models are presented for the three selected profiles. There is reasonable agreement between Res2DInv (Figures 8–10b) and BERT chargeability models (Figures 8–10d), whereas the BERT models appear less spotty thanks to the new regularisation. The chargeability residuals obtained are reasonable, 11.5 mV/V, 19.3 mV/V, and 18.9 mV/V for G1, G3, and G4, respectively. This adds confidence to the interpretation of the ground-based chargeability models. Like for the Res2DInv RMS, these chargeability residuals reveal that the data are noisier toward the north with the presence of black shale. As for the Res2DInv models, a contiguous chargeability contrast traces the sediment–bedrock interface. This feature is in accordance with the preliminary geological model. In addition, some strong chargeability anomalies are observed within the bedrock: near x = 340 m along G1, between x = 200 m and 400 m along G4 and along most of G3. These coincide with the conductive regions and observations of black shale.

AEM test survey

A small AEM test survey was carried out with the SkyTEM 304 time domain system (Sørensen and Auken 2004) as part of a bigger survey (Lysdahl *et al.* 2015). Raw data were processed using the Århus Workbench package (www.aarhusgeo.com) and inverted using a spatially constrained inversion (SCI, Viezzoli *et al.* 2008). The AEM time gates range from 8.21 μs to 8.90 ms. Figure 11 shows a sample of the AEM data collected during 2 minutes of flights. The raw data quality suffers from the noisy background caused by the urban area. However, unlike for the ground-based IP data, the AEM data can be edited through careful inspection of the transients, carried out using available ancillary geographic information system (GIS) data (e.g., Auken *et al.* 2009). Failure to do so can result in significant artefacts in the models (Viezzoli, Jørgensen and Sørensen 2012). The data coverage is sparse because the helicopter could not fly above buildings. The penetration depth of the AEM method is in excess of 100 m in this area, more than twice that of the short ERT profiles. The nominal spacing between AEM sounding points was 30 m. The 1D vertical resistivity models were projected along the Gran tunnel and are depicted in Figure 12a. Although the resulting profile does not perfectly coincide with the ground investigation lines (c.f. map in Figure 1), the AEM resistivity depth section agrees with those obtained with BERT (Figure 4a) and the geological mapping (Figure 4b). The very conductive black shale (Galgeberg and Alum shales, dark blue on the resistivity colour scale) is easily identified in the AEM resistivity section: the small-scale undulations are not recovered, but the black shale layer deepens toward the south.

The spatial distribution of the AEM resistivity is presented in map views at three different elevations (Figure 13). The very high conductivity ($\rho < 1$ Ωm, dark blue on the resistivity colour scale) is in agreement with the presence of Alum shale near the northern end of the tunnel. The distribution of radioactive nuclides (Th, U, K) was mapped with a light gamma spectrometer mounted on the helicopter. It measured the intensity of gamma radiation emitted from the ground, from the isotopes the isotopes thorium-232, uranium-238, and potassium-40. The U distribution is also depicted in Figure 13, and it presents a strong anti-correlation with the AEM resistivity distribution at the highest of the three elevation slices (210–220 m). As expected, the U level is the strongest where the Alum shale layer is shallowest near the northern end of the tunnel. This method therefore can be used for efficient large-scale investigation of Alum shale; however, Heincke *et al.* (2008) have noticed that clayey marine sediment covers can strongly attenuate gamma radiation. It might therefore not be as reliable as resistivity/IP surveying.

The presence of strong IP signals in the laboratory and ground data suggested the possibility of modelling IP from the SkyTEM data. It has long been known that chargeability can affect time domain AEM systems (e.g., Smith and Klein 1999). A better understanding and monitoring on AEM systems' responses, associated with recent developments in inversion codes (e.g., Fiandaca *et al.* 2013) has renewed interest in this topic and its applicability (Kratzer and Macnae 2012, Kaminsky and Viezzoli 2017). The AEM data need proper pre-processing; then a dispersive resistivity formulation takes place of the standard non dispersive resistivity. Negative raw time domain (TD) EM data are a sure indication of IP effects, for a concentric TDEM system. Negatives develop more easily in the presence of resistive bedrock, which is not present in this area. Lack of negatives, however, does not exclude the presence of an IP component, which could be associated with an increase of signal at the early times and/or a slightly faster decay at later times (e.g., Smith and West 1989). IP modelling was therefore attempted, using the Cole–Cole model. On average, the data misfit decreased by approximately 15%. The resistivity changed only marginally. The sensitivity on the Cole–Cole models is generally low, with a depth of investigation for chargeability on the order of 50 m (Christiansen and Auken 2012). However, the chargeability distribution inverted from the AEM dataset (Figure 12b) shows a strong correlation with the presence of Alum shale just below or in the tunnel, from distance x = 400 to 600 m and an even stronger correlation toward the northern end of the tunnel from distance x = 1250 to 1400 m (the purple colour Figure 12b indicates chargeability levels > 200 mV/V).

DISCUSSION

ERT surveys are widely used for site investigations during the design stage of construction projects. IP surveys however are hardly ever used. In this study, the benefit of the IP measurements in conjunction with the resistivity measurements was examined. Although the ground-based IP data are very noisy and the TDIP setup was not optimal for a chargeability investigation, the ground-based IP models (Figures 8–10d) clearly indicate a strong polarisation where the black shale was mapped by geologists (direct observation in the tunnel and cores). This black shale could have been imaged by the ground-based resistivity survey alone, but they were confirmed by the TDIP survey with no extra cost and, therefore, decreased the overall project risk. Further data pre-processing should be considered to improve TDIP data quality in the future. The new inversion approach in the BERT/GIMLi algorithm substantially improved the quality of the chargeability models compared with the linearised inversion.

As already mentioned by Wennermark *et al.* (2015), the two different types of IP acquisition (time domain in the field and frequency domain in the laboratory) are qualitatively connected, but it is difficult to proceed to a quantitative comparison. Exploiting the full-decay spectrum of the ground-based IP data may allow such comparison in the future. The TDIP field experiment uses a transmitter frequency of ~0.2 Hz. At this frequency, all three Alum shale samples show a significant phase lag (6° to 8°) and a chargeability level of ~200 mV/V over the Terrameter bandwidth range. There is, thus, good agreement between the ground-based TDIP and the SIP laboratory test. It would be interesting to address whether different types of black shale have different phase peak frequencies and chargeability levels in future investigations. If so, SIP field surveys would be able to discriminate between the different types of black shale.

The SIP measurements show two peaks in the phase spectra, whereas the Cole–Cole model should in theory have a single peak. Therefore, a multiple Cole–Cole model should be involved (Vanhala 1997). The highest frequencies (100 Hz to 100 KHz) of the SIP spectrum, which overlap with SkyTEM low-moment bandwidth, show a rather small-phase lag (< 4°, Figure 3b). The phase lag is the largest, 2.6° and 3.8°, for E2 and E3 samples (the two samples that contain the most sulphides) at 117 Hz, which corresponds to the latest SkyTEM gates. This could explain why the chargeability distribution inverted from the AEM dataset shows a strong correlation with the presence of Alum shale in the tunnel (Figures 4b and 12b). The chargeability level estimated from the relative drop of SIP resistivity over the SkyTEM band-

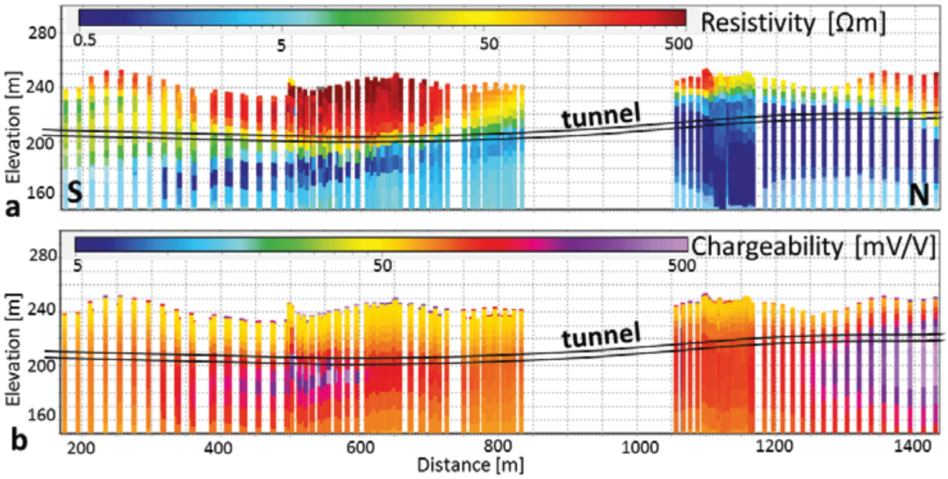

Figure 12 AEM derived resistivity (a) and chargeability m_o (b) vertical sections projected along the tunnel, obtained with the SCI of a dispersive resistivity model (Cole–Cole). C.f. Figure 4 for the coincident geological section where the resistivity colours scale and the horizontal distances are the same.

width ranges between 52 mV/V and 126 mV/V for the three samples (Figure 3a). This is in agreement with the chargeability values inverted from the AEM dataset (Figure 12b).

Although we observe a correlation across the three types of measurements, more research is needed to investigate the IP spectra in natural soils and the relationships between laboratory results and the inverted spectral parameters measured in the field, both from ground IP (Johansson, Fiandaca and Dahlin 2015) and from airborne EM.

CONCLUSIONS

Electrical resistivity investigations at an early phase of a tunnel project can minimise the number of drillings and decrease the geological uncertainty. The two resistivity datasets (ground-based and airborne investigations) show the following: (i) AEM provides high enough resolution for tunnel investigations; (ii) ERT is useful for small-scale evaluation, but it is limited in depth of investigation. AEM possesses the advantage of a large depth of investigation while covering large areas in a relatively short time without requiring access to the ground. In addition, it is particularly sensitive to conductive anomalies. AEM is however limited in densely populated areas (for safety reasons) and in the presence of infrastructure (for data quality reasons). Its high mobilisation cost limits its application to medium and large geotechnical projects, but combining several nearby surveys can be an economical option. The heavily folded shale along our study area illustrates the superior lateral resolution of ERT versus AEM, whereas both methods are consistent in terms of resolving the vertical boundary of the resistor/conductor interface.

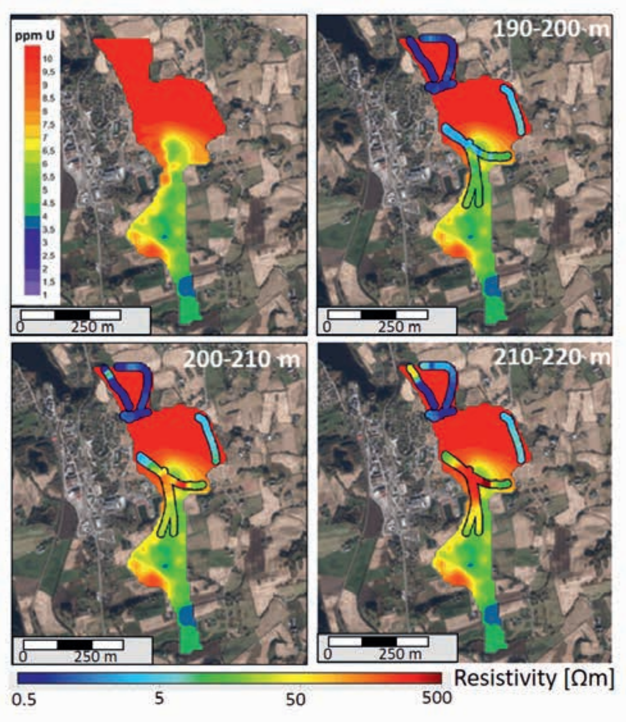

Figure 13 Maps showing the AEM-derived resistivity models near Gran tunnel during the test survey (point themes) compared with the radiometry data (solid map, only the U distribution is shown). The average resistivity maps are taken at three different elevation slices intersected by the tunnel.

The laboratory results suggest that the amplitude of the SIP phase peak might be a good proxy for the toxicity level of the Alum shale. Chargeability investigations obtained from ground-based methods have a strong potential for black shale mapping. However, the standard and efficient ground-based time-domain acquisition method reveals some limitation due to the high noise level in the voltage data when acquired in a conductive environment. The preliminary results presented on the chargeability derived from AEM method are also promising for contributing to the mapping of these shales. Even at a noisy site, the airborne time-domain IP data present a good correlation with the presence of Alum shale. More research is needed on the induced polarisation in black shale to bridge the gap between small-scale laboratory measurements and the inverted parameters in field, both ground and airborne.

Airborne gamma radiation, in particular U distribution, is also very sensitive to the presence of Alum shale, but it can be attenuated by clayey overburdens. Fortunately, the data quality does not deteriorate with the presence of infrastructures, as it does for AEM. The two methods are therefore complementary.

ACKNOWLEDGEMENT

The authors thank the Norwegian Public Road authority (SVV) for financing this study and giving permission to publish. The authors are grateful to Stian Ellingsen and Tore Thomassen (SVV) for permission to publish the geological data used in this study. Valuable comments on Alum shale have been provided by E. Endre (formerly NGI). The authors express gratitude to Flemming Effersø (SkyTEM Surveys Aps) for effective survey planning as well as Århus University for the continuous support and early access to their latest inversion development. The authors further thank the editor and the three anonymous reviewers for providing thoughtful comments to this manuscript. Funding was also provided by the Research Council of Norway through NGI research programs.

REFERENCES

ABEM 2010. Terrameter LS Instruction Manual. http://abem.se, pp 63.

AGI 1972. Glossary of Geology American Geological Institute, pp 805.

Anschütz H., Bazin S., Kåsin K., Pfaffhuber A.A. and Smaavik T. in press. Airborne sensitive clay mapping - stretching the limits of AEM resolution and accuracy. *Near surface Geophysics.*

Anschütz H., Vöge M., Lysdahl A., Bazin S., Sauvin G., Pfaffhuber A.A. *et al*. 2017. From manual to automatic AEM bedrock mapping. Special issue Airborne Geophysics of *Journal of Environmental and Engineering Geophysics* **22**, 35–49.

Auken E., Christiansen A.V., Jacobsen B.H., Foged N. and Sørensen K.I. 2005. Piecewise 1D laterally constrained inversion of resistivity data. *Geophysical Prospecting* **53**, 497–506.

Auken E., Christiansen A.V. Kirkegaard C., Fiandaca G., Schamper C., Behroozmand A.A., Binley A. *et al*. 2014. An overview of a highly versatile forward and stable inverse algorithm for airborne, ground-based and borehole electromagnetic and electric data. *Exploration Geophysics* **46***, 223-235.*

Auken E., Christiansen A.V., Westergaard J.H., Kirkegaard C., Fopged N., Viezzoli A. 2009. An integrated processing scheme for high-resolution airborne electromagnetic surveys, the SkyTEM system. *Exploration Geophysics* **40**, 184–192.

Bazin S., Anschütz H., Lysdahl A.K., Pfaffhuber A.A. and Scheibz J. 2015. ERT inversion industry standard versus cutting edge developments, time for a change? Symposium on the Application of Geophysics to Engineering and Environmental Problems (SAGEEP)*,* TX, USA, 535-538.

Christiansen A.V. and Auken E. 2012. A global measure for depth of investigation. *Geophysics* **77**, 171–178.

Dahlin T. 2000. Short note on electrode charge-up effects in DC resistivity data acquisition using multi electrode arrays. *Geophysical Prospecting* **48**(1), 181–187.

Dahlin T. and Zhou B. 2006. Gradient array measurements for multi-channel 2D resistivity imaging. *Near Surface Geophysics* **4**, 113–123.

Dahlin T. and Leroux V. 2012. Improvement in time-domain induced polarisation data quality with multi-electrode systems by separating current and potential cables. *Near Surface Geophysics* **10**, 545–565.

Dahlin T. and Loke M.H. 2015. Negative apparent chargeability in time-domain induced polarisation data. *Journal of Applied Geophysics* 1**23**, 322–332.

Danielsen B.E. and Dahlin T. 2009. Comparison of geoelectrical imaging and tunnel documentation at the Hallandsås Tunnel, Sweden. *Engineering Geology* **107***,* 118-129.

Fiandaca G., Ramm J., Binley A., Gazoty A., Christiansen A. V. and Auken E. 2013. Resolving spectral information from time domain induced polarization data through 2-D inversion. *Geophysical Journal International* **192**, 631–646.

Günther T., Rücker C., and Spitzer K. 2006. 3D modelling and inversion of dc resistivity data incorporating topography – II. Inversion. *Geophysical Journal International* **166**, 506–517.

Günther T. and Martin T. 2016. Spectral two-dimensional inversion of frequency-domain induced polarization data from a mining slag heap. *Journal of Applied Geophysics* **135***,* 436-448.

Heincke B.H., Smethurst M.A., Bjørlykke A., Dahlgren S., Rønning J.S. and Mogaard J.O. 2008. Airborne gamma-ray spectrometer mapping for relating indoor radon concentrations to geological parameters in the Fen region, southeast Norway. *Geology for Society, Geological Survey of Norway* **11**, 131–143.

Johansson S., Fiandaca G. and Dahlin T. 2015. Influence of non-aqueous phase liquid configuration on induced polarization parameters: conceptual models applied to a time-domain field case study. *Journal of Applied Geophysics* **123**, 295–309.

Kaminsky V. and Viezzoli A. 2017. Modeling induced polarization effects in helicopter time-domain electromagnetic data: field case studies. *Geophysics* **82**, 49–61.

Kratzer T. and Macnae J.C. 2012. Induced polarization in airborne EM. *Geophysics* **77**, E317–E327.

Lysdahl A.K., Bazin S., Anschütz H. and Pfaffhuber A.A. 2015. Black shale mapping by AEM for geotechnical applications. *EAGE European Airborne Electromagnetics Conference*, Turin, Italy.

Lysdahl A.K., Endre E. and Radic T. 2016. The IP response of black shales in the Oslo graben, Norway. *5th international workshop on Induced Polarization*, Århus, Denmark.

Loke M.H. 2010. RES2DINV version 3.59.102. Geoelectrical Imaging 2D and 3D. Instruction Manual. *Geotomo Software*, http://www.geotomosoft.com.

NGI 2013. Tunnel Gran Jaren: identifisering og karakterisering av skiferhorisonter i tunneltrasé. NGI report 20120110-01R, 43.

NGI 2015. Identifisering og karakterisering av syredannende bergarter. NGI report 20120842-01R, 57. Public document in Norwegian for the Norwegian Environment Agency. http://www.miljodirektoratet.no/Documents/publikasjoner/M310/M310.pdf.

NGU 2009. A compilation of previously published geochemical data on the lower Cambro-Silurian sedimentary sequence, including the alum shales in the Oslo region. NGU report 2009.053, 25.

Nielsen A.T. and Schovsbo N.H. 2007. Cambrian to basal Ordovician lithostratigraphy in southern Scandinavia. *Bulletin of the Geological Society of Denmark* **53**, 82–84.

Nyland B. and Teigland J. 1984. *Sedimentologisk og geokjemisk undersøkelse av de kambriske og underordoviciske marine sedimenter i Oslofeltet*. *Thesis*, Geologisk institutt, Universitetet i Oslo, pp. 196.

Okazaki K., Mogi T., Utsugi M., Ito Y., Kunishima H., Yamazaki T. *et al.* 2011. Airborne electromagnetic and magnetic surveys for long tunnel construction design. *Physics and Chemistry of the Earth* **36**, 1237–1246.

Oldenburg D.W. and Li Y. 1994. Inversion of induced polarization data. *Geophysics* **59**, 1327–1341.

Olsson P.-I., Dahlin T., Fiandaca G. and Auken E. 2015. Measuring time-domain spectral induced polarization in the on-time: decreasing acquisition time and increasing signal-to-noise ratio. *Journal of Applied Geophysics* **123***,* 316–321.

Pelton W.H., Ward S.H., Hallof P.G., Sill W.R. and Nelson P.H. 1978. Mineral discrimination and removal of inductive coupling with multi-frequency IP. *Geophysics* **43**, 588–609.

Pfaffhuber A.A., Grimstad E., Domaas U., Auken E., Halkjær M. and Foged N. 2010. Airborne EM mapping of rock slides and tunneling hazards, EAGE 16th European Meeting of Environmental and Engineering Geophysics, Zurich, Switzerland, B10.

Radic T. 2014. Measuring IP effects at high frequencies: first lab and field data from 0.001 Hz–250 kHz. *3rd International Workshop on Induced Polarization*, Boulder Colorado, USA.

Revil A., Mao D., Shao Z., Sleevi M.F. and Wang D. 2016. Induced polarization response of porous media with metallic particles — Part 6: the case of metals and semimetals. *Geophysics* **82**, E77-E96.

Smith R.S. and West G.F. 1989. Field examples of negative coincident-loop transient electromagnetic responses modeled with polarizable half-planes. *Geophysics* **54**, 1491–1498.

Smith R.S. and Klein J. 1999. A special circumstance of airborne induced polarization measurements. *Geophysics* **61**, 6–73.

Sørensen K.I. and Auken E. 2004. SkyTEM – a new high-resolution helicopter transient electromagnetic system. *Exploration Geophysics* **35**, 191–199.

Vanhala H. 1997. *Laboratory and field studies of environmental and exploration applications of the spectral induced-polarization (SIP) method*. PhD thesis, Geologian Tutkimuskeskus, Helsinki University of Technology, Espoo, Finland.

Viezzoli A., Christiansen A.V., Auken E. and Sørensen K.I. 2008. Quasi-3D – modeling of airborne TEM data by spatially constrained inversion. *Geophysics* **73**, F105–F113.

Viezzoli A., Jørgensen F and Sørensen C. 2012. Flawed processing of airborne EM data affecting hydrogeological interpretation. *Groundwater* **51** (2), 191–202.

Viezzoli A. and Kaminski V. 2016. Airborne IP: examples from the Mount Milligan deposit, Canada, and the Amakinskaya kimberlite pipe, Russia. *Exploration Geophysics*.

Wang Z., Gelius L.J. and Kong F.N. 2009. Simultaneous core sample measurements of elastic properties and resistivity at reservoir conditions employing a modified triaxial cell - a feasibility study. *Geophysical Prospecting* **576**, 1009–1026.

Wennermark M., Olsson P.-I., Johansson S. and Hellman K. 2015. A comparison of DCIP Inversion Software. *EAGE European Airborne Electromagnetics Conference*, Turin, Italy.

4.5 La géophysique pour la surveillance des glissements de terrain

Grace à mon expérience en instrumentation géophysique pour la surveillance volcanologique et sismologique, j'ai naturellement participé à un projet de recherche sur les systèmes de surveillance et de préalerte (EWS pour Early Warning System) juste après mon arrivée au NGI. J'ai ainsi intégré un grand projet de recherche financé par le 7ème Programme-Cadre de l'Union Européenne pour 2007-2013 pour la recherche et le développement technologique (en abrégé FP7) et intitulé SafeLand. Les objectifs du consortium européen formés de 18 instituts de recherche étaient de développer des outils et des stratégies d'évaluation quantitative sur la gestion des risques liés aux glissements de terrain à l'échelle locale, régionale et européenne. Il s'agissait d'établir une base de référence sur les études des glissements de terrain en Europe, afin d'améliorer notre capacité à anticiper et à atténuer les risques associés. J'étais impliquée dans deux des cinq ateliers de travail. J'ai participé à la rédaction d'un rapport sur l'état de l'art dans les techniques de détection des glissements de terrain, leur caractérisation rapide et leur cartographie (rapport SafeLand D4.1, Michoud et al., 2010). Mon travail a consisté à dresser la liste et les caractéristiques des méthodes géophysiques de proche surface utiles pour cartographier les glissements de terrain. Parallèlement, j'ai piloté l'atelier de travail sur l'évaluation et le développement de procédures et de technologies fiables pour l'alerte dans les EWS. Pour cela je me suis aidée du sondage fait avec un doctorant de l'Université de Lausanne, Clément Michoud, pour dresser un état des lieux des EWS existants dans le monde. Cette enquête a par la suite été publiée et l'article est présenté dans ce chapitre. Les analyses des résultats de l'enquête nous ont permis d'établir des procédures adaptées aux différents cas possibles. Nous avons abordé les questions techniques et pratiques liées à la surveillance et à l'alerte précoce. J'ai rédigé le rapport final (rapport SafeLand D4.8, Bazin, 2012) et présenté nos résultats à différents ateliers de travail et conférences internationales (e.g. Bazin et al., 2012). Une fois encore, l'accent était mis sur l'intérêt de combiner plusieurs méthodes géophysiques pour surveiller des paramètres physiques différents en mesurant des phénomènes avec des dimensions géométriques et des échelles de temps variées. J'ai par la suite continué à travailler sur la thématique des méthodes géophysiques pour cartographier les zones susceptibles de provoquer des glissements de terrains en participant à la rédaction d'un livre (Malehmir et al., 2016).

Nat. Hazards Earth Syst. Sci., 13, 2659–2673, 2013
www.nat-hazards-earth-syst-sci.net/13/2659/2013/
doi:10.5194/nhess-13-2659-2013

Natural Hazards
and Earth System
Sciences
Open Access

Experiences from site-specific landslide early warning systems

C. Michoud[1], **S. Bazin**[2], **L. H. Blikra**[3], **M.-H. Derron**[1], **and M. Jaboyedoff**[1]

[1]University of Lausanne, Lausanne, Switzerland
[2]Norwegian Geotechnical Institute, Oslo, Norway
[3]Åknes/Tafjord Beredskap, Stranda, Norway

Correspondence to: C. Michoud (clement.michoud@unil.ch)

Received: 30 November 2012 – Published in Nat. Hazards Earth Syst. Sci. Discuss.: –
Revised: 20 September 2013 – Accepted: 25 September 2013 – Published: 22 October 2013

Abstract. Landslide early warning systems (EWSs) have to be implemented in areas with large risk for populations or infrastructures when classical structural remediation measures cannot be set up. This paper aims to gather experiences of existing landslide EWSs, with a special focus on practical requirements (e.g., alarm threshold values have to take into account the smallest detectable signal levels of deployed sensors before being established) and specific issues when dealing with system implementations. Within the framework of the SafeLand European project, a questionnaire was sent to about one-hundred institutions in charge of landslide management. Finally, we interpreted answers from experts belonging to 14 operational units related to 23 monitored landslides. Although no standard requirements exist for designing and operating EWSs, this review highlights some key elements, such as the importance of pre-investigation work, the redundancy and robustness of monitoring systems, the establishment of different scenarios adapted to gradual increasing of alert levels, and the necessity of confidence and trust between local populations and scientists. Moreover, it also confirms the need to improve our capabilities for failure forecasting, monitoring techniques and integration of water processes into landslide conceptual models.

1 Introduction

Landslides are frequent phenomena in many natural environments, and remediation measures ought to be implemented in areas with high risk due to the presence of populations or infrastructures. Structural remediation measures have been extensively used for reducing and even eliminating the hazard (Piteau and Peckover, 1978; Holtz and Schuster, 1996; Wyllie and Mah, 2004; Cornforth, 2005; Vaciago et al., 2011). However, classical countermeasures, such as modifications of mass distributions or water regimes, are often too expensive or difficult, if not impossible, when dealing with complex instabilities of large volumes (Crosta and Agliardi, 2003; Blikra, 2012).

In such situations, other types of mitigations have to be performed in order to decrease the risk, mainly imposed on human lives. A proper measure is to reduce the number of exposed people by implementing reliable landslide early warning systems (EWSs) that are capable of alerting and evacuating populations based on the monitoring of stability conditions of the landslide (e.g., parameter values exceeding established thresholds). Indeed, EWSs are defined by the United Nations as "the set of capacities needed to generate and disseminate timely and meaningful warning information to enable individuals, communities and organizations threatened by a hazard to prepare and to act appropriately and in sufficient time to reduce the possibility of harm or loss" (UN-ISDR, 2009). Efficient landslide EWSs require four major elements that have to be well integrated: (1) risk assessment, (2) phenomenon monitoring and forecasting, (3) warning communication and alert dissemination, and (4) local response aptitudes (UN-ISDR, 2009).

These elements have been described in detail in many papers, and useful concepts and recommendations can be extracted, such as in (1) Turner and Schuster (1996) or Fell et al. (2005) for hazard and risk assessments, (2) Stumpf et al. (2011), Michoud et al. (2012) or Tofani (2013) for monitoring techniques, (3) Saito (1969), Fukuzono (1990), Crosta and Agliardi (2003) or Meyer et al. (2012) for slope failure and flow initiation forecasts and (4) Basher (2006) or Dash and Gladwin (2007) for alerts and associated social

Published by Copernicus Publications on behalf of the European Geosciences Union.

processes. Furthermore, some papers describe how to integrate all tasks together (Angeli et al., 2000; Lacasse and Nadim, 2009). For shallow landslides and debris flows, a huge effort has been performed in order to develop complete and efficient EWSs at regional scales; they are based on rainfall intensity forecasting, soil moisture content and/or antecedent water index, etc. (Keefer et al., 1987; Aleotti, 2004; Baum and Godt, 2010; Jakob et al., 2012; Mercogliano et al., 2013). Nevertheless, it seems that there are only few reviews dealing with practical considerations and specific requirements in order to implement reliable single landslide EWSs that are site-related.

For this purpose, the SafeLand project (2009–2012), funded by the European Commission in the 7th Framework Programme (Grant Agreement No. 226479), intended to develop generic risk management tools and strategies for landslides. Thus, one of its main objectives has been to provide guidelines that would facilitate the establishment of new EWSs and increase the quality of existing systems (Bazin, 2012; Intrieri et al., 2013). Consequently, the first step of this study was to gather experiences from existing EWS strategies and expert judgments. In this way, we prepared a four-page questionnaire that has been filled by 15 institutions in charge of 24 landslide EWSs. Primary analyses were first presented in Bazin (2012). This paper therefore aims to present the results of experiences of those European and North American landslide EWSs, focusing on implementation requirements and potential practical issues of importance for landslide specialists dealing with risk management.

2 Design of the questionnaire

As a part of the SafeLand project, a screening study was intended to gather information about the state of the technologies and existing strategies for the establishment of landslide EWSs. A four-page questionnaire was compiled to illustrate the wide spectra of monitoring and integrated platforms, and to merge actual knowledge and expert judgments from existing systems. It aimed to collect information about:

- operational units in charge of the EWS;
- monitored landslide settings and consequences of past events (if any);
- pre-investigations used to design the EWSs;
- monitoring parameters, thresholds and sensors;
- warnings, communication and decision-making processes.

Questions were focused on practical considerations and specific requirements, such as technical challenges in installing and maintaining the EWSs. In addition, it was also oriented towards understanding advantages and disadvantages and revealing the potential lack of existing techniques to propose directions that current research should follow.

In order to maximize the number of potential answers, the questionnaire has been designed to be as short, user-friendly and simple as possible (Lapointe et al., 2010). Indeed, it mainly contained a list of closed questions with pre-established answers clickable in checkboxes. Moreover, a few open questions were also kept in order to leave the compiler free to provide any further considerations and points of view, especially about:

- advantages, limitations and upcoming improvements of current monitoring systems;
- how actual EWSs could be improved.

In practice, units in charge of EWSs often have the responsibility for several landslides, and the questionnaire was therefore designed to fit systems that monitor multiple sites as well as single landslides. The questionnaire was then compiled into a Portable Document Format (pdf) document, one of the most standard formats, in order to ensure that everyone could open and read it. Finally, each user had the possibility to include some supplementary material such as extra text and maps with his answer.

The questionnaire is available in the Supplement.

3 Results and interpretations

The questionnaire was sent and spread in June 2011 to about one-hundred institutions in charge of landslide hazard and risk management. These Asian, European and North American institutions were identified within the professional network of SafeLand's participants, national experts and colleagues in the landslide scientific community. The list was also completed by reviewing EWS publications, conferences on landslides and also by looking for internet websites. Finally, in autumn 2011, we received answers from experts belonging to 15 operational units from 9 different countries and related to 24 landslides, i.e., 23 site-specific landslides and 1 regional EWS. Among them, 21 systems are in operation, 1 is under construction and 2 have been stopped. Table 1 sums up the list of institutions (and investigated landslides) that answered the questionnaire. Some slope movements are well known within the landslide community, such as the landslides of Åknes in Norway (Blikra, 2008, 2012; Oppikofer et al., 2009; Jaboyedoff et al., 2011), Ancona (Cotecchia, 2006; Cardellini, 2011) and Ruinon in Italy (Agliardi et al., 2001; Crosta and Agliardi, 2003; Tarchi et al., 2003), Turtle Mountain in Canada (Terzaghi, 1950; Cruden and Krahn, 1973; Benko and Stead, 1998; Froese and Moreno, 2011) and Vallcebre in Spain (Gili et al., 2000; Corominas and Santacana,

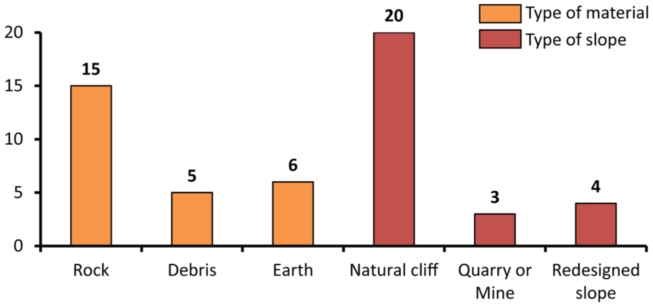

Fig. 1. Type of landslide materials and slopes involved in this study. The total number is over 23, due to multiple possible settings.

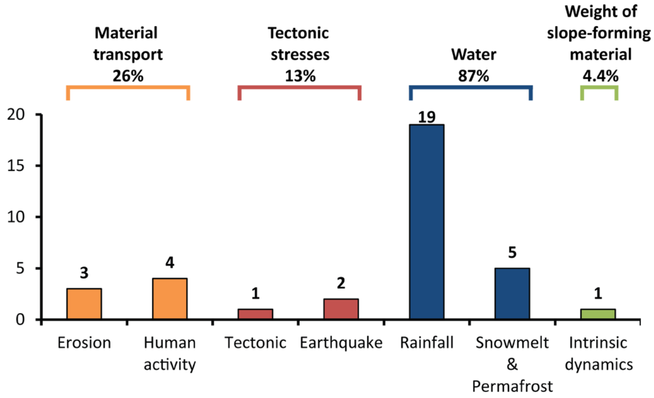

Fig. 2. Triggering mechanisms involved for the 23 reported instabilities and grouped according to Terzaghi's (1950) agents. The total can be over 23 (and 100 %), since the reported studies can be affected by more than one triggering mechanism.

2003; Corominas et al., 2005). On the other hand, the Hong Kong Engineering Office provided the only response dealing with a regional EWS for shallow landslides (Hong Kong Slope Safety, 2012); this case is not included hereafter, since many questions were not designed and thus not applicable for regional systems and also since this singular experience is too different from the other 14 operational units and their 23 related site-specific case studies.

Although 23 answers do not have a high statistical significance, interesting practical trends can still be extracted from the dataset, especially since some of them are among the most studied landslides worldwide, and valuable experiences have thus been accumulated for many years.

3.1 Units in charge of the EWSs

The first part of the questionnaire relates to the functioning of operational units. The 14 reported institutions in charge of site-specific landslide monitoring and/or EWSs operate mostly at national and regional level; however, two thirds of them are also responsible for monitoring other natural processes such as weather conditions, volcanoes and/or earthquakes. These units employ especially for their EWSs between 0 (monitoring carried out by universities) and 15 people (IPGP – Martinique). All these institutions are financed by public funds, except one that receives additional private resources. On average, they need about EUR 175 000 per year to operate, with a minimum of EUR 60 000 for a Czech office in charge of 10 landslides and a maximum of EUR 500 000 for the *Centro di Monitoraggio Geologico of the ARPA Lombardia* in charge of 24 single landslides. However, annual operational costs are highly dependent on the different living standards in each country and also on how the unit is organized; moreover, the funding for replacing and implementing new monitoring systems can highly change from year to year. This highly changing budget and resources from year to year can be a reason why only 7 institutions answered this question.

3.2 Landslide settings

3.2.1 Hazard

The second part of the questionnaire relates to the context of the 23 monitored instabilities, their previous displacement activities and their potential consequences. It includes a wide range of phenomena (Fig. 1) mostly related to natural slopes, from small rockfalls of less than 10 m^3 to large rockslides of more than 50 million m^3, or regional debris flows and earth slides. Moreover, landslide events had already occurred for 20 of them.

The studied instability crises are mainly triggered by intensive rainfall (Fig. 2). Snowmelt and permafrost, human activities, erosion processes, tectonic activities, or even their intrinsic dynamics are the other triggering mechanisms sometimes involved. Half of the events happened due to a combination of several factors. Furthermore, classifying triggering factors according to the four physical agents responsible for slope destabilizations described by Terzaghi in 1950 (i.e., material transport, tectonic stresses, water and weight of slope-forming material), water is surely the most important agent, destabilizing more than 87 % of the slopes (Fig. 2).

3.2.2 Risk

As introduced before, remediation measures have to be considered when there is an unacceptable risk. Indeed, as shown in Fig. 3, these 23 landslides are directly threatening infrastructures such as roads or railways (for 20 of them), buildings (for 14 of them) and human lives (for 12 of them). Moreover, 8 of them could even lead to significant indirect consequences, such as tsunami induced by rockslides (Blikra, 2008, 2012; L'Heureux et al., 2011) or outbursts resulting from landslide dam failures (Costa and Schuster, 1988; Korup, 2002). In the past, the 20 reported landslides that are now active or dormant (cf. the classification of

Table 1. Exhaustive list of the monitored landslides and their related operational units that answered the questionnaire during summer 2011.

Country	Operational unit	Monitored landslide
Canada	Alberta Geological Survey	Turtle Mountain[a]
	University of Laval	Gascon Rockslide[b]
Czech Republic	Geo-Tools	*unnamed*[a]
	National Park Bohemian Switzerland	Hrensko[a]
France	Service de Restauration des Terrains en Montagne	La Valette[a]
	Institut de Physique du Globe de Paris à la Martinique	Prêcheur River[c]
China	Geotechnical Engineering Office	Entire Hong Kong province[a,x]
Italy	Ancona Monitoring Center	Ancona[a]
	Centro di Monitoraggio Geologico – ARPA Lombardia	Ruinon[a]
	Servizio Geologico Aosta	Becca di Nona[a]
		Bosmatto[a]
		Chervaz[a]
		Citrin[a]
		La Saxe[a]
		Vollein[a]
	Università degli Studi di Firenze	Torgiovannetto[c]
Norway	Åknes/Tafjord Early warning Centre	Åknes[a]
		Hegguraksla[a]
		Jettan[a]
		Mannen[a]
	Nebbet Monitoring Center	Nebbet Mountain[a]
Slovakia	State Geological Institute of Diunyz Stur	Okolicne[a]
		Velka Causa[a]
Spain	Universitat Politècnica de Catalunya	Vallcebre[a]

[a] system in operation. [b] system under construction. [c] stopped system. [x] results not included in this study.

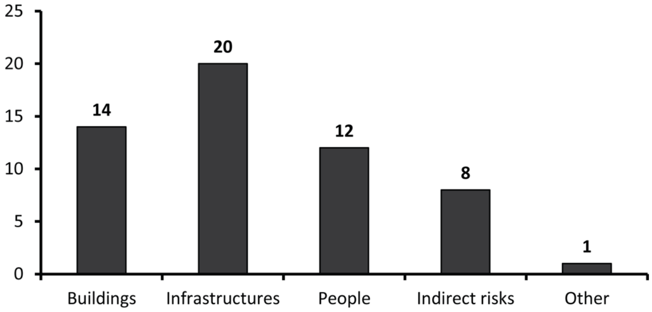

Fig. 3. Number of landslides that are endangering buildings, transportation infrastructures and people, and creating indirect risks or even other issues. The total number is over 23, because consequences of a landslide can affect more than a single target.

Cruden and Varnes, 1996) produced considerable economic losses that are difficult to quantify (even if estimated at about EUR 400 million by their operational units). Furthermore, they had important social consequences, destroying roads and villages, isolating populations and even killing more than 110 people. For example, the rock avalanche at Turtle Mountain in 1903 buried more than 70 citizens of the village of Frank during their sleep (McConnell and Brock, 1904). In 1934, the Hegguraksla rockslide indirectly killed 40 people due to the landslide-induced tsunami that destroyed several villages along the fjord with a wave reaching a maximum height of 62 m a.s.l. (Kaldhol and Kolderup, 1936; Bugge, 1937).

For 10 of the reported landslides, some physical mitigation works were performed to prevent new catastrophic events, such as retaining basins for debris flows or retaining walls for rockfalls when the context allowed it. Moreover, revision of the land-use plans has been implemented in the hazard zones for almost 75 % of the reported landslides, essentially updating land-use restrictions and construction norms for new inhabitants and infrastructures to reduce the number of elements at risk, their vulnerability and/or the population exposition.

3.2.3 Pre-investigations for EWSs

The third part of the questionnaire was related to investigations performed before the design of the monitoring systems.

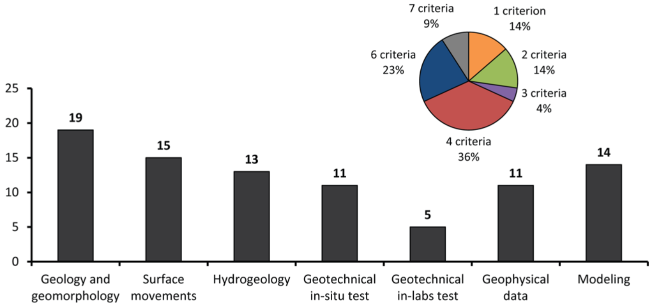

Fig. 4. Inventory of investigations performed before designing the 23 reported EWSs performed and percentage of total number of criteria investigated per site. The total number of investigations is over 23, because 86 % of the landslides required more than one type of criterion.

Several issues are usually investigated in order to get a sufficient understanding of the unstable systems, which is required for designing a proper and pertinent monitoring network (Fig. 4).

The most investigated criteria are obviously the landslide geology and the geomorphology (for 19 of them), completed by surface movement data (for 14 of them). Indeed, geological and geomorphological studies are crucial for understanding unstable slope behavior and for providing relevant conceptual models. This includes mapping of landslide features (e.g., main and minor scarps, open fractures, surfaces of rupture and compression zones) and evidence of recent activities. Furthermore, investigating surface and sub-surface displacements is often crucial for making reliable landslide conceptual models. The coupling of geological, geomorphological and displacement maps is an important foundation for designing monitoring networks and sensor locations. The monitoring network of the Norwegian rockslide in Mannen (Fig. 5) illustrates how a monitoring network can be designed, with in-place instrumentations in the accessible upper areas close to the open fractures, and with ground-based remote-sensing techniques to cope with less accessible lower parts. Moreover, sub-surface monitoring in deep boreholes is performed at two accessible localities in order to fulfill the Norwegian requirements for EWSs.

In addition, numerical models are computed for 14 instabilities in order to (1) determine stability factors and (2) map potential run-out areas of rockfalls, rock avalanches, debris flows, as well as rockslide-induced tsunamis. Therefore, simulation models are essential for identifying exposed populations and infrastructures. Geophysical measurements (mainly seismic refraction and electrical resistivity) and geotechnical in situ tests (such as standard or cone penetration tests) are performed in approximately 50 % of the cases, providing useful complementary information on subsurface conditions. Geotechnical in-lab tests are usually less employed than other criteria.

Surprisingly, hydrogeological conditions are only investigated for half of the cases (mainly piezometers and/or rain gauges). It contrasts with the fact that in the 2nd part of the questionnaire, water is considered as a physical destabilizing agent for 87 % of the reported instabilities (Fig. 2), and groundwater conditions are also required for reliable landslide models. For example, Bonnard and Steiger (2012) advise a minimum of two years of water-table monitoring before designing any drainage systems.

Finally, it is also important to note the common use of a multi-criteria approach. Thus, as seen in Fig. 4, operational units have designed their EWS on 4 types of criteria and even more in 69 % of the cases. The use of only one criterion is a method used for 14 % of the cases, and this is mostly implemented for cases where debris flows are triggered by heavy precipitations.

3.3 Monitoring systems

3.3.1 Sensor network

The fourth part of the questionnaire relates to instruments and sensors used to monitor the instabilities. Two of our partners, monitoring fragmental rockfall events, reported difficulties in filling this section table to us because of its pdf format; the following interpretations are thus based on the other 21 case studies. Figure 6 displays the different types of observed parameters and Fig. 7 sums up the different setup sensors. Detailed theoretical and technical aspects on all these landslide monitoring sensors are developed in Stumpf et al. (2011) and Michoud et al. (2012).

The large majority of the EWSs is based on the monitoring of surface and sub-surface displacements (for 18 of them), certainly because they show direct evidence of active deformations. In order to measure movements, half of the networks are based on extensometers and/or Global Navigation Satellite Systems (GNSS); crackmeters and inclinometers are also frequently used. These sensors deliver reliable data and are robust and cheap (except for GNSS). Regarding GNSS, even if antennas and receivers are more expensive than other systems and the data processing more complicated, they have the major advantage that they provide 3-D displacement information. Other techniques such as ground-based interferometric radar (GB-InSAR), total station, laser, or tiltmeters are less used. Up to now they were considered to be expensive as well as to create some difficulties related to setup and data processing in comparison with other methods. Furthermore, some instruments such as crackmeters or GB-InSAR may become fragile in harsh environments, and good protection (against heavy rainfall, snow load or snow creep for example) has to be considered to protect them. Sub-surface monitoring in boreholes is common in some of the largest and more complex landslides, and is used in 6 of the reported cases. Several of the landslide monitoring systems have now changed the instrumentation from traditional

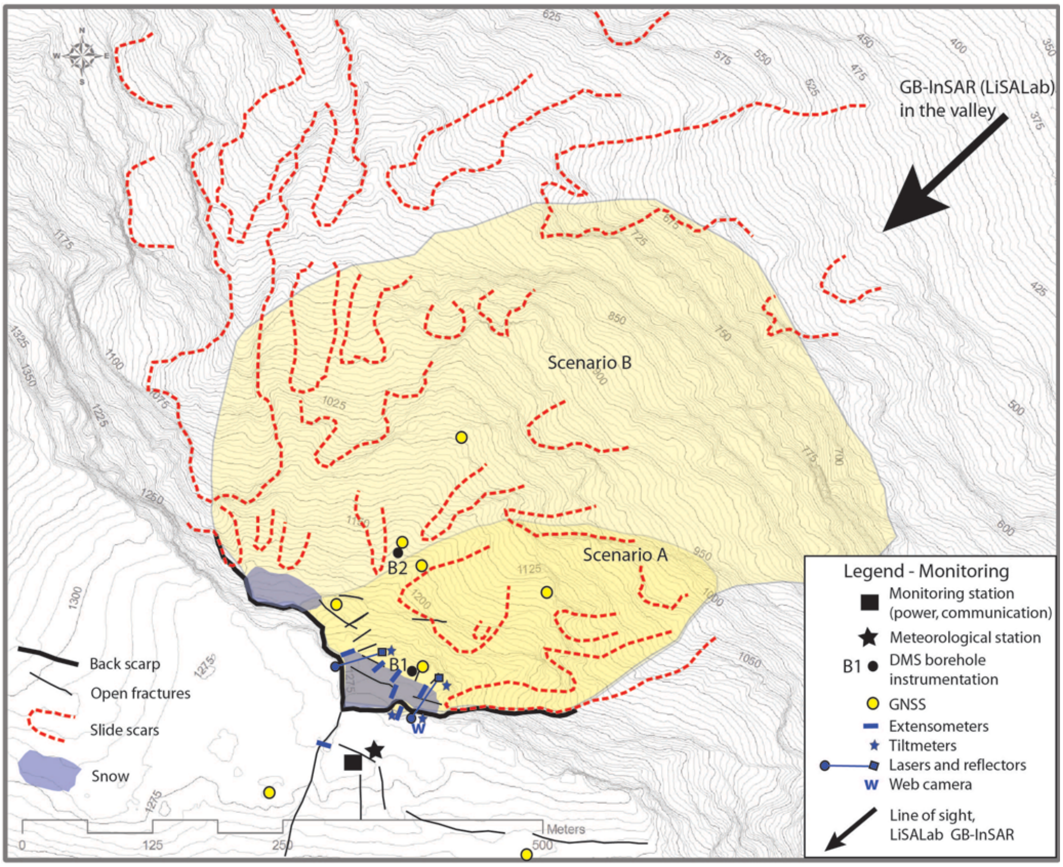

Fig. 5. Mannen rockslide monitoring network. Ground-based in-place instrumentation is concentrated close to the back scarp, while the GB InSAR system is placed in the valley below. Two deep boreholes are instrumented by 120 m-long DMS columns. Open fractures and slide scars were identified and mapped during previous field investigations. Theoretical and technical details of those techniques are developed in Stumpf et al. (2011) and Michoud et al. (2012).

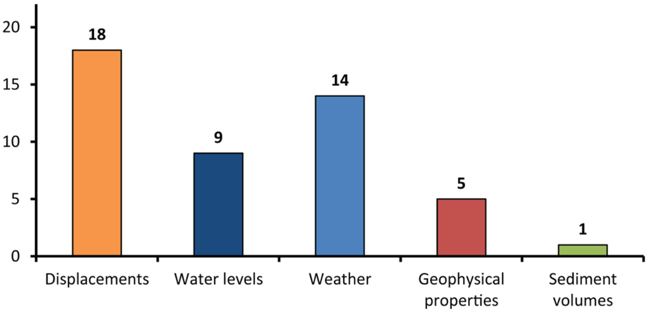

Fig. 6. Inventory of monitored parameter types for the 21 reported monitoring networks. The total number is over 21, because more than one parameter is monitored for 15 of the landslides.

manual inclinometric probe measurements to automatic and long columns, such as the DMS system (Lovisolo et al., 2003), consisting of a large number of sensors managing to monitor continuous sequences.

It is also interesting to note that the Turtle Mountain and Åknes instabilities are monitored using spaceborne radar interferometry (InSAR) techniques as well. Even if it does not provide real-time data and de facto cannot be used for operative early warnings, it is a useful approach to understand and update the landslide dynamics using images from space agencies' archives. Moreover, Spaceborne InSAR can be helpful during pre-investigation work and can also provide EWSs with complementary information. Indeed, an overview of the regional stability in the neighborhood of the monitored slopes is important in many cases, since large landslides as sackungs are able to destabilize small monitored landslides inside the large deformed masses (Agliardi et al., 2001).

In addition to displacement data, meteorological parameters are crucial to be monitored, since rainfall, snowmelt and permafrost are considered as a triggering factor for 20 (87 %) of the instabilities (Fig. 2). Meteorological parameters are thus very frequently measured (in 14 EWSs) as well as water table levels and water discharge in streams (in 9 EWSs); indeed, rain gauges are included in half of the monitoring networks, and piezometers and temperature gauges in 7 of them.

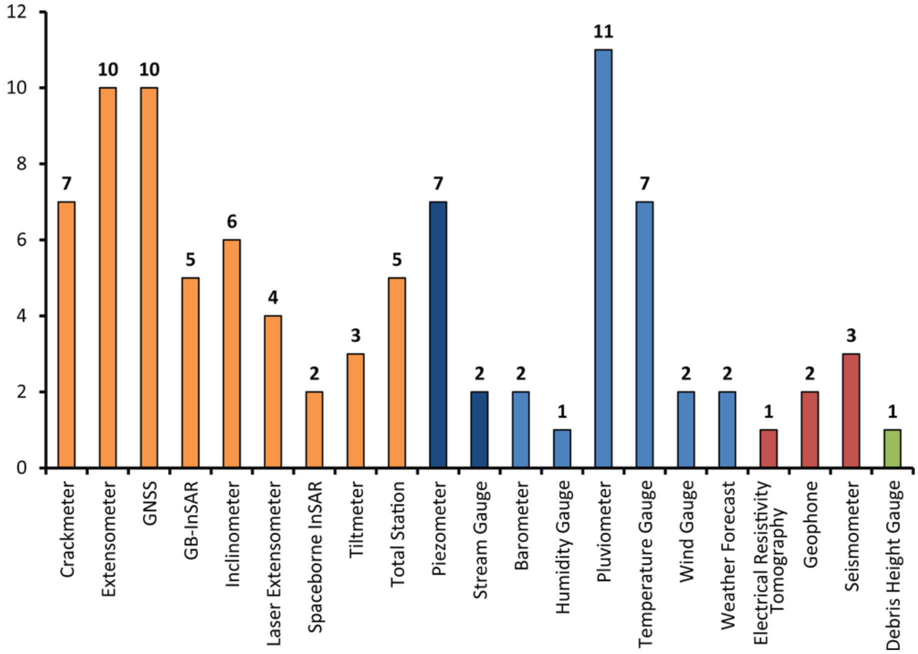

Fig. 7. Inventory of the different techniques used for the 21 reported monitoring networks in order to measure surface and sub-surface displacements (in orange), water and groundwater table levels (in dark blue), weather conditions (in light blue), geophysical properties (in red) and available sediment volumes (in light green). Theoretical and technical details of those techniques are developed in Stumpf et al. (2011) and Michoud et al. (2012).

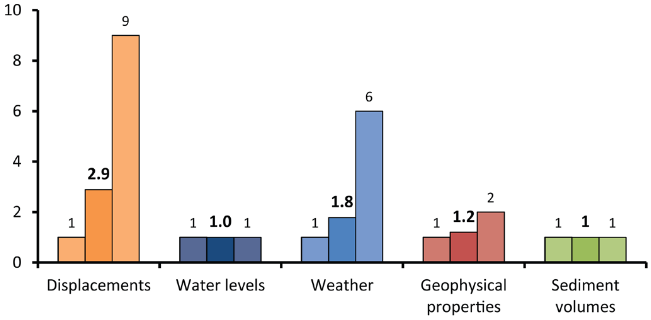

Fig. 8. Minimum, mean and maximum instrument types used to monitor each parameter (when it is done) per landslide.

Near-surface geophysical methods have been considerably improved during the last two decades, and their uses for landslide investigation purposes have been reviewed in Jongmans and Garambois (2007). Nevertheless, geophysical applications for operational EWSs are still under development (Spillman et al., 2007; Roth, 2012; Mainsant et al., 2012; Navratil et al., 2013), largely explaining why they are applied for only 5 of the 21 reported case studies.

An EWS implemented in debris and earthflow source areas also monitors the volume of available sediments that can be mobilized in case of heavy rainfall, using gauges that measure the sediment heights in order to be able to forecast potential event intensities.

Redundancy is important in EWSs (Figs. 8 and 9). This is particularly evident for robust monitoring networks that measure displacements and groundwater. For example, in the Åknes instability, displacements are monitored by 8 instrument types: 8 crackmeters, 8 GNSS antennas, 2 laser devices, 1 ground-based radar, 3 extensometers, 1 total station coupled with 30 prisms, 2 surface tiltmeters and 3 deep boreholes instrumentated with inclinometers and water-pressure measurement cells (DMS columns). It allows one to (1) monitor several sectors with different dynamics and displacement rates on the surface and the sub-surface, (2) discriminate unwanted false alarms coming from large noise or one defective sensor and (3) have instruments fed by several power supply and data communication lines. On the contrary, only one meteorological station (e.g., with rainfall, temperature, snow depth or humidity gauges) is usually installed to monitor weather conditions, since landslides are usually confined to small areas with relatively similar conditions.

In conclusion, based on the experiences of the reported institutions in charge of landslide EWSs, a good monitoring network is characterized by:

1. simplicity;
2. robustness;
3. presence of multiple sensors;
4. power and communication lines backups (detailed in Sect. 3.3.2).

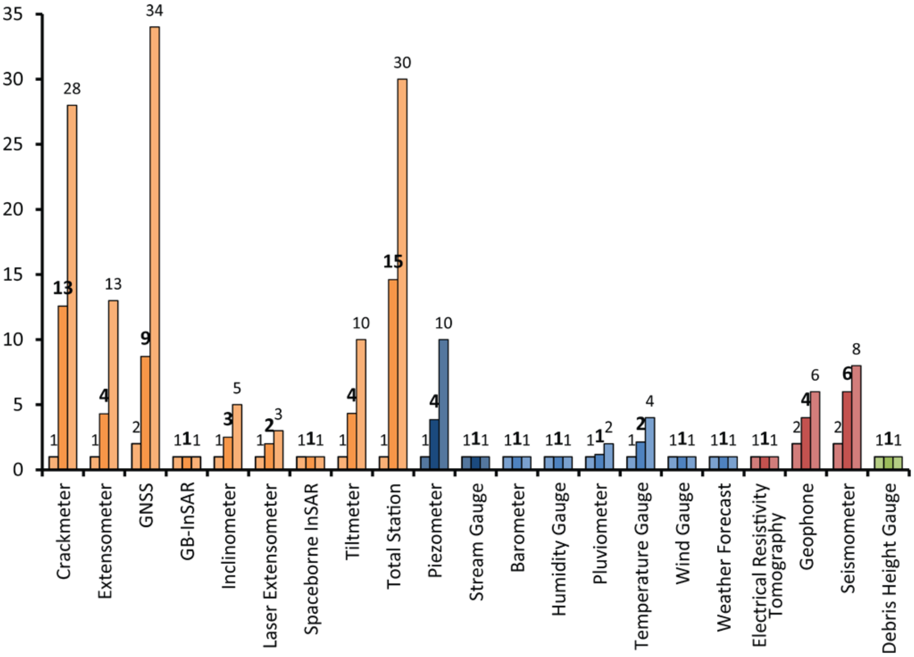

Fig. 9. Minimum, mean and maximum number of sensors of each type per landslide, when used, in order to monitor surface and sub-surface displacements (in orange), water and groundwater table levels (in dark blue), weather conditions (in light blue), geophysical properties (in red) and available sediment volumes (in light green). Theoretical and technical details of those techniques are developed in Stumpf et al. (2011) and Michoud et al. (2012).

The following characteristics are also important for the choice of instrumentation:

1. implication for understanding the landslide evolution;
2. high life expectancy;
3. robustness;
4. price;
5. level of real-time data;
6. noise level of the sensors.

On the other hand, a system is limited if it is based only on surface displacements and if it can be damaged by weather conditions and/or landslide events themselves before sending data or alarms to the operational center. Present monitoring networks can still be improved by a better integration and near real-time compilation of all monitoring data, for example by coupling displacements with weather conditions, groundwater and/or seismic activities.

3.3.2 Power and data management networks

The principle of redundancy is also important for power and data management networks, as shown in detail in Froese and Moreno (2011). Those networks supply monitoring sensors with electricity, and allow manual remote data access for experts' periodic checks and automatic data transmission to operational units based on Internet protocols. Regarding the 23 reported sites, two thirds of monitoring networks are equipped with power supplies, communication lines and systems backups for monitoring sensors and for operational centers, in order to ensure continuous data measurement, transmission and analysis.

3.3.3 Alarms

The fifth and last part of the questionnaire is focused on the way to use monitored data, establishing alarms and associated responses to protect endangered populations and infrastructures.

Threshold values for alarm messages are normally based on the evaluation of different sensors and an expert interpretation of the stability conditions, mainly during the pre-investigation work (Blikra, 2008; Froese and Moreno, 2011). Because they are direct evidence of activity, almost all threshold parameters are based on displacement data (for 13 of the 15 reported answers), sometimes coupled with rainfall data (for 6 cases). More rarely, 2 earthslides in Slovakia use the groundwater table level monitored by piezometers as a threshold parameter.

Figure 10 highlights essential characteristics for the establishment of alarm procedures. In order to limit false alarms, threshold values are based on multiple identical devices and/or several redundant types of sensor for 19 of the EWSs.

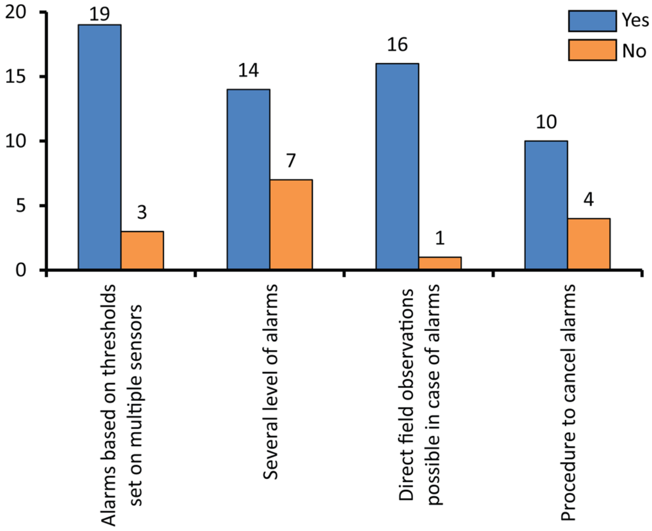

Fig. 10. Inventory of the essential characteristics of alarm procedures for the 23 reported monitoring networks.

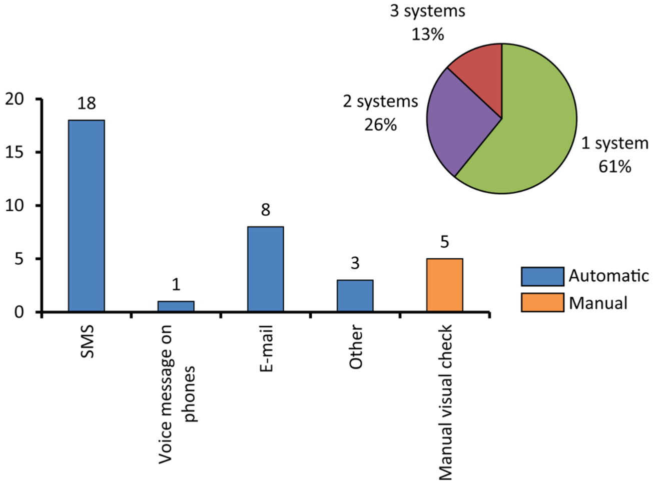

Fig. 11. Inventory of automatic and manual techniques used to send alarms from the monitoring network to the operational unit and percentage of number of techniques used simultaneously for the 23 reported monitoring networks. The total number is above 23, since 39 % of the monitoring networks use more than one technique.

Curiously however, only 9 of the threshold values take technical sensor limitations such as the smallest detectable signal and noise levels into account before establishing them, even if it allows the alarm's reliability to be increased. Furthermore, several levels of alarms (such as Table 2) have been established for one third of the reported systems.

As soon as a threshold value is reached by a predefined number of sensors, 22 of the 23 monitoring networks automatically send an alarm message to an operator on call 24/7. The most used communication technique is largely an automatic SMS sent to cellular operators and is too rarely coupled with other redundant systems such as emails or voice phone messages (Fig. 11). These alarms prompt the person on duty to inspect the monitored data. Moreover, direct field observations are possible in many cases to get additional information about the stability conditions, especially during critical stages, by checking visible changes such as local activities (e.g., sliding and/or falls) within the whole landslide area. Finally, according to expert judgments based on the monitored data and these field observations, procedures to manually cancel alarms have been established for two thirds of the reported case studies.

3.4 Dealing with populations

3.4.1 Decision-making processes

Tailored strategies have to be adopted depending on the landslide state of activity, and two thirds of the reported EWSs have established different thresholds for different scenarios. For example, the *Emergency Preparedness Centre in Stranda* established gradual alert postures based on different threshold values and expert evaluations, leading to appropriate responses such as the evacuation of endangered populations (Table 2). The execution of these strategies requires close collaboration between the operational units and local and/or regional authorities. Rigorous protocols have to be established in order to clearly define the roles and responsibilities of each institution according to the alert levels; a detailed example of the Turtle Mountain Monitoring Project protocols is illustrated in Moreno and Froese (2009). The flowchart is a common representation that gives an evident checklist reviewing necessary procedures, as shown for instance in Fig. 12.

The design of decision-making processes should take care of legislation and cultural issues, as well as of the prerogatives of the involved agencies. Three fourths of the reported strategies have been designed by the operational units, with the help for about one third of them from local authorities and/or regional and governmental institutions (Fig. 13). Moreover, the procedures have almost all been reviewed by operational checklists (in 16 cases), completed in 8 cases by reviews from external groups.

3.4.2 Alert broadcasts

When circumstances require the evacuation of local populations, the most used communication vectors to inform people are radio, siren and SMS, coupled sometimes with telephone and television (Fig. 14); however, normal evacuation approaches by policemen walking door-to-door are also important routines. Websites and e-mails are rarely used, since it is not sure that they manage to reach the population in time for imminent danger. Regarding the closing of road sections, the most frequent system is simple traffic lights that can actually be completed by policemen. According to our ability to predict in advance the time to slope failure or to

Table 2. Example from the Emergency Preparedness Centre in Stranda (Norway) of gradual alert levels based on different threshold values and expert evaluations leading to planned responses (modified from Blikra et al., 2007).

Velocities [mm day^{-1}]	Alarm level	Activities and alarms	Response
0.1–0.5	Level 1 – Green Normal situation	Minor seasonal variations No alarm	Technical maintenance EPC staff
0.5–2	Level 2 – Blue Awareness	Important seasonal fluctuations for individual and multiple sensors Values < excess thresholds for Level 2	Increase frequency of data review and comparison of different sensors EPC staff
2–5	Level 3 – Yellow Increase awareness	Increased displacement velocity, seen on several individual sensors Values < excess thresholds for Level 3	Do continuous reviews and field survey Geo-expert team at EPC full time Inform police and emergency preparedness teams in municipalities
5–10	Level 4 – Orange High hazard	Acceleration in displacement velocity observed on multiple sensors Values < excess thresholds for Level 4	Increase preparedness, continuous data analysis Alert municipalities to stand prepared for evacuation
> 10	Level 5 – Red Critical situation	Further acceleration Values >excess thresholds for Level 4	Evacuation

flow initiation (Fukuzono, 1990; Crosta and Agliardi, 2003; Baum and Godt, 2010; Federico et al., 2012; Meyer et al., 2012) and the stakes of each site, reaction times after warning are from 10 min to close roads, as in Torgiovanetto, to 72 h to evacuate populations, as for Norwegian rockslides.

Prior to real evacuations, operational units and local units have imperatively to ensure that the public has been well informed about the adopted strategies, in order to guarantee that the plan comes together with proper cooperation and behavior of the local populations (as detailed in Sect. 3.4.3). In addition, evacuation exercises, which have been performed once or twice for 12 reported case studies, have recently turned out to be necessary for testing the efficiency of established plans and procedures (Moreno and Froese, 2009).

3.4.3 Risk communications

The trust of local populations in EWSs and proper risk perception are fundamental to the success of an EWS (Dash and Gladwin, 2007), since cooperative and collective actions are required in case of alerts. Due to socio-cultural heritages, fair judgments need openness, involvement and good consultation processes. Ostrom (1998) further recommends face-to-face communication. It provides the best positive effects on cooperative tasks, allowing, among other things, the exchange of mutual commitments and the assurance of proper expectations of population behaviors in case of evacuation, for instance. For half of the reported cases, the information is given thanks to public meetings, reports, as well as websites (Fig. 15). Other solutions, such as newspapers, are still anecdotal. No answers referred to any information provided by TV programs. Good risk communication also means that public meetings have to be organized to inform and consult local populations during and/or after every round of the decision-making process.

Finally, a last point is also clear: monitoring centers are in charge of sensitive and complex data. Indeed, even if they are all partially or totally financed by public funds, two thirds of the institutions still do not provide free and easy access to data for anyone. It can be also a question about letting the public have access to raw data that can be difficult to interpret due to noise in the sensor measurements. Although not communicating the monitored data could make local people suspicious, incorrect readings could also certainly lead to major misunderstandings and unnecessary concerns (Mileti and Sorensen, 1990). Therefore, the right communication level is difficult to reach.

3.5 Practical challenges

The last part of the questionnaire relates to practical challenges encountered during the design, the construction and the maintenance of the EWSs (Fig. 16). Most of them (20) related some problems during the installation and the maintenance of the sensors. Indeed, more than half of the instrumentation deals with harsh weather and site conditions, suffering from heavy rainfall, ice, thick snow cover, avalanches, wind, etc. On the other hand, funding and human resources are sources of problems for less than one third of the EWSs.

Of the 8 participating countries, only Norway legislated on EWS in order to define the roles of institutions in charge of landslide EWSs and to direct them (technical requirements in the Norwegian building codes). In addition, Slovakia produced a guideline about general strategies to adopt and Canada is on the way (Couture et al., 2012). As a consequence, the operational units in charge of EWSs have to look for scientific and practical support from other expert groups and/or international experience.

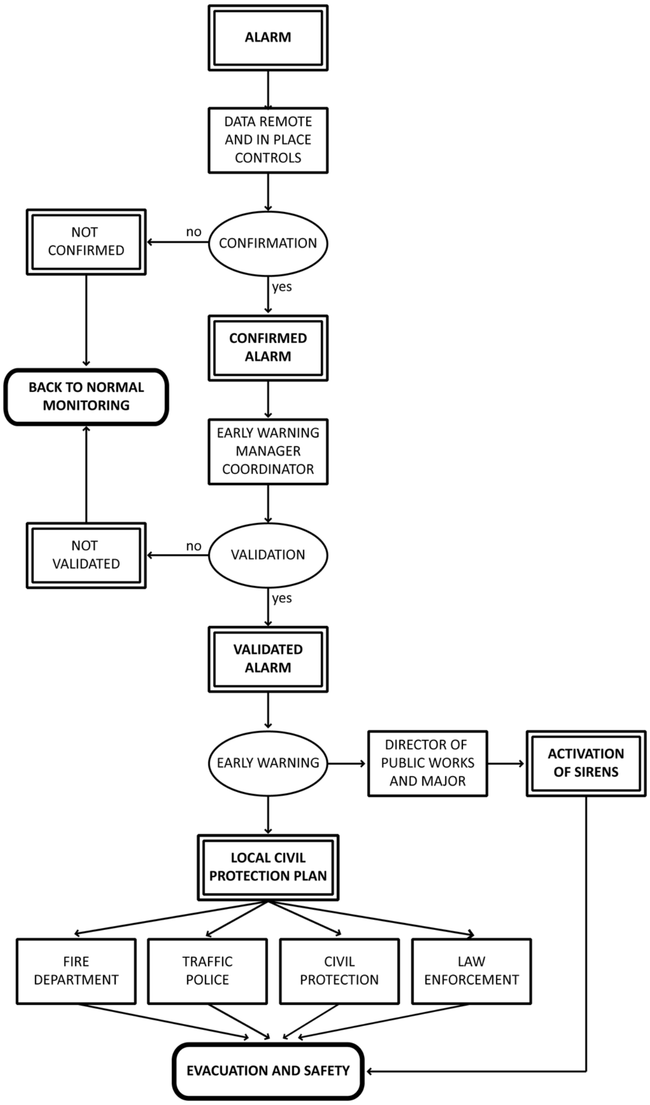

Fig. 12. Flowchart of the protocol that has to be followed in case of alarm in Ancona, Italy (modified after Cardellini, 2011).

4 Discussions and conclusions

This paper aims to present some reflections for implementing site-specific landslide EWSs, focusing on specific requirements and practical issues based on current ongoing experiences. A questionnaire on these purposes was created and sent to about one-hundred institutions in charge of landslide management. About one fourth of the requests received an answer. One reason could be the lack of availability of the persons in charge. Another reason could be the questionnaire format (a pdf file including questions and tables sent by emails), even if it seemed to be easily accessible for everybody. Several institutions indeed reported difficulties in filling some parts of the questionnaire to us, and had to print it to write answers by hand. For future investigations, we would recommend the use of interactive web-based survey tools (e.g., as in Tofani et al., 2013); they are indeed more user-friendly to fill by respondents (maximizing the number of potential answers as shown in Lapointe et al., 2010) and also to analyze afterwards. Although the small number of answers does not have a high statistical significance, several of the reported EWSs are among the most studied landslides in Western countries. They have also accumulated high-quality knowledge after many constructive studies and experiments; valuable results and future recommendation can thus be extracted from these sites.

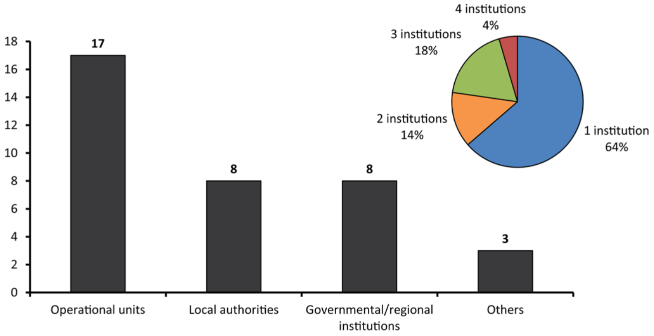

Fig. 13. Inventory of institutions involved in the establishment of strategies in case of alerts and percentage of number of institutions involved together for the 23 reported EWSs. The total number is above 22, because 36 % of the strategies have been designed by more than one institute.

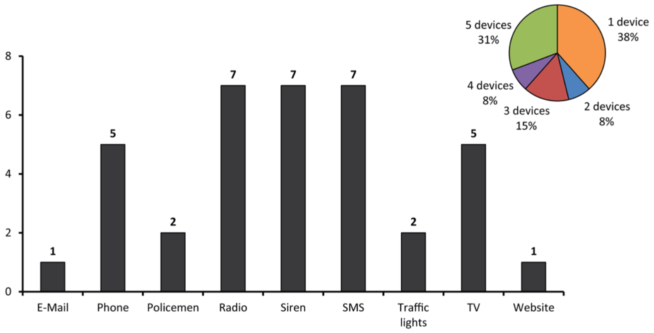

Fig. 14. Inventory of the different ways used to issue the alerts to local populations and percentage of number of communication devices coupled for the 13 reported answers got from questionnaires. The total number of communication vectors for alerts is over 13, because 38 % of the systems use more than one type of device.

There are no standard requirements for designing and operating EWSs. Actually, we cannot provide solutions to all questions, since every situation is unique, depending on landslide hazard and risk settings, local legislations and available resources. Such guidelines are provided in a comprehensive report (Bazin, 2012). Nevertheless, this review based on current experiences highlights specific requirements and potential practical issues that operational units would have to take into consideration when designing their system:

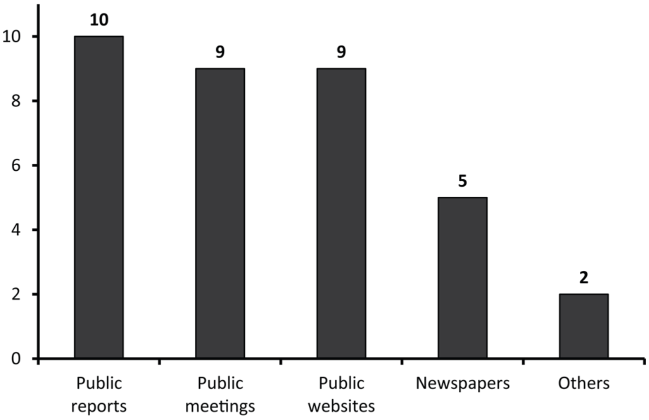

Fig. 15. Inventory of communication vectors used to inform local populations for the 23 reported EWSs. The total number of vectors is over 23, because several institutions communicated in several ways.

- it is crucial to acquire a proper understanding of instabilities through hazard and risk pre-investigations, and to constantly update landslide conceptual models with the newer monitored data of EWSs;

- redundancy, simplicity, robustness, communication and power supply backups are necessary for a reliable monitoring system. This should support a near real-time interpretation of the stability conditions by experts;

- the establishment of different scenarios adapted to gradual increasing of alert levels based on reliable landslide models is important. Procedures should clearly define the role and the responsibilities of all involved institutions. Alerts should be as quick and as direct as possible;

- public meetings for properly informing and consulting local populations are important in order to ensure a trust atmosphere and appropriate behavior of people in case of alert.

Nevertheless, some EWSs are limited by theoretical and practical issues that are currently being investigated:

- First, operational units also underline that, most of the time, monitoring networks are located in harsh conditions and therefore that it is difficult to install and maintain sensors. This point emphasizes the importance for manufacturers to improve long-term sensor robustness and for operational units to ensure a proper maintenance budget.

- EWSs could be significantly improved by current research, focusing on a better near real-time integration of monitoring data from different sensor types (Bichler et al., 2004; Travelletti et al., 2012; Michoud et al., 2013). Sensors and their data processing are undergoing fast development (Tofani et al., 2012), getting to the continuous integration of GB-InSAR data (Casagli et al., 2010; Chantry et al., 2013; Montserrat et al., 2013), LiDAR data (Riegl, 2013) and geophysical measurements (Mainsant et al., 2012; Navratil et al., 2013) to monitor landslides. Due to this fast evolution, monitoring systems have to be regularly updated, having once again an impact on EWS deployments and maintenance costs (Froese, 2013).

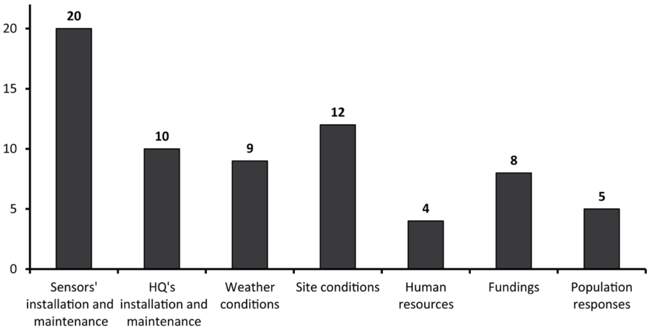

Fig. 16. Inventory of practical challenges met by the 23 reported EWSs. The total number of challenges is over 23, because EWSs usually encountered more than one issue during their life cycles.

- In addition to technical limitations, this survey also highlights some EWS conceptual issues. For instance, it seems there is a lack of investigations into hydrological factors in landslide processes, since water is involved in about 86 % of slope destabilizations and/or landslide triggering, but is investigated with rain gauges or piezometers for only half of the cases.

- Moreover, an important challenge is to improve the reliability and pertinence of automatic alarms in the future. Surprisingly, about half of the reported systems did not take into consideration technical sensor limitations before establishing threshold values, even if it would surely decrease the frequency of false alarms. In addition, recent research is focused on failure forecasting and/or flow initiations by looking for mass movement indicators (Baroň et al., 2012) such as precursory displacements (Abellán et al., 2010; Federico et al., 2012), changes in slope rheological settings (Mainsant et al., 2013), strain rates (Jaboyedoff et al., 2012), or hydrological conditions (Abellán et al., 2013; Mercogliano et al., 2013).

We can also add that a recent workshop ("The 1st International Workshop on Warning Criteria for Actives Slides"), held in Courmayeur, Italy, during the review process of this paper (10–12 June 2013), showed one additional issue. After a decade of service, it indeed seems that some EWSs need to be redeployed because of low activity of the landslides and budget issues. This leads to learning how to go from expensive and complex EWS to simpler and cheaper monitoring systems (Troisi and Negro, 2013; Froese, 2013).

Finally, the collected feedback and experiences, in addition to current research, will therefore contribute to modifying and improving existing and future EWS strategies.

Supplementary material related to this article is available online at http://www.nat-hazards-earth-syst-sci.net/13/2659/2013/nhess-13-2659-2013-supplement.pdf.

Acknowledgements. The present work has been partially supported by the SafeLand "Living with landslide risk in Europe: Assessment, effects of global change, and risk management strategies" project (7th Framework Programme of the European Commission, Grant Agreement No. 226479). This support is gratefully acknowledged. We would also like to thank our SafeLand partners, and more particularly Ivo Baroň, for their essential and appreciated support. Thanks also to Marie Charrière, who recommended valuable references on risk communication. Moreover, Veronica Tofani, Simone Frigerio and Emanuele Intrieri helped us to significantly improve the present document thanks to pertinent remarks and suggestions. Finally, we thank all the institutions that responded to the screening study.

Edited by: V. Tofani
Reviewed by: E. Intrieri and S. Frigerio

References

Abellán, A., Calvet, J., Vilaplana, J. M., and Blanchard, J.: Detection and spatial prediction of rockfalls by means of terrestrial laser scanner monitoring, Geomorphology, 119, 162–171, 2010.

Abellán, A., Moya, J., Jaboyedoff, M., and Corominas, J.: Prediccion de la velocisas de un deslizamiento en base a la precipitación, Applicación en la zona de studio piloto de Vallcebre (Pirineos Catalanes), in: Proceedings of the VII Simposio Nacional sobre Taludes y Laderas Inestables, Palma de Mallorca, Spain, 11–14 June 2013, 1081–1092, 2013 (in Spanish).

Agliardi, F., Crosta, G. B., and Zanchi, A.: Structural constraints on deep-seated slope deformation kinematics, Eng. Geol., 59, 83–102, 2001.

Aleotti, P: A warning system for rainfall-induced shallow failures, Eng. Geol., 73, 247–265, 2004.

Angeli, M.-G., Pasuto, A., and Silvano, S.: A critical review of landslide monitoring experiences, Eng. Geol., 55, 133–147, 2000.

Baroň, I., Supper, R., and Ottowitz, D. (Eds.): SafeLand deliverable 4.6.: Report on evaluation of mass movement indicators, European Project SafeLand, Grant Agreement No. 226479, 382 pp., available at: http://www.safeland-fp7.eu, 2012.

Basher, R.: Global early warning systems for natural hazards: systematic and people-centered, Phil. Trans. R. Soc., 364, 2167–2182, 2006.

Baum, R. L. and Godt, J. W.: Early warning of rainfall-induced shallow landslides and debris flows in the USA, Landslides, 7, 259–272, 2010.

Bazin, S. (Ed.): SafeLand deliverable 4.8.: Guidelines for landslide monitoring and early warning systems in Europe – Design and required technology, European Project SafeLand, Grant Agreement No. 226479, 153 pp., available at: http://www.safeland-fp7.eu, 2012.

Benko, B. and Stead, D.: The Frank Slide: A reexamination of the failure mechanism, Can. Geotech. J., 35, 299–311, 1998.

Bichler, A., Bobrowsky, P., Best, M., Douma, M., Hunter, J., Calvert, T., and Burns, R.: Three-dimensional mapping of a landslide using a multi-geophysical approach: the Quesnel Forks landslide, Landslides, 1, 29–40, 2004.

Blikra, L. H.: The Åknes rockslide: Monitoring, threshold values and early-warning, in: Landslides and Engineering Slopes: From the Past to the Future, Proceedings of the 10th International Symposium on Landslides and Engineering Slopes, Xi'an, China, 30 June–4 July 2008, 1089–1094, 2008.

Blikra, L. H.: The Åknes rockslide, Norway, in: Landslides: Types, Mechanisms and Modeling, edited by: Clague, J.J. and Stead, D., Cambridge, 323–335, 2012.

Bonnard, C. and Steiger, H.: Control of an unstable slope by horizontal drainage boreholes and soil nailing during the widening of a major road, Laubegg gorge Switzerland, in: Landslides and Engineering Slopes: Protecting Society through Improved Understanding, Proceedings of the 11th International and 2nd North American Symposium on Landslides and Engineered Slopes, Banff, Canada, 3–8 June 2012, 1575–1580, 2012.

Bugge, A.: Fjellskred fra topografisk og geologisk synspunkt, Norsk Geografisk Tidsskrift, 6, 342–360, 1937.

Cardellini, S.: The Early Warning System of Ancona for Managing and Reducing Landslide Risks, Climate change adaptation and disaster risk reduction, making cities resilient conference, Stockholm, Sweden, 17 May 2011, available at: http://www.unisdr.org/we/inform/events/19823 (last access: 15 October 2013), 2011.

Casagli, N., Catani, F., Del Ventisette, C., and Luzi, G.: Monitoring, prediction, and early warning using ground-based radar interferometry, Landslides, 7, 291–301, 2010.

Chantry, R., Pedrazzini, A., Jaboyedoff, M. and Stampfli, E.: Caractérisation, suivi et assainissement des instabilities rocheuses à la carrier d'Arvel, in: Les dangers naturels en Suisse: pratiques et développement, Comptes rendus de la deuxième Journée de Rencontre sur les Dangers Naturels, Lausanne, Switzerland, 18 February 2011, 243–261, 2013 (in French).

Cornforth, D. H.: Landslides in Practice: Investigation, Analysis and Remedial/Preventive Options in Soils, John Wiley & Sons, Hoboken, New Jersey, 624 pp., 2005.

Corominas, J. and Santacana, N.: Stability analysis of the Vallcebre translational slide, Eastern Pyrenees (Spain) by means of a GIS, Nat. Hazards, 30, 473–485, 2003.

Corominas, J., Moya, J., Ledesma, A., Lloret, A., and Gili, J.: Prediction of ground displacements and velocities from groundwater level changes at the Vallcebre landslide (Eastern Pyrenees, Spain), Landslides, 2, 83–96, 2005.

Costa, J. E. and Schuster, R. L.: The formation and failure of natural dams, Geol. Soc. Am. Bull., 100, 1054–1068, 1988.

Cotecchia, V.: The Second Hans Cloos Lecture: Experience drawn from the great Ancona landslide of 1982, Bull. Eng. Geol. Env., 65, 1–41, 2006.

Couture, R., Bobrowsky, P. T., Blais-Stevens, A., Wang, B., and VanDine, D. F.: An introduction to the Canadian technical guidelines and best practices related to landslides, in: Landslides and Engineering Slopes: Protecting Society through Improved Understanding, Proceedings of the 11th International and 2nd North American Symposium on Landslides and Engineered Slopes, Banff, Canada, 3–8 June 2012, 217–222, 2012.

Crosta, G. B. and Agliardi, F.: Failure forecast for large rock slides by surface displacement measurements, Can. Geotech. J., 40, 176–191, 2003.

Cruden, D. and Krahn, J.: A re-examination of the geology of Frank Slide, Can. Geotech. J., 10, 581–591, 1973.

Cruden, D. and Varnes, D.: Landslides Types and Processes, in: Landslides, Investigations and Mitigations, Transportation Research Board, Special Report 247, edited by: Turner, A. and Schuster, R., Washington, DC, 36–75, 1996.

Dash, N. and Gladwin, H.: Evacuation Decision Making and Behavioral Responses: Individual and Household, Nat. Hazards Rev., 8, 69–77, 2007.

Federico, A., Popescu, M., Elia, G., Fidelibus, C., Internò, G., and Murianni, A.: Prediction of time to slope failure: a general framework, Environ. Earth Sci., 66, 245–256, 2012.

Fell, R., Ho, K. K. S., Lacasse, S., and Leroi, E.: A framework for landslide risk assessment and management, in: Landslide Risk Management, edited by: Hungr, O., Fell, R., Couture, R., and Eberhardt, E., Proceedings of the International Conference on Landslide Risk Management in Vancouver, Canada, 31 May–3 June 2005, 3–25, 2005.

Froese, C.: Lessons Learned from 10 Years of Early Warning at Turtle Mountain, Alberta, Canada, in: Proceedings of the 1st International Workshop on Warning Criteria for Active Slides, Courmayeur, Italy, 10–12 June 2013, 48–49, available at: http://www2.ggl.ulaval.ca/iwwcas/, 2013.

Froese, C. and Moreno, F.: Structure and components for the emergency response and warning system on Turtle Mountain, Alberta, Canada, Nat. Hazards, 24 pp., doi:10.1007/s11069-011-9714-y, 2011.

Fukuzono, T.: Recent Studies on Time Prediction of Slope Failure, Landslide News, 4, 9–12, 1990.

Gili, J., Corominas, J., and Riuz, J.: Using Global Positioning System techniques in landslide monitoring, Eng. Geol., 55, 167–192, 2000.

Holtz, R. D. and Schuster, R. L.: Stabilization of soil slopes, in: Landslides, Investigations and Mitigations, Transportation Research Board, Special Report 247, edited by: Turner, A. and Schuster, R., Washington, DC, 439–473, 1996.

Hong Kong Slope Safety: available at: http://hkss.cedd.gov.hk/hkss/eng/index.aspx, last access: 19 November 2012.

Intrieri, E., Gigli, G., Casagli, N., and Nadim, F.: Brief communication "Landslide Early Warning System: toolbox and general concepts", Nat. Hazards Earth Syst. Sci., 13, 85–90, doi:10.5194/nhess-13-85-2013, 2013

Jaboyedoff, M., Oppikofer, T., Derron, M.-H., Blikra, L. H., Böhme, M. and Saintot, A.: Complex landslide behaviour and structural control: a three-dimensional conceptual model of Åknes rockslide, Norway, in: Slope Tectonics, Special Publication 351, edited by: Jaboyedoff, M., Geological Society of London, 147–161, 2011.

Jaboyedoff, M., Derron, M.-H., Pedrazzini, A., Blikra, L., Froese, C., Hermanns, R. H., Oppikofer, T., Böhme, M., and Stead, D.: Fast assessment of susceptibility of massive rock instabilities, in: Landslides and Engineering Slopes: Protecting Society through Improved Understanding, Proceedings of the 11th International and 2nd North American Symposium on Landslides and Engineered Slopes, Banff, Canada, 3–8 June 2012, 459–465, 2012.

Jakob, M., Owen, T., and Simpson, T.: A regional real-time debris-flow warning system for the District of North Vancouver, Canada, Landslides, 9, 165–178, 2012.

Jongmans, D. and Garambois, S.: Geophysical investigations of landslides. A review, Bulletin de la Société Géologique de France, 178, 101–112, 2007.

Kaldhol, H. and Kolderup, N.-H.: Skredet i Tafjord 7. April 1934, Bergens Museums Årbok 1936 Naturvitenskapelig Rekke, 11, 1–15, 1936.

Keefer, D. K., Wilson, R. C., Mark, R. K., Brabb, E. E., Brown, W. M., Ellen, S. D., Harp, E. L., Wieczorek, G. F., Alger, C. S., and Zatkin, R. S.: Real time landslide warning system during heavy rainfall, Science, 238, 921–925, 1987.

Korup, O.: Recent research on landslide dams – a literature review with special attention to New Zealand, Progr. Phys. Geogr., 26, 206–235, 2002.

Lacasse, S. and Nadim, F.: Landslide Risk Assessment and Mitigation Strategy, in: Landslides – Disaster Risk Reduction, edited by: Sassa, K. and Canuti, P., Springer-Verlag Berlin Heidelberg, 31–61, 2009.

Lapointe, F., Baulne, J., Bélanger, L., Breton, A., Camirand, J., Chevalier, R., Cloutier, R., Godbout, M., Lepage, H., Thibault, M.-T., Vecerina, C., Bilodeau, D., des Groseilliers, L., and Haché, M.: Gestion de la qualité – Document de principes sur la qualité dans les enquêtes, Public report, Institut sur la statistique du Québec, Québec, Canada, 65 pp., 2010 (in French).

L'Heureux, J.-S., Glimsdal, S., Longva, O., Hansen L., and Harbitz, C. B.: The 1888 shoreline landslide and tsunami in Trondheimsfjorden, central Norway, Mar. Geophys. Res., 32, 313–329, 2011.

Lovisolo, M., Ghirotto, S., Scardia, G., and Battaglio, M.: The use of Differential Monitoring Stability (D.M.S.) for remote monitoring of excavation and landslide movements, in: Proceedings of the Sixth International Symposium on Field Measurements in Geomechanics, edited by: Myrvol, A., Oslo, Balkema, 519–524, 2003.

Mainsant, G., Larose, E., Brönnimann, C., Jongmans, D., Michoud, C., and Jaboyedoff, M.: Ambient seismic noise monitoring of a clay landslide: Toward failure prediction, J. Geophys. Res., 117, F01030, doi:10.1029/2011JF002159, 2012.

Mainsant, G., Jongmans, D., Chambon, G., Larose, E., and Baillet, L.: Shear-wave velocity as an indicator for rheological changes in clay materials: Lessons from laboratory experiments, Geophys. Res. Lett., doi:10.1029/2012GL053159, in press, 2013.

McConnell, R. G. and Brock, R. W.: Report on the Great Landslide at Frank, Alberta, in: Annual Report for 1903, Canada Department of the Interior, 1904.

Mercogliano, P., Segoni, S., Rossi, G., Sikorsky, B., Tofani, V., Schiano, P., Catani, F., and Casagli, N.: Brief communication "A prototype forecasting chain for rainfall induced shallow landslides", Nat. Hazards Earth Syst. Sci., 13, 771–777, doi:10.5194/nhess-13-771-2013, 2013.

Meyer, N. K., Dyrrdal, A. V., Frauenfelder, R., Etzelmüller, B., and Nadim, F.: Hydrometeorological threshold conditions for debris flow initiation in Norway, Nat. Hazards Earth Syst. Sci., 12, 3059–3073, doi:10.5194/nhess-12-3059-2012, 2012.

Michoud, C., Abellán, A., Derron, M.-H., and Jaboyedoff, M. (Eds.): SafeLand deliverable 4.1.: Review of Techniques for Landslide Detection, Fast Characterization, Rapid Mapping and Long-Term Monitoring, 2nd Edition, European Project SafeLand, Grant Agreement No. 226479, 401 pp., available at: http://www.safeland-fp7.eu, 2012.

Michoud, C., Derron, M.-H., Jaboyedoff, M., Abellán, A., Bazin, S., and Blikra, L.: On the importance of landslide conceptual models by integrating and coupling different souces of data to set pertinent thresholds and proper EWS, in: Proceedings of the 1st International Workshop on Warning Criteria for Active Slides, Courmayeur, Italy, 10–12 June 2013, 19–20, available at: http://www2.ggl.ulaval.ca/iwwcas/, 2013.

Mileti, D. and Sorensen, J.: Communication of emergency public warnings – A social science perspective and state-of-the-art assessment, Oak Ridge National Laboratory, Tennessee, USA, 166 pp., 1990.

Monserrat, O., Moya, J., Luzi, G., Crosetto, M., Gili, J. A., and Corominas, J.: Non interferometric GBSAR measurement – Application to the Vallcebre Landslide (Eastern Pyrenees, Spain), Nat. Hazards Earth Syst. Sci., submitted, 2013.

Moreno, F. and Froese, C.: ERCB/AGS Roles and Responsibilities Manual for the Turtle Mountain Monitoring Project, Alberta, ERCB/AGS, Open File Report 2009-06, 35 pp., available at: http://www.ags.gov.ab.ca/geohazards/turtle_mountain/, 2009.

Navratil, O., Liébault, F., Bellot, H., Travaglini, E., Theule, J., Chambon, G., and Laigle, D.: High-frequency monitoring of debris-flow propagation along the Réal Torrent, Southern French Prealps, Geomorphology, 201, 157–171, 2013.

Oppikofer, T., Jaboyedoff, M., Blikra, L., Derron, M.-H., and Metzger, R.: Characterization and monitoring of the Åknes rockslide using terrestrial laser scanning, Nat. Hazards Earth Syst. Sci., 9, 1003–1019, doi:10.5194/nhess-9-1003-2009, 2009.

Ostrom, E.: A Behavioral Approach to the Rational Choice Theory of Collective Action: Presidential Address, American Political Science Association, 1997, The American Political Science Review, 92, 1–22, 1998.

Piteau, D. R. and Peckover, F. L.: Engineering of Rock Slope, in: Landslides, Analysis and Control, Transportation Research Board, Special Report 176, edited by: Schuster, R. L. and Krizek, R. J., Washington, DC, 192–228, 1978.

Riegl: available at: http://www.riegl.com/media-events/newsletter/0512-rimonitor-and-rimining/, last access: 11 July 2013.

Roth, M.: Microseismic monitoring at the unstable rock slope at Åknes, Norway, in: SafeLand deliverable 4.1.: Review of Techniques for Landslide Detection, Fast Characterization, Rapid Mapping and Long-Term Monitoring, 2nd Edn., edited by: Michoud, C., Abellán, A., Derron, M.-H., and Jaboyedoff, M., European Project SafeLand, Grant Agreement No. 226479, 313–317, available at: http://www.safeland-fp7.eu, 2012.

Saito, M.: Forecasting time of slope failure by tertiary creep. In: Proceedings of the 7th International Conference on Soil Mechanics and Foundation Engineering, Mexico City, Mexico, 677–683, 1969.

Spillman, T., Maurer, H., Green, G. A., Heincke, B., Willenberg, H., and Husen, S.: Microseismic investigation of an unstable mountain slope in the Swiss Alps, J. Geophys. Res., 112, B07301, doi:10.1029/2006JB004723, 2007.

Stumpf, A., Kerle, N., and Malet, J.-P. (Eds.): SafeLand deliverable 4.4.: Guidelines for the selection of appropriate remote sensing technologies for monitoring different types of landslides, European Project SafeLand, Grant Agreement No. 226479, 91 pp., available at: http://www.safeland-fp7.eu, 2011.

Tarchi, D., Casagli, N., Moretti, S., Leva, D., and Sieber, A. J.: Monitoring landslide displacements by using ground-based synthetic aperture radar interferometry: Application to the Ruinon landslide in the Italian Alps, J. Geophys. Res.-Solid Earth, 108, 2387, doi:10.1029/2002JB002204, 2003.

Terzaghi, K.: Mechanism of Landslides, The Geological Society of America, Engineering Geology (Berkley) Volume, 83–123, 1950.

Tofani, V., Segoni, S., Catani, F., and Casagli, N. (Eds.): SafeLand deliverable 4.5.: Evaluation report on innovative monitoring and remote sensing methods and future technology, European Project SafeLand, Grant Agreement No. 226479, 280 pp., available at: http://www.safeland-fp7.eu, 2012.

Tofani, V., Segoni, S., Agostini, A., Catani, F., and Casagli, N.: Technical Note: Use of remote sensing for landslide studies in Europe, Nat. Hazards Earth Syst. Sci., 13, 299–309, doi:10.5194/nhess-13-299-2013, 2013.

Travelletti, J. and Malet, J.-P.: Characterization of the 3D geometry of flow-like landslides: A methodology based on the integration of heterogeneous multi-source data, Eng. Geol., 128, 30–48, 2012.

Troisi, C. and Negro, N.: Managing of EW systems by public agencies: related problems, in: Proceedings of the 1st International Workshop on Warning Criteria for Active Slides, Courmayeur, Italy, 10–12 June 2013, 43–45, available at: http://www2.ggl.ulaval.ca/iwwcas/, 2013.

Turner, A. and Schuster, R. (Eds.): Landslides, Investigations and Mitigations, Transportation Research Board, Special Report 247, Washington, DC, 685 pp., 1996.

UN-ISDR: Terminology on Disaster Risk Reduction, United Nation International Strategy for Disaster Reduction, Geneva, Switzerland, 35 pp., 2009.

Vaciago, G., Rocchi, G., Riba, I., Davì, M., Bianchini, A., Callerio, A., and Costi, M. (Eds.): SafeLand deliverable 5.1.: Compendium of tested and innovative structural, non-structural and risk-transfer mitigation measures for different landslide types, European Project SafeLand, Grant Agreement No. 226479, 340 pp., available at: http://www.safeland-fp7.eu, 2011.

Wyllie, D. C. and Mah, C. W.: Rock Slope Engineering, Civil and Mining, 4th Edn., Taylor & Francis, London and New-York, 2004.

5. Hydroacoustique

A l'échelle mondiale, les réseaux sismologiques terrestres permettent une étude en temps réel de tous les séismes dont la magnitude est suffisante pour générer des ondes clairement analysables. Cette magnitude seuil est de l'ordre de 5.5-6. Cette couverture trouve ses limites lorsqu'on s'intéresse aux détails du processus de rupture. Les années 1990 puis 2000 ont vu l'augmentation du nombre de stations large-bande mondiales. Aujourd'hui, même si la distribution reste hétérogène sur les continents, la limite principale reste la quasi-absence de sismomètres sous-marins. La surveillance hydroacoustique est une façon de palier à cette absence.

L' hydroacoustique consiste à appliquer à la sismologie une méthode qui a initialement été développée pour la surveillance d'essais nucléaires et la localisation de sous-marins : l'enregistrement acoustique par des hydrophones immergés dans le canal SOFAR (Sound Fixing and Ranging). Les ondes T sont des signaux hydroacoustiques qui peuvent être générés par des éruptions volcaniques, des tremblements de terre, des vocalisations de mammifères marins, des fractures d'icebergs, etc. La propagation des ondes T dans l'océan a lieu grâce à un guide d'onde naturel, le canal SOFAR, qui est situé à 500-1000m de profondeur aux latitudes moyennes. Grâce à l'efficacité de cette canalisation, les ondes hydroacoustiques se propagent sur des milliers de kilomètres et la faible atténuation dans l'eau rend possible l'enregistrement d'événements sismiques de faible magnitude (Figure 12). En effet, la surveillance sismologique de la dorsale Médio-Atlantique à l'aide d'un réseau de 6 hydrophones autonomes du PMEL (Pacific Marine Environment Laboratory, NOAA) a montré que le réseau d'hydrophones a permis de descendre le seuil de détection à Mb = 2,5. Ainsi, un réseau hydroacoustique permet de localiser en un an autant de séismes que le réseau sismologique mondial en 50 ans.

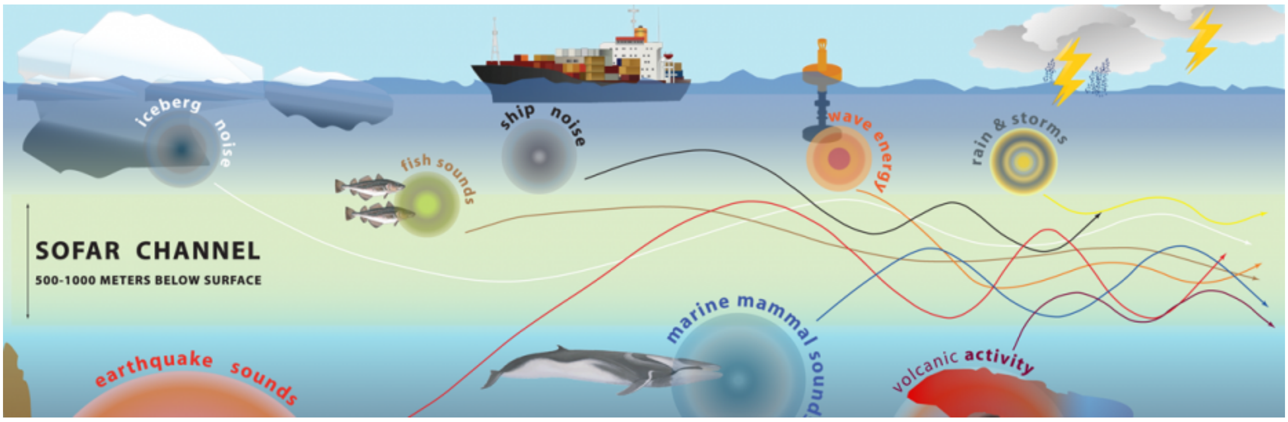

Figure 12: Illustration montrant la diversité des sources acoustiques dont les ondes sont piégées dans le canal SOFAR et qui peuvent être enregistrées par des hydrophones mouillés à la profondeur du canal (Figure 10). Source www. noaa.gouv.

5.1 Mes travaux antérieurs sur la dorsale médio-Atlantique

Mes premiers travaux en poste à l'IPGP ont été le développement un prototype d'hydrophone SOFAR grâce à un financement Bonus Qualité Recherche en 2001-2002 avec Laurent Béguery (Figure 13 centre). Ce dernier a été déployé sur le site de MOMAR.

Figure 13: : Gauche: schéma simplifié d'un hydrophone autonome déployé dans le canal SOFAR (dessin modifié de Fox et al., 2001). Centre: Prototype que j'ai développé avec L. Béguery dans le laboratoire de St Maur de l'IPGP. Droite: mission océanographique SIRENA (2002) avec les concepteurs de la méthode: Chris Fox et Haru Matsumoto.

Je me suis par ailleurs formée à l'interprétation des données hydroacoustiques avec Deborah Smith (Woods Hole Oceanographic Institute) lors de son séjour à l'IPGP. Cette coopération a donné lieu à une publication en commun (Smith et al., 2003).

J'ai aussi participé au déploiement de 6 hydrophones au nord des Açores (campagnes SIRENA en 2002 et 2003, chef de mission Jean Goslin, Figure 13 droite) pour compléter le réseau du PMEL déjà installé au sud. Cette collaboration a permis la publication de plusieurs articles en commun, dont le premier significatif est présenté ici. Ce réseau est resté en fonctionnement jusqu'en 2020 (réseau HYDROMOMAR, responsable : Julie Perrot).

Geochemistry Geophysics Geosystems G³

Published by AGU and the Geochemical Society

Article
Volume 13, Number 2
24 February 2012
Q02010, doi:10.1029/2011GC003828
ISSN: 1525-2027

Spatiotemporal distribution of the seismicity along the Mid-Atlantic Ridge north of the Azores from hydroacoustic data: Insights into seismogenic processes in a ridge–hot spot context

J. Goslin, J. Perrot, J.-Y. Royer, and C. Martin
Domaines Océaniques, UMR 6538, Université Européenne de Bretagne, Université de Brest, CNRS, IUEM, Place N. Copernic, F-29280 Plouzané, France

N. Lourenço
Estrutura de Missão para a Extensão da Plataforma Continental, 2770-057 Paço de Arcos, Portugal

J. Luis
Centro de Investigação Marinha e Ambiental, Universidade do Algarve, Campus de Gambelas, 8005-139 Faro, Portugal

R. P. Dziak, H. Matsumoto, J. Haxel, and M. J. Fowler
Pacific Marine Environmental Laboratory, Hatfield Marine Science Center, Oregon State University, NOAA, Newport, Oregon 97365, USA

C. G. Fox
NGDC, NESDIS, NOAA, Boulder, Colorado 80303, USA

A. T.-K. Lau
Pacific Marine Environmental Laboratory, Hatfield Marine Science Center, Oregon State University, NOAA, Newport, Oregon 97365, USA

S. Bazin
Institut de Physique du Globe de Paris, Paris, France

Now at Norwegian Geotechnical Institute, Sognsveien 72, N-0855 Oslo, Norway

[1] The seismicity of the North Atlantic was monitored from May 2002 to September 2003 by the 'SIRENA array' of autonomous hydrophones. The hydroacoustic signals provide a unique data set documenting numerous low-magnitude earthquakes along the section of the Mid-Atlantic Ridge (MAR) located in a ridge-hot spot interaction context. During the experiment, 1696 events were detected along the MAR axis between 40°N and 51°N, with a magnitude of completeness level of $m_b \approx 2.4$. Inside the array, location errors are in the order of 2 km, and errors in the origin time are less than 1 s. From this catalog, 15 clusters were detected. The distribution of source level (SL) versus time within each cluster is used to discriminate clusters occurring in a tectonic context from those attributed to non-tectonic (i.e. volcanic or hydrothermal) processes. The location of tectonic and non-tectonic sequences correlates well with regions with positive and negative Mantle Bouguer Anomalies (MBAs), indicating the presence of thinner/colder and thicker/warmer crust respectively. At the scale of the entire array, both the complete and declustered catalogs derived from the hydroacoustic signals show an increase of the seismicity rate from the Azores up to

43°30′N suggesting a diminishing influence of the Azores hot spot on the ridge-axis temperature, and well correlated with a similar increase in the along-axis MBAs. The comparison of the MAR seismicity with the Residual MBA (RMBA) at different scales leads us to think that the low-magnitude seismicity rates are directly related to along-axis variations in lithosphere rheology and temperatures.

Components: 9300 words, 10 figures, 2 tables.

Keywords: Azores hot spot–ridge interaction; autonomous hydrophone; seismicity; spreading center.

Index Terms: 7230 Seismology: Seismicity and tectonics (1207, 1217, 1240, 1242); 8416 Volcanology: Mid-oceanic ridge processes (1032, 3614); 9325 Geographic Location: Atlantic Ocean.

Received 4 August 2011; **Revised** 20 January 2012; **Accepted** 20 January 2012; **Published** 24 February 2012.

Goslin, J., et al. (2012), Spatiotemporal distribution of the seismicity along the Mid-Atlantic Ridge north of the Azores from hydroacoustic data: Insights into seismogenic processes in a ridge–hot spot context, *Geochem. Geophys. Geosyst.*, *13*, Q02010, doi:10.1029/2011GC003828.

1. Introduction

[2] Studies of active accretion processes at the axes of slow spreading mid-ocean ridges, either based on field studies [*Lin et al.*, 1990; *Gente et al.*, 1995; *Thibaud et al.*, 1998] or on analog or numerical modeling [*Gac et al.*, 2003, 2006] have promoted the now well-accepted image that seafloor spreading results from a succession, in space and time, of magmatic and tectonic episodes. In such models, most of the heat output focuses near the centers of ridge segments, resulting from the emplacement of greater amounts of new basaltic crust [*Bell and Buck*, 1992; *Cannat*, 1993; *Gente et al.*, 1995; *Magde et al.*, 1997]. In contrast, seafloor spreading at relatively colder segment-ends is mostly accounted for by tectonic processes, resulting in the emplacement of a thinner crust with a thicker brittle upper layer [*Lin et al.*, 1990; *Bell and Buck*, 1992; *Cannat*, 1993; *Gac et al.*, 2003, 2006]. Such variations in crustal and lithospheric thermal state at the segment scale directly influence the rheology of the crust and lithosphere. Moreover, these along-axis variations in the rheology should be reflected by the along-axis spatiotemporal distributions of the seismicity; testing this intuitive idea requires access to low-level (background) seismicity recorded over large sections of mid-ocean ridges.

[3] Here we report the results of a hydroacoustic experiment carried out over a >1000 km-long section of the north Mid-Atlantic Ridge. There are several previous examples of experiments where arrays of autonomous underwater hydrophones (AUH) were deployed for a year on the flanks of mid-oceanic ridges were able to capture the low-level seismicity associated with seafloor spreading processes [e.g., *Dziak et al.*, 1995; *Fox et al.*, 2001; *Dziak*, 2001; *Smith et al.*, 2002; *Goslin et al.*, 2005]. Earthquakes occurring at mid-ocean ridge axes generate both seismic phases that will travel within the lithosphere and a hydroacoustic phase which will propagate in the water column and through the SOund Fixing And Ranging (SOFAR) channel, over long distances (>1000 km) with very little attenuation [*Fox et al.*, 1994]. This waterborne phase results from the conversion of seismic to acoustic waves at the crust/water interface on the seafloor [*Talandier and Okal*, 1998; *Okal*, 2008; *Balanche et al.*, 2009]. The SOFAR channel is a low-velocity layer in the water column, typically located at depths from 700 to 1000 m at midlatitudes in the North Atlantic Ocean, and thus acts as a waveguide trapping acoustic signals. The acoustic phase is referred to as the Tertiary (or T-) phase, since it has a lower velocity (~1.5 km/s) than crustal seismic phases and thus arrives third on-land seismic stations, after the P- and S-waves (compressional and shear waves, respectively) [*Leet et al.*, 1951; *Johnson et al.*, 1963]. For the vast majority of small-magnitude events, only the T-phase is recorded by hydrophone arrays [*Dziak et al.*, 2004a]. In some cases, for an event with its epicenter close enough to an autonomous hydrophone (typically less than 150/200 km), all the P-, S- and T-phases can be recorded by the instrument. This occurs when the seismic phases traveling through the crust reach the vicinity of the instrument where they are locally converted to acoustic signals.

[4] This paper presents data from, and our analysis of, the north Atlantic hydrophone experiment (called SIRENA which means stands for Seismic Investigation by REcording of Acoustic Waves in

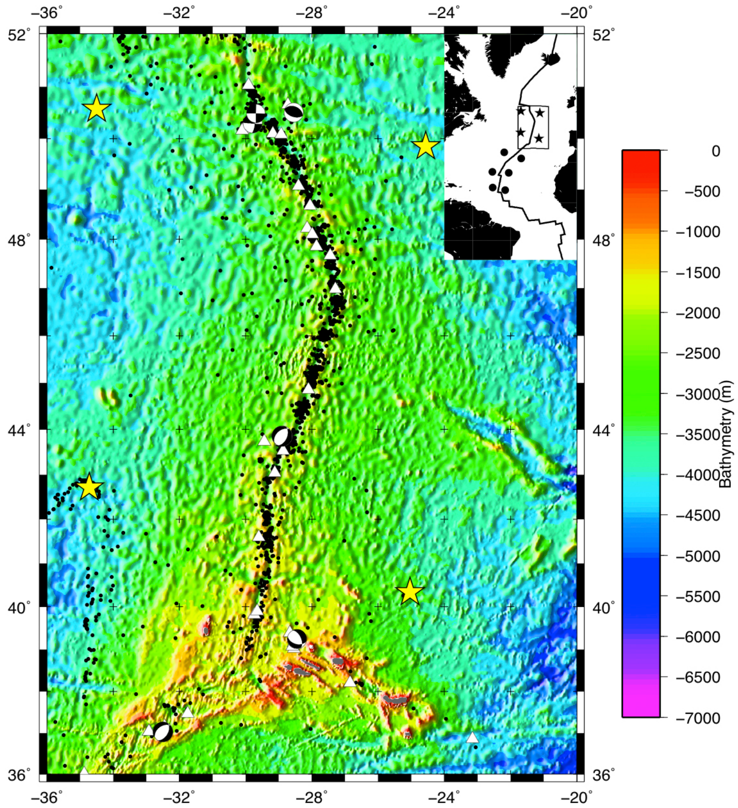

Figure 1. Acoustic events located from June 1, 2002 to September 30, 2003 during the SIRENA experiment. Yellow stars show the positions of the 4 hydrophones used to locate the earthquakes represented by the black dots. White open triangles are the epicenters of the few large magnitude earthquakes listed in the NEIC catalog for the same period. Beach balls are from the Global Centroid Moment Tensor (GCMT) solutions catalog. The inset shows the location of the hydrophones of the SIRENA array (stars) and of the NOAA/PMEL South Azores array (circles).

the North Atlantic). We discuss the spatiotemporal distribution of the seismicity recorded by the SIRENA array along the MAR between 40°20′N and 50°30′N, how these distributions may be related to the large scale influence of the Azores hot spot and how segment scale clusters of events may provide information on seafloor spreading processes.

2. The SIRENA Experiment

[5] SIRENA was a France-USA-Portugal cooperative experiment specifically aimed at studying the seismicity of the MAR north of the Azores [*Goslin*, 2004]. To take full advantage of the SOFAR channel propagation properties and to avoid acoustic shadowing by the Azores Plateau, the autonomous hydrophones were moored north of the Plateau, and on either side of the northern Mid-Atlantic Ridge between 40°20′N and 50°30′N (Figure 1). The array was deployed by *R/V Le Suroit* during a cruise from Ponta Delgada (Azores) to Brest 17 May to 3 June 2002 and was recovered by the *RRS Discovery* during a cruise from Govan (Scotland) to Ponta Delgada 12 September to 1 October 2003 [*Goslin*, 2004].

[6] Initially, the SIRENA array was comprised of six instruments, but one hydrophone stopped recording after a week and another was not recovered. Our catalog of events is thus mainly derived from the 4 hydrophones of the SIRENA array, with the addition of two hydrophones deployed by NOAA/PMEL south of the Azores from early 1999 to mid 2005 [*Smith et al.*, 2002] (Figure 1). The seismic events were detected and located with analysis software developed in-house by personnel at the U.S. NOAA/Pacific Marine Environmental Laboratory. The earthquake locations are derived by using the arrival times of the energy maxima of the acoustic signals recorded by at least three of the four instruments. The location software uses a non-linear regression algorithm to derive an event's

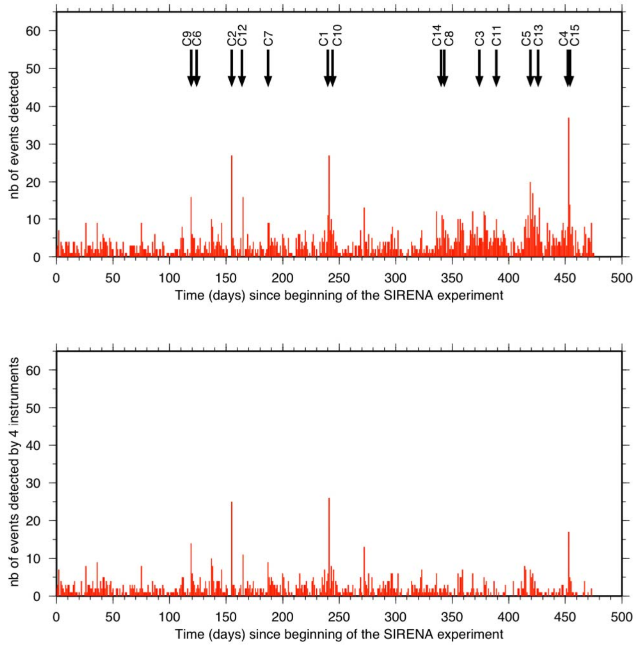

Figure 2. Number of events located inside the SIRENA array as a function of time since the completion of the deployment (i.e. when all the SIRENA array instruments started recording acoustic signals). (top) Daily seismicity rates from the catalog. The vertical arrows show the date of the clusters listed in Table 1. (bottom) Daily seismicity rates derived from the sub-catalog limited to the events detected and localized by four instruments.

latitude, longitude and origin time, where the error in locations is provided by the output of the co-variance matrix [*Fox et al.*, 2001]. The "epicenter" derived in this manner is the point at which the acoustic waves enter the sound channel after they have been converted from seismic waves at the seafloor-ocean interface. Moreover, because our hydroacoustic location technique utilizes oceanographic sound velocity models, which are well known and adjusted for seasonal variations, and our array geometry provides good azimuthal coverage of the MAR, the magnitude of completeness for hydroacoustic arrays is expected to be an order of magnitude lower than what can be achieved using regional or teleseismic earthquake monitoring. In remote areas from land-based network, the locations of earthquakes recorded by four or more hydrophones are generally more accurate than land-based derived locations [*Bohnenstiehl and Tolstoy*, 2003; *Pan and Dziewonski*, 2005]; added to a lower detection threshold, hydrophone arrays are thus fully suitable for detailed studies of the low-level seismicity.

[7] The SIRENA catalog lists almost 6000 events, nearly 1700 of which occurred inside the array during its 16 month deployment (1 June 2002 to 19 September 2003). It should be noted that, for the same area and time period, only 19 earthquakes are listed in the National Earthquake Information Center (NEIC) catalog. The SIRENA array thus increases by more than 70-fold the detection and localization of MAR earthquakes north of the Azores. Between 1 June 2002 and 2 May 2003, we also incorporated the northernmost hydrophones deployed by NOAA/PMEL south of the Azores. These two hydrophones south of the Azores were used only in a complementary role to derive the SIRENA earthquake catalog, with nearly all of the events being located using three or more SIRENA array hydrophones.

[8] The long-term temporal distribution of events, as derived from the SIRENA catalog are shown in Figure 2. The top histogram shows that the mean seismicity rate derived from the catalog remained fairly constant throughout the duration of the SIRENA experiment until day ~340, after which the seismicity rate increases from 2.8 to 5.2 events/day. This increase in earthquake rate may be due to increased crustal stress that occurred from 7 May through August 2003 with the occurrence of four $M_w > 5.0$ earthquakes (Table 1). As noted above, the SIRENA catalog was obtained by simultaneously processing the data from the

Table 1. Clusters Detected Inside the SIRENA Array With the Coordinates of the Main Shock, Its Date, Time, and SL, the Numbers of Events and Duration in Days[a]

Cluster	Lat (deg)	Lon (deg)	Date	Time	SL (dB)	Number	Duration (days)	Type	Axis Location/ Segment	Comments
C1	41.568	−29.435	2003-01-27	15:32:47.1	216	25	5	Sw	on/c	m_b = 4.7(NEIC)
C2	41.745	−29.277	2002-11-03	08:38:31.5	217	24	19	Sw	on/c	
C3	43.333	−29.569	2003-06-10	20:13:30.0	215	20	10	Sw	off	
C4	43.797	−28.645	2003-08-27	14:40:35.4	237	38	20	Ma	on/e	M_w = 5.4(GCMT), m_b = 4.1(NEIC), studied by *Simão et al.* [2010]
C5	44.349	−28.465	2003-07-25	03:46:55.9	215	15	40	Sw	on/c	
C6	44.369	−28.119	2002-10-03	06:22:10.3	218	20	37	Sw	on/c	
C7	44.954	−28.006	2002-12-05	01:43:04.0	220	15	32	Sw	on/c	
C8	46.112	−27.577	2003-05-10	15:12:16.5	216	15	16	Sw	on/?	
C9	47.894	−27.776	2002-09-28	05:09:45.3	238	48	35	fMa	on/?	m_b = 4.6(NEIC)
C10	48.656	−28.195	2003-01-31	16:15:25.7	221	28	36	Sw	on/?	
C11	49.987	−28.984	2003-06-25	06:24:29.8	216	15	36	Nc	on/?	
C12	50.013	−28.972	2002-11-12	21:52:54.7	220	20	40	Sw	on/?	m_b = 4.2(NEIC)
C13	50.263	−29.085	2003-08-01	09:22:58.5	215	17	35	Sw	on/?	
C14	50.232	−29.996	2003-05-07	13:10:21.0	242	27	36	Ma	off	M_w = 5.1(GCMT), M_w = 5.0(GCMT)
C15	50.489	−28.648	2003-08-29	07:07:17.5	234	16	2	Ma	off	M_w = 5.2(GCMT), m_b = 4.4(NEIC)

[a] Following *Mogi* [1963] and *Sykes* [1970] classification, clusters are sorted in 3-types: Sw for swarm, Ma for main shock-aftershock sequence, fMa for foreshock-main shock-aftershock sequence, and Nc for unclassified type. Cluster location are denoted *off* for an off-axis location and *on* for an on-axis location. In the latter case, the location of the cluster in the segment is noted *c* for a center location, *e* for an end-segment location and ? for an undetermined location. The M_w magnitude from the GCMT catalog, or if not available, the m_b from the NEIC catalog are given.

SIRENA and the South Azores arrays. The recovery of the southern array in March 2003 explains the decrease in the rate of events (from 2.4 to 1.6 events/day) after day 334.

3. Methods

[9] A total of 1696 earthquakes were located within the SIRENA array during 16 months recording period; 1013 events were located using 4 hydrophones or more. We estimated the magnitude of completeness of our event catalog and derived location errors for all events. These values were then used in our review of the space-time distribution of the seismicity and as the basis for our earthquake cluster analysis.

3.1. Source Level and Magnitude of Completeness

[10] Our estimate of the source Level of completeness (SL_c) for the SIRENA catalog was limited to the events located inside the array and is needed to assess the earthquake cluster search. The SL_c is the minimum value of the source level at which the logarithm of cumulative number of events having a given SL departs from a linear relationship. The SL_c is similar to the magnitude of completeness M_c computed from fitting the Gutenberg-Richter law to a seismically derived earthquake catalog:

$$\log(N) = a_t + b_t \, \mathrm{SL},$$

where N is the number of events having a size equal to or greater than SL, a_t is a constant dependent on the total number of events and b_t is representative of the frequency-size distribution [*Bohnenstiehl et al.*, 2002].

[11] SL_c's were computed from the catalog for the MAR events within two-degree boxes of latitude between 40°30′N and 50°30′N. These SL_c's range from 206 dB to 210 dB, with a mean of 207.8 dB. The narrow range of SL_c's allows us to rule out possible detection biases of the SIRENA array which could be due to the presence of shallow bathymetry along the propagation path between the earthquake source and hydrophones. Relationships between source levels and magnitudes are difficult to assess. Only empirical relations have yet been proposed [*Dziak et al.*, 2004a], based on simultaneous observation of large earthquakes by land-stations and hydrophone arrays. The magnitude of completeness M_c of the hydrophone array can then

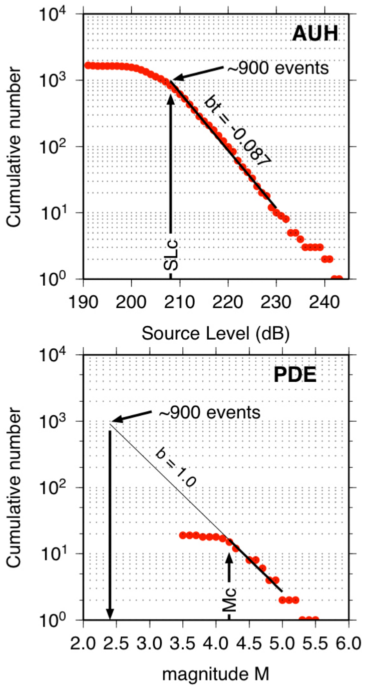

Figure 3. (top) Logarithm of the cumulative number of events from the SIRENA AUH catalog plotted versus Source Level (SL). The Source Level of completeness SL_c is defined as the minimum SL where the distribution of the cumulative number of events departs from the linear Gutenberg-Richter law (shown as a black line). SL_c equals ~208 dB and corresponds to ~900 events. Least squares regression estimate of the slope of the data (b_t) is 0.087 between 208 and 230 dB. Data with SL > 230 dB are excluded due to the clipping of the hydrophone sensors. (bottom) Logarithm of the cumulative number of events from the National Earthquake Information Center's (NEIC) Preliminary Determination of Epicenters (PDE) catalog detected within the SIRENA array during the SIRENA deployment plotted versus their m_b magnitude. The magnitude of completeness (M_c) is the minimum magnitude where the distribution of the cumulative number of events departs from the linear Gutenberg-Richter law (shown as a black line); M_c is equal to 4.2. A b-value of 1.0 is obtained by least squares regression of data. Extrapolating the linear trend of the Gutenberg-Richter law toward smaller magnitudes, yields a M_c ~2.4 corresponding to the ~900 events, number of events detected at the SL_c. It means that the threshold detection of the SIRENA array is in the order of m_b ~2.4.

be evaluated as follows. First the source level of completeness for the SIRENA array is derived from Figure 3 and equals ~208 dB and corresponds to ~900 events detected within the array during its deployment. Second, the linear fit between the cumulative number of events and their magnitude is extrapolated toward smaller magnitudes (Figure 3, bottom). This line intersects the 900-event horizontal line close to a magnitude m_b value of 2.4, which we consider to be the magnitude of completeness M_c or essentially the detection threshold of the SIRENA array.

3.2. Location Error Distribution

[12] To interpret a distribution of seismic events with respect to accurately mapped bathymetric features or faults, their uncertainties in time and in location need to be assessed. These errors can be computed only using four or more hydrophones. Histograms in Figure 4 show that 90% of the events inside the array have an error in origin time lower than 1 second and latitudinal and longitudinal errors less than ~2 km. These results confirm that the hydroacoustic technique can be successfully used for detailed seismicity studies of mid-oceanic ridges.

3.3. Earthquake Cluster Identification

[13] Cluster analyses provide many useful insights on processes occurring along mid-oceanic ridges, for instance to distinguish tectonic events with main shock-aftershock sequence from non-tectonic, possibly magmatic, sequences [e.g., *Bohnenstiehl et al.*, 2002; *Simão et al.*, 2010].

[14] In order to delineate clusters, we adapted the program "cluster" included in the seismic analysis SEISAN package [*Haskov and Ottemoller*, 2008] to the acoustic magnitude or SL. A minimum SL of 215 dB was chosen as the minimum value of possible main shocks. The cluster was then defined as including all events that occurred within 40 days after and 1 day before these main shocks and located within a radius of 30 km from the main shock. Thirty kilometers was chosen because it corresponds to the maximum fault length expected in a slow-rate spreading ridge environment [*Bohnenstiehl and Kleinrock*, 2000]. The time window of forty days after the main shock corresponds to the greater time window observed in previous studies on the MAR [*Bohnenstiehl et al.*, 2002; *Simão et al.*, 2010]. Our analysis is limited to the clusters having 15 events. Fifteen clusters were thus detected along the MAR between 40°N and 51°N during the SIRENA deployment (Table 1), with the maximum number of earthquakes in a swarm being 48 events. Among the 19 earthquakes listed by the NEIC catalog during the SIRENA experiment,

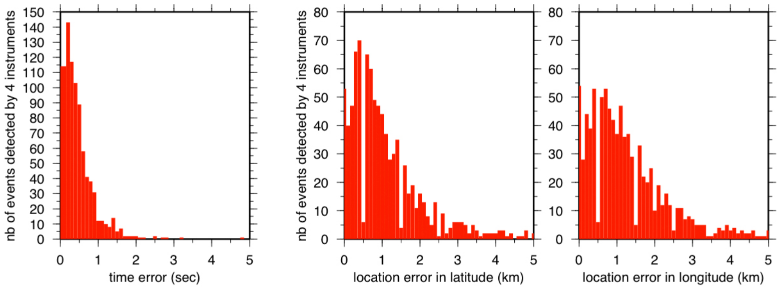

Figure 4. Histograms (left) of time errors in origin time and of location errors in (middle) latitude and (right) longitude of the events located within the SIRENA array. Errors are computed only for the events detected by the four instruments.

we detected 9 clusters associated with these large earthquakes. The 10 remaining events from the NEIC catalog are isolated in time and space in the SIRENA catalog and therefore do not appear as being part of a sequence.

3.4. Temporal Distribution of the Clusters and Modified Omori Law

[15] The patterns of earthquake clusters were classified into the following three types [*Mogi*, 1963]; (1) A large earthquake followed by aftershocks, (2) large earthquakes preceded by foreshocks and

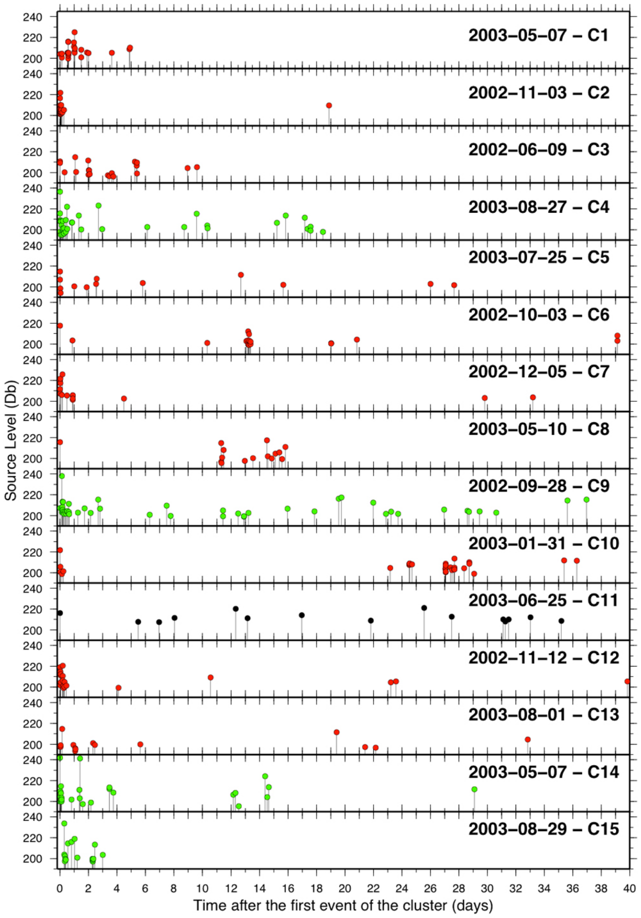

Figure 5. Source level versus time relative to the main shock for clusters including 15 or more events. The color of circles reflects the processes which generated the clusters: green for a main shock-aftershock or fore-main-aftershock sequence, red for swarms and black for an unclassified cluster following *Mogi* [1963] and *Sykes* [1970].

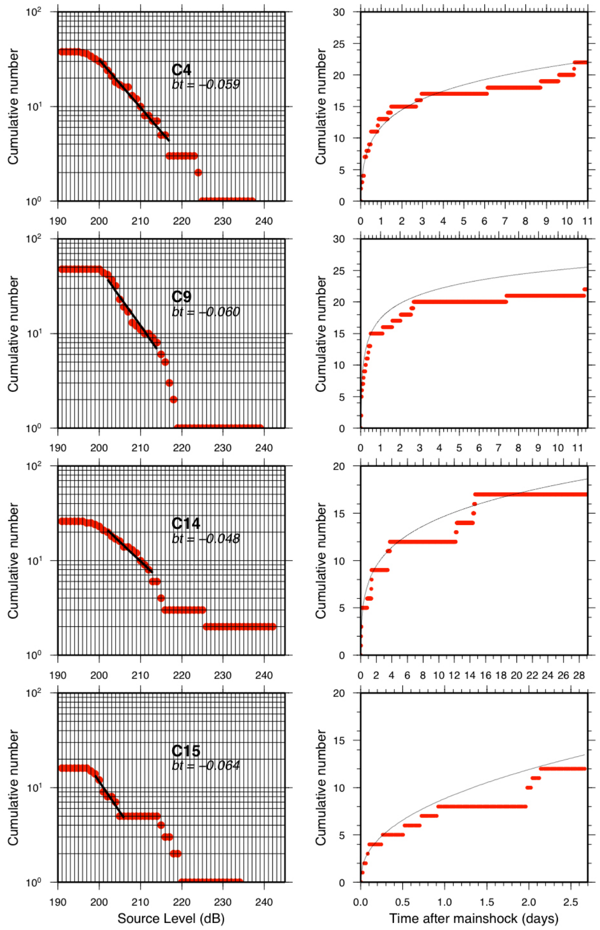

Figure 6. (left) Cumulative-number of events above a given source level (SL) versus the source level and (right) the cumulative number of events versus time after the main shock, for sequences *C*4, *C*9, *C*14 and *C*15. An SL_c value of 202 dB is obtained for *C*9 and *C*14, a value of 200 dB for *C*4 and a value of 199 dB for *C*15. The b_t value is indicated on each plot. Events with a SL ≤ 199, 200 or 202 dB and a $SL_c > 230$ dB were excluded from the MOL fitting and parameter computations. The solid line in Figure 6 (right) is the predicted cumulative distribution for the maximum likelihood estimates of the MOL parameters reported in Table 2. Red lines and circles are the data.

followed by aftershocks and (3) earthquake swarms with events of roughly equivalent magnitude but do not show a dominant earthquake. The type (1) and (2) clusters were attributed to slip on transform faults, and are likely of tectonic origin. In an analysis of magnitude versus time distribution of large earthquakes along the East Pacific Rise (EPR) and the MAR, *Sykes* [1970] interpreted the type (3) swarm as precursors of volcanic eruptions or as seismic activity related to magmatic processes that did not reach the surface and for which fault activation is a response to magma emplacement into the shallow crust. This cluster classification proved very useful for further analyses of Ocean Bottom Seismometer data [*Tolstoy et al.*, 2001] or hydrophone array data [*Bohnenstiehl et al.*, 2002; *Dziak et al.*, 2004b, 2009; *Simão et al.*, 2010].

[16] We next analyzed the SL variation with time distribution of each cluster (Figure 5). Among the fifteen identified clusters, three fit a typical a main shock-aftershock distribution, one fit a foreshock-main shock-aftershock style of sequence, ten clusters reflect a swarm type and one cluster could not be classified (Table 1). All the identified sequences include a dominant earthquake (SL>=230 dB) with a more or less rapid SL decrease in time. The events of the swarm sequences are concentrated over a short period (less than 10 days) with similar moderate to low SLs (all below 230 dB) and without a dominant SL. Last, the only cluster that does not fit into our classification shows constant activity during the 40 day time window with no single large event.

[17] A validation of the main shock-aftershock sequence can be performed by matching the cumulative number of events versus time and fitting a Modified Omori Law (MOL) [*Ogata*, 1983; *Utsu*, 1995]. Events following such a main shock-aftershock distribution generally occur in a tectonic context. Events are considered as aftershocks if the frequency per unit time $n(t)$ follow a MOL within a time interval $[S, T]$:

$$n(t) = K(c + t)^{-p},$$

where K, c and p are empirically derived constants, T is the duration of the sequence and $T\text{min} = 0$ corresponds to the time of the main shock. These parameters are estimated using the method of maximum likelihood carried out within the software package SAseis using a Fletcher-Powell optimization procedure [*Utsu and Ogata*, 1997]. To evaluate the goodness-of-fit, we compute the Anderson-Darling statistic (A^2). The values of A^2 less than 1 indicate that a sequence's distribution of aftershocks with time can be adequately fitted by a MOL. It may be difficult to identify the aftershock in the main shock coda and because of their complicated nature in the initial stage. To avoid this bias, Tmin is found to best fit to the data in the [Tmin, Tmax] time interval. A SL_c is determined for each individual sequence and aftershocks with SL <= SL_c are removed before calculating the MOL parameters [*Bohnenstiehl et al.*, 2002].

Table 2. Properties of Aftershock Sequences[a]

Sequence	[Tmin, Tmax]	N	p	c (days)	K	AIC	A^2
C4	[0.002, 17.6]	28	0.74 (0.10)	0.000 (0.005)	3.80 (0.76)	−16	1.50
	[0.002, 11.0]	22	0.89 (0.21)	0.024 (0.050)	3.82 (1.08)	−20	0.61
	[0.002, 3.0]	17	0.91 (0.39)	0.035 (0.085)	4.19 (1.33)	−38	0.30
C9	[0.005, 36.9]	39	0.75 (0.09)	0.000 (0.019)	4.46 (0.90)	5	1.90
	[0.005, 11.5]	24	1.05 (0.18)	0.013 (0.025)	3.57 (0.90)	−55	0.42
	[0.005, 3.0]	17	0.91 (0.39)	0.001 (0.010)	4.35 (1.28)	−70	0.31
C14	[0.007, 29.1]	19	0.82 (0.16)	0.008 (0.039)	2.39 (0.76)	13	0.69
	[0.007, 1.39]	9	0.86 (0.60)	0.012 (0.071)	2.36 (1.47)	−23	2.10
	[1.39, 29.1]	10	0.73 (1.00)	0.000 (7.013)	1.94 (5.81)	42	1.34
C15	[0.002, 2.7]	13	0.57 (0.22)	0.000 (0.012)	3.80 (1.23)	−17	0.93

[a] The time interval [Tmin, Tmax] in days is relative to the main shock during which the data are modeled. N is the number of aftershocks within this interval used in determining p, c and K. A^2 is the Anderson-Darling statistic. The sequences with $A^2 \approx 1$ are well fit by the MOL model.

[18] Special attention was given to four sequences with a high SL value for the main shock: *C*4, *C*9, *C*14 and *C*15 (fMa or Ma type in Table 1). The SLc is estimated to be 202 dB for C9 and C14 sequences, 200 dB, for C4 sequence and 199 dB for C15 (Figure 6). Calculations for each sequence over the whole time interval yields A^2 values that fit the MOL for *C*14 and *C*15. A good fit of the MOL for the *C*4 and *C*9 sequences is obtained at shorter time intervals (Table 2 and Figure 6). For these two sequences, we search for the largest time interval with A^2 values below 1 and the MOL parameters for the best A^2 value (Table 2). The C14 sequence shows a second high SL event after the first main shock (Figure 6), with both the main shock and first large aftershock listed in the Global Centroid Moment Tensor (GCMT) catalog with equivalent M_w. We attempted to fit individually a MOL for these two main shocks, but the high values of A^2 (Table 2) suggest that these sequences do not follow a MOL.

4. North Azores Seismicity

[19] We present in this section the seismicity observed inside the array from 40° to 52°N and 25° to 33°W at the large-scale to investigate the thermal state of the lithosphere and at segment-scale to analyze spreading center processes. We propose that the along-ridge seismicity distribution has a combined origin of (1) a large-scale trend reflecting large-scale variations of the thermal state of the MAR axis resulting from a variable along-ridge influence of the Azores hot spot [e.g., *Goslin et al.*, 1998]; (2) short-scale variations due to more local seismogenic processes which are considered to be mainly dependent on intrasegment variations of the thermal state of the ridge axis, such as those observed by *Kuo and Forsyth* [1988], *Lin et al.* [1990] and *Thibaud et al.* [1998] and also modeled by *Gac et al.* [2003].

4.1. Large-Scale MAR's Seismicity Distribution

[20] Figure 7 shows all earthquakes from the SIRENA catalog between 40°N and 51°N superimposed on a bathymetric map. Scattered seismicity is observed between latitudes 40°N and 43°30′N. Conversely, north of 43°30′N, the events are generally more tightly grouped although not necessarily constituting clusters. In order to distinguish between the large-scale trend of the seismicity and seafloor spreading processes generating seismic clusters, the SIRENA catalog was declustered, meaning we removed events belonging to the 15 clusters from the catalog. Figure 8 displays the latitudinal distribution of the seismicity rate, derived from the total and from the declustered SIRENA catalogs.

[21] The declustered seismicity rate versus latitude, summed for the total duration of the SIRENA experiment, shows two characteristic trends: (1) the seismicity rate increases with latitude, that is with increasing distance away from the Azores hot spot. Such a trend is consistent with the existence of an along-ridge hot spot influence on the MAR upper mantle and crustal regime, and (2) in addition to this first-order trend, the seismicity rate shows a distinctive step near 43°N, increasing drastically from an average of ∼76 events, from 40°30′N to 43°N, to an average of 142 (or almost double) from 43°N to 50°N (Figure 8). This evidence would set the northernmost limit of the along-ridge influence of the Azores hot spot in the relay zone located near 43°30′N, as initially proposed by *Goslin et al.* [1998] from an interpretation of the along-ridge distribution of upper mantle velocities and Sr isotope data. Analyzing the declustered catalog is further warranted by the strongly variable contribution

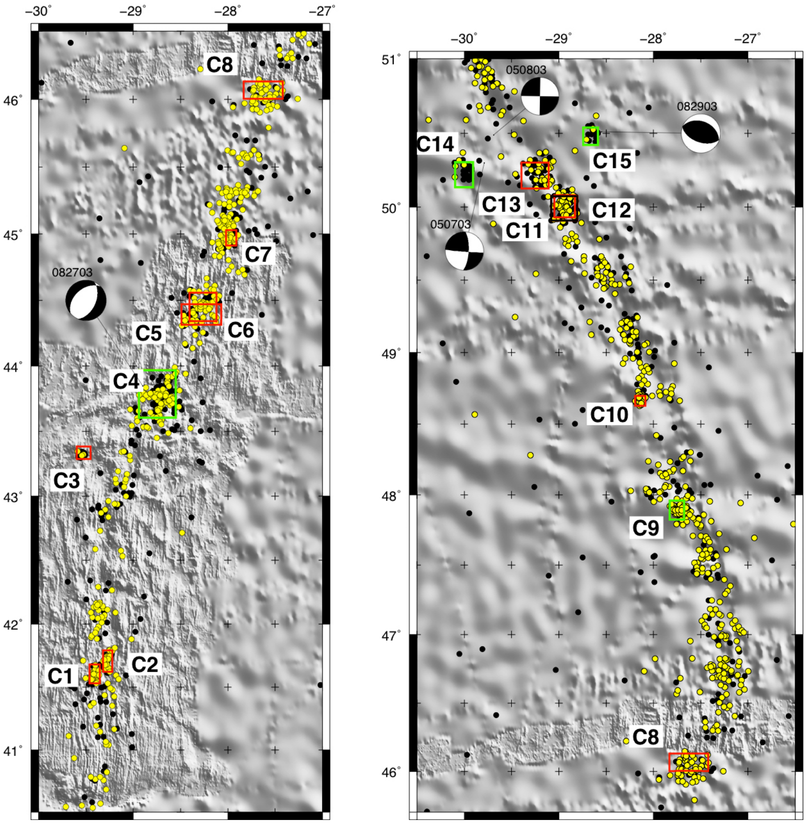

Figure 7. Composite bathymetric map combining the ETOPO1 grid and the high-resolution TRIATNORD multibeam bathymetric grid [*Goslin et al.*, 1999] between 40° and 45°N. Circles show earthquakes located with 4 or more hydrophones (yellow) and with 3 hydrophones (black). All the identified cluster (Table 1) are indexed from South (C1) to North (C15). Available focal mechanism solutions from the GCMT catalog are also shown. The boxes encompass the events of each cluster, their color are relative to their cluster classification (Figure 5 and Table 1).

of the clusters to the total seismicity rate with latitude, below and above 43°30′N. There are 12 clusters, comprising 257 events, that occurred north of 43°30′N, while 3 clusters totaling 69 events occurred south of 43°30′N. A cluster including a large number of events (*C*4) is located near 43°30N within the relay zone itself [*Maia et al.*, 2007].

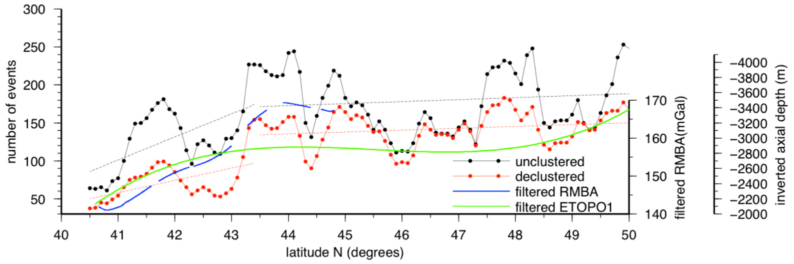

Figure 8. Number of events detected by the SIRENA array as a function of latitude. Both curves are obtained by calculating the cumulative number of events within a 1° latitudinal window, moving by steps of 0.1°. The black upper curve is computed from the full SIRENA catalog, the red lower curve represents the seismicity derived from the declustered catalog. We computed linear trends by least squares regression for the two curves, both present a positive slope, with a higher factor for the trend of the declustered curve. The blue line shows the filtered Residual Mantle Bouguer Anomaly (RMBA), corresponding to the MBA after the removal of the gravity effect of a cooling lithosphere, computed by *Maia et al.* [2007] from 40.7°N to 44.8°N. The green line shows, in an inverted scale, the overall trend of the axial depth filtered from the ETOPO1 grid [*Amante and Eakins*, 2009].

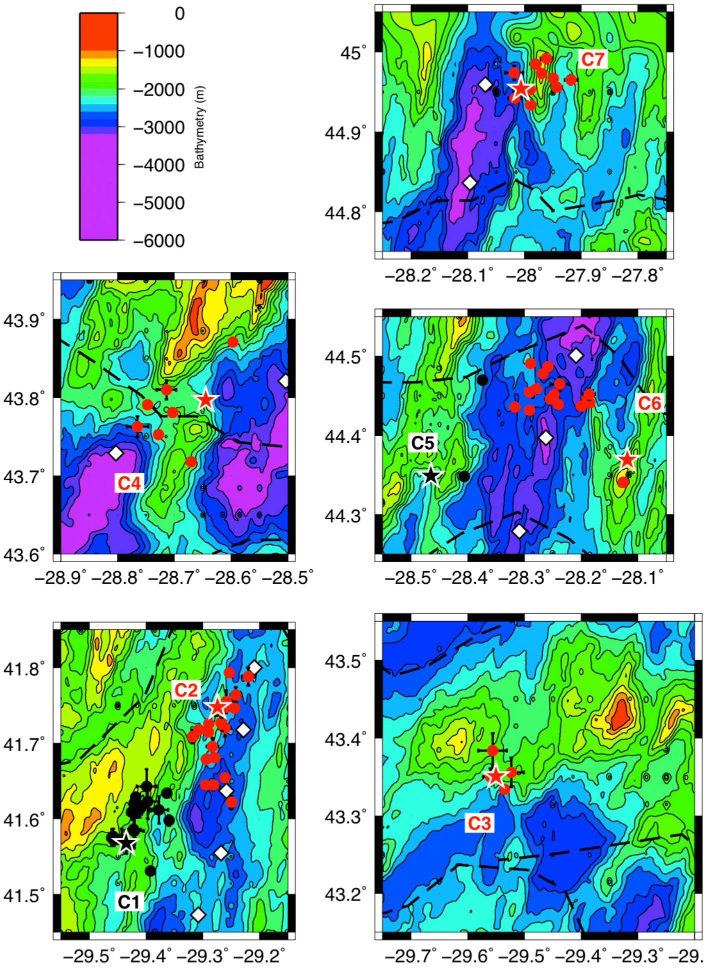

Figure 9. Selection of earthquakes superimposed on the TRIATNORD bathymetric map [*Goslin et al.*, 1999]. Only earthquakes detected by four hydrophones with latitude and longitude errors smaller than 2.5 km are shown on the map. The red or black stars show the position of the larger earthquakes (main shock) of each sequence resulting from the cluster search and circles of the corresponding color, the subsequent events (aftershocks). Errors bars are shown for all events. Segments boundaries identified by *Maia et al.* [2007] are shown by the black dashed lines. The white diamonds show the locations of the ridge axis deduced from magnetic anomalies [*Maia et al.*, 2007].

[22] This large-scale trend of seismicity, despite the short 16-month duration of the SIRENA experiment, can be interpreted as an effect of the Azores hot spot and can be compared to other observations, such as gravity. For instance, the Residual Mantle Bouguer Anomaly (RMBA) which corresponds to the MBA after removal of the gravity effect due to the cooling of the lithosphere is interpreted in terms of anomalous crustal thickness variations and/or mantle thermal structures [*Kuo and Forsyth*, 1988]. *Maia et al.* [2007] computed the RMBA along the MAR from 40°42′N to 44°48′N using the method of *Rommevaux et al.* [1994]: the RMBA displays a similar trend with an important increase from 40°42′N to 43°30′N, followed by a constant and positive value around 10 mGal up to 44°48′N (blue dashed line on Figure 8). *Maia et al.* [2007] interpreted this change at 43°30′N as an effect of a thicker and warmer crust underneath the relay zone, which is consistent with the increasing number of earthquakes up to this zone. Thus the Sr isotope, mantle seismic velocities, RMBA, seismicity rate data all indicate the northern limit of the Azores plume influence is at 43°30′N.

4.2. Spatial Distributions of Earthquakes at Segment Scales

[23] During the 16 months hydroacoustic observations of the SIRENA array, we found 15 clusters with more than 15 events. In their analysis, *Simão et al.* [2010] found only one cluster based on a threshold of 40 events. Most single events and clusters are located along the ridge-axis. However,

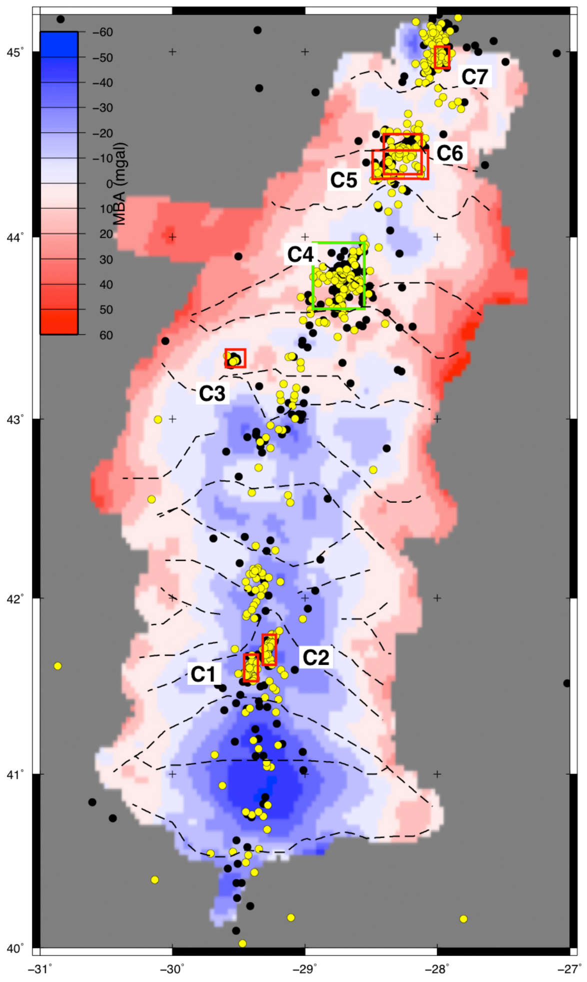

Figure 10. Earthquake locations superimposed on the Mantle Bouguer Anomaly (MBA) [*Maia et al.*, 2007]. Circles show earthquakes located with 4 or more hydrophones (yellow) and with 3 hydrophones (black). The tectonic cluster (green box) is located in a region with the highest MBA values, whereas magmatic swarms (red boxes) are located in areas with low MBA values (Figure 5 and Table 1).

there is also a significant amount of seismicity off the ridge-axis (Figure 7) including three clusters. We note that most of the scattered off-axis events were located using only 3 hydrophones.

4.2.1. Sequences Located Off-Axis

[24] The three off-axis sequences are *C*3, *C*14 and *C*15. The *C*14 and *C*15 sequences are located close to 50°30′N on both sides of the axial valley. The GCMT solutions indicate a strike-slip mechanism in the *C*14 sequence and a compressive mechanism in the *C*15 one (Figure 7). As both *C*14 and *C*15 clusters were considered above as tectonic sequences, the *C*14 sequence could be due to the reactivation of a fracture zone [*DeLong et al.*, 1977; *Wiens and Stein*, 1984] and the *C*15 or activity along an inside corner transform [*Engeln et al.*, 1986] or due to a thrust fault previously observed by *Galindo-Zaldívar et al.* [2000] on multichannel seismic profiles. As mentioned above, the *C*3 swarm shows a magmatic type of distribution in time. The spatial distribution of the events is concentrated in a small 7 × 7 km area. If this seismic activity is truly magmatic in origin, then it implies magmatic activity can occur up to 50 km off-axis, a surprising observation along a slow-spreading ridge. Aside from scattered events, the off-axis seismic activity is restricted to these three swarms.

4.2.2. Sequences Located On-Axis

[25] Swarms of earthquakes recorded on 4 hydrophones and located between 40°N and 45°N with location errors smaller than 2.5 km are plotted on the TRIATNORD bathymetric map [*Goslin et al.*, 1999; *Maia et al.*, 2007] (Figure 9). In this latitudinal range, seven swarms were identified.

[26] Among these sequences, only the *C*4 sequence fits a MOL (Figure 6 and Table 2), indicative of a tectonic-type sequence. The region of the *C*4 sequence has the highest seismic rates with 0.29 earthquake/day (consistent with similar rates near 22.5°N of the MAR [*Smith et al.*, 2002]) and nearly continuous seismic activity during the SIRENA experiment. It is located at the end of a spreading segment in a relay zone where the gravimetric crust is thin and peridotites were sampled [*Maia et al.*, 2007], corresponding probably to a non-transform discontinuity. The spatial distribution of the events on the map may reflect the projection at the seafloor surface of aftershocks located on a dipping fault plane. The *C*4 sequence probably represents a tectonic episode that lasted 11 days (Table 2), however we are unsure we recorded the whole sequence because it began 23 days before the end of the SIRENA experiment. The intrusion of a magma dike at the same time as the tectonic episode has also been proposed by *Simão et al.* [2010] for this sequence. As only 8 events were detected by four hydrophones (Figure 9), it is difficult to conclude with any certainty that migration of earthquakes associated with magma intrusion occurred. We derived a p value of 1 (Table 2) for this sequence which indicates a slow decay rate. Thus the *C*4 sequence may be the result of the activation of a fault within relatively cold lithosphere. The apparent spatial distribution of the aftershocks along a

dipping fault plane and the presence of peridotites indicate this area is a detachment fault, similar to those observed by *Cann et al.* [1997] which allows exhumation of mantle rocks [*Cannat*, 1993, 1996; *Ildefonse et al.*, 2007].

[27] *C*1 and *C*2 swarms are located near the center of Segment 3 as identified by *Maia et al.* [2007]. Swarm *C*2 occurred on an active volcanic ridge, consistent with a magmatic character for these two sequences. C1 is located on the western wall of the rift valley. Normally this location indicates a tectonic origin for the events, however *Cannat et al.* [1995] observed a volcanic cone on the western ridge flank near the Lucky Strike segment. Neither of these two sequences appeared to propagate in space and time. However, *C*2 swarm occurred in November 2002 approximately 10 km north of *C*1, which occurred three months later. The occurrence of *C*2 may have triggered *C*1 by changing pressure within the magma source reservoir, a process which has been recently documented in subaerial volcanoes in rift-zones-[e.g., *Baer et al.*, 2008; *Albaric et al.*, 2010]. The same spatial distribution on one of the ridge flanks is observed for *C*7 swarm.

[28] The *C*6 sequence, located in the center of Segment 10 [*Maia et al.*, 2007], shows a different spatial behavior, since the main shock occurred about 10 km away from the majority of the events that occurred 12 days later (Figure 5). Swarm *C*5 also occurred in Segment 10 but was located along the Eastern flank. There is a ten month lag between these two swarms; possibly, the stress release during *C*6 events could have triggered *C*5 sequence. However, there may also be no spatial and time relationship between these two clusters. The different seismic pattern on both flanks of this segment may be due the presence of a thinner crust under the west flank than under the east flank as evidenced by *Maia et al.* [2007].

[29] No migration pattern is observed for any of these swarms, but we may have missed all the events with a magnitude lower than our estimated SL_c (2.4). Nevertheless, a possible interpretation for this lack of migration pattern could be the occurrence of multiple vertical magmatic pulses as observed by *Tolstoy et al.* [2001] along the Gakkel Ridge which is the slowest spreading ridge on the planet. An alternative interpretation could also be a shallow intrusion of magmatic bodies, as imaged by *Magde et al.* [2000] within a MAR segment.

[30] From the spatial observations of clusters between 40°N and 45°N, its apparent that the tectonic event (*C*4) is isolated at the end of a segment whereas the other events (swarm type) are spatially concentrated or organized along structures such as the neovolcanic on-axis ridge, in the center of ridge segments. At a shorter scale, Figure 10 shows the location of the sequences superimposed on the Mantle Bouguer Anomaly (MBA) map computed by *Maia et al.* [2007]. The locations of tectonic and magmatic clusters are well correlated with regions with positive and negative MBA values, respectively. This indicates the presence of thinner/colder and thicker/warmer crust, respectively. The good spatial correlation between "non-tectonic" clusters and active volcanic structures of the MAR (e.g. neovolcanic ridges and negative MBAs) indicates the presence of a warmer and thicker crust consistent with magmatic source for these earthquake clusters.

5. Conclusions

[31] The SIRENA hydroacoustic experiment recorded monitored for 16 months the seismic and volcanic activity along a one-thousand-kilometer section of the Mid-Atlantic Ridge north of the Azores. This survey provides a key data set to understand the volcanic and tectonic processes occurring along a slow-spreading ridge in a ridge/hot spot interaction context, at various spatial and temporal scales. The spatial and temporal distribution of the seismicity recorded during the SIRENA experiment brings insights both into large-scale ridge-hot spot interactions and segment-scale active accretion processes.

[32] The long-term declustered distribution of the small-magnitude seismicity provides further evidence that the Azores hot spot exerts a strong influence on recent MAR accretion processes. The long-trend variations of this distribution further indicates that this influence has a rather limited northward extension, up to the relay zone located near 43°30′N [*Goslin et al.*, 1998; *Maia et al.*, 2007]. At a segment-scale, tectonic and non-tectonic earthquake-generating processes can be viewed through the analysis of the time-distribution of earthquakes from several sequences. The locations of tectonic and "non-tectonic" sequences correlate well with regions exhibiting positive and negative MBAs, respectively. Detachment faults can also be evidenced using aftershocks spatial distribution. Such a correlation is in favor of the now-classical image of a thermally segmented slow-spreading Mid-Atlantic Ridge.

Acknowledgments

[33] Funding from several sources made the SIRENA experiment possible. The cost of ship-time for the two cruises was provided by the French Ministry of Research. The development of the autonomous hydrophones, their building and deployment costs were provided by the NOAA Ocean Exploration Program and National Science Foundation (OCE-01). Finally, data interpretation was initiated while R. Dziak stayed in Brest for two months as an invited professor by the University of Brest. We thank the masters and crews of the *R/V Le Suroit* and *RRS Discovery* for their help and seamanship during the deployment and recovery of the instruments. Discussions with A. Deschamps, M. Maia and C. Tisseau are gratefully acknowledged. This is NOAA/PMEL contribution 3792 and IPGP contribution 3262. We thank two anonymous reviewers and one associate editor who significantly contributed to improve the quality of the manuscript.

References

Albaric, J., J. Perrot, J. Déverchère, A. Deschamps, B. L. Gall, R. W. Ferdinand, C. Petit, C. Tiberi, C. Sue, and M. Songo (2010), Contrasted seismogenic and rheological behaviours from shallow and deep earthqauke sequences in the North Tanzanian Divergence, East Africa, *J. Afr. Earth Sci.*, *58*, 811–899.

Amante, C., and B. W. Eakins (2009), Etopo1 1 arc-minute global relief model: Procedures, data sources and analysis, *NOAA Tech. Memo., NESDIS NGDC-24*, Natl. Geophys. Data Cent., Boulder, Colo., March.

Baer, G., Y. Hamiel, Y. Shamir, and R. Nof (2008), Evolution of a magma-driven earthquake swarm and triggering of the nearby Oldoinyo Lengai eruption as resolved by InSAR, ground observations and elastic modeling, East African Rift, 2007, *Earth Planet. Sci. Lett.*, *272*, 339–352.

Balanche, A., C. Guennou, J. Goslin, and C. Mazoyer (2009), Generation of hydroacoustic signals by oceanic subseafloor earthquakes: A mechanical model, *Geophys. J. Int.*, *177*, 476–480.

Bell, R. E., and W. R. Buck (1992), Crustal control of ridge segmentation inferred from observations of the Reykjanes Ridge, *Nature*, *357*, 583–586.

Bohnenstiehl, D. R., and M. C. Kleinrock (2000), Evidence for spreading-rate dependence in the displacement-length ratios of abyssal hill faults at mid-ocean ridges, *Geology*, *28*, 395–398.

Bohnenstiehl, D. R., and M. Tolstoy (2003), Comparison of teleseismic- and hydroacoustic-derived earthquake locations along the north-central Mid-Atlantic Ridge and equatorial East Pacific Rise, *Seismol. Res. Lett.*, *74*, 790–801.

Bohnenstiehl, D. R., M. Tolstoy, R. P. Dziak, C. G. Fox, and D. K. Smith (2002), Aftershock sequences in the mid-ocean ridge environment: An analysis using hydroacoustic data, *Tectonophysics*, *354*, 49–70.

Cann, J. R., D. K. Blackman, D. K. Smith, E. McAllister, B. Janssen, S. Mello, E. Avgerinos, A. R. Pascoe, and J. Escartin (1997), Corrugated slip surfaces formed at ridge-transform intersections on the Mid-Atlantic Ridge, *Nature*, *385*,329–332.

Cannat, M. (1993), Emplacement of mantle rocks in the seafloor at mid-ocean ridges, *J. Geophys. Res.*, *98*, 4163–4172.

Cannat, M. (1996), How thick is the magmatic crust at slow-spreading ridge?, *J. Geophys. Res.*, *101*, 2847–2857.

Cannat, M., et al. (1995), How thick is the magmatic crust at slow-spreading ridge?, *Earth Planet. Sci. Lett.*, *101*, 2847–2857.

DeLong, S. E., J. Dewey, and P. J. Fox (1977), Displacement history of oceanic fracture zone, *Geology*, *5*, 199–202.

Dziak, R. P. (2001), Empirical relationship of t-wave energy and fault parameters of northeast Pacific Ocean earthquakes, *Geophys. Res. Lett.*, *28*, 2537–2540.

Dziak, R. P., C. G. Fox, and A. E. Schreiner (1995), The June–July 1993 seismo-acoustic event at CoAxial Segment, Juan de Fuca Ridge: Evidence for a lateral dike injection, *Geophys. Res. Lett.*, *22*, 135–138.

Dziak, R. P., D. R. Bohnenstiehl, H. Matsumoto, C. G. Fox, D. Smith, M. Tolstoy, T.-K. Lau, J. Haxel, and M. Fowler (2004a), P- and T-wave detection thresholds, Pn velocity estimate, and detection of lower mantle and core P-waves on ocean sound-channel hydrophones at the Mid-Atlantic Ridge, *Bull. Seismol. Soc. Am.*, *95*, 665–677.

Dziak, R. P., D. K. Smith, D. R. Bohnenstiehl, C. G. Fox, D. Desbruyeres, H. Matsumoto, M. Tolstoy, and D. J. Fornari (2004b), Evidence of a recent magma dike intrusion at the slow spreading Lucky Strike segment, Mid-Atlantic Ridge, *J. Geophys. Res.*, *109*, B12102, doi:10.1029/2004JB003141.

Dziak, R. P., D. R. Bohnenstiehl, H. Matsumoto, M. J. Fowler, J. H. Haxel, M. Tolstoy, and F. Waldhauser (2009), January 2006 seafloor-spreading event at 9°50′N, East Pacific Rise: Ridge dike intrusion and transform fault interactions from regional hydroacoustic data, *Geochem. Geophys. Geosyst.*, *10*, Q06T06, doi:10.1029/2009GC002388.

Engeln, J. F., D. A. Wiens, and S. Stein (1986), Mechanisms and depths of Atlantic transform earthquakes, *J. Geophys. Res.*, *91*, 548–577.

Fox, C., R. Dziak, H. Matsumoto, and A. Schreiner (1994), Potential for monitoring low-level seismicity on the Juan de Fuca Ridge using military hydrophone arrays, *Mar. Technol. Soc. J.*, *27*, 22–30.

Fox, C. G., H. Matsumoto, and T.-K. Lau (2001), Monitoring Pacific Ocean seismicity from an autonomous hydrophone array, *J. Geophys. Res.*, *106*, 4183–4206.

Gac, S., J. Dyment, C. Tisseau, and J. Goslin (2003), Axial magnetic anomalies over slow-spreading ridge segments: Insights from numerical 3-D thermal and physical modelling, *Geophys. J. Int.*, *154*, 618–632.

Gac, S., C. Tisseau, J. Dyment, and J. Goslin (2006), Modelling the thermal evolution of slow-spreading ridge segments and their off-axis geophysical signature, *Geophys. J. Int.*, *164*, 341–358.

Galindo-Zaldívar, J., A. Jabaloy, A. Maldonado, J. M. Martínez-Martínez, C. S. de Galdeano, L. Somoza, and E. Surinach (2000), Deep crustal structure of the area of intersection between the Shackleton fracture zone and the West Scotia Ridge (Drake Passage, Antartica), *Tectonophysics*, *320*, 123–139.

Gente, P., R. A. Pockalny, C. Durand, C. Deplus, M. Maia, G. Ceuleneer, C. Mével, M. Cannat, and C. Laverne (1995), Characteristics and evolution of the segmentation of the Mid-Atlantique Ridge between 20°N and 24°N during the last10 million years, *Earth Planet. Sci. Lett.*, *129*, 55–71.

Goslin, J., J.-L. Thirot, O. Noel, and J. Francheteau (1998), Slow-ridge/hotspot interactions from global gravity, seismic tomography and ^{87}Sr/^{86}Sr isotopedata, *Geophys. J. Int.*, *135*, 700–710.

Goslin, J., et al. (1999), Extent of Azores plume influence on the Mid-Atlantic Ridge north of the hotspot, *Geology*, *27*, 991–994.

Goslin, J., et al. (2004), Interactions between the MAR and the Azores hotspot as imaged by seismicity distributions using autonomous hydrophone arrays, paper presented at Workshop on Seismo-acoustic Applications in Marine Geology and Geophysics, Woods Hole Oceanogr. Inst., Woods Hole, Mass., 24–26 March.

Goslin, J., N. Lourenço, R. P. Dziak, D. R. Bohnenstiehl, J. Haxel, and J. Luis (2005), Long-term seismicity of the Reykjanes Ridge (North Atlantic) recorded by a regional hydrophone array, *Geophys. J. Int.*, *162*, 516–524.

Haskov, J., and L. Ottemoller (2008), Seisan: The earthquake analysis software for Windows, Solaris, Linux and MacOSX, version 8.2, technical report, 281 pp., Dep. of Earth Sci., Univ. of Bergen, Bergen, Norway.

Ildefonse, B., D. K. Blackman, B. E. John, Y. Ohara, D. J. Miller, C. J. MacLeod, and Integrated Ocean Drilling Program Expeditions 304/305 Science Party (2007), Oceanic core complexes and crustal accretion at slow-spreading ridges, *Geology*, *35*, 623–626.

Johnson, R. H., J. Northrop, and R. Eppley (1963), Source of Pacific T-phases, *J. Geophys. Res.*, *68*, 4251–4260.

Kuo, B.-Y., and D. W. Forsyth (1988), Gravity anomalies of the ridge-transform system in the South Atlantic between 31 and 34.5°S: Upwelling centers and variations in crustal thickness, *Mar. Geophys. Res.*, *10*, 205–232.

Leet, L. D., D. Linehan, and P. Berger (1951), Investigation of the T-phases, *Bull. Seismol. Soc. Am.*, *41*, 123–141.

Lin, J., G. M. Purdy, H. Schouten, J.-C. Sempere, and C. Zervas (1990), Evidence from gravity data for focused magma accretion along the Mid-Atlantic Ridge, *Nature*, *344*, 627–632.

Magde, L. S., D. W. Sparks, and R. S. Detrick (1997), The relationship between buoyant mantle flow, melt migration and gravity bull's eyes at the Mid-Atlantic Ridge between 33°N and 35°N, *Earth Planet. Sci. Lett.*, *148*, 59–67.

Magde, L. S., A. H. Barclay, D. R. Toomey, R. S. Detrick, and J. A. Collins (2000), Crustal magma plumbing within a segment of the Mid-Atlantic Ridge, 35°N, *Earth Planet. Sci. Lett.*, *175*, 55–67.

Maia, M., J. Goslin, and P. Gente (2007), Evolution of the accretion processes along the Mid-Atlantic Ridge north of the Azores since 5.5 Ma: An insight into the interactions between the ridge and the plume, *Geochem. Geophys. Geosyst.*, *8*, Q03013, doi:10.1029/2006GC001318.

Mogi, K. (1963), Some discussionson aftershocks, foreshocks, and earthquake swarms—The fracture of a semi-infinite body caused by an inner stress origin and its relation to the earthquake phenomena, *Bull. Earthquake Res. Inst. Univ. Tokyo*, *41*, 615–658.

Ogata, Y. (1983), Estimation of the parameters in the modified Omori formula for aftershocks frequencies by the maximum likehood procedure, *J. Phys. Earth*, *31*, 115–124.

Okal, E. A. (2008), The generation of T-waves by earthquakes, *Adv. Geophys.*, *49*, 1–70.

Pan, J., and A. M. Dziewonski (2005), Comparison of mid-oceanic earthquake epicentral differences of travel time, centroid locations, and those determined by autonomous underwater hydrophone arrays, *J. Geophys. Res.*, *110*, B07302, doi:10.1029/2003JB002785.

Rommevaux, C., C. Deplus, P. Patriat, and J.-C. Sempéré (1994), Three-dimensional gravity study of the mid-atlantic ridge: Evolution of the segmentation between 28° and 29°N during the last 10 m.y., *J. Geophys. Res.*, *99*, 3015–3029.

Simão, N., J. Escartin, J. Goslin, J. Haxel, M. Cannat, and R. Dziak (2010), Regional seismicity of the Mid-Atlantic Ridge: Observations from autonomous hydrophone arrays, *Geophys. J. Int.*, *183*, 1559–1578.

Smith, D. K., M. Tolstoy, C. G. Fox, D. R. Bohnenstiehl, H. Matsumoto, and M. J. Fowler (2002), Hydroacoustic monitoring of seismicity at the slow-spreading Mid-Atlantic Ridge, *Geophys. Res. Lett.*, *29*(11), 1518, doi:10.1029/2001GL013912.

Sykes, L. R. (1970), Earthquake swarms and sea-floor spreading, *J. Geophys. Res.*, *32*, 6598–6611.

Talandier, J., and E. A. Okal (1998), On the mechanism of conversion of seismic waves to and from T-waves in the vicinity of island shores, *Bull. Seismol. Soc. Am.*, *88*, 621–632.

Thibaud, R., P. Gente, and M. Maia (1998), A systematic analysis of the Mid-Atlantic Ridge morphology and gravity between 15°N and 40°N: Constraints on the thermal structure, *J. Geophys. Res.*, *103*, 24,223–24,243.

Tolstoy, M., D. Bohnenstiehl, M. Edwards, and G. Kurras (2001), Seismic character of volcanic activity at the ultraslow-spreading Gakkel Ridge, *Geology*, *29*, 1139–1142.

Utsu, T. (1995), The centenary of the Omori formula for a decay law of aftershock activity, *J. Phys. Earth*, *43*, 1–33.

Utsu, T., and Y. Ogata (1997), Statistical analysis of seismicity, in *IASPEI Software Library*, vol. 6, edited by J. H. Healy, V. I. Kelis-Borok, and W. H. K. Lee, pp. 13–94, Int. Assoc. of Seismol. and Phys. of the Earth's Inter., Trieste, Italy.

Wiens, D. A., and S. Stein (1984), Intraplate seismicity and stresses in young oceanic lithosphere, *J. Geophys. Res.*, *89*, 11,442–11,464.

5.2 Mes projets en hydroacoustique

L'OSU-IUEM s'est engagé depuis 2002 dans l'observation hauturière avec la sismicité des domaines océaniques. Ces systèmes d'observations consistent principalement à enregistrer en continu de longues séries de signaux acoustiques réalisées à l'aide de réseaux hydroacoustiques. Ces réseaux permettent à la fois de caractériser la sismicité de faible magnitude associée à différents processus géologiques et ouvrent notamment de nouvelles perspectives concernant l'activité sismo-tectonique des dorsales, la nucléation des séismes dans les failles sous-marines, l'hydrothermalisme et le rôle des fluides en général, ainsi que les déformations intraplaques. Ce type d'observations est particulièrement bien adapté à l'étude des dorsales où l'expansion océanique résulte d'une succession, dans l'espace et le temps, des épisodes magmatiques et tectoniques. Ils sont par ailleurs complémentaires de ceux d'études plus ciblées menées grâce au déploiement d'OBS. Pour tester les différents modèles d'expansion, il faut avoir accès à une sismicité de faible magnitude sur de grandes sections des dorsales et sur de longues périodes de temps, afin de quantifier la récurrence des évènements magmatiques et tectoniques. Les hydrophones autonomes présentent de nombreux avantages avec une technologie relativement simple et bien maîtrisée (150+ déploiements effectués par l'UMR6538 depuis 2010, Figure 14) et une longue autonomie (jusqu'à deux années d'observation). Cette activité est soutenue par l'INSU qui a labellisé comme Site National Instrumenté (SNI) deux projets d'observatoire du laboratoire. Le premier réseau est autour du site MOMAR sur la dorsale Atlantique au sud des Açores (HYDROMOMAR) maintenu par J. Perrot, et qui est l'un des 3 sites d'observation long terme en domaine profond « EMSO-France » dans lesquels la communauté française est impliquée.

Figure 14: Gauche : récupération d'un hydrophone avec son système d'acquisition protégé dans une bouée cylindrique. L'ensemble est attaché à un mouillage pour que l'instrument soit immergé dans le canal SOFAR. Droite: le Marion Dufresne permet la maintenance du réseau OHA-SISBIO avec ses sites placés sur routes des Terres Australes et Antarctiques Françaises.

5.2.1. Hydroacoustique pour étudier les dorsales indiennes

Le Site National Instrumenté (SNI) OHASIS-BIO, labelisé par l'INSU depuis 2010, comprend 9 hydrophones et couvre tout l'Océan Indien Austral (Figure 15). Il est étendu sur plus de 2000 km et permet d'enregistrer la sismicité quasi-continue mais de faible magnitude le long de la dorsale océanique. Il permet ainsi une couverture simultanée des trois dorsales présentes dans l'océan indien et qui ont des taux d'expansion très contrastés (ultra-lent, lent, et intermédiaire). Leur activité sismique est ponctuée par des essaims de quelques jours à quelques semaines, concentrés sur certains segments de la dorsale. La géométrie du réseau a été adaptée pour satisfaire à la fois les objectifs scientifiques et les contraintes logistiques, les sites étant placés sur les routes du N.O. Marion Dufresne (Figure 14) vers les îles australes (Crozet, Kerguelen, Amsterdam).

J'ai récemment rejoint l'équipe hydroacoustique (J.-Y. Royer, J. Perrot, A. Sukhovich, M. Beauverger, C. Guenou) et je participe à l’acquisition et au suivi des séries. J'ai participé au pointé manuel et à l'interprétation de la dernière année des données acquises par OHASIS-BIO (Figure 15 de gauche). Les réseaux d'hydrophones ne permettent pas d’accéder aux mécanismes au foyer des séismes. Comme ils sont plus sensibles aux évènements de faible magnitude que les réseaux sismologiques mondiaux, ils donnent néanmoins accès à la répartition spatio-temporelle des essaims et localisent les processus actifs au niveau des dorsales océaniques. En collaboration avec J.-Y. Royer, nous avons étudié 2 essaims sismiques qui se sont produits en juillet et en septembre 2018 sur la partie extrêmement lente de la dorsale Sud-Ouest Indienne (taux d'expansion de 14 mm/an). Le premier essaim (en bleu sur la Figure 15 de droite) comprend 410 séismes enregistrés pendant 3,5 jours. Le second essaim (en rouge sur la Figure 15 de droite) comprend 253 séismes pendant 12 jours. La répartition géographique, leur occurrence et leur niveau acoustique peuvent apporter des informations sur leur origine tectonique ou magmatique et sont révélateurs de l'état thermique et mécanique de la lithosphère de ce segment de dorsale. Ce travail conjoint a été présenté à l'AGU en 2019 (Royer et al., 2019).

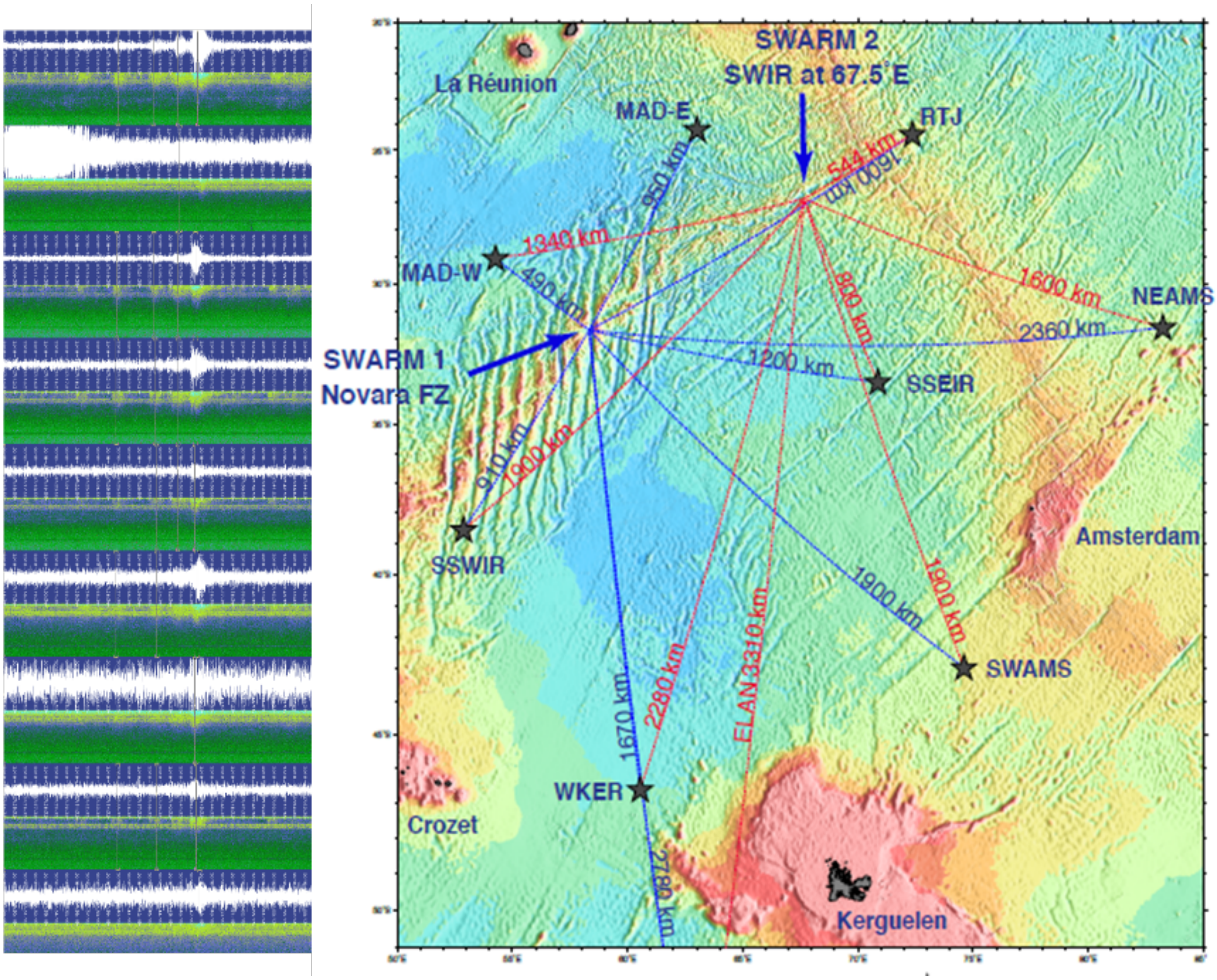

Figure 15: Gauche: enregistrement des ondes acoustiques générées par les éruptions volcaniques et les tremblements de terre sous-marins sur la dorsale Sud-Ouest Indienne. Droite: deux 2 essaims sismiques se sont produits en 2018 sur la partie extrêmement lente de la dorsale et sont détectés par l'ensemble du réseau. Figure d'après Royer et al., 2019.

Cette première analyse se prolonge actuellement par le co-encadrement d'une thèse intitulée «Dynamique de l’accrétion océanique vue par l’analyse d’essaims de séismes détectés depuis 10 ans sur trois dorsales à taux d’ouverture contrastés» avec Vaihab Ingale. Les 10 années d'enregistrement de la sismicité acquises par le réseau OHASIS-BIO permettront d'analyser systématiquement les essaims et les caractéristiques des séquences choc principal/répliques.

Tenant compte des résultats déjà obtenus et des problèmes rencontrés pour la surveillance hydroacoustique, quelques propositions d'actions dans lesquelles je souhaiterais m'investir avec mes collègues dans les années à venir pourraient être les suivantes :

- Participer au traitement manuel des bases de données et l'élaboration des catalogues de sismicité.
- Les données des réseaux hydroacoustiques s'étendent sur de longues durées et sont laborieuses à traiter. Nous souhaitons pouvoir appliquer une méthode de détection automatique par intelligence artificielle en utilisant les périodes déjà labellisées comme données d'entraînement (training data).
- Obtenir le label des Services Nationaux d’Observation (SNO) pour le Site National Instrumenté (SNI) de OHASISBIO. Les SNO mettent en œuvre sur plusieurs années voire plusieurs dizaines d’années des dispositifs d’observation et d’acquisition de données des milieux naturels. Ces dispositifs ont une vocation de service au bénéfice de toute la communauté par la production et l’accès aux données et permettent de faire progresser la connaissance des systèmes étudiés. Les décisions de labélisation sont prises par l'INSU après évaluation scientifique par la commission Terre Solide suivant des critères portant notamment sur la justification scientifique, la taille de la communauté servie, l’impact du service, etc.

5.2.2. Hydroacoustique pour étudier la crise sismo-volcanique de Mayotte

Mayotte appartient à l’archipel volcanique des Comores situé dans le Canal du Mozambique entre l’Afrique et Madagascar. C’était une région sismique considérée comme modérée et la dernière activité volcanique sur l’île datait de moins de 7000 ans. Depuis mai 2018, une forte activité sismique affecte la région. Celle-ci forme deux essaims avec des épicentres regroupés en mer, entre 5 et 15 km à l'est de Petite-Terre pour l’essaim sismique principal, et à 25 km à l’est de Petite-Terre pour le secondaire, à des profondeurs comprises majoritairement entre 25 et 50 km (Figure 16 à gauche ; Lemoine et al., 2020). L’analyse de la sismicité se base sur les données issues du réseau de stations à terre, qui s’est largement densifié depuis le début de la crise et qui est maintenant distribué dans toute la région, et depuis 2019 d’un parc d’OBS relevés tous les 3 à 4 mois. La majorité des séismes est de faible magnitude, mais plusieurs évènements de magnitude modérée (max. Mw5,9 le 15 mai 2018) ont été fortement ressentis par la population et leur succession a endommagé certaines constructions. De plus, l’île a aussi subi une forte subsidence au début de la crise. Les stations GPS dont le réseau a aussi été densifié indiquent un déplacement vers l’est de ~21-24 cm et un affaissement de ~10 -19 cm. Un ralentissement des déplacements est observé depuis le printemps 2019 (Bulletins du REVOSIMA, www.ipgp.fr/revosima).

Une campagne océanographique (MD220-MAYOBS1) sur le Marion Dufresne a permis la découverte d’un nouveau volcan sous-marin à 50 km à l’est de Mayotte, formant un édifice de 820 m de hauteur à 3500 m de profondeur (Feuillet, 2019). Depuis cette première campagne, de nouvelles coulées de lave autour de l’édifice sont régulièrement observées par différentiel bathymétrique. La dernière campagne MAYOBS15, en octobre 2020, a capturé les premières images de lave incandescente sur une coulée active au nord-ouest du sommet du volcan ; celles-ci ont été prises avec la caméra tractée du SCAMPI. En l’état actuel des connaissances, l’éruption a produit un volume cumulé estimé d’environ 6,55 km^3. Par ailleurs, la région dite du Fer à Cheval, est située elle à l’aplomb de l’essaim sismique principal (5-15 km à l’Est de Petite-Terre), est une structure préexistante à la crise sismo-volcanique mais son âge reste à déterminer. Plusieurs panaches acoustiques associés à des anomalies géochimiques ont été détectés dans la colonne d’eau au-dessus de cette structure et ils semblent s’intensifier dans le temps.

L’activité sismo- volcanique est analysée par le Réseau de surveillance Volcanologique et Sismologique de Mayotte (REVOSIMA). L’IPGP opère le REVOSIMA à travers l’Observatoire volcanologique du Piton de la Fournaise, avec l'appui du BRGM et en étroite association avec l’IFREMER et le CNRS. Le REVOSIMA est soutenu par un consortium scientifique avec l’IPGS et le RENASS-BCSF, l’IRD, l’IGN, l’ENS, l'Université de Paris, l’Université de la Réunion, l’Université Clermont Auvergne, LMV et l'OPGC, l'Université de Strasbourg, l'Université Grenoble Alpes et ISTerre, l’Université de La Rochelle, l'Université Paul Sabatier, Toulouse et le GET- OMP, GéoAzur, le CNES, Météo France, le SHOM, les TAAF, et collaborateurs. De par mon expérience dans les observatoires sismologiques de volcanologiques, ma participation à de nombreuses campagne OBS et mon statut CNAP, j’ai naturellement souhaité participer aux études coordonnées par le REVOSIMA. Dans un premier temps, j'ai participé aux astreintes journalières pilotées par l'IPGP pour le pointé à distance de l'activité sismo-volcanique. Aussi, je souhaite continuer à participer aux *pickathons* après les relèves des OBS. Ces pointés collectifs sont réalisés en différé environ tous les 4 mois, en présentiel ou distanciel, et ont pour but de compléter les catalogues de sismicité construits au jour le jour à partir des seuls enregistrements continus des stations à Terre. J'ai aussi déployé lors de la campagne MD228-MAYOBS15 en octobre 2020 4 hydrophones SOFAR (Figure 16 à droite). Ce réseau hydroacoustique situé à 50 km autour du volcan a pour objectif de compléter les réseau d’OBS pour suivre le développement des deux essaims sismiques (Figure 16 à gauche). Ce type d'observation est particulièrement bien adapté à l'étude des volcans sous-marins car ils peuvent enregistrer les sons associés aux coulées volcaniques et aux explosions. En effet, les hydrophones installés sur les cadres des OBS ont déjà pu détecter des signaux acoustiques au niveau de toute dernière coulée, probablement générés par le contact explosif entre la lave chaude et l’eau de mer. Les hydrophones permettront aussi de caractériser et suivre l’évolution du bruit océanique ambient, notamment celui généré par les grands mammifères marins. Une première rotation des hydrophones est pour l’instant programmée en mars 2021 (GEOFLAMME) à bord du N/O Pourquoi Pas, et nous attendons les données avec impatience. D’autres rotations seront programmées en fonction des navires sur la zone.

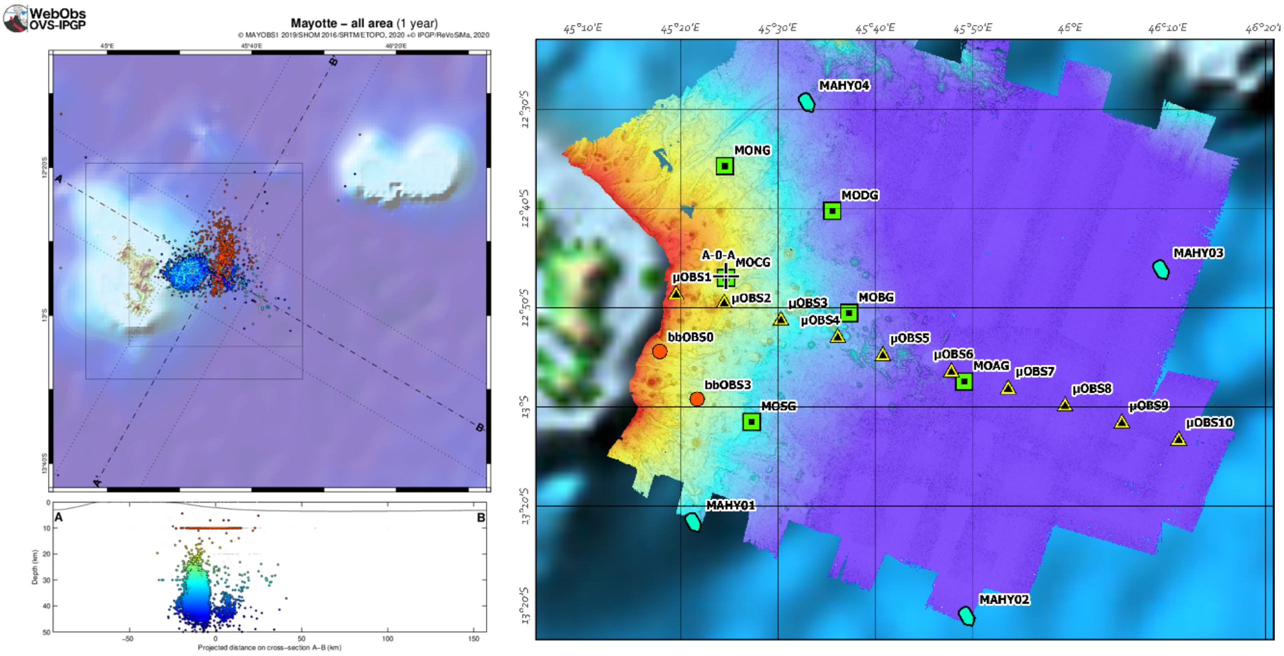

Figure 16: Gauche : sismicité détectée par le REVOSIMA pendant l'année 2019 autour de l'île de Mayotte (document de travail WebObs-IPGP). Droite : positions des stations de mesures déployées pendant la campagne MD228-MAYBOS15 en octobre 2020. Les points MAHY01 à MAHY04 correspondent aux lignes de mouillages équipées d' hydrophones dans le canal SOFAR.

6. Perspectives et conclusions

Les premiers chapitres de ce manuscrit étaient consacrés à présenter les travaux que j'ai menés essentiellement dans le domaine terrestre. J'envisage de continuer ma carrière dans le domaine marin et d'y poursuivre mes développements multi-méthodes. L'interdisciplinarité est un mot à la mode, mais au-delà de cet effet de mode, il me semble opportun de chercher à croiser les disciplines car de nombreux phénomènes géologiques interagissent.

Les crises sismiques et volcaniques génèrent des besoins et des d'attentes sociétales mais apportent aussi des opportunités pour la communauté scientifique. De telles périodes sont de rares occasions d'étudier des processus dynamiques et sont de ce fait un élément clé pour développer des modèles prédictifs afin de prévoir l'avenir. Je souhaite pouvoir continuer à travailler sur ces phénomènes passionnants grâce à des observations géophysiques multi-méthodes.

Au moment où j'écris ces lignes, un projet ambitieux est proposé par la communauté française avec la création d'un parc instrumental sous-marin mutualisé et porté par RESIF dans le cadre du Programme d'Investissement d'Avenir (PIA3) EQUIPEX. Ce projet de grande ampleur (20 M€) s'intitule MARMOR pour **M**arine **A**dvanced geophysical **R**esearch equipment and **M**ayotte multidisciplinary **O**bservatory for research and **R**esponse (équipement géophysique de recherche marine avancée et observatoire multidisciplinaire pour la recherche et la surveillance à Mayotte). L'un des objectifs de MARMOR est de prolonger les études sismologiques en mer mais aussi de faciliter la combinaison des études géodésiques et sismologiques en fond de mer. En effet, les zones où les populations sont les plus exposées aux aléas naturels (séisme, tsunami, éruption, modification du littoral, instabilité gravitaire) se situent souvent dans les régions côtières. Appréhender ces aléas nécessite une observation continue Terre-Mer, au plus proche de la source de ces aléas souvent situés en mer. L'un des objectifs du projet MARMOR est la caractérisation de la déformation et de la sismicité aux frontières de plaque, l'étude des processus physiques menant à l'occurrence des grands séismes et leur relation avec la génération de tsunamis. Au-delà des études fondamentales, l'infrastructure améliorera le suivi opérationnel des crises sismiques ou volcaniques. De plus, MARMOR prévoit un axe de travail pour développer l'observation en continu de l'aléa sur Mayotte et la réalisation de prototypes d'observatoire sous-marin, en continu et en temps réel pour aller vers la surveillance. J'ai contribué à l'élaboration et à la soumission du projet en juin 2020. S'il est financé, je souhaite participer à la gestion du parc d'hydrophones SOFAR mutualisés (Figure 17) ainsi qu'à celui d'OBS dédié aux interventions rapides (après un séisme fort comme dans le cas de GUADOBS après les séismes des Saintes en 2004 ou de MARTOBS après le séisme au Nord de la Martinique en 2007). Le parc d'hydrophones sera hébergé à l'IUEM alors que le parc d'OBS d'intervention sera hébergé à Ifremer. Pour le quinquennal 2022-2026, l'UMR6538 « Laboratoire Géosciences Océan » de l'IUEM et l'Unité de Recherche « Géosciences Marines » d'Ifremer présentent un projet de fusion pour devenir « Geo-Ocean Brest ». Cette fusion va faciliter les collaborations et renforcer nos synergies.

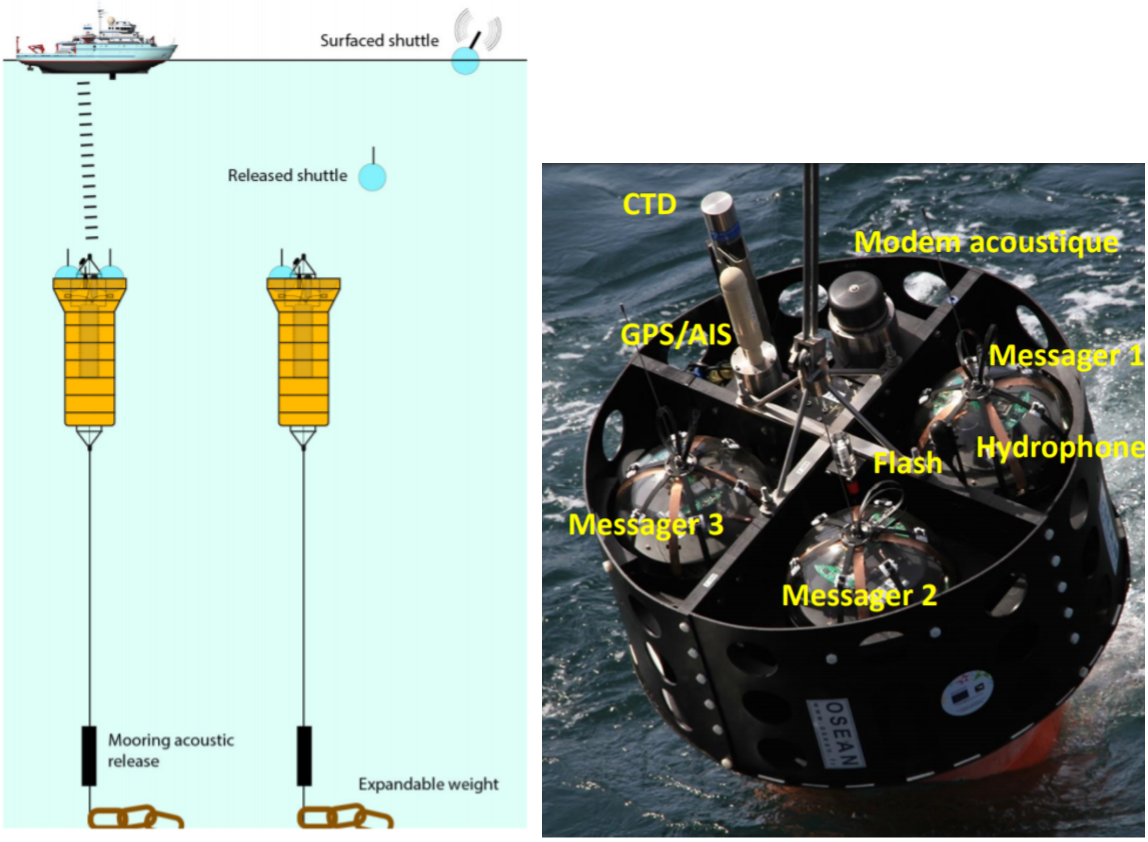

Figure 17: les hydrophones « communiquants » tels que ceux qui seraient choisis pour le parc communautaire de MARMOR sont des instruments autonomes communiquant les données à la demande par messagers. Une bouée contenant un disque peut être larguée à la demande et récupérée par un navire d'opportunité. Une prototype HYDROBS fabriqué par la société OSEAN est actuellement déployé dans le réseau OHASISBIO (source: J.Y. Royer).

Par ailleurs, j'explore la manière dont on pourrait prolonger le réseau sismologique du Grand Ouest Français en mer. Depuis les années 2010, en plus de la modernisation des stations sismologiques, l'infrastructure de recherche RESIF a permis de densifier le réseau de surveillance. Actuellement, le réseau large-bande permanent (RLBP) est constitué d'environ 120 stations opérées par différents partenaires de RESIF. Historiquement, ces stations sont principalement localisées dans les zones où l'activité sismique est la plus importante. Un effort important est engagé depuis plusieurs années pour homogénéiser cette répartition en France. RESIF a donc permis l'installation de 26 nouvelles stations sismologiques dans le Nord-Ouest de la France, sous la responsabilité de l'OSUNA à l'université de Nantes. Cette nouvelle couverture instrumentale permet depuis quelques mois de mieux localiser la sismicité du Nord-Ouest de la France mais aussi de descendre le seuil de détection. De plus petits séismes sont maintenant catalogués par rapport aux années précédentes. Néanmoins, les performances du réseau de surveillance sont bien moindres sur la façade Ouest que dans le reste du territoire, du fait de l'absence de stations en mer dans l'Atlantique et dans la Manche (Figure 18). Du fait de la géométrie des côtes françaises, une bonne partie des régions sismiquement actives sont mal couvertes. Avec le stage de M2 de Maël Thomas, nous avons réalisé un travail exploratoire pour dimensionner une éventuelle extension du réseau sismologique en mer au large de la Bretagne. Développer un réseau de surveillance OBS dans le Grand Ouest serait une lourde tâche mais nous avons les compétences et les outils nécessaires. Ce projet pourrait bénéficier à la connaissance scientifique mais aussi aux étudiants, qui pourraient ainsi se former au travail d'observation en participant à la maintenance des stations.

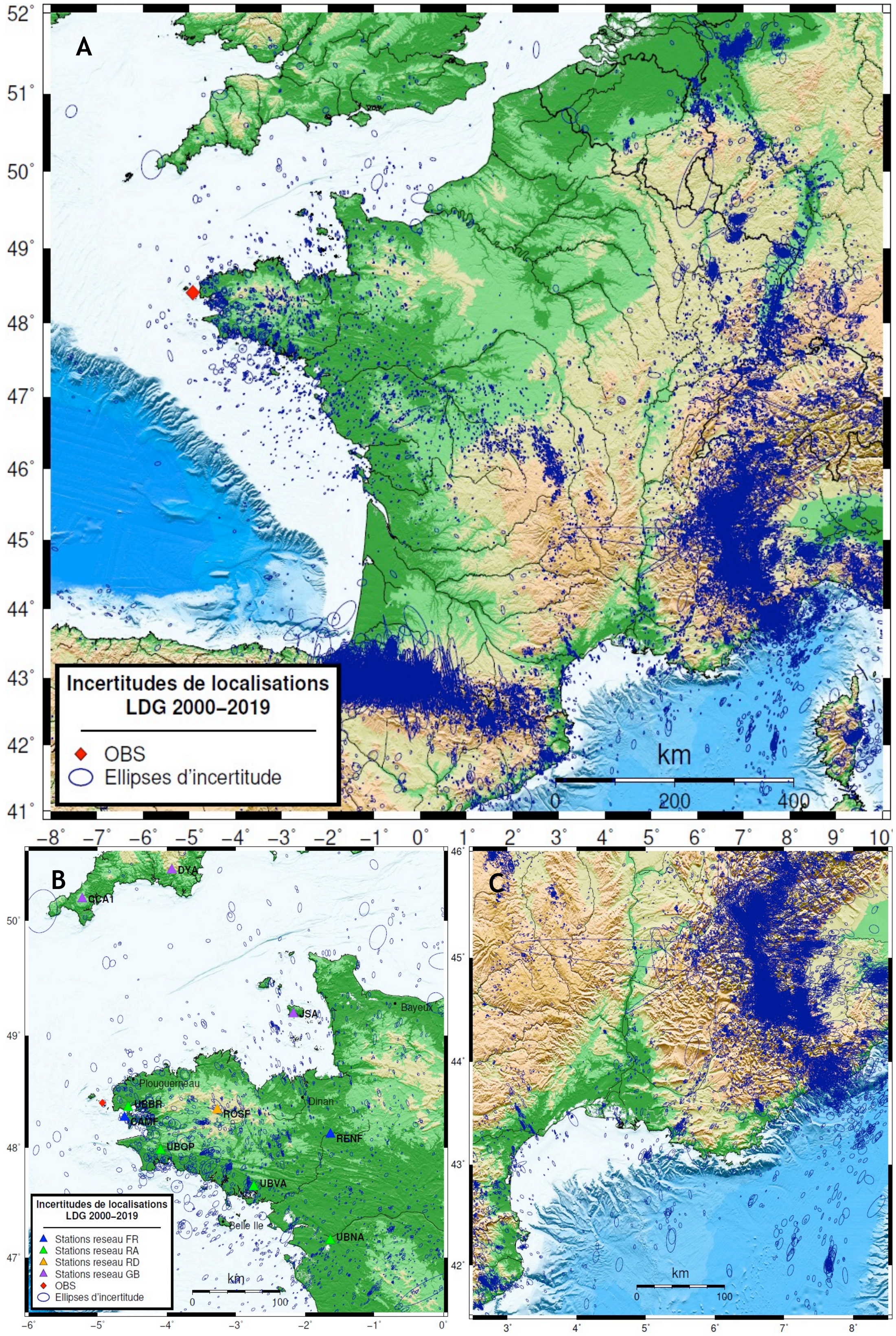

Figure 18: Incertitudes épicentrales de la sismicité entre 2000 et 2019 (données LDG) en France (A), dans le Grand Ouest (B) et par comparaison dans le Sud Est (C). Figure issue du rapport M2 de Maël Thomas (2020).

Un autre projet que je souhaite développer dans ce chapitre de perspectives est celui du développement instrumental. Dans ce contexte, j'ai déposé un pré-dossier en mai 2020, puis un dossier complet en septembre 2020 à l'appel à projet européen MarTERA ERA-NET COFUND. Nous souhaitons avec le projet Listen2Bubbles (An autonomous observatory for monitoring deep-sea gas emissions), construire une plateforme autonome multi-capteurs. En effet, il est toujours intéressant d'acquérir et d'archiver conjointement plusieurs paramètres environnementaux pour mieux comprendre les phénomènes observés. C'est un enseignement que j'ai appris en travaillant dans les observatoires volcanologiques où c'est seulement la multitude des types de monitoring qui nous permet de comprendre les processus étudiés. Par ailleurs, il apparaît important d'intégrer le rôle des fluides et de leurs interactions avec le substrat en fond de mer. Les failles en mer sont naturellement des zones riches en fluides. C'est un enseignement que j'ai appris avec la campagne GUADOBS en étudiant la crise sismique des Saintes, qui apparait fortement influencée par la circulation de fluides dans le plan de faille. D'une façon générale, les fluides influent sur le comportement sismogénique des failles. Il a été montré que ces fluides avaient un rôle dans la distribution (géographique et temporelle) des séismes (e.g., Henry et al., 2018), dans le mécanisme dans les séismes lents (e.g., Davis et al., 2015), mais aussi dans la sismicité induite (e.g., Ellsworth, 2013). Notre plateforme autonome sera capable de détecter et de caractériser les bulles émises en fond de mer et remontant dans la colonne d'eau. Le système combinera des capteurs chimiques avec des capteurs acoustiques. Les hydrophones et géophones ont de faibles besoins en énergie et seront utilisés pour déclencher les capteurs les plus gourmands en énergie, notamment un sonar acoustique et un capteur chimique pour analyser les panaches de bulles. Cette conception à faible consommation d'énergie permettra une surveillance à long terme des sites d'intérêt, sans avoir besoin de câbles ou d'autres infrastructures. Les principales applications scientifiques du système sont d'aider à estimer la quantité de méthane rejetée dans les océans et susceptible d'atteindre l'atmosphère et, par conséquent, de contribuer à l'effet de serre. D'un point de vue industriel, ce serait un outil précieux contribuant à la sécurité des opérations de forage pétrolier et gazier, et permettant la surveillance à distance des puits abandonnés. D'un point de vue scientifique, cet outil pourrait apporter des séries temporelles pour mieux comprendre l'interaction entre les sorties de fluides et l'activités sismiques ou volcaniques. Ce projet est une collaboration entre des partenaires français (IUEM, Ifremer, CEREGE, et Quiet Oceans), norvégiens (NGI et Kongsberg Maritime) et turcs (Istanbul Technical University). Nous proposons de tester le prototype en Mer de Marmara pour étudier les interactions entre les failles actives et les fluides, mais la zone active de Mayotte serait aussi un beau terrain de jeu.

Il me parait évident que le Laboratoire Géosciences Océan offrira les conditions favorables pour me permettre de développer mes activités d'observation, d'enseignement et de recherche. A travers les exemples de projets exposés ici, je pense que mon rôle s'inscrira dans une démarche d'élargissement interdisciplinaire sur les thématiques de la géophysique marine et mais aussi de la géophysique de proche surface.

7. Références

Anglade A., A. Lemarchand, J.-M. Saurel, V. Clouard, M.-P. Bouin, J.-B. de Chabalier, S. Tait, C. Brunet, A. Nercessian, F. Beauducel, R. Robertson, L. Lynch, M. Higgins, and J. Latchman, 2015. Significant technical advances in broadband seismic stations in the Lesser Antilles, *Adv. Geosci.*, 40, 43–50, doi:10.5194/adgeo-40-43-2015.

Anschütz, H., Vöge, M., Lysdahl, A., **Bazin, S.**, Sauvin, G., Pfaffhuber, A.A., Berggren, A.L., 2017. From manual to automatic AEM bedrock mapping. Special issue Airborne Geophysics *of J. of Environmental and Engineering Geophysics*, doi: 10.2113/JEEG22.1.35.

Bazin S., D. Bertil, F. Beauducel, M. Bengoubou-Valérius, 2005. Le séisme des Saintes du 21 novembre 2004. *Lettre d'Information du Réseau Accélérométrique Permanent*, n°2, juillet 2005.

Bertil D., **S. Bazin**, D. Mallarino, F. Beauducel, 2004. Séisme des Saintes du 21 novembre 2004. Rapport de Synthèse, *Centre de Données Sismologique des Antilles*, 8 décembre 2004.

Bazin C., 2012. SafeLand deliverable 4.8. Guidelines for landslide monitoring and early warning systems in Europe – Design and required technology. Edited for the SafeLand European project, Grant Agreement No.: 226479.

Bazin, S., and the SafeLand Team, 2012. SafeLand guidelines for landslide monitoring and early warning systems in Europe - Design and required technology, *Geophysical Research Abstracts*, Vol. 14, EGU2012-1347-1, EGU General Assembly.

Bazin, S., Lysdahl, A., Olaus Harstad, A., Frauenfelder, R., 2019. Resistivity and Induced Polarization (ERT/IP) Survey for Bedrock Mapping in Permafrost, Svalbard. *25th European Meeting of Environmental and Engineering Geophysics*, doi: 10.3997/2214-4609.2019023622019.

Bjerrum, L., 1954. Geotechnical properties of Norwegian marine clays. *Géotechnique*, 4(2), 49–69.

Davis, E., H. Villinger, T. Sun, 2015. Slow and delayed deformation and uplift of the outermost subduction prism following ETS and seismogenic slip events beneath Nicoya Peninsula, Costa Rica. *Earth Planet. Sci. Lett.* 410, 117–127 doi:10.1016/j.epsl.2014.11.015.

Ellsworth, W.L., 2013. Injection-induced earthquakes. *Science*, 341, 10.1126/science.1225942.

Feuillet, N., I. Manighetti, P. Tapponnier, 2001. Active arc-transverse normal faulting in Guadeloupe (French Lesser Antilles), C. R. Acad. Sci. Ser. IIa, 333, 583–590.

Feuillet, N., 2019. MAYOBS1 cruise, RV Marion Dufresne, doi :10.17600/18001217

Fox, C. G., H. Matsumoto, T.-K. Lau, 2001. Monitoring Pacific Ocean seismicity from an autonomous hydrophone array, *J. Geophys. Res.,* 106, 4183–4206.

Geist, E. L., 2002. Complex earthquake rupture and local tsunamis, *J. Geophys. Res*., 107(B5), 2086, doi:10.1029/2000JB000139.

Günther, T., Rücker, C., Spitzer, K., 2006. Three-dimensional modelling and inversion of DC resistivity data incorporating topography - II. Inversion. *Geophys. J. Int.,* 166, 506–517.

Henry, P., C. Grall, J. Kende, S. Viseur, M.S. Özeren, A.M.C. Şengör, S. Dupré, C. Scalabrin, L. Géli, 2018. A statistical approach to relationships between fluid emissions and faults: The Sea of Marmara case, Deep Sea Research Part II: *Topical Studies in Oceanography:* special issue edited by L. Ruffine, N. Çagatay, L. Géli. doi.org/10.1016/j.dsr2.2018.05.010.

Lander J. F., L. S. Whiteside, P. A Lockridge, 2002. A brief history of tsunamis in the Caribbean Sea, *Science of Tsunami Hazards*, 20, 57-94.

Le Friant, A., P. Heinrich, G. Boudon, 2008. Field survey and numerical simulation of the 21 November 2004 tsunami at Les Saintes (Lesser Antilles). *Geophys. Res. Lett.*, 35, L12308, doi:10.1029/2008GL034051.

Lemoine, A., Briole P., Bertil D., Roullé A., Foumelis M., Thinon I., Raucoules D., de Michele M., Valty P., Colomer R. H., 2020. The 2018–2019 seismo-volcanic crisis east of Mayotte, Comoros islands: seismicity and ground deformation markers of an exceptional submarine eruption. *Geophys. J. Int.,* https://doi.org/10.1093/gji/ggaa273

L'heureux, J.-S. et M. Long, 2017. Relationship between Shear-Wave Velocity and Geotechnical Parameters for Norwegian Clays. *Journal of Geotechnical and Geoenvironmental Engineering*, 143 (6), doi.org/10.1061/(ASCE)GT.1943-5606.0001645.

Loke, M.H., 2002. RES2DMOD Version 3.01.80. Rapid 2D Resistivity Forward Modeling Using the Finite-difference and Finite Element Methods. Instruction Manual. Geotomo Software.

Long, M. et S. Donohue, 2007. In situ shear wave velocity from multichannel analysis of surface waves (MASW) tests at eight Norwegian research sites. *Can. Geotech. J.,* 44(5), 533–544.

Long, M., et S. Donohue,2010. Characterisation of Norwegian marine clays with combined shear wave velocity and CPTU data. *Can. Geotech. J*., 47(7), 709–718.

Lysdahl, A.K., Pfaffhuber, A.A., Anschütz, H.,Kåsin, K., **Bazin, S.**, 2017. Probability of Sensitive Clay from AEM Data. *23rd European Meeting of Environmental and Engineering Geophysics*, DOI: 10.3997/2214-4609.201702007.

Michoud, C., Abellán A., Derron M.-H. and Jaboyedoff M., 2010. SafeLand deliverable 4.1. Review of Techniques for Landslide Detection, Fast Characterization, Rapid Mapping and Long-Term Monitoring. Edited for the SafeLand European project, Grant Agreement No.: 226479.

Okada, Y., 1985. Surface deformation due to shear and tensile faults in a half-space, *Bull. Seismol. Soc. Am.,* 75, 1135–1154.

O'loughlin K. F. et J. F. Lander, 2003. Caribbean tsunamis: a 500-year history from 1498-1998, Springer

Pfaffhuber, A., A.O. Lysdahl, C.W. Christensen, M. Vöge, H. Kjennbakken , J. Mykland, 2019. Extraction of depth to bedrock from airborne electromagnetic data using artificial neural networks. *32nd Annual Symposium on the Application of Geophysics to Engineering and Environmental Problems*.

Royer, J.-Y., **S. Bazin**, M. Beauverger, M. Torterot, J. Lecoulant, 2019. Seismic crisis along the Sousthwest Indian Ridge: insights from hydroacoustic observations. *AGU Fall meeting* San Francisco, T131-0284.

Salichon, J., A. Lemoine, H. Aochi, 2009. Validation of teleseismic inversion of the 2004 M-w 6.3 Les Saintes, Lesser Antilles, earthquake by 3D finite-difference forward modeling, *Bull. Seismol. Soc. Am*., 99, 3390–3401.

Skurdal, G., Pfaffhuber, A.A., Davis, A., **Bazin, S.**, 2019. Improved near-surface resolution in geotechnical applications using very early AEM time gates. *Exploration Geophysics.* doi: 10.1080/08123985.2019.1691441.

Smith, D.K., J. Escartin, M. Cannat, M. Tolstoy, C.G. Fox, D.R. Bohnenstiehl, **S. Bazin**, 2003. Spatial and Temporal Distribution of Seismicity Along the Northern Mid-Atlantic Ridge (15-35°N). *J. Geophys. Res.*, doi: 10.1029/2002JB001964.

Söderblom, R., 1969. Salt in Swedish clays and its importance for quick clay formation. Results from some field and laNboratory studies. Proceedings, 22. Swedish Geotechnical Institute, Stockholm.

Thomas, M. Complémenter les enregistrements sismiques en mer dans le Grand Ouest, 2020. *Mémoire de stage de Master 2*, Université de Bretagne Occidentale, pp46.